



Fluid-Rock Interactions in a Carbon Storage Site Analogue, Green River, Utah

Niko Jan Sterland Kampman

Darwin College

University of Cambridge

A thesis submitted for the degree of

Doctor of Philosophy

10th January 2011

Declaration

Except where indicated, this thesis describes my own work and contains nothing which is the outcome of work done in collaboration with others. No part of this dissertation is substantially the same as any work that has been, or will be submitted for any other qualification at any other University. The number of pages is within the prescribed limit.

NIKO KAMPMAN
January 2011

Acknowledgments

I would like to take this opportunity to first thank Mike Bickle for his insight, wisdom and witticisms throughout this project. This project has challenged and stretched both my understanding and appreciation of the sciences; I am grateful for Mike's patience and guidance on both aspects of this work and the direction of my career. Special thanks must also go to John Becker whose sound words, patient instruction and provoking conversation laid the groundwork for that which was to follow. During the course of this study I have been assisted in my analyses by many people in the Department, and I would like to thank Hazel Chapman, Nelly Assayag, Fatima Khan, Keith Gray, Martin Walker, Chiara Petrone, Tony Dickson, Steven Reed, Jason Day and Mike Hall for their time. Fluid inclusion analyses at the University of Leeds were only made possible with the support and encouragement of Bruce Yardley.

This research would not have been possible were it not for the generosity (and undemanding) financial support of Shell Renewables International. I am greatly indebted to Bruce Levell, Claus Otto and Andreas Busch for this, and for their kind words and (continued) support.

Field work in Utah benefited tremendously from the logistical support of Steve Nelson, Brigham Young University, whose kindness, patience and generosity made many aspects of the 2007 field season. This field work was greatly enriched by discussions with, and support from Zoe Shipton and Neil Burnside, for which I am extremely grateful. I would like to send special thanks to Jay Beach of Delta Petroleum for his generous insights, amusing anecdotes and for bringing a true sense of Americana to the occasion. A small, but not insignificant mention must also go to the chef at Rays Tavern for his continuing contributions to heart disease.

I have shared offices with many outstanding individuals throughout my time in the Department. Special thanks go to Mike Cook who helped instil in (un)equal parts, a tireless work ethic and workless tiredness during my first year, and to Andy Smye and Ben Winpenny who made the last two years of deskbound solitude especially enjoyable. Conversations on the (geological) significance of god, the graces, beards that shall remain nameless, and various aspects of 'science' have had a profound and lasting impact. I will forever be indebted for their enduring tolerance of my introspections and (mainly fruitless) cogitations, and the organic mass that my desk became. To Ben, Julie and Damien I owe many things, not least of which have been your tireless and rewarding friendship, and your moral and intellectual support throughout the trials and tribulations of my write-up. For which also, special recognition must go to the enduring support of G. Innes and T.O Nicolson.

The various residence/inmates of 57 Coleridge Road have made the last three years in Cambridge a joy, and an emotional, linguistic and culinary experience; Lesley, Loizos, Jen, Antoine, Romain, Laia, Raul, Greg, Jan, Pete, Alison, Marion, Justin, Andrea, Spanish.1 and Spanish.2, I thank you all. Innumerable thanks, love and affection go especially to Lesley and Loizos without whom I would surely have been finished, before the thesis ever was. Finally, to my Mum, Dad, Anneke, Colin, Landy, Steve and Rory I am eternally grateful for your support, friendship and sound advice in the face of the many challenges that have befallen this long journey.

Fluid-Rock Interactions in a Carbon Storage Site Analogue, Green River, Utah

Niko Jan Sterland Kampman

Reactions between CO₂-charged brines and reservoir minerals might either enhance the long-term storage of CO₂ in geological reservoirs or facilitate leakage by corroding cap rocks and fault seals. Modelling the progress of such reactions is frustrated by uncertainties in the absolute mineral surface reaction rates and the significance of other rate limiting steps in natural systems. This study uses the chemical evolution of groundwater from the Jurassic Navajo Sandstone, part of a leaking natural accumulation of CO₂ at Green River, Utah, in the Colorado Plateau, USA, to place constraints on the rates and potential controlling mechanisms of the mineral-fluid reactions, under elevated CO₂ pressures, in a natural system.

The progress of individual reactions, inferred from changes in groundwater chemistry is modelled using mass balance techniques. The mineral reactions are close to stoichiometric with plagioclase and K-feldspar dissolution largely balanced by precipitation of clay minerals and carbonate. Mineral modes, in conjunction with published surface area measurements and flow rates estimated from hydraulic head measurements, are then used to quantify the kinetics of feldspar dissolution. Maximum estimated dissolution rates for plagioclase and K-feldspar are 2×10^{-14} and 4×10^{-16} mol·m⁻²·s⁻¹, respectively. Fluid ion-activity products are close to equilibrium (e.g. ΔG_r for plagioclase between -2 and -10 kJ/mol) and lie in the region in which mineral surface reaction rates show a strong dependence on ΔG_r . Local variation in ΔG_r is attributed to the injection and disassociation of CO₂ which initially depresses silicate mineral saturation in the fluid, promoting feldspar dissolution. With progressive flow through the aquifer, feldspar hydrolysis reactions consume H⁺ and liberate solutes to solution which increase mineral saturation in the fluid and rates slow as a consequence. The measured plagioclase dissolution rates at low ΔG_r would be compatible with far-from-equilibrium rates of $\sim 1 \times 10^{-13}$ mol·m⁻²·s⁻¹ as observed in some experimental studies. This suggests that the discrepancy between field and laboratory reaction rates may in part be explained by the differences in the thermodynamic state of natural and experimental fluids, with field-scale reactions occurring close to equilibrium whereas most laboratory experiments are run far-from-equilibrium.

Surface carbonate deposits and cementation within the footwall of the local fault systems record multiple injections of CO₂ into the Navajo Aquifer and leakage of CO₂ from the site over ca. 400,000 years. The $\delta^{18}\text{O}$, $\delta^{13}\text{C}$ and $^{87}\text{Sr}/^{86}\text{Sr}$ of these deposits record rapid rates of CO₂ leakage (up to ~ 1000 tonnes/a) following injection of CO₂, but rates differ by an order of magnitude between each fault, due to differences in the fault architecture. Elevated $p\text{CO}_2$ enhances rates of feldspar dissolution in the host aquifer and carbonate precipitation in fracture conduits. Silicate mineral dissolution rates decline and carbonate precipitation rates increase as pH and the CO₂ charge dissipate. The Sr/Ca of calcite cements record average precipitation rates of $\sim 2 \times 10^{-6}$ mol/m²/s, comparable to laboratory derived calcite precipitation rates in fluids with elevated Mn/Ca and Fe/Ca, at Ω_{cc} of ~ 1 to 3. This suggests that far-from-equilibrium carbonate precipitation, which blocks fracture conduits and causes the leaking system to self-seal, driven by CO₂ degassing in the shallow subsurface, can be accurately modeled with laboratory derived rates. Sandstones altered in CO₂ leakage conduits exhibit extensive dissolution of hematite grain coatings and are chemically bleached as a result. Measurements of Eh-pH conditions in the modern fluid, and modeling of paleo-Eh-pH conditions using calcite Fe and Mn concentrations, suggests that the CO₂-charged groundwaters are reducing, due to their low dissolved O₂ content and that pH suppression due to high $p\text{CO}_2$ is capable of dissolving and transporting large concentrations of metals. Exhumed paleo-CO₂ reservoirs along the crest of the Green River anticline have been identified using volatile hosting fluid inclusions. Paleo-CO₂-charged fluids mobilized hydrocarbons and CH₄ from deeper formations, enhancing the reductive dissolution of hematite, which produced spectacular km-scale bleached patterns in these sediment.

Contents

Contents.....	i
List of Figures	v
List of Tables	vii
Chapter 1.....	1
<i>Introduction.....</i>	
1.1. Global Warming.....	1
1.1.1. Global Warming Mitigation	2
1.2. Carbon Capture and Storage	2
1.2.1. CO ₂ Storage Integrity	3
1.2.2. Modeling Long-term Storage Integrity: Insights at the Field-Scale.....	4
1.2.3. Natural Analogues.....	7
1.3. Project Aims and Scope	8
1.4. Thesis Outline	9
Chapter 2.....	11
<i>Hydrogeology and Geochemistry of a CO₂ Leaking Groundwater System, Green River, Utah.....</i>	
2.1. Introduction.....	11
2.2. Regional Geology of the Paradox Basin	12
2.2.2. Local Structure	17
2.2.3. CO ₂ -charged Springs.....	18
2.3. Geochemical Sampling and Results.....	24
2.3.1. Field Sampling Methods	24
2.3.2. Analytical Methods	25
2.4. Discussion	26
2.4.1. CO ₂ -Water-Rock Interactions	26
2.4.2. CO ₂ Sources: Isotopic Constraints	32
2.4.3. CO ₂ Sources for Springs.....	36
2.4.4. Hydrology and Fluid Geochemistry	39
2.4.5. Fluid Geochemistry	44
2.4.6. Thermodynamic Constraints on Fluid-Rock Reaction.....	53
2.4.7. Redox Conditions.....	58
2.4.8. Time Series Fluid Chemistry: Crystal Geysers.....	61
2.5. Conclusions.....	69
Chapter 3.....	71
<i>Silicate Mineral Dissolution Kinetics.....</i>	
3.1. Introduction	71
3.2. Review of Experimental Studies on Feldspar Dissolution Kinetics.....	71
3.2.1. Dissolution Mechanism.....	72
3.2.2. Solution Composition	76
3.3. Methodology: Calculating Reaction Rates.....	78
3.3.1. Introduction.....	78
3.3.2. Mass Balance	78
3.3.3. Calculation of Reaction Rates.....	81
3.4. Results and Discussion.....	82

3.4.1.	Reaction Rates	82
3.4.2.	Approach to Equilibrium - ΔG_r	86
3.4.3.	Uncertainties in Reaction Rates and Solution Saturation States	89
3.4.4.	Comparison of Reaction Rates with Laboratory and Field Estimates	91
3.5.	Conclusions	93
Chapter 4		94
<i>Geochemistry of an Ancient CO₂-Leaking Groundwater System, Green River, Utah</i>		
4.1.	Introduction.....	94
4.1.1.	Diagenetic Bleaching of Jurassic Sandstones, Paradox Basin	95
4.2.	Objectives	96
4.3.	Methodology	97
4.3.1.	Isotopic Systems and Fluid Rock Interaction.....	97
4.3.2.	Faults and CO ₂ Leakage	98
4.3.3.	Isotopes: Equilibrium versus kinetic fractionation.....	98
4.3.4.	Carbonate Precipitation in CO ₂ -rich Fluids.....	100
4.3.5.	Carbonate Cement Compositions.....	103
4.3.6.	Redox	107
4.3.7.	Eh-pH Diagrams.....	108
4.3.8.	Analytical Methods	109
4.4.	Results and Discussion.....	110
4.4.1.	Field Observations.....	110
4.4.2.	Petrology, Cathodoluminescence, SEM and XRD.....	116
4.4.3.	Carbonate Trace Element Compositions and Paleo-Fluid Chemistry	129
4.4.4.	Stable Isotope Geochemistry.....	145
4.4.5.	Modern Travertine Deposits.....	146
4.4.6.	CO ₂ Degassing, Carbonate Precipitation and Kinetic Isotope Fractionation	147
4.4.7.	Ancient Travertine Deposits.....	151
4.4.8.	Aragonite Veins.....	153
4.4.9.	Altered Host Rock.....	155
4.4.10.	Implications for modern and ancient travertine formation.....	156
4.4.11.	Reconstructing the CO ₂ Leakage History.....	157
4.4.12.	Controls on Leakage.....	161
4.5.	Conclusions.....	165
Chapter 5		166
<i>Fluid Inclusion Petrography of Diagenetic Bleaching in the Entrada Sandstone, Green River.....</i>		
5.1.	Introduction.....	166
5.2.	Methodology	167
5.1.1.	Fluid Inclusions	167
5.1.2.	Raman Microspectroscopy	169
5.1.3.	Sample Material	176
5.1.4.	Analytical Methods	176
5.3.	Results.....	177
5.1.5.	Field Observations.....	177
5.1.6.	Petrology and Cathodoluminescence	180
5.1.7.	Scanning Electron Microscopy	185
5.1.8.	XRD and XRF.....	186
5.1.9.	Discussion: Petrology of Diagenetic Bleaching in the Entrada Sandstone	186
5.1.10.	Isotope Geochemistry.....	188
5.1.11.	Fluid Inclusion Petrography	193

5.1.12.	Raman Spectroscopy	197
5.1.13.	Microthermometry	200
5.4.	Discussion: Fluid Inclusion Petrology	202
5.5.	Conclusions.....	207
Chapter 6		209
<i>Discussion and Conclusions</i>		
6.1.	Carbon Storage Site Analogue, Green River, Utah.....	210
6.1.1.	Summary of the CO ₂ -charged Groundwater Hydrogeochemistry.....	210
6.1.2.	Fluid-Mineral Reaction Kinetics	211
6.1.3.	CO ₂ Leakage from Fault Systems	214
6.1.4.	Future Work	216
References.		217
Appendix A		A-1
A.1.	Gas Isotope Geochemistry	A-1
A.2.	CO ₂ -spring Fluid Chemistry & Isotope Data	A-2
A.3.	Crystal Geyser Fluid Chemistry & Isotope Data.....	A-3
A.4.	Paradox Formation Brine Analyses.....	A-4
A.5.	Uncertainty Analysis	A-6
Appendix B		B-1
B.1.	XRF Analyses.....	B-1
B.2.	Electron Probe Data: Navajo Sandstone.....	B-2
B.3.	Petrophysical Data: Navajo Sandstone.....	B-6
B.4.	Sample Details.....	B-8
B.5.	Rock Isotope Data	B-11
B.6.	Point Counting Data: Entrada Sandstone	B-14
B.7.	Aragonite Vein Isotope Data.....	B-15
Appendix C		C-1
C.1.	Calculation of Mn-oxyhydroxide solubility	C-1

List of Figures

1.2-1 Serial and parallel reactions occurring during the dissolution of anorthite.....	5
1.2-2 Field and laboratory dissolution rates for plagioclase	6
1.2-3 The Colorado Plateau.....	8
2.2-1 Geological features of the Paradox Basin	14
2.2-2 Generalized stratigraphic section for the Green River area.	15
2.2-3 Main geographic features of the Green River.	20
2.2-4 Surface geology of the Green River anticline	21
2.2-5 Photographs of springs and geysers	22
2.2-6 Photographs of springs and geysers	23
2.2-7 Field photographs of modern Crystal Geyser	24
2.4-1 CO ₂ solubility as a function of temperature	28
2.4-2 Carbonate speciation for the system CO ₂ -H ₂ O and CaCO ₃ -CO ₂ -H ₂ O	29
2.4-3 Temperature dependent dissociation constant for H ₂ CO ₃	30
2.4-4 Capacity diagrams for the CO ₂ -springs.....	32
2.4-5 $\delta^{13}\text{C}_{\text{DIC}}$ measured versus that calculated from the $\delta^{13}\text{C}$ of CO ₂ (g)	36
2.4-6 Histogram of the $\delta^{13}\text{C}_{\text{CO}_2(\text{g})}$ for the 2006 and 2007 sampling programs	36
2.4-7 Profile of the instantaneous carbon isotopic composition	37
2.4-8 CO ₂ / ³ He ratios	39
2.4-9 Map showing the location of CO ₂ -charged springs.....	42
2.4-11 Local structure and the potentiometric surface within the Navajo Sst.....	44
2.4-12 Piper diagrams for the CO ₂ -springs	46
2.4-13 (a) Oxygen and hydrogen stable isotopes and (b) ⁸⁷ Sr/ ⁸⁶ Sr versus Sr ²⁺	47
2.4-14 CO ₂ solubility versus depth	48
2.4-15 Field alkalinity versus the sum of the base cations	50
2.4-16 1/Sr versus ⁸⁷ Sr/ ⁸⁶ Sr.....	50
2.4-17 Solute chemistry versus distance along the modelled flow path.....	51
2.4-18 In-situ DIC, pH and pCO ₂	53
2.4-19 Calcite and plagioclase saturation indices.....	54
2.4-20 aSiO ₂ (aq) as a function of temperature	55
2.4-21 Activity-activity diagrams.....	56
2.4-22 Alumino-silicate phase stability diagrams	57
2.4-23 Alumino-silicate phase stability diagrams.	58
2.4-24 Calcite saturation index as a function of pCO ₂	59
2.4-25 FeCSOH and MnCSOH Eh-pH equilibrium phase diagrams	61
2.4-26 Cold water geysering.....	62
2.4-27 Times series solute and isotope geochemistry for Crystal Geyser.....	63
2.4-28 $\delta^{18}\text{O}$ versus Cl ⁻	64
2.4-29 Cl ⁻ versus major solute chemistry.....	65
2.4-30 Cross plots of Sr ²⁺ and ⁸⁷ Sr/ ⁸⁶ Sr versus Mg/Ca.....	66
2.4-31 Accumulation of CO ₂ -charged brine.....	68
3.2-1 Laboratory dissolution rates for feldspars	72
3.4-1 Feldspar mineral modes with distance along the flow path	83

3.4-2 Variation in feldspar dissolution rate versus pH	84
3.4-3 Feldspar mineral modes with distance along the flow path	86
3.4-4 The variation in feldspar dissolution rate with ΔG_r	89
3.4-5 The variation in plagioclase dissolution rate with ΔG_r	90
3.4-6 Variation in plagioclase dissolution rate with ΔG_r	92
4.3-1 The dependence of D_{Sr} on the precipitation rate	106
4.4-1 Distribution of surface travertines along	111
4.4-2 Field photographs of ancient travertine mounds	112
4.4-3 Field photographs of ancient travertine mounds	113
4.4-4 Field photographs of ancient travertine mounds	114
4.4-5 Formation of a fault related travertine deposit.....	115
4.4-6 Photomicrographs of micro-wafers from thick aragonite veins	117
4.4-7 XRD patterns.....	118
4.4-8 Photomicrographs from aragonite micro-veins	119
4.4-9 Cold cathodoluminescence photomicrographs.....	121
4.4-12 SEM photomicrographs	123
4.4-13 Photomicrographs of representative samples of Entrada Sandstone.....	124
4.4-14 SEM photomicrographs	125
4.4-15 Cold CL photomicrographs.....	126
4.4-16 Photomicrographs from pore occluding calcite cement	127
4.4-17 Cold CL photomicrographs of pore filling calcite	128
4.4-18 Cumulative frequency plot of Sr^{2+}	129
4.4-19 Cumulative frequency plot of Mg^{2+}	129
4.4-20 Cumulative frequency plot of Fe^{2+}	130
4.4-21 Cumulative frequency plot of Mn^{2+}	130
4.4-22 Cumulative frequency plot of Na^+	131
4.4-23 Tr/Ca of calcites	132
4.4-24 Cumulative frequency plot of crystallization temperature	133
4.4-25 Parent fluid Fe^{2+} and Mn^{2+} concentrations	133
4.4-26 Parent fluid Na^+ and K^+ concentrations.....	134
4.4-27 Parent fluid Mg^{2+} and Sr^{2+} concentrations	134
4.4-28 Calcite precipitation rate	136
4.4-29 Laboratory derived calcite precipitation	137
4.4-30 Eh-pH diagrams for the system FeSCOH and MnSCOH	138
4.4-31 Measured calcite Fe and Mn contents	139
4.4-32 Fluid Fe^{2+} concentration as a function of pCO_2	139
4.4-33 Tr/Ca of calcites.....	141
4.4-34 Mg/Ca and Sr/Ca covariation.....	143
4.4-35 Stable Isotope analyses for carbonate deposits	145
4.4-36 $\delta^{18}O$ and $\delta^{13}C$ of HCO_3^-	146
4.4-37 Kinetic fractionation of $\delta^{18}O$ and $\delta^{13}C$	147
4.4-38 Evolution of the $\delta^{13}C$ of the reactant DIC pool.....	148
4.4-39 $\delta^{18}O$ and $\delta^{13}C$ of HCO_3^-	150
4.4-40 $\delta^{18}O$ and $\delta^{13}C$ of HCO_3^- of travertine	153
4.4-41 The $\delta^{18}O$ and $\delta^{13}C$ of HCO_3^- of aragonite veins.....	155
4.4-42 The $\delta^{18}O$ and $\delta^{13}C$ of HCO_3^- of altered Entrada Sandstone.....	155
4.4-43 Deformation and alteration beneath travertine mounds	156
4.4-45 $\delta^{13}C$ and $\delta^{18}O$ of aragonite with time	159
4.4-46 $\delta^{13}C$ and $\delta^{18}O$ of HCO_3^- of aragonite veins from LGF.....	161

4.4-47 Cumulative travertine volume.....	162
4.4-48 The spatial distribution of individual travertine mounds.....	164
5.2-1 NaCl-H ₂ O phase diagram.....	168
5.2-2 Fundamental vibrations of CO ₂	171
5.2-3 Typical Raman spectrum of CO ₂	171
5.3-2 Field photographs of the bleaching front.....	179
5.3-3 Point counted mineralogies.....	180
5.3-4 CL photomicrographs from bleached Entrada Sandstone.....	182
5.3-5 Plane polarized light photomicrographs from bleached Entrada Sst.....	183
5.3-6 Photomicrographs from bleached Entrada Sandstone.....	184
5.3-7 SEM images from bleached Entrada Sandstone.....	185
5.3-8 XRD pattern from bleached Entrada Sandstone.....	186
5.3-9 Stable isotope analyses for calcite cements and veins.....	189
5.3-10 ⁸⁷ Sr/ ⁸⁶ Sr of aragonite, calcite and gypsum veins.....	189
5.3-11 δ ¹⁸ O _{H₂O} and δ ¹³ C _{HCO₃}	191
5.3-12 δ ¹³ C of CO ₂ (g).....	192
5.3-13 Photomicrographs of fluid inclusions in aragonite.....	194
5.3-14. Photomicrographs of fluid inclusions in gypsum.....	195
5.3-15. Photomicrographs of fluid inclusions in quartz.....	196
5.3-16. Raman spectra.....	198
5.3-17. Close up of the region 1200-1800 cm ⁻¹	198
5.3-18. Raman spectra.....	199
5.3-19. Close up of the region 1200-1800 cm ⁻¹	199
5.3-20. Close up of the region 2825-3000 cm ⁻¹	200
5.3-21. Fluid salinities.....	201
5.3-22. Homogenization temperatures.....	201
5.3-23. Fluid salinities versus homogenization temperatures.....	202
5.4-1 Burial and thermal model for the Paradox Basin.....	204
5.4-2 Paragenesis of the Entrada Sandstone.....	206

List of Tables

2.4-1 Measured DIC versus DIC calculated for CO ₂ -saturation.....	54
3.4-1 Mineral mol transfers	82
5.3-1 Modal Mineralogy.....	186
5.5-1 Fluid inclusion gas composition and densities	208
A.1-I δ ¹³ C of CO ₂ (g) collected from CO ₂ -charged springs.....	A-1
A.2-I Major and minor element and isotope data from the CO ₂ -charged springs	A-2
A.3-I Major and minor element and isotope data from Crystal Geyser.....	A-3
A.4-I Major solute chemistry of brine analyses from the Paradox Formaiton.....	A-4
B-I Major element XRF analyses for Entrada and Navajo Sandstone samples	B-1
B-II Recalculated probe data for Navajo Sandstone samples	B-2
B-III Porosity, permeability and hydraulic conductivity of the Navajo Sandstone	B-6
B-IV Sample localities, rock types and analyses.....	B-8
B-V Petroleum exploration wells	B-10
B-VI δ ¹⁸ O, δ ¹³ C and ⁸⁷ Sr/ ⁸⁶ Sr for rock samples.....	B-11
B-VII δ ¹⁸ O and δ ¹³ C for rock sample from petroleum exploration wells.....	B-13
B-VIII Point count estimates	B-14
B-IX Aragonite vein isotope data	B-15

Chapter 1

Introduction

1.1. Global Warming

Climate change is one of the primary environmental concerns of the 21st century. Over the past century, atmospheric carbon dioxide (CO₂) concentrations have steadily increased, having now risen to over 387 ppm from the pre-industrial level of 280 ppm and are expected to continue rising at 2 ppm annually (IPCC, 2007). Increases in CO₂ concentrations are attributed predominantly to the burning of oil, gas and coal for electrical generation, transportation, industrial and domestic uses, with deforestation and cement production making significant contributions.

Interpretation of the temperature record on a scale of centuries to millennia indicates a slight increase in global average annual temperatures in the last 150 years, in the order of 0.76 °C (IPCC, 2007), and predictions are that, if emissions growth continues unabated, a warming of 1.1 to 6.3 °C will be observed by the end of this century (IPCC, 2007). It is very likely and generally accepted that the main cause of the observed global warming is the increase in atmospheric concentrations of greenhouse gases, primarily carbon dioxide (CO₂), methane (CH₄) and nitrous oxide (N₂O) (IPCC, 2007). Although a direct causal link between the rise in greenhouse gas concentrations in the atmosphere and global warming has not been demonstrated, significant circumstantial evidence points toward this link, which has been generally accepted by a broad segment of the scientific community (e.g. IPCC, 2007; AGU, 2003). And in agreement, increasing empirical evidence points to a causal relationship between elevated concentrations of green house gases in the atmosphere and changes in the radiative heat forcing, global surface temperatures and atmospheric *p*CO₂ within the recent geological past (e.g. Crowley *et al.*, 2003; Indermuhle *et al.*, 1999; Keeling and Whorf, 2005; Petit *et al.*, 1999; Tripathi *et al.*, 2009). The detailed response of the highly nonlinear climate system to increasing CO₂ concentration in the atmosphere, and to the resulting increased heat load, is uncertain because of the inherent complexity of the climate system and natural variability; however, the close coupling between the carbon cycle, including CO₂ and CH₄, and palaeo-climate suggests that changes in the former will be accompanied by changes in the latter (AGU, 1999).

1.1.1. Global Warming Mitigation

Scientific consensus on global warming and the fear of abrupt climate change (IPCC, 2007; Schneider, 2004) is leading to increased efforts to develop new technologies and sciences in an attempt to mitigate global warming. Such climate change mitigation strategies include reducing demand for emissions-intensive goods and services, increasing efficiency gains, increasing use and development of low-carbon technologies, and reducing fossil fuel emissions (Parry *et al.*, 2007). A reduction in the release rate of CO₂ to the atmosphere is considered an essential first step in the control of global warming. It is widely agreed that for a rapid reduction in global CO₂ emissions to be successful a spectrum of new technologies and energy policies is required. Principally this will involve an increase in the utilization of non-fossil fuel based energy sources such as solar, wind, wave, nuclear and geothermal power and the sequestration of gas emissions from existing and future fossil or bio-fuel based power stations. Given predictions that a significant fraction of global energy production will continue to be generated from bio- or fossil fuels, CO₂ emissions will continue into the next century (Coyle, 2009; Faiman *et al.*, 2007; Shafiee and Topal, 2008). Thus a safe and secure method of sequestering CO₂ out with the atmospheric system is being sought. Carbon sequestration can take many forms, including the direct sequestration of CO₂ from the atmosphere through enhancement of surface silicate weathering, stimulation of surface ocean productivity, reforestation, physical sequestration of CO₂ in the deep ocean and in geological environments, as well as mineral carbonation on exhumed or in-situ geological strata. Among these CO₂ capture and geological storage, which entails CO₂ capture from large industrial processes and injection into deep geological formations, plays an important role (IEA, 2005, 2006).

1.2. Carbon Capture and Storage

The capture of CO₂ from large anthropogenic point sources and storage in geological formations including depleted oil and gas reservoirs, coal beds and aquifers has received increasing scientific attention as a safe and long-term storage option (Gale, 2004; Holloway *et al.*, 2005). Geological storage can in addition be used in combination with enhanced oil or gas exploitation (CO₂-EOR) (e.g. Damen *et al.*, 2005). Whilst no immediate technological barriers inhibit the implementation of carbon capture and storage, uncertainty in our understanding of aspects of the physical and chemical impacts of long-term storage of CO₂ in the subsurface undermines our ability to satisfy operational, regulatory and public acceptance criteria (Rudnicki and Wawersik, 1999). Globally distributed saline aquifers represent the largest single reservoir type for geological storage of anthropogenic CO₂ (Bachu *et al.*, 2005; Saylor and Zerai, 2004). The feasibility of storing CO₂ in aquifers has been thoroughly discussed in the literature and continues to be debated. These

studies include an evaluation of the feasibility of CO₂ aquifer storage (summarized in Cook, 2006; Gale, 2004; Bachu, 2008). Recently, extensive experimental, field, and modeling studies of geological carbon storage have been conducted (Gaus, 2009; Gaus *et al.*, 2005; Giammar *et al.*, 2005; Gunter *et al.*, 1997; Holloway *et al.*, 2007; Horita, 2002; Hovorka, *et al.*, 2006, 2005; Johnson *et al.*, 2001; Jones *et al.*, 2006; Kaszuba, *et al.*, 2003, 2005; Knauss *et al.*, 2002; McPherson and Lichtner, 2001; Oelkers *et al.*, 2005, 2008; Palandri and Kharaka, 2002, 2005; Pearce *et al.*, 2006; Pruess *et al.*, 2003; Rochelle *et al.*, 1999; Rosenbauer, and Koksalan, 2002; Soong, *et al.*, 2004; Strazisar and Zhu, 2002; White *et al.*, 2001; Xu *et al.*, 2004, 2005, 2007). Whilst the engineered aspects of geological storage have been successfully demonstrated through a small number of commercial scale CO₂-injection projects including Sleipner, Norwegian North Sea (Korbol and Kaddour, 1995); Snøhvit, Norway (Maldal and Tappel, 2004) and In Salah, Algeria (Rutqvist *et al.*, 2009); and an increasing number of small-scale experimental projects including Ketzin, Germany (Schilling *et al.*, 2009); Nagaoka, Japan (Kikuta *et al.*, 2004); Frio, USA (Hovorka *et al.*, 2006; Kharaka *et al.*, 2006a, 2006b) and large-scale CO₂-EOR projects at Weyburn, Canada (Emberley *et al.*, 2004, 2005; Wilson and Monea, 2004) and Otway, Australia. A comprehensive summary of geological carbon storage is given by Bickle, (2009).

1.2.1. CO₂ Storage Integrity

Carbon dioxide injected into saline aquifers below ~ 800 m water-depth will form a supercritical phase. The critical pressure and temperature of CO₂ are 7.4 MPa and 31.1°C, corresponding to a critical density of 0.468 g/cm³ (Leitner, 2000). This is equivalent to reservoir depths of ca 800-1500 m depending on local land surface temperature, heat flow and lithology. Supercritical CO₂ combines gas- (e.g. low viscosity, typically around 10⁻⁴ to 10⁻³ Pa·s for supercritical gases), and liquid- (e.g. high density, relative to gas) properties. A supercritical fluid is liable to very large changes of density, especially close to the critical point.

Carbon dioxide is retained in geologic formations in four ways. First, CO₂ can be trapped as a gas or supercritical fluid under a low-permeability caprock. The safety of the injected CO₂ on a short timescale is related to buoyancy-driven flow of the immiscible part of the injected CO₂ and the trapping capabilities of the formation. Second, CO₂ can become physically trapped within the reservoir pore space via residual or capillary trapping owing to surface tension phenomena in multiphase systems (e.g. Suekane *et al.*, 2008; Taku Ide *et al.*, 2007). Third, CO₂ can dissolve into the groundwater, becoming trapped as a soluble phase. The dissolution of CO₂ in groundwater increases the acidity of water and affects the solubilities of minerals composing the host rock matrix. Fourth, CO₂ can react directly or indirectly with minerals and organic matter in the geologic formation leading to the precipitation of secondary carbonates and the solubilization of organic matter. The former process, so-called ‘mineral trapping’, is potentially attractive because

it could immobilize CO₂ for long time-scales, and prevent its easy return to the atmosphere. The interaction of CO₂ with alkaline aluminosilicate minerals will also result in the formation of soluble carbonates and bicarbonates in solution, thereby enhancing “solubility trapping”.

The long-term containment of CO₂ in the subsurface will depend on the performance of the materials sealing the host formation. Acceptable performance will need to be demonstrated in order to satisfy operational, regulatory and public acceptance criteria (Friedmann *et al.*, 2007). Some of the CO₂ injected into geological reservoirs is expected to dissolve relatively rapidly into formation waters and the resulting acidic solution will undergo geochemical reactions with host reservoir minerals and the reservoir seal which will ultimately control the long term containment and integrity of the stored CO₂. These reactions may either stabilise the CO₂ or enhance leakage. The nature and kinetics of the geochemical interactions between CO₂, formation fluids, carbonate and silicate minerals in the reservoirs and their clay-rich caprocks are inadequately known (Gale, 2004).

Short term leakage from geological storage sites (see Oldenburg, (2007) for a complete summary) will involve process related to the buoyant migration of free phase CO₂ laterally and vertically within the subsurface and may lead to introduction of CO₂ into shallow potable aquifers (e.g. Nicot, 2008; Wang and Jaffe, 2004) and surface leakage (e.g. Beaubien *et al.*, 2004). CO₂ leakage within the wellbore, via the cement casing and through existing wells is also of concern (e.g. Preuss, 2004; Nordbotten *et al.*, 2005). Additionally, the leakage of CO₂ from its host reservoir on longer timescales may be facilitated by migration through the caprock (Fleury *et al.*, 2009; Gherardi *et al.*, 2007; Li *et al.*, 2005; Morris *et al.*, 2009) and via fracture networks and through the reactivation of local faults (Barnes *et al.*, 1978; Irwin and Barnes, 1975; Kennedy *et al.*, 1997; Pruess, 2005) under conditions of over-pressuring (e.g. Lewicki *et al.*, 2007). The surface leakage of CO₂ has a range of environmental (see Oldenburg and Unger, 2003) and economic impacts (see Zwaan and Gerlagh, 2009), a comprehensive summary is given by Bachu (2008).

1.2.2. Modeling Long-term Storage Integrity: Insights at the Field-Scale

Understanding the geochemical behaviour of anthropogenic carbon dioxide stored in geological reservoirs, over a range of time-scales, is crucial for quantifying the risk of leakage and the evolution of the sequestered form of that CO₂ through the life of an individual storage site. The relatively low temperatures expected in typical storage sites imply rate-controlled systems that deviate from thermodynamic equilibrium (e.g. Lasaga, 1998; Lasaga and Luttge, 2004; Stumm and Morgan, 1996). Prediction of the long-term fate of this carbon dioxide requires determination of the relevant gas-fluid-mineral reactions and their chemical kinetics (e.g. Xu *et al.*, 2004).

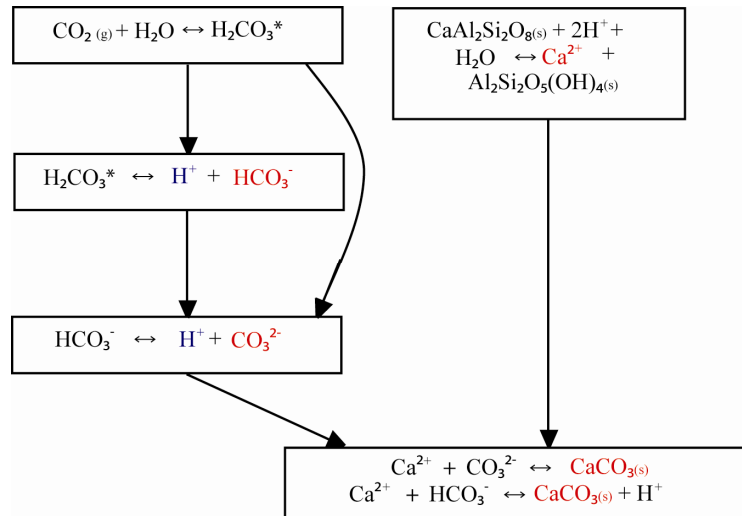


Figure 1.2-1 Reaction schemes showing the serial and parallel reactions occurring during the dissolution of anorthite. The protons formed by the CO_2 -dissolution branch (blue) will hydrolyse the plagioclase, resulting in the release of Ca^{2+} ions. The calcium and bicarbonate or carbonate ions form the parallel branches (red) will together result in the precipitation of calcite. For a complete discussion see Chapter 2.

These gas-fluid-mineral reactions may act either to increase the stability of stored CO_2 by precipitating carbonate minerals or enhance leakage by corroding well cements, existing boreholes, cap rocks and fault seals. Solubilisation of heavy metal bearing minerals in shallow groundwater systems is also of concern for the contamination of potable water sources (e.g. Wang and Jaffe, 2004). In addition, changes to the reservoir porosity and permeability structure, through clay and carbonate mineral precipitation, may alter injectivity and flow within the reservoir.

The main gas-fluid-mineral reactions that will occur as a result of CO_2 injection can be summarised by a number of serial and parallel reactions, as shown in Fig. 1.2-1. The rate-limiting step in such serial-parallel reaction sequences will in general be the slowest step of the fastest parallel branch. Amongst the above reactions, it is well established that the silicate dissolution reactions are likely to be the slowest and hence most important in controlling reaction progress (e.g. Sorai *et al.*, 2005). The accurate modelling of CO_2 -fluid-mineral reactions therefore requires a robust knowledge of the dissolution kinetics as well as the solubilities of silicate and aluminosilicate minerals.

Experimentally determined reaction rates and reaction product pathways have to-date been the major source of data used to constrain simulation of multicomponent, multiphase CO_2 -fluid-rock systems (Gunter, 1996; Knauss *et al.*, 2001; Johnson *et al.*, 2001; Johnson and Nitao, 2003, Xu *et al.*, 2004, 2005, 2007). However, significant discrepancies have been found between the mineralogical products and reaction kinetics of natural and experimental systems (Brantley *et al.*, 1993, 2007; Kim, 2002; Malmstrom *et al.*, 2000; Taylor and Blum, 1995, 2000; White *et al.*, 1996; White and Brantley, 2003).

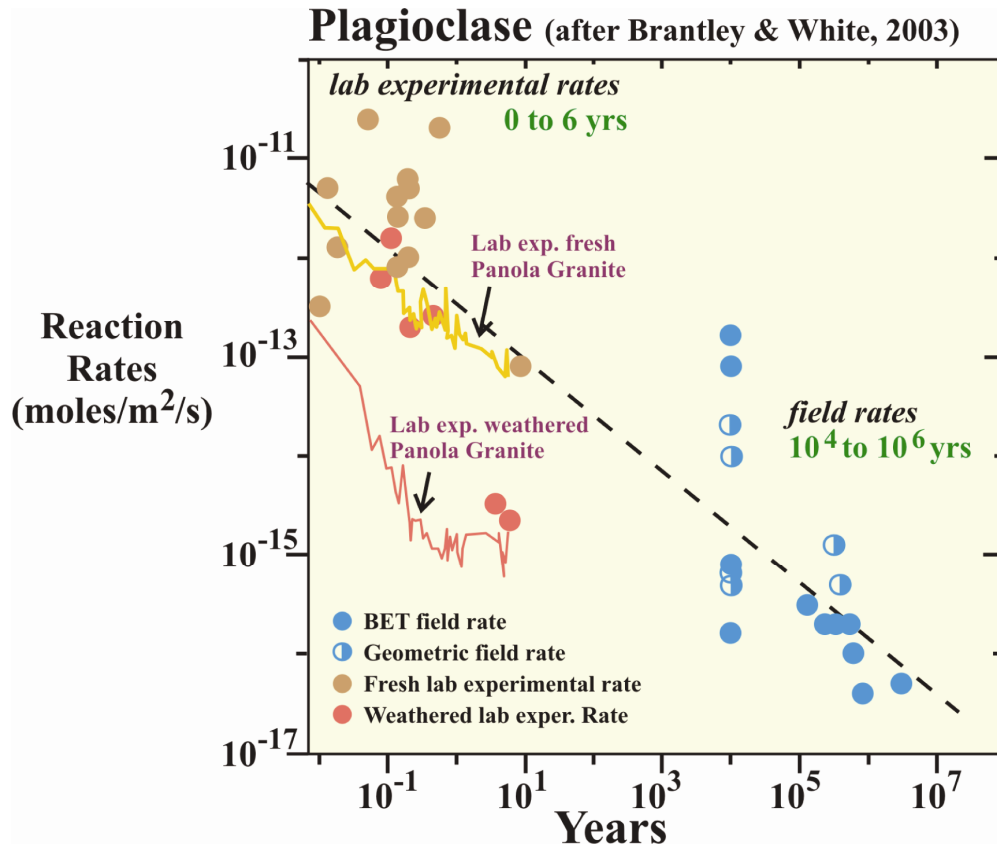


Figure 1.2-2 A compilation of field and laboratory dissolution rates for plagioclase plotted against the duration of the ‘experiment’. Significantly the natural dissolution rates are up to 5 orders of magnitude slower than, far-from-equilibrium, laboratory-derived rates at similar pH and temperature conditions. The cause of the discrepancy between experimental and in-situ reaction rates is uncertain but may reflect the proximity of natural systems to equilibrium, efficiency of solution/mineral contact, ageing of mineral surfaces, the nature of defects, etch pits and leached layers on mineral surfaces, surface coatings, gradients in solution chemistry in micro-pores and overestimates of dissolution rate for minerals with slow dissolution kinetics due to the lag in step density decrease following the change in dissolution mechanism from etch pit to step retreat as equilibrium is approached (e.g. Brantley and White, 2003).

Modelling the progress of such reactions is frustrated by uncertainties in the absolute mineral surface reaction rates and the significance of other rate-limiting steps in natural systems (see White and Brantley, 2003 for a complete review). It is well established that silicate dissolution rates in the natural environment are typically 2 to 5 orders of magnitude slower than, far-from-equilibrium, laboratory-derived rates at similar pH and temperature conditions (Fig. 1.2-2) (White and Brantley, 2003), and the laboratory rates are typically the only rates available for simulations (e.g. Knauss *et al.*, 2005; White *et al.*, 2005; Xu *et al.*, 2004). Quantification of the kinetics of fluid-mineral reactions in natural systems, rich in CO₂, is thus required for the accurate prediction of the long-term performance of geological storage sites.

1.2.3. Natural Analogues

Carbon dioxide occurs naturally as a result of geologic processes in large, often high-purity (>90%) deposits in many sedimentary basins forming an ideal analogue to the subsurface storage of anthropogenic CO₂ (Allis *et al.*, 2005; Czernichowski-Lauriol *et al.*, 1999; Evans *et al.*, 2004; Gaus *et al.*, 2005; Haszeldine *et al.*, 2005; May, 2005; Moore *et al.*, 2003, 2005; Pauwels *et al.*, 2007; Pearce *et al.*, 1996, 1999, 2004; Stevens *et al.*, 2001; Worden, 2006). Several CO₂ fields in the United States, Hungary, France, Australia and Argentina have been exploited to provide injectant for enhanced oil recovery projects and industrial quality CO₂ (Wycherley *et al.*, 1999).

The introduction of a volatile species such as CO₂, be it anthropogenic or naturally produced, into subsurface geological reservoirs will result in chemical disequilibria and the initiation of various chemical reactions. Its abundance and the rapid kinetics of reactions involving dissolved carbonate species make it an important buffer of pH and a volatile component which dominates the overall equilibrium state of many natural systems (e.g. Coudrain-Ribstein *et al.*, 1997; Hutcheon and Abercrombie, 1989, 1990; Hutcheon *et al.*, 1992). In sedimentary formations the partial pressure of CO₂ ($p\text{CO}_2$) can be more than 10–100 times greater than atmospheric $p\text{CO}_2$ at 25 °C (Coudrain-Ribstein *et al.*, 1998; Gaucher *et al.*, 2007). The mechanism of CO₂ generation in some sedimentary basins and magmatic systems produces large quantities of CO₂ which are able to migrate from its source through the basin interacting with reservoir fluids and minerals.

Examination of natural analogue sites allows characterization of physiochemical processes, important for predicting the fate of geologically stored CO₂, which cannot be captured at the laboratory scale and which, otherwise, would only be available through multiple, costly experimental CO₂ injection projects. These include observations, at the field-scale, of 1) multiphase flow where geophysical or isotopic constraints (such as stable or noble gas isotope systematics) are available; 2) gas-fluid-mineral reaction kinetics (and their inherent complexity in natural reservoirs with highly complex mineralogies, fluid chemistries and permeability structures); 3) the structural, hydrodynamic and geochemical controls on CO₂ leakage, at a variety of temporal scales, which can only be made from natural observations (or from the failure of industrial CO₂ storage projects).

Access to fluids and gas samples from the deep subsurface is often difficult and costly. This thesis examines the geochemistry of a natural, leaking accumulation of carbon dioxide at Green River, Utah, in the Colorado Plateau, USA (Fig. 1.2-3) where fluid and gas effusion allows direct observation of physiochemical processes occurring in the subsurface.

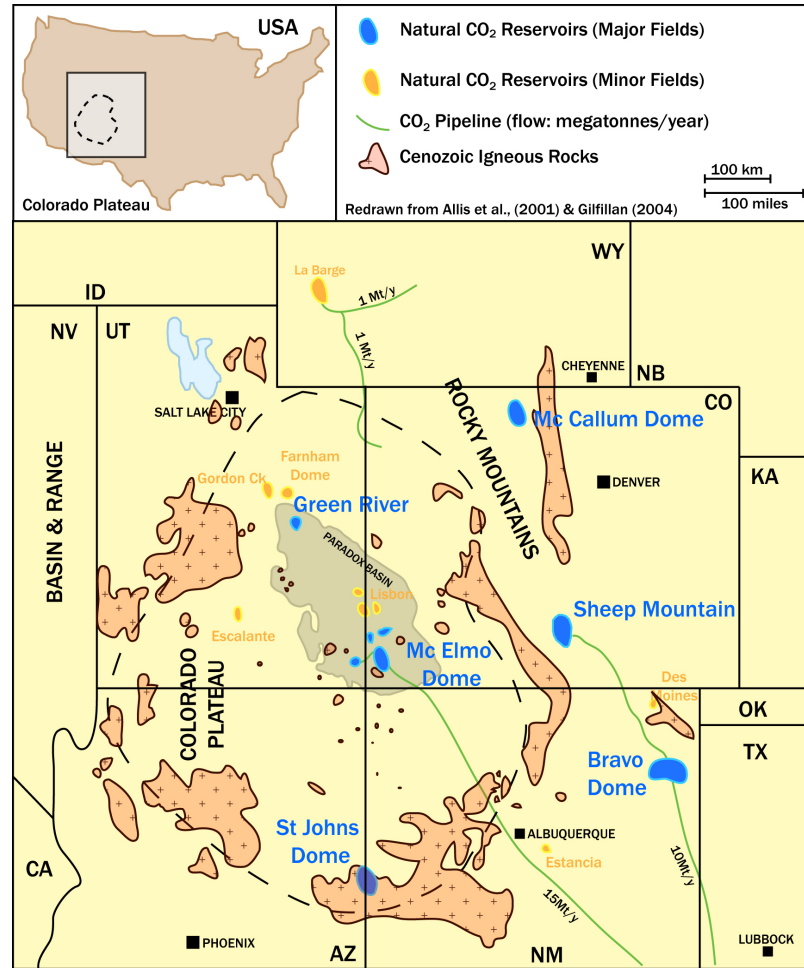


Figure 1.2-3 The Colorado Plateau, located in the south western USA, is an extensive uplifted region covering portions of Utah, Colorado, Arizona and New Mexico. Natural accumulations of subsurface CO₂ gas are common in this province and the adjacent southern Rocky Mountain region, where eighteen CO₂ fields have been identified (Allis *et al.*, 2001). Some CO₂ fields, notably Bravo Dome (NM), McElmo and Sheep Mountain (CO), Farnham Dome (UT), Springerville (AZ), and Big Piney-LaBarge (WY) have been exploited for commercial purposes, mainly for enhanced oil recovery and dry ice production (Allis *et al.*, 2001). The source of the CO₂ is considered to be dominantly volcanogenic, juvenile CO₂ generated from Cenozoic magmatic activity and mantle degassing (Gilfillan *et al.*, 2005, 2008, 2009). The gas reservoirs, usually sandstone or dolomite, lie in four way dip closed or anticlinal structures with mudstone or anhydrite top seals. Fault seals are common along the margins of the reservoirs (Allis *et al.*, 2001; Shipton *et al.*, 2004). The commercially producing fields contain from 28 to 2800 billion m³ of CO₂ gas (Allis *et al.*, 2001). The gases from the fields can be > 98% CO₂ with trace quantities of N₂ (4%), He (0.1-1%), Ar, and CH₄ (Allis *et al.*, 2001). Associated with these large subsurface CO₂ accumulations is a region of surface CO₂ leakage near Green River, Grand and Emery County, Utah, the focus of this thesis. Significant volumes of CO₂ escape to the surface in intimate association with the Little Grand and Salt Wash fault zones, along the northern edge the Paradox Basin.

1.3. Project Aims and Scope

Understanding the geochemical behaviour of anthropogenic carbon dioxide stored in geological reservoirs, over a range of time-scales, is crucial for quantifying the risk of leakage and the

evolution of the sequestered form of that CO₂ through the life of an individual storage site. Observations from natural analogue sites provide insights into physical and chemical processes which differ at the field and laboratory scales. Direct measurement of the rate of CO₂-promoted fluid-mineral reactions and quantification of their geochemical dependencies, in natural CO₂-charged groundwater systems can provide important insights into these processes over large physical and temporal scales. Several approaches have been employed in this project to assess the nature and rates of CO₂-promoted fluid-mineral reactions and their controls. These have included hydrological and geochemical modelling of an active CO₂-charged groundwater system from which rates of reactions were quantified using mass balance techniques and from petrological constraints on the reacting mineral properties. Measurement of the composition of secondary carbonate minerals, in conjunction with theoretical aspects of trace element incorporation in carbonates, was used to measure in-situ calcite precipitation rates. The synthesis of these approaches allowed quantification of their chemical controls and provides a possible explanation for the orders of magnitude difference in field-scale and laboratory mineral-fluid reaction rates.

Observations of the long term performance of CO₂ leakage from natural sites, via the examination of the geochemical and isotopic composition of dated near-surface carbonate deposits, is used to constrain the interplay of structural and chemical processes in controlling leakage sites and rates, the role of fluid-mineral interactions in generating and closing leakage pathways and their relation to geochemical processes in the host aquifer. These methods provide insights into leakage processes which cannot be discerned from present day measurements alone. Additionally, the relationship between the modern CO₂-system and exhumed paleo-reservoirs, which exhibit extensive chemical bleaching where hematite grain coatings have been dissolved by the passage of diagenetic fluids, is investigated. Various isotopic, petrological and geochemical methods, and observations from volatile-hosting fluid inclusions, are employed to investigate the mineralogical impact and nature of the volatile-rich diagenetic fluids. The identification of exhumed CO₂ reservoir analogues has important implications for the future examination of CO₂-fluid-mineral reactions and transport processes at the field scale.

1.4. Thesis Outline

In **Chapter 2** the general geology of the field area at Green River, Utah is briefly discussed and the CO₂-leaking groundwater system is introduced. The thermodynamics of CO₂ and CO₂-fluid-mineral reactions is then briefly discussed, the theory of which, is applied in many subsequent chapters. The CO₂-spring geochemistry is then addressed. The isotopic composition of the effused fluids and gases are used to place constraints on the origin of the groundwater and CO₂. Hydrological modelling is then used to place constraints on the flow paths between individual

springs. The fluid geochemistry is then addressed, supported by the hydrological modelling and thermodynamic considerations, to place constraints on the nature of the fluid-mineral reactions that control solute composition. Thermodynamic modelling is then used to quantify the in-situ CO₂ solubility and place an upper limit on the degree of CO₂ degassing experienced by the fluids during ascent to the surface. Finally, time series fluid geochemistry from the largest of the CO₂-degassing springs, Crystal Geysir, is used to place constraints on the origin of the fluids, mixing processes in the subsurface and the role of cold water geysiring in stimulating leakage from CO₂-rich groundwater systems.

Chapter 3 utilizes the geochemical and hydrological models of Chapter 2, in conjunction with mass balance modelling techniques, and petrological measurements on the reacting mineral phases, to place constraints on the kinetics of the controlling fluid-mineral reactions, and their chemical dependencies, in the modern groundwater system. Comparable laboratory experiments are reviewed, the discrepancies discussed, and the implications for field-scale silicate mineral dissolution rates are evaluated.

Chapter 4 uses petrological, isotopic and geochemical methods to investigate the history of CO₂-leakage from the Green River anticline, recorded in surface and shallow subsurface carbonate deposits. Isotopic measurements on U-Th dated carbonate deposits are used to reconstruct the last 400,000 year leakage history of the CO₂ system and to place constraints on the style, location and duration of leakage and its relationship to fluid-mineral reactions in the host reservoir and in fracture conduits. Carbonate mineral compositions are used to constrain calcite precipitation rates in the modern setting and their controls and chemical dependencies are discussed.

Chapter 5 uses petrological, isotopic and geochemical methods, in conjunction with a Raman microspectroscopy study of volatile hosting fluid inclusions, to investigate the nature of volatile rich diagenetic fluids which caused widespread chemical bleaching in Jurassic sandstones outcropping along the crest of the Green River anticline. Fluid inclusion Raman microspectroscopy and microthermometry are used to place constraints on the composition of the volatile phase(s) and the timing of this alteration. Its relation to chemical bleaching within Jurassic sediments of the wider Paradox Basin region is discussed. Additionally, volatile hosting fluid inclusions in bleached portions of travertine feeder systems are investigated using Raman spectroscopic techniques and the two systems are compared.

Finally, tabulated analytical results for water chemistry, gas analyses, XRF, point counting, electron microprobe, and fluid and mineral, stable and radiogenic isotope geochemistry are presented for reference.

Chapter 2

Hydrogeology and Geochemistry of a CO₂ Leaking Groundwater System, Green River, Utah

2.1. Introduction

CO₂-charged fluids and gas escape to the surface along faults and through abandoned petroleum exploration wells in the vicinity of Green River, Utah, USA. This provides an opportunity to examine a CO₂-rich groundwater system as an analogue to processes occurring in anthropogenic CO₂ storage sites. A number of studies have examined various aspects of the origin of the carbon dioxide and effused groundwaters (Baers and Rigby, 1978; Gilfillan, 2004; Heath, 2004; Wilkinson *et al.*, 2008), the nature and magnitude of CO₂ leakage from this site, (Allis *et al.*, 2005), rates of CO₂ effusion from the largest of the CO₂ degassing geysers (Gouveia *et al.*, 2005; Gouveia and Friedmann, 2006), and the role of the local structure and fault architecture on controlling the sites of CO₂ leakage (Dockrill, 2005; Dockrill *et al.*, 2010, Shipton *et al.*, 2004, 2005).

CO₂-rich groundwaters are widely reported, (e.g. Chernichowski-Lauriol *et al.*, 1996; Pearce *et al.*, 1996) although few contain sufficiently quantities of dissolved CO₂ to sustain cold water geysering (Glennon and Pfaff, 2005; Rinehart, 1980). Many studies have suggested that much of the CO₂ gas in these CO₂-charged groundwater systems has a deep origin being sourced from magma and/or mantle contributions (Cartwright *et al.*, 2002; Gilfillan *et al.*, 2006, 2008; Pauwels and Fouillac, 1997). Other sources of CO₂ production in the geosphere have been identified including the metamorphism of carbonate rocks, diagenetic reactions between carbonate and silicate minerals, the thermal alteration of coal and other organic material, the biodegradation of oil and gas and the dissolution of carbonate rocks (Hutcheon and Abercrombie, 1990; Wycherley *et al.*, 1999). CO₂-rich groundwaters typically show very high alkalinity and solute concentrations [1.3-110 mEq L⁻¹ alkalinity, 200-10,400 mg L⁻¹ total dissolved solids] (Choi *et al.*, 2005). It is generally accepted that H⁺ from the dissociation of carbonic acid enhances fluid-rock reactions in these systems, elevating the solute load of these groundwaters (e.g. Schofield and Jankowski, 2004). This however, is somewhat inconsistent with laboratory experimental results. Many experimental studies agree that dissolution of silicate minerals is enhanced by high H⁺ concentrations in acidic solutions. However, the reactions have been shown

to be independent of pH (e.g. Drever 1994; Oxburgh et al. 1994) in neutral solutions $5 < \text{pH} < 9$. Almost all CO₂-charged groundwaters fall within this pH range (Choi et al., 2005 and references therein). CO₂ rich groundwaters with pH < 5 are rarely observed in the field, because only very dilute solutions can exhibit pH values less than 5 by dissolution and dissociation of CO₂. This is due to the complexing effect of base cations on speciation in the carbonate system (see section 2.5.1.2).

Subsurface reservoirs imbue rocks with mineral assemblages of highly different solubilities and dissolution kinetics. The extent to which CO₂-charged groundwater chemistries are controlled by equilibrated reactions with soluble minerals (e.g. carbonates, sulphates and oxides) and kinetically controlled reactions with relatively insoluble minerals with more complex frameworks (e.g. silicates, aluminosilicates) is largely unevaluated. The complex relationship between mineral hydrolysis in multi-mineral assemblages, pH buffering and alkalinity generation is important as it impacts greatly on the reactivity of stored CO₂, on the stability and precipitation of CO₂ trapping carbonate minerals, on the potential for CO₂-rich waters to corrode cap-rocks and on the ultimate solubility of the stored CO₂.

This chapter presents geochemical data from CO₂-charged springs and geysers emanating along the crest of the Green River anticline, Northern Paradox Basin, Utah. The general geology of the Paradox Basin is discussed with emphasis on the stratigraphic and structural setting of the Green River anticline and its impact on local hydrology. Spring water chemistry and fluid and gas isotope geochemistry is discussed and used to illuminate the source of the groundwater and the CO₂. Published measurements of hydraulic head are then used to constrain flow paths between individual springs and aid in the interpretation of the evolution of the groundwater solute chemistry. The degree to which spring water chemistry is controlled by equilibrated fluid-mineral reactions is then evaluated using activity-activity diagrams. The evolution of the solute chemistry will be used in Chapter 3 to place constraints on the rates of the kinetically controlled fluid-rock reactions.

The solute and isotope geochemistry of fluid sampled prior to, and during the course of, a large-scale eruption of Crystal Geyser is then discussed. Observations of changes in the chemical and isotopic composition of the fluid is then used to place constraints on the origin of the solute chemistry and fluid mixing processes in the subsurface.

2.2. Regional Geology of the Paradox Basin

This region of SE Utah is underlain by the Paradox basin (Fig. 2.2-1a) a late Palaeozoic intracratonic basin filled with a mixture of carbonate, clastic, and evaporite sediments (Nuccio and Condon, 1996). The Paradox Basin is defined by the maximum extent of salt in the Middle

Pennsylvanian Paradox Formation (Nuccio and Condon, 1996). The basin was primarily a Pennsylvanian and Permian feature (320-245 Ma) that accumulated thick deposits of carbonate, halite, and clastics in response to tectonic down-warping and simultaneous uplift along its north-eastern border (Baars and Stevenson, 1981). The shape of the basin was modified by later tectonic events, primarily the Laramide orogeny (80-35 Ma) (Dickinson and Snyder, 1978). Today, the basin has been dissected in places by uplift of the Colorado Plateau (25 Ma – present) and down-cutting by the Colorado River and its tributaries (Flowers *et al.*, 2008). The basin is bordered on the northeast by the Uncompahgre Plateau, a broad anticline cored by Precambrian rocks. The east side of the basin is bounded by the San Juan dome. The southeast end of the basin is defined by the northeast-trending Hogback monocline. The north-western, Green River, side is bounded by the San Rafael Swell (Fig. 2.2-1b), a Laramide aged monocline, and the far northern end of the basin merges with the southern Uinta Basin.

Sedimentary rocks of the Paradox Basin (Fig. 2.2-2) overlie an Early Proterozoic metamorphic basement that is locally intruded by granite (Nuccio and Condon, 1996). Cambrian through Jurassic strata unconformably overlies the basement rocks. Remnants of Cretaceous rocks are also present, especially in the north-western and south-eastern part of the basin, but, except for the igneous intrusive centres, Tertiary rocks have been completely eroded away (Nuccio and Condon, 1996). At the surface, the subhorizontal, north-dipping rocks in the study area (Fig.2.2-3) consist of Jurassic and Cretaceous clastic sedimentary rocks that include from oldest to youngest: Entrada Sandstone, Curtis Sandstone, Summerville Formation, Morrison Formation, Cedar Mountain Formation, Dakota Sandstone, and Mancos Shale (Fig.2.2-4).

2.2.1.1 Pre-Pennsylvanian Rocks

Cambrian through Devonian sedimentation in Eastern Utah was on a stable shelf in mainly shallow marine conditions (Blakey, 2008). Sub-Pennsylvanian rocks consist of the Lower and Middle Cambrian Tintic Quartzite, Upper Cambrian Ignacio Quartzite, Middle Cambrian Ophir Formation, Middle Cambrian Maxfield Limestone, Middle and Upper Cambrian Lynch Dolomite, Upper Devonian Aneth and Elbert Formations and Ouray Limestone, and the Mississippian Leadville Limestone.

2.2.1.2 Pennsylvanian and Permian Rocks

During the Pennsylvanian and Permian, the Uncompahgre Plateau experienced rapid and large-scale uplift, and the adjacent north-eastern side of the Paradox Basin subsided, accumulating sediments of great thickness (as much as 3650m) (Nuccio and Condon, 1996). Deposits within the oldest Pennsylvanian formation, the Molas Formation, are transitional from nonmarine to marine, later being deposited and reworked by streams. The upper part has, in addition to fluvial strata, marine limestone beds deposited by the transgressive Middle Pennsylvanian Sea.

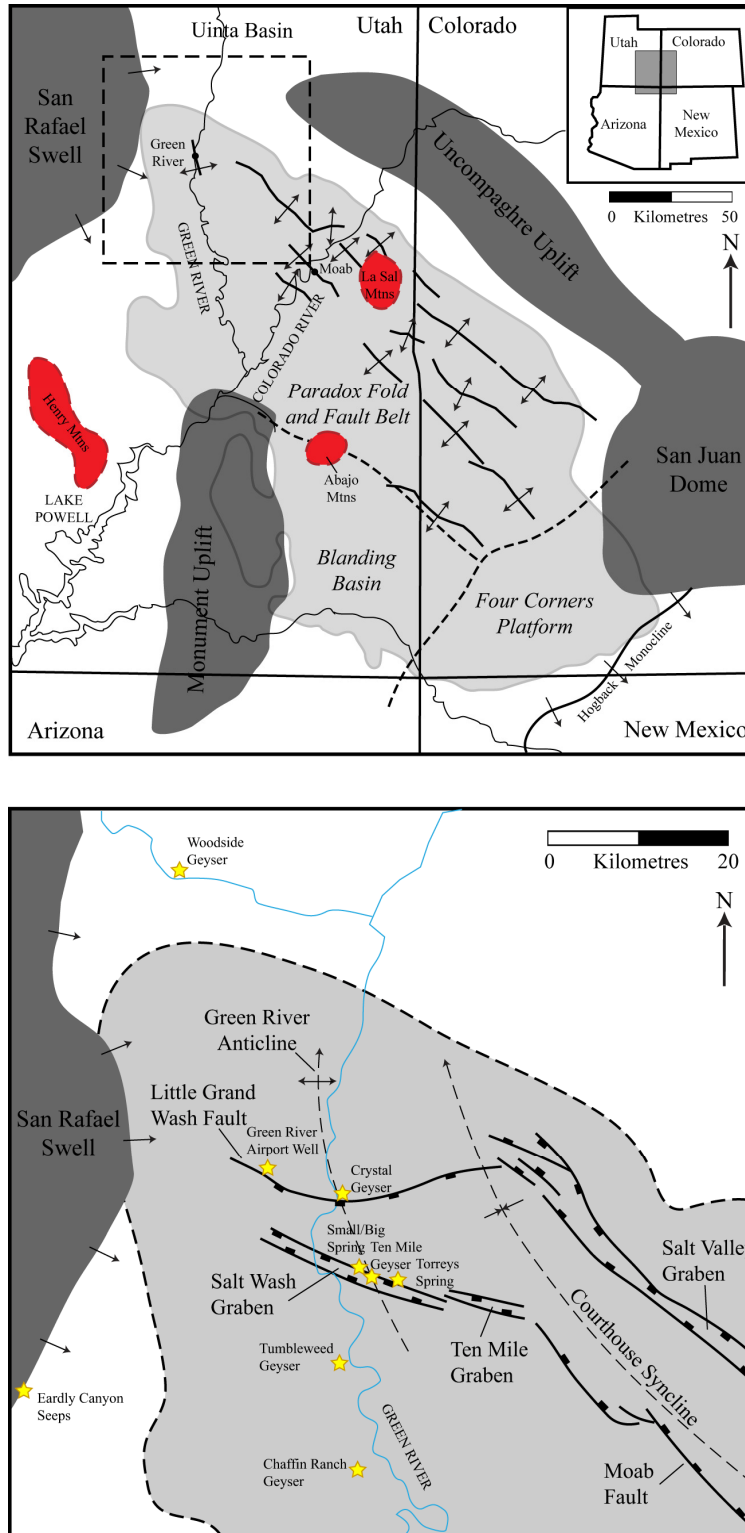


Figure 2.2-1 Geological features of the Paradox Basin and surrounding region. (a) Structural provinces of the Paradox Basin and bordering uplifts (after Condon, 1997). (b) Main structural features of the Northern Paradox Basin, in the vicinity of the study area. The outlined area in grey is the maximum extent of the Pennsylvanian evaporite formations which demarks the extent of the Paradox Basin. Yellow stars denote the locations of CO₂-charged springs or regions of dry CO₂ exhalations.

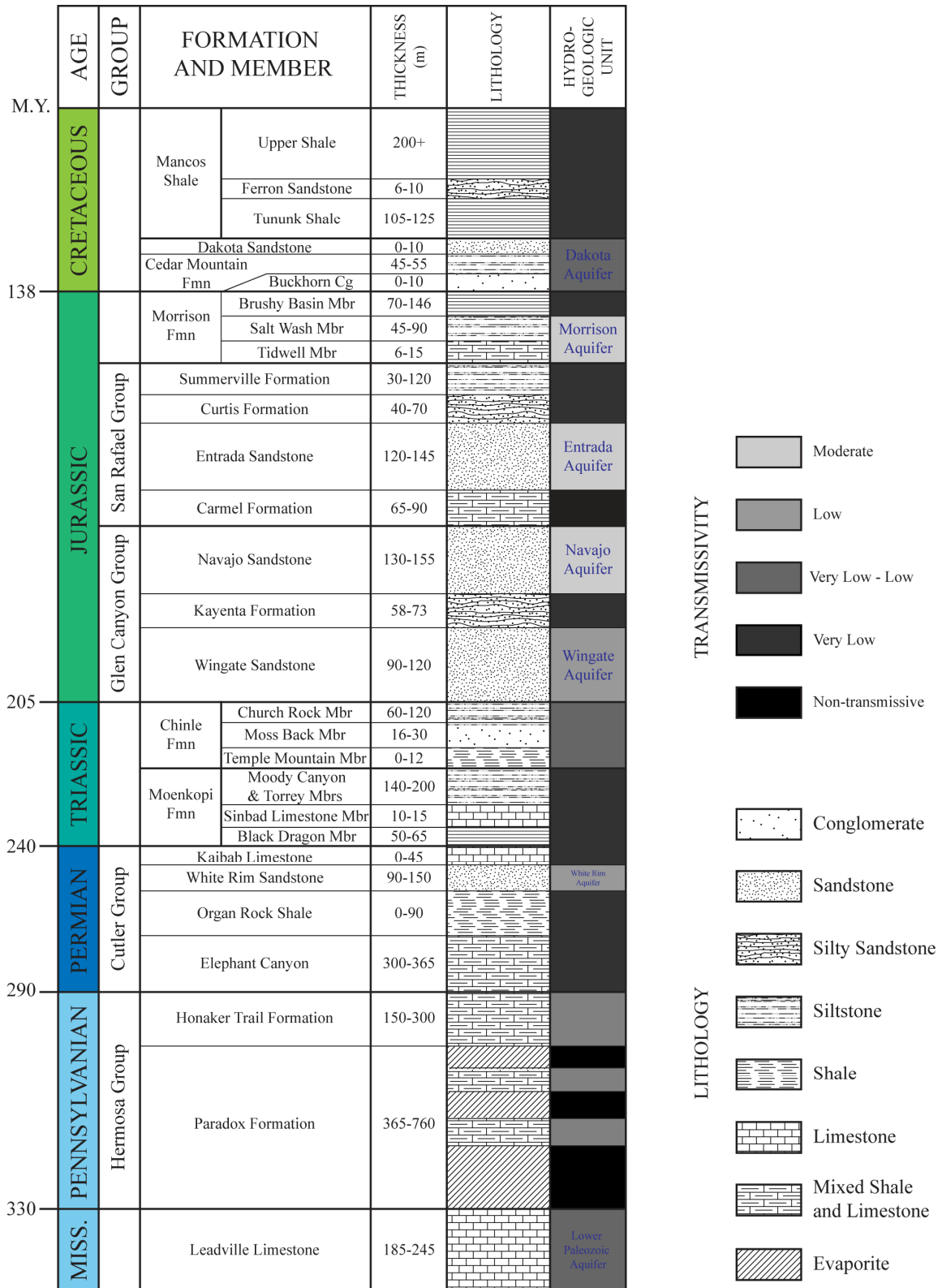


Figure 2.2-2 Generalized stratigraphic section for the Green River area. Thickness data compiled from Trimble and Doelling (1978) and Hintze (1993). Hydrological data from Hanshaw and Hill (1969) and Hood and Patterson (1984).

The Middle and Upper Pennsylvanian Hermosa Group includes the Middle Pennsylvanian Pinkerton Trail and Paradox Formation and the Middle and Upper Pennsylvanian Honaker Trail Formations (Doelling, 1988). The Pinkerton Trail consists of interbedded marine limestone and dark shale, deposited in shallow-marine conditions of normal salinity. The cyclic Paradox Formation is composed of dolomite, black shale, anhydrite, halite, and other salts (Hite and Buckner, 1981). Halite is the most abundant constituent of the Paradox, occurring in beds tens of feet thick. The Honaker Trail Formation is composed of cyclically deposited limestone, sandstone, and shale. It represents a return to normal marine conditions in contrast to the evaporitic marine conditions of the Paradox Formation (Condon, 1997). The thickness of the formation varies significantly throughout the basin due to salt flowage in the underlying Paradox Formation during deposition.

Continued uplift of the Uncompahgre Plateau in Late Pennsylvanian and Early Permian time eventually unroofed the Precambrian basement rocks (Nuccio and Condon, 1996). The Permian Cutler Formation is mostly a product of this unroofing process and consists of arkose sandstone, deposited in a series of alluvial fans (Campbell, 1980). In the study area, the Cutler Group includes the Elephant Canyon Formation, the Cedar Mesa Sandstone, the Organ Rock Formation, and the White Rim Sandstone (Baars, 1962).

2.2.1.3 Triassic and Jurassic Rocks

In the Triassic and Jurassic, sedimentation in the area of the Paradox Basin was influenced to a great degree by development of magmatic arcs to the south and west of the current basin (Currie, 1997). Development of the arcs produced periodic uplift in source areas and provided sediment to the Paradox Basin (Nuccio and Condon, 1996). Triassic and early Jurassic sedimentary units contain large volumes of ash derived from volcanic activity in the arcs, creating thick regional aquitards. Times of less tectonic activity, especially in the Middle Jurassic, led to deposition of marine, sabkha, and eolian deposits of high hydraulic conductivity.

Deposition of Permian, Triassic, and Jurassic sediment onto thick sequences of salt in the Middle Pennsylvanian Paradox Formation led to the diapiric rise of the salt in several anticlines in the fold and fault belt. Individual Triassic and Jurassic units thin on the flanks of these anticlines (Doelling, 1988). The basal Triassic unit in the basin is the Early and Middle Triassic Moenkopi Formation. Uplift south of the Paradox Basin in Late Triassic time led to development of a north-westward flowing fluvial system depositing the Upper Triassic Chinle Formation (Huntoon *et al.*, 2002). The thickness of Jurassic sediment is dominated by the Lower Jurassic Glen Canyon Group, which is composed of the Wingate Sandstone, Kayenta Formation, and Navajo Sandstone (Doelling, 1988). The Wingate and Navajo are massive eolian units, the Kayenta is fluvial. Contacts between formations of the group are gradational; an unconformity lies at the top of the

Navajo Sandstone (Doelling, 1988). Unconformably overlying the Glen Canyon Group is the Middle Jurassic San Rafael Group. The San Rafael Group consists of the Page Sandstone, Carmel Formation, Entrada Sandstone, Curtis Formation, and the Summerville Formation. These formations were deposited in and on the margins of an inland sea (Nuccio and Condon, 1996).

2.2.1.4 Cretaceous and Tertiary Rocks

Late Tertiary to Holocene erosion removed Cretaceous and Tertiary rocks throughout most of the Paradox Basin (Nuccio and Condon, 1996). The remaining Cretaceous rocks comprise the Early Cretaceous Morrison Formation and Cedar Mountain Formation (Molenaar, 1981) and the Upper Cretaceous Dakota Sandstone and Mancos Shale. The dominant event of latest Cretaceous and Tertiary time was the development of uplifts and adjacent basins associated with the Laramide orogeny. Major structural features in the Paradox Basin region are the Uncompahgre Plateau, San Rafael Swell, Monument Upwarp, San Juan Dome, and Uinta Basin. Records of Tertiary sedimentation in the Paradox Basin are absent due to late Tertiary uplift and erosion; however, it is very likely that Palaeocene, Eocene, and possibly even Oligocene, Miocene, and Pliocene rocks were once present in the northernmost part of the basin (Nuccio and Condon, 1996).

2.2.2. Local Structure

The northern part of the Paradox Basin, pertinent to this study (Fig. 2.2-1, Fig. 2.2-3), has been termed the Paradox fold and fault belt (Kelley, 1958). This includes the area encompassing the Green River and the major structural features of the Little Grand Wash and Salt Wash fault zones, the sites of natural CO₂ leakage (Dockrill, 2005; Shipton *et al.*, 2004, 2005) (Fig. 2.2-4). This area consists of a series of parallel, northwest-trending faults, anticlines, and synclines. Dissolution of salt along the crests of some anticlines in this region has caused down-faulting and the development of grabens at the crests (Doelling *et al.*, 1988). Rocks as old as Pennsylvanian are exposed in the cores of some anticlines, and remnants of Cretaceous rocks are present in some synclines.

The Little Grand Wash fault is a steeply south-dipping, listric normal fault, with an arcuate surface trace length of about 61 km (Shipton *et al.*, 2004). The fault splays into two strands for ~ 3.3 km of its length (Shipton *et al.*, 2004). The throw of the fault near the Green River is about 290 m and much of the displacement is concentrated along the southern strand (Heath, 2004). The fault may cut rocks from Pennsylvanian to early Cretaceous and sole into the halite-rich Pennsylvanian Paradox Formation (Heath, 2004). To the south, the Salt Wash and the Tenmile Grabens are together about 31 km long and are separated by a step-over zone (Dockrill, 2005). The faults strike about N 70° W (Dockrill, 2005). The southeast end of the Salt Wash faults may link to the northwest tip of the Moab fault (Shipton *et al.*, 2004). At least some

movement of these faults may be related to salt flow, since the faults are located on the northern plunging limb of the broad Cane Creek-Big Flat salt anticline. Doelling *et al.*, (1988) and Condon, (1997) concluded that salt migration commenced in the Permian and continued to the mid Jurassic. Local sedimentation patterns reveal a period of salt movement between Triassic to mid Jurassic resulting in the development of the Green River anticline and adjacent Courthouse Syncline (Dockrill, 2005). Fault movement may also be due to interaction of the Uncompahgre and San Rafael blocks to the east and west, respectively (Campbell and Baer, 1978). Unpublished illite age analysis dates fault movement at 40 Ma \pm 10 corresponding to the early tertiary Laramide orogeny (Dockrill, 2005).

2.2.3. CO₂-charged Springs

Almost pure CO₂ gas [95.7-99.4 % CO₂; 3.4-0.5 % N₂; 0.1-0.9 % O₂, 0.01-0.05 % Ar; 0.00-0.01 % He; Heath (2004)] is discharged from the Green River anticline along the Little Grand and Salt Wash fault systems, in the vicinity of Green River forming a series of geysering, cold water springs and dry exhalations (Fig. 2.2-5). CO₂-charged springs and mofettes emanate along and within complexities of the local normal fault systems or as fluid escapes from abandoned petroleum exploration and water wells (Fig. 2.2-6). Most springs occur in the northern fault footwalls of Little Grand Fault (Green River Airport Well [Grand Fault Unit 14-24], Crystal Geyser [Glen Ruby #1-X]) or Salt Wash Graben (Small Bubbling Spring, Big Bubbling Spring, Pseudo Tenmile Geyser, Torry's Spring [Delaney Petro Corp #1]) where these faults intersect with the crest of the Green River anticline (Fig 2.2-4). Two springs lying off the normal fault systems (Tumble Weed Geyser and Chaffin Ranch Geyser), are located towards the anticlines axis and are sourced from abandoned water wells. Tenmile Geyser lies in the hangwall of the northern fault of the Salt Wash Graben and is thought to represent effusion from a well penetrating to considerable depth, through to the footwall of the fault, but no record of this well could be found. Fluid discharge varies between individual springs typically being greater in the open conduits formed by wells. All the springs have been observed to geyser at some point in their history, but the height of these eruptions and volumes of expelled fluid vary considerably. Only Chaffin Ranch Geyser and Crystal Geyser erupt with any regularity. The most dramatic of these is Crystal Geyser on the eastern bank of the Green River in the footwall of the Little Grand Wash fault zone. This cold-water geyser has erupted at 8-22 hour intervals since the Glen Ruby #1-X well was drilled to the base of the Triassic section (TD 801 m) in 1935 (Baer and Rigby, 1978). The well was spudded into a 21.5m thick travertine mound attesting to a long history of leakage from this site prior to drilling of the well (Shipton *et al.*, 2004). Layered, ochre coloured travertine deposits accumulate within the immediate vicinity of all the emanations (Fig. 2.2-7). Many springs are also demarked by the precipitation of salt crusts as surface runoff evaporates.

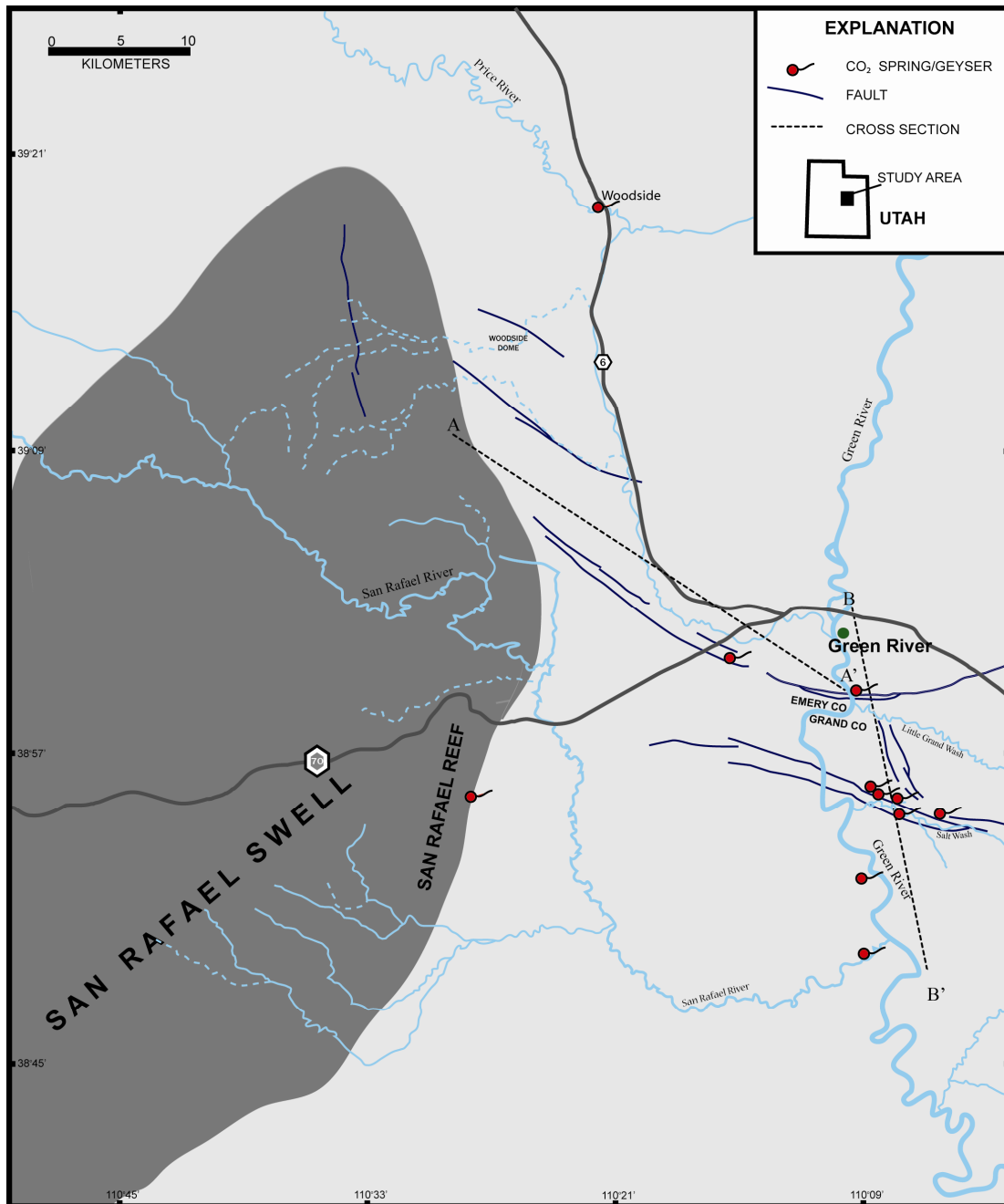


Figure 2.2-3 Map showing the main geographic features of the region surrounding Green River and the locations of all known CO₂-escapes. Dotted lines show the location of the cross sections in Figure 2.4-10.

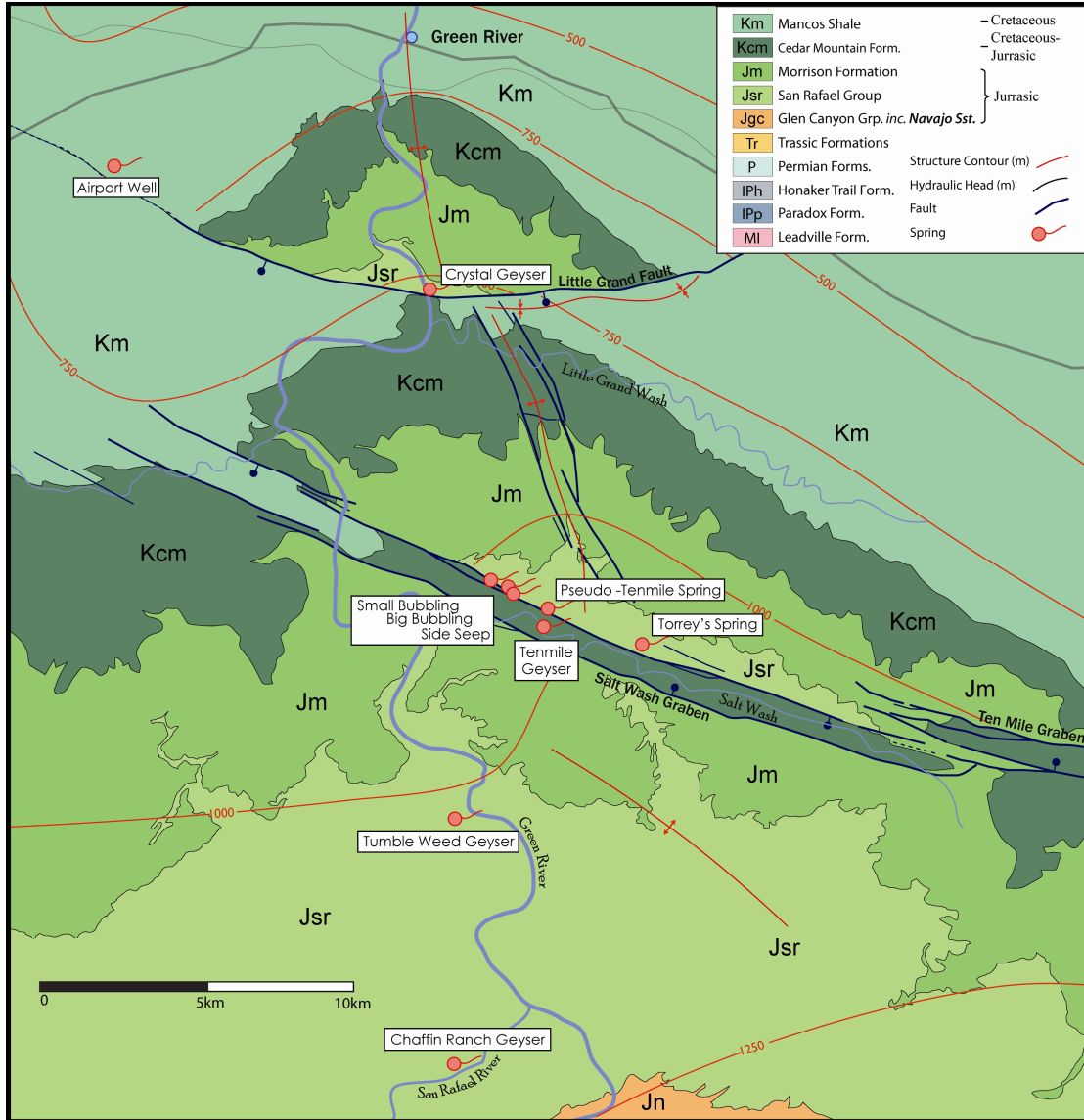


Figure 2.2-4 Surface geology of the Green River anticline redrawn after Doelling (2000). Structure contours are for the top of the Navajo Sandstone (after Dockrill, 2005). The map shows the clustering of springs along the axis of the anticline, within the damage zones of the Little Grand Fault and the northern fault of Salt Wash Graben.

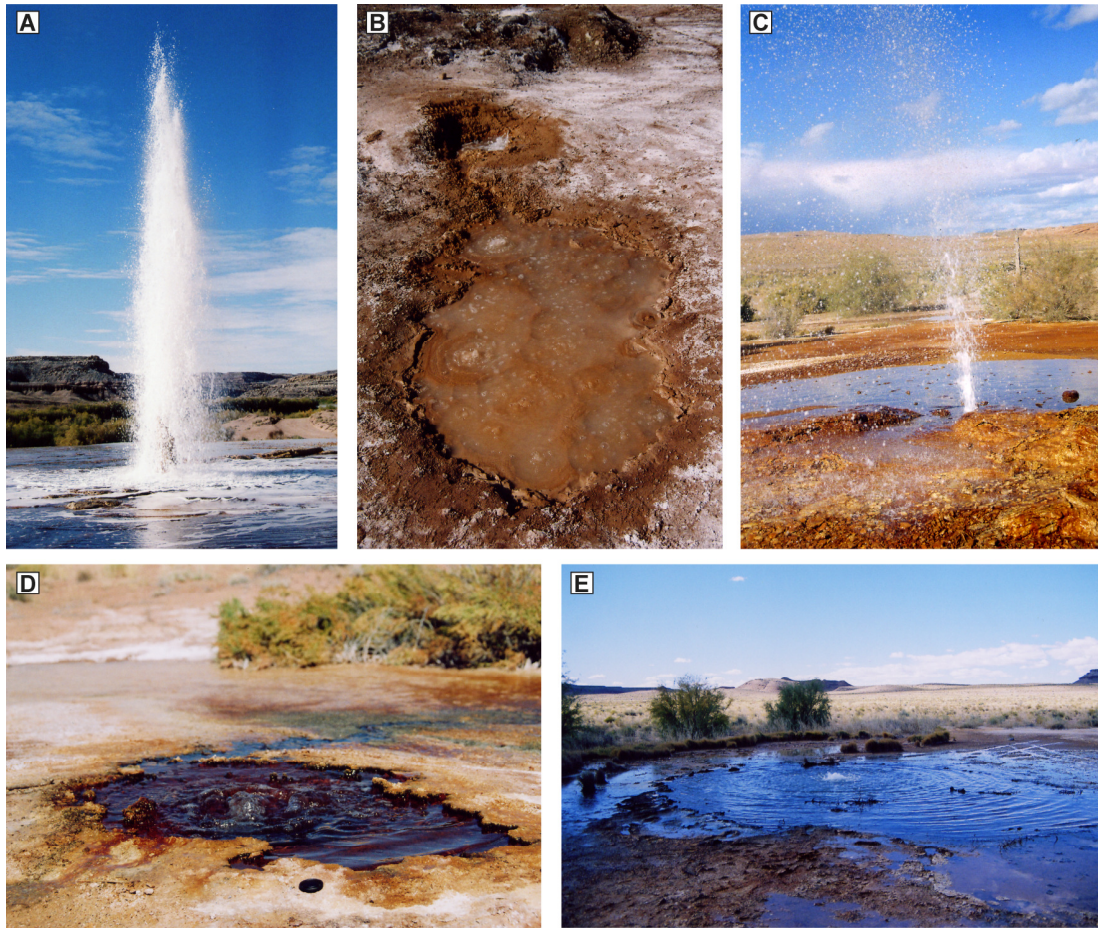


Figure 2.2-5 Photographs of springs, geysers, and groundwater leakage from abandoned wells. (a) Crystal Geyser. This geyser erupts periodically about once every 16 hours to a height of ~20 m from the Glen Ruby #1-X abandoned oil exploration well drilled during 1935 and 1936 (b) a side seep ~8m from Crystal Geyser. (c) Chaffin Ranch Geyser; regularly geysers, sourced from a water well drilled for livestock.(d) Torreys spring sourced from the Delaney Petroleum Co. #1 well (e) Tumble Weed Geyser, sourced from a water well drilled for livestock

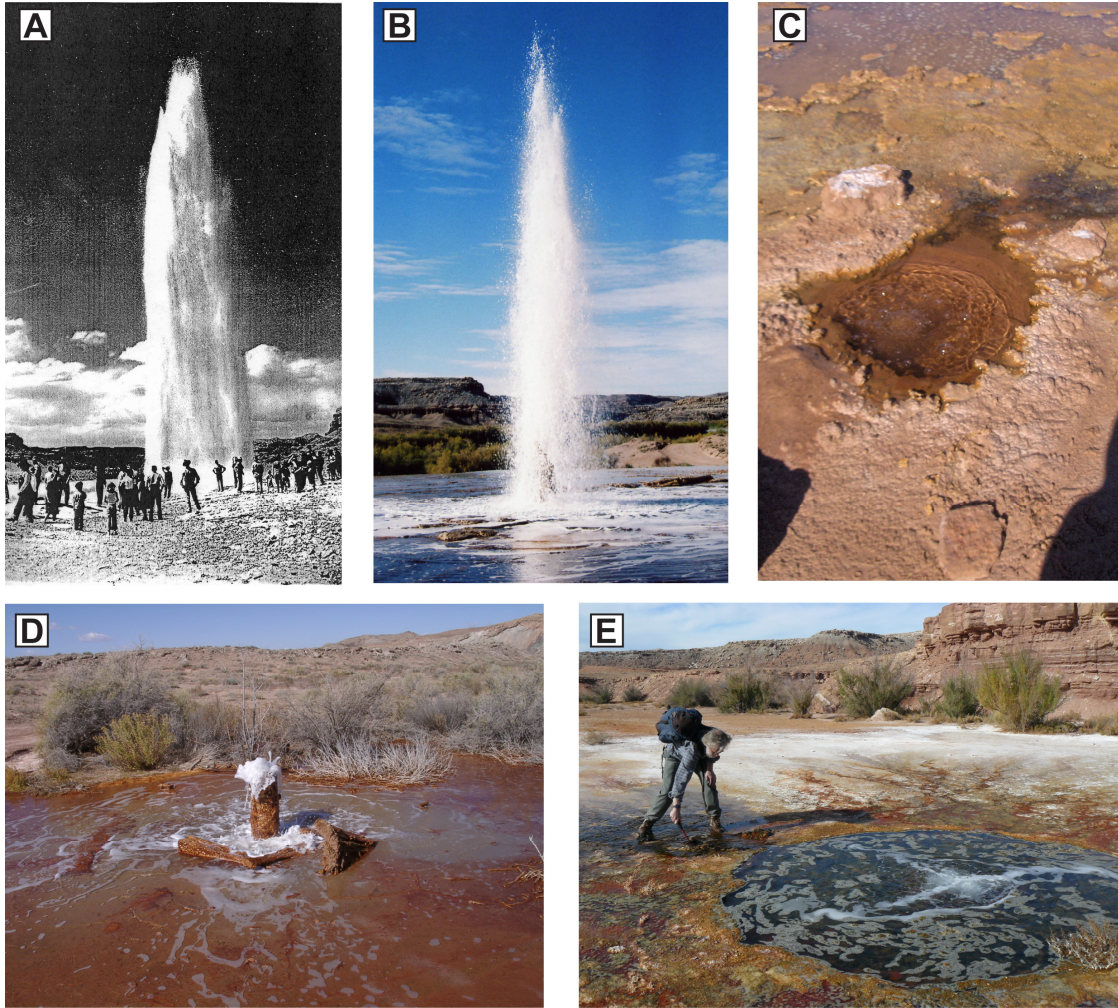


Figure 2.2-6 Photographs of springs, geysers, sourced from abandoned wells and natural leaks. (a) Past eruption from Crystal Geyser showing a large discharge of water, much greater than what is seen today; estimated eruption high 23m (Shipton, 2004) (b) Modern eruption of Crystal Geyser, exhibiting its maximum height of ~12m (c) Pseudo-tenmile Geyser, a natural seep at the intersection of the Salt Wash Graben and the apex of the Green River anticline (d) Tenmile Geyser with well casing; thought to be an exploration well drilled within the Salt Wash Graben through to the underlying footwall. (e) Big Bubbling Spring, a natural seep at Salt Wash Graben.



Figure 2.2-7 Field photographs of modern Crystal Geyser (a,e) travertine mound and travertine formed around Green River Airport Well (b), Chaffin Ranch Geyser (c) and Tumble Weed Geyser (d). (a) Hemispherical pools that form the terrace morphology on travertine surface (b) Friable travertine poor in Fe, iron content of the travertine has a significant impact on its strength. (c) Fe-rich irregular travertines when the fluid flux is low (d) Large pools form around some of the springs where discharge can exceed local evaporation. The pools contain a travertine substrate. (e) Fe-rich, down-stepping lobate mounds that radiate out from geyser vent, with conically shaped speleothems on sub-vertical surfaces of the mound.

2.3. Geochemical Sampling and Results

Knowledge of any groundwater system is often limited to the chemical data collected from surface spring waters. Manipulation of chemical data allows a valuable window into the deep workings of a groundwater system, provided that hydrology and geology of the site are sufficiently understood. Of particular importance when quantifying physiochemical controls on solute composition from spring fluids are: 1) knowledge of the conditions from which the fluids were sourced (e.g. host lithology, *P*, *T*) and; 2) any geochemical processes which may alter groundwater chemistry as fluids ascend to the surface, such as CO₂ degassing and calcite precipitation. These aspects of CO₂-spring chemistry are discussed in this section, especially with relevance to the carbonate system and fluid-mineral reactions controlling solute chemistry.

2.3.1. Field Sampling Methods

Water samples collected from the springs were filtered through 0.2 µm nylon filters on site and stored in pre-cleaned high-density polyethylene bottles, prewashed with filtrate, one sample acidified to ~pH 2-3 with HNO₃ for analyses of cations and one un-acidified sample for analysis of anions. All samples were stored in 60 mL plastic bottles free of air to minimise degassing and oxidation. pH, alkalinity (by Gran titration (Stumm and Morgan, 1996)) and temperature were measured in the field. The pH probe was calibrated daily with 4.0 and 7.0 pH standards.

Oxidation-reduction potential (mV) was measured in-situ using a Hach Lange MC3051Pt-9 ORP platinum electrode filled with an Ag/AgCl reference electrode and saturated KCl filling solution. These measurements were then converted to Eh values by using measured temperature values in order to establish standard hydrogen electrode corrections. ORP standard (Orion ® #967961) was used to perform ORP electrode checks where the measured value of the standard was 220 ± 3 mV at 25°C. The platinum electrode was cleaned at the end of each sampling day and stored according to manufacturer's guidelines. ORP electrodes can be erratic when used in ground water and often do not stabilize rapidly (Stumm and Morgan, 1981). For each spring, measurements were recorded every five minutes over a thirty minute sampling interval and the average reported.

Exsolved gases were collected in 10 mm diameter, internally polished, refrigeration-grade copper tubes (EAWAG, 2000). Individual sampling units comprise two sections of copper pipe separated by a Swagelok® needle valve closed at either end with high grade thread sealing nuts. During sampling polyethylene tubing and funnels were connected to either end of the piping to create a sampling environment isolated from the atmosphere. The tube is flushed through with gas or water for at least 30 minutes to remove air contamination before the copper tube was submerged and sealed using sealing nuts.

2.3.2. Analytical Methods

Water samples were collected from springs and geysers, during the 2006 and 2007 field season, for the analysis of $\delta^{18}\text{O}$, $^{87}\text{Sr}/^{86}\text{Sr}$, ^3H , K^+ , Na^+ , Ca^{2+} , Mg^{2+} , Sr^{2+} , Ba^{2+} , Fe , Mn , Al^{3+} , SiO_2 , Cl^- and SO_4^{2-} (Table 1, Appendix A). Time series samples through a large-scale eruption of Crystal Geyser were collected during the 2007 season. Dissolved inorganic carbon (DIC) was calculated from field alkalinity and pH using the computer code PHREEQC (Pankhurst and Appelo, 1999). Cation analyses were measured on acidified samples using a Varian Vista-PRO simultaneous inductively coupled plasma atomic emission spectrometer (ICP-AES) and anion concentrations were analysed on a Dionex Ion Chromatography System at the University of Oxford (2006 sample set) and the University of Cambridge (2007 sample set). Spring samples were diluted to fit the calibration range. For the 2006 data set all water samples were interspersed with standards SPSSW2 and T-167 which indicate accuracies better than $\pm 5\%$ for Na, K, Ca, Mg, Al, S and Si. For the 2007 data set multiple analysis of standard T-167 by AES again indicates accuracies of better than $\pm 5\%$ (2σ).

Total dissolved inorganic carbon (DIC) was measured at the University of Cambridge. CO₂ was released from 5–15 mL aliquots of spring water by acidification with $>100\%$ H₃PO₄ in vacuum. CO₂ released on acidification in the reaction vessel was extracted while water was trapped at $-80\text{ }^\circ\text{C}$. Total CO₂ was measured manometrically before being converted to mmol L^{-1} .

Analyses for $^{87}\text{Sr}/^{86}\text{Sr}$ at the University of Cambridge follow Bickle *et al.* (2003) with analyses of NBS987 giving 0.710258 ± 0.000008 (2σ , $n = 11$) over the period of the analyses (2006 data set). $\delta^{13}\text{C}$ of dissolved inorganic carbon (DIC) and the $\delta^{18}\text{O}$ of H₂O were analysed in the Godwin Labs, University of Cambridge and are expressed in $\delta\text{‰}$ deviation relative to Peedee Belemnite (PDB) and VSMOW standards with analytical precisions estimated at ± 0.06 and ± 0.08 ‰ respectively. Analysis for $\delta^{13}\text{C}_{\text{CO}_2(\text{g})}$ of the sampled gas where performed at the University of Cambridge using VG PRISM Mass Spectrometer.

Enriched ^3H was counted at Brigham Young University using a PerkinElmer Quantulus 1220 Liquid Scintillation Counter with a detection limit of ± 0.8 tritium units and a precision of about ± 0.3 TU.

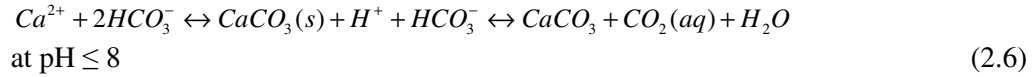
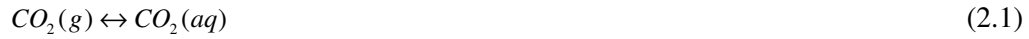
$\delta^{13}\text{C}$ of CO₂(g) from collected gas samples are presented in Appendix A and detailed in figure 2.4-6. Major cation, anion and isotope analyses for the CO₂-spring waters and for time-series fluid chemistry from Crystal Geyser are presented as data tables in Appendix A.

2.4. Discussion

2.4.1. CO₂-Water-Rock Interactions

2.4.1.1 CO₂ Solubility and the Carbonate System

The theoretical aspects of carbonate equilibria are covered in great detail elsewhere (e.g. Drever, 1997; Garrels and Christ, 1965; Plummer *et al.*, 1979; Stumm and Morgan, 1981), and only a brief overview of the carbonate equilibria necessary for understanding CO₂ dissolution and speciation, CO₂ degassing and CO₂ promoted fluid-rock interaction is discussed here. As is well known, dissolution of CO₂, and subsequent precipitation of calcite, is determined by the chemical exchange equilibria:



where H₂CO₃^{*} represents H₂CO₃ + CO₂(aq) and the overall defining reaction for calcite precipitation may be written



Where the calcite saturation index (*SI_{cc}*), the logarithm of the saturation state (*Ω*), is defined as

$$SI_{cc} = \log \left(IAP_{cc} / K'_{sp} \right) \quad (2.8)$$

where

$$K'_{sp} = \frac{a_{Ca^{2+}} \cdot a_{HCO_3^-}}{a_{H^+}} = \frac{\gamma_{Ca^{2+}} [Ca^{2+}] \cdot \gamma_{HCO_3^-} [HCO_3^-]}{\gamma_{H^+} [H^+]}, \quad (2.9)$$

the activities at equilibrium, and

$$IAP_{cc} = \frac{a_{Ca^{2+}} \cdot a_{HCO_3^-}}{a_{H^+}} = \frac{\gamma_{Ca^{2+}} [Ca^{2+}] \cdot \gamma_{HCO_3^-} [HCO_3^-]}{\gamma_{H^+} [H^+]}, \quad (2.10)$$

the activities in the water sample. Where a is activity, $[]$ is concentration, and γ is an activity coefficient. $SI = 0$, if there is equilibrium between the mineral and the solution; $SI < 0$ reflects subsaturation, and $SI > 0$ supersaturation (see for example Appelo and Postma, 2005, Drever, 1997).

Initially, CO₂ transfers across the gas-water interface to become an aqueous ion, a kinetically slow process [Eq. (2.1), (2.2)] (Dreybrodt, 1996). The solubility of CO₂ increases with pressure, but decreases with temperature and salinity (Joyce and Holloway, 1993; Duan and Sun, 2003) (Fig. 2.4-1). At 25 °C and 1 bar, the solubility of CO₂ in an aquifer fluid equivalent to a 3 M NaCl solution is approximately one-third its solubility in pure water. The dissolution of CO₂ and subsequent speciation can be described by equations (2.1-2.4).

The removal of CO₂(g) from solution drives equation (2.1) to the left and equation (2.7) to the right, driving calcite precipitation in CO₂-degassing springs and the formation of travertine. However, numerous studies (e.g. Dreybrodt *et al.*, 1992; Herman & Lorah, 1987, 1988; Lorah & Herman, 1988; White, 1997) show that calcite does not precipitate instantaneously at the point of saturation. Precipitation requires a finite supersaturation because of activation barriers to calcite nucleation and crystal growth (White, 1997). In most circumstances this implies a saturation index (SI_{CC}) of +0.5, although Dreybrodt *et al.* (1992) suggest that saturation indices of at least +1.0 are required.

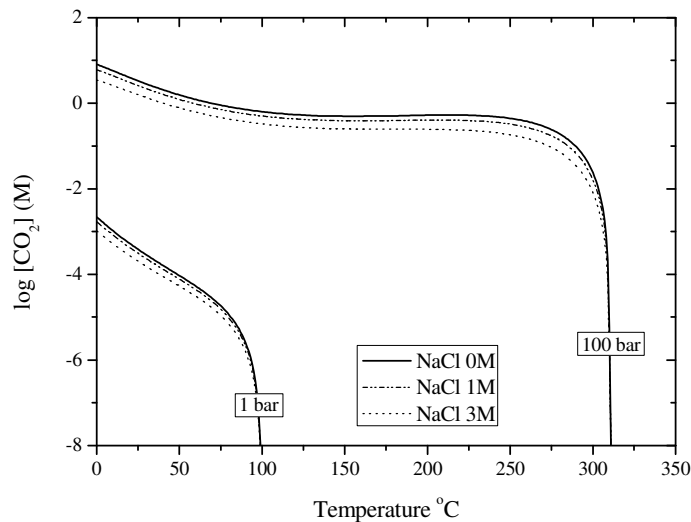


Figure 2.4-1 CO₂ solubility (mol kg⁻¹) as a function of temperature and various salinities at pressures of 1 and 100 bar. Calculations performed using the CO₂ solubility model of Duan *et al.*, 2006.

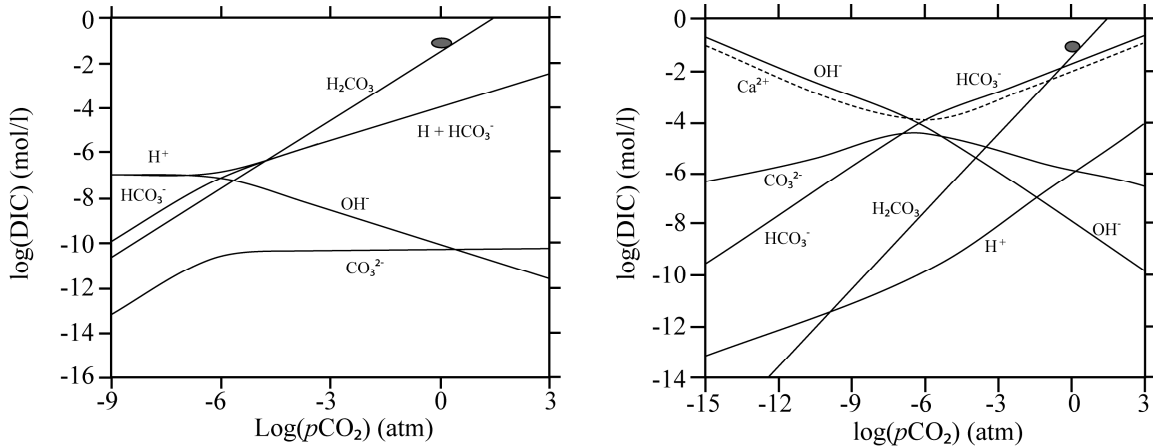


Figure 2.4-2 Carbonate speciation for the system CO₂-H₂O and CaCO₃-CO₂-H₂O assuming open system equilibrium and externally fixed pCO₂ (calculations performed in PHREEQC). (a) Speciation in the simple system CO₂-H₂O illustrates that H₂CO₃^{*} is the dominant species in solution at the pCO₂ of the springs. (b) The addition of calcite to the CO₂-H₂O system greatly affects the speciation of carbon in solution. The most dramatic change is [H₂CO₃^{*}] becoming subordinate to [HCO₃⁻]. HCO₃⁻ stability increases up to 4 orders of magnitude (compared to the CO₂-H₂O system) before [H₂CO₃^{*}] exceeds [HCO₃⁻] at -log pCO₂ of 0.4.

2.4.1.2 Carbonate System Speciation

The simplest speciation system (after Garrels and Christ, 1965) is the dissociation of carbon dioxide in water and follows from equation (2.1-2.4). All the other controlling species are assumed devoid from water, and hence the electrical neutrality may be written

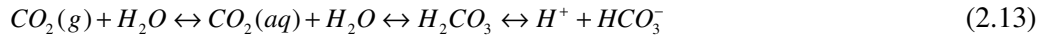
$$[H^+] = [OH^-] + [HCO_3^-] + 2[CO_3^{2-}] \quad (2.11)$$

Temperature has little effect on the speciation of the system (Garrels and Christ, 1965), with speciation being largely dependent on the pressure of the system (Fig. 2.4-2). As pCO₂ goes to zero, the solution pH approaches 7, while increasing pCO₂ causes the system to become more acidic. In this simple system the speciation of CO₂ in the Green River springs would be dominated by H₂CO₃^{*}. Most H₂CO₃^{*} remains as CO₂(aq); only about 0.3% actually forms carbonic acid (Drever, 1997). Fluid chemistry in groundwater system however, involves interaction with additional components, most importantly Ca²⁺, whose presence alters the electrical neutrality of the system and the subsequent carbonate speciation such that

$$2[Ca^{2+}] + [H^+] = [OH^-] + [HCO_3^-] + 2[CO_3^{2-}] \quad (2.12)$$

Addition of CaCO₃ to the system significantly affects the speciation. At 25 °C the shift in speciation between H₂CO₃^{*} and HCO₃⁻ implies an approximately even distribution of these two species in the CO₂-charged groundwaters.

Upon dissolution of CO₂, the formation of bicarbonate ion, HCO₃⁻ and production of acidity by release of H⁺ leads to a series of secondary reactions with complex feedbacks that buffer solution properties and mineral reactivity (Gunter *et al.*, 1993). In the absence of any fluid-mineral interaction the disassociation of this dissolved CO₂ results in an acidic solution of pH 3.4 due to the dissociation of carbonic acid:



A temperature-dependent dissociation constant K can be defined for Eq. (2.13):

$$\log K_{H_2CO_3} = \frac{a_{H^+} \cdot a_{HCO_3^-}}{a_{H_2CO_3}} = \frac{\gamma_{H^+} [H^+] \cdot \gamma_{HCO_3^-} [HCO_3^-]}{\gamma_{H_2CO_3} [H_2CO_3]} \quad (2.14)$$

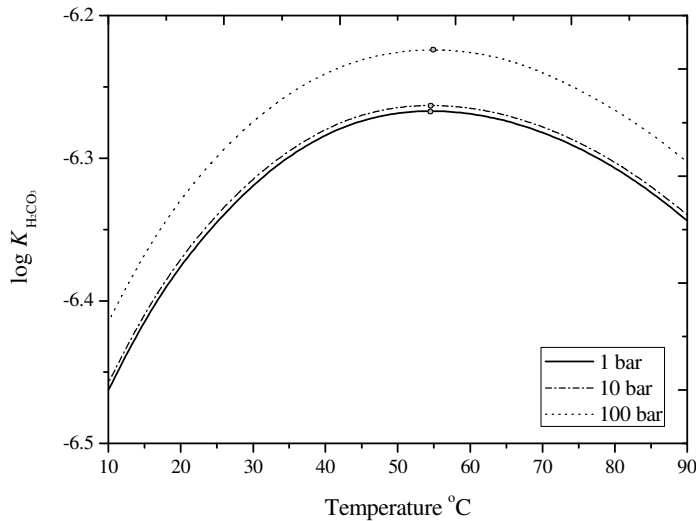


Figure 2.4-3 Temperature dependent dissociation constant for H₂CO₃ showing maxima at ~55°C

Calculations of log K (Eq. (2.14)) using SUPCRT92 (Johnson *et al.*, 1992) show a maximum of dissociation for reaction (2.13), occurring at about 55 °C above which log K decreases continuously with increasing temperature such that an initially weak acid becomes increasingly weaker at elevated temperature (Fig. 2.4-3). Thus, at low temperatures, the increased availability of H⁺ might be expected to cause higher rates of mineral hydrolysis. Overall the larger relative solubility of CO₂ and the effective disassociation of H₂CO₃, means that even at very low temperatures CO₂-charged fluids have a significant effect on the promotion of mineral-fluid reactions.

2.4.1.3 Alkalinity

Alkalinity [Alk] is a measure of the ability of a solution to neutralize acids to the equivalence point of carbonate or bicarbonate (Stumm and Morgan, 1981). It is equal to the stoichiometric sum of the bases in solution. In groundwater systems carbonate alkalinity tends to make up most of the total alkalinity due to the common occurrence and dissolution of carbonate minerals and the ubiquitous presence of dissolved CO₂ (Drever, 1997). Other aqueous species that can contribute to alkalinity include BO₃³⁻, PO₄³⁻, SiO₂ and NH₃ although these have low concentrations in groundwaters (Drever, 1997). Alkalinity may be defined either as:

$$[Alk] = [HCO_3^-] + 2[CO_3^{2-}] + [OH^-] - [H^+] \quad (2.15)$$

or, the excess of positive charges over the anions of strong acids:

$$[Alk] = [Na^+] + [K^+] + 2[Ca^{2+}] + 2[Mg^{2+}] + \dots - [Cl^-] - 2[SO_4^{2-}] - [NO_3^-] - \dots \quad (2.16)$$

Removal or addition of CO₂ modifies DIC and pH without changing [Alk] as the net reaction produces the same number of equivalents of positively contributing [H⁺] as negative contributing species [HCO₃⁻ and/or CO₃²⁻]. This concept is typically illustrated in a capacity diagram (Deffeyes, 1965) which plots alkalinity against DIC to expediently show contours of pH. Accurate determination of pH, field alkalinity and DIC can be assessed by comparison of the measure values of [Alk], DIC and pH with the position of pH isopleths predicted from equilibrium conditions. If extensive CO₂ degassing had occurred prior to sampling the measured values of pH should be significantly large than those predicted by equilibrium considerations. Figure 2.4-4 shows the relation between measured DIC (mmol L⁻¹), field alkalinity (mEq L⁻¹) and pH for the Green River springs. Measured values of pH are close to or within error of values predicated by theoretical considerations suggesting that equilibration within the carbon system is largely maintained during ascent of fluid to the surface and sampling.

Addition of CO₂ to a solution in contact with rock forming minerals can affect alkalinity. Hydrolysis of silicate, alumino-silicate and carbonate minerals consumes [H⁺] increasing [Alk], while releasing cations to solution which do not contribute to alkalinity. Precipitation of carbonate minerals consumes HCO₃⁻ and/or CO₃²⁻ buffering [Alk] towards lower values. Alkalinity is therefore an important measure of the degree of fluid-rock interaction in a groundwater system. CO₂-rich groundwater systems should evolve to higher alkalinity due to the progressive hydrolysis of rock forming minerals.

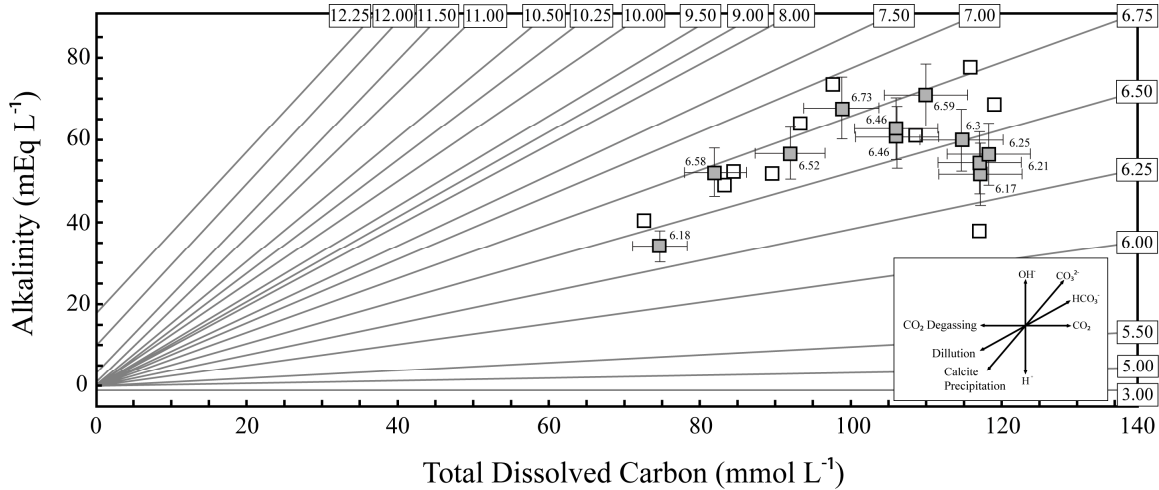


Figure 2.4-4 Capacity (Deffeyes) diagrams for the CO₂-springs. pH measurements made in the field are labeled next to each sample (2006 data). Data for the 2007 sampling program is included for reference. Constant pH isopleths are labeled about the margins of the diagrams for equilibrium at 25 °C. Change in temperature has negligible effect on the location of the important isopleths (between pH's of 6 and 9). Springs are invariably characterized by higher [Alk] than DIC when compared to corresponding pH isopleths. The deficiency in DIC is interpreted to represent CO₂-degassing (which maintains [Alk]).

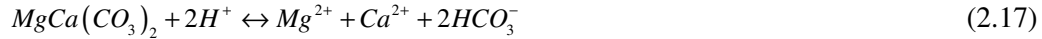
2.4.1.4 Fluid-Mineral Reactions

After introduction of CO₂ into a geological reservoir, initial rapid carbonate, sulphate and oxide acid hydrolysis is expected to be followed by more sluggish ion-exchange reactions and then hydrolysis of silicate phases accompanied by re-precipitation of carbonate in excess of that dissolved. Upon consumption of these phases and as the fluid-mineral system moves towards saturation with respect to these minerals, kinetically slower and energetically less favourable reactions will begin to dominate the geochemical evolution of these fluids. The dissolution of silicate and phyllosilicate minerals, which are typically undersaturated in near surface and shallow subsurface geological fluids (Brantley and White, 2003), will be enhanced by the reduction in pH afforded by the dissolution and speciation of CO₂ and by the overall availability of H⁺ (e.g. Casey and Bunker, 1990; Oelkers *et al.*, 1994). A variety of secondary reactions (e.g. clays, silicates, carbonate, oxide, sulphates and salts) will be promoted by the availability of carbonate ions sourced from CO₂ and carbonate dissolution, cations sourced from mineral dissolution and exchange reactions and the relative increase in saturation of secondary phases as a result of solubilisation of primary minerals and increases in pH. Reactions involving H₂CO₃* with reservoir minerals are thus many and varied, depending on the chemical composition of the fluid and the mineralogy of the host rock.

Porosity volume in sedimentary basins is dominant by contributions from porous and permeable sandstone formations (e.g. Bethke, 1989). The mineralogy of terrestrial and marine sandstones is dominated by silicate minerals; including quartz and feldspars, and phyllosilicate minerals, including smectites, illites and chlorites (e.g. Cox and Lowe, 1995). Sandstones are

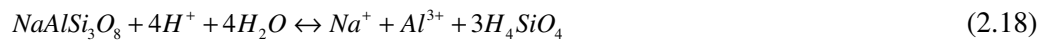
typically variably cemented by carbonate minerals including calcite, dolomite, siderite and ankerite (e.g. Cox and Lowe, 1995). Thus the dominant pH buffering reactions in mixed mineralogies are likely to vary with duration of reaction as the initial pH buffering will be dominated by minerals with fast dissolution kinetics;

Dolomite



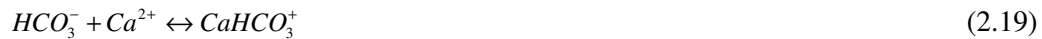
Followed by slower reaction of minerals with more complex frameworks, and lower solubilities, e.g.

Albite



At low temperatures, energy barriers prevent this reaction being reversible and these reactions are dominantly uni-directional. As a result, increases in porefluid [Al³⁺], [H₄SiO₄] and mono- and divalent cations results in an increase in the solution saturation state of a range of phyllosilicate minerals whose formation is favoured by thermodynamic considerations, but whose composition and precipitation will be fundamentally controlled by chemical kinetics (Lasaga, 1995).

Dissolved bicarbonate species will form soluble complexes with dissolved cations sourced from fluid-rock reactions, e.g.



which will ultimately increase the solubility of the dissolved CO₂. Dissolved HCO₃⁻ will then react with divalent cations, in solution, to form carbonate minerals (e.g. calcite, siderite, magnesite) which will form a sink of CO₂ from the fluid following Eq. (2.6). Rates of these reactions are known to be fast, relative to the slow kinetics of CO₂ dissolution and aqueous speciation, but have a complex dependence on reactant concentrations, in situ pH, temperature and fluid composition (e.g. Morse and Arvidson, 2002; Zuddas and Mucci 1998). Additionally, within porous media the growth of secondary precipitates may be ultimately limited by solute supply and solute transport, as apposed to true mineral surface reaction.

2.4.2. CO₂ Sources: Isotopic Constraints

Carbon isotopes aid in the elucidation of the carbon history of groundwaters and CO₂ gases due to the large spread in isotopic composition of the various sources of geospherically derived carbon (Clark and Fritz, 1997). However, assessment of the degree of isotopic equilibration between sampled fluids and CO₂ gas is important before the observed compositions can be considered

characteristic of the original source carbon, due to the potential effects of CO₂ degassing and non-equilibrium fractionation as fluids ascend to the surface. To determine whether the waters and gases are in equilibrium with respect to carbon isotopes, calculations can be made to derive theoretical, predicted $\delta^{13}\text{C}_{\text{DIC}}$ values based on the $\delta^{13}\text{C}$ of exsolved CO₂ gases.

2.4.2.1 Stable Isotope Fractionation: Notation Review

The isotope fractionation factor between two substances A and B is defined as

$$\alpha_{A-B} = R_a / R_b \quad (2.20)$$

$$\text{Where } R_a = {}^hE / {}^lE \quad (2.21)$$

The ratio of the heavy isotope over the light stable isotope in phase A, such as ¹⁸O/¹⁶O or ¹³C/¹²C. Rather than determining the absolute ratio of a substance it is easier and more precise to determine the relative difference between that substance and a reference such that

$$\delta_A = \frac{R_A - R_{std}}{R_{std}} \times 10^3 \quad (2.22)$$

where R_{std} is the absolute ratio in the standard. The relation between δ values and fractionation factors (which are equilibrium constants that describe how isotopes are portioned between two phases) is

$$\alpha_{A-B} = \frac{1 + \delta_A/1000}{1 + \delta_B/1000} = \frac{\delta_A + 1000}{\delta_B + 1000} \quad (2.23)$$

Values of α are commonly close to unity so that isotopic fractionation factors are expressed as per mil (‰) fractionations, which can be approximated as

$$10^3 \ln \alpha_{A-B} \approx \delta_A - \delta_B \quad (2.24)$$

2.4.2.2 Carbon Isotopic Composition of DIC and CO₂(g)

The mass balance defining the contributions of H₂CO₃^{*} and HCO₃⁻ forming the total dissolved carbon pool at the pH range of interest can be defined as:

$$\delta^{13}\text{C}_{\text{DIC}} = X_{\text{H}_2\text{CO}_3^*} \delta^{13}\text{C}_{\text{H}_2\text{CO}_3^*} + X_{\text{HCO}_3^-} \delta^{13}\text{C}_{\text{HCO}_3^-} \quad (2.25)$$

Where X_{H₂CO₃^{*}} and $\delta^{13}\text{C}_{\text{H}_2\text{CO}_3^*}$, and X_{HCO₃⁻} and $\delta^{13}\text{C}_{\text{HCO}_3^-}$ are the mole fractions of each component and their isotopic composition, respectively. Although H₂CO₃^{*} is composed of both CO₂(aq) and H₂CO₃, the contribution of H₂CO₃ is small and for these calculations all H₂CO₃^{*} is assumed to be

CO₂(aq). The fractionation factor, α , is related to δ values for the species CO₂(aq), HCO₃⁻ and CO₂(g) by (Clark and Fritz, 1997):

$$\alpha_{CO_2(aq)-CO_2(g)} = \left(\delta^{13}C_{CO_2(aq)} + 1000 \right) / \left(\delta^{13}C_{CO_2(g)} + 1000 \right) \quad (2.26)$$

$$\alpha_{HCO_3^- - CO_2(g)} = \left(\delta^{13}C_{HCO_3^-} + 1000 \right) / \left(\delta^{13}C_{CO_2(g)} + 1000 \right) \quad (2.27)$$

Where the temperature dependent fraction factors are determined using (Mook et al., 1974; Vogel et al., 1970):

$$10^3 \ln \alpha_{CO_2(aq)-CO_2(g)} = -0.373 \times 10^3 T^{-1} + 0.19 \quad (2.28)$$

$$10^3 \ln \alpha_{HCO_3^- - CO_2(g)} = 9.552 \times 10^3 T^{-1} - 24.1 \quad (2.29)$$

Which can be combined with the equation of mass balance to yield the isotopic composition of individual carbon species from the analysed $\delta^{13}C_{CO_2(g)}$ using the measured values of DIC, pH and the distribution of carbon species calculated using PHREEQC (Parkhurst and Appelo, 1999).

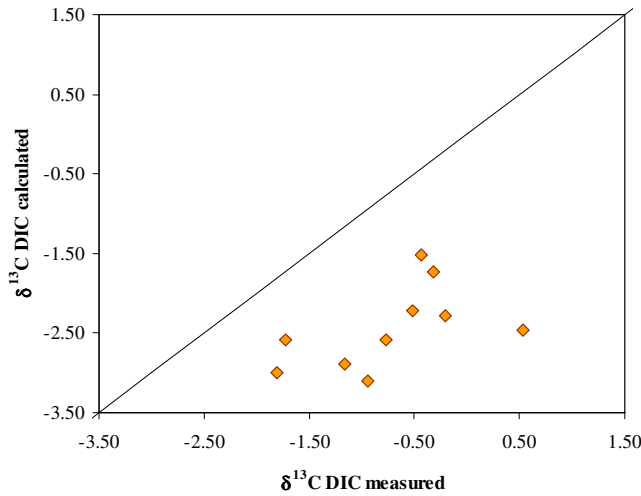


Figure 2.4-5 $\delta^{13}C_{DIC}$ measured versus that calculated from the $\delta^{13}C$ of CO₂(g) using equilibrium fractionation factors and the distribution of HCO₃⁻ and H₂CO₃^{*} at the measured pH and DIC.

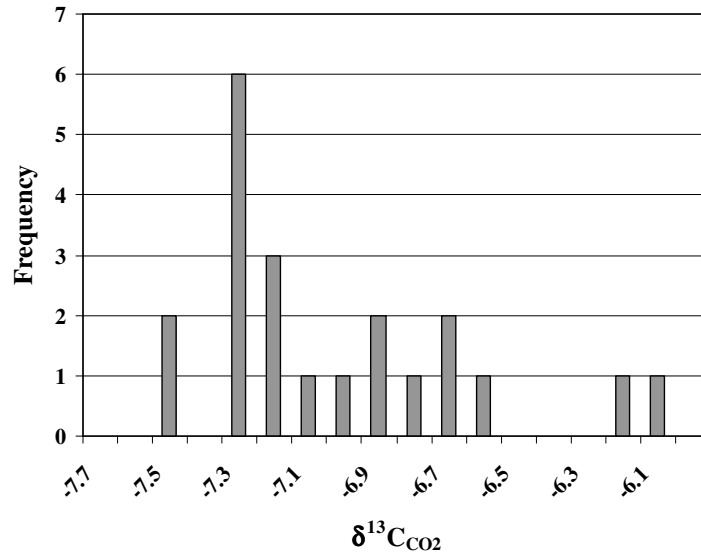


Figure 2.4-6 Histogram of the $\delta^{13}\text{C}_{\text{CO}_2(\text{g})}$ for the 2006 and 2007 sampling programs and from the analyses of Gilfillan (2006) and Heath (2004). $\delta^{13}\text{C}_{\text{CO}_2(\text{g})}$ analyses show a relatively narrow range from -8.4 to -5.8 ‰ and a skewed distribution towards isotopically light values.

The $\delta^{13}\text{C}_{\text{DIC}}$ calculated from the $\delta^{13}\text{C}_{\text{CO}_2(\text{g})}$ and the measured $\delta^{13}\text{C}_{\text{DIC}}$ do not exhibit a 1:1 relationship (Fig. 2.4-5). During ascent to the surface spring waters degas CO₂ as a result of changes in the ambient pressure. The sampled CO₂ gas represents the weighted average of gas degassed over the whole degassing region, whereas the sampled waters represent the cumulative fractionation effects up until the point of sampling at the surface. $\delta^{13}\text{C}_{\text{CO}_2(\text{g})}$ for the CO₂-springs exhibit a skewed distribution towards lower values (Fig. 2.4-6). This results from a Rayleigh type fractionation of the DIC pool as degassing takes place; with the bulk of the exsolved gas having more negative values, becoming increasingly negative as degassing progresses and occurs at shallower depths. The observed negative correlation in DIC and $\delta^{13}\text{C}_{\text{DIC}}$ during a large-scale eruption of Crystal Geyser fits a Rayleigh fractionation model (of pure CO₂ degassing) to a first order (Assayag et al., 2009), but the narrow range of composition observed and lack of corresponding measurements on the gas phase does not put useful constraints on the initial undegassed fluid composition.

The apparent disequilibrium between DIC and CO₂ maybe due to: 1) the large uncertainty in $\delta^{13}\text{C}_{\text{DIC}(\text{calculated})}$ due to uncertainty in measured pH and the resulting calculation of carbonate speciation; 2) kinetic fractionation resulting from diffusion into growing gas bubbles; 3) Bulk CO₂ gas measurements representing a cumulative composition resulting from degassing over a degassing region as apposed to a true instantaneously degassed values. Constraints on the degree of degassing are important for the accurate characterisation of fluid chemistry and the calculation of mineral saturation state in the fluid.

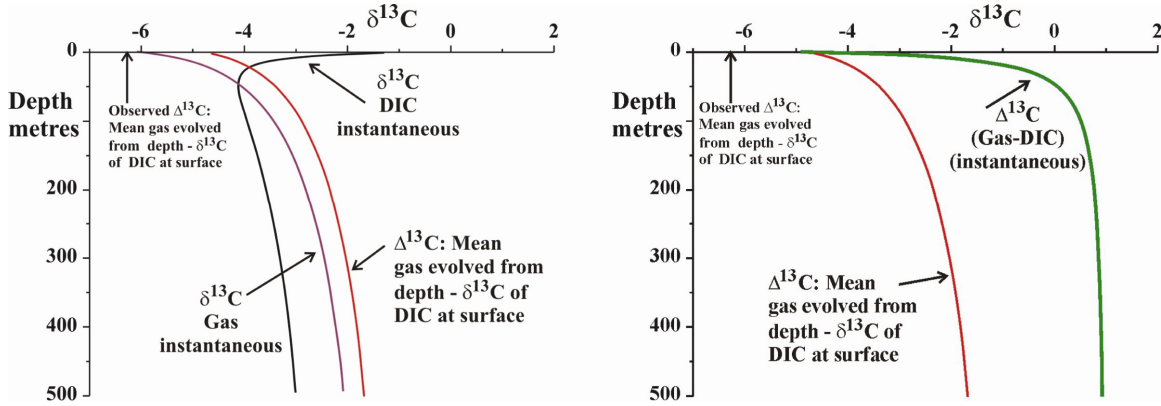


Figure 2.4-7 Profile of the instantaneous carbon isotopic composition of the DIC and of the CO₂ versus depth. This illustrates how the equilibrium carbon isotopic fractionation between the instantaneous DIC and CO₂ changes from a small positive value at greater than 100 m depth to increasingly larger values at depths shallower than 100m and b) that the observed large negative isotopic fractionations are dominated by the degassing processes at shallow depths. From Assayag *et al.*, (2009).

Analysis of carbon isotopic fractionation during ascent of the fluid by Assayag *et al.*, (2009) concluded that degassing must occur at shallow depths <100m inferred from the magnitude of the overall fractionation between DIC and CO₂ gas (Fig. 2.4-7). The average of the fractionation between CO₂(g) and DIC ($\Delta_{\text{CO}_2\text{-DIC}} = \delta^{13}\text{C}_{\text{CO}_2} - \delta^{13}\text{C}_{\text{DIC}}$) for all springs and geyser ranges from -4.8 to -7.5 ‰ with an average of ~ -6.4 ‰. Isotopic fractionation resulting from CO₂ degassing of a solution will be dominated by exchange in both the system H₂CO₃^{*}-CO₂ and HCO₃⁻-CO₂. Given that H₂CO₃^{*} is largely CO₂(aq) fractionation will be dominated by isotopic exchange in the system CO₂(aq)-CO₂(g), at $p\text{CO}_2 > 1$ atm and by HCO₃⁻-CO₂ at $p\text{CO}_2 < 1$ atm (Fig. 2.4-2). This means that the overall fractionation of a degassing solution will change with depth of degassing due to changes in the speciation and thus the magnitude of the observed fractionation is an approximate indication of the depth at which degassing started. The results suggest that in-situ values of $\delta^{13}\text{C}_{\text{CO}_2}$ and $\delta^{13}\text{C}_{\text{DIC}}$ are between 3.0 to 4.0 ‰ and 2.0 to 3.0 ‰ more positive and more negative respectively, depending on the measured surface $\delta^{13}\text{C}_{\text{CO}_2(\text{g})}$ and $\delta^{13}\text{C}_{\text{DIC}}$, and the depth of the host reservoir. Recalculated values of $\delta^{13}\text{C}_{\text{CO}_2(\text{g})}$ are used for further discussion of the carbon dioxide source. This also indicates that variation in the $\delta^{13}\text{C}_{\text{DIC}}$ is overprinted by degassing effects and is thus not an accurate constraint on fluid-rock reactions occurring in the host aquifer.

2.4.3. CO₂ Sources for Springs

Possible geological processes that may generate high concentrations of CO₂ gas in crustal reservoirs include (Cappa and Rice, 1995): 1) gases derived from mantle or magmatic sources; 2) the degradation of organic matter; 3) diagenetic reactions involving clay and carbonate rocks; and 4) thermal decarbonation of carbonate rocks by metamorphic processes.

The $\delta^{13}\text{C}$ values of the CO₂ gas phase emitted by the Green River springs show little spread, ranging from -6.61 to -7.55 ‰ ($1\sigma = 0.29\text{‰}$) (Table 1.). This suggests a common source for all the escaping CO₂, and implies that the flux of the CO₂ gas phase to the surface is sufficient to suppress transport related fractionation of the gas isotopic composition. However, degassing effects during fluid ascent imply a 3 to 4 ‰ fractionation on the original values of $\delta^{13}\text{C}_{\text{CO}_2(\text{g})}$, implying in-situ values in the region ~ -3 to -5 ‰. The $\delta^{13}\text{C}$ of CO₂ is within the compositional range of mantle-derived carbon (-3 to -8 ‰ V-PDB, Wycherley *et al.*, 1999), but is also largely within the range of bulk crustal carbon (-5 to -7 ‰ V-PDB).

Discriminating between magmatic, crustal and biogenic sources of CO₂ is not possible with stable isotopes alone, because the ranges of $\delta^{13}\text{C}$ in magmatic and crustal CO₂ are non-unique (Sherwood Lollar *et al.*, 1997). In contrast, ³He is an unambiguous tracer of magmatic volatiles (Oxburgh *et al.*, 1986), and ⁴He which is derived from radioactive decay of U, Th and K, elements concentrated in the crust, is a tracer of crustal components. Because the rate of He diffusion is relatively low in magmatic/crustal fluids (Ballentine, 1997), magmatic ³He must be carried, or advected, into shallow systems. The carrier fluid is inferred to be CO₂ (e.g. Sherwood Lollar *et al.*, 1997). Differences in their production mechanisms and diffusivities partition ³He and ⁴He into terrestrial reservoirs with different concentrations. Mantle helium is dominated by primordial ³He, with a ³He/⁴He ratio (R) of 1 to 3×10^{-25} and R/R_{air} of 3 to 30. Crustal He, dominated by ⁴He from a decay of U and Th has a radiogenic ³He/⁴He ratio of 1 to 3×10^{-28} or R/R_{air} of 0.007 to 0.04 (Andrews, 1987). The clearest indication of a mantle-derived fluid is therefore shown by the presence of ³He (Ballentine, 1997).

Because He is lost from the atmosphere, with a residence time of approximately 10⁶ years, the concentration of ³He in air is two orders of magnitude smaller than in typical magmatic gases (Oxburgh *et al.*, 1986). Helium is present within the atmosphere at only low concentrations (5×10^{-6} vol/vol at STP; Ballentine *et al.*, 2002). The production mechanisms of crustally sourced CO₂ do not typically introduce additional ³He and as such crustally sourced CO₂ has high CO₂/³He ratios. CO₂-rich groundwaters therefore have CO₂/³He ratios dominated by the CO₂ source, with crustally sourced CO₂ systems having CO₂/³He elevated relative to MORB (CO₂/³He = 1 to 2×10^9).

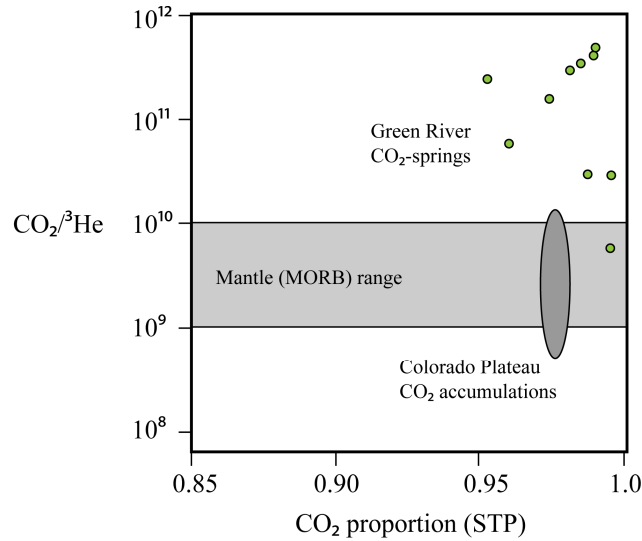


Figure 2.4-8 The majority of the CO₂-springs have CO₂/³He ratios above the MORB range indicating a predominantly crustal CO₂-source (Sherwood Lollar *et al.*, 1997; Ballentine *et al.*, 2002). Also plotted is the data range from the deep CO₂ reservoirs documented by Gilfillan *et al.*, (2006), from McCallum Dome, Sheep Mountain, Bravo Dome, McElmo Dome, Doe Canyon and St John's Dome. All error bars are smaller than printed symbols. Drawn after Gilfillan (2004).

Figure 2.4-8 shows CO₂/³He ratios plotted against CO₂ concentration for all of the major CO₂ gas fields of the Colorado Plateau and the Green River CO₂-springs (Gilfillan, 2004). All of the samples from the major gas fields have CO₂/³He ratios around the MORB range, distinct from the elevated CO₂/³He ratios of at Green River. Many of these samples have elevated ³He/⁴He. This indicates that the CO₂ within all the major CO₂ fields of the Colorado Plateau is dominated by mantle derived CO₂ but implies a predominantly crustal source for the CO₂ at Green River.

³He/⁴He ratios of Gilfillan (2004) for Green River show a small variation from 0.224 to 0.256 Ra and CO₂/³He ratios are significantly elevated relative to MORB. Despite the distinctly crustal CO₂/³He ratios, measured ³He/⁴He values are well above the expected 0.02 Ra of pure crust. This indicates either a small contribution of mantle derived CO₂ (1-15 %; c.f. Wilkinson *et al.*, 2007) diluted by large crustal contributions or the entrainment of atmospherically derived noble gases in the groundwater system. The observed CO₂/³He and ³He/⁴He imply a predominantly crustal source for this CO₂.

Heath (2004) concluded that the CO₂ was sourced in the uppermost Palaeozoic section. Drilling reports from petroleum exploration in the vicinity of Green River document small accumulations of CO₂-rich fluid throughout the stratigraphy, within formations that include the Jurassic Navajo Sandstone, Permian White Rim Sandstone, Honaker Trail Hermosa Formation and within multiple clastic units of the predominantly evaporitic Pennsylvanian Paradox Formation. Of the deeper formations, the Mississippian Leadville Limestone is the most likely CO₂ source, as it possesses a suitable clay and carbonate mineralogy, petrographic evidence of

replacement and breakdown of carbonate to produce a high secondary porosity (Chidsey *et al.*, 2005) and is known to contain accumulations of free phase CO₂ in other regions of the Paradox Basin (Cappa and Rice, 1995). Nuccio and Condon (1996) infer that the Leadville Limestone was heated to ~ 170 °C between ~ 70 and 38 Ma, temperatures thought sufficient to drive decarbonation reactions (e.g. Hutcheon and Abercrombie, 1990).

2.4.4. Hydrology and Fluid Geochemistry

2.4.4.1 Water Sources for CO₂-Springs

Aquifers within the Phanerozoic sequence include the Jurassic Entrada Sandstone, the Jurassic 'N-aquifer' dominated by the Navajo Sandstone but including the Wingate Sandstone and the Kayenta Formation, the Permian White Rim Sandstone and a Palaeozoic aquifer comprising the Lower Pennsylvanian and Mississippian limestone and dolomite formations (Fig. 2.2-2) (Hanshaw and Hill, 1969).

The N-aquifer is the dominant local aquifer and the temperatures of waters in the CO₂-springs and geysers (Table 1) are consistent with their derivation from depths appropriate to the local depth of the Jurassic Navajo Sandstone, assuming a constant thermal gradient of 22.1 °C/km (estimated from local bottom hole temperature measurements) and no conductive cooling as fluids ascend to the surface. The flow rates estimated in Chapter 3 imply a thermal Peclet Number ~ 1 and therefore, that there is limited advection of heat within the Navajo Aquifer where it shallows in the anticline at Green River. Uncertainty on the local heat flow and thermal conductivities (Bodell and Chapman, 1982) and the magnitude of advective heat transport result in temperature estimates for the slightly shallower Entrada Sandstone which overlap those of the Navajo Sandstone. However, the deeper aquifers of the White Rim Sandstone and the Pennsylvanian formations would be significantly hotter (> 40 °C). The similarity of fluid chemistry and isotopic composition, and the constancy of the superposition of fluid temperature with reservoir depths appropriate for the Navajo Sandstone suggest a common source reservoir for all the springs.

2.4.4.2 Reservoir Geology

The Navajo Sandstone, along with the Wingate Sandstone and Kayenta Formation, forms the regionally extensive Lower Jurassic 'N-aquifer', of which the Navajo Sandstone is the most productive unit.

The aeolian Navajo Sandstone in the northern Paradox Basin is fine grained (0.1 to 0.25 mm) and is dominated by quartz (72–86 wt%) and K-feldspar (7–11 wt%) with minor amounts of plagioclase (3–6 wt%) and trace heavy mineral fractions of tourmaline, apatite and rutile (<1 wt%) (Beitler *et al.*, 2005; Bowen, 2004; Cooley *et al.*, 1969; Harshbarger *et al.*, 1957; Parry *et*

al., 2004). Primary quartz and feldspar grains are rimmed with hematite and goethite (Chan *et al.*, 2000) and feldspar grains are altered to illite, smectite and kaolinite (Zhu *et al.*, 2005, 2006). Authigenic illite is disseminated across both feldspar and quartz surfaces. Portions of the feldspar surface are locally altered to kaolinite and a 1–3 μm thick layer of authigenic smectite. Diagenetic pore fillings of kaolinite, illite and smectite occur predominantly in larger pore spaces. Interstitial dolomite and calcite, and quartz overgrowths are present as sporadic cements.

2.4.4.3 *Local Hydrology and Fluid Flow Paths*

The Mesozoic and Permian aquifers are recharged seasonally from precipitation principally in the San Rafael Swell (Hood and Patterson, 1984). The distribution of hydraulic head in wells penetrating the Navajo Sandstone delineates groundwater flow paths from zones of recharge in the San Rafael Swell, southeast towards the centre of the basin, where artesian conditions prevail (Fig. 2.4-9; 2.4-10). Groundwater is subsequently discharged into both the Green and Colorado Rivers (Hood and Patterson, 1984).

Individual flow paths, which map the source of fluid feeding each spring, are taken as down-slope on the potentiometric surface in the Navajo Sandstone from the potentiometric height of the Green River Airport Well, the upstream spring (Fig. 2.4-11). Spring solute chemistries show a progressive change along these flow paths attributed to fluid-mineral reactions (see section 2.5.7). Tritium abundances for measured springs (Table 1) exhibit values within error of zero, providing a minimum age constraint of >60 yrs for the groundwater samples. This precludes significant mixing with shallow, modern groundwater. Fluid flow rates estimated in Chapter 3. imply groundwater transit times between the most up-stream spring (Green River Airport Well) and the most down gradient spring (Chaffin Ranch Geysir) on the order of ~10,000 years.

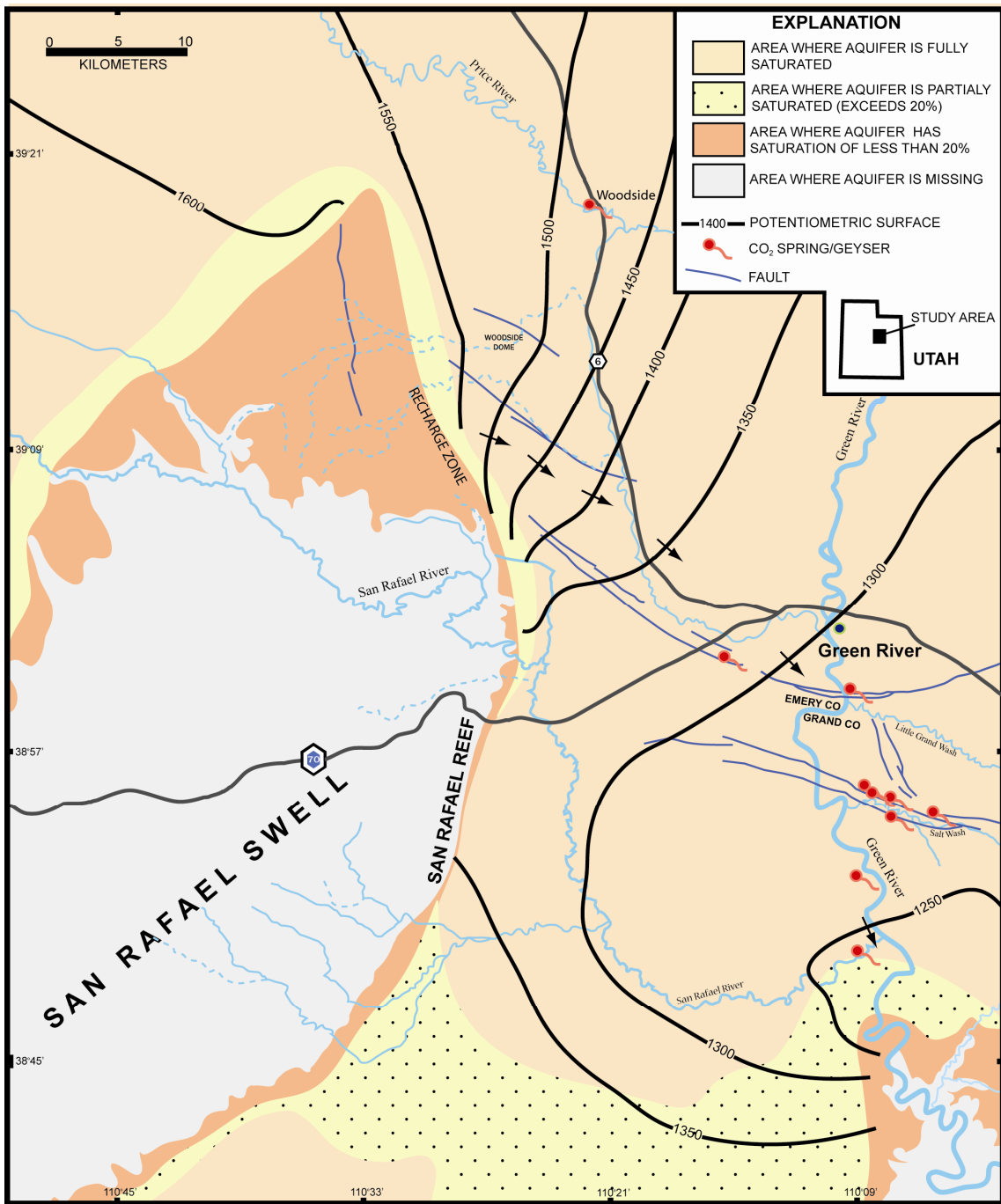


Figure 2.4-9 Map showing the location of CO₂-charged springs, local geological structure and the relative saturation of groundwater within the Navajo Sandstone. Arrows indicate the direction of groundwater flow within the Navajo Sandstone defined by the topology of the potentiometric surface. Modified from Hood and Patterson (1984).

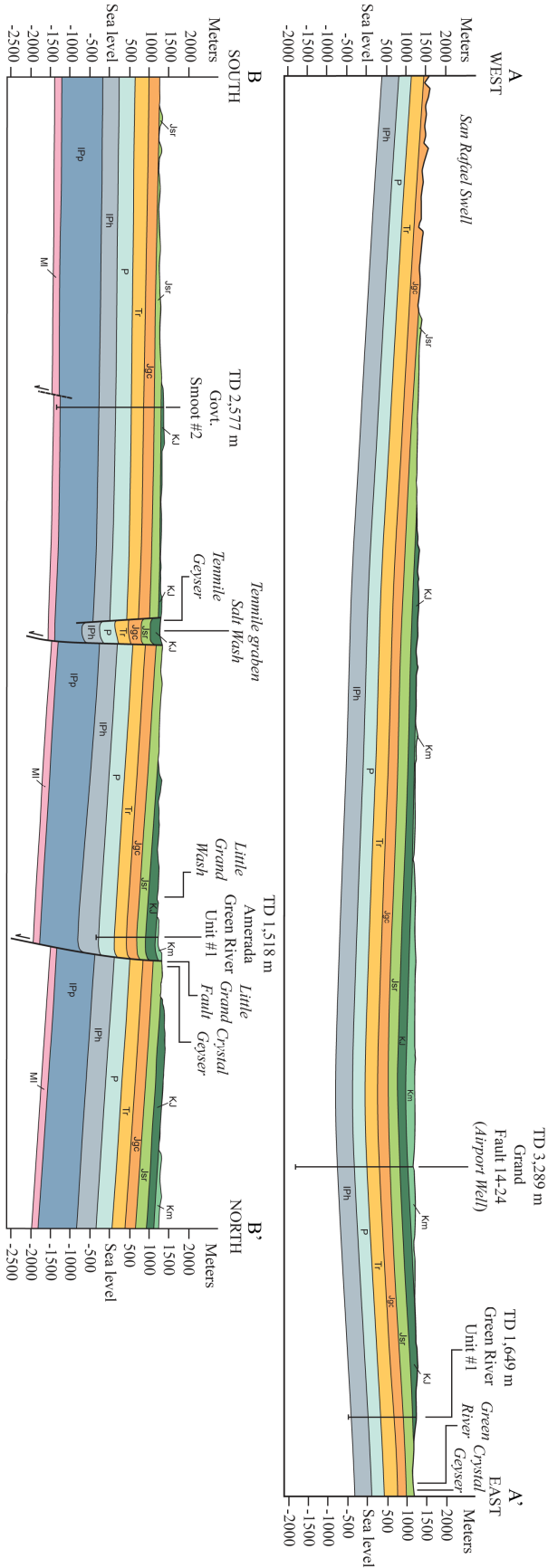


Figure 2.4-10 Cross section through the Phanerozoic stratigraphy from: A-A': Zone of meteoric recharge in the San Rafael Swell to the vicinity of Crystal Geysers and B-B': The axis of the Green River anticline.

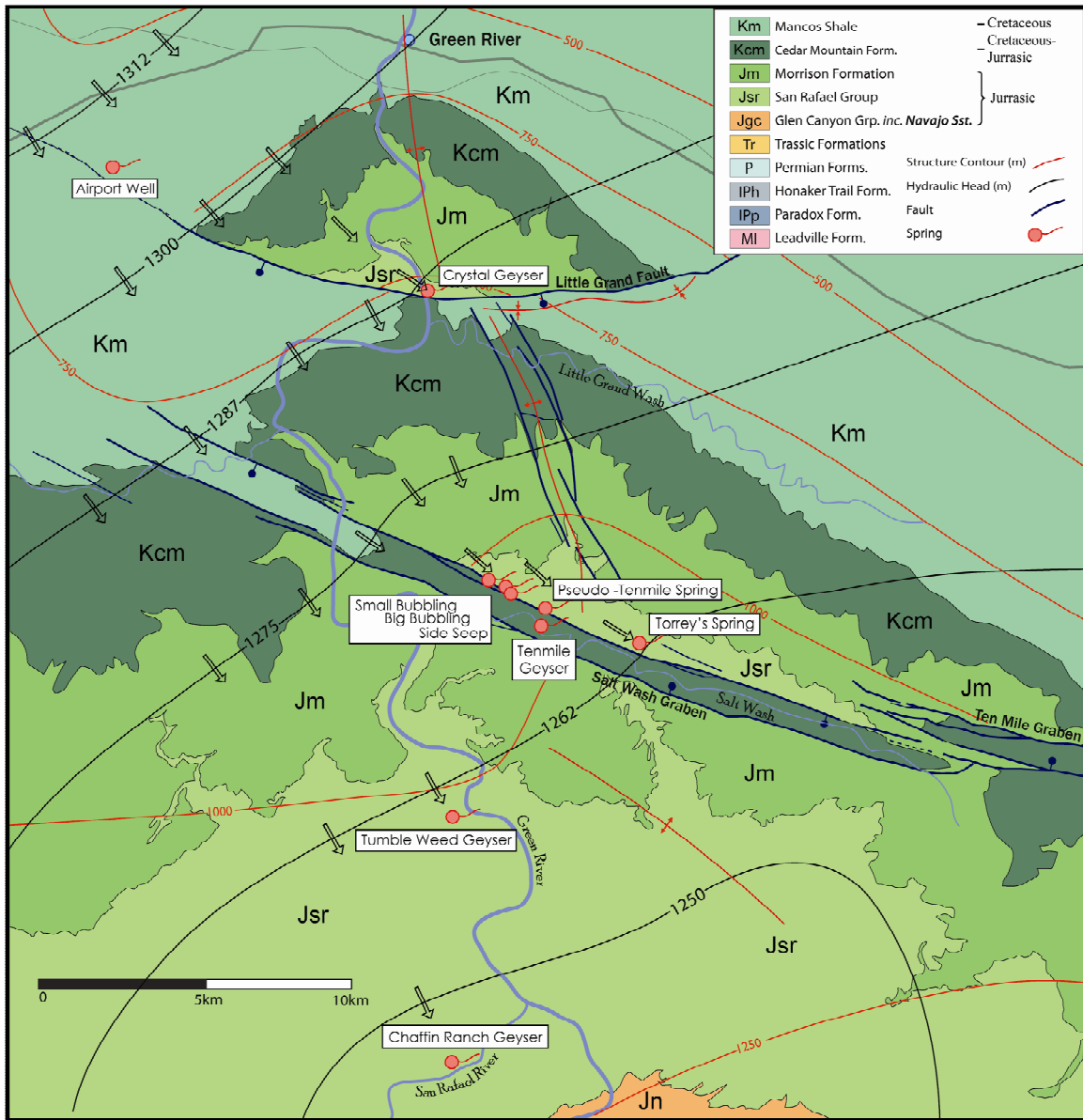


Figure 2.4-11 Map illustrating the relationship between local structure and the potentiometric surface within the Navajo Sandstone. The northerly plunging Green River anticline is transected by the approximately east-west trending Little Grand Wash and Salt Wash fault systems. Flow paths are deflected by the normal faults where throws exceed ~100m. Structure contours are of the top surface of the Navajo Sandstone. Redrawn after Doelling (2002) & Dockrill (2005).

Flow is assumed to be homogeneous and springs are projected up to 6km laterally onto the ~ 30 km flow path from the upstream Green River Airport Well (Fig. 2.4-11 & 2.4-17). Dockrill (2005) assessed sealing mechanisms on the Little Grand Wash Fault and northern fault of the Salt Wash Graben and concluded that cross-fault flow should occur at low throws (<100m), towards the fault tips but that the faults were sealed at higher throws (>100m), towards the axis of the Green River anticline, due to reservoir–non-reservoir juxtaposition and development of a

continuous clay smear. It is probable that the flow path through Crystal Geyser is deflected along the Little Grand Wash Fault and that flow paths are deflected along the northern margin of the Salt Wash Graben. Flow paths to Tumble Weed and Chaffin Ranch geysers pass through the fault tips of the Salt Wash Graben and, on the basis of the analysis of Dockrill (2005), should not be deflected. Below we show that data from the geysers on the north side of the Salt Wash Graben, as well as Ten Mile, Tumble Weed and Chaffin Ranch Geysers can be modelled as a continuous geochemical sequence although the extent to which this results from comparable hydrologies remains untested.

2.4.5. Fluid Geochemistry

2.4.5.1 Origin of the Fluid Isotopic Composition

The consistent $\delta^{18}\text{O}$ and $^{87}\text{Sr}/^{86}\text{Sr}$ ratios of the Green River spring waters suggest a common source for all ten springs (Table 1, Appendix A). The spring waters are initially of the $\text{Ca}^{2+}\text{-Mg}^{2+}\text{-HCO}_3^-$ type, where they flow from the recharge zone to the westerly limb of the Green River anticline (Fig. 2.4-12). The waters then evolve to $\text{Na}^+\text{-HCO}_3^-\text{-Cl}^-$ type as they ascend and cool in the anticline and mix with deeply derived brines.

Regionally, chloride concentrations in the Navajo Sandstone are low (0.1–1mmol/l) (Zhu, 2000), being derived from atmospheric inputs in recharge waters. Halite is not present in the Navajo Sandstone and is thus not a potential source of Cl^- (Zhu, 2005). Elevated chloride concentrations in the Green River springs are attributed to input of basinal brines most probably associated with the inputs of CO_2 .

Heath (2004) shows that the spring waters lie close to the global meteoric water line on a plot of D/H versus $\delta^{18}\text{O}$, and attributed these fluids to a purely meteoric source. We interpret $\delta^{18}\text{O}$ values $\sim 2\text{‰}$ more positive than local Green River surface waters (Mayo *et al.*, 2003) as resulting from mixing between the meteoric source and isotopically heavy brine (Fig. 2.4-13a), (c.f. Wilkinson *et al.*, 2008).

$^{87}\text{Sr}/^{86}\text{Sr}$ ratios (Table 1.) in the Green River spring waters are elevated compared with formation waters from the Navajo Sandstone elsewhere (0.70976 ± 0.0007) (Spangler *et al.*, 1996). Strontium concentration versus $^{87}\text{Sr}/^{86}\text{Sr}$ data (Fig. 2.4-13b) fall along a two component mixing hyperbola between Paradox Formation waters (Spangler *et al.*, 1996), with values close to that of Pennsylvanian seawater (0.7081 to 0.7087, Burke *et al.*, 1982), and a radiogenic end-member comprising silicate minerals in the host aquifer.

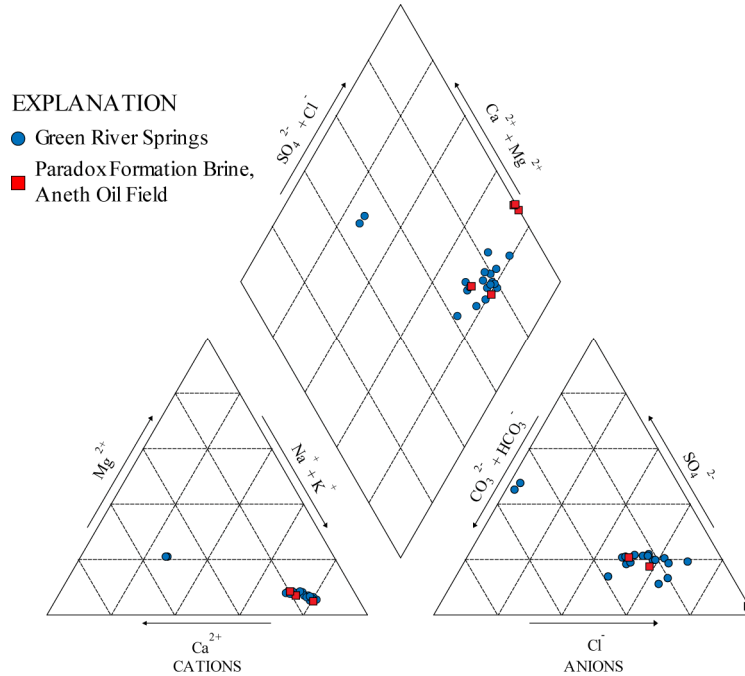


Figure 2.4-12 Piper diagrams for the CO₂-springs and basinal brine from the Paradox formation and Paleozoic Aquifers. Concentrations in mEq L⁻¹.

Assuming that chloride behaves conservatively and is derived solely from brine, the solute chemistry in each spring can be corrected for the brine input:

$$k_c = k_S - \left[\frac{(Cl_S / Cl_B) \cdot k_B}{1 - (Cl_S / Cl_B)} \right] \quad (2.27)$$

where k_c , k_S and k_B are the corrected, spring and brine concentrations (mmol/l) of the k th element, respectively. Cl_S and Cl_B are the chloride concentrations in the spring and the formation brine. This is equivalent to treating brine inputs as an additional phase and allows the quantification of solutes derived from fluid-rock interaction alone (Fig. 2.4-17). Compilations of regional brine analyses are present in Appendix A.

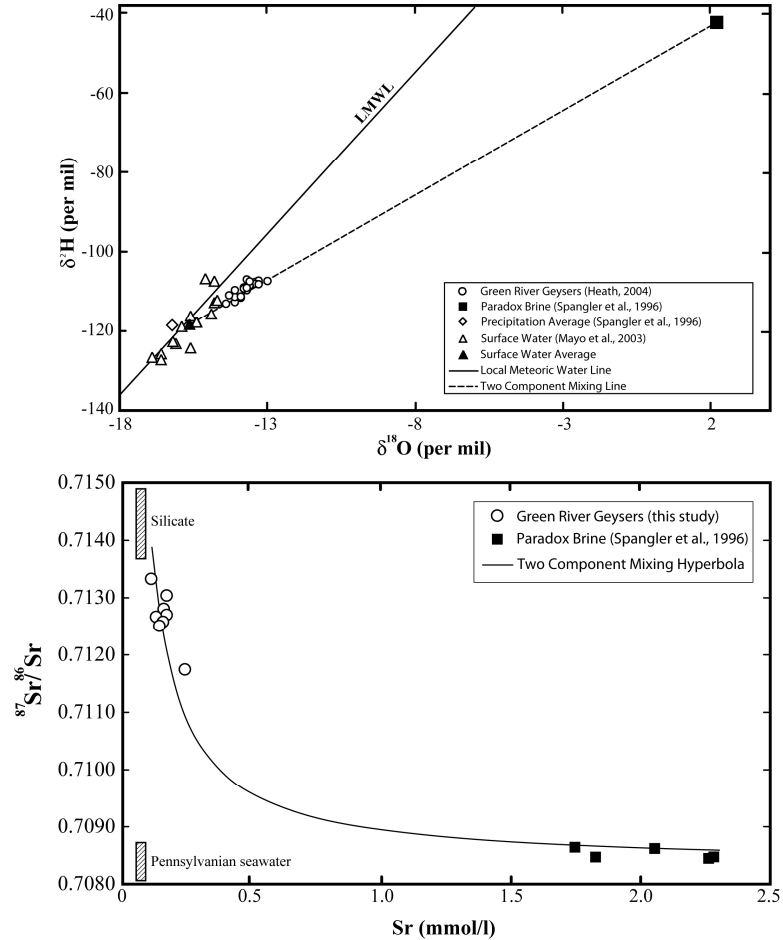


Figure 2.4-13 (a) Cross plot of oxygen and hydrogen stable isotopic compositions of the Green River springs (Heath, 2004), local surface waters (Mayo *et al.*, 2003) and Paradox Formation brine (Spangler *et al.*, 1996). The isotopic composition of the CO₂-charged springs is explained by mixing between isotopically light meteorically derived fluids with a small component of isotopically heavy basinal brine from the Paradox Formation. **(b)** ⁸⁷Sr/⁸⁶Sr versus Sr²⁺ concentration for the CO₂-charged springs and Paradox Formation brine (Spangler *et al.*, 1996), showing mixing of strontium derived from brine with a composition close to that of Pennsylvanian seawater (Burke *et al.*, 1982) and a radiogenic end-member attributed to strontium derived from silicates in the host aquifer (Truini and Longworth, 2003).

2.4.5.2 CO₂ Solubility and transport

Figure 2.4-14 depicts the maximum dissolved CO₂ concentration in pore fluid through the stratigraphy of the Paradox Basin, in the vicinity of Green River. This model assumes a constant porewater temperature from the surface to where this intersects the geothermal gradient at the reservoir top. The local geothermal gradient is calculated as 21.2 °C/km based on bottom-hole temperature measurements from exploration well Pan American 1#, Salt Wash. Fluid salinities are based on measured values for the Navajo Aquifer system (Crystal Geyser water) and on a compilation of published analyses for fluids of the White Rim, Paradox Formation (Spangler *et al.*, 1996) and Paleozoic Aquifer systems. The solubility of CO₂ was determined using the P, T and salinity dependent expressions of Duan *et al.*, (2006). Because of the interplay of increasing

temperature and pressure deeper into the subsurface, the solubility of CO₂ in porefluid has a minimum at the surface and a maximum at between 500 and 900 m depending on the thermal profile and fluid salinities. Below this depth solubility decreases sharply at the transition from dilute meteoric aquifers to brine-rich aquifers with high salinities, due to the salting out effect (Duan *et al.*, 2006) and then continues to decrease slowly due to the effects of temperature. The transport of deeply derived CO₂ in solution from the Paleozoic Aquifer to the shallow White Rim and Navajo Aquifers will be limited by the solubility of CO₂ within the saline Paradox Formation brine – a maximum concentration of ca. 0.8 mol L⁻¹ can be expected in the brine rich formations and ca. 1.6 mol L⁻¹ in the shallower Navajo and White Rim Aquifers. If CO₂ is transported in solution from the Paleozoic Aquifer, exsolution of a free phase is unlikely due to the increased solubility in the shallow aquifers due to salinity, temperature and pressure effects.

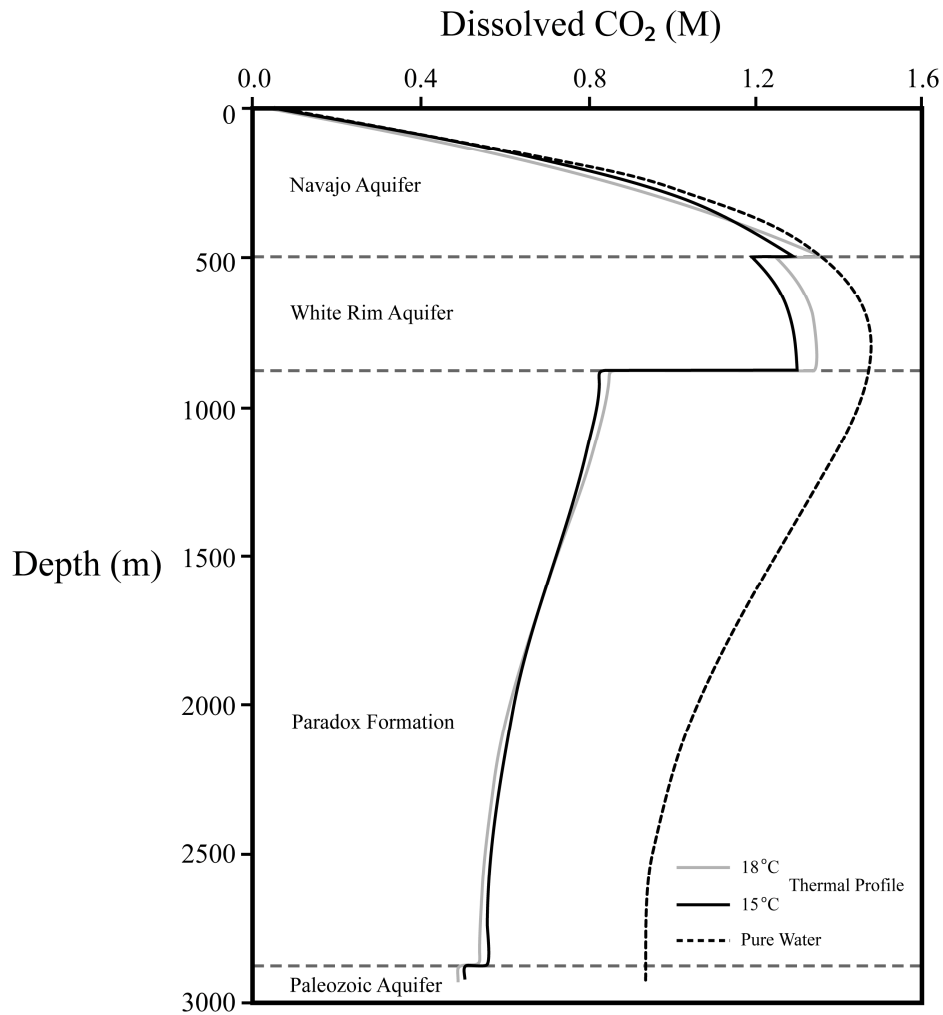


Figure 2.4-14 CO₂ solubility versus depth for a typical profile through the Green River anticline, and for different thermal profiles. See text for method of derivation and details of fluid compositions in the different aquifer systems.

2.4.5.3 Fluid Rock Reaction: Evolution of the Fluid Chemistry

Fluid chemistries of groundwater systems are controlled largely by the hydrolysis of rock forming silicate, aluminosilicate and carbonate minerals and to a lesser extent by the dissolution of halides and sulphates (Drever, 1997). Fluid-rock reactions in groundwater systems are driven by the dissolution and redistribution of CO₂ which promotes mineral dissolution via the production and dissociation of carbonic acid. Shallow and/or young groundwater systems are dominated by reactions involving carbonate minerals, when present, due to the high solubility and rapid dissolution kinetics of these minerals. When there are no carbonates present, or saturation with respect to carbonate phases is reached, the ion chemistry will be controlled by the dissolution of silicate and aluminosilicate minerals. Determination of groundwater saturation state using PHREEQC (Parkhurst and Appello, 1999) indicates that groundwaters are undersaturated with respect to the predominant silicate minerals in the host aquifer; K-feldspar, albite and anorthite, and are oversaturated with respect to typical weathering product aluminosilicate minerals kaolinite, smectite and illite. Groundwaters are oversaturated with calcite and dolomite.

Silicate mineral dissolution reactions consume CO₂ and increase the dissolved cation and bicarbonate concentrations. Alkalinity is therefore frequently invoked as a variable which reflects the extent of fluid-rock interaction (Plummer *et al.*, 1983) because it can increase concurrently with the base cations (Ca, Mg, Na, K) that are released during mineral dissolution. The stoichiometry of typical mineral dissolution reactions implies that alkalinity should show a 1:1 relation with respect to Ca + Mg + Na + K in equivalent when the water chemistry is regulated by the weathering of silicate and/or carbonates. Dissolution of halide and sulphate minerals does not affect alkalinity (Garrels and Mackenzie, 1967). The 1:1 relationship between the total base cations and alkalinity observed in the fluid chemistry of the CO₂ springs (Fig. 2.4-15) indicates that the dissolved solutes, in excess of those derived from brine inputs, are sourced predominantly from the dissolution of silicate and/or carbonates.

The fluid chemistry exhibits a systematic increase in Na⁺, K⁺, Ca²⁺, Sr²⁺, Al³⁺ and ⁸⁷Sr/⁸⁶Sr along the flow path attributed to feldspar dissolution (Fig. 2.4-17). In general, DIC and alkalinity increase down stream from Green River Airport Well due to the progressive addition of CO₂ to the fluid along flow and the consumption of CO₂ and H⁺ during silicate hydrolysis.

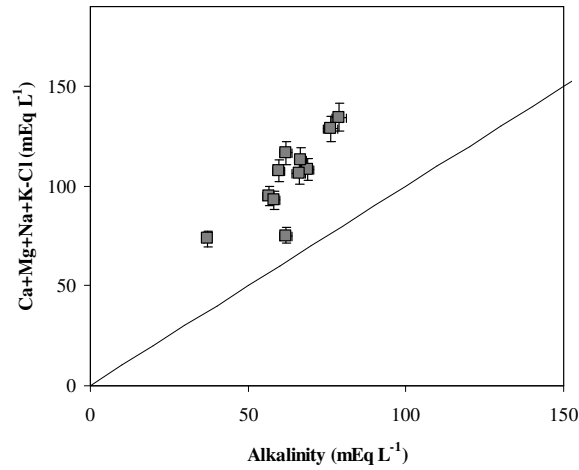


Figure 2.4-15 Cross plot of field alkalinity versus the sum of the base cations corrected for brine derived N⁺ and K⁺ by subtraction of Cl⁻.

⁸⁷Sr/⁸⁶Sr is highest for the most up gradient spring, Green River Airport Well, which is devoid of brine inputs. ⁸⁷Sr/⁸⁶Sr decreases to Crystal Geyser and Small Bubbling Spring reflecting brine inputs close to the site of these springs. ⁸⁷Sr/⁸⁶Sr and Sr²⁺ then increase progressively down stream reflecting increased proportions of silicate derived Sr²⁺ in the fluid. This trend mirrors that observed for other silicate derived components. Tenmile Geyser lies off this trend in both ⁸⁷Sr/⁸⁶Sr and Sr²⁺ reflecting the high proportion of Sr²⁺ rich, low ⁸⁷Sr/⁸⁶Sr brine in this spring. On a plot of 1/Sr versus ⁸⁷Sr/⁸⁶Sr the spring waters down stream of Small Bubbling Spring form an array reflecting increasing quantities of silicate derived Sr²⁺ with increasing groundwater age and degree of fluid rock interaction (Fig. 2.4-16).

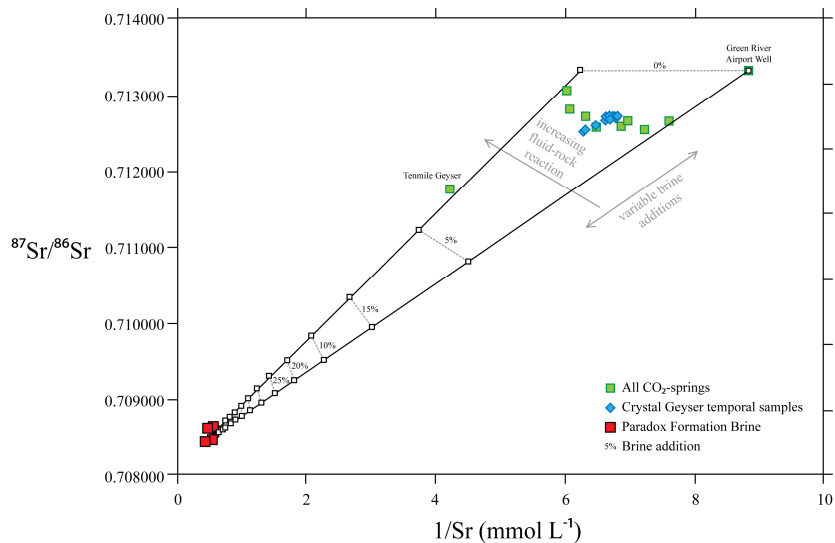


Figure 2.4-16 Cross plot of 1/Sr versus ⁸⁷Sr/⁸⁶Sr illustrating the effects of both fluid mixing and fluid-rock reaction on the composition of the groundwater.

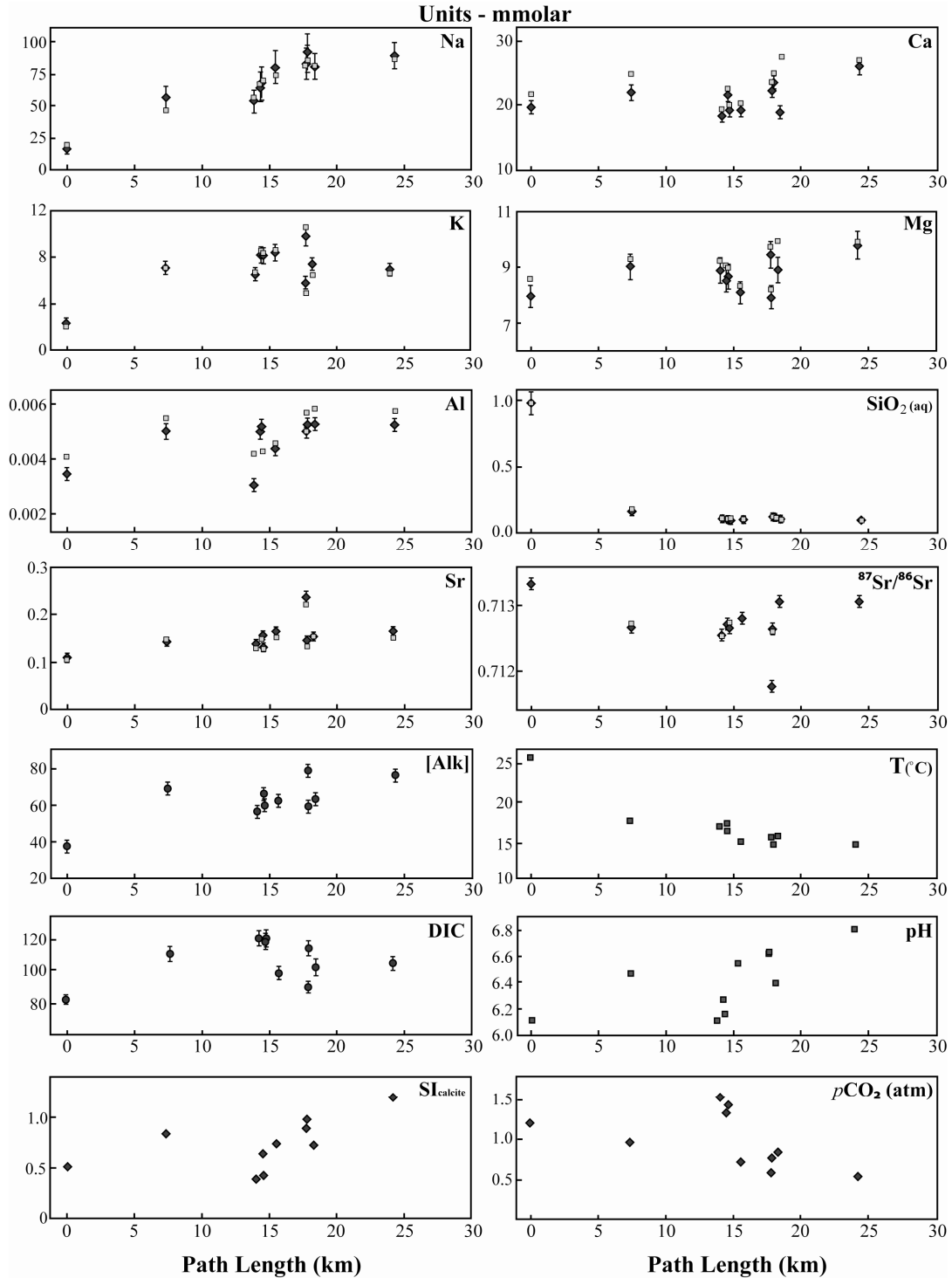


Figure 2.4-17 Solute chemistry versus distance along the modelled flow path. Little Grand Fault and the northern fault of Salt Wash Graben are located approximately 8 and 14 km along the flow path, respectively. Trends in the data are discussed in the text. Concentrations of N^+ and K^+ are corrected for brine additions. Na^+ and K^+ error bars are uncertainty after correction for brine inputs (Appendix A) and analytical uncertainties for all other solutes. For cations and $^{87}\text{Sr}/^{86}\text{Sr}$ both 2006 and 2007 data sets are presented. Values are generally within the measured uncertainties adding validity to the trends and suggest spring chemistries are temporally invariant. (DIC = Dissolved Inorganic Carbon, [Alk] = Alkalinity (mEq/l)).

The primary Mg²⁺ source is diagenetically early dolomite cement ubiquitous to aeolian Jurassic sediments of the Paradox Basin (Desborough and Poole, 1992). Mg²⁺ initially increases during the earliest portions of the flow path, interpreted to reflect dissolution of dolomite. Increases in Mg²⁺ along various portions of the flow path are matched by relative increases in Sr²⁺ and decreases in ⁸⁷Sr/⁸⁶Sr, which reflect Mg²⁺ liberation from dolomite dissolution. Further along flow Mg²⁺ concentrations are variable suggesting its concentration is largely regulated by precipitation of secondary weathering products.

The SiO₂ content decreases sharply as fluid flows from the Green River Airport Well, which samples deeper, warmer (27°C), fluids on the NE limb of the Green River anticline, to springs along the crest of the anticline which consistently sample cooler fluids (16–18°C). On the projected profile (Fig. 2.4-17), pH shows a minimum at Green River Airport Well and increases to Crystal Geysers, decreases to Small Bubbling Spring and then increases at a decreasing rate in geysers downstream of Small Bubbling Spring. This is interpreted to reflect injection of CO₂ at, or upstream, of Green River Airport Well and near Small Bubbling Spring on the northern margin of the Salt Wash Graben. The downstream increase in pH is interpreted to reflect progressive neutralization of this acidity by dissolution of silicate minerals.

2.4.5.4 CO₂ Degassing: In-situ DIC and pH

The measured pH and DIC may not directly reflect the in-situ values of these quantities if extensive CO₂ degassing has taken place as fluids ascend to the surface. Elucidation of the true in-situ values of these quantities is important for the interpretation of the fluid-rock interaction histories of these groundwaters and for the correct determination of mineral saturation state. Without direct measurement of the fluid and gas flux in each spring or isotopic constraints on the degassing process (from for example an inert tracer such as noble gases) it is impossible to precisely constrain the degree of CO₂ degassing in individual springs. As has previously been discussed (section 2.4.2.2) stable isotopic constraints imply degassing takes place in the shallower portions of each spring. This implies that saturation with respect to CO₂ in the ascending fluid is not reached until some finite depth (unless fluid velocities are very fast relative to the critical overstep in saturation required for bubble nucleation and growth) and that fluids are not saturated with CO₂ at reservoir conditions. However, the in-situ solubility of CO₂ at the site of each spring is a readily calculable quantity and provides a maximum constraint on the degree of CO₂ degassing experienced by each spring.

Calculation of the maximum in-situ CO₂ solubility for each spring was made using the model of Duan *et al.*, (2006) and analyzed fluid chemistries, at reservoir depths estimated from the fluid emanation temperature or from well constraints, where available. In-situ pH, SI_{cc} and pCO_2 were then calculated in PHREEQC (Parkhurst and Appello, 1999) using the modeled DIC,

analyzed water compositions and field alkalinity (Fig. 2.4-18). Measured values of alkalinity provide an important constraint on in-situ pH and calcite saturation, being unaffected by the degassing process. If alkalinity of the groundwaters was controlled purely by equilibria in the carbonate system (i.e. by equilibrium between CO₂(aq), HCO₃⁻ and calcite) the decrease in the modeled CO₂ solubility with distance along the flow path would impose a decrease in alkalinity also. This is not observed in the field measurements and thus alkalinity, and subsequently pH, must be elevated by progressive fluid-rock reaction along the flow path. The trends in in-situ DIC and pH with distance along the flow path mirror those observed in the measured values of these quantities. These calculated CO₂ solubilities are a maximum for individual springs. Whilst the actual in-situ CO₂ concentrations maybe somewhere close to, or below saturation this provides an upper limit on the degree of CO₂ degassing experience by each spring (Table. 2.4-1) and a minimum possible value for in-situ pH. Importantly, elevated CO₂ concentrations at the measured values of alkalinity lower mineral saturation in the fluid through a reduction in pH (Fig. 2.4-18). However, absolute changes in in-situ pH remain a result of progressive fluid-rock reaction and pH neutralization through hydrolysis reactions.

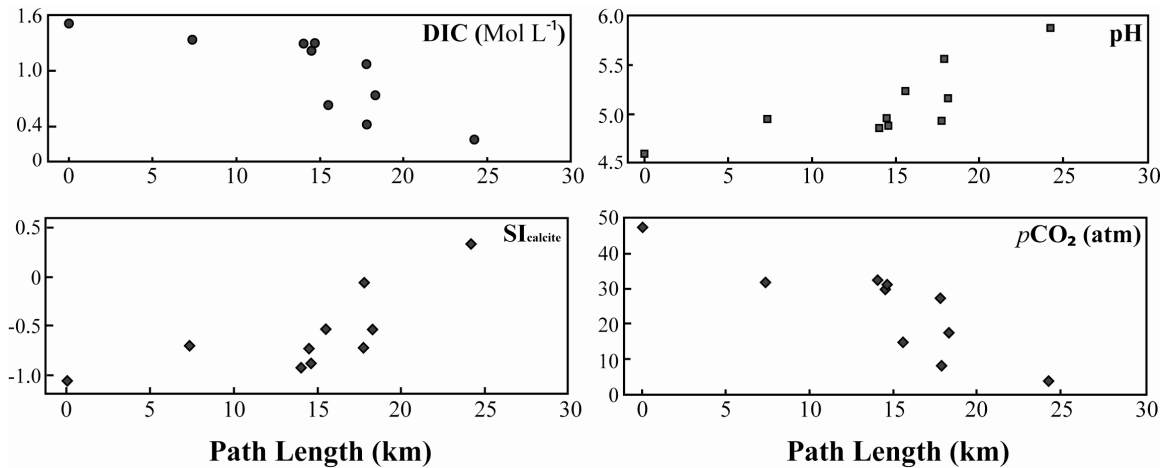


Figure 2.4-18 In-situ DIC, pH and $p\text{CO}_2$ and the resulting SI_{cc} calculated using the Duan *et al.*, (2006) CO₂ solubility model and PHREEQC.

Well	Modelled DIC	Measured DIC	% Degassed
	mmol L ⁻¹		
Crystal Geyser	1334	107	92
Torreys Spring	411	112	73
Tenmile Geyser	1079	83	92
Pseudo-Tenmile Geyser	617	93	85
Chaffin Ranch Geyser	239	100	58
Green River Airport Well	1537	76	95
Big Bubbling Spring	1215	116	90
Small Bubbling Spring	1298	119	91
Side Seep Big Bubbling	1288	119	91
Tumble Weed Geyser	737	98	87

Table 2.4-1 Measured DIC versus DIC calculated for CO₂-saturation at reservoir depth, and the implied degree of CO₂ loss through degassing.

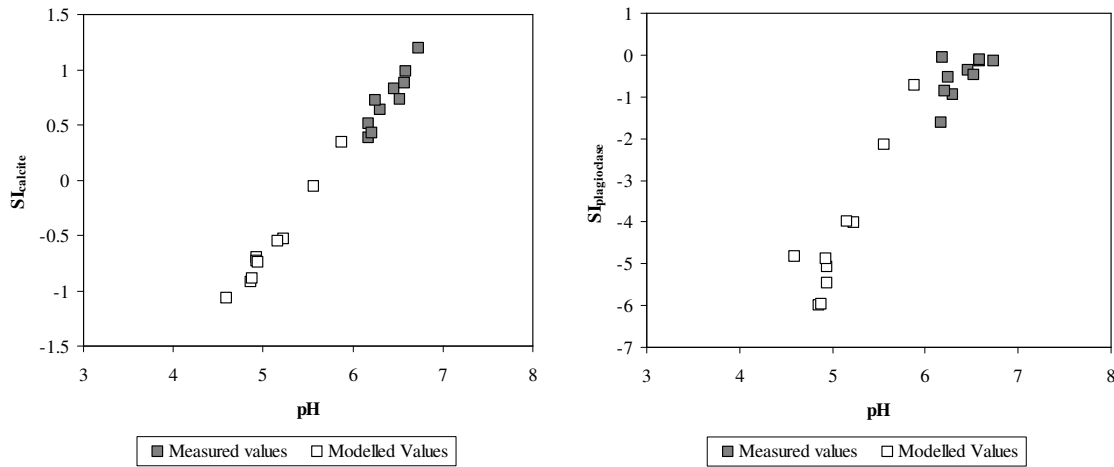


Figure 2.4-19 Calcite and plagioclase saturation indices for the measured spring compositions (black squares) and the compositions recalculated for CO₂ saturation in the host reservoir (open symbols).

2.4.6. Thermodynamic Constraints on Fluid-Rock Reaction

Although a weathering process must be regarded as a nonequilibrium process, a common approach to obtain information on the regulation of natural water composition is through equilibrium calculations. In principle this approach is valid since an irreversible pathway as a whole may be seen as a series of consecutive reactions each of which is in equilibrium with the next (Wernberg, 1998). Besides their relative simplicity, the equilibrium models always show the direction towards which the system is striving.

One of the most common applications of equilibrium models is to relate analysed concentrations of different species to stability diagrams of some selected minerals. If the analysed species are approximately located along the boundary of two different phases, these phases are interpreted as concentration controlling. In order to define the different equilibrium model

systems (Figs. 2.4-20 to 2.4-23) a certain number of chemical species, i.e., components, were chosen (see Ingri, 1978). These components, H⁺-SiO₂(aq)-Al³⁺-Na⁺-K⁺-Mg²⁺-Ca²⁺-H₂CO₃, are the minimum number of chemical species required to describe the composition of all phases and solute species (after Marini, 2007). H₂O is not considered since its activity is set to unity in the calculations. The anions Cl⁻ and SO₄²⁻ are not considered since they are not included in the silicate minerals.

It should be noted that the application of equilibrium constants of silicate minerals to natural water model systems is associated with some difficult problems. First, the equilibrium constants are usually not experimentally obtained but extrapolated using data (e.g. heat capacities, entropies) from elevated temperatures. In some cases even the thermodynamic data at elevated temperatures are estimated. Secondly, the silicate phases occurring in nature are not idealized pure phases, but instead solid solutions are ubiquitous. Thus inferences about controlling reactions in groundwater systems based on activity diagrams are a general guide at best. The superposition of groundwater composition outwith a specific mineral field does not always imply that that mineral may not form or be an important buffer of composition.

The concentration of dissolved silica, derived from the dissolution of silicate minerals, is controlled by equilibrium with an amorphous silica phase in the majority of springs (Figs. 2.4-20). Theoretically dissolved silica may be either controlled by kinetic factors during the dissolution of silicate minerals or by precipitation of secondary minerals. It has been noted in several studies (e.g. Barnes and Hem, 1973; Paces 1978) that secondary silica formation in low temperature groundwaters typically involves amorphous forms of silica, with variable solubilities (between chalcedony and true amorphous silica), rather than direct precipitation of quartz. Although, tentatively the dissolved silica may be controlled by a more soluble silica phase or by the transformation of K-feldspar and smectite to illite at higher temperatures (Aagaard and Helgeson, 1983).

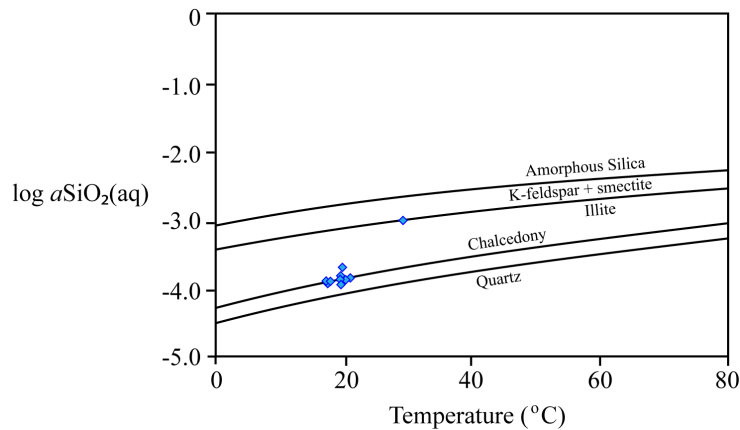


Figure 2.4-20 The $a_{\text{SiO}_2(\text{aq})}$ as a function of temperature showing the superposition of measured values with the stability boundaries for chalcedony (for the low temperature springs) and for the reaction of K-feldspar and smectite to illite for Green River Airport Well.

Kaolinite and Ca-smectite are the dominant stable clay minerals (Fig. 2.4-21 to 2.4-23). Equilibrium with the aforementioned silica phases maintains most groundwater samples within the kaolinite stability field. Al³⁺ concentrations are essentially independent of pH suggesting a non equilibrium control on this species. Because $a\text{SiO}_2(\text{aq})$ is fixed by the precipitation of an amorphous silica phase, kaolinite will not regulate the dissolved Al³⁺ concentration (Deutsch, 1997) and its concentration will be regulated by the dissolution of silicate minerals.

Groundwater composition trajectories are from the stability field of smectite as waters at moderate temperature flow from depth up the NW-limb of the Green River anticline (Fig. 2.4-21). Accumulation of base cations and attenuation of pH as the fluids ascend induces trajectories towards the stability field of the dissolving silicate minerals (K-feldspar and plagioclase). Cooling of the fluid results in a decrease in solubility of the silica phase and results in a decrease in $a\text{SiO}_2(\text{aq})$, moving the fluids into the stability field of kaolinite.

A second introduction of CO₂ further along the flow path suppresses silicate saturation in the fluid and they transpose vertically in $a\text{K}^+/\text{aH}^+$, $a\text{Na}^+/\text{aH}^+$, $a\text{Ca}^{2+}/(\text{aH}^+)^2$, $a\text{Mg}^{2+}/(\text{aH}^+)^2$ compositional space. Further dissolution of silicate minerals drives compositions back towards the silicate mineral stability fields. The groundwaters are oversaturated with respect to calcite and therefore secondary calcite formation is thermodynamically favourable (Fig. 2.4-24). However, numerous studies (e.g. Dreybrodt *et al.*, 1992; Herman and Lorah, 1987, 1988; Lorah and Herman, 1988; Michaelis *et al.*, 1985; Segnit *et al.*, 1962; White, 1997) show that calcite does not precipitate instantaneously at the point of saturation. Precipitation requires a finite supersaturation because of activation barriers to calcite nucleation and crystal growth (White, 1997). Activation barriers may be accentuated by calcite inhibitor ions, e.g. Mg (Berner, 1975; Bischoff, 1968; Pytkowicz, 1965), or the presence of organic matter (Berner, 1975; Raiswell & Fisher, 2004). In most circumstances this implies a saturation index (SI_{CC}) of +0.5, although Dreybrodt *et al.* (1992) suggest that saturation indices of at least +1.0 are required. The measured spring compositions fall within this +0.5 to +1.0 range. $p\text{CO}_2$ recalculated for reservoir CO₂ saturation (section 2.4.5.4) displaces SI_{CC} to values of undersaturation in the upper portions of the flow path, moving to saturated to moderately saturated in the later portions of flow.

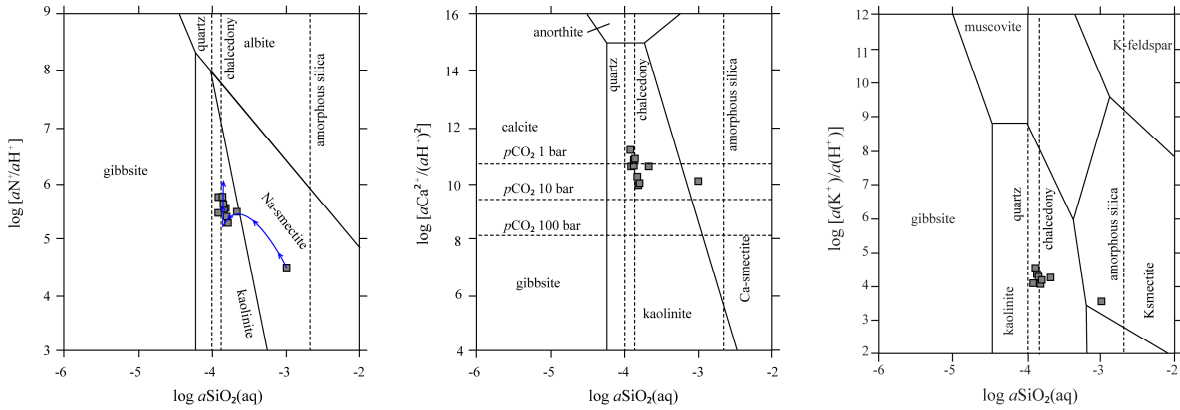


Figure 2.4-21 Activity-activity diagrams for Na⁺, Ca²⁺ and K⁺ at 25 °C for the CO₂-springs (modified after Helgeson *et al.*, 1969), showing generalized mineral stability boundaries assuming that the activity of aqueous SiO₂ is fixed by equilibrium with chalcedony. Blue path is the generalized trajectory for the evolution of the fluid along the length of the flow path. Lower in-situ pH would depress data points to lower values of log(aX/aH⁺).

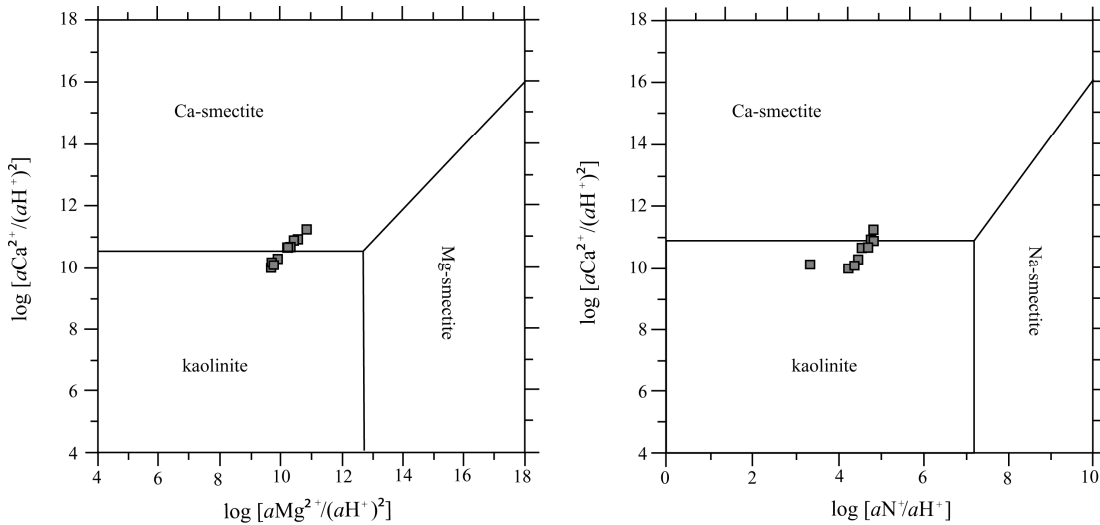


Figure 2.4-22 Alumino-silicate phase stability diagrams for Na⁺, Ca²⁺ and Mg²⁺ at 25 °C. Approximately linear correlations with slopes of 1:1 and 2:1 are characteristic of groundwater systems where Na⁺, Ca²⁺ and Mg²⁺ aqueous activities are regulated by silicate dissolution reactions (Helgeson, 1969, 1970; Norton, 1974). Kaolinite and a Ca-rich smectite are the most thermodynamically favored reaction products.

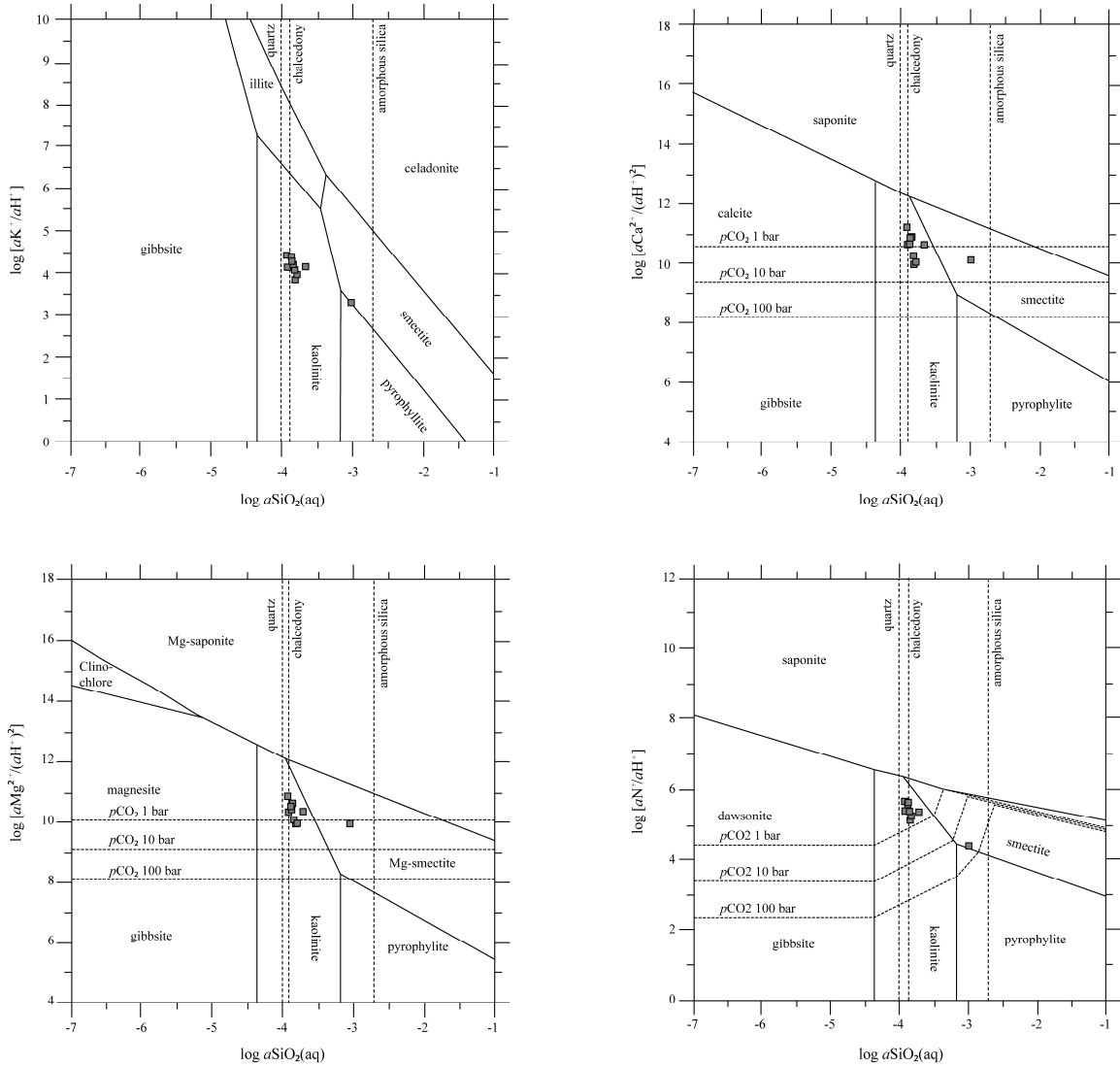


Figure 2.4-23 Aluminosilicate phase stability diagrams at 25 °C for all the potential low temperature reaction products (modified after Marini, 2007).

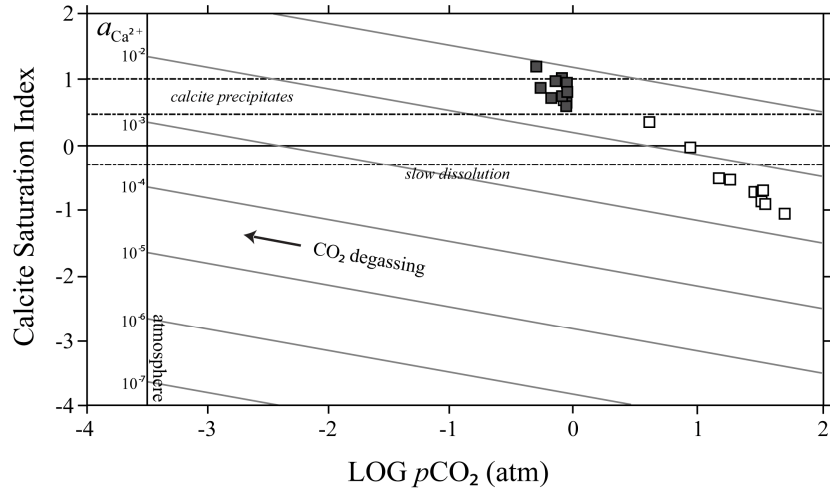


Figure 2.4-24 Calcite saturation index as a function of $p\text{CO}_2$ for measured CO_2 -spring water analyses (black squares) and for the modelled in-situ values (open symbols). The solid horizontal line at $SI_{cc} = 0$ describes water in equilibrium with calcite, while the dashed horizontal lines indicate kinetic thresholds for dissolution and precipitation (White, 1997). Vertical lines labeled ‘atmosphere’ represent $p\text{CO}_2$ at sea level (1 atm total pressure).

2.4.7. Redox Conditions

Groundwaters typically contain Fe concentrations in the region of $5 \mu\text{mol L}^{-1}$ (Drever, 1997) but values as high as $2000 \mu\text{mol L}^{-1}$ have been reported in reducing groundwater systems (Deutsch, 1997) due to the increased solubility of Fe phases in reduced and acidic fluids (e.g. Welham et al., 2000). Analysed spring waters have Fe concentrations in the range 60 to $270 \mu\text{mol L}^{-1}$ and Mn concentrations in the range 2 to $30 \mu\text{mol L}^{-1}$.

Measured Eh values for spring waters are in the range 6 to -42 ± 3 mV, indicating that the groundwater system is in a reduced state and that Fe and Mn are predominantly present in 2+ oxidation state (Fig. 2.4-25a). Superposition of measured Eh, pH and $a_{\text{Fe}^{2+}}$ indicate that dissolved iron concentrations are largely controlled by equilibrium with an iron oxide phase (Fig. 2.4-25b) with a solubility close to that of hematite or goethite (see Appendix C for a complete discussion) via the reductive dissolution reaction at acidic pH:



or



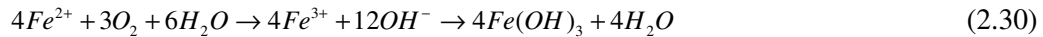
It should be noted that various authors suggest caution in using Eh to quantify redox condition (e.g. Lindberg and Runnells, 1984). The difficulty in interpreting redox from Eh measurements results from using an equilibrium approach to describe a highly dynamic system (James and Bartlett, 2000). Eh is a simple measure, but it gives at best only qualitative assessment of water redox conditions because the Pt electrode may not respond to many important redox couples

(Lovely and Goodwin, 1998). Thus, a wide range of Eh has been observed for the same redox couple and, as a result, several redox reactions may be relevant within the same Eh range (Lovely and Goodwin, 1998).

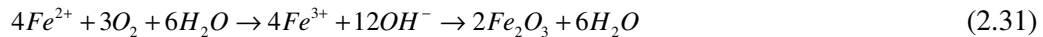
In the absence of soluble phase redox couples such as SO₄²⁻-H₂S or CO₂-CH₄ groundwater redox reaction potential is largely a function of the oxygen fugacity of the fluid (Drever, 1997).

Equilibrium redox potentials for the SO₄²⁻-H₂S and CO₂-CH₄ redox couples are in the region of 0 to -200 mV and -200 to -500mV, respectively (Drever, 1997). Dissolved oxygen concentrations typically decrease within increasing depth and groundwater age (e.g. Edmunds, Miles and Cook, 1984; Lin-Hua and Atkinson, 1985). This is largely due to the interaction of the groundwater with organic rich sediments, reduced mineral phases and bacterial activity in the subsurface (Drever, 1997). Gas compositional analyses of Heath (2004) suggest that these groundwaters are largely free of dissolved CH₄ or H₂S. However, circumstantial evidence in the form of a detectible odour of H₂S during large-scale eruptions of Crystal Geyser suggests that dissolved H₂S at least, may be present in small quantities in these groundwaters. This suggests that the groundwater redox reaction potential is largely controlled by the dissolved oxygen content of the fluid (and possibly by the presence of trace H₂S), whilst the measured redox potential is determined by the Fe³⁺/Fe²⁺ redox couple.

Effused spring water interacts with the atmosphere accumulating dissolved oxygen such that Fe moves from the ferrous to ferric state and as a result of the change in relative solubility is removed from solution:



or



Fe is precipitated as goethite or hematite. Reprecipitated Fe imparts a distinctive ochre colour to the precipitated carbonate in travertines.

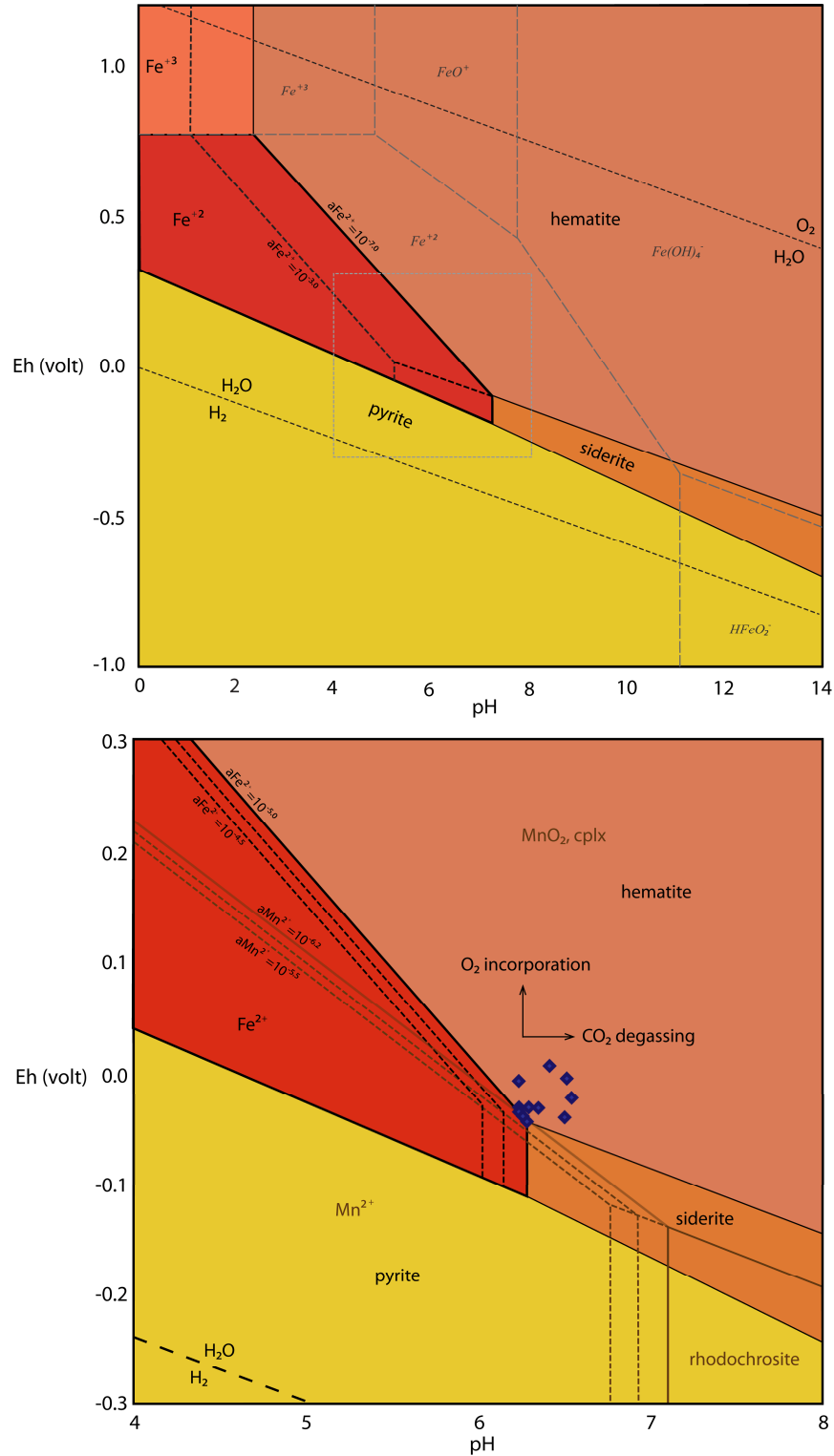


Figure 2.4-25 a) Equilibrium phase diagram, calculated using CHNOSZ (Dick, 2008), for iron oxide-hydroxides and sulphides in the system FeCSOH and MnCSOH at 18°C; $a_{\text{CO}_2} = -1.4$, $a_{\text{S}_{\text{TOT}}} = -2.4$ and $a_{\text{Fe}_{\text{TOT}}}$ at -3 and -7. b) As above but including equilibrium boundaries for Mn-oxides and aqueous species, and data points for the measured values of Eh and pH for each spring. Some scatter in the data is attributed to CO₂ degassing and the incorporation of atmospheric O₂ in the surface layers of the spring waters.

2.4.8. Time Series Fluid Chemistry: Crystal Geysers

Modern eruptions of Crystal Geysers exhibit a bimodal pattern of size and frequency with short duration (~20 minutes), low flux (~0.17 kg/sec CO₂) eruptions occurring approximately every 8 hours and large explosive eruptions (~4.2 kg/sec CO₂) occurring every 22 hours, lasting on average 115 minutes (Gouveia and Friedmann, 2006).

Time series fluid chemistry from Crystal Geysers exhibits two distinct compositional patterns which are related to changes in the style of fluid and gas effusion (Fig. 2.4-26). During the build-up period to a large-scale eruption small-scale 'bubbling events' occur periodically (five small scale 'bubbling events' occurred during the sampling period, at regular 25 minute intervals) and fluid chemistry evolves towards increasing Na-K-Cl-SO₄ rich and Ca-Mg-Sr-Fe-Mn poor compositions. During a large-scale eruption this trend reverses and the fluid chemistry then changes systemically through the course of the eruption (with the sampled eruption lasting two hour and ten minutes).

The major changes in solute chemistry during this period are a systematic decrease in the Na⁺, K⁺, Cl⁻, SO₄²⁻, δ¹⁸O, DIC, ⁸⁷Sr/⁸⁶Sr and an increase in Ca²⁺, Mg²⁺, Sr²⁺, Fe²⁺, Mn²⁺ and δ¹³C_{DIC}. Systematic changes in Cl⁻ and δ¹⁸O through both portions of the geyser cycle are interpreted to reflect two-component end-member mixing between a saline, isotopically heavy Na-K-Cl-SO₄ type fluid (representing the 'typical' groundwater previously discussed; a mixture of meteorically derived formation fluid and deeply derived Paradox Formation brine) and an isotopically light, dilute Ca-Mg-Sr-Fe-Mn type fluid (representing 'typical' groundwater without addition of brine, similar to that of the fluid expelled from the Green River Airport Well further up the flow path) (Fig. 2.4-17). Cl⁻ versus δ¹⁸O defines a hyperbolic mixing line (Langmuir *et al.*, 1978). This hyperbola lies as a mixing curve between an isotopically light, dilute meteoric end-member and an earlier mixture of dilute meteoric fluid and isotopically heavy, saline brine. Thus, the chemistry changes observed in Crystal Geysers largely represent the dilution of an earlier fluid formed by mixing isotopically light formation fluid and Paradox Formation brine.

Cross plots of major cations and anions versus Cl⁻ define approximately linear trends. Linear trends of decreasing Na⁺, K⁺ and SO₄²⁻ with decreasing Cl⁻ reflect dilution of a high Na/Cl, K/Cl and SO₄/Cl fluid with increasing proportions of a dilute, isotopically light, Mg-Ca-HCO₃⁻ end-member. Approximately linear trends of increasing divalent cation (Ca²⁺, Mg²⁺, Sr²⁺, Fe²⁺, Mn²⁺) concentrations with decreasing Cl⁻ reflect dilution of the pre-eruption water with increasing proportions of the Ca-Mg-HCO₃ end-member. Increase in these cation concentrations reflects that fact that the divalent cation/Cl of the Ca-Mg-HCO₃ end-member are greater than that of the Na-K-Cl type pre-eruption waters.

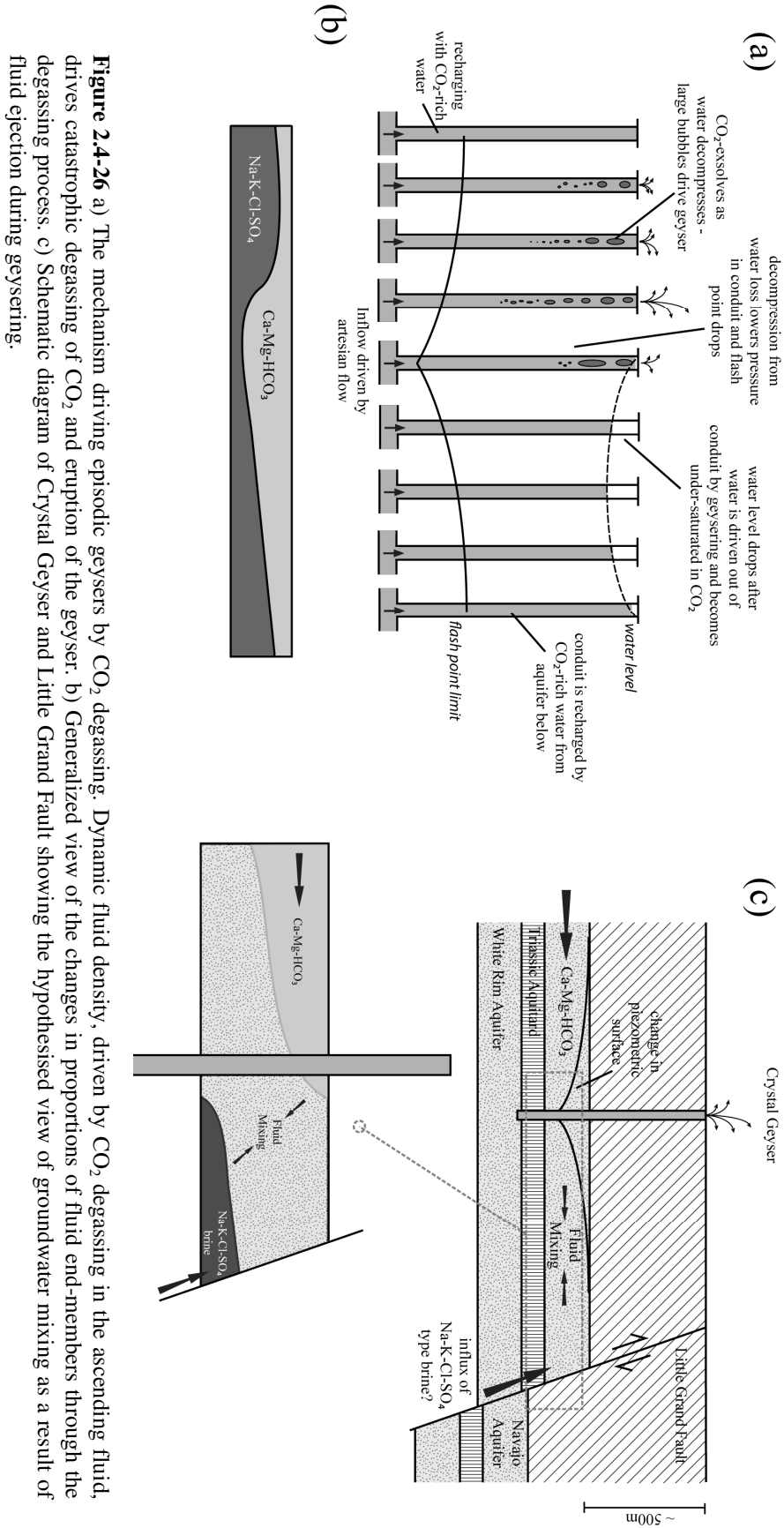


Figure 2.4-26 a) The mechanism driving episodic geysers by CO₂ degassing. Dynamic fluid density, driven by CO₂ degassing in the ascending fluid, drives catastrophic degassing of CO₂ and eruption of the geyser. b) Generalized view of the changes in proportions of fluid end-members through the degassing process. c) Schematic diagram of Crystal Geyser and Little Grand Fault showing the hypothesised view of groundwater mixing as a result of fluid ejection during geysering.

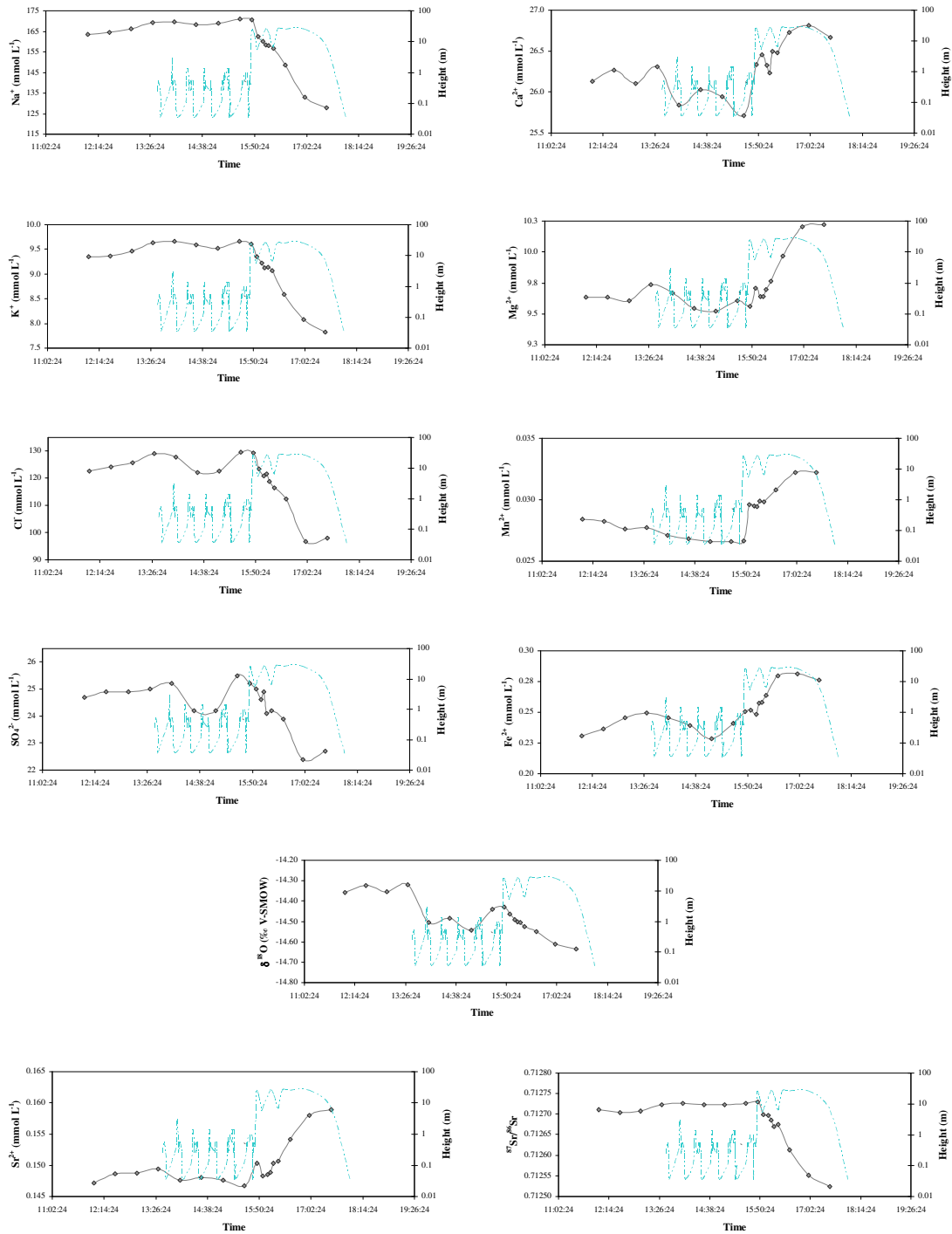


Figure 2.4-27 Times series solute and isotope geochemistry for the time series samples of Crystal Geyser. Dashed line is the eruption height (m), solid line are the solute or isotope values.

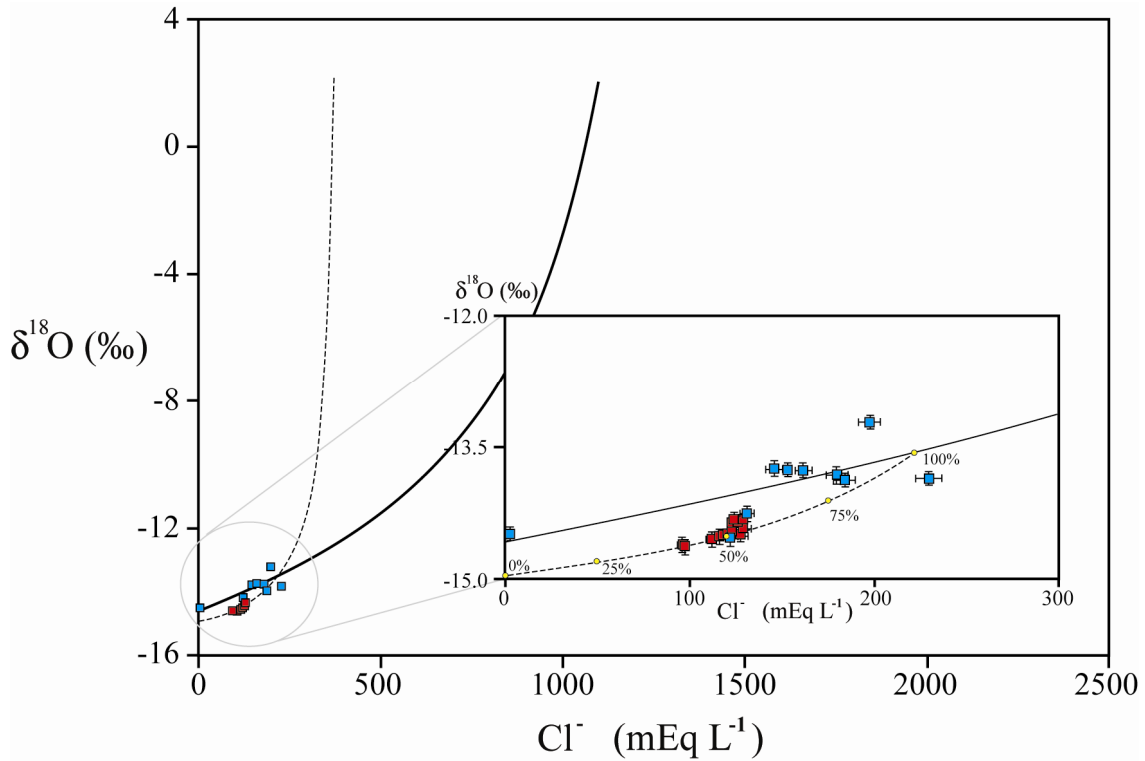


Figure 2.4-28 $\delta^{18}\text{O}$ versus Cl^- for all the CO₂-springs (blue squares) and for the time series samples of Crystal geyser (red squares) showing the least squares hyperbolic fit to the data (Langmuir *et al.*, 1978). The figure demonstrates the mixing between two end-member fluids: a saline brine with high Cl^- and heavy $\delta^{18}\text{O}$; and dilute meteoric fluid with low Cl^- and light $\delta^{18}\text{O}$. The Crystal geyser samples are a further dilution of a mixture already formed from these end-members, with a third lighter meteoric end-member. Differences in the $\delta^{18}\text{O}$ of the meteoric end-members is interpreted as reflecting variability in the $\delta^{18}\text{O}$ of rainwater through the Holocene (c.f. Zhu, 2000)

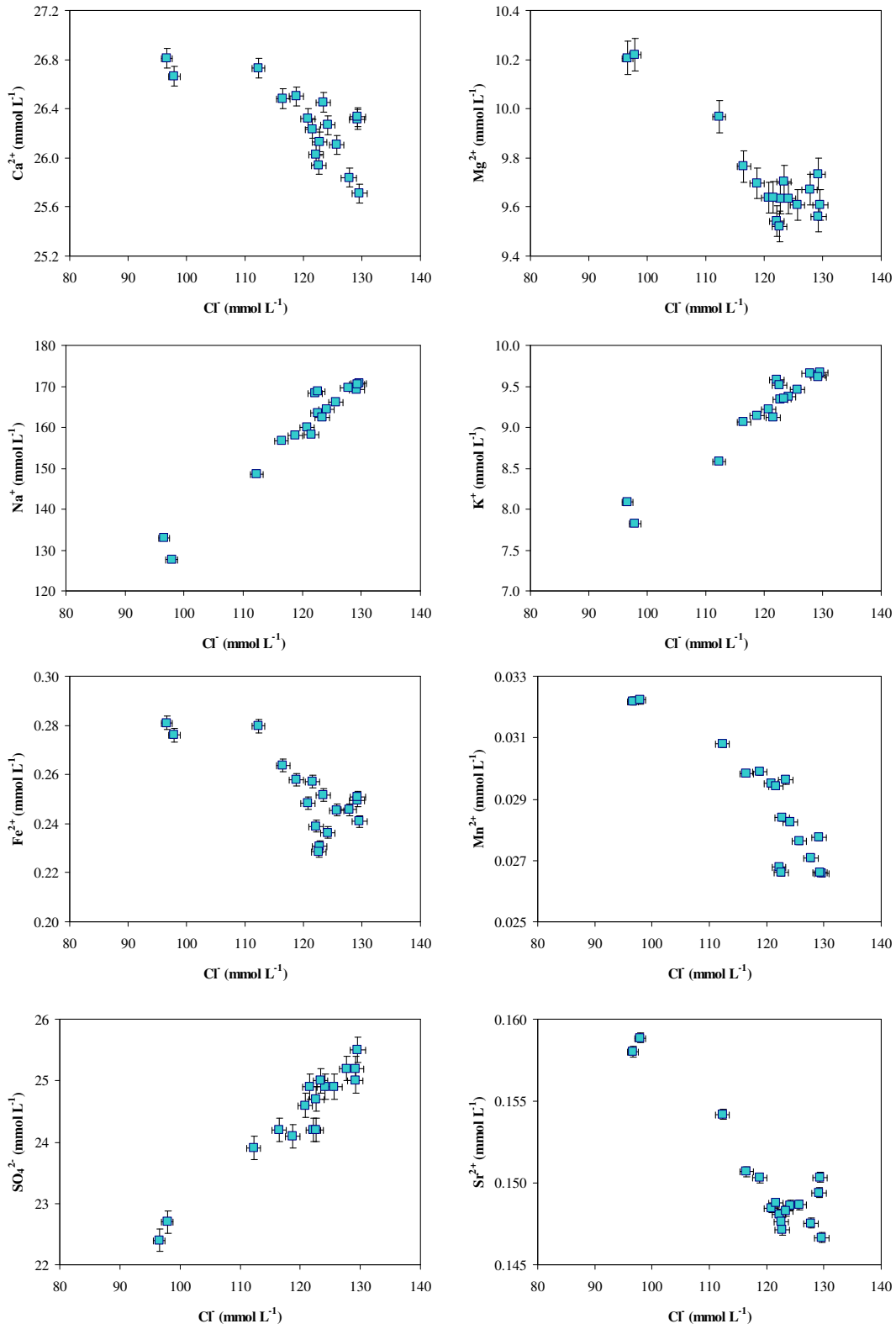


Figure 2.4-29 Cl⁻ versus major solute chemistry for the time series samples of Crystal Geyser.

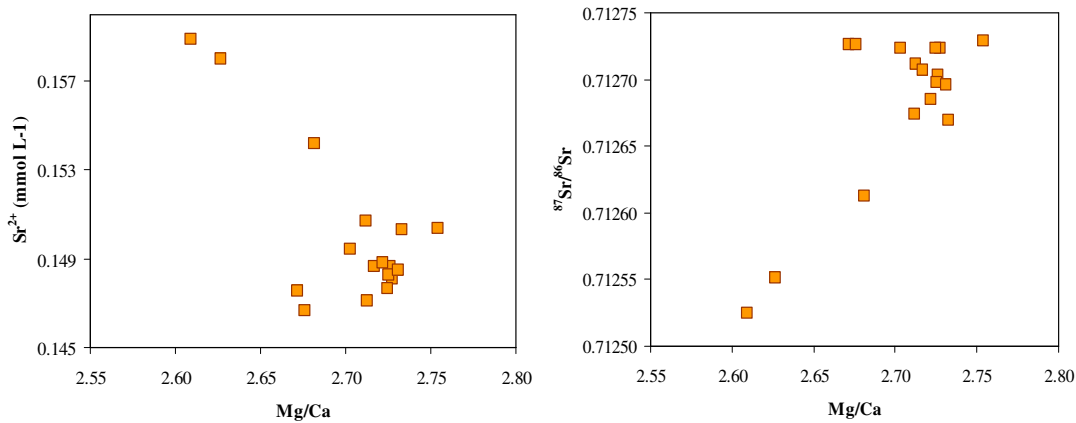


Figure 2.4-30 Cross plots of Sr²⁺ and ⁸⁷Sr/⁸⁶Sr versus Mg/Ca illustrating the derivation of low ⁸⁷Sr/⁸⁶Sr Sr, Ca and Mg from dolomite dissolution.

The magnitude of the variation in ⁸⁷Sr/⁸⁶Sr observed in the time series samples (0.712524 to 0.712729, n = 17) is small compare to the observed range in ⁸⁷Sr/⁸⁶Sr observed between all samples (0.711755 to 0.713327, n = 10). ⁸⁷Sr/⁸⁶Sr decreases 1) through the course of an eruption, 2) with decreasing Cl⁻ and 3) with increasing Sr²⁺ concentration. The hyperbolic mixing trends between ⁸⁷Sr/⁸⁶Sr and various cations implies; a) the pre-eruption fluid has ⁸⁷Sr/⁸⁶Sr higher than the Ca-Mg-HCO₃ end-member. b) trends in ⁸⁷Sr/⁸⁶Sr versus major cations reflect mixing between the two fluid end-members and the dilution effects previously discussed. c) ⁸⁷Sr/⁸⁶Sr decreases with increasing Sr²⁺. The lower ⁸⁷Sr/⁸⁶Sr and higher Sr, Ca and Mg of the Ca-Mg-HCO₃ end-member are attributed to a higher proportion of carbonate derived from dissolution of dolomite in the host aquifer, in the earlier portions of the flow path (Fig. 2.4-30).

Temperature measurements of Gouveia and Friedmann, (2006) using rugged thermistors record systemic variations in temperature of the effused fluid during the build up to an eruption, and through the course of an eruption, which are generally consistent with our measurements of temperature variation. Time series measurements reveal a gradual but systematic increase in temperature of ~ 1.5 °C from 17 °C to 18.5 °C at the onset of eruption. During the course of an eruption temperature decreases systematically from the pre-eruptive maximum (18.7 °C) to close to the pre-eruptive minimum (16.6 °C), at the end of the eruption. These systematic temperature changes covary with changes in the proportion of two fluid end-members. The temperature variation may thus be related to mixing of two distinct water bodies of different temperature, and from different depths. This temperature variation is equivalent to a ~ 85 m variation in the depth of the source fluid. The Navajo Sandstone is ~ 95 m thick in the vicinity of Crystal Geyser (Green River Unit 1#). Differences in the densities of the fluid end-members may impart differences in the hydrodynamics of these fluids and stratification within the host reservoir. It can thus be

inferred that the Na-Cl type end-member is sourced from deeper portions of the formation and the Mg-Ca-HCO₃⁻ from shallower (Fig. 2.4-26).

This variation in fluid chemistry and temperature is interpreted to reflect the drawing in and mixing of distinct water types within the near wellbore region, within the host aquifer. It seems likely that these fluid mixing processes are in part stimulated by the excess (e.g. a fluid flux greater than that driven by hydraulic head) of fluid withdrawn from the aquifer during geysering. This rapid fluid effusion is driven by the buoyant uplift and explosive ejection of fluid from the well by rising CO₂ bubbles (Lu et al., 2005; 2006; Pruess, 2006, 2008). This results in a rapid decline in the height of the column of fluid sitting in the well, causing a pressure perturbation in the reservoir itself, which must impose increased fluid velocities in the subsurface. The observed pattern of fluid mixing implies that CO₂-charged brines influx into the Navajo Aquifer in close proximity to Crystal Geyser, on the timescale of the geysering events. It suggests that the geysering processes itself acts as an active groundwater pump, stimulating the vertical migration of fluid between reservoir and leakage to the surface.

The presence of an active flux of CO₂-charged brine from a reservoir deeper than the Navajo Aquifer can be assessed from information on the effusion of CO₂ and fluid from Crystal Geyser. The rate of CO₂ effusion from Crystal Geyser has been measure as ~11,000 t/a (tones per annum) (Gouveia *et al.*, 2005; Gouveia and Friedmann, 2006). The presence of a continuous free gas phase close to the site of Crystal Geyser is improbable as this well is close to the apex of the anticline and would thus be likely to directly penetrate any buoyantly accumulated gas cap. However, the exsolution of small volumes of CO₂ within the host aquifer may occur due to the depression of CO₂ solubility as fluids ascend the anticline.

If the reservoir fluid was close to CO₂ saturation (as it would likely be if an exsolved phase could be maintained) fluid entering the bottom of the Crystal Geyser well would degas instantaneously upon rising a short distance vertically. The geysering processes intrinsically requires that the point of gas exsolution be mobile and able to rise and fall vertically through the well (Fi.g 2.4-26), thus regulating the development of periodic, large-scale degassing events which drive large eruptions. A CO₂-saturated reservoir would degas continuously from the well base, producing a continuous violent gas stream and would not exhibit periodicity in eruption style or strength.

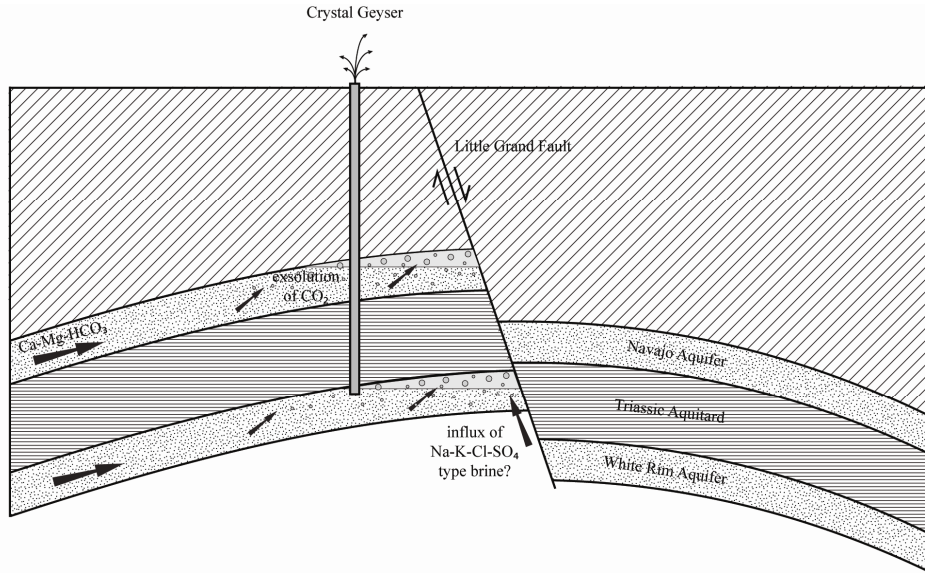


Figure 2.4-31 Schematic diagram illustrating the accumulation of CO₂-charged brine at the intersection of the Little Grand Fault with the apex of the Green River anticline. Free phase CO₂ may accumulate as isolated, capillary trapped bubbles due to the change in solubility as fluids ascend the anticline.

Measurement of the recovery rate of fluid within the well following a large eruption allows calculation of the fluid velocity (1.03×10^{-4} m/sec) and volumetric fluid flux ($1.17 \text{ m}^3/\text{day}$). This value match closely with that expected for a pressure head driven fluid flux calculated using the equations of Bernoulli, and is equivalent to the artesian fluid flux. Additional fluid is expelled from the well during large eruptions due to the buoyant uplift of water by large, rising gas bubbles. The rate of water flux from Crystal Geyser during large-scale eruptions was measured in the early 1970's (although the method was not specified) and was reported by Baer and Rigby (1978) as $27.5 \pm 2 \text{ m}^3/\text{hr}$, with eruptions lasting on average 4.25 hours. However, anecdotal evidence suggests that the modern flux has decreased since this measurement (Waltham, 2001; Fig. 2.2-6), possibly due to reduction in local hydraulic head as a result of fluid and pressure depletion in the surrounding reservoir, or depletion of a CO₂-charged fluid reservoir. Scaled to the duration of a modern eruption these flux estimates imply that in the course of an eruption $60 \pm 3 \text{ m}^3$ of fluid (or a 527m x 38cm column) is emptied from the well; equivalent to the entire well volume. Assuming that this flux was similar over the period prior to the flux measurements this implies that for the given reservoir thickness (95 m) and porosity (20%) a $3.2 \pm 0.8 \text{ km}$ radius around the geyser was emptied of fluid prior to the 1970's and $5.5 \pm 1.4 \text{ km}$ radius over the 74 year life of the geyser (scaling for the decrease in eruption length since the 1970's). This large volume of fluid effusion is most likely balanced by influx of fluid from aquifers below the Navajo Aquifer and from increase in the fluid velocity within the aquifer itself.

From eruption frequency data and the estimates of fluid and gas expulsion during eruptions and the background fluid and gas flux during periods of quiescence, annual estimates of

the CO₂ and water discharge, and the yearly, average CO₂ concentration can be made. Average annual CO₂ emissions range from 5694 ± 1708 t/a to 12702 ± 3810 t/a using upper and lower limits for the CO₂ flux observed in individual, large eruptions and uncertainty estimates in the sampling method (Gouveia *et al.*, 2005). Estimates of fluid flux during periods of eruption and quiescence yield 2.7×10⁴ m³/a and 368 m³/a, respectively. This results in average CO₂ concentrations of ~4 to 10 mol L⁻¹, greatly exceeding the maximum solubility of CO₂ in the Navajo Aquifer. This strongly implies that CO₂ must be added to the Navajo Aquifer close to the site of Crystal Geysers.

2.5. Conclusions

Crustally sourced CO₂, produced from diagenetic reactions in the Leadville Limestone, at depth within the Paradox Basin, migrates vertically through the stratigraphy mixing with and dissolving into basinal brines of the Paradox Formation. These CO₂-charged brines migrate along the Little Grand and Salt Wash fault systems into the shallow White Rim and Navajo Aquifers where they mix with meteorically derived groundwaters, flowing along hydraulic gradients from zones of recharge in the San Rafael Swell to zones of discharge near the confluence of the Green and Colorado Rivers. This passive migration of CO₂ is analogous to leakage of a deep geological CO₂ reservoir into shallower aquifer systems. CO₂ entering the shallow groundwater systems suppresses pH and mineral saturation in the fluid promoting dissolution of silicate and carbonate minerals in the host aquifer. The introduction of this high partial pressure CO₂ gas increases the capacity to accept dissolved solids by lowering the pH and the saturation state of the groundwater, enhancing mineral dissolution. As a result, the CO₂-rich groundwaters can evolve towards very high solute concentrations after prolonged water-rock interaction. In geological CO₂ storage sites this processes will ultimately enhance the fluids capacity to accept dissolved CO₂, through ionic complexing, thereby enhancing solubility trapping. With progressive flow through the aquifer the hydrolysis of plagioclase and K-feldspar consume H⁺, releases solutes and alkalinity to the solution driving the groundwaters towards saturation with respect to these phases. pH attenuation and elevation in mineral saturation will ultimately reduce the reactivity of migrating CO₂-charged fluids reducing the rate of corrosion of caprocks and fault seals encountered by the migrating plume. Thermodynamic constraints imply that the dominant reaction products are smectite, kaolinite and chalcedony. Importantly equilibrium with chalcedony fixes $a_{\text{SiO}_2(\text{aq})}$, maintains groundwater compositions in the stability field of kaolinite and prevents kaolinite equilibrium from regulating Al³⁺.

The CO₂-charged groundwaters contain high quantities of dissolved Fe²⁺ and Mn²⁺. Superposition of Eh, pH and $a_{\text{Fe}^{2+}}$ suggests that the redox state of the fluid is controlled by low

oxygen fugacity and fixed by the Fe³⁺/Fe²⁺ redox couple through equilibration with hematite. This has important implications for the mobilization and transport of metals in CO₂ storage sites and is analogous to iron mobilization processes recently observed at the Frio test CO₂-injection site (Hovorka *et al.*, 2006; Karaka *et al.*, 2006; Smyth *et al.*, 2009). This suggests that, even in the absence of an additional reductant, deep O₂ depleted groundwaters in CO₂ storage sites will derive high metal concentrations from the pH suppression induced by large quantities of dissolved CO₂.

Cold water geysering of Crystal Geysir, driven by CO₂-degassing, causes pressure depletion in the Navajo Aquifer. This stimulates influx of CO₂-charged brines from deeper formations, on the time-scale of the geysering events, which mix with chemically distinct fluids in the host aquifer. The physical process of CO₂ gas-driven geysering is therefore an important mechanism for the stimulation of vertical fluid and gas migration in the subsurface and will be important for prolonging effusion from leaking wells in CO₂ storage sites.

Chapter 3

Silicate Mineral Dissolution Kinetics

3.1. Introduction

The majority of estimates of field-based mineral dissolution rates have previously been determined by mass balance techniques in soil profiles and watersheds (reviewed in Drever and Clow, 1995; White and Brantley, 1995; White and Brantley, 2003), at surface pressure and temperature conditions. A smaller number of studies have focused on understanding reaction rates in natural porous media (e.g. Brantley *et al.*, 2001; Hereford *et al.*, 2007; Keating and Bahr, 1998; Kenoyer and Bowser, 1992a, 1992b; Kim, 2002; Maher *et al.*, 2006; Malmstrom *et al.*, 2002; Rowe and Brantley, 1993; Zhu, 2000, 2005). Few attempts have been made to determine field scale reaction rates in clastic reservoirs with high $p\text{CO}_2$ (Matter *et al.*, 2007).

In this chapter the groundwater chemistry, thermodynamic and hydrological modelling described in Chapter 2 is used, in conjunction with petrological observations and a compilation of published porosity and hydraulic conductivity measurements, to estimate rates of the controlling fluid-mineral reactions in the CO_2 -charged groundwaters. The main results of this work were published by Kampman *et al.*, (2009) and this chapter builds on this work. Emphasis is placed on the feldspar dissolution reactions, as they are likely to be the slowest and hence the most important in controlling reaction progress. Prior to this the most relevant aspects of the experiment studies of feldspar dissolution are reviewed with emphasis on aspects of fluid chemistry and the dissolution mechanisms relevant to the conditions expected in natural CO_2 -charged groundwaters.

3.2. Review of Experimental Studies on Feldspar Dissolution Kinetics

Dissolution rate experiments on feldspars have been conducted in three ways: 1) batch experiments (Amrhein & Suarez, 1992; Casey *et al.*, 1991; Hamilton *et al.*, 2001); 2) flow-through experiments (Berg & Banwart, 2000; Hellmann, 1994; Knauss & Wolery, 1986; Oxburgh *et al.*, 1994); or, 3) surface titration experiments (Blum and Lasaga, 1991; Oxburgh *et al.*, 1994). Fluid samples and effluents of the former two experimental methods were analysed for various elements, e.g. Al, Si, Na and Ca and, using this data, dissolution rates were calculated by mass

balance techniques. The latter was mainly used to derive reaction rate equations as a function of surface charge.

In general feldspar dissolution rates can be divided into three different pH-dependent regions (Fig 3.2-1) (Blum and Lasaga, 1991; Hamilton et al., 2001; Knauss and Wolery, 1986; Oxburgh et al., 1994): 1) low pH region (pH < 5): the dissolution rate decreases with increasing pH; 2) near-neutral pH region (pH 5 to 8): the dissolution rate shows no dependence on pH; 3) high pH region (pH > 8): the dissolution rate increases with increasing pH, though this pH dependence is less pronounced than for the “low pH” region. As temperature increases, the dissolution rates become more pH dependent in the acid and alkaline pH regions. The activation energy required for dissolution is also higher (~ 80 kJ/mol) in more acid and alkaline environments, than in the near-neutral pH region (~ 65 kJ/mol).

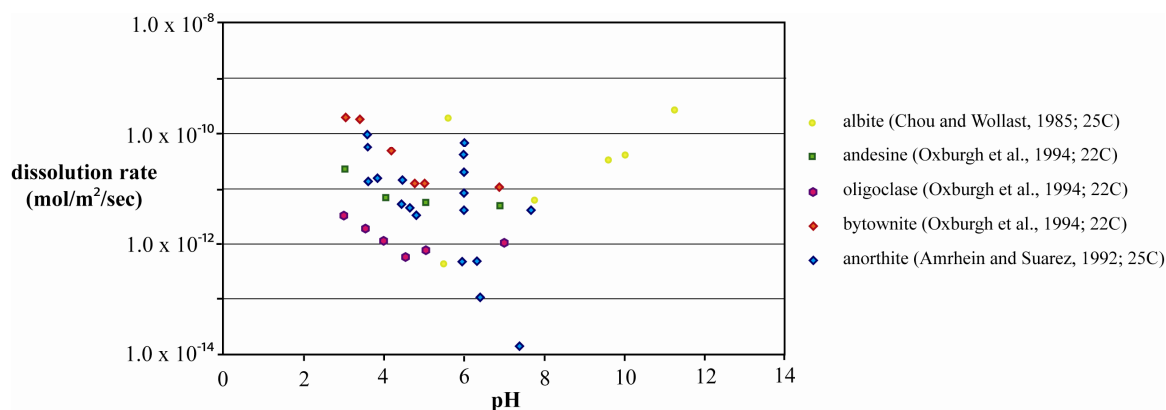


Figure 3.2-1 Laboratory dissolution rates for feldspars of different composition at various pH.

3.2.1. Dissolution Mechanism

The dissolution mechanism of the feldspar mineral surface has been a point of debate among various authors. Essentially, there are three main contentious aspects: 1) the surface-controlled dissolution reaction; important aspects of which include a) the reactive site density (Amrhein and Suarez, 1992; Holdren Jr. and Speyer, 1987), which in turn is related to the “reactive surface area”, though not in a proportional manner; b) the formation of surface complexes (Brady and Walther, 1992; Hellmann, 1999; Oxburgh et al., 1994) c) mineral heterogeneities, e.g. more rapid dissolution of Ca-rich phases than Na- or K-rich phases (Casey et al., 1991; Inskeep et al., 1991); and 2) formation of a leached or altered layer at the mineral-solution interface (Amrhein and Suarez, 1992; Hellmann et al., 2003; Muir et al., 1990; Muir and Nesbitt, 1991; Nesbitt and Muir, 1988); and 3) formation of protective coatings at the crystal surface (Amrhein and Suarez, 1992; Berner and Holdren Jr., 1977; Nugent et al., 1998).

3.1.1.1. Surface Controlled Reaction

Knauss and Wolery (1986), as well as Hamilton et al. (2001) and Berner and Holdren (1977), suggest that dissolution was controlled by the reactive site density due to non-uniform attack at the surface, preferentially at high energy crystal defects, along twin boundaries or at dislocations, which intersect the surface. However, Amrhein and Suarez (1992) have shown that the relation between dissolution rate and specific surface area is not a simple one, and though the density of reactive surface sites per unit area varies systematically with grain size, it does not do so in a linear way (Holdren Jr. & Speyer, 1985). Laboratory estimates of mineral surface areas are typically measured using the BET technique which relates the adsorption of a measured volume of inert gas (usually N₂) to the mineral surface area (e.g. Gregg and Sing, 1982). Geometric estimates, considering idealized sediment grains, typically underestimate mineral surface areas by orders of magnitude, when compared to BET measurements, due to the effects of surface roughness and topology (e.g. Brantley *et al.*, 2000, White *et al.*, 1996). In naturally weathered materials surface roughness and thus total mineral surface area increases with the duration of weathering (White *et al.*, 2003) but how this relates to the total reactive surface area of the mineral is still uncertain.

Further complexity surrounds the formation of surface complexes on the mineral surface, prior to detachment and dissolution of the grain, which relate the surface dissolution mechanism to the solution pH. At low pH values the feldspar surface is positively charged due to the formation of $\equiv\text{Al-OH}_2^+$ surface complexes, and at high pH values $\equiv\text{Si-O}^-$ surface complexes are dominant, resulting in a negative surface charge. As a result of the formation of these surface complexes, at acid pH dissolution will be mainly concentrated at the Al-surface site, while, at alkaline pH, dissolution focuses on the Si-surface sites (Brady and Walther, 1989; Hellmann, 1999; Oxburgh et al., 1994). At near-neutral pH, however, the dissolution rate is independent of surface charge, as it is mainly occupied by neutral $\equiv\text{Si-OH}$ and $\equiv\text{Al-OH}$ surface complexes. Oxburgh et al. (1994) suggested that, at near-neutral pH, reaction occurs at neutral Al-surface sites, due to the fact that an Al-O-Si bond is weaker than a Si-O-Si bond (Hamilton et al., 2001).

Further, the role of compositional heterogeneity may introduce variable dissolution rates across the mineral surface. In general, it is suggested that the dissolution rate of feldspars increases with anorthite content (Casey et al., 1991; Oxburgh et al., 1994). This is related to the higher solubility of more Ca-rich feldspar compared to Na-rich feldspar. TEM imaging of a zoned labradorite by Inskeep et al. (1991) has shown that the more Ca-rich lamellae were dissolved preferentially over the more Na-rich ones. These mineralogical heterogeneities influence the measured dissolution rate significantly.

Hamilton et al. (2001) and Oxburgh et al. (1994) showed that the Al/Si ratio also affects the dissolution rate. For feldspars with varying Al content it is seen that the dissolution rate

increases with increasing Al/Si ratio (Hamilton et al., 2001). In addition, Hamilton et al. (2001) and Oxburgh et al. (1994) both concluded that variations in Al content among feldspars could explain the observed increase in dissolution rate going from albite to anorthite. This difference is explained by the difference in feldspar structure, which is related to the interconnection between AlO_4 and SiO_4 tetrahedra (Hellmann, 1999). Increasing the Al/Si ratio means replacement of Si atoms by Al atoms, which results in an increase in Si-O-Al bond length (Hamilton et al., 2001). As a result of this bond length increase AlO_4 tetrahedra are preferentially removed from the feldspar framework. Albite contains SiO_4 tetrahedra that are interconnected, and therefore the loss of AlO_4 tetrahedra will not affect the kinetics of surface SiO_4 tetrahedra detachment, i.e. $\equiv\text{Si-OH}$ complexes, in albite. This is in contrast to anorthite, which contains completely isolated SiO_4 tetrahedra, and therefore anorthite dissolution requires only the breaking of, weaker, Al-O-Si bonds, instead of both Al-O-Si and Si-O-Si bonds, as is the case for albite dissolution (Hellmann, 1999).

3.1.1.2. Leached Layer

The mineral surface dissolution of feldspar is also influenced by the formation of leached layers and precipitates. Coating of the feldspar grains by these layers is assumed to change the dissolution mechanism from transport-controlled to diffusion-controlled, as released ions must now first diffuse through the coating before being released to solution. Leached layers are the result of non-stoichiometric dissolution and near-surface alteration at acid to neutral pH, and are not generally observed at basic pH (Casey et al., 1988, 1991; Hellmann et al., 2003). Depth profiles of these altered zones typically show depletion in interstitial cations, i.e. Na, K, Ca, and framework elements, i.e. Al, retention of Si and O (Hellmann et al., 2003; Muir et al., 1990), and enrichment in aqueous species, i.e. H (Casey et al., 1988).

There is a significant difference between naturally formed leached layers and laboratory produced layers: naturally formed leached layers are Al-rich (Nesbitt and Muir, 1988), while laboratory produced layers are Si-rich (Hellmann et al., 2003; Inskeep et al., 1991; Muir et al., 1990). These altered layers usually have a thickness of several hundreds of angstroms, and this thickness may also vary with feldspar composition (Muir et al., 1990), increasing with increasing Al content. The mechanism of leached layer formation is thought to involve three consecutive steps (Chou and Wollast, 1985; Muir et al., 1990): 1) rapid replacement of Ca^{2+} and Na^+ by H^+ or H_3O^+ ; 2) hydrolysis reactions, resulting in the breaking of Si-O-Al and Si-O-Si bonds preferentially and the depolymerisation of the silicate structure, eventually resulting in a Al-depleted layer; 3) slow dissolution of the residual layer at the solid-solution interface, together with diffusion of ions from the fresh feldspar surface, leading to steady state dissolution. This results in the formation of a layer composed of Si, O and H, most likely a hydrated silica gel, overlying the fresh feldspar mineral (Chou and Wollast, 1985; Hellmann et al., 2003; Muir et al.,

1990). The effect of this layer on inhibiting dissolution remains uncertain. Additionally, the presence of a cation depleted surface layer in highly weathered natural minerals may adversely influence BET or geometric estimates of the reactive mineral surface area, resulting in overestimation of the reactive surface of natural feldspars.

3.1.1.3. Secondary mineral precipitation

Part of the discrepancy between laboratory and field-scale reaction rates may be explained by the presence of surface coatings formed by the precipitation of secondary minerals, which may influence the dissolution rates. Weathered minerals in nature are often coated by clays (Berner & Holdren Jr., 1977; Nugent et al., 1998; Zhu, 2005), organic material and oxyhydroxides of Al, Fe, and Mn. This coating can either be discontinuous (Berner & Holdren Jr., 1977; Nugent et al., 1998), or continuous. Even if the coating is discontinuous, as a result of its porosity or patchy distribution, it may affect the dissolution of the mineral where this is in contact with the coating rather than with the solution (Hodson, 2003).

Investigation of natural mineral coatings on feldspars (Berner & Holdren Jr., 1977; Nugent et al., 1998; Zhu, 2005) has shown that the weathering of feldspar minerals indeed results in the formation of a patchy hydrous coating consisting of aluminosilicates, e.g. kaolinite or other clay minerals. In spite of the presence of this clay-like coating the underlying feldspar showed the same textural features as laboratory weathered feldspar without a coating. Therefore, Berner and Holdren Jr. (1977) concluded that it is unlikely that the presence of this coating inhibited dissolution. However, they did not take into account the possibility that the observed dissolution textures, e.g. etch pits, could either have developed before the precipitation of the coating, or just developed more slowly below the coating (Hodson, 2003).

To investigate the effect of coatings on the dissolution rate of feldspar under conditions where effect of solution saturation state can be discounted Hodson (2003) studied the dissolution behaviour on anorthite in the presence of a, laboratory produced, Fe-rich coating. He concluded that the formed coating was porous, containing both meso- and micropores, and that this porous coating of secondary minerals did not inhibit the dissolution of the feldspar mineral, as the obtained dissolution rates were in the same order of magnitude as those for uncoated minerals. This also means that the presence of porous surface coatings on minerals does not explain the observed discrepancy between mineral dissolution rates obtained in the field and those in the laboratory.

A similar study was performed on anorthite (Murakami et al., 1998), but with different secondary mineral precipitates; boehmite, “modified” boehmite, and kaolinite, which are reaction products derived from the dissolving feldspar. Though their obtained dissolution rates were in the same order of magnitude as those for uncoated minerals, they concluded, on the basis of

calculated Gibbs free energies for anorthite dissolution, that the precipitation of secondary minerals promoted dissolution. They stated that, even though the dissolution rate decreased as a result of precipitation, the formation of the coating required elements present in solution, thereby reducing the saturation state of the fluid, and hence, promoting more dissolution of the feldspar.

3.2.2. Solution Composition

Other factors affecting the dissolution rate of feldspars are: 1) solution saturation state (Aagaard and Helgeson, 1977, 1982; Lasaga, 1981; Oeklers et al., 1994); 2) cations in solution, e.g. aqueous Al (Amrhein and Suarez, 1992; Muir and Nesbitt, 1991); and 3) ligand absorption, e.g. oxalate (Berg and Banwart, 2000; Blake and Walter, 1999), citrate (Blake & Walter, 1999), or carbonate (Berg & Banwart, 2000);

3.1.1.4. Solution Saturation State

Within the framework of transition state theory (TST) (Lasaga, 1981), the rate of an elementary reaction is proportional to the concentration of the activated complex (or the energy maximum that the reactants should pass to be converted into products) and to the concentration of the surface species precursor of the activated complex (precursor complex) (Wieland et al., 1998). Although feldspar dissolution likely involves several elementary reactions, TST can still be applied to the overall rate if it is controlled by a single elementary rate-limiting step (Lasaga, 1981). Within this context, silicate dissolution rates can be described using (Lasaga, 1981):

$$r = k^+ \prod a_i^{-n_i} \{1 - \exp(\Delta G_r / \sigma RT)\} \quad (3.1)$$

where r defines the net reaction rate, k^+ denotes a dissolution rate constant, a corresponds to the activity of the i^{th} aqueous species, n_i signifies the reaction coefficient of the i^{th} species in the reaction forming the precursor complex, σ refers to the reaction order, ΔG_r denotes the change in free energy for the overall reaction, T stands for absolute temperature, and R represents the gas constant. The product $\prod a_i^{-n_i}$ describes the effect on the overall rate of the activities of the aqueous species involved in precursor complex formation. The terms within the brackets describe the effect of solution saturation state. For highly undersaturated solutions, ΔG_r has a large negative value and the term within the brackets is equal to 1. At these conditions the dissolution rate is independent of bulk solution saturation state, but is still dependent on the activities of the aqueous species that participate in the formation of the precursor complex. For small deviations from equilibrium (i.e. when $\Delta G_r / \sigma < RT$), the rate becomes linearly related to chemical affinity.

When applying Eq. (3.1) to silicate dissolution rates, it has commonly been assumed that 1) H^+ , OH^- and H_2O are the only aqueous species involved in precursor complex formation, 2) a

single reaction mechanism controls the overall rate at all ΔG_r , and 3) $\sigma = 1$. These assumptions lead to the following rate equation (Lasaga, 1981):

$$r = k'_+ (a_{H^+})^n H^+ \{1 - \exp(\Delta G_r / RT)\} \quad (3.2)$$

where k'_+ refers to the dissolution rate constant for the hydrolytic process. This rate law has been used extensively to model fluid-rock interactions. However, the functional form of the dissolution rate: ΔG_r dependence is not well established and published expressions include simple exponentially decreasing rates as ΔG_r tends to zero (e.g. Aagaard and Helgeson, 1977, 1982; Lasaga, 1981) as well as combinations of two or more exponential terms attributed to multiple dissolution mechanisms such as the development of etch pits as saturation states deviate further from equilibrium (e.g. Hellman and Tisserand, 2006; Taylor *et al.*, 2000).

3.1.1.5. Cation Effects

The addition of cations to solution could affect the dissolution rate of feldspars, though not all cations have this effect (Amrhein & Suarez, 1992; Muir & Nesbitt, 1991). Addition of “feldspar building” ions, e.g. Ca, Na, Si, and Al, to solution resulted in different effects on the dissolution rate. In general, Ca, Na, and Si ions appeared to have no effect on the dissolution rates of labradorite (Muir & Nesbitt, 1991), and anorthite (Amrhein & Suarez, 1992) in acid solutions. This is in contrast to Al, which significantly inhibited dissolution at pH 3.6 to 6.0 at 25 °C (Amrhein & Suarez, 1992; Muir & Nesbitt, 1991), though not at pH 3.0 (Amrhein & Suarez, 1992), and only at concentrations above ca 0.5 mM. Inhibition of dissolution by Al was assumed to be the result of the blocking or retardation of H^+ supply from the bulk solution to the surface by aqueous aluminium. As the release of Al from the silicate surface to solution depends on the concentration gradient between the solid and solution, addition of aluminium to solution decreases this gradient and therefore slows down the release of Al from the solid, and hence the dissolution rate (Muir & Nesbitt, 1991).

3.1.1.6. Ligand Complexation

The addition of ligands to solution also affects the dissolution rate, as they tend to form surface complexes. Carbonate is believed to form $\equiv Al-CO_3^-$ surface complexes with positively charged Al-surface groups (Berg & Banwart, 2000). A similar process is applicable to organic acids (Blake & Walther, 1999). Blake and Walther (1999) have studied the effect of citric and oxalic acid on the dissolution rate of albite, labradorite, and orthoclase. They concluded that there is a similarity in dissolution behaviour of alkali feldspars with similar Al content, i.e. albite and orthoclase, and a greater solubility of the more Al-rich feldspar, labradorite, in the presence of organic acids.

3.3. Methodology: Calculating Reaction Rates

3.3.1. Introduction

The rate of individual mineral-fluid reactions occurring in the Navajo Sandstone, have been determined by the solution of the mass balance equations which relate changes in fluid chemistry between a single initial spring (Green River Airport Well) and down-gradient springs (Fig. 2.4-17), to addition or subtraction of specific mineral phases. Fluid compositions sampled at each CO₂ spring are corrected for the addition of brine entrained in the CO₂ stream. Reaction progress (M_j) is then calculated by difference from a single initial well. The flow path and its length (z) are estimated from potentiometric surface measurements. Fluid velocity is calculated from a compilation of published porosity, hydraulic conductivities and local hydraulic head measurements for the Navajo Sandstone (Appendix B). Mineral proportions and surface areas are estimated from physical, chemical and petrological measurements on Navajo Sandstone samples locally, and from sites elsewhere in the Paradox Basin. The extent of mineral-fluid thermodynamic disequilibrium (ΔG_r) is calculated from the fluid chemistry, uncorrected for the brine additions

3.3.2. Mass Balance

Reaction progress, the net transfer of a mineral j to the fluid, M_j (negative for precipitation, positive for dissolution), was calculated from the evolution of solute chemistry between springs. Mineral mole transfers, M_j , in units of moles per m³ of fluid, were calculated between the brine corrected chemistry of the upstream spring, Green River Airport Well, and the brine corrected chemistry of all down-gradient springs. Positive M_j denotes dissolution, negative M_j denotes precipitation. The chemical evolution of component k (concentration m_k moles/l), in the water between two points along the flow path is given by

$$\Delta m_k = \sum_{j=1}^J M_j b_{j,k} \quad (3.3)$$

where $\Delta m_{r,k} = m_{k_{final}} - m_{k_{initial}}$ and $b_{j,k}$ are the stoichiometric mole fraction of component k in mineral phase j (c.f. Plummer *et al.*, 1990). The solute flux mass balance model is non-unique to the extent that there may be phases additional to the ten (including brine) constrained by the ten components (including Cl⁻) modelled here. The possible reacting phases are defined by petrographic observations of outcrop samples of fresh unaltered Navajo Sandstone obtained from the San Rafael Swell, and core chips from petroleum exploration wells that penetrate the Navajo Sandstone along the Green River anticline, as well as published petrography of the Navajo

Sandstone (Harshbarger *et al.*, 1957; Zhu *et al.*, 2006). Primary and secondary mineral compositions were analysed by electron microprobe, average compositions are presented bellow (see Appendix B for tabulated probe data). The following mineral compositions were used to constrain the mass balance model

K-feldspar:	$K_{0.95}Na_{0.05}Al_{1.00}Si_{3.00}O_8$	
Plagioclase:	$Na_{0.62}Ca_{0.38}Al_{1.38}Si_{2.62}O_8$	
Smectite:	$K_{0.26}Na_{0.03}[Mg_{0.35}Fe_{0.13}Al_{1.52}][Si_{3.51}Al_{0.49}]O_{10}(OH)_2$	
Kaolinite:	$Al_2Si_2O_5(OH)_4$	*
Dolomite:	$Ca_{1.06}Mg_{0.93}(CO_3)_2$	
Calcite:	$CaCO_3$	*
Quartz:	SiO_2	*
Gypsum:	$CaSO_4 \cdot 2H_2O$	(*ideal composition used)

Nine components (Na^+ , K^+ , Ca^{2+} , Mg^{2+} , Al^{3+} , SiO_2 , SO_4^{2-} , C and alkalinity), and nine phases (plagioclase (An38), K-feldspar, silica, kaolinite, smectite, calcite, gypsum, dolomite and $CO_2(g)$) were considered, giving:

(i) solute mass balance

$$\Delta m_{T,Na} = 0.62M_{plagioclase} + 0.05M_{K-feldspar} + 0.03M_{smectite} \quad (3.4)$$

$$\Delta m_{T,K} = 0.95M_{K-feldspar} + 0.26M_{smectite} \quad (3.5)$$

$$\Delta m_{T,Mg} = 0.35M_{smectite} + 0.93M_{dolomite} \quad (3.6)$$

$$\Delta m_{T,Si} = M_{silica} + 2.62M_{plagioclase} + 3M_{K-feldspar} + 2M_{kaolinite} + 3.51M_{smectite} \quad (3.7)$$

$$\Delta m_{T,Al} = 1.38M_{plagioclase} + M_{K-feldspar} + 2M_{kaolinite} + 2.01M_{smectite} \quad (3.8)$$

$$\Delta m_{T,Ca} = M_{calcite} + M_{gypsum} + 0.38M_{plagioclase} + 1.06M_{dolomite} \quad (3.9)$$

$$\Delta m_{T,C} = M_{calcite} + M_{dolomite} + M_{CO_2} \quad (3.10)$$

$$\Delta m_{T,S} = M_{gypsum} \quad (3.11)$$

(ii) alkalinity mass balance

$$\Delta m_{T,Alkalinity} = 2M_{calcite} + 4M_{dolomite} + 2M_{kaolinite} + 5.94M_{smectite} + 2.76M_{plagioclase} + 2M_{k-feldspar} \quad (3.12)$$

$$where \text{Alkalinity} = [HCO_3^-] + 2[CO_3^{2-}] + [OH^-] - [H^+] \quad (3.13)$$

In addition to the solute mass balance equations mineral mass transfers are further constrained by the solution of an alkalinity mass balance. The stoichiometric coefficients constraining individual mineral mole transfers in equation 3.12 are the number of equivalents (mEq/l) of alkalinity produced or consumed per mole of phase dissolved or precipitated. Silicate dissolution and clay precipitation reactions modify local alkalinity by consuming or releasing protons, respectively. Reactions involving carbonate minerals modify alkalinity through the consumption or release of protons and bicarbonate ions. The dissolution and dissociation of CO₂ has no net effect on alkalinity as it produces both HCO₃⁻ and H⁺ ions via the dissociation reaction CO₂ + H₂O → HCO₃⁻ + H⁺.

The mole transfers for plagioclase can be independently constrained by separate solution of the mass balance equations for Sr and ⁸⁷Sr/⁸⁶Sr (Eq. 3.14 to 3.16), assuming all Sr, corrected for brine additions, is derived from the dissolution of plagioclase and dolomite, and $M_{dolomite}$ is derived from the solute mass balance model:

$$\Delta Sr = Sr_{final} - Sr_{initial} \quad (3.14)$$

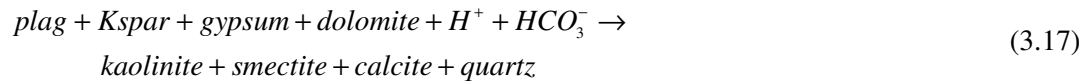
$$\Delta \frac{{}^{87}\text{Sr}}{{}^{86}\text{Sr}} \cdot Sr = \left(\frac{{}^{87}\text{Sr}}{{}^{86}\text{Sr}} \cdot Sr \right)_{final} - \left(\frac{{}^{87}\text{Sr}}{{}^{86}\text{Sr}} \cdot Sr \right)_{initial} \quad (3.15)$$

$$\Delta \frac{{}^{87}\text{Sr}}{{}^{86}\text{Sr}} \cdot Sr = \left(\frac{{}^{87}\text{Sr}}{{}^{86}\text{Sr}} \cdot Sr \right)_{plagioclase} \cdot M_{plagioclase} + \left(\frac{{}^{87}\text{Sr}}{{}^{86}\text{Sr}} \cdot Sr \right)_{dolomite} \cdot M_{dolomite} \quad (3.16)$$

The average Sr concentration in analysed plagioclase and dolomite are ~ 320 ppm and 205 ppm, respectively. ⁸⁷Sr/⁸⁶Sr_{plag} (0.724102) is taken to be the average ⁸⁷Sr/⁸⁶Sr reported for whole rock analyses of Truini and Longworth, (2003). ⁸⁷Sr/⁸⁶Sr_{dolomite} is taken as the average ⁸⁷Sr/⁸⁶Sr for early dolomite cements (0.71030) reported by Goldstein *et al.*, (2008).

Whilst illite clays are present as altered products of feldspar they are thought to represent the products of higher temperature diagenetic reactions during burial and are not thought to participate in these reactions either as dissolving phases due to their relative super-saturation or as precipitates due to the presence of other, thermodynamically more stable phases.

The solutions of equations 3.4 to 3.12 for the changes of brine-corrected water compositions between the Green River Airport Well and the nine downstream wells are consistent with: 1) dissolution of plagioclase, K-feldspar, dolomite and gypsum, 2) precipitation of calcite, kaolinite, smectite and quartz, and 3) consumption of CO₂. The proportions of the phases are consistent with the stoichiometry of the reaction



3.3.3. Calculation of Reaction Rates

Feldspar dissolution rates in mole·m⁻²·s⁻¹ were calculated from 1) the gradient of the mineral modes in the fluid with distance along the flow path, 2) the fluid flux and 3) mineral surface areas within the aquifer. Porosity and hydraulic conductivity data are compiled in Appendix B. Mineral mode against distance plots show an inflection where there is a drop in pH (Figs. 2.4-17 & 3.4-1) and we model the best constrained part of the profile downstream of this point. The rate of change of mineral mode with distance was calculated by modelling the variation of mineral modes (M_j) with distance (z), by a least-squares fit to the empirical expression

$$M_j = A \cdot (1 - \exp^{-Bz}) \quad (3.18)$$

which was then differentiated to obtain the rate of change of the slope, dM_j/dz .

$$\frac{dM_j}{dz} = AB \cdot \exp^{-Bz} \quad (3.19)$$

The differential equation describing the variation in moles of a reacted phase in the fluid phase with time may be approximated by

$$\phi \frac{\partial M_j}{\partial t} = R_j \cdot S_j - \omega_o \phi \frac{\partial M_j}{\partial z} \quad (3.20)$$

where ω_o is the fluid velocity (ms⁻¹), ϕ is the porosity, R_j is the reaction rate for phase j (mole·m⁻²·s⁻¹) and S_j is the surface area of mineral j (m²/m³). For flow systems where S_j varies slowly, the quasi stationary state approximation (Lichtner 1988), $\partial M_j/\partial t = 0$, simplifies equation (3.20) to

$$\frac{\partial M_j}{\partial z} = \frac{R_j S_j}{\omega_o \phi} \quad (3.21)$$

The fluid flux ($\omega_o \phi$) was calculated from the gradient in hydraulic head dh/dz , and the mean of a compilation of laboratory derived hydraulic conductivity values from the Navajo Sandstone, K (ms⁻¹) (Hood and Patterson, 1984; Weigel, 1986), where

$$\omega_o \phi = K \cdot \frac{dh}{dz} \quad (3.22)$$

Reaction rate R_j for the j th mineral phase, was then calculated as

$$R_j = \frac{\partial M_x}{\partial z} \frac{\omega_o \phi}{S_j} \quad (3.23)$$

S_j , the surface area of the j th mineral (m^2/m^3) is calculated from the whole rock specific surface area, ($s_j = 0.7 \text{ m}^2/\text{g}$ from BET measurements on Navajo Sandstone by Zhu (2005) assuming that individual mineral surface areas are proportional to their volume fractions and allowing for the mean porosity of the Navajo ($\phi = 0.20 \pm 0.04$ 1 σ , from Navajo Sandstone samples collected from the northern Paradox Basin, (Cooley *et al.*, 1969; Freethy, 1988; Hood and Patterson, 1984; Weigel, 1986) as

$$S_j = s_j \cdot v_j \cdot (1 - \phi) \cdot \rho \quad (3.24)$$

Mineral volumetric abundances, v_j , were determined from normative mineral abundances calculated using the mineral compositional data obtained in this study and a compilation of whole rock chemical analyses of Navajo Sandstone from this study (Appendix B) and Bowen (2004). Modal mineralogy was calculated from least squares mixing of mineral proportions to match whole rock compositions using the program MINSQ (Hermann & Berry, 2002). Calculated mineral surface areas for plagioclase and K-feldspar are $51 \times 10^3 \pm 6 \times 10^3 \text{ m}^2/\text{m}^3$ and $112 \times 10^3 \pm 10 \times 10^3 \text{ m}^2/\text{m}^3$ respectively.

3.4. Results and Discussion

3.4.1. Reaction Rates

Reaction progress in terms of net dissolution of plagioclase and K-feldspar and precipitation of kaolinite, smectite and calcite calculated relative to Green River Airport Well (Table 3.4-1) show an inflection after Crystal Geysir but then increase at an exponentially decreasing rate downstream (Fig. 2.4-17). These rate changes are attributed to progressive neutralization of pH downstream from the sites of CO_2 injection and the approach to mineral-fluid equilibrium. The inflexion in gradient after Crystal Geysir is consistent with the drop in pH and increase in CO_2 consumed (Fig. 2.4-17) at Small Bubbling Spring attributed to additional CO_2 injection.

We therefore fit the empirical equation 3.18 to the change in mineral modes against distance for springs downstream of Small Bubbling Spring (Fig. 3.3-1). These fits include the downstream Ten Mile, Tumble Weed and Chaffin Ranch Geysers which have a more tenuous hydrological connection with the upstream wells. Excluding these springs from the fits makes only a $\sim 25\%$ difference to the gradient except where it is poorly defined towards the ends of the flow paths.

The rates of mineral dissolution are calculated from the gradients in molar transfer with distance (equation 3.18) and from the steady state solution to the transport equation 3.21. The rates of plagioclase and K-feldspar dissolution are in the ranges 2×10^{-14} to 2×10^{-19} and 4×10^{-16} to 4×10^{-18} $\text{mol} \cdot \text{m}^{-2} \cdot \text{s}^{-1}$ respectively, within the range observed for other field studies at near-neutral pHs but slower than most laboratory studies (Fig. 3.4-2).

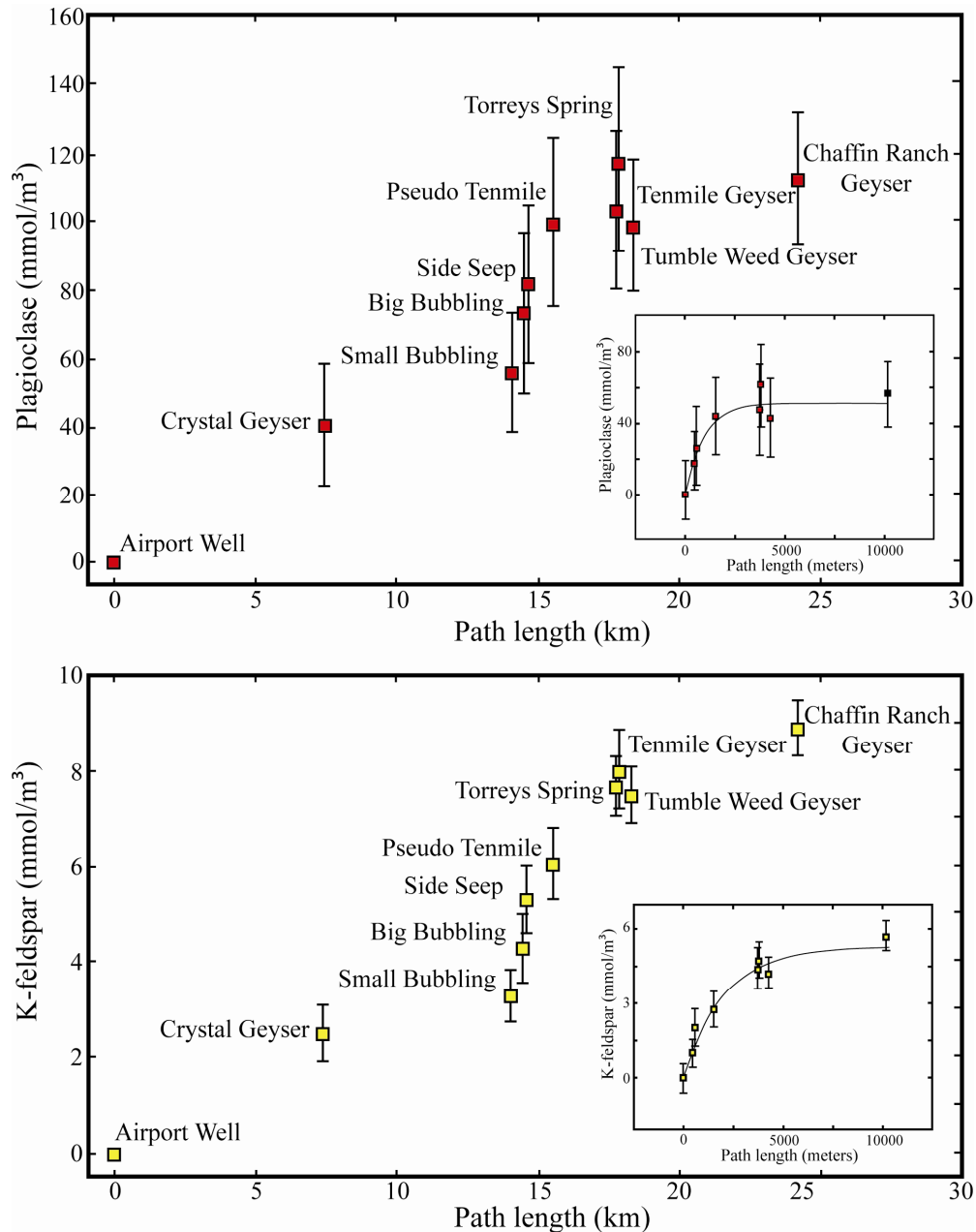


Figure 3.4-1 Calculated changes in the feldspar mineral modes with distance along the flow path. The rate of change of mineral mode with distance was calculated by a least-squares fit to the variation of mineral modes (M_i) with distance (z) over the well-constrained portion of the flow path, downstream of Small Bubbling Spring. Error bars are the propagated errors derived from analytical uncertainty, uncertainty associated with the brine correction and mass balance modeling (see Appendix A of details).

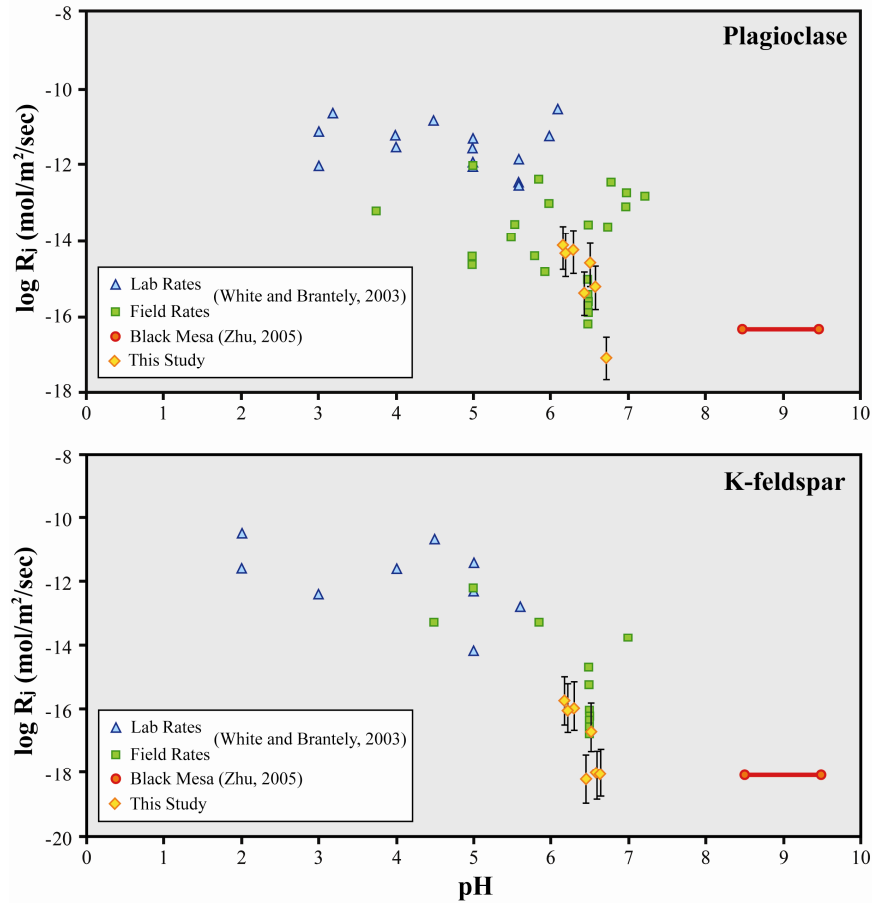


Figure 3.4-2 Variation in feldspar dissolution rate versus pH for a compilation of laboratory (White and Brantley, 2003) and in-situ dissolution rates (Hereford et al., 2007; Malstrom et al., 2004; White and Brantley, 2003), feldspar dissolution rates in the Navajo Sandstone at Black Mesa (Zhu, 2005) and the rates calculated at Green River.

	Plag	Kspar	Kao	Smc	Cc	Si	Gyp	Dol	CO ₂
Spring	<i>mmol/l</i>								
Crystal Geyser	40.18	2.53	-28.38	-3.80	-14.06	-58.46	3.03	2.58	40.68
Small Bubbling	55.85	3.26	-35.50	-8.00	-26.17	-73.25	2.05	4.01	61.44
Big Bubbling	73.30	4.25	-47.97	-10.13	-32.75	-98.56	0.14	4.46	64.58
SS Big Bubbling	81.99	5.27	-51.01	-13.63	-38.47	-106.14	1.75	5.89	69.88
Pseudo Tenmile	99.86	6.01	-61.98	-16.26	-46.50	-127.72	1.18	6.27	51.72
Torreys	117.80	7.97	-73.25	-19.66	-48.41	-151.66	3.64	7.38	69.70
Tenmile	103.50	7.63	-49.01	-32.05	-35.09	-110.67	18.77	13.67	15.35
Tumble	98.87	7.45	-55.00	-21.46	-40.16	-117.34	9.87	9.10	44.30
Chaffin	112.68	8.96	-58.32	-28.54	-36.90	-127.03	15.10	12.70	16.59

Table 3.4-1 Mineral mol transfers (mmol/l) calculated using the mass balance model detail in section 3.3.2.

Error propagation analyses, using Gaussian error propagation, give uncertainties of approximately 20-25% of the calculated rates (the formulation of error analysis is detailed in Appendix A). Error propagation takes into account the errors associated with mass transfer calculations arising from analytical uncertainty, the uncertainties in correction for brine inputs taken as the standard error of brine compositions compiled from Spangler *et al.*, (1996) and Breit (2002), the scatter in BET specific surface area measurements, mineral abundances and porosity. Calculation of plagioclase mole transfers depends primarily on changes in fluid Na concentrations which have relatively large uncertainty due to the scatter in brine Na/Cl ratios. If the brine inputs in the Green River system are of relatively homogeneous compositions then plagioclase exhibits smooth changes in mole transfer with distance comparable with the better constrained K-feldspar mole transfers (Figs. 3.4-1). However the magnitude of plagioclase mole transfers and resultant inferred reaction rates are sensitive to the assumed brine Na/Cl ratio. If this is varied over the full range observed (0.73 to 0.99), then average calculated plagioclase dissolution rates decrease from $\sim 3 \times 10^{-14}$ to $\sim 8 \times 10^{-15} \text{ mol} \cdot \text{m}^{-2} \cdot \text{s}^{-1}$.

Plagioclase dissolution rates determined independently with $^{87}\text{Sr}/^{86}\text{Sr}$ and Sr mass balance vary from 4×10^{-14} to $1 \times 10^{-25} \text{ mol} \cdot \text{m}^{-2} \cdot \text{s}^{-1}$ in good agreement with rates derived from solute mass balance. However, uncertainties associated with rates derived from Sr are on the order of 50% of the calculated rates, given the compounding effects of the large variation in $^{87}\text{Sr}/^{86}\text{Sr}_{\text{plag}}$, Sr_{plag} , $^{87}\text{Sr}/^{86}\text{Sr}_{\text{dol}}$, Sr_{dol} , $^{87}\text{Sr}/^{86}\text{Sr}_{\text{brine}}$ and Sr_{brine} . Depressed Sr and $^{87}\text{Sr}/^{86}\text{Sr}$ for Torreys Spring and Big Bubbling side seep are probably due to the addition of a low $^{87}\text{Sr}/^{86}\text{Sr}$ Sr source not accounted for in the model, variability in the brine $^{87}\text{Sr}/^{86}\text{Sr}$ and Sr concentration or to heterogeneity in mineral $^{87}\text{Sr}/^{86}\text{Sr}$ and Sr concentrations at the aquifer scale.

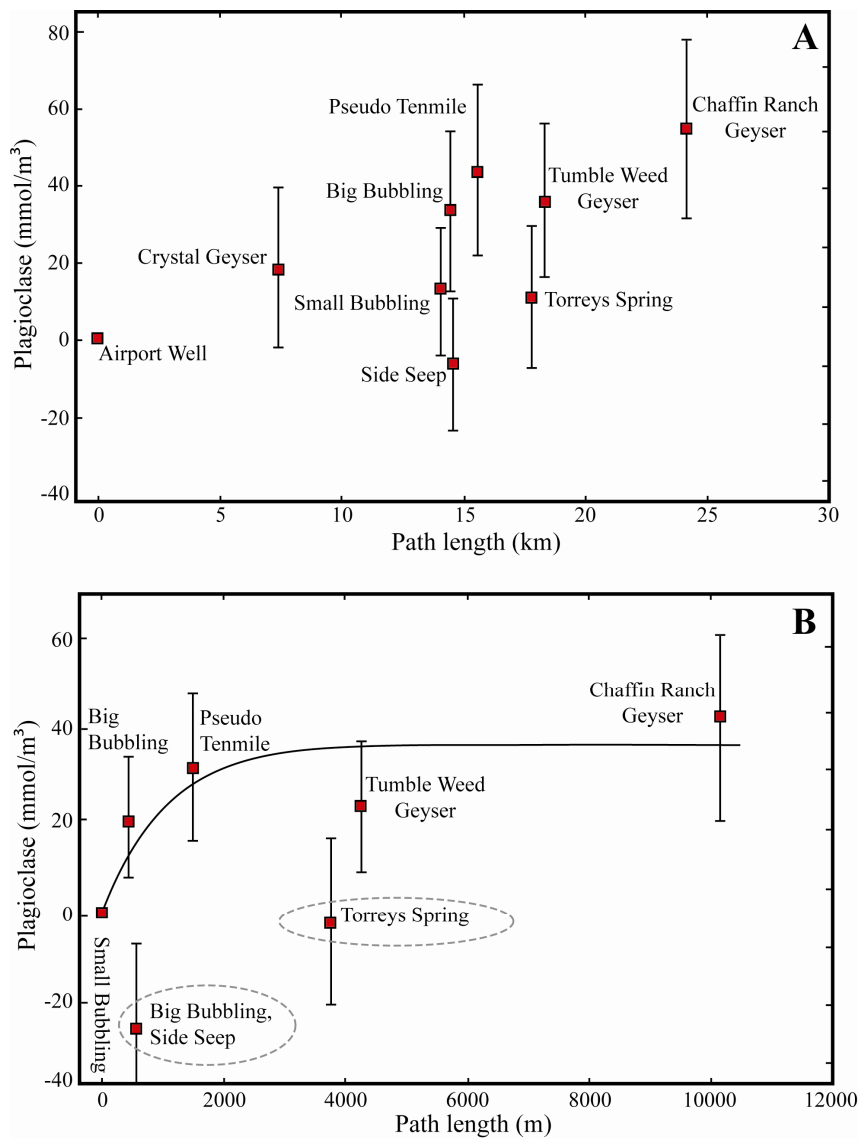


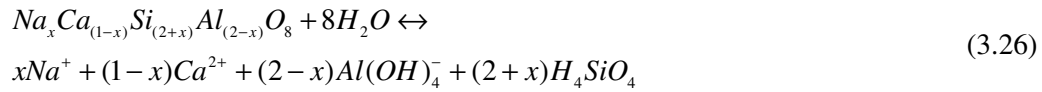
Figure 3.4-3 (A) Calculated changes in the plagioclase mineral modes with distance along the flow path, using Sr mass balance. (B) Least squares fitting of equation 3.18 yields mole transfers and calculated rates that are of the same order of magnitude as those derived from solute mass balance. Torrey's spring and Big Bubbling side seep are discounted from the fit as they have negative mole transfers, suggesting that the model does not accurately account for their measured fluid composition.

3.4.2. Approach to Equilibrium - ΔG_r

Reaction rates decrease as minerals approach equilibrium with co-existing fluids (e.g. Lasaga, 1998). We have therefore calculated the degree of solution saturation state for each spring with respect to the individual feldspar dissolution reactions. The deviation from equilibrium is expressed in terms of the Gibbs free energy of reaction, ΔG_r (kJ mol⁻¹),

$$\Delta G_r = RT \ln \left[\frac{IAP}{K_{eq}} \right] \quad (3.25)$$

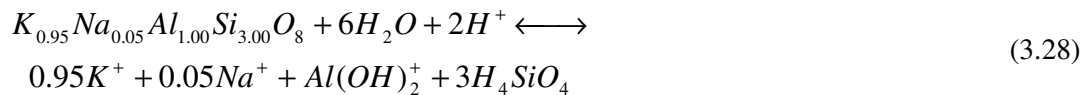
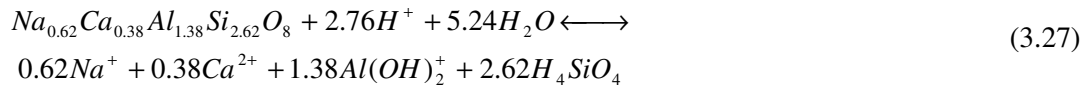
where R is the gas constant ($\text{kJ}\cdot\text{K}^{-1}\cdot\text{mol}^{-1}$), T is the absolute temperature (K), IAP is the ion activity product and K_{eq} is the equilibrium constant. The general reaction for the dissolution of plagioclase feldspar in water can be described as (Arnórsson and Stefánsson, 1999):



In general, feldspars dissolve congruently at acid and alkaline pH, and incongruently at neutral pH. Studies of mineral saturation in aqueous solutions involve two steps: (1) derivation of equilibrium constants (K_{eq}) for mineral hydrolysis from thermodynamic data taking into account the effects of variable composition of the minerals and ordering, as appropriate; and, (2) calculation of individual aqueous species activities from analytical data on the waters to retrieve values for the respective activity product (IAP). Comparison between the two allows evaluation of saturation states of waters with respect to feldspars as a function of their composition and Al-Si ordering (Arnórsson & Stefánsson, 1999).

The distribution of aqueous species and their activities were calculated using the geochemical computer code PHREEQC (Parkhurst and Appelo, 1999). ΔG_f° , T_r , P_r , V° , S° , C_p of feldspar solid solutions were calculated after Arnórsson and Stefánsson, (1999). Equilibrium constants (K_{eq}) for the reactions considered were calculated using the SUPCRT92 code (Johnson *et al.*, 1992) modified with the thermodynamic data for Al species of Tagirov and Schott (2001).

ΔG_r values for the feldspar dissolution reactions were computed from equation 3.25. Values of the ion activity product, IAP in equation 3.25, for the congruent dissolution of plagioclase and K-feldspar, consistent with the reactions



were computed using

$$IAP_{plag} = \frac{a_{Na^+}^{0.62} \cdot a_{Ca^{2+}}^{0.38} \cdot a_{Al(OH)_2^+}^{1.38} \cdot a_{H_4SiO_4}^{2.62}}{a_{H^+}^{2.76}} \quad (3.29)$$

$$IAP_{Kspar} = \frac{a_{K^+}^{0.95} \cdot a_{Na^+}^{0.05} \cdot a_{Al(OH)_2^+} \cdot a_{H_4SiO_4}^3}{a_{H^+}^2} \quad (3.30)$$

The modelled plagioclase and K-feldspar reactions exhibit a strong inverse relationship between dissolution rate and mineral-fluid free energy difference over a -10 to -2kJ mol⁻¹ and a -6 to 0 kJ mol⁻¹ transition region, respectively (Fig. 3.4-3). These free energies lie close to equilibrium in the very low ΔG_r , low dissolution rate region that is characterized by a strong functional dependence of the dissolution rate on ΔG_r . Laboratory studies on feldspars (Beig and Lüttge, 2006; Burch *et al.*, 1993; Hellman *et al.*, 2006; Hellmann and Tisserand, 2006; Taylor *et al.*, 2000) and other silicate minerals (e.g. Nagy & Lasaga, 1992) confirm theoretical predictions that dissolution rates are independent of saturation state far from equilibrium (but see Oeklers *et al.*, 1994) and decrease in a transition region as equilibrium is approached. However, the functional form of the dissolution rate: ΔG_r dependence is not well established and published expressions include simple exponentially decreasing rates as ΔG_r tends to zero (e.g. Aagaard and Helgeson, 1977, 1982; Lasaga, 1981) as well as combinations of two or more exponential terms attributed to multiple dissolution mechanisms such as the development of etch pits as saturation states deviate further from equilibrium (e.g. Hellman and Tisserand, 2006; Taylor *et al.*, 2000).

The results here for plagioclase and K-feldspar dissolution rates (Fig. 3.4-3), suggest that at $\Delta G_r > -10$ kJ/mol rates decrease exponentially over 5 orders of magnitude as equilibrium is approached. This is the most difficult region to investigate in laboratory experiments because of the very slow reaction rates, and field results, such as those here which reflect reactions over the ~ 1000 year time scales for water flow between the springs, offer an alternative approach.

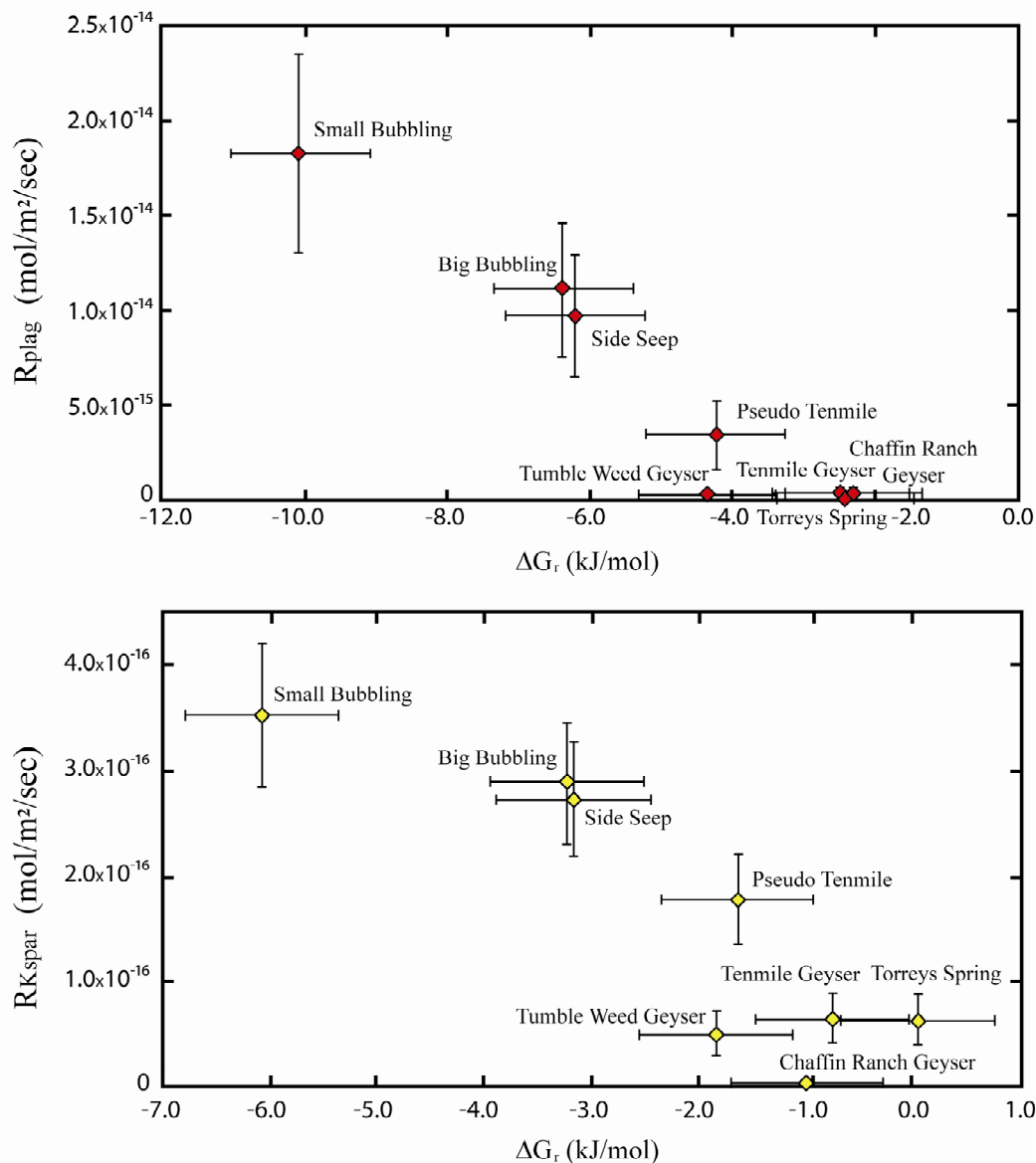


Figure 3.4-4 The variation in feldspar dissolution rate with ΔG_r at Green River, illustrating the strong dependence of rate on degree of under-saturation, the wide range of rates observed and the overall proximity of the system to equilibrium. Error bars are the propagated uncertainty in dissolution rate and ΔG_r , detailed in Appendix A.

3.4.3. Uncertainties in Reaction Rates and Solution Saturation States

The uncertainties in the reaction rates recovered from the field measurements should not be underestimated. However several of the most significant of these may cause systematic uncertainty in the absolute magnitude of the reaction rates but not the form of the functional dependence on ΔG_r . A major uncertainty is that the BET method may over-estimate mineral surface areas. However, it is unlikely that mineral surface areas will vary significantly along the

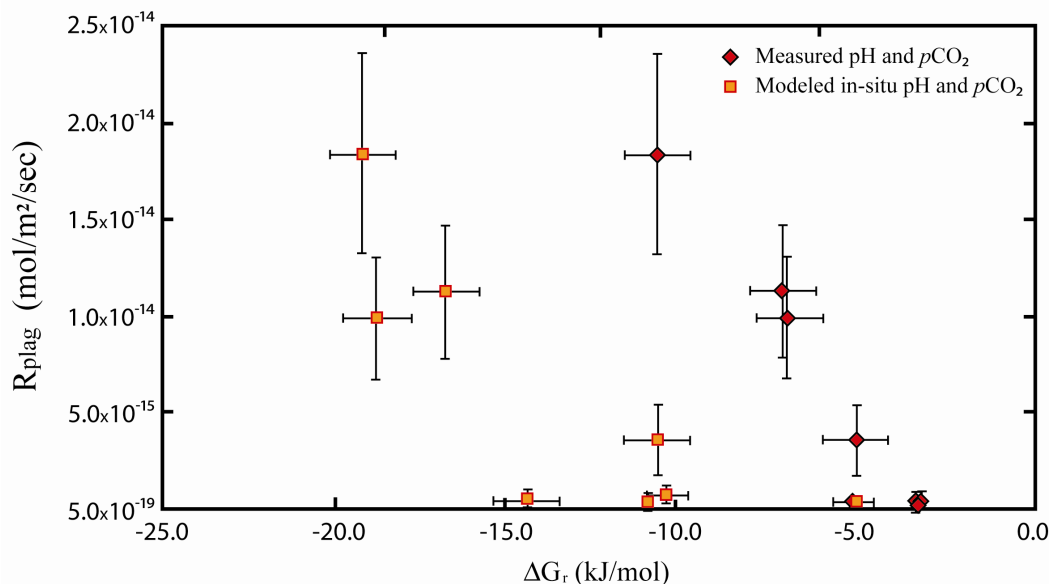


Figure 3.4-5 The variation in plagioclase dissolution rate with ΔG_r , comparing estimates of ΔG_r , from measured pH and $p\text{CO}_2$ to those derived from recalculation of in-situ $p\text{CO}_2$ and pH described in Chapter 2.

flow path and any systematic error in surface areas will result in a corresponding systematic error in the absolute values of dissolution rates but not their functional dependence on ΔG_r . K-feldspar and plagioclase geometric surface areas, are 27% and 41% less than BET determined surface areas, respectively, and would imply calculated rates that are faster than BET normalized rates by the same factors, with peak K-feldspar and plagioclase rates of 4.5×10^{-16} and $4.5 \times 10^{-14} \text{ mol} \cdot \text{m}^{-2} \cdot \text{s}^{-1}$. Complications in the hydrology could invalidate the calculation of reaction rates but the results from closely spaced springs are consistent. Again, systematic errors in estimating flow rates would not change the form of the relationship with ΔG_r .

Uncertainties in the calculation of ΔG_r are more difficult to estimate because confidence limits on the thermodynamic data are not available for the fluid species. In addition there are two further potential sources of uncertainty: 1) the filtration of water samples through $0.2 \mu\text{m}$ filters may not remove all particulate Al, although the consistency of the results suggest that this is not a serious problem in these relatively clean spring waters: 2) fluid pH and alkalinity measurements are taken from samples collected after degassing during ascent in the spring. Modelling of the carbon isotope versus pH changes during the degassing process (Assayag *et al.*, 2009) suggests that degassing must be a relatively shallow process and even so the observed CO_2 -gas to DIC $\delta^{13}\text{C}$ fractionations need to include an extra $\sim 1 \text{‰}$ kinetic fractionation. Precise estimates of the uncertainty in DIC and pH are therefore difficult to ascertain. Depth-dependent degassing may result in over-estimates of local fluid pH which would introduce systematic uncertainty in ΔG_r , and erroneously high ΔG_r estimates for each spring. Recalculation of in-situ pH and $p\text{CO}_2$ (Chapter 2, section 2.4.5.4) for the plagioclase dissolution reaction results in $\sim -10 \text{ kJ/mol}$ lower

estimates of ΔG_r for the springs closest to the site of CO₂ injection, decreasing to between -5 and 0 kJ/mol for the springs furthest along the flow path (Fig. 3.4-5). Even at the maximum in-situ pH ΔG_r estimates are still close to or within the experimentally determined close to equilibrium region, where rates are predicted to exhibit strong ΔG_r dependence.

3.4.4. Comparison of Reaction Rates with Laboratory and Field Estimates

The observed proximity of Green River Navajo Sandstone fluids to plagioclase and K-feldspar equilibrium and the dependence of feldspar dissolution rates on deviation from these equilibria may explain a significant part of the apparent discrepancy with comparable laboratory-derived rates, which typically characterize systems far from equilibrium.

For example, the experiments of Taylor *et al.*, (2000) on plagioclase (An61) dissolution at 25°C and pH 3 (Fig. 3.4-6) imply that plagioclase (An61) dissolution rates at $\Delta G_r = -10$ kJ/mol are about 18% of those measured at far from equilibrium (Fig. 3.4-6). If so, the calculated rates at low ΔG_r of $\sim 2 \times 10^{-14}$ mol·m⁻²·s⁻¹ would be compatible with far-from-equilibrium rates of $\sim 1 \times 10^{-13}$ mol·m⁻²·s⁻¹ as observed in some experimental studies (e.g. Amrhein and Suarez, 1992; White and Brantley, 2003). If geometric surface area normalized rates are considered, close to equilibrium rates derived here imply far from equilibrium rates of $\sim 3 \times 10^{-13}$ mol·m⁻²·s⁻¹ within error, of the mean of circum-neutral pH laboratory derived plagioclase dissolution rates ($\sim 4.6 \times 10^{-13}$ mol·m⁻²·s⁻¹) (White and Brantley, 2003).

The effect of inhibiting ions, namely Al and CO₃²⁻ are difficult to assess in any natural system due to the competing and interdependent effects of pH, ΔG_r , and ion activities. Al concentrations are on the order of 3 to 6 μmol L⁻¹ significantly lower than the 500 μmol L⁻¹ required for significant Al inhibition at 25 °C reported by Amrhein and Suarez, (1992). Amrhein and Suarez, (1992) report a 31% decrease in anorthite dissolution rate at 25 °C and pH 6 in the presence of Al concentrations of 4 μmol L⁻¹. Correction of the calculated rates for this magnitude of Al inhibition makes a negligible difference to the peak plagioclase dissolution rates, which become 2.4×10^{-14} mol·m⁻²·s⁻¹. Oeklers *et al.*, (1994) reported a ~16% decreasing in albite dissolution rates at 150°C and pH 9 in the presence of 1000 μmol L⁻¹ Al. A ~10% decrease in K-feldspar dissolution rate at 150°C and pH 2 was reported by Gautier *et al.*, (1994) for similar Al concentrations. Whilst the presence of dissolved Al may have a small effect on suppressing the overall magnitude of the dissolution rates in this system, its effect is probably small and cannot explain the overall variation in the magnitude of rates observed. However without experimental studies at the relevant feldspar compositions, temperature and pH this is difficult to assess quantitatively. No applicable experimental work has been conducted on CO₃²⁻ at the relevant temperature and *p*CO₂ and as CO₃²⁻ surface complexation is likely to increase solubility, its effect on retarding dissolution rate can be negated.

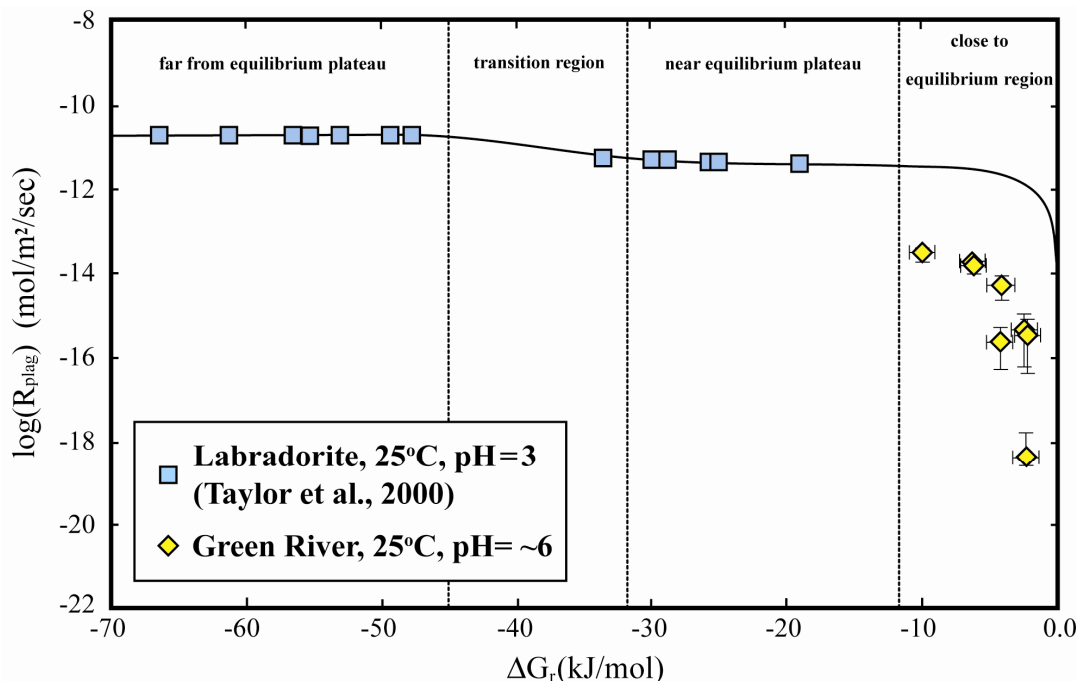


Figure 3.4-6 Variation in plagioclase dissolution rate with ΔG_r at Green River compared to experimentally determined rates at similar pH and temperature (after Taylor *et al.*, 2000). Green River rates have been normalized to 25°C using the Arrhenius equation and an activation energy of 80 kJ/mol from Blum and Stillings (1995). Line fit to the experimental data is the dissolution rate law of Taylor *et al.*, (2000). The figure illustrates the main ΔG_r regions over which free energy-rate dependence and independence is observed in experimental studies. It should be noted that differences in the magnitude of our rates compared to the predicted rates at $\Delta G_r > -10$ kJ/mol of Taylor *et al.*, (2000) are attributed to differences in An content and pH between their experiment and the groundwater system, but this is the only study of ΔG_r dependence at a 'comparable' plagioclase composition and at low temperature.

Differences in feldspar dissolution rates observed between surface weathering environments and aquifer systems (White and Brantley, 2003) are attributed to the difference in proximity of these two systems to equilibrium. The difference in proximity to equilibrium found here as compared to the lower ΔG_r values (-30 to -50 kJ mol⁻¹) for feldspar dissolution observed in surface weathering environments (Velbel, 1989) with high percolation velocities suggests that slow flow velocities and long solution-mineral contact times in aquifers maybe important in holding silicate weathering reactions close to thermodynamic equilibrium. It should be noted that the slow rate of fluid percolation through the Navajo Sandstone favours mineral surface control, as apposed to transport control on fluid-mineral reaction rate.

Additionally the apparent pH dependence observed in compilations of field-scale dissolution rates at circum-neutral pH (Fig. 3.4-2) is attributable to the combined effects of a) their proximity to equilibrium and b) the strong variation in ΔG_r observed over a small change in pH between pH 6 and 7.

3.5. Conclusions

In-situ feldspar dissolution rates under conditions of high $p\text{CO}_2$, within the saturated Navajo Sandstone at Green River, Utah have been determined in this chapter. The close to equilibrium plagioclase dissolution rates derived from mass balance and hydrological modelling range from $10^{-13.74 \pm 0.11/0.15} \text{ mol}\cdot\text{m}^{-2}\cdot\text{s}^{-1}$ to $10^{-18.63 \pm 0.6/1.5} \text{ mol}\cdot\text{m}^{-2}\cdot\text{s}^{-1}$. K-feldspar dissolution rates range from $10^{-15.45 \pm 0.08/0.09} \text{ mol}\cdot\text{m}^{-2}\cdot\text{s}^{-1}$ to $10^{-17.42 - 0.27/0.81} \text{ mol}\cdot\text{m}^{-2}\cdot\text{s}^{-1}$. These rates are 1 to 3 orders of magnitude slower than rates determined by laboratory experiments at similar temperatures and pH, and 1 to 3 orders of magnitude faster than rates determined in the same aquifer under alkaline groundwater conditions. The enhancement of feldspar dissolution rates in this study area, relative to those determined by Zhu (2005) for alkaline groundwater, is attributed to the introduction of CO_2 which depresses silicate mineral saturation in the fluids. The finding that the Green River system is close to thermodynamic saturation adds to the evidence that the 2–5 orders of magnitude discrepancy between laboratory and field rates may, in part, be explained by differences in the thermodynamic state of experimental and natural fluids (c.f. Burch *et al.*, 1993; White and Brantley, 2003).

The range of rates and the rate: ΔG_r dependence observed at Green River suggest that feldspar dissolution rate laws should include exponentially declining rates close to equilibrium ($\Delta G_r < -10\text{kJ/mol}$), over a wider range (and slower absolute values) of dissolution rate than previously suggested by experimental studies. These findings suggest that mineral-fluid reactions in CO_2 hosting reservoirs will be promoted by the state of disequilibrium induced by the introduction of CO_2 and highlight the importance of including a rate: ΔG_r dependence in the geochemical modelling of the long term interactions of CO_2 -fluid-rock in geological storage reservoirs. This suggests that in the earliest stages of CO_2 injection in storage sites systems can be expected to be highly undersaturated with respect to minerals comprising the host reservoir and reaction rates will be fast, occurring at low ΔG_r . The continued study of fluid-rock interactions in natural settings may help further elucidate the relationship between rate and ΔG_r for a range of mineral phases, in the close-to-equilibrium region which is so difficult to assess experimentally.

These results must be tempered with the understanding that large uncertainties exist in the quantification of modelling parameters in natural settings, especially reactive mineral surface area, indirect sampling of reservoir fluids and the hydro-geological setting. The long duration of reaction accessible in natural studies, whilst allowing access to controlling factors of real mineral weathering such as near equilibrium rate dependence, also introduces uncertainty as many model parameters may change through the duration of the ‘experiment’. The change in porosity and reacting mineral surface through the duration of the natural experiment cannot easily be factored into the calculation of the controlling rates. Heterogeneity in reservoir hydraulic properties, mineralogy and fluid chemistry also lead to uncertainty in the calculation of rates.

Chapter 4

Geochemistry of an Ancient CO₂-Leaking Groundwater System, Green River, Utah

4.1. Introduction

Surface travertine deposits, and carbonate cementation and veining within Jurassic sandstones within the footwall of Little Grand Fault (LGF) and Salt Wash Graben (SWG) record a history of CO₂ leakage from the Green River anticline. The origin and evolution of fluids responsible for surface travertine formation, shallow subsurface carbonate veining and host rock alteration may be delineated from petrographic observations, and from the chemical and isotopic composition of mineral products. Further, processes important for controlling the leakage of CO₂ from the fault systems, and the coupling of physical and geochemical processes during subsurface CO₂ leakage, can be investigated through the analysis of chemical and isotopic systems. Understanding the evolution of leakage behaviour in fault systems both in time and space, and under conditions of differing fluid infiltration, mineral-fluid reactions, fault architecture and lithological properties is of great importance for predicting the potential leakage behaviour of geological CO₂ storage sites. Physical and geochemical observations from naturally leaking faults allows prediction to be made about the interplay of structural and chemical processes in controlling leakage sites and rates, the role of fluid-mineral interactions in generating and closing leakage pathways and their relation to geochemical processes in the host aquifer, such as the volume of the CO₂-charge, and subsequent in-situ $p\text{CO}_2$, and the dissolved mineral load.

The petrology and mineral chemistry of altered host rock, carbonate cements and veins from fracture networks in the fault damage zone and in travertine feeder systems provide constraints on the pathways and rates of CO₂-promoted fluid-mineral reactions. Minor and trace element contents of carbonate cements reflect pore water chemistries prevailing during carbonate precipitation (Veizer, 1983) and with knowledge of the relevant mineral-fluid partition coefficients can be used to reconstruct the chemistry of the parent fluid. In addition, if the composition of the parent fluid is known, a posteriori, mineral and fluid chemistry can be used to constrain the magnitude of this partitioning. For some trace elements, experimental studies have shown that the magnitude of the partitioning is dependent on the kinetics of the incorporation of the element into the carbonate mineral structure. Thus, if past fluids associated with ancient

travertine formation were compositionally similar to the modern CO₂-charged fluids, this fluid composition, in conjunction with measured carbonate cement compositions can be used to estimate the rate of carbonate mineral precipitation. Information on the rates of carbonate cementation in fault zones, and their geochemical controls, is of great importance in predicting the sealing behaviour of faults and fracture zones as a result of the passage of CO₂-charged fluids. This will allow prediction of the time required for leaking faults in geological carbon storage sites to self seal through carbonate mineral precipitation.

4.1.1. Diagenetic Bleaching of Jurassic Sandstones, Paradox Basin

The aeolian Lower to Middle Jurassic sandstones of the Paradox Basin are typically characterized by a uniform red color that results from thin hematite coatings on sand grains, formed during early diagenesis (Walker, 1975). Across the Paradox Basin, adjacent to faults and preferentially in coarser grained sandstone units, these reddish sandstones are frequently bleached pale-yellow or white where hematite grain coatings have been dissolved by the passage of diagenetic fluids (Foxford et al., 1996; Garden et al., 1997, 2001). The nature of the fluid(s) responsible for this bleaching are still highly debated as many volatile species are capable of altering the Eh-pH conditions of subsurface fluids, facilitating dissolution of minerals such as hematite, which are otherwise relatively insoluble in typical, low temperature groundwater systems. These extra-formational fluids may include hydrocarbon liquids, carbon dioxide, organic acids, methane, hydrogen sulphide (Chan et al., 2000; Eichhubl et al., 2009; Garden et al., 2001; Surdam et al., 1993) and de-oxygenated fluids. Previous studies of bleaching in the Paradox Basin have mainly attributed the bleaching fluid directly to hydrocarbons (Beitler et al., 2003; Bowen, 2004; Chan et al., 2000; Garden et al., 2001; Hansley, 1995; Parry et al., 2004) or fluids directly associated with them (Eichhubl et al., 2009). Although alternative volatile phases, such as CO₂ + H₂S, have been proposed (Haszeldine et al., 2005). What ever the mechanism, such extensive dissolution of hematite must involve reductive hydrolysis via the reaction; $Fe_2O_3 + 2e + 6H^+ \leftrightarrow 2Fe^{2+} + 3H_2O$, given the very low solubility of Fe³⁺ in typical groundwaters.

At Green River bleaching of Jurassic sandstones occurs to varying degrees in the footwalls of both Little Grand Fault (Curtis Formation) and Salt Wash Graben (Entrada Sandstone) (Dockrill, 2005). The distribution of bleaching in the footwalls of both faults is focused at the intersection of the faults and the fold axis of the Green River anticline. Two distinct generations of sandstone bleaching are observable in the field. The first is large-scale bleaching which is m's thick and 10's to 1000's m in lateral extent, separated from unbleached rock by a sharp contact and constrained to the lower portions of individual formations. This bleaching is associated with calcite cementation and gypsum and calcite veining. The second is small-scale bleaching which is confined to the base of ancient travertine deposits. This occurs as:

a) thin, 10's cm thick bleached sandstone beds which extend laterally 10's meters from the alteration zone; b) as halos, mm's-cm's thick, around fractures within the alteration zone and; c) as diffuse bleaching in zones of complex alteration, and calcite and aragonite cementation and veining. The origin of both bleaching events, and their relationship to each other, is uncertain but the localization of bleaching in travertine feeder zones implies at least some relation between this geochemical processes and the passage of CO₂-charged fluids.

This chapter discusses the petrology, isotope geochemistry and mineralogy of bleaching associated with ancient travertine feeder zones, within the Entrada Sandstone, Salt Wash Graben. In this chapter mineral composition from calcite cements associated with bleaching below travertine mounds are used to constrain the Eh-pH conditions prevailing in the ancient CO₂-system. The petrology and isotope geochemistry of the large-scale bleached zones is discussed in Chapter 5, where observations from fluid inclusions are used to constrain the volatile phase responsible for bleaching in each system.

4.2. Objectives

Carbonate cemented host rock and carbonate veins from the Entrada Sandstone, in the footwall of Salt Wash Graben, were collected for geochemical, petrological and isotopic analysis. Samples collected during the 2007 field season were supplemented with chips of U-Th dated carbonate veins from both Little Grand Fault and Salt Wash Graben provided by Neil Burnside, University of Glasgow. Isotopic analysis of their ⁸⁷Sr/⁸⁶Sr, δ¹⁸O and δ¹³C performed at the University of Cambridge allows a reconstruction of the evolution of the isotopic composition of CO₂-charged groundwaters, sourced from the Navajo Aquifer, over the ca 413 ka year leakage history (Burnside, 2009) recorded in these deposits.

Detailed petrology, cathodoluminescence and SEM mapping of thin sections, and EDS, XRD and XRF were used to characterize the mineralogy of the original host rock and the mineralogical products of interaction with CO₂-charged fluids. Detailed compositional analysis of the carbonate minerals can be used to constrain the chemistry of the parent fluid, Eh-pH conditions prevailing during its deposition and to asses the role of kinetic processes in controlling carbonate formation and to quantify their precipitation rates. A petrological and isotopic study of carbonate mineral products within the fault zones was carried out in order to investigate the following:

- 1) What was the nature and origin of the fluid associated with ancient travertine deposition and did that fluid vary compositionally with time (i.e. modification of major chemistry through fluid-mineral reactions; degassing or carbonate precipitation modification of the δ¹³C_{DIC})? Was it compositionally similar to the active CO₂ system?

- 2) What were the Eh-pH conditions prevailing in the ancient CO₂-charged groundwaters? Were the groundwaters sufficiently reduced, due to low dissolved oxygen content, that pH suppression due to high concentrations of dissolved CO₂, was sufficient to dissolve hematite grain coatings?
- 3) What geochemical factors control the mineralogy, chemistry and rates of carbonate cementation in travertine feeder zones? Can carbonate chemistry be used to infer carbonate precipitation rates and if so how do these rates compare to predictions from experimental studies on surface controlled mineral precipitation rates? What geochemical factors, such as the presence of inhibiting ions, the state of saturation with respect to carbonate and the degree of CO₂-degassing, are most important in controlling precipitation rates?
- 4) What are the timescales of active CO₂ injection, from deeper formations, into the Navajo Aquifer? Does surface leakage occur immediately upon injection of CO₂ into the Navajo Aquifer or is there a delay reflecting the time required for physical and geochemical interactions to occur, facilitating leakage? How long does this CO₂-charge take to dissipate? Is there a coupling between CO₂ injection, surface leakage and the rate of mineral- and gas-fluid reactions?
- 5) What controls the spatial and temporal distribution of leakage sites? Do these sites vary as a result of geochemical processes, such as the plugging of leakage pathways by carbonate deposition? Are overall properties of the fault lithologies, fault architecture and local hydrology important in controlling rates of leakage?

4.3. Methodology

4.3.1. Isotopic Systems and Fluid Rock Interaction

When information is desired regarding the past properties of a hydrological system information recorded in minerals deposited in past regimes is of great value (e.g. Bottomley and Veizer, 1992; Hendry and Marshall, 1991; Marshall *et al.*, 1992, Paces *et al.*, 1994; Whelan and Stuckless, 1992). The stable-isotope geochemistry of carbonate phases can be analyzed to help constrain pore-water evolution. The isotope ratios of O and C record the isotope ratios of the parent fluid, modified by temperature-dependent fractionations. Oxygen isotopic signatures may provide information about fluid flow, fluid sources and fluid–rock interaction (e.g. Burkhard and Kerrich, 1988; Burkhard *et al.*, 1992; Janssen *et al.*, 1997, 1998). Commonly pore waters can be attributed to end-member compositions (e.g. meteoric, seawater, basinal brine) or to mixing lines between these end member compositions (e.g. Lee and Krothe, 2001).

The carbon isotopic signature of carbonate can be used to study the origin and evolution of the pore water carbon reservoir from which inferences about the nature of the original carbon source can be made, if precipitation temperature can be independently estimated. Further, the stable isotopic composition of the parent fluid may be fractionated by reactions resulting from

physical processes, such as volatile loss and mineral precipitation, important for understanding the physical and geochemical controls on fluid chemistry and the evolution of pore fluid chemistry and mineral products as a result of these processes.

The isotope ratios of Sr and other ‘nonfractionating’ elements in solution deposited minerals are always equal to those of the parent water; thus these isotope ratios directly record water conditions prevailing at the time of precipitation, with possible alteration due to subsequent cation exchange. The ⁸⁷Sr/⁸⁶Sr ratios in groundwater reflect the water-rock reaction histories and flow pathways of the waters and the mixing of distinct water sources. Several studies have used ⁸⁷Sr/⁸⁶Sr as a natural tracer of groundwater flow and fluid-rock interaction (e.g., Blum *et al.*, 1993; Bullen *et al.*, 1997; Clow *et al.*, 1997; Johnson and DePaolo, 1994; Katz and Bullen, 1996; Musgrove and Banner, 1993). ⁸⁷Sr/⁸⁶Sr in groundwater evolve toward the ratio of Sr acquired from the host rock, primarily from silicate minerals (e.g. plagioclase, K-feldspar, mica). Although ⁸⁷Sr is radiogenic the roughly forty seven billion year half life of the decay process is so long that on the timescale of groundwater evolution, ⁸⁷Sr/⁸⁶Sr of Sr sources is essentially stable.

4.3.2. Faults and CO₂ Leakage

Fluid infiltration into faults and the resulting fluid–rock interaction influence the chemical and mechanical behaviour of faults (Hubbert and Rubey, 1959). In particular, elevated pore fluid pressures, which reduce the effective confining stress and allow frictional slip at low fault stress, have been invoked to explain the remarkable weakness of major fault zones (Chester *et al.*, 1993; Chester and Logan, 1986; Lachenbruch and Sass, 1980; Miller *et al.*, 1996). Since areas of CO₂ discharge globally coincide with regions of seismic activity, CO₂ exsolution may increase pore fluid pressures within fault zones (e.g. Barnes *et al.*, 1978; Irwin and Barnes, 1975), and corrode minerals comprising the fault surface, inducing fault weakening (Kennedy *et al.*, 1997). Recent detailed studies on fault zones have revealed that faults act both as important fluid conduits during fault-related deformation and as barriers to fluid flow (Caine *et al.*, 1996). This conduit-barrier behaviour of faults varies in space and time during the active fault stages (Goddard and Evans, 1995; Logan and Decker, 1994). Structural and geochemical studies have been used to characterize fault-related alteration processes both along and across major fault zones (e.g. Chester, 1994; Cox, 1995; Hadizadeh, 1994)

4.3.3. Isotopes: Equilibrium versus kinetic fractionation

4.3.3.1. Carbon Isotopes

Various mechanisms can lead to the precipitation of calcium carbonate from groundwaters. Precipitation of calcite can precede either by slow reactions close to equilibrium or by rapid

irreversible reactions. In the first forward and backward reaction rates are almost equal. The products formed escape from the solution and do not interact with it again. Under such conditions the products are in carbon and oxygen isotopic equilibrium with the solution, when they are generated. This, however, requires slow deposition rates, whereby the Ca-concentration at the surface of the solid must be close to saturation with respect to calcite. The fractionation factors α_{eq} in this case are the corresponding equilibrium values. For the carbonate system, in the pH range of interest, they can be defined from experimental studies (Clark and Fritz, 1997; Deines *et al.*, 1974; Romanek, 1992) as:

$$10^3 \ln \alpha_{CO_2(aq)-CO_2(g)} = -0.373 \times 10^3 T^{-1} + 0.19 \quad (4.1)$$

$$10^3 \ln \alpha_{H_2CO_3-CO_2(g)} = (-0.91 + 0.0063 \times 10^6) / T^2 \quad (4.2)$$

$$10^3 \ln \alpha_{HCO_3^- - CO_2(g)} = 9.552 \times 10^3 T^{-1} - 24.1 \quad (4.3)$$

$$10^3 \ln \alpha_{cc-CO_2(g)} = 2.988 \times 10^6 T^{-2} - 7.6663 \times 10^3 T^{-1} + 2.4612 \quad (4.4)$$

$$10^3 \ln \alpha_{arag-CO_2(g)} = 13.88 - 0.13 \times T \quad (4.5)$$

$$\delta^{13}C_{dol} - \delta^{13}C_{HCO_3^-} = 38.832 - \frac{31.506 \times 10^3}{T} + \frac{7.698 \times 10^6}{T^2} - \frac{0.388 \times 10^9}{T^3} \quad (4.6)$$

Where

$$\alpha_{CO_2(aq)-CO_2(g)} = (\delta^{13}C_{CO_2(aq)} + 1000) / (\delta^{13}C_{CO_2(g)} + 1000) \quad (4.7)$$

$$\alpha_{H_2CO_3-CO_2(g)} = (\delta^{13}C_{H_2CO_3} + 1000) / (\delta^{13}C_{CO_2(g)} + 1000) \quad (4.8)$$

$$\alpha_{HCO_3^- - CO_2(g)} = (\delta^{13}C_{HCO_3^-} + 1000) / (\delta^{13}C_{CO_2(g)} + 1000) \quad (4.9)$$

$$\alpha_{CaCO_3-CO_2(g)} = (\delta^{13}C_{CaCO_3} + 1000) / (\delta^{13}C_{CO_2(g)} + 1000) \quad (4.10)$$

can be employed to yield the individual equilibrium fractionation factors between all of the various carbonate species and from which the isotopic composition of HCO₃⁻ in equilibrium with measured values of calcium carbonate $\delta^{13}C$ can be estimated.

For non-equilibrium fractionation the other extreme is irreversible fast precipitation as a consequently of rapid changes in solution composition which produce and maintain an elevated saturation state of calcium carbonate (Ω_{cc}). Such processes include very rapid changes in pH via H⁺ consuming mineral dissolution reactions with fast kinetics and CO₂ degassing. Three

processes determine the value of the rate constant of calcium carbonate precipitation: (a) the precipitation kinetics at the surface of the mineral. (b) Mass transport of the reacting species from and towards this surface, respectively. (c) The slow conversion of HCO₃⁻ to CO₂ and the chemical reactions of carbonate chemistry (Buhmann and Dreybrodt, 1985; Dreybrodt, 1988, Dreybrodt *et al.*, 1996). Such irreversible processes result in kinetic fractionation with different fractionation factors α_{kin} , caused by the different reaction rates of the light and the heavy molecules (Zeebe and Wolf-Gladrow, 2001). However, the magnitude of these fractionations is largely unknown.

4.3.3.2. Oxygen Isotopes

During calcium carbonate precipitation, in contrast to carbon where all atoms are contained in HCO₃⁻ and CO₂(aq) molecules and to a negligible amount in CO₃²⁻, the oxygen atoms are exchanged not only within the carbonate species but also with the huge amount of oxygen atoms in the water. These represent a large reservoir with about 10⁴ times more atoms than contained in the carbonate species.

The oxygen isotopic composition of water in equilibrium with calcite, aragonite and dolomite can be derived from (Kim and O'Neil, 1997, 2007; Zhou and Zheng, 2003):

$$10^3 \ln \alpha_{cal-H_2O} = 18.03 \times 10^3 T^{-1} - 32.42 \quad (4.11)$$

$$10^3 \ln \alpha_{arag-H_2O} = 20.44 \times 10^3 / T^{-1} - 41.48 \quad (4.12)$$

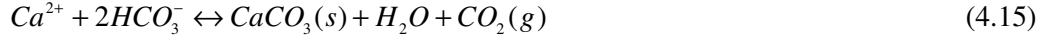
$$10^3 \ln \alpha_{dol-H_2O} = 2.73 \times 10^6 T^{-2} + 0.26 \quad (4.13)$$

Equilibrium isotopic fractionation between HCO₃⁻ and H₂O can be assumed in instances where the precipitation rate of carbonate is sufficiently slow to allow equilibration of HCO₃⁻ in solution with H₂O. Since the slowest of the reactions taking place in solution during the precipitation of calcium carbonate is the dehydration of bicarbonate ions, and the hydration of aqueous carbon dioxide (Williams, 1983) and since this is the only step in which isotopic exchange can take place between the oxygen of the water and the oxygen of the carbon compounds in solution, equilibrium between these species is necessary for the carbonate to be precipitated in oxygen isotopic equilibrium with the water. Positively correlated $\delta^{18}O$ versus $\delta^{13}C$ with a slope that deviates from that expected for changes in fractionation due to temperature variations is a general indication that kinetic processes may ultimately govern $\delta^{18}O_{CaCO_3}$.

4.3.4. Carbonate Precipitation in CO₂-rich Fluids

Dissolved CO₂ will react with divalent cations, in solution, to form carbonate minerals (e.g. calcite, siderite, magnesite) which will form a sink of CO₂ from the fluid. Overall reaction

stoichiometries show that calcite precipitation consumes bicarbonate ion while either increasing acidity in a closed system or liberating CO₂(g) in a system open to CO₂ loss (i.e. CO₂ degassing):



Increase in HCO₃⁻ concentrations, Ca²⁺ liberation and H⁺ consumption through mineral dissolution, or CO₂ loss through degassing, drives overall equations (4.14) and (4.15) to the right, resulting in the precipitation of calcite.

Rates of these reactions are known to be fast, relative to the slow kinetics of CO₂ dissolution and aqueous speciation, but have a complex dependence on reactant concentrations, in situ pH, temperature and fluid composition (e.g. Morse 1986; Mucci and Morse, 1983, 1984; Zuddas and Mucci 1998). Additionally, carbonate precipitation rates may be ultimately limited by solute supply and solute transport, as apposed to true mineral surface reaction (e.g. Given and Wilkinson, 1985; Lee *et al.*, 1996; Wilkinson and Dampier, 1990).

Surface controlled mineral precipitation and dissolution rates have most often been expressed in terms of a disequilibrium functional dependence. Since the net growth rate of calcium carbonate is, a priori, a function of calcium and bicarbonate concentrations, rate data has been commonly fitted to the following rate equation (Arvidson and Mackenzie, 2000; Berner and Morse, 1974; Gledhill and Morse, 2006; Morse and Arvidson, 2002; Nancollas and Reddy, 1971):

$$R = k(\Omega_{cc} - 1)^n \quad (4.16)$$

or its logarithmic form:

$$\log R = \log k + n \log (\Omega_{cc} - 1) \quad (4.17)$$

where R is the precipitation rate normalized to the reacting surface area (mol m⁻² s⁻¹), k is the rate constant, n is the order of the overall reaction (Lee and Morse, 1999; Morse, 1987; Mucci and Morse, 1984; Nancollas and Reddy, 1971) and Ω_{cc} is the saturation state defined as

$$\Omega_{cc} = \frac{[HCO_3^-] \cdot [Ca^{2+}]}{K_{cc}^* \cdot [H^+]} \quad (4.18)$$

where K_{cc}^* is the calcite stoichiometric solubility constant at a given temperature, and [HCO₃⁻] and [Ca²⁺] are the bicarbonate and calcium ion concentrations, respectively. This model is commonly adopted for precipitation from aqueous solutions of minerals such as calcite and

involves alternating incorporation of cations and anions (Ca²⁺ and CO₃²⁻) into the lattice. In this case, the growth rate also depends on the relative abundance of the cations and anions in solutions in addition to Ω_{cc} .

Within porefluids at, or close to saturation with CO₂ the [HCO₃⁻] >> [Ca²⁺] and the macroscopic variation in carbonate precipitation rates will be partly limited by the availability of Ca²⁺ and other divalent ions. Given the order of magnitude differences between [HCO₃⁻] and [Ca²⁺] in typical porefluids the microscopic variability in precipitation rate will be governed by variation in Ω_{cc} due to variable activities of [HCO₃⁻] and [H⁺]. Variation in [HCO₃⁻] and [H⁺] will primarily be caused by changes in *p*CO₂, the extent of reaction and the degree of pH buffering.

Numerous studies (e.g. Dreybrodt *et al.*, 1992; Herman & Lorah, 1987, 1988; Lorah & Herman, 1988; White, 1997) show that calcite does not precipitate instantaneously at the point of saturation. Precipitation requires a finite supersaturation because of activation barriers to calcite nucleation and crystal growth (White, 1997). Activation barriers may also be accompanied by calcite inhibitor ions, e.g. Mg (Arvidson *et al.*, 2006; Berner, 1975; Bischoff, 1968; Pytkowicz, 1965), or the presence of organic matter (Berner, 1975; Raiswell & Fisher, 2004). In most circumstances this implies a saturation index (*SI_{cc}*) of +0.5, although Dreybrodt *et al.*, (1992) suggest that saturation indices of at least +1.0 are required.

The rate of calcite growth in porefluids is strongly influenced by its relative supersaturation, the *p*CO₂, the concentration of inhibitor ions and organic molecules and the trace ion/Ca²⁺ of the parent fluid (Arvidson *et al.*, 2003; Busenberg and Plummer, 1986; House *et al.*, 1981; Inskeep and Bloom, 1985; Morse, 1983; Nancollas and Reddy, 1971; Reddy *et al.*, 1981; Shiraki and Brantley, 1995; Zhong and Mucci, 1993; Zuddas and Mucci, 1994). It is expected that, in fluids with complex chemistry calcite precipitation will be suppressed by a decrease in the density of active growing sites due to the blocking of growth steps and kink sites by the adsorption of divalent ions such as Fe²⁺, Mn²⁺ and Mg²⁺ (Chen *et al.*, 2006; Dromgoole and Walter, 1990b; Gutjahr *et al.*, 1996; Katz *et al.*, 1993; Meyer, 1984; Reddy and Wang 1980). This effect decreases with increasing super-saturation due to higher intrinsic growth rates and the rapid 'burial' of the absorbed ion. The ratio of trace ion (Tr) concentrations of components forming solid solutions with that of the pure endmember, Tr²⁺/Ca²⁺, (e.g. Mg²⁺, Mn²⁺, Fe²⁺) have been shown to lower calcite precipitation rates where the concentration of the trace ion in the parent fluid is high and where the solubility of the TrCO₃ endmember is greater than that of pure calcite (Berner, 1975, Dromgoole & Walter, 1990b; Meyer, 1984; Mucci, 1988). This may be especially important in diagenetic systems where Fe²⁺ and Mn²⁺ concentrations in pore fluids can be large. Additionally the precipitation kinetics of calcite increase with increasing *p*CO₂ at (constant supersaturation) due to an increase in the activity of the component carbonate species in solution. Water soluble organic ligands and ions such as PO₄³⁻ and SO₄²⁻ have been known to act as

precipitation inhibitors by blocking crystal growth sites (Katz *et al.*, 1993; Kitano and Hood, 1965; Paquette *et al.*, 1996; Reddy, 1977)

4.3.5. Carbonate Cement Compositions

Interpreting the mode and environment of formation of secondary carbonates deposited from CO₂-charged fluids is best achieved by examination of the chemical and isotopic composition of the secondary phases themselves. Minor and trace element contents (Mg, Fe, Mn, Sr, Ba, Na, K) of carbonate cements reflect pore water chemistries prevailing during carbonate precipitation (e.g. Rimstidt, 1998; Veizer, 1983). The systematic dependence of the coprecipitation of these ‘foreign’ ions in calcite, dolomite and aragonite with various physical and chemical processes provides an important tool in understanding paleo-fluid chemistry and the pathways by which fluid-mineral reactions have occurred. Numerous studies have focused on the measurement and application of partition coefficients, which relate the composition of the carbonate mineral to that of the solution from which it precipitated (e.g. Brand and Veizer, 1980; Budd *et al.*, 1993; Fairchild *et al.*, 2000; Oomori *et al.*, 1987). For instance, the temperature dependence of Mg²⁺ incorporation into the calcite lattice makes it an important tool in interpreting paleo-temperatures (e.g. Morse *et al.*, 1997). Efforts have been made to use the Na⁺ contents of carbonates as indicators of paleosalinities and salinity (e.g. Veizer *et al.*, 1977; Ishkawa and Ichikumi, 1984) but Na probably occupies interstitial positions in the calcite structure and its incorporation is thus partly dependent on the number of surface defect sites (see Busenberg and Plummer, 1984).

Concentrations of the redox sensitive elements Fe and Mn in calcite have been used, in conjunction with cathodoluminescence (CL) microscopy, to interpret paleo-redox conditions of pore waters prevailing during diagenesis (see Barnaby and Rimstidt, 1989 for a thorough review). Variation in CL brightness is primarily a function of Fe²⁺ and Mn²⁺ content, with Fe²⁺ the main quencher and Mn²⁺ the main activator of luminescence (Sommer, 1972; Fairchild, 1983; Machel, 1985; Mason, 1987). Natural calcite cements may contain 1000's of ppm Fe or Mn, and a minimum of ~ 10 ppm Mn is necessary to activate CL (Ten Have and Heijnen, 1965). Variations in CL brightness may record changes in Fe²⁺ and Mn²⁺ concentrations which reflect changes in the Eh-pH conditions of the parent fluids (e.g., Frank *et al.*, 1982).

The equilibrium partitioning of a component between two phases can be represented as a simple chemical reaction:



With an equilibrium constant (K) for the reaction of:

$$K = a_{X_{\text{phaseA}}} / a_{X_{\text{phaseB}}} \quad (4.20)$$

Where a_X is activity and the equilibrium constant K is equivalent to a distribution coefficient of X between the two phases. This equilibrium constant can only be equal to the concentration ratio of X in the two phases when the activity coefficient of X in both phases is unity (or the same). Given the difficulty in determining activities and the non-equilibrium state of many experimental and natural systems the concentration of a trace component (Tr) is typically related to a carrier component (Cr) in the solid (S) and liquid (L) phases (e.g. Ca^{2+}) by the non-thermodynamic partition coefficient, D , where:

$$D = \frac{(Tr / Cr)_S}{(Tr / Cr)_L} \quad (4.21)$$

D can be theoretically related to a true thermodynamic equilibrium constant by solid (f_i) and liquid (γ_i) activity coefficients (after Morse and Bender, 1990). Using the exchange reaction for a hypothetical trace component (Tr) in calcite as an example, we have:



$$K_d = \frac{a_{Ca^{2+}} a_{TrCO_3}}{a_{Tr^{2+}} a_{CaCO_3}} \quad (4.23)$$

$$= \frac{(a_{TrCO_3} / a_{CaCO_3})}{(a_{Tr^{2+}} / a_{Ca^{2+}})} \quad (4.24)$$

$$= \frac{(f_{TrCO_3} m_{TrCO_3} / f_{CaCO_3} m_{CaCO_3})}{(\gamma_{Tr^{2+}} m_{Tr^{2+}} / \gamma_{Ca^{2+}} m_{Ca^{2+}})} \quad (4.25)$$

and

$$D = \frac{(m_{Tr} / m_{Ca})_{calcite}}{(m_{Tr} / m_{Ca})_L} \quad (4.26)$$

Since the molar ratios of Tr to Ca in the solid phase and $TrCO_3$ to calcite are the same, D is related to K_d as:

$$D = K_d \left[\frac{(\gamma_{Tr^{2+}} / \gamma_{Ca^{2+}})}{(f_{TrCO_3} / f_{CaCO_3})} \right] \quad (4.27)$$

Taking the activities of the solid phases as unity and substituting (4.26) into (4.27) we have:

$$(m_{Tr}/m_{Ca})_{calcite} = K_d \left(\gamma_{Tr^{2+}} / \gamma_{Ca^{2+}} \right) \cdot (m_{Tr}/m_{Ca})_L \quad (4.28)$$

The dependence of partition coefficients on both the crucial thermodynamic properties of pressure, temperature and composition and the kinetics of carbonate precipitation have been determined for a number of minor and trace elements in calcite: Mg and Sr (Gascoyne, 1982; Huang and Fairchild, 2001; Lorens, 1980; Mucci and Morse, 1982; Oomori *et al.*, 1987; Pingitore and Eastman, 1986; Tesoriero and Pankow, 1996); Mn and Fe (Böttcher, 1998; Dromgoole and Walter, 1990a; Lorens, 1978, 1981; Mucci, 1988, Pingitore *et al.*, 1988); Ba (Tesoriero and Pankow, 1996; Tunusoglu, 2007); Na (Busenberg and Plummer, 1986; Ishkawa and Ichikumi, 1984); and some trace elements (Zhong and Mucci, 1989, 1995). Experimentally determined partition coefficients for minor and trace element incorporation in dolomite and aragonite (Busenberg and Plummer, 1984; Gaetani and Cohen, 2006; Kinsman and Holland, 1969; Zhong and Mucci, 1989), are less ubiquitous or are absent and as such values must be determined from theoretical thermodynamic calculations (e.g. Curti, 1999, Wang and Xu, 2001). However, given its easy substitution for Ca, Sr incorporation in aragonite (Kinsman and Holland, 1968; Gabitov *et al.*, 2008; Gaetani and Cohen, 2006) and dolomite (Baker and Burns 1985; Vahrenkamp and Swart, 1990) is reasonably well constrained. The application of experimentally determined (K_d) values or those based on thermodynamic calculations of mineral solubilities are complicated by the fact that true thermodynamic equilibrium is rarely attained in low temperature experimental or natural systems.

Kinetic processes effecting the distribution of trace elements within precipitating carbonate crystals include the tendencies of Ca and *Tr* to attach at kink sites on the growth steps of an actively growing crystal (Watson and Liang, 1995, Rakovan and Reeder 1996). This is due to differences in the surface energies of different absorption sites in the crystal. This process results in heterogeneous trace element distributions and sector and intersectoral zoning in carbonate crystals due to the low rates of diffusion of trace elements in the solid phases relative to the rates of crystal growth (Rakovan and Reeder 1996).

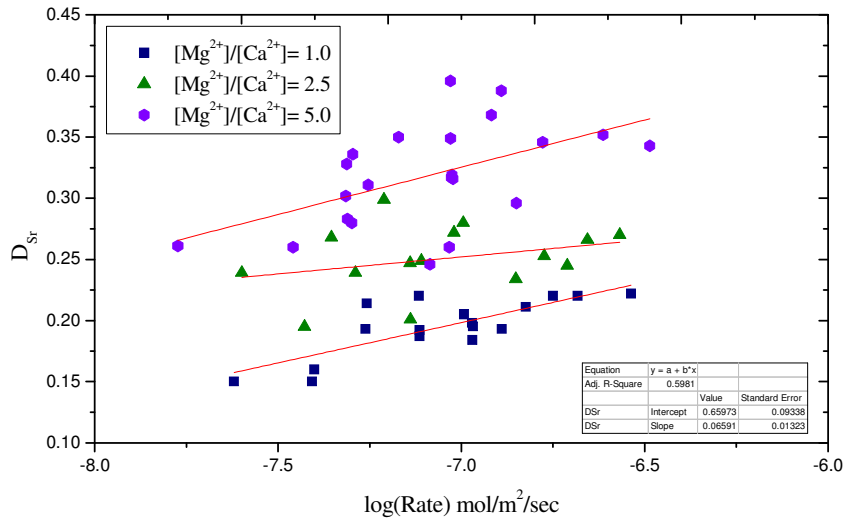


Figure 4.3-1 The dependence of D_{Sr} on the precipitation rate of calcite at various fluid Mg/Ca. Compiled from Mucci (1986) and Mucci and Morse (1983).

The second process is related to surface-solution boundary processes which result in the incorporation of Tr into the growing crystal at a different rate to the incorporation of Ca , so that (mTr/mCa) ratio is either large or smaller than the contacting solution. This differential incorporation is dependent on the rate of transport of the ions from the solution to the mineral surface (Lasaga, 1981; 1982).

Experimental distribution coefficients show a systematic pattern of behaviour that differs from that expected if the distribution were controlled by equilibrium thermodynamics alone (Rimstidt *et al.*, 1998), suggesting that experiments are effected by kinetic processes. As such calculations of pore fluid chemistry from carbonate cement composition using equilibrium distribution coefficients can predict general trends but they must be tempered with an understanding of the kinetic processes affecting the specific system of interest. This does however allow the Tr/Ca of calcite to be used to infer precipitation rates where the original fluid Tr/Ca value is known and the dependence of D_{Tr} on precipitation rate is experimentally well constrained.

In the case of calcite, the value of trace element partition coefficients varies with increasing rate of precipitation in a systematic manner (Beck *et al.*, 1992; Kinsman and Holland, 1969; Lorens, 1981; Morse and Bender, 1990; Mucci, 1986; Pingitore and Eastman, 1986). Mucci (1986) precipitated magnesian calcites at room temperature from solutions of various $[Mg^{2+}]/[Ca^{2+}]$ and at Ω_{cc} values ranging from 2.0 to 14.4. The results, combined with those of Mucci and Morse (1983) (Fig. 4.3-1) were used to obtain the empirical relationship

$$D_{Sr} = 0.65973 + 0.06591 \cdot \log R \quad (4.29)$$

where R is the precipitation rate in mol/m²/sec, D_{Sr} is the Sr/Ca^{cc} partition coefficient, at a $[Mg^{2+}]/[Ca^{2+}]$ of 1.0. It is noted that the exact nature of this rate-dependence is not clear, nor are the effects of Mg and pCO_2 rigorously known. Eq. (4.29) is the result of a least square fit with a correlation coefficient of 0.60. Beck *et al.*, (1992) in agreement with the results of Mucci and Morse (1983, 1990) and Jacobson and Usdowski (1976), reported no significant effect on D_{Sr} due to increase in pressure. These workers observed only a slight increase in D_{Sr} value with increasing temperature in experiments carried out to 400°C and 10 MPa.

4.3.6. Redox

Various studies (Carpenter and Oglesby, 1976; Grover and Read, 1983; Niemann and Read 1988; Oglesby, 1976) have suggested that progressive changes in Fe and Mn contents reflect variation in porewater pH and Eh during diagenesis. Implicit in this geochemical model is the assumption that the Mn²⁺ and Fe²⁺ concentrations in the fluid were governed by equilibrium reactions with Mn- and Fe-bearing mineral phases whose solubilities were controlled by the pH and Eh conditions of the groundwater and that these minerals were present in the system during the precipitation of carbonate. The Mn and Fe content of this pore water is determined by the Mn/Ca and Fe/Ca ratios of the calcite precipitate and the corresponding distribution coefficients D_{Mn} and D_{Fe} . Application of Eq. (4.27) requires knowledge of the aCa^{2+} in pore waters and activity coefficients for Ca²⁺, Mn²⁺ and Fe²⁺. Given the apparent similarity of chemistry of modern CO₂-charged fluids and those responsible for calcite deposition (see section 4.4.3) Ca concentration and activity coefficients from the modern fluid have been used in the calculation of element distributions in calcite cements. The distribution coefficients for Mn and Fe in calcite are influenced by precipitation rate (Dromgoole and Walter, 1990a; Lorens, 1981; Mucci, 1988) and temperature (Bodine *et al.*, 1965). Lorens (1981) indicated that D_{Mn} varies from 5 at rapid precipitation rates to almost 70 at very slow rates of precipitation. A similar behaviour is observed for D_{Fe} (Lorens, 1981). In subsequent calculations values of $D_{Mn}=7$ and $D_{Fe}=3$ were used. If the effective distribution coefficients for Mn and Fe during calcite precipitation varied by even an order of magnitude from these values due to rate effects, the estimated solution Eh and pH would be in error by only 0.06 volts and 0.25 pH units, respectively. This would not significantly effect the conclusions about approximate Eh & pH ranges of paleo-CO₂-charged fluid. Temperature is not of a significant concern given the narrow range of temperatures observed in modern CO₂-charged fluids and the lack of a significant variation in D_{Mn} and D_{Fe} at temperatures lower than 100°C (Bodine *et al.*, 1965)

4.3.7. Eh-pH Diagrams

The redox couples of interest Fe²⁺/Fe₂O₃ and Mn²⁺/MnO₂ more closely approximate equilibrium with respect to measured Eh than to Eh computed from other parameters such as dissolved O₂ (Lindberg and Runnells, 1984). It is thus reasonable to conclude that Pt electrode measured Eh closely resembles groundwater Eh as reflected by the Fe and Mn equilibria, and that redox conditions inferred on the basis of calcite Fe and Mn contents should be compatible with measured Eh values for modern CO₂-charged fluids. A crucial component of this model is the identification of the correct redox coupled Mn- and Fe-oxyhydroxide phases whose solubilities govern the fluid Mn and Fe content. For the Navajo and Entrada Sandstones the potential Fe-oxyhydroxide phases include hematite, goethite, magnetite and amorphous ferric hydroxide; potential Mn-oxyhydroxides include pyrolusite, manganite, amorphous MnO₂ and ‘complex’ MnO₂ (Chan, 2000).

Identification of the oxyhydroxide phases controlling groundwater Fe²⁺ and Mn²⁺ content can be made based on the assumption that Mn and Fe contents are controlled by equilibrium with an appropriate oxyhydroxide and that measured spring Eh and pH values adequately reflect subsurface Eh/pH conditions. Superposition of measured Eh-pH values for CO₂-charged fluids, with the stability boundary of hematite, and its ubiquitous presence in these sediments suggest this phase largely controls fluid Fe (Chapter 2, section 2.4.7). Manganese chemistry in natural systems is complex and not well understood (e.g. Barnaby and Rimstidt, 1989; Bricker, 1965; Potter and Rossman 1979). Mn exists in several possible oxidation states and commonly forms complex nonstoichiometric oxyhydroxides, with highly variable crystallinity (Ponnamperuma *et al.*, 1969). Detailed studies of Mn-oxide mineralogy from various sedimentary environments indicate that insoluble Mn oxides other than pyrolusite (MnO₂) are the dominant controls on dissolved Mn (see Taylor *et al.*, 1964). Consequently it is assumed that Mn²⁺ concentrations are controlled by equilibrium with a relatively insoluble ‘complex’ MnO₂ phase. Details of the calculation of the solubility of this phase are presented in Appendix C.

Relating values for measured Eh in CO₂-charged waters to activities of redox elements in solution may be problematic given that internal disequilibrium for any given redox couple is common (Lindberg and Runnells, 1984); however given the time scale of groundwater residence (>10³ yrs), redox reactions between cations in solution are comparatively instantaneous (e.g. Basolo and Pearson, 1967); furthermore, the dissolution and precipitation rates of Fe- and Mn-oxyhydroxides are also fast (e.g. Cornell and Giovanoli, 1993; Melbourne *et al.*, 1991; Surana and Warren, 1969; Schwertmann, 1991). Thus it is reasonable to assume redox equilibria between groundwaters and oxyhydroxide phases and that Fe and Mn contents of authigenic calcite will reflect this fact.

4.3.8. Analytical Methods

Representative thin sections of altered and unaltered Entrada sandstone and veins were qualitatively investigated petrographically using transmitted light microscopy. Percent mineralogy and porosity were estimated by point counting (200 points) at a spacing of 0.1 mm, on representative samples. Polished thin sections were examined with cathodoluminescence using a cold cathode machine and a mono-CL attached to a Jeol JSM 6100 SEM. SEM imaging and SEM-EDS analyses were undertaken on flat, well-polished specimens following Reed, (2005). Samples were analysed using a Jeol JSM 6100 scanning microscope, combined with an Oxford Instruments INCA EDS suite. The accelerating voltage for X-ray intensity measurement and for SEM image capture was 15 kV, using a probe current of 0.3 nA and a mean dead time of 20%. X-ray diffraction analysis was conducted on a Bruker AXS D8 diffractometer at the University of Cambridge. Diffraction patterns were recorded by step scanning from 2-80°2θ, with a step size of 0.013605° and counting for 0.7s per step. The Eva 9.0 software by SOCABIM (2003) was used to identify the mineral phases. The major and minor element chemistry of carbonate cements and veins were analysed using a Cameca SX-100 electron microprobe. The operation conditions were a filament voltage of 15 kV and a current of 10 nA with a beam diameter of 5.5 μm for the carbonates. Whole rock major element concentrations were determined by X-ray fluorescence (XRF) spectrometry at the Open University. Analyses were performed on fused discs following Potts *et al.*, (1984). Modal mineralogy was calculated from least squares mixing of mineral proportions to match whole rock compositions using the method of Hermann & Berry, (2002).

Carbon and oxygen isotopes, ¹⁸O/¹⁶O and ¹³C/¹²C, were measured in carbonates from cements and veins. Powdered carbonate micro-samples (~0.5g) taken from homogenized bulk samples (15g) were reacted at 90°C in pure orthophosphoric acid. The resultant CO₂ gas was purified cryogenically and analyzed for ¹⁸O/¹⁶O and ¹³C/¹²C using a Thermo Finnigan MAT253 Gas Bench II stable isotope mass spectrometer. δ¹³C and δ¹⁸O are expressed in ‰ deviation relative to Peedee Belemnite (PDB) and VSMOW standards with analytical precisions, based on the repeat analysis of in house standards, estimated at ±0.06 and ±0.08 ‰ respectively (1σ).

Samples of U-series dated aragonite veins provided by Neil Burnside, University of Glasgow, were analyzed for ⁸⁷Sr/⁸⁶Sr, δ¹⁸O and δ¹³C. Chips taken from dated samples were ground to a powder and duplicated 0.3 to 0.5 mg samples were taken for analysis. The samples were analyzed using a Thermo Gas Bench attached to a Thermo MAT 253 mass spectrometer in continuous flow mode. Results are quoted to the international standard VPDB and the precision is better than ±0.10 ‰ for δ¹⁸O and better than ±0.06 ‰ for δ¹³C (1σ). Results are reported as averages of the two analyses. Approximately 0.3 g of each sample was dissolved in 6 M HCl in Teflon beakers for the analysis of ⁸⁷Sr/⁸⁶Sr. The solutions were evaporated to dryness on a hot plate at approximately 70°C. Each residue was dissolved in 1 M HCl and 0.4 ml was loaded on a

cation-exchange resin column to separate Sr from Ca and Rb. Eluant was 3 M HCl. The strontium-containing volume of eluant was then evaporated to dryness. After final evaporation to dryness the sample was dissolved in 1 M HNO₃ and approximately 0.5 µg of strontium were loaded on a single tungsten filament. Isotopic analyses were performed on the T40 Sector 54 VG mass spectrometer at Cambridge following Bickle *et al.*, (2003). Analyses of NBS987 gave 0.710258 ± 0.000008 (1σ , $n = 20$) over the period in which the samples were analysed.

4.4. Results and Discussion

4.4.1. Field Observations

Exposed along Little Grand Fault and the northern fault of Salt Wash Graben are a series of partial to complete remnants of ancient travertine deposits that parallel the fault trace (Fig. 4.4-1). The ancient travertine deposits form resistant caps to sandstone buttes and are topographically higher than modern, actively-forming travertines. All deposits originate in the footwall proximal to areas where the fold axis of the Green River anticline is cut by normal faults. However, there are variations in the distribution and development of the ancient deposits between the two faults. The Little Grand Fault contains a series of discrete, well-developed, thick (1 to 10 m) deposits that are located in various footwall lithologies from the variably sand-rich Curtis Formation to clay-rich sections of the Morrison Formation (Fig. 4.4-2). The deposits form in the immediate footwall but generally drape over the fault into the hanging wall (Fig. 4.4-3). Additionally, the deposits are confined to sections where the two main fault strands are close together and/or there are pronounced structural complexities such as fault bends and relay ramps (Dockrill, 2005). The northern fault of the Salt Wash Graben contains mainly thinner (0.5 to 4 m) deposits compared to the Little Grand Fault (Fig. 4.4-4). They are located in the sand-rich Entrada Sandstone. The deposits are predominantly confined to the immediate footwall, occasionally draping into the adjacent graben. However, around the Green River fold axis deposits increase in number and form further into the footwall. The easternmost travertine deposits are associated with a breached relay ramp (Dockrill, 2005) (Fig. 4.4-1). In both fault systems the fault gouge is locally well exposed and consists of a zone up to 5m thick of slices of host lithologies separated by clay rich foliated gouge. Where the footwall Upper Jurassic units are juxtaposed against shales in the hanging-wall, the fault core is dominated by low-permeability clay-rich gouge (Dockrill, 2005). Conversely, the surrounding damage zone is dominated by fractures both in the high permeability reservoir units and in the low-permeability seal units (Dockrill and Shipton, 2010). Fracture orientation range and frequency are enhanced in zones of structural complexity improving fracture connectivity and providing pathways for fluids to migrate vertically, parallel to the fault (Dockrill and Shipton, 2010).

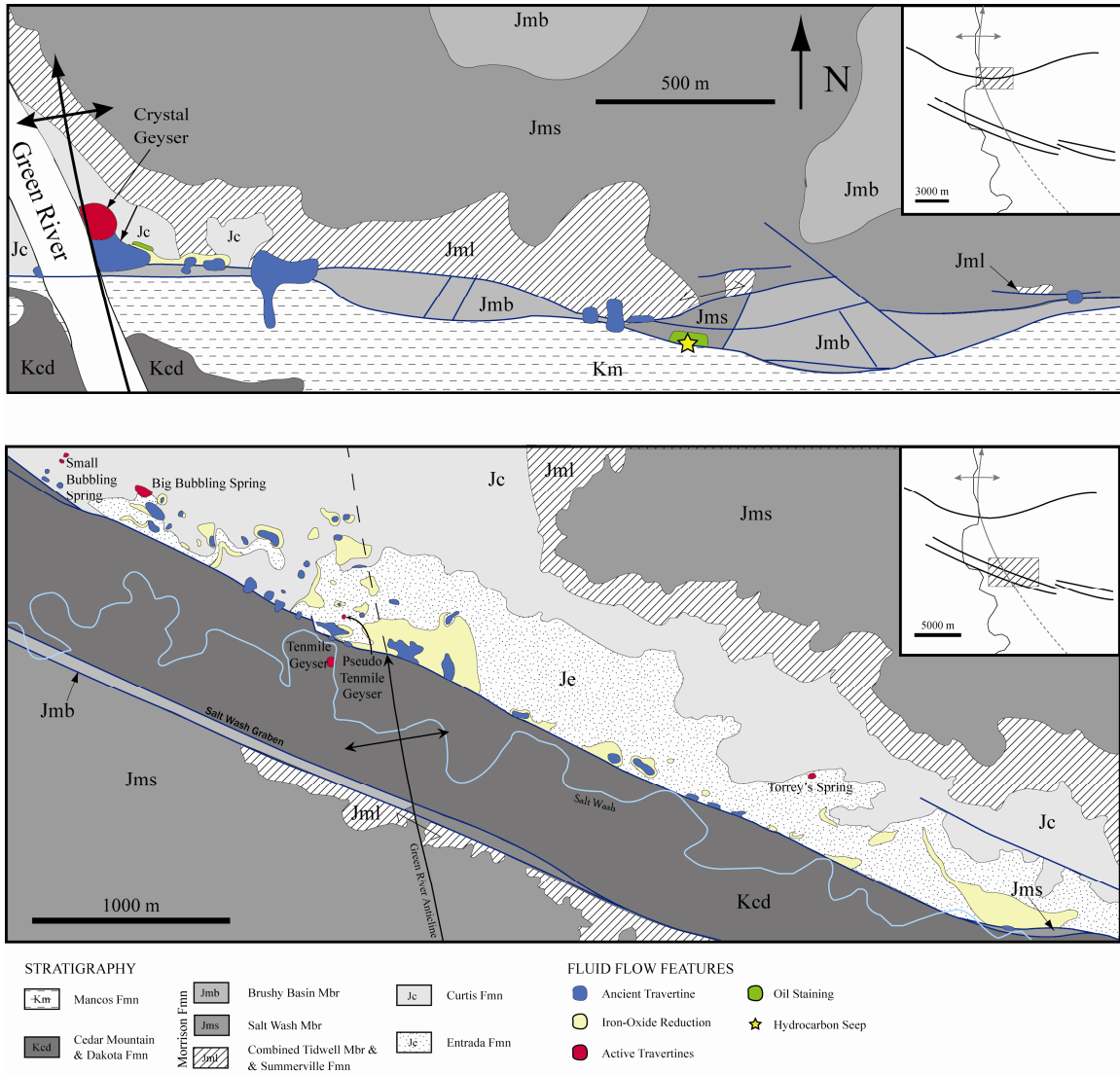


Figure 4.4-1 Distribution of surface travertines along (a) Little Grand Wash Fault and (b) the northern fault of Salt Wash Graben. Also shown is the distribution of iron oxide dissolution and bleaching in the Entrada Sandstone. Insets show the location of each map relative to the Green River, the axis of the Green River Anticline and the two fault systems. Modified after Dockrill (2005).

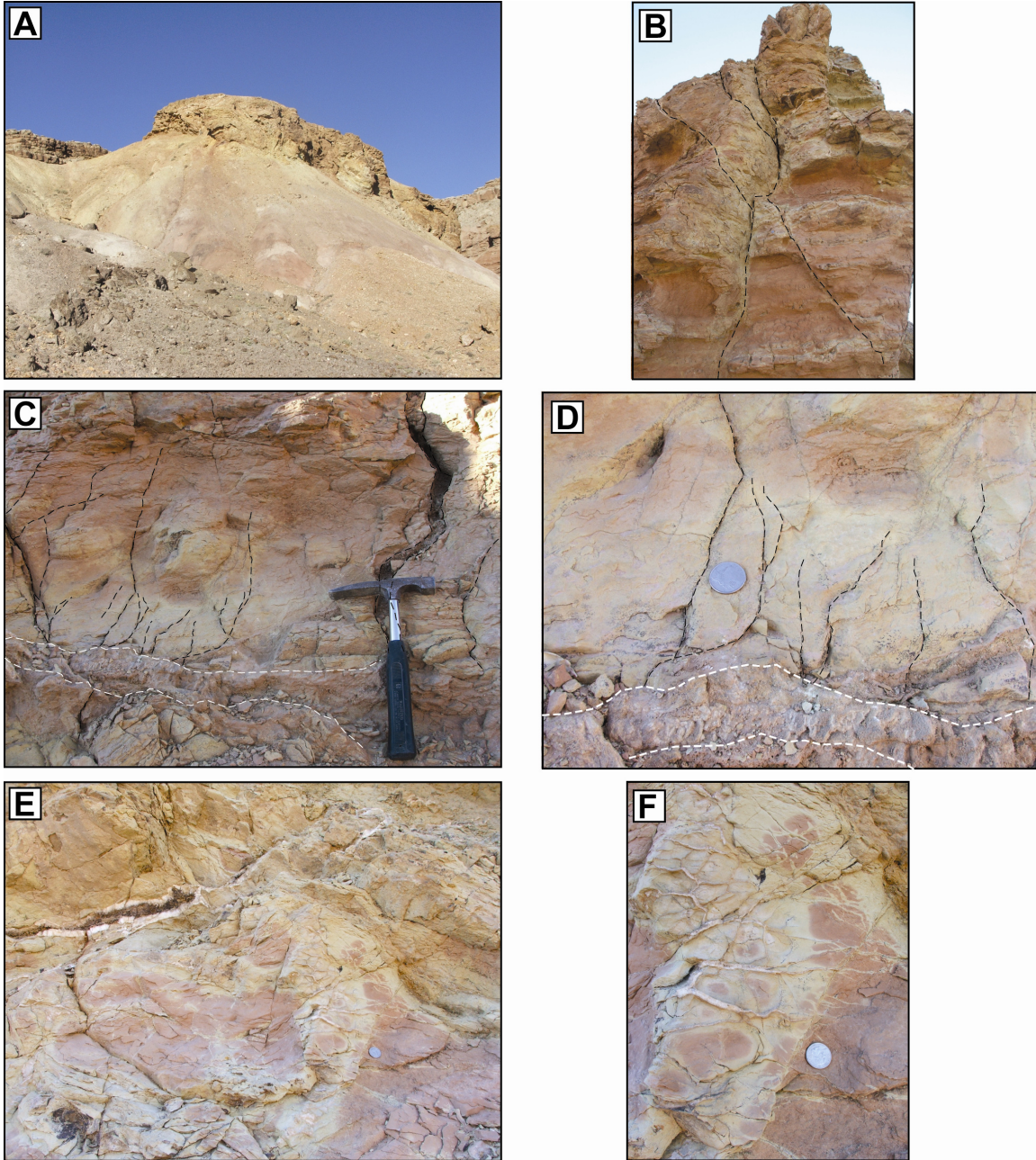


Figure 4.4-2 (a-f) Field photographs of ancient travertine mounds from the Little Grand Fault showing distribution of: (a) A layered travertine mound emplaced on partially bleached Mancos Shale. In mud-dominated lithologies, networks of thin boxwork veins (5 to 10 mm thick) are more common than the thicker white-banded veins, locally destroy the host rock fabrics, and have thin reduction haloes (1 to 5 mm). (b) The faulted and fractured feeder zone to a travertine mound with associated reduction halo in the partially sandy Curtis Formation. (c-f) Horizontal and vertical aragonite veins with diffuse bleaching paralleling the vein trace and following fine fractures radiating from the veins.

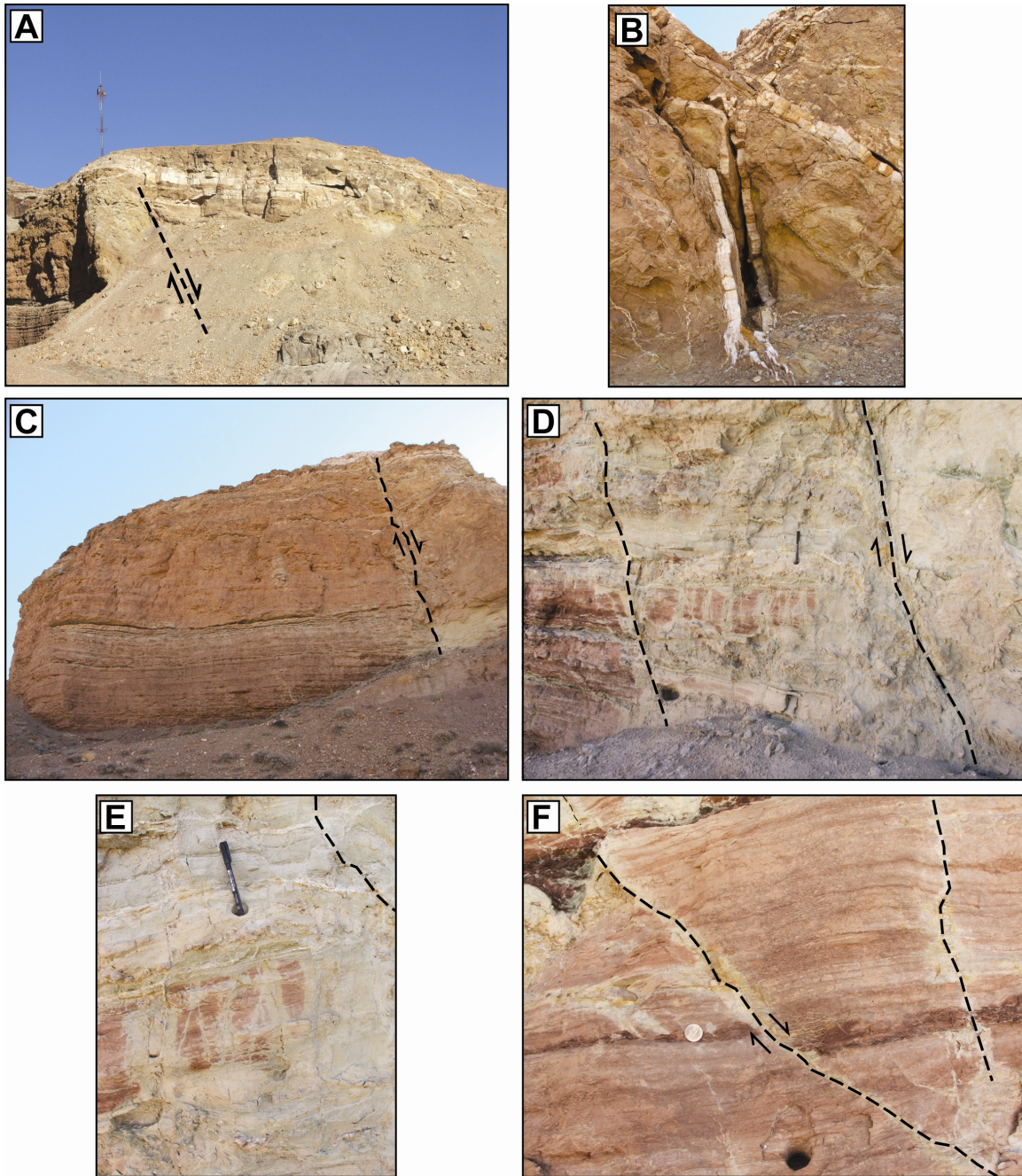


Figure 4.4-3 Field photographs of ancient travertine mounds from the Little Grand Fault showing distribution of (a) A thick mound draping across the fault, dominated by a thick aragonite vein that down turns to the left hand side of the photo, into the fault zone. (b) Large vertical aragonite vein with open cavity feeding travertine (a). (c) Feeder fault cross cutting the Curtis formation (left hand side of (a)) with partial bleaching and extensive bedding parallel calcite cementation, aragonite veining and bleaching (d-e). (f) Close up of the fault zone in (c).

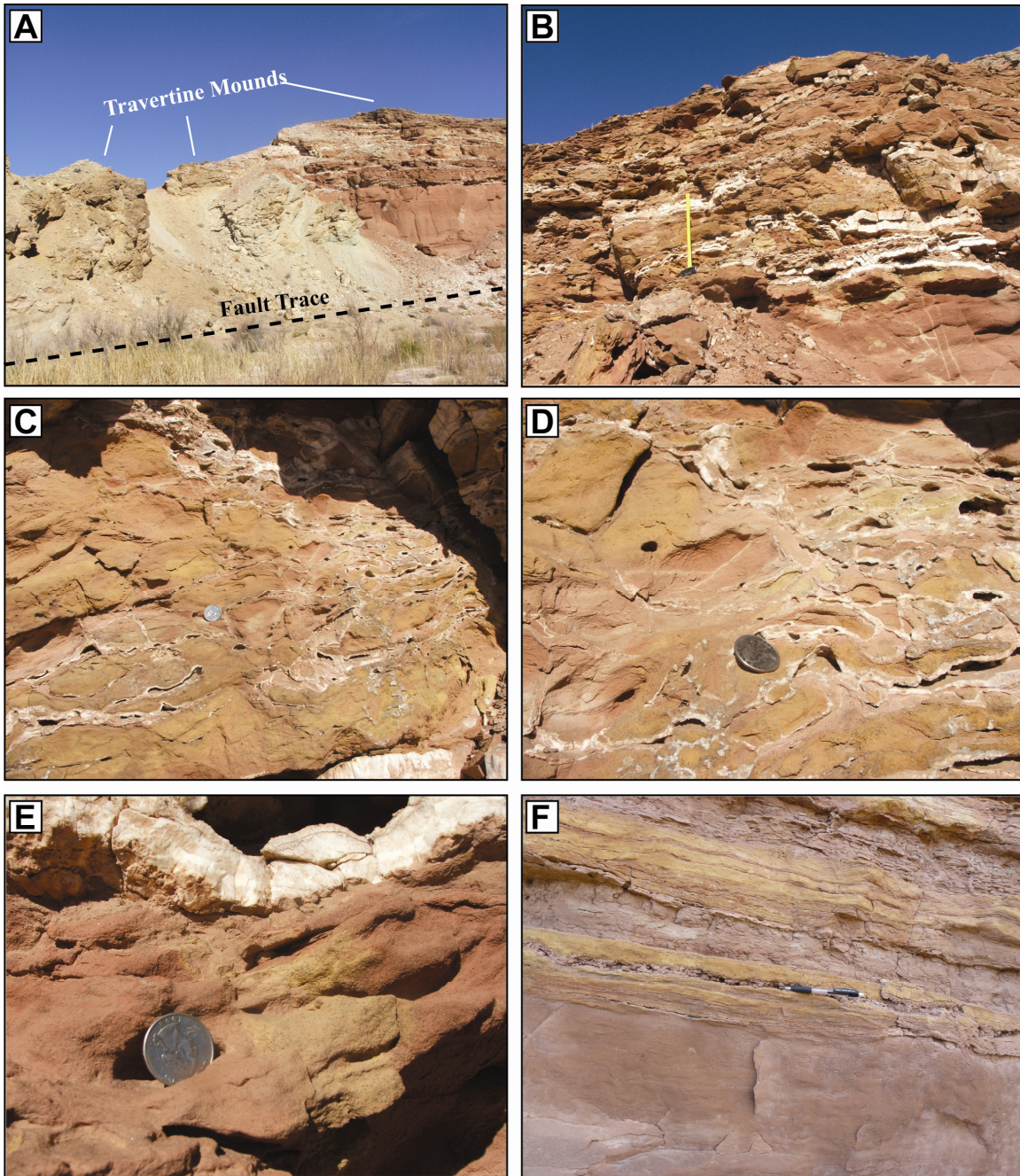


Figure 4.4-4 Field photographs of a) a travertine mound (Tenmile Butte) collapsing to the south, from the footwall of the northern fault of Salt Wash Graben into the graben itself. (b) Close up of righthand side of photo (a) showing extensive horizontal aragonite veining ~15 m beneath the top of Tenmile Butte which is capped with travertine deposits. (c-e) increasingly close up images of (b) showing aragonite veining and cavity formation within the partially bleached and heavily cemented Entrada Sandstone. Iron is dissolved and locally precipitated on the mm-cm scale as coarse dark Fe-oxides (e). (f) Bedding parallel bleaching and cementation halos in sandy layers surrounding thin bedding parallel aragonite veins, accumulating beneath and between impermeable silty horizons.

4.4.1.1. Ancient Travertine Deposits

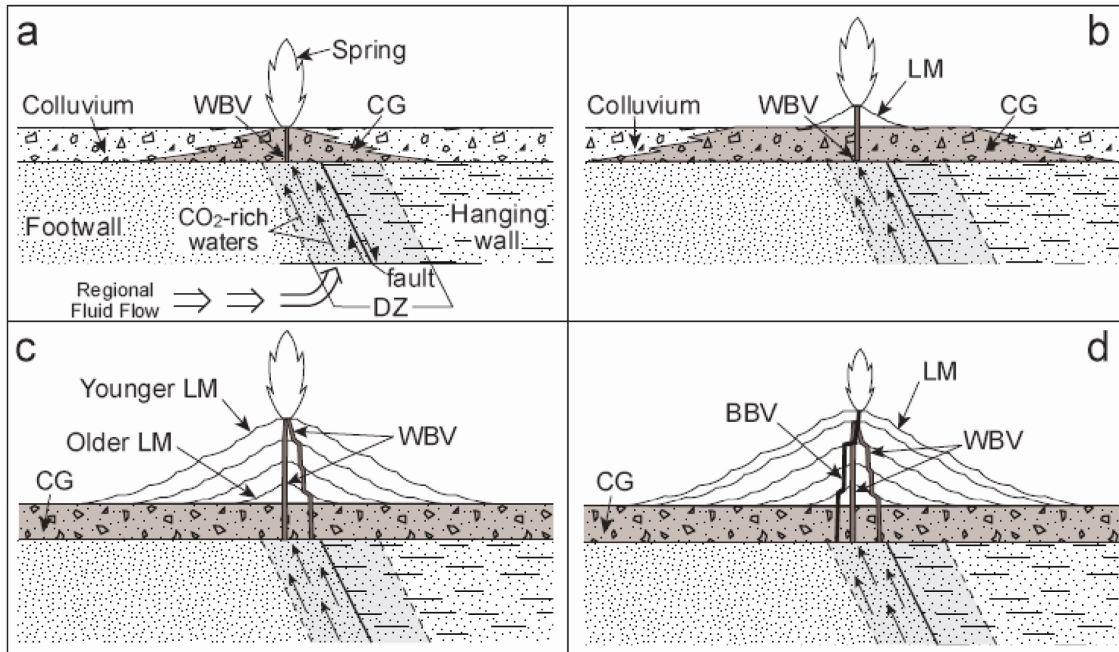


Figure 4.4-5 Figure (from Dockrill, 2005) showing the different stages involved in the formation of a fault related travertine deposit. (a) CO₂-charged waters migrate up the fault damage zone (DZ) through pre-existing fractures. Discharged waters percolate through the surrounding colluvium and flow across the land surface, degassing CO₂ and cementing conglomerate (CG). (b) Sealing of the colluvium initiates layered carbonate (LM) deposits at the surface. Aragonite veins (WBV or BBV) begin to form in the colluvium and host rock beneath the layered deposit. (c-d) Travertine builds up laterally and vertically. Eventually the springs become inactive and the travertine begins to erode.

The morphology and formation of travertine mounds is discussed thoroughly by Dockrill (2005); a brief over view is given here. Travertine mounds essentially comprise (Fig. 4.4-5): a) Calcite-cemented colluvium conglomerate which forms the base of the mound. b) A subhorizontal, layered carbonate deposit with moderate to high visible porosity, situated above the conglomerate. The morphology of the layered carbonate varies considerably in texture and packing, but is generally composed of layered, subhorizontal alternating porous and dense horizons. Each layer contains subvertical, dendritic precipitates that branch out from a thin, laminated substrate. The substrate commonly has an irregular, sinuous shape similar to the pool-and-rim geometries of microterraces on the present-day travertines. c) Horizontally and vertically orientated banded aragonite veins cross cut the travertine mounds and extend to depth beneath individual deposits.

4.4.2. Petrology, Cathodoluminescence, SEM and XRD

4.4.2.1. Entrada Sandstone

The aeolian sandstones of the Slick Rock and Earthy members of the Entrada are fine- to medium-grained quartz arenites to subarkose sandstones (Trimble, 1978). These sandstone units alternate with siltstone and silty sandstone of the Dewey Bridge Member at the base of the Entrada Sandstone. The sandstones are red in colour due to the presence of hematite and goethite grain coatings (Beitler *et al.*, 2005, Bowen *et al.*, 2007, Chan *et al.*, 2000, Parry *et al.*, 2004). Regionally, the detrital mineralogy of dune facies sandstones comprises subangular to rounded grains of 76-89 wt% quartz, 8.5-16.5 wt% K-feldspar, 2.2-6.5 wt% plagioclase and trace muscovite (<0.4 wt%), tourmaline, apatite and zircon (<0.5 wt%) (Cullers, 1995; Mirsky and Treves, 1962). All samples vary somewhat in grain size (0.12-0.56 mm), sorting and packing. Type and amount of cement varies considerably and includes quartz, dolomite, calcite, illite, smectite, kaolinite, hematite and goethite.

Point counted samples from SWG average 72.2 vol% quartz grains and 9.8 vol% feldspar grains (both K-feldspar and plagioclase). Quartz grains show occasional quartz overgrowths (0.1 vol%) that exhibit a euhedral outline and occasionally preserve illite and haematitic grain coatings on the original grain rim. Samples average 3.3 vol% illite and 0.2 vol% kaolinite. Two illite textures are present: illite coatings on quartz and K-feldspar grains and pore filling illite, which may replace K-feldspar. Samples average 1.8 vol% illite coating and 1.5 vol% pore filling illite. Samples average 7.6 vol% rhombohedral dolomite and trace (detrital?) calcite (0.1 vol%). Cryptocrystalline hematite averages 1.2 vol% in red dune facies samples and they contain trace detrital oxides (0.1 vol%)

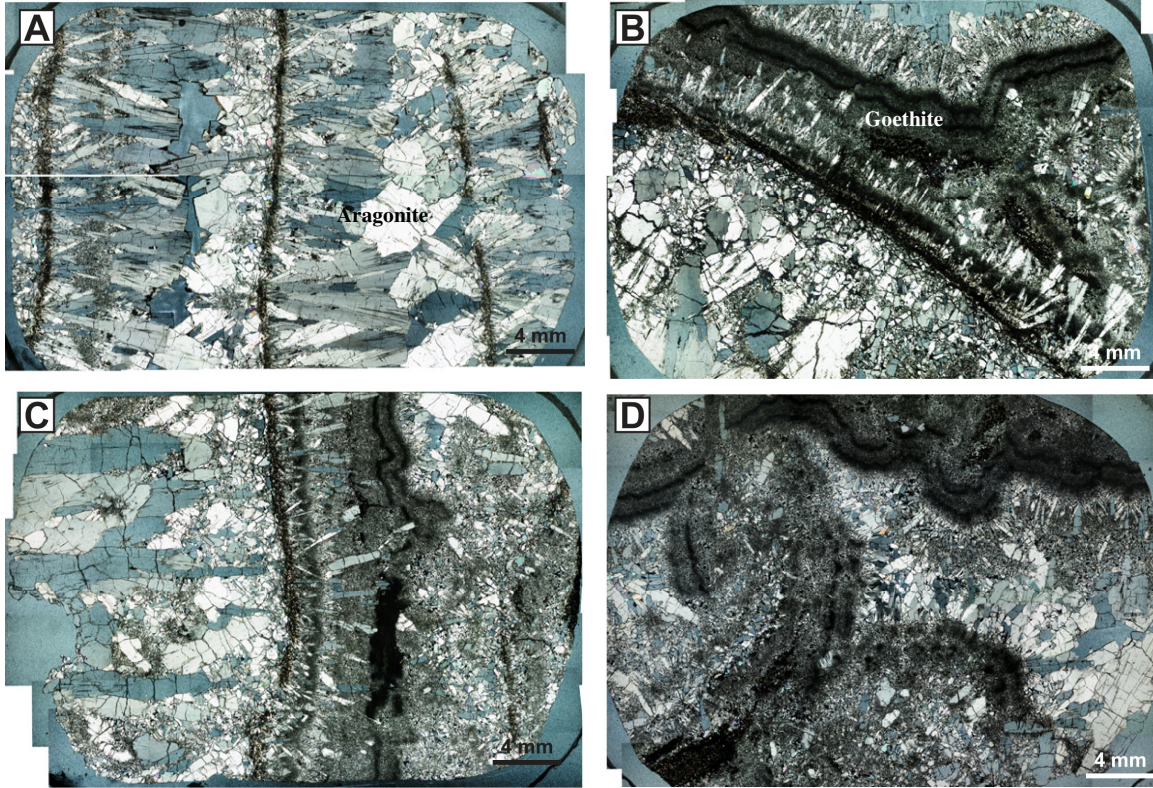


Figure 4.4-6 Typical crossed polarized light photomicrographs of micro-wafers from thick aragonite veins illustrating the typical pattern of grain morphology and size through an individual growth set. Also prominent in the images are the Fe and Mn rich layers that occur on inception of a new growth surface

4.4.2.2. Aragonite Veins

Aragonite and calcite veins parallel bedding or infill open joints and are observed at depths up to ~30m below ancient travertine mounds. Thick aragonite veins are composed of multiple sets of growth surfaces, generally 5 to 30 mm thick, defined by radial and ray crystals elongate perpendicular to the plane of the veins (Fig. 4.4-6). Thin veins are composed of equant and euhedral, occasionally twinned, pseudohexagonal aragonite crystals which grow in open fractures and within the porosity (Fig. 4.4-8). Individual veins grew primarily from the fracture walls inwards (Figs. 4.4-2 to 4.4-4). The carbonate lining the fracture walls are usually equidimensional and occasionally separated by a central cavity. At the inception of a new growth surface aragonite crystals are equant and pigmented containing micro-inclusions of Fe- and Mn-oxides and crystallize with cryptocrystalline hematite and goethite (Fig 4.4-6 & 4.4-7). With distance from the growth surface towards the vein centre crystals increase in size and become elongate, acicular and prismatic. Thick veins thin laterally and terminate in networks of thin veins, occluding lenses of the local host rock, which becomes heavily altered. Fe-oxyhydroxides precipitate on the inner surface of the vein occluding sections of the host rock. Feldspar grains included in these vein segments exhibit evidence of extensive dissolution and reprecipitation of silica, kaolinite and smectite within the pore volume formed by the occluding vein (Figs. 4.4-10 to 4.4.12).

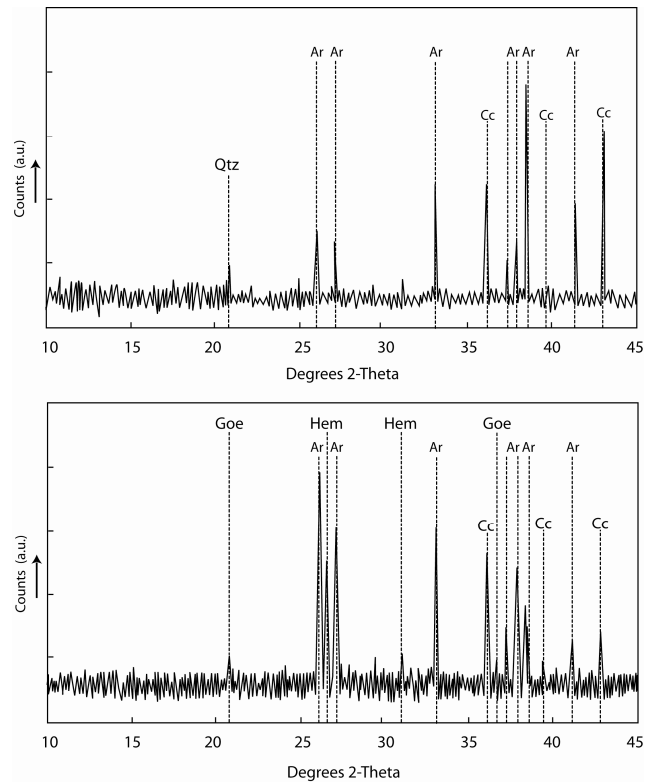


Figure 4.4-7 XRD patterns from a) coarsely crystalline transparent aragonite and b) from one of the pigmented growth surfaces in Fig. 4.4-6 illustrating the presence of hematite and goethite.

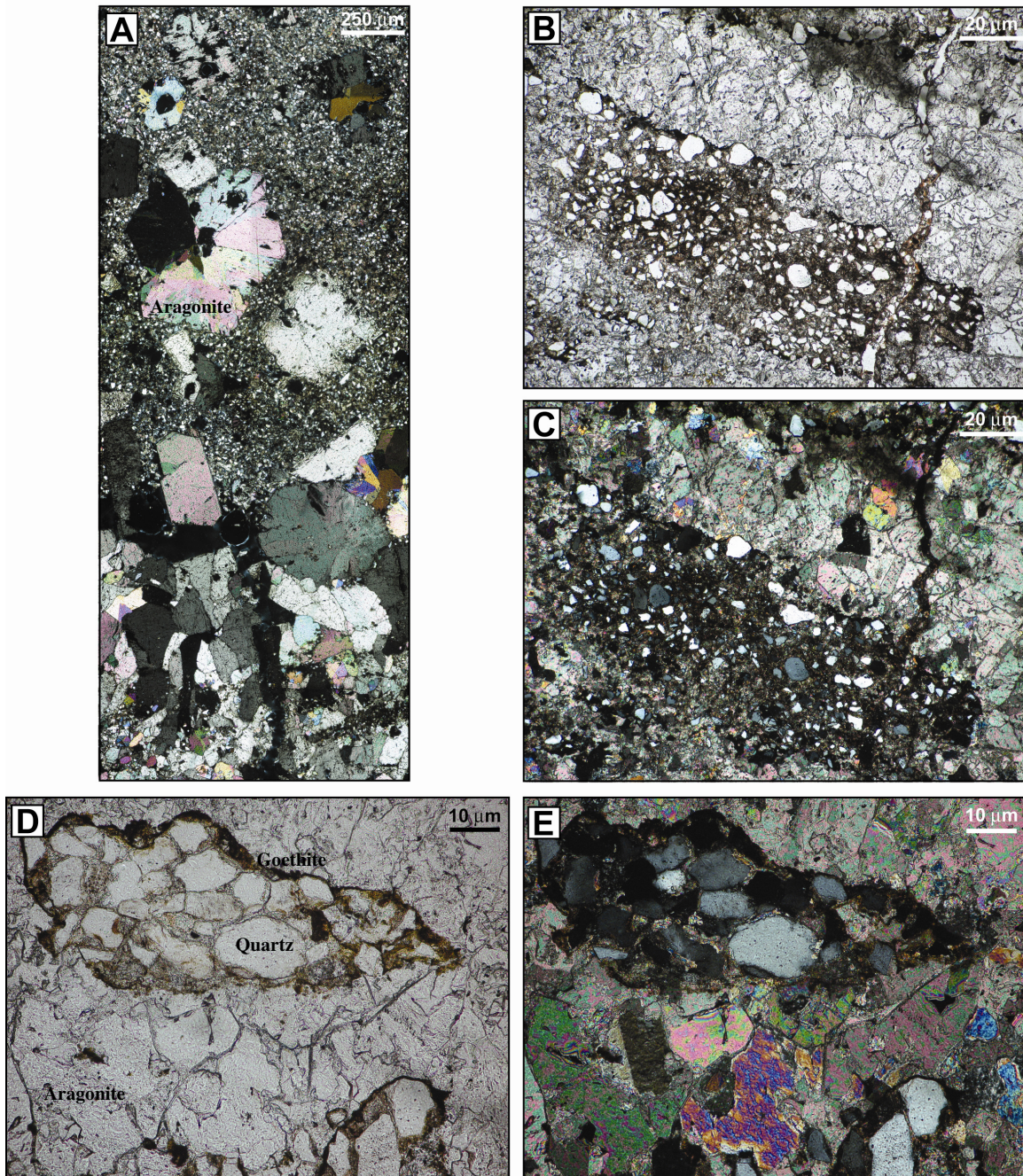


Figure 4.4-8 Typical plane and crossed polarized light photomicrographs from aragonite micro-veins growing either a) at ~ 30 m below the paleo-land surface or b-e) at the lateral termination of a shallow thick aragonite vein. a) Illustrates the variety of twinned and pseudo-hexagonal habits of the aragonite crystals which grow in thin micro-veinlets within fractures or the porosity of the local host rock. b-e) Illustrates inclusion of host rock, Fe-mobilization and reprecipitation on the inner surface of the occluding veinlet.

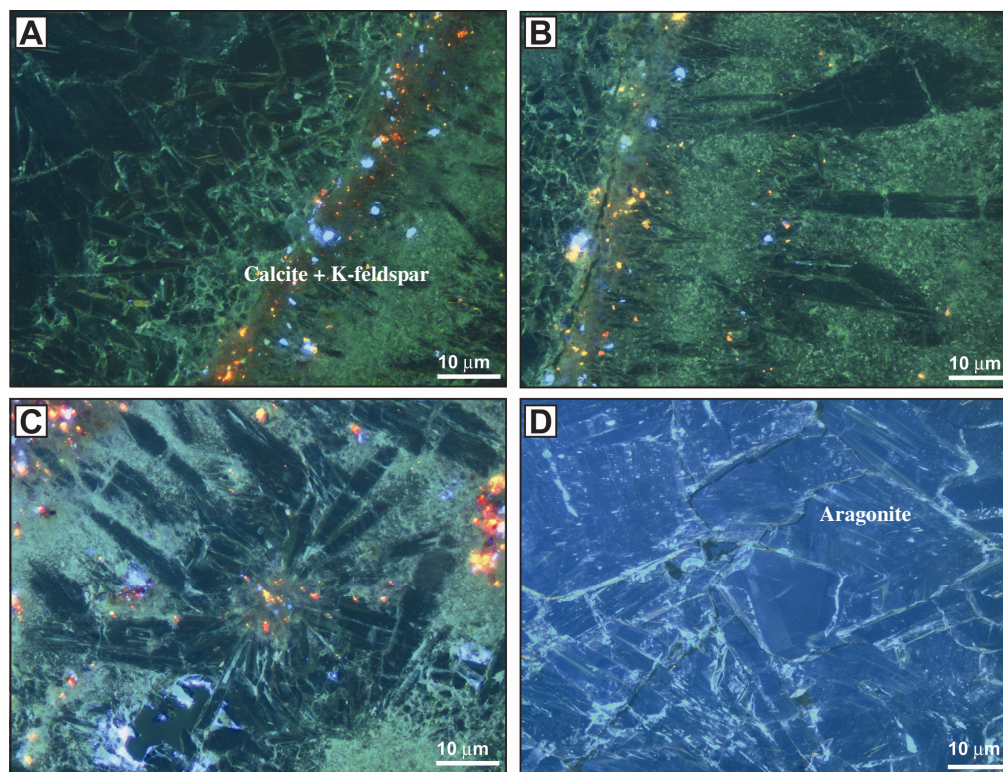


Figure 4.4-9 Cold cathodoluminescence photomicrographs of thick aragonite veins exhibiting a-c) Inclusion of fragments of host rock grains, at the inception of a new growth surface, around which new crystals or rosettes of crystals nucleate. d) CL image from the coarse portion of a vein showing the generally homogeneous nature of the CL pattern.

Cathodoluminescence patterns for aragonite veins are homogeneous reflecting relatively uniform fluid compositions throughout the precipitation of a single vein (Fig. 4.4-9). Some difference in CL brightness is observed on individual crystal facets reflecting the preferential attachment of ions to surfaces which grow at different rates. Bright yellow-orange (calcite) and blue (K-feldspar) CL patterns observed at the inception of a new growth surface represent grains from the host rock lithology entrained into the vein cavity. These sites comprise amalgams of many small crystals reflecting rapid crystal nucleation due to the density of nucleation sites on the surface of the entrained grains.

Back-scatter electron (BSE) and mono-CL images of micro-aragonite veins (Figs. 4.4-10 to 4.4-11) from the lateral tip of a thick horizontal vein reveals that individual micro-veins are composed of a single, or up to three, growth events and that early growth stages are broken apart and then occluded by later growth stages. Electron intensity increases with proximity to an included portion of host rock reflect dissolution of silicate grains in the matrix and increased incorporation of foreign ions into the aragonite. Increased electron intensity, where no concurrent change in CL intensity is observed reflects an increase in Sr²⁺, Na⁺ and K⁺ content. Later stages of vein growth have higher CL intensities but lower electron intensities reflecting a decreased Fe²⁺,

Sr²⁺, Na⁺ and K⁺ content. This general pattern reflects a decrease in wall rock interaction in these fine veins as fluid becomes isolated from the host rock by precipitation of aragonite on the fracture surface. EDS patterns and SEM imaging reveal extensive kaolinite veining in these micro-veins where they interact with the host rock, deriving SiO₂ and Al³⁺ locally, from the dissolution of silicate minerals.

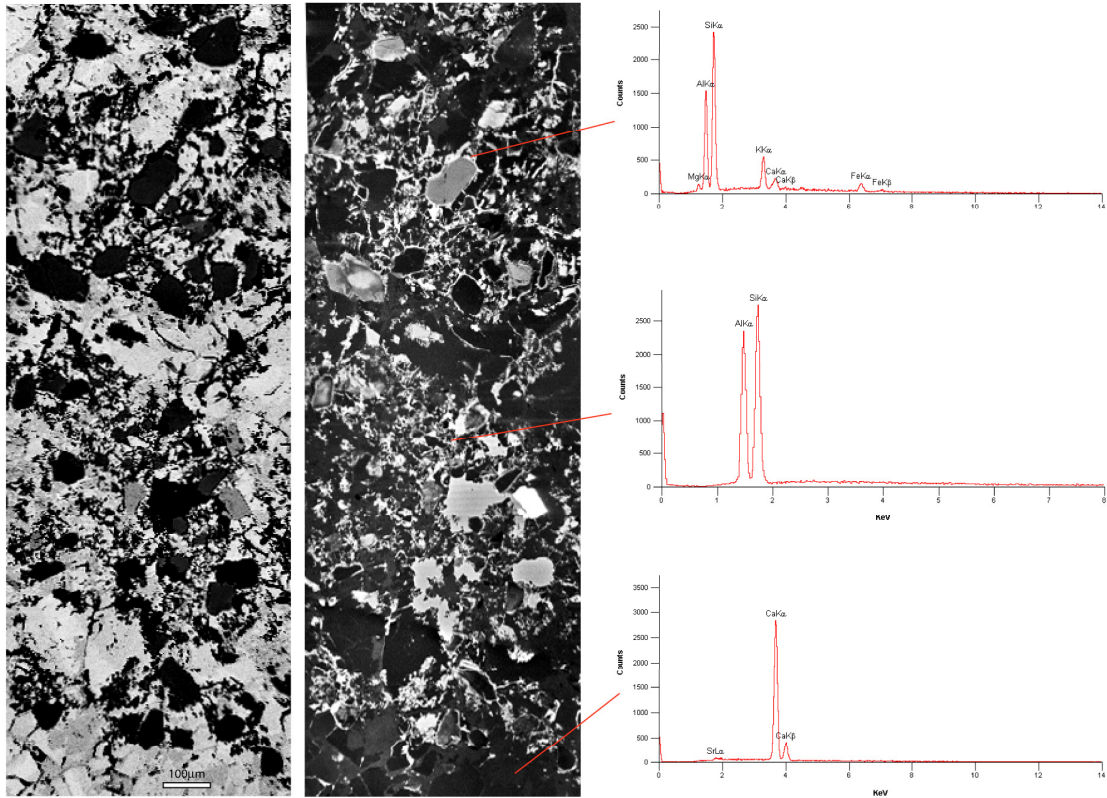


Figure 4.4-10 a) BSE and b) Mono-CL photomicrographs of an aragonite micro-veinlet and alteration of occluded portions of the local host rock. EDS spectral for various secondary products including a) smectite surrounding a dissolving K-feldspar grain, b) kaolinite precipitating as fine micro-veins surrounding sand grains and intergrowing with CaCO₃ and c) the aragonite vein.

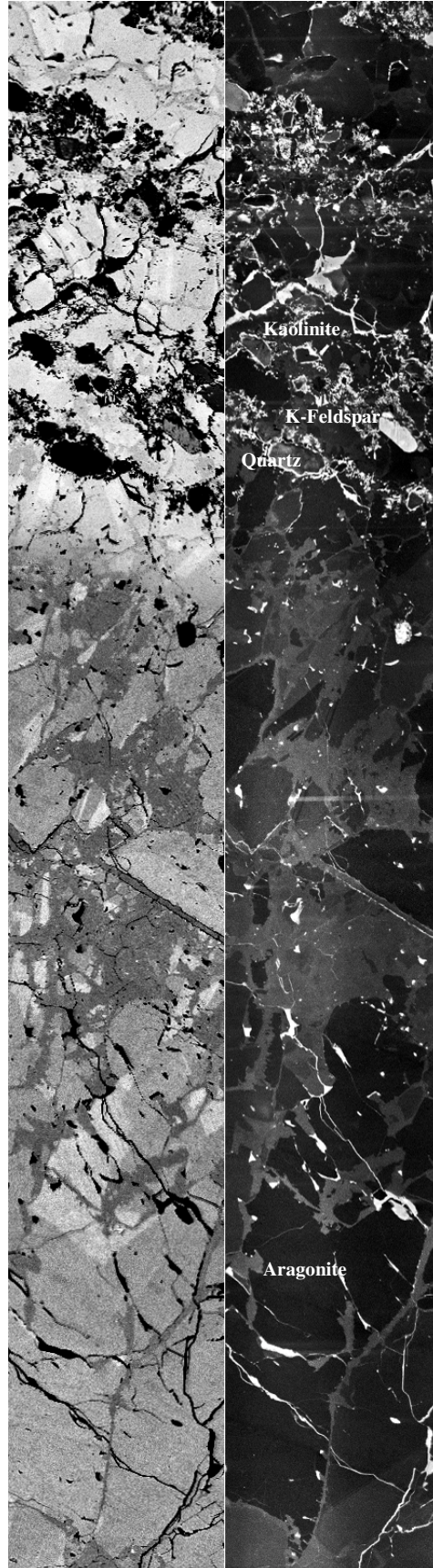


Figure 4.4-11 a) BSE and b) Mono-CL photomicrographs of an aragonite micro-veinlet showing the two major stages of vein deposition and the variation in BSE and CL intensities with proximity to the occluded portions of host rock (top of image).

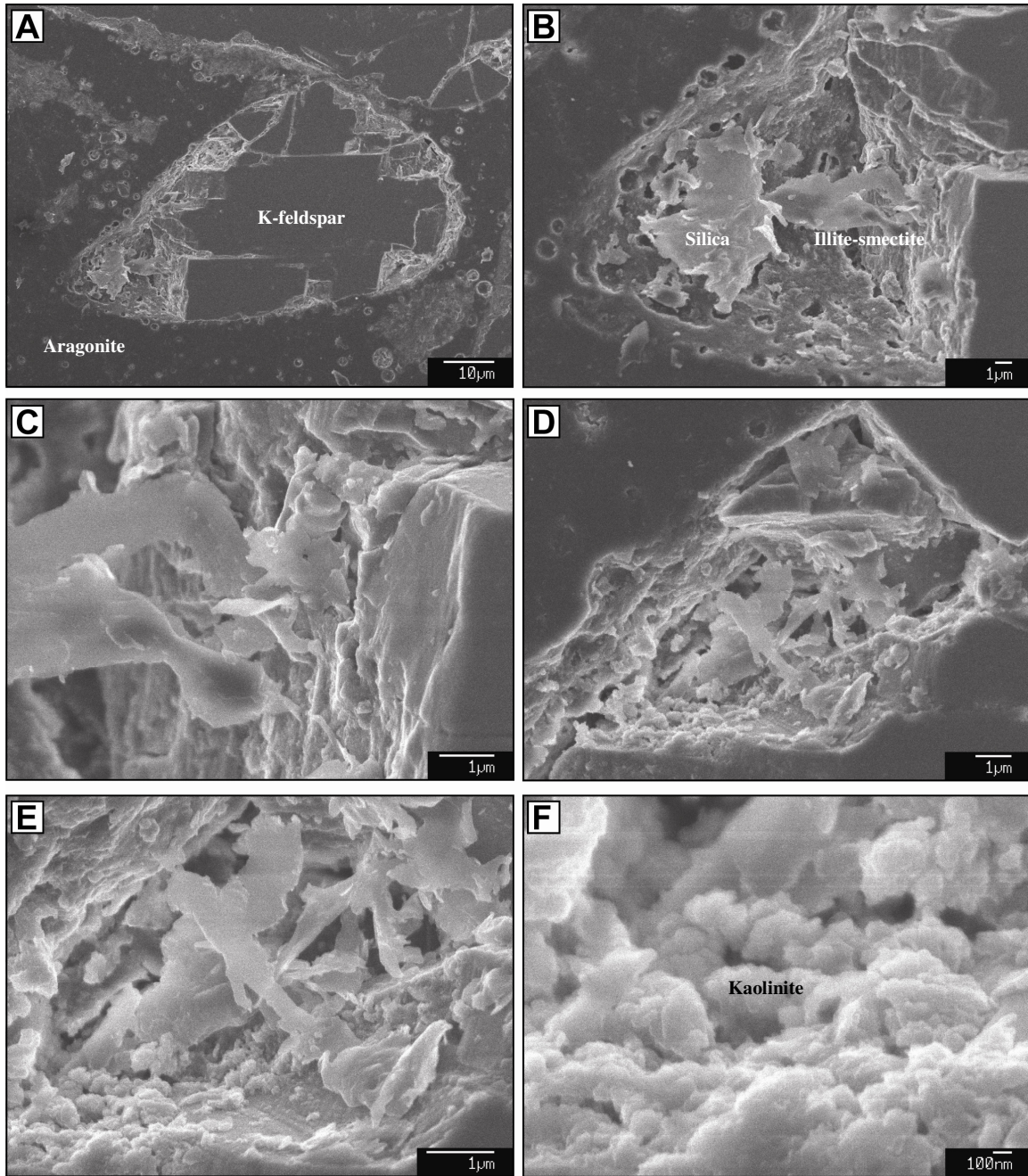


Figure 4.4-12 SEM photomicrographs at various scales of a single feldspar grain occluded by an aragonite micro-vein. a) The grain is heavily corroded and is preferentially dissolved along cleavage planes. b-f) The feldspar surface is largely free of secondary mineral coatings. Dissolved components are reprecipitated within the porosity volume created by the dissolved grains as flakes of silica, smectite and micro-platelets of kaolinite on portions of the grain surface and the cavity wall. Clay gains adhering to the aragonite crystal surface inhibit carbonate nucleation, creating pockets of clay occluded in the growing vein.

4.4.2.3. Altered Entrada Sandstone

The host rock below individual ancient travertine mounds are generally altered along fractures and bedding planes (Fig. 4.4-4 & 4.4-13). Alteration includes; pervasive calcite, aragonite and

silica cementation, and calcite and aragonite veining. Poikilitic aragonite crystals occur in zones away from fracture conduits. Point counted bleached yellow-orange dune facies samples average 6.5 vol. % feldspar (both K-feldspar and plagioclase), much of which is heavily corroded (Fig. 4.4-12 & 4.4-14), and 65.5 vol. % detrital quartz grains, which are commonly overgrown by euhedral and irregular quartz overgrowths (2.4 vol. %). Overgrowths surround both hematite and illite grain coatings, grains from which the haematitic coatings have been dissolved and commonly include calcite. Grain rimming illite/smectite (1.8 vol. %) and kaolinite (0.5 vol. %) are common and many feldspar grains have 2-10µm coatings of clay intergrowths (Fig. 4.4-14). Samples contain trace, heavily corroded fragments of dolomite (0.2 vol. %) and abundant pore filling calcite (13.7 vol. %) (Fig. 4.4-15 to 4.4-17). Grain rimming, cryptocrystalline hematite and coarse crystalline oxides average 0.4 % and 2.6 %, respectively.

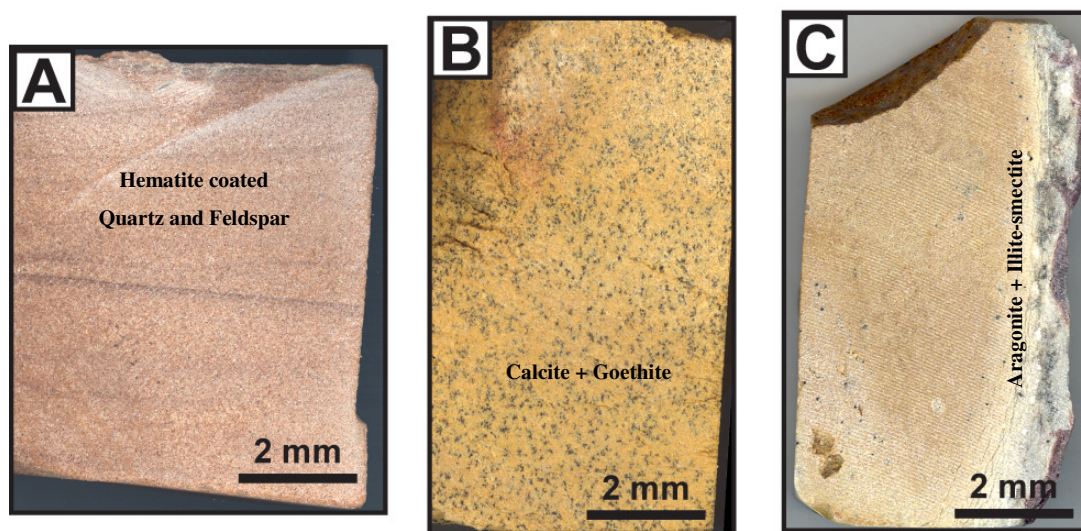


Figure 4.4-13 Photomicrographs of representative samples of Entrada Sandstone showing a) Unaltered diagenetically red dune facies sandstone from SWG. Dark pigmented layers are zones with thicker (4-6µm) hematitic grain coatings. b) Altered sandstone from a travertine feeder zone at SWG. Cryptocrystalline haematitic grain coatings have been dissolved and the Fe locally reprecipitated as coarse hematite and goethite grains. The pore space is completely occluded by calcite cement. c) Altered Entrada Sandstone from SWG adjacent to an aragonite filled fracture (left hand side of image). Grain coatings have been removed and some Fe has been locally reprecipitated and some mobilized to the fluid. The fracture is filled with aragonite, kaolinite and smectite. Some fine fracturing in the host rock adjacent to the fracture is observable in the sample due to alteration of the adjacent host rock and the growth of the fracture fill.

Dissolved hematite grain coatings are locally reprecipitated, at the mm-cm scale, as goethite, and occasionally as coarse hematite grains (Fig. 4.4-13). Calcite occurs as granular to blocky, equant to poorly prismatic poor rimming and filling cements. Individual calcite crystals typically contain a pigmented core reflecting a high Fe and Mn content in the crystal and the inclusion of microcrystalline inclusions of Fe-oxyhydroxides (Fig. 4.4-15). CL patterns for samples close to fracture conduits exhibit a dominant single stage of calcite growth, with no pronounced concretionary zoning and gradational changes in Fe and Mn content from calcite core to rim (Fig. 4.4-16).

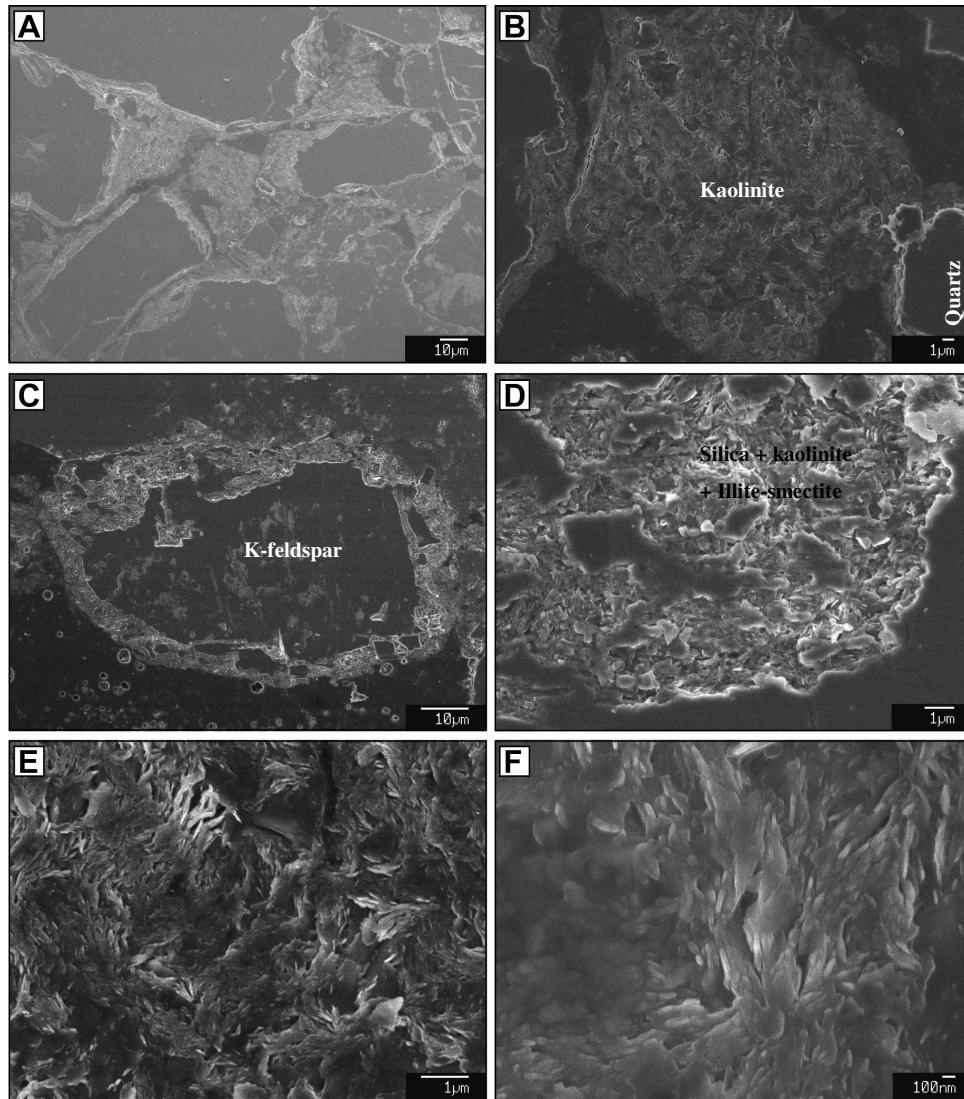


Figure 4.4-14 SEM photomicrographs at various scales of a sand grains in the altered portions of the host rock surrounding an aragonite vein. a) heavily corroded feldspar grains and local reprecipitation of kaolinite and smectite. b) pore-filling kaolinite. c) Dissolving feldspar grain which continues to dissolve even though it is surrounded by a 5 to 10 µm thick layer of reprecipitated silica and clay. d-f) close up of secondary products surrounding c).

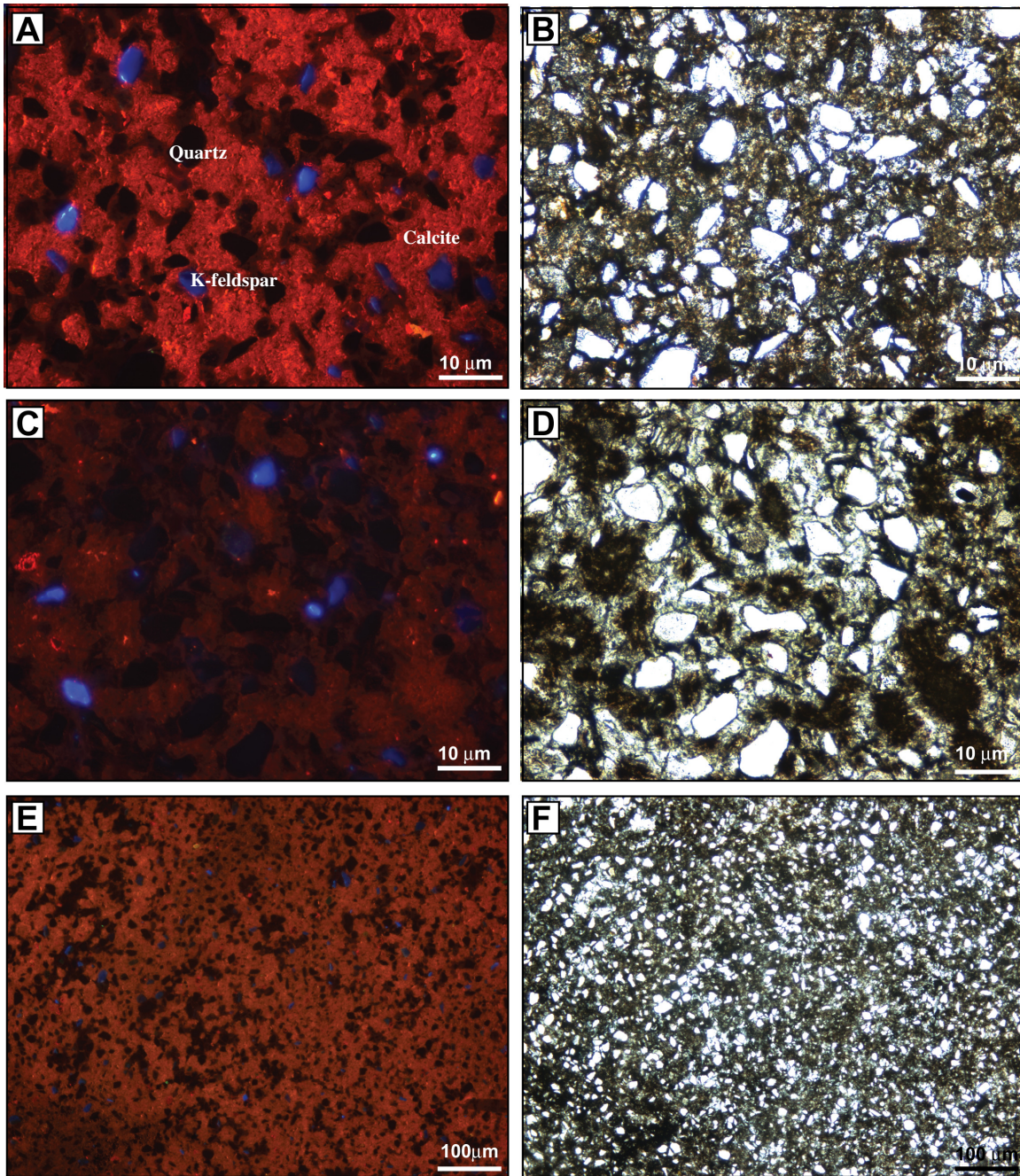


Figure 4.4-15 Cold CL photomicrographs of pore occluding calcite (a-f) cement close to a fracture conduit. The calcite fills pore space and is gradationally zoned suggesting continuous precipitation from a fluid of relatively homogenous composition. The cores of most grains are pigmented contain high concentrations of Fe and Mn and micro inclusions of oxyhydroxides, whilst the rims are transparent. Large-scale image of the same sample showing the homogenous nature of the calcite.

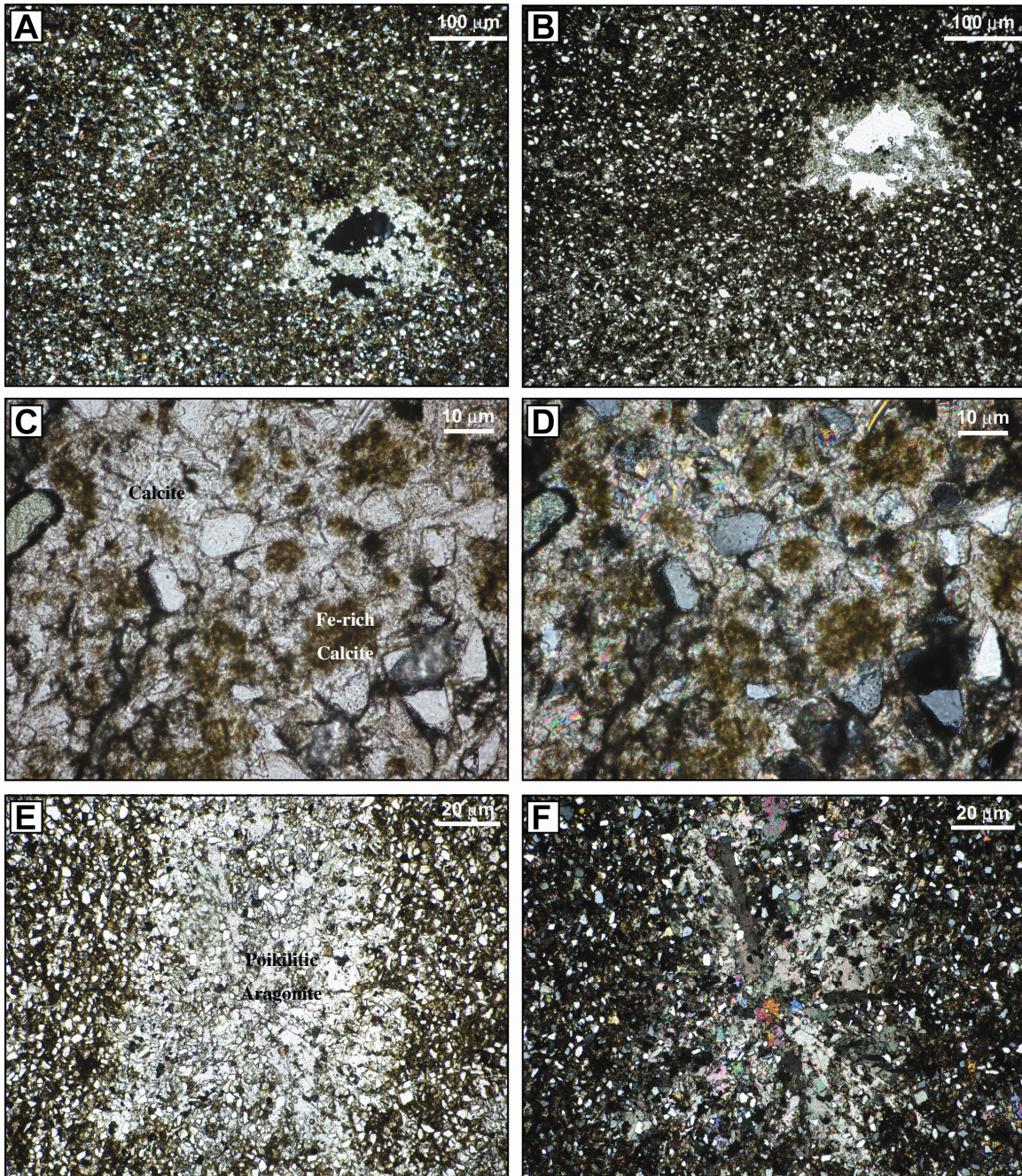


Figure 4.4-16 Typical plane and crossed polarized light photomicrographs from a-d) pore occluding calcite cement close to a fracture conduit in Fig. 4.4-14; e-f) poikilitic aragonite in calcite cemented host rock ~ 3m from the fracture conduit.

Where calcite cementation is associated with joints or open fractures a systematic increase in cement volume is observed with proximity to the conduit. Typically the calcite cementation occludes the majority of the porosity in individual samples.

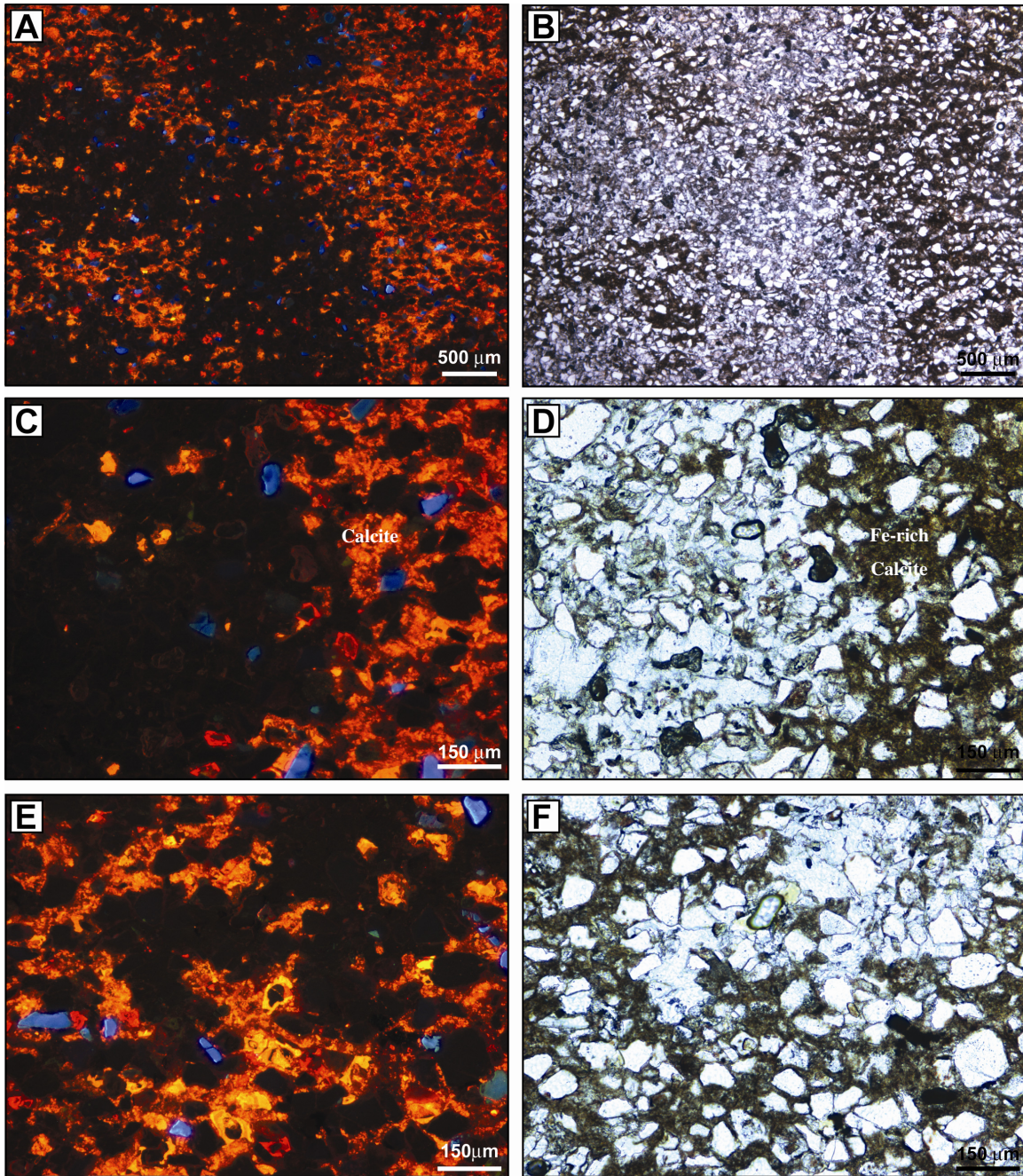


Figure 4.4-17 Cold CL photomicrographs of pore filling calcite and poikilitic aragonite in cemented host rock ~3 m from a fracture conduit.

Other samples (Fig. 4.4-17), typically forming some distance from fracture conduits or at the edges of calcite cemented halos, around veins, exhibit more complex CL patterns, concretionary and concentric zoning and abundant poikilitic aragonite cements

4.4.3. Carbonate Trace Element Compositions and Paleo-Fluid Chemistry

A single representative sample from each of the two distinct cementation zones; zones containing only calcite cements and zones containing calcite and aragonite cements, were analyzed for major and minor element chemistry (Figs 4.4-18 to 4.4-22).

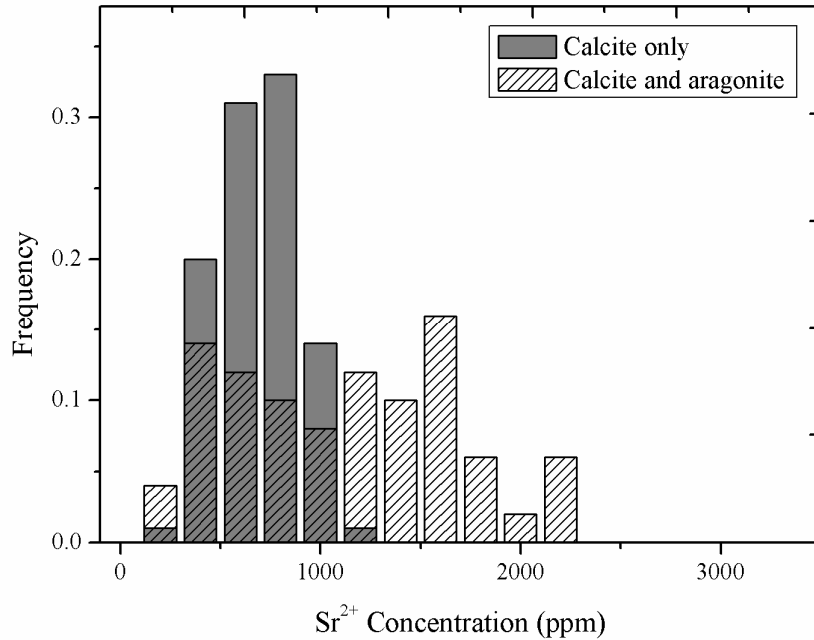


Figure 4.4-18 Cumulative frequency plot of Sr²⁺ concentrations in a) calcite only and b) calcite and aragonite cemented host rock.

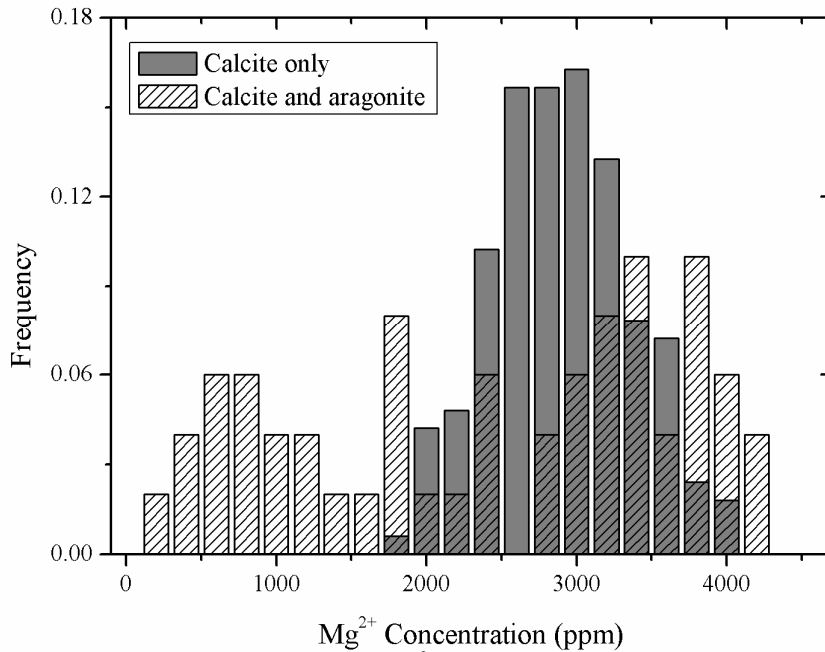


Figure 4.4-19 Cumulative frequency plot of Mg²⁺ concentrations in a) calcite only and b) calcite and aragonite cemented host rock.

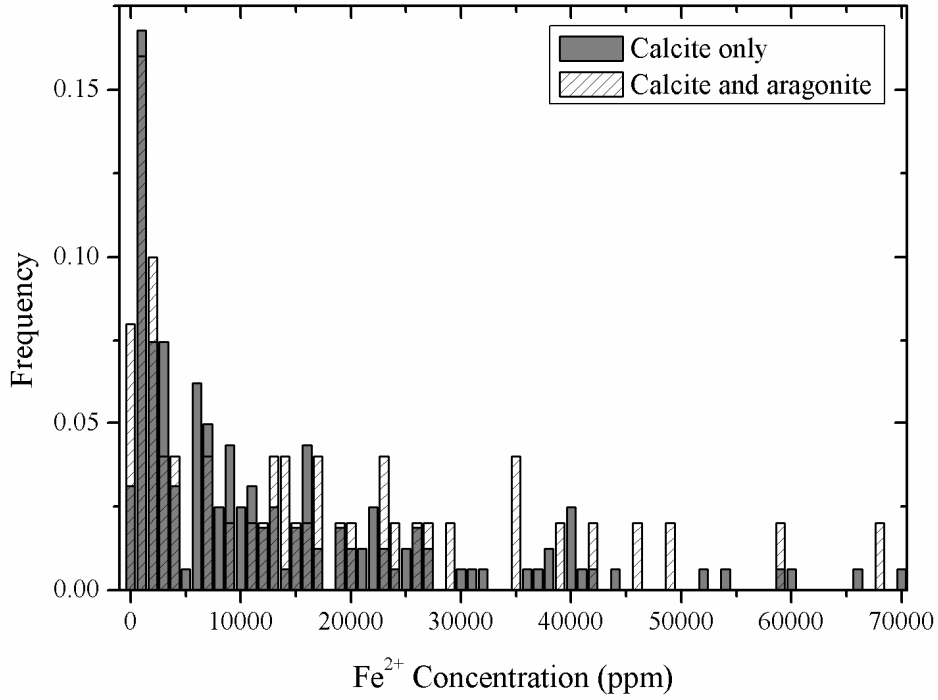


Figure 4.4-20 Cumulative frequency plot of Fe²⁺ concentrations in a) calcite only and b) calcite and aragonite cemented host rock.

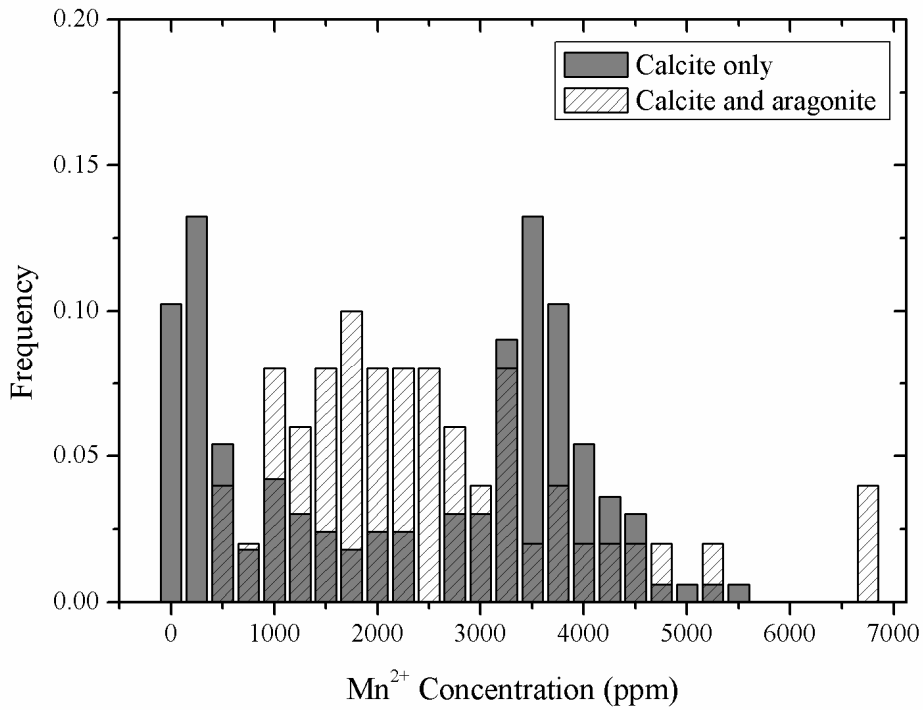


Figure 4.4-21 Cumulative frequency plot of Mn²⁺ concentrations in a) calcite only and b) calcite and aragonite cemented host rock.

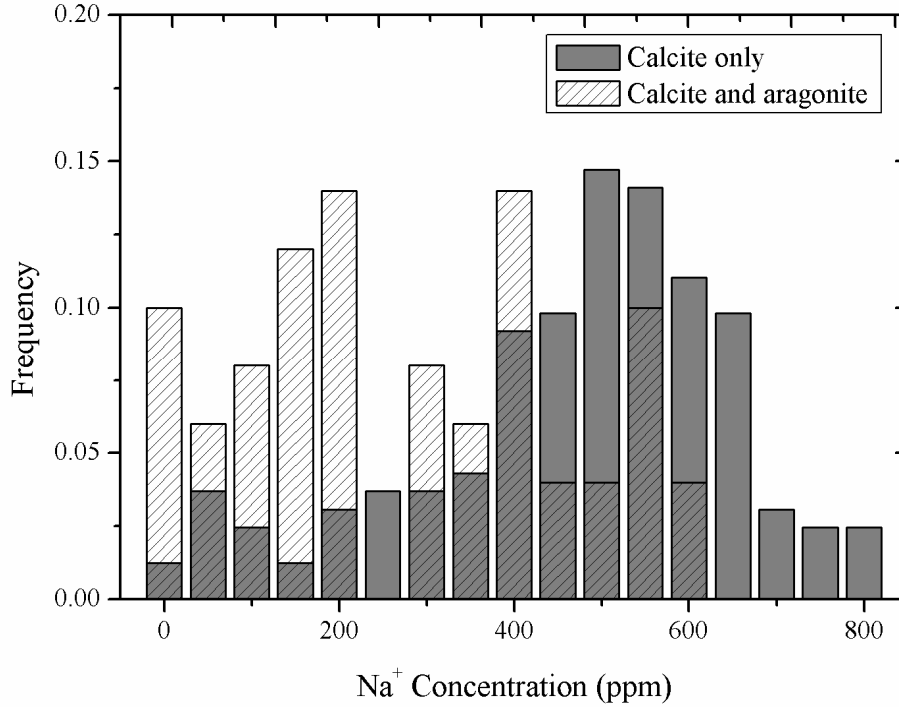


Figure 4.4-22 Cumulative frequency plot of Na⁺ concentrations in a) calcite only and b) calcite and aragonite cemented host rock.

4.4.3.1. Calcite Cements

Calcite cements, in samples containing only calcite, contain a gradational zonation in Fe and Mn from core to rim (Figs. 4.4-15, 4.4-16 & 4.4-23). Mg²⁺, Sr²⁺, Na⁺ and K⁺ concentrations are essentially homogenous (Figs. 4.4-23). Mg contents reflect crystallization at low temperatures: crystallization temperatures calculated from the temperature dependent D_{Mg} (Oomori *et al.*, 1987) have a mean (~15 °C) close to the average emanation temperature of CO₂-charged springs in SWG (Fig. 4.4-24). Parent fluid Sr²⁺, Na⁺ and K⁺ concentrations calculated from the distribution coefficients of Mucci and Morse (1982) and Ishkawa and Ichikumi, (1984) overlap with the Sr²⁺, N⁺ and K⁺ contents of the modern CO₂ charged fluids at SWG and exhibits similar co-variation of these solutes (Figs. 4.4-25 to 4.4-27). N⁺ and K⁺ range to higher values in part due to the effects of ion incorporation into interstitial sites (Busenberg and Plummer, 1984). Superposition of calculated parent fluid chemistry and crystallization temperature suggest deposition from a fluid of comparable composition to that of the modern CO₂-charged fluids at SWG.

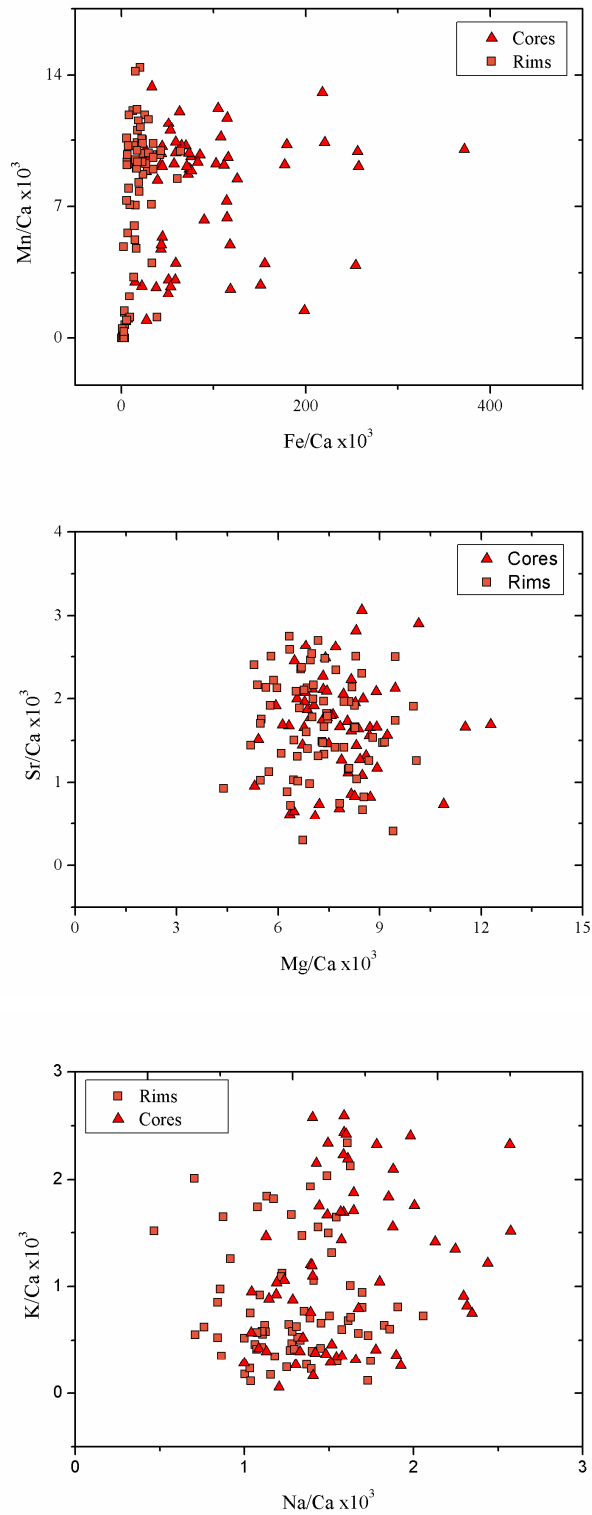


Figure 4.4-23 Tr/Ca of calcites in samples containing only calcite cements showing the variation in cement composition between crystal cores and rims.

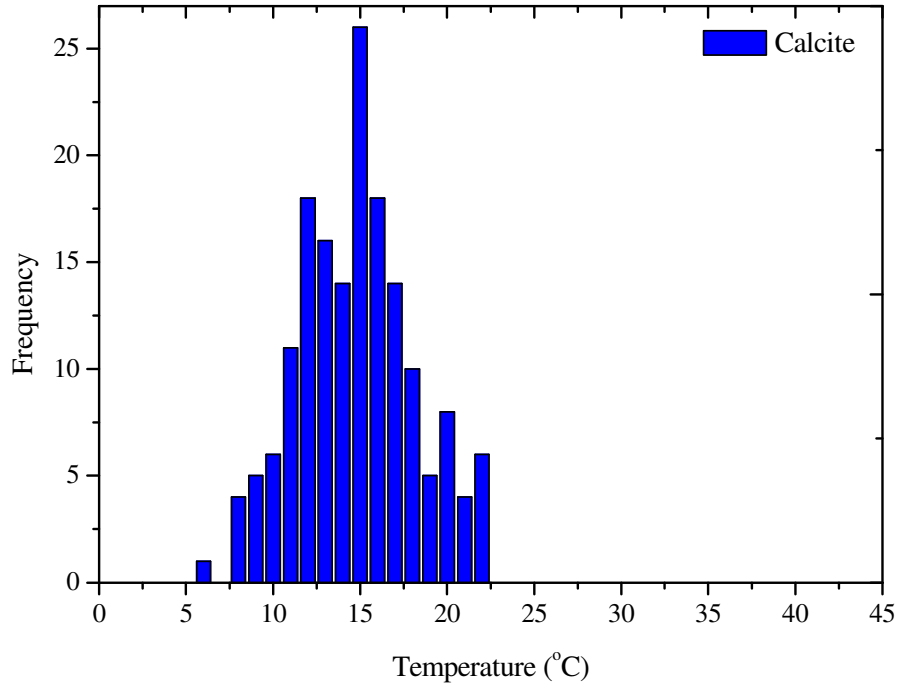


Figure 4.4-24 Cumulative frequency plot of crystallization temperature calculated from the temperature dependent D_{Mg} expression of Oomori *et al.*, (1987) and using the average Mg/Ca of the modern CO₂-charged fluids (0.51) at SWG.

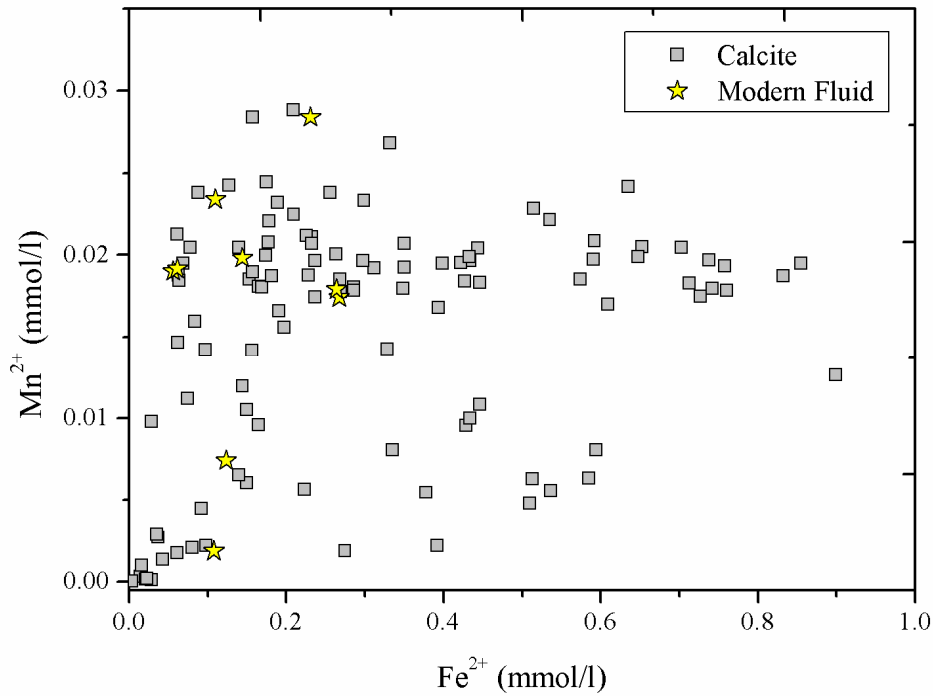


Figure 4.4-25 Parent fluid Fe²⁺ and Mn²⁺ concentrations calculated using the distribution coefficients of Lorens (1981).

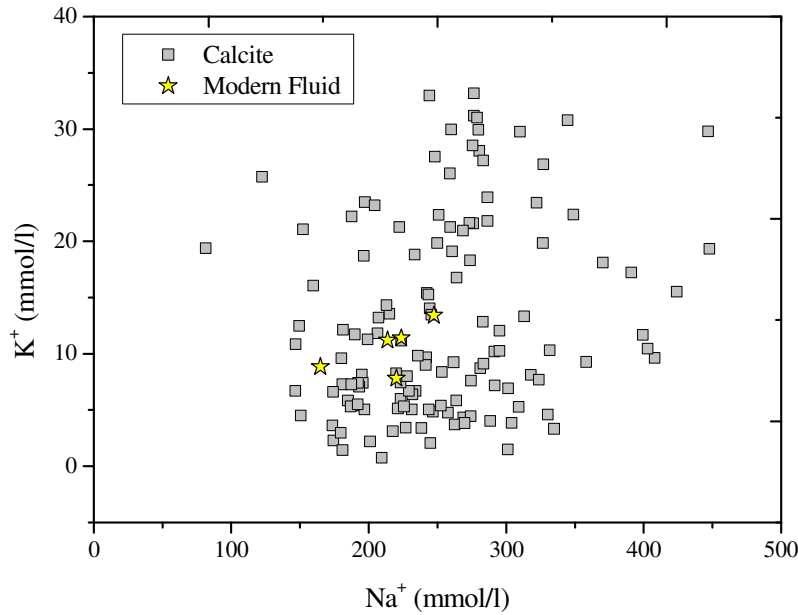


Figure 4.4-26 Parent fluid Na⁺ and K⁺ concentrations calculated using the distribution coefficients of Ishkawa and Ichikumi, (1984). The range of Na/Ca and K/Ca observed in calcite cements suggests Na⁺ and K⁺ concentrations in the paleo-CO₂-charge fluids that overlap with those of the modern fluid but ranged to higher concentrations. However, both Na and K probably occupy interstitial positions in the calcite structure and their incorporation is thus partly dependent on the number of surface defect sites (see Busenberg and Plummer, 1984) which probably explains the high concentrations observed in some cements.

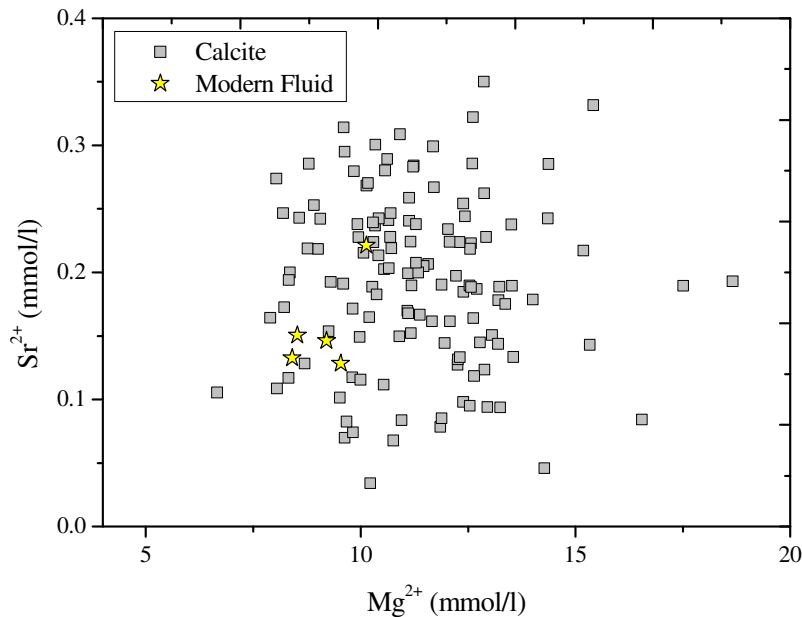


Figure 4.4-27 Parent fluid Mg²⁺ and Sr²⁺ concentrations calculated using the distribution coefficients of Mucci and Morse (1982). Sr²⁺ concentrations in the paleo-fluids largely overlap those of the modern fluids. Mg²⁺ concentrations range to higher values suggesting Mg²⁺ concentrations in the paleo-CO₂-charged fluids where probably higher, but not significantly so, than those observed in the modern fluids.

4.4.3.2. Calcite Precipitation Rates

Given the similarity in composition of the parent fluid and the modern CO₂-charged fluids, in-situ distribution coefficients can be derived from measured calcite compositions and the Tr/Ca and activity coefficients of the modern fluid. Using the rate dependent expression for D_{Sr} (Equation 4.29) derived from experimental studies (section 4.3.5) the rate of calcite precipitation can then be calculated from the Sr/Ca^{cc}. Average calcite precipitation rates calculated for calcite core compositions are 2.1×10^{-6} mol/m²/s and from rim compositions are 1.3×10^{-6} mol/m²/s (Fig. 4.4-28). The values approximate a Gaussian distribution and fall within the range of experimentally observed calcite precipitation rates (e.g. Morse, 1987; Mucci and Morse, 1984; Lee and Morse, 1999; Nancollas and Reddy, 1971) (Fig. 4.4-29). Implicit in this model is that fluid Sr/Ca is invariant throughout the precipitation of calcite; this is likely to be a significant simplification. However, uncorrelated Sr and Mg, and the range of values observed, suggest that fluid Mg/Ca and Sr/Ca are not significantly fractionated by calcite precipitation. Varying the calculation through the full range of Sr/Ca^{fluid} observed at SWG (0.006 to 0.009, average = 0.007, $n = 6$) changes the mean rate by only +11 to -17 %. The mean values of Sr/Ca^{cc} are probably derived from fluids with Sr/Ca values close to that observed in the modern fluid and mean calculated precipitation rates will reflect this fact. Modern fluid Mn/Ca and Fe/Ca ratios are ~0.001 and ~0.005 respectively, values sufficient to suppress calcite precipitation but only by a small degree (e.g. Dromgoole and Walter, 1990b). Paleo-CO₂ charge fluids had up to an order of magnitude higher Fe/Ca ratios (although similar Mn/Ca ratios) than modern CO₂ charged fluids (Fig. 4.4-25 & assuming [Ca²⁺] was of the same order of magnitude as the modern fluid). The dependence of precipitation rate on Fe/Ca has not been quantified but if it exhibits a similar magnitudinal relationship as Mn (Dromgoole and Walter, 1990b) this would imply an order of magnitude inhibition of rate. The variation in calculated rate probably reflects a variety of factors including changes in the solution saturation state, $p\text{CO}_2$, small variations in the Tr/Ca of inhibiting trace ions (mainly Mn and Fe) and nucleation site density and the variation of all these parameters in pores of different sizes and degrees of connectivity.

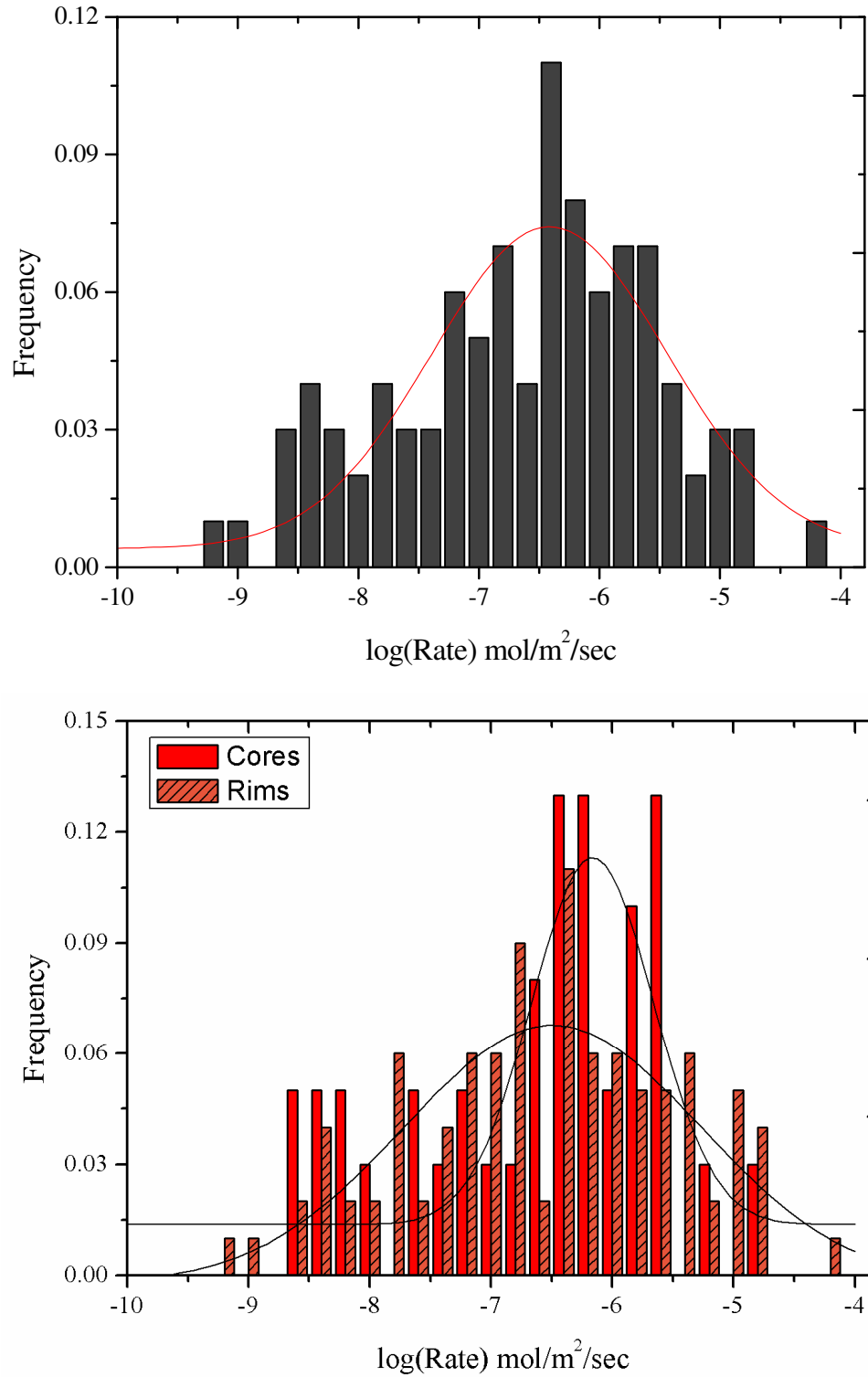


Figure 4.4-28 Calcite precipitation rate calculated from Sr/Ca^{CC} and Sr/Ca^{fluid} and the D_{Sr} rate dependence derived from a least square fit to the data of Mucci and Morse (1983) and Mucci (1986). Displayed are the rates for all a) calcite compositions and b) the rates for core and rim compositions. Curves are best fit Gaussian distributions.

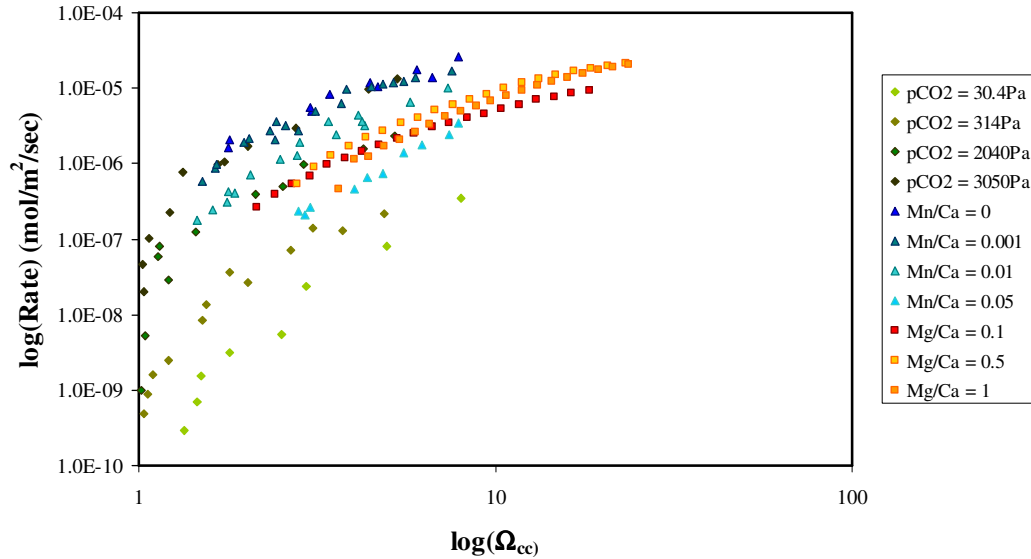


Figure 4.4-29 Laboratory derived calcite precipitation rates as a function of solution saturation state for fluids of various compositions. Data for the variation in rate with: $p\text{CO}_2$ are from Zuddas and Mucci 1993 (25°C, pH 8, [Mg/Ca] = ~5, 1.2 M NaCl); for [Mn/Ca] from Dromgoole and Walter, 1990b (25°C, pH 8, [Mg/Ca] unknown, 0.1 M NaCl, $p\text{CO}_2 = 100$ Pa); and for [Mg/Ca] from House *et al.*, 1988 (25°C, pH 8, 1.0 M NaCl, $p\text{CO}_2 = \sim 100$ to 1000 Pa).

4.4.3.3. Paleo-fluid Eh-pH

Constrains on paleo-fluid Eh-pH conditions, base on calcite Fe and Mn contents, the distribution coefficients of Lorens (1981) and simultaneous Fe₂O₃-MnO₂ equilibria (section 4.3.7) imply Eh-pH conditions comparable to that of the modern CO₂-charged fluids (Figs. 2.4-25 & 4.4-30) but which range to lower pH. Actual variations in calcite Mn and Fe reflect variation in the Eh-pH conditions of the fluid and variations in precipitation rate (Fig. 4.4-30 & 4.4-31); although the effects of variation in D_{Fe} and D_{Mn} due to variations in precipitation rate are relatively small compared to the magnitude of the partitioning (see section 4.3.7). Differences in the Fe and Mn content between cores and rims reflect a progressive increase in pH through the course of precipitation. Any major variation in pH in these fluids is most likely a result of differing degrees of CO₂ saturation modified either by degassing during ascent of the fluids to the surface or as the initial CO₂-charge in the aquifer dissipates.

Modelling the solubility of hematite as a function of $p\text{CO}_2$, at different fixed Eh conditions (Fig. 4.4-32), highlights the high solubility of hematite in fluids with high $p\text{CO}_2$ even at relatively oxidizing conditions.

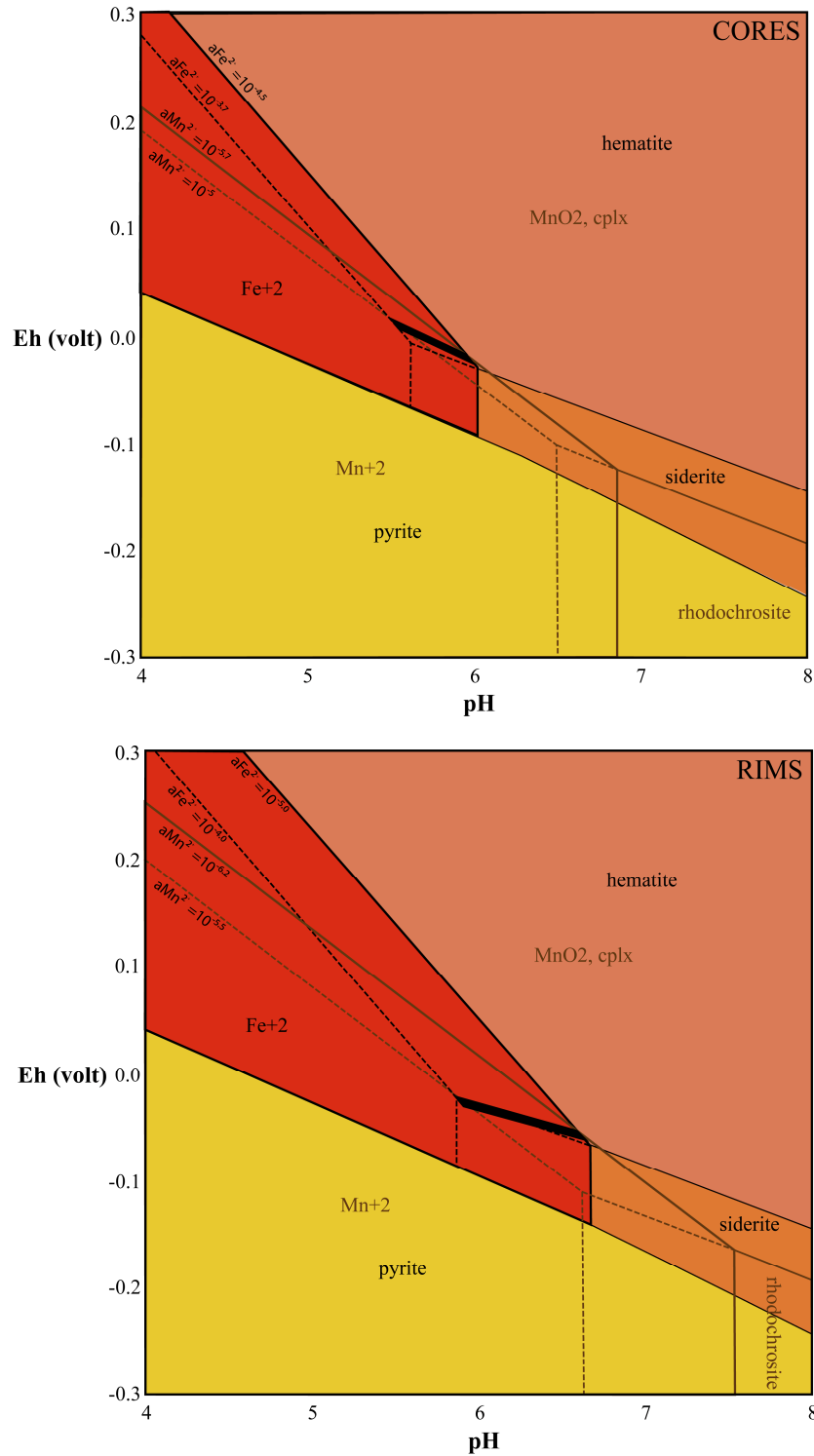


Figure 4.4-30 Eh-pH diagrams for the system FeSCOH and MnSCOH, calculated using CHNOSZ (Dick, 2008) at 15°C; $\log(a_{\text{CO}_2}) = -1.4$, $\log(a_{\text{S}_{\text{TOT}}}) = -2.4$. Black bands are the projected Eh-pH range of parent fluids calculated for calcite core and rim Fe and Mn contents showing upper and lower Eh-pH limits for maximum and minimum Fe and Mn contents observed in each zone. $D_{\text{Mn}} = 7$ and $D_{\text{Fe}} = 3$ were used based on the rate dependent expressions of Dromgoole and Walter (1990a), calculated for the rates derived in section 4.4.3.1. The calculated trajectory for Eh-pH evolution between cores and rims suggests mainly a transition towards higher pH rather than a change in Eh.

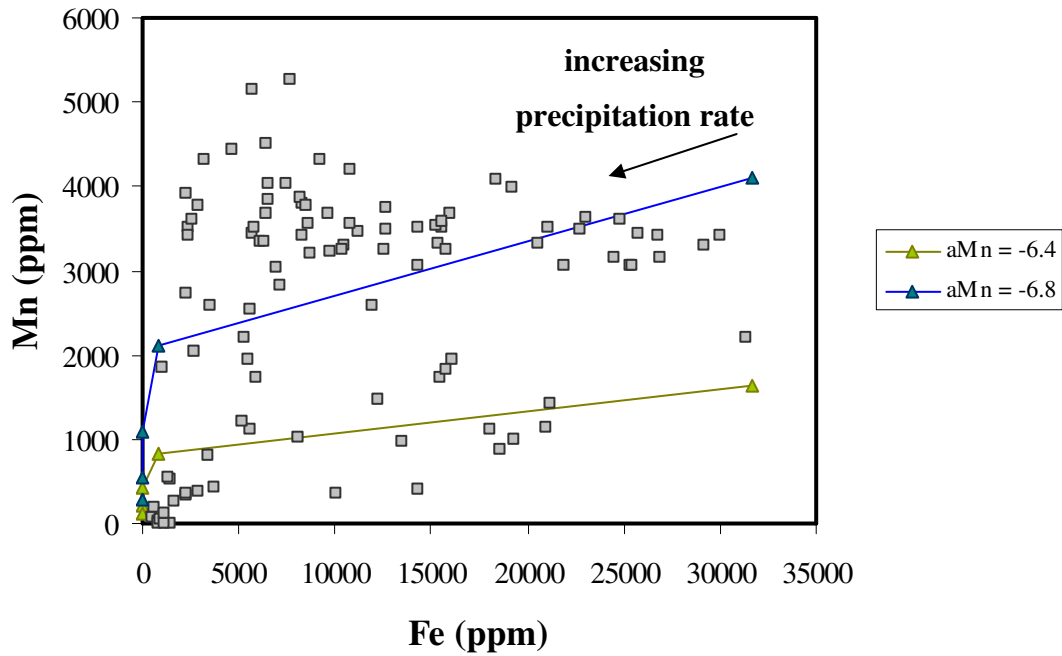


Figure 4.4-31 Measured calcite Fe and Mn contents (grey squares) versus calcite Fe and Mn contents modelled for the modern CO₂ charged fluids at varying precipitation rates using expressions from Dromgoole and Walter (1990a); $\log(a\text{Fe}^{2+}) = -4.5$ and $\log(a\text{Ca}^{2+}) = -2.3$. Differences in the dependence of D_{Mn} and D_{Fe} on precipitation rate produce non-linear correlations in calcite Mn-Fe and most likely explains some of the variation in measured concentrations. The bimodal distribution of Mn concretions may be explained by precipitation from two generations of fluid with varying $a\text{Mn}^{2+}$ but similar $a\text{Fe}^{2+}$ and $a\text{Ca}^{2+}$.

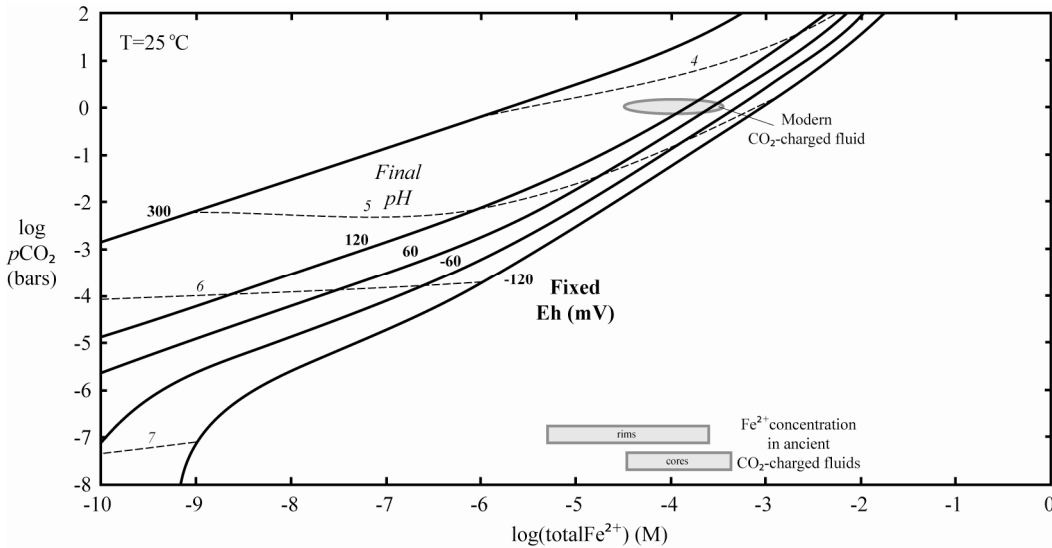


Figure 4.4-32 Fluid Fe²⁺ concentration in equilibrium with hematite as a function of $p\text{CO}_2$, up to 100 bar and for different fixed values of Eh, from -120mV to +300mV. A wide range in Fe²⁺ concentrations is observed over the full range of $p\text{CO}_2$, and hematite is relatively soluble at high $p\text{CO}_2$ even at relatively oxidizing conditions. Calculations performed in PHREEQC; 0.1M NaCl solution, hematite equilibrium, fixed Eh using O₂ fugacity, progressive titration of CO₂

4.4.3.4. Calcite and Aragonite Cements

Fe, Mn, Na, K contents of these calcites (Fig. 4.4-33) are similar to the concentrations in samples containing only calcite but Sr and Mg concentrations range to higher values and exhibit a strong positive correlation. Positively correlated Mg/Ca and Sr/Ca suggest calcite precipitation from a closed fluid reservoir. Thus cation concentrations cannot be accurately used to estimate temperature or precipitation rate due to the highly variable nature of the parent fluid composition. Given the rate independence of Mg-incorporation into calcite, and an insignificant variation in D_{Sr} with temperature, only variation in the composition of the parent solution can explain correlated Mg/Ca and Sr/Ca. Positively correlated variation in Tr/Ca for multiple cations in calcite (e.g., Mg/Ca, Sr/Ca, Na/Ca), where both D_{Tr} are either <1 , $=1$ or >1 is indicative of a Rayleigh fractionation process occurring during precipitation. Precipitation from a closed system results in modification of the fluid Tr/Ca due to the non-uniform incorporation of Tr into calcite relative to Ca^{2+} .

Rayleigh fractionation as applied to individual trace element behaviour has been discussed thoroughly elsewhere (e.g. McIntire, 1963). When examining multiple Tr/Ca²⁺ systems where the incorporation of one trace component (e.g. Mg²⁺) modifies the degree or rate of incorporation of a second trace component (e.g. Sr²⁺) one must consider a modified form of the Rayleigh relationship where by D_{Sr}^{cc} varies as a function of Mg/Ca.

The Sr/Ca of calcite $[(Sr/Ca)^{cc}]$ precipitated at any point during a Rayleigh process from a closed solution of initial Sr/Ca can be calculated from the initial solution composition $[(Sr/Ca)_o^{fluid}]$ assuming a constant effective partition coefficient (D_{Sr}^{cc}):

$$\left(\frac{Sr}{Ca}\right)^{cc} = D_{Sr}^{cc} \cdot \left(\frac{Sr}{Ca}\right)_o^{fluid} \cdot F^{D_{Sr}^{cc}-1} \quad (4.30)$$

where the extent of precipitation is defined as:

$$F = \left(\frac{Ca}{Ca_o}\right)_{fluid} \quad (4.31)$$

Mg/Ca can be described similarly to Eq. (4.30), where Sr/Ca is replaced by Mg/Ca and D_{Sr}^{cc} by D_{Mg}^{cc} . Since Mg/Ca and Sr/Ca are linked by the extent of precipitation, F , the expressions can be combined, eliminating F , yielding a linear log–log relationship:

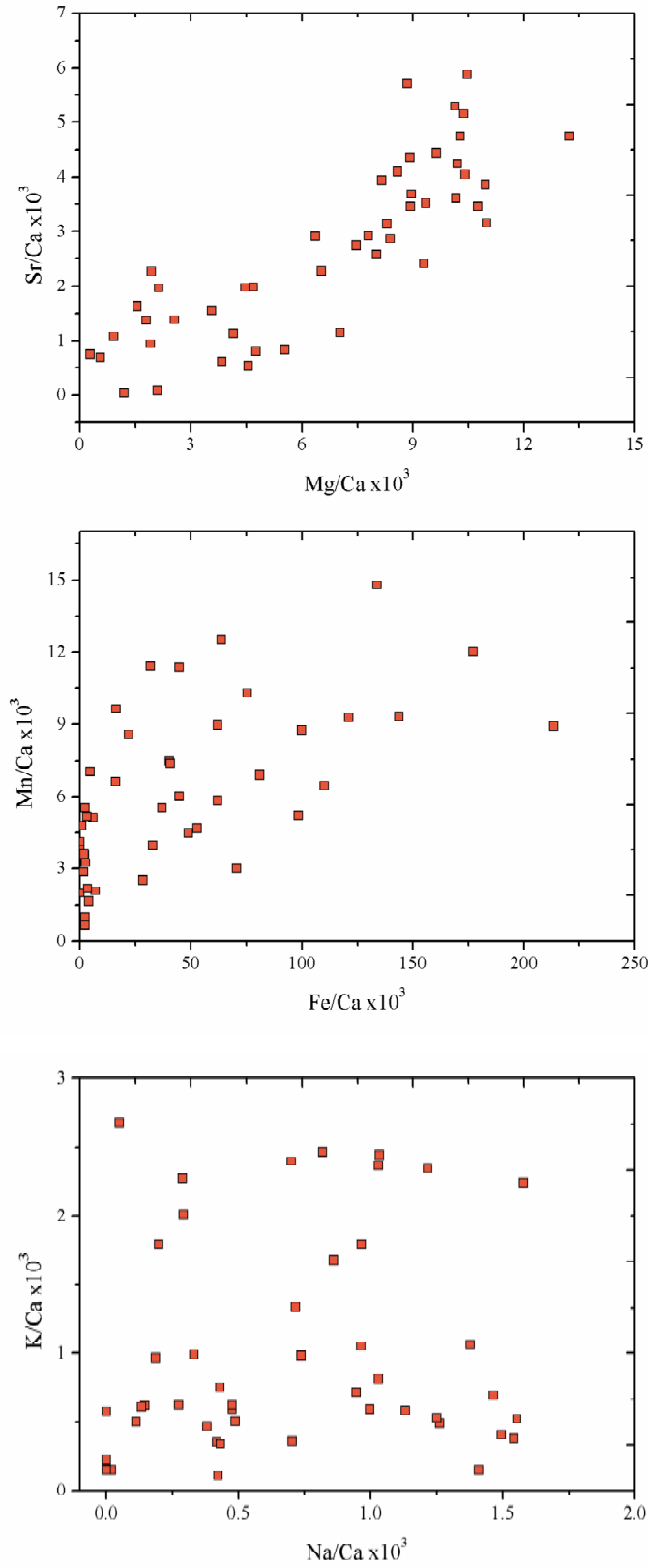


Figure 4.4-33 Tr/Ca of calcites in samples containing both calcite and aragonite cements.

$$\ln \left[\frac{(Sr/Ca)^{cc}}{D_{Sr}^{cc} \cdot (Sr/Ca)_o^{fluid}} \right] / D_{Sr}^{cc} - 1 = \ln \left[\frac{(Mg/Ca)^{cc}}{D_{Mg}^{cc} \cdot (Mg/Ca)_o^{fluid}} \right] / D_{Mg}^{cc} - 1 \quad (4.32)$$

For the incorporation of Sr²⁺ and Mg²⁺ into calcite where the (Mg/Ca)^{fluid} modifies the D_{Mg}^{cc} and D_{Sr}^{cc} and the functional relationship (Fig. 4.4-34) can be derived from a least means squared fit to the experimental data of Mucci and Morse (1983) giving:

$$D_{Mg}^{cc} = 0.0275 \cdot (Mg/Ca)_{fluid}^{-0.3197} \quad (4.33)$$

and

$$D_{Sr}^{cc} = 0.146 + 1.833 \cdot \chi_{Mg}^{cc} \quad (4.34)$$

where χ_{Mg}^{cc} is the mole fraction of Mg in calcite at a given (Mg/Ca)_{cc}. Combining Eq. (4.32) to (4.34) yields

$$(Sr/Ca)^{cc} = \exp \left\{ \frac{\ln \left[\frac{(Mg/Ca)^{cc}}{0.0275 \cdot (Mg/Ca)_{fluid}^{-0.3197} \cdot (Mg/Ca)_o^{fluid}} \right] / \left[(0.0275 \cdot (Mg/Ca)_{fluid}^{-0.3197}) - 1 \right]}{\left[(0.146 + 1.833 \cdot \chi_{Mg}^{cc}) - 1 \right]} \right\} \cdot \left[(Sr/Ca)_o^{fluid} \right] \quad (4.35)$$

Under the conditions of closed system precipitation with constant partition coefficients and any initial fluid composition, trace-trace behaviour is predicted to follow Eq. (4.32) In Eq. (4.32) the slope of the log-log relationship is determined by the partition coefficients of each Tr and the intercept is influenced by both the initial solution composition and the partition coefficients. The slope in Eq. (4.32) is relatively less sensitive to variations in D_{Mg}^{cc} than D_{Sr}^{cc}, since D_{Mg}^{cc} is << D_{Sr}^{cc}.

First we can consider the simple model of constant D_{Mg}^{cc} and D_{Sr}^{cc}. We can calculate a value for D_{Mg}^{cc} and D_{Sr}^{cc} from the composition of the calcites precipitated from the unfractionated reservoir, and the modern fluid (D_{Mg}^{cc} = 0.0131 close to the value of 0.0154 predicted from the temperature dependence of Mg incorporation into calcite (Oomori *et al.*, 1987) and D_{Sr}^{cc} = 0.23).

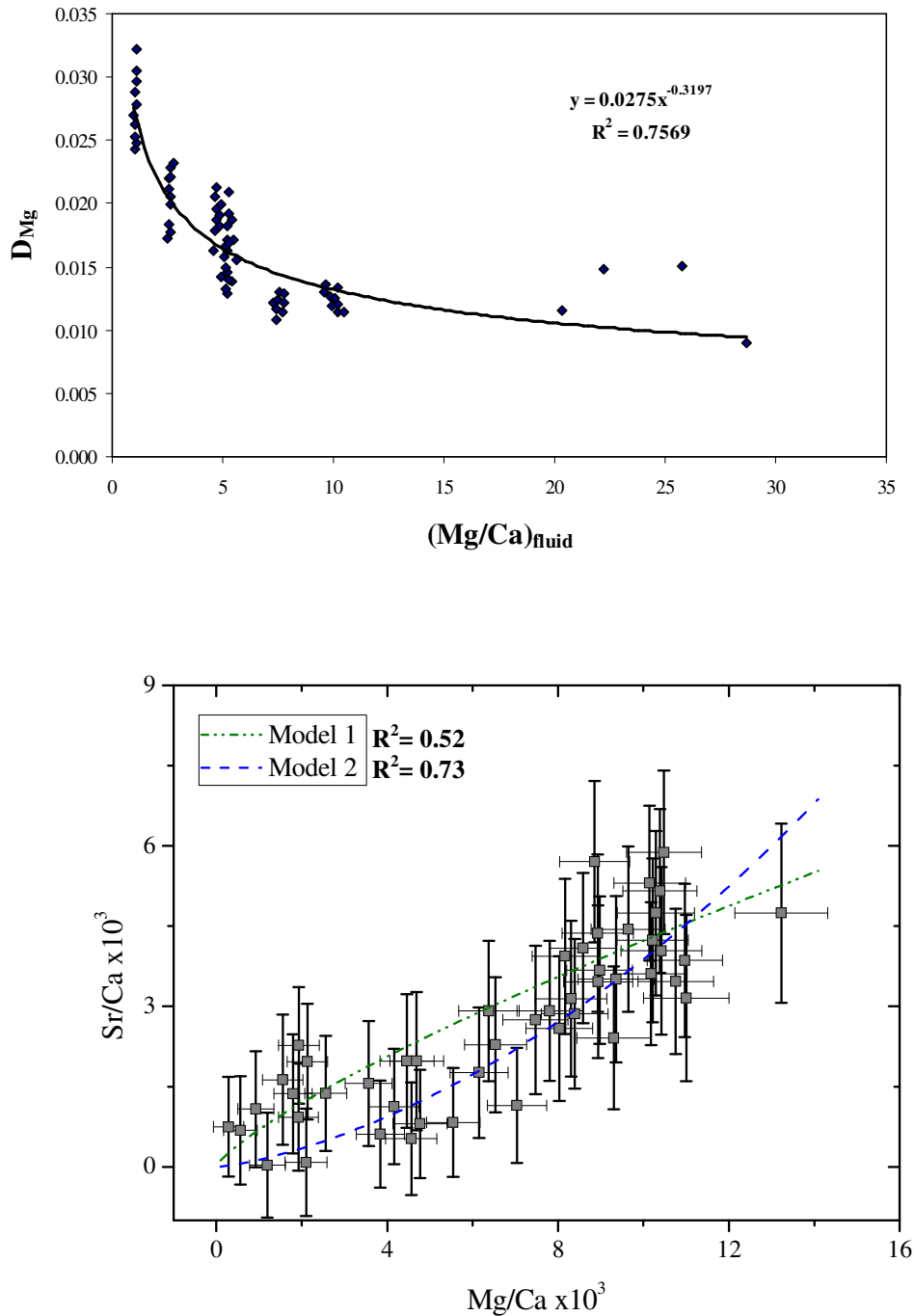


Figure 4.4-34 a) Variaiton in D_{Mg}^{cc} as a functon of $(Mg/Ca)_{fluid}$ (Mucci and Morse, 1983). b) Mg/Ca and Sr/Ca covariation in samples containing calcite and aragonite cements. Curves are the Rayleigh fractionation models previously described. Model 1) Constant D_{Mg}^{cc} and D_{Sr}^{cc} . Model 2) Variation in the fluid Mg/Ca as a result of fraction of the fluid composition due to calcite precipitation modifies D_{Mg}^{cc} and D_{Sr}^{cc} resulting in a non-linear relationship which best describes the measured data. Error bars are 2σ uncertainties in the deviation of repeat analysis of points.

We can also consider a second model describing the Sr/Ca of calcite precipitating from a closed system where the fluid composition is undergoing a Rayleigh type fractionation and the resulting modification of $(Mg/Ca)_{fluid}$ results in a progressive modification of D_{Mg}^{cc} and D_{Sr}^{cc} . Fitting these two models to the measured data (Fig. 4.4-34) suggests the functional form of the variation in Mg/Ca and Sr/Ca is best described by the second model, consistent with the experimental prediction that the incorporation of Mg²⁺ into the calcite lattice is dependent on the Mg/Ca of the parent solution and that the X_{Mg} in calcite exerts a control on the incorporation of Sr²⁺ as discussed. Further this suggest that closed system fraction of the solution composition results in elevated $(Mg/Ca)_{fluid}$ and Mg²⁺.

It has been well established that the presence of dissolved Mg²⁺ favours the precipitation of CaCO₃ as aragonite, rather than the more stable calcite, from magnesium-rich aqueous solutions (Lippmann, 1973). Also, other studies (e.g. Taft, 1967; Bischoff and Fyfe, 1968) indicate that Mg²⁺ inhibits the low temperature transformation, via dissolution-reprecipitation, of aragonite to calcite. A commonly accepted explanation of these observations is that Mg²⁺ inhibits calcite nucleation and/or crystal growth, and, as a result aragonite, which precipitates more rapidly, is kinetically 'stabilized' (Bischoff, 1968). Dissolved Mg is not readily absorbed on to the surface of aragonite, nor is Mg²⁺ taken up to any extent into the aragonite crystal lattice. As a result aragonite crystal growth is relatively unaffected by the presence of dissolved Mg²⁺. By contrast Mg²⁺ is readily absorbed on to the surface of calcite and incorporated into its crystal structure. Most of the Mg inhibition is believed to be due to the non-equilibrium incorporation of Mg into growing calcite crystals, which causes them to be considerably more soluble than pure calcite (e.g. McIntire, 1963). Also, the presence of Mg²⁺ ions in solution inhibits nucleation kinetics of calcite as hydrated magnesium is adsorbed onto the surfaces of the pre-critical nuclei of the calcite (i.e., crystallites that are too small to be stable in solution and quickly dissolve) and poisons the active growth sites (Fernández-Díaz *et al.*, 1996).

The findings of Fernández-Díaz *et al.*, (1996) and Given and Wilkinson (1985) suggest that carbonate mineralogy and morphology are not controlled by a single parameter but by interplay between super-saturation and solution Mg/Ca ratios. These findings are further supported by the fact that aragonite can be precipitated from low-Mg²⁺ solutions at very high super-saturations (González and Lohmann 1988), indicating that CO₃²⁻-controlled kinetics also play a major role in aragonite precipitation in fluids with low Mg/Ca, such as dilute surface and ground waters.

Thus the presence of pokiolitic aragonite cements growing with calcite can be attributed to the modification of $(Mg/Ca)_{fluid}$ through closed system fractionation of the parent fluid resulting in elevated Mg/Ca ratios suitable for the inhibition of calcite precipitation and the kinetic stabilization of aragonite. The additional role of CO₃²⁻ and thus Ω_{cc} is difficult to asses in

this situation. Significant modification of the Ω of carbonate minerals in this setting is probably best achieved by H⁺ consumption by CO₂ degassing following the conversion of CO₂ (aq) → CO₂ (g).

4.4.4. Stable Isotope Geochemistry

Twenty samples of bleached and altered Entrada Sandstone and twenty samples of aragonite veins, from travertine feeder systems, were collected from Salt Wash Graben. Table B-VI and B-VII (Appendix B) displays the $\delta^{13}\text{C}$ and $\delta^{18}\text{O}$ of samples of carbonate cemented Entrada Sandstone associated with travertine mounds, aragonite veins and modern travertine samples obtained in this study. These samples were supplemented with 16 chips of U-Th dated aragonite veins from travertine feeder systems (Burnside, 2009) from both LGF and SWG (Table B-IX, Appendix B). U-Th dated samples were obtained from the thickest portions of homogeneous veins in order to limit the effects of wall rock interaction. This data is presented in figure (4.4-35) together with data from Dockrill (2005) for aragonite veins, ancient travertine deposits and travertine samples from the actively forming mound at Crystal Geyser.

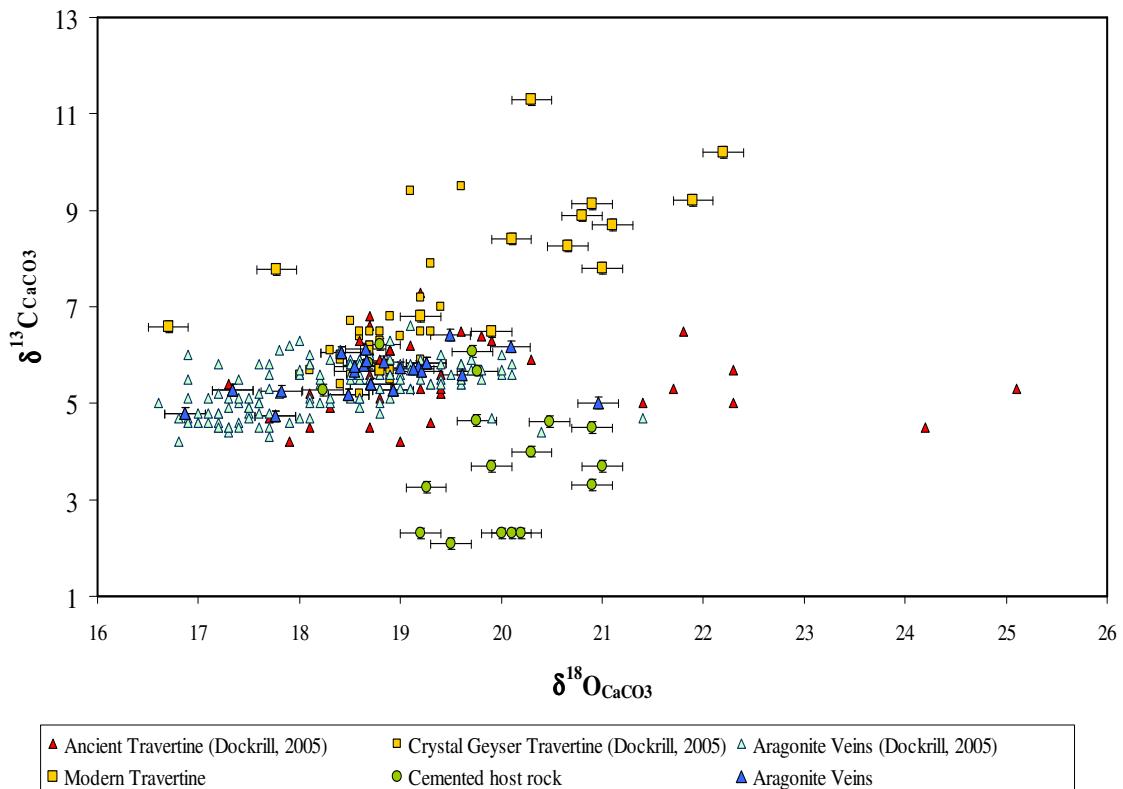


Figure 4.4-35 Stable Isotope analyses for carbonate deposits associated with the modern CO₂ systems from this study and from Dockrill (2005).

4.4.5. Modern Travertine Deposits

Modern travertine deposits exhibit extreme enrichment in ¹³C with values of δ¹³C_{CaCO₃} ranging from 5.2 to 11.3 ‰ V-PDB (Fig. 4.4-36). This ~6 ‰ variation is attributed to CO₂ degassing and carbonate precipitation driven ¹³C enrichment in the out-gassing fluid. Positively correlated δ¹³C and δ¹⁸O is attributed to kinetic isotope effects during the degassing processes (see section 4.4.6). The range in δ¹⁸O_{CaCO₃} of these modern deposits is largely attributed to kinetic degassing effects (but see section 4.4.7). The least fractionated values of δ¹⁸O_{CaCO₃} are consistent with the δ¹⁸O_{HCO₃⁻} beginning controlled by equilibration with δ¹⁸O_{H₂O} of modern CO₂-charged waters. The fraction models suggest that the modern fluid undergoes ~20% degassing before the initiation of calcite precipitation (Figs. 4.4-36 & 4.4-40).

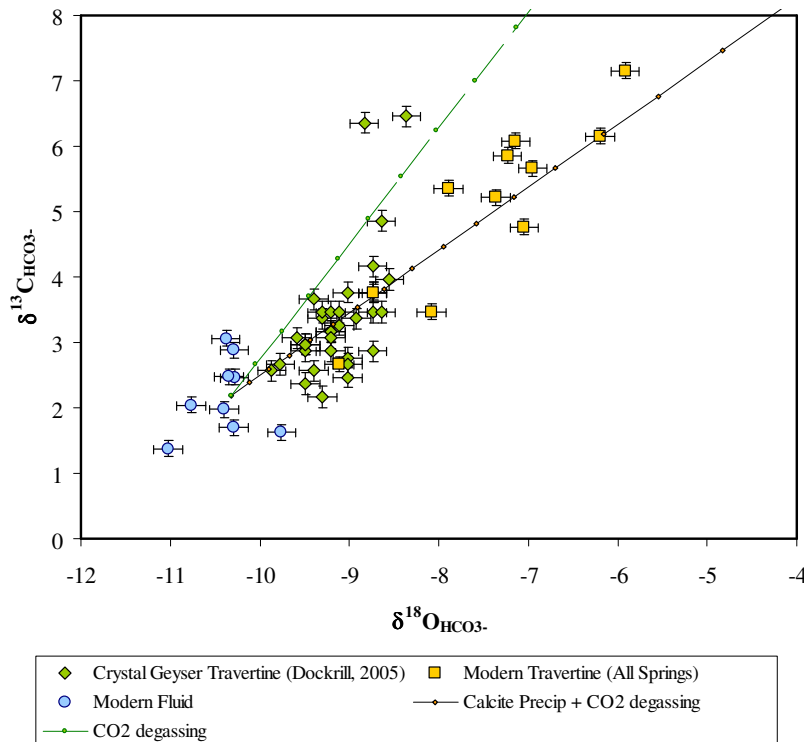


Figure 4.4-36 The δ¹⁸O (PVB) and δ¹³C (PVB) of HCO₃⁻ calculated from the isotopic composition of modern travertine samples from springs in Salt Wash Graben and from samples of travertine from Crystal Geyser (Dockrill, 2005) using appropriate equilibrium fractionation factors calculated for the emanation temperature of each spring. Also plotted is the δ¹⁸O and δ¹³C of HCO₃⁻ in modern CO₂-charged fluids calculated from the measured δ¹⁸O_{H₂O} and δ¹³C_{CO₂(g)}. Lines are Rayleigh distillation models of kinetic fraction of the average HCO₃⁻ of modern fluid resulting from for CO₂ degassing only, and coupled CO₂ degassing and calcite precipitation (see section 4.5.2 for a complete discussion). Error bars are the 2σ of analytical uncertainty.

4.4.6. CO₂ Degassing, Carbonate Precipitation and Kinetic Isotope Fractionation

Carbonate precipitation in shallow subsurface and surface systems will be driven by changes in $p\text{CO}_2$ resulting from changes in ambient pressure. As CO₂-charged fluids ascend through the shallow subsurface the water will move toward chemical equilibrium with its new environment by degassing CO₂, dissolved as CO₂(aq). During this first stage of out gassing of CO₂(aq) from the solution the concentrations of Ca²⁺ and HCO₃⁻ will stay constant (Dulinski and Rozanski, 1990). The equilibrium concentrations of HCO₃⁻ and Ca²⁺ with respect to CaCO₃ are determined by the initial $p\text{CO}_2$ at depth and consequently the fluid becomes quickly supersaturated with respect to CaCO₃ as $p\text{CO}_2$ decreases. After the first stage of out gassing of CO₂, carbonate precipitation starts, the stoichiometry of the overall reaction;



requires that for each CaCO₃ molecule deposited one CO₂ molecule is created. In fluids with high DIC the rate of CaCO₃ precipitation will ultimately be governed by the state of CaCO₃ saturation which will be a direct function of the amount of degassing experience by the fluid. The rate of CaCO₃ precipitation is therefore dependent on the CO₂ degassing rate of the solution.

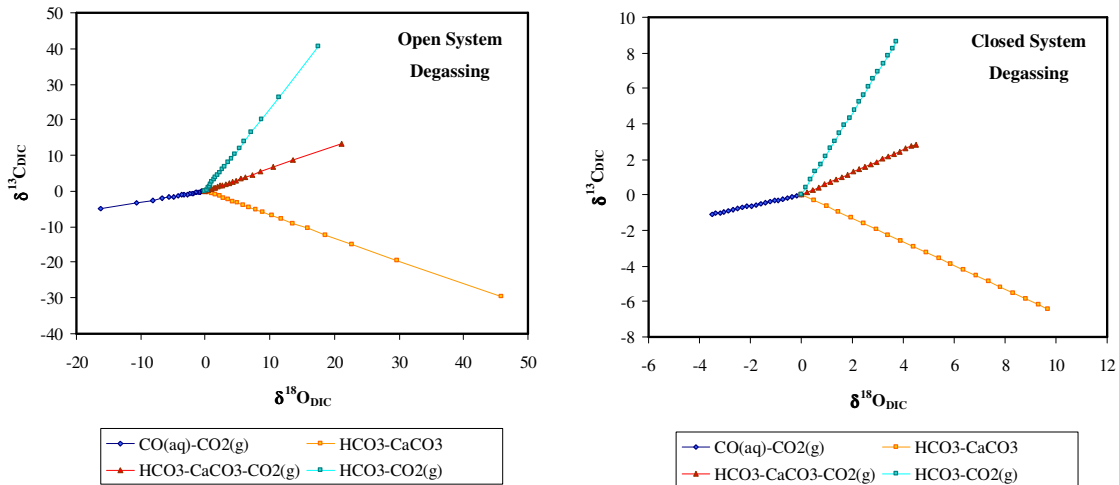


Figure 4.4-37 Evolution of the isotopic composition of the reactant DIC pool during the kinetic fractionation of $\delta^{18}\text{O}$ and $\delta^{13}\text{C}$ (from an initial $\delta^{18}\text{O}$ and $\delta^{13}\text{C}$ of both 0‰) during different mechanism of DIC loss from an open and closed fluid reservoir. Only CO₂ degassing from an HCO₃⁻ reservoir and coupled CO₂ degassing and CaCO₃ precipitation can lead to positively correlated $\delta^{18}\text{O}$ and $\delta^{13}\text{C}$. Open system behaviour leads to large fractionations in the reacting DIC pool.

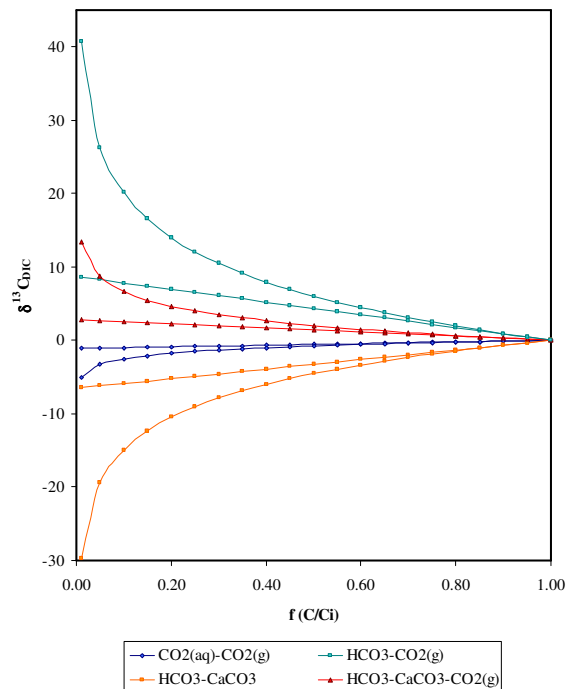


Figure 4.4-38 Evolution of the $\delta^{13}\text{C}$ of the reactant DIC pool as a function of various degrees of C loss during the kinetic fractionation of $\delta^{13}\text{C}$ (from an initial $\delta^{13}\text{C}$ of 0 ‰) under different mechanism of DIC loss from an open (exponential functions) and closed (linear functions) fluid reservoir.

As calcium carbonate precipitation and CO₂ degassing, progresses, the HCO₃⁻ reservoir in the fluid will undergo ¹³C enrichment (Fig. 4.4-37 & Fig. 4.4-38) if C isotope exchange reactions between DIC and CO₂(g) are sufficiently slow and/or fluid/gas velocities is small. This ¹³C enrichment results from the relatively low $\delta^{13}\text{C}$ value of the CO₂ that is lost from the fluid by degassing. The extent of ¹³C enrichment is a function of the fractionation factors between the C species and the fraction of total DIC lost to CO₂ degassing and CaCO₃ precipitation. Only relatively slow hydration-dehydration reactions permit oxygen isotope exchange between CO₂(aq) and H₂O, so if the precipitation of calcium carbonate proceeds rapidly, there may be progressive ¹⁸O enrichment in the HCO₃⁻ and in the CO₃²⁻ that is ultimately incorporated into the calcium carbonate. Both batch (closed) and Rayleigh distillation (open) models can be used to describe the covariation in $\delta^{13}\text{C}$ and $\delta^{18}\text{O}$ of the precipitated CaCO₃ during CO₂ degassing and CaCO₃ precipitation from a fluid. Batch and Rayleigh distillation can be used to model the C and O isotope evolution of precipitating calcium carbonate because if C and O isotopes are fractionated during calcium carbonate precipitation, there must be an effect on the isotope composition of the remaining reactant. It is assumed that an instantaneous isotopic equilibrium fraction occurred among the degassed CO₂, remaining HCO₃⁻ and precipitated CaCO₃. During rapid mineral precipitation it is not uncommon for isotopic disequilibrium to occur (e.g. Fantidis

and Ehhalt, 1970; Hendy, 1971). However, equilibrium fractionation factors are used as a best first approximation because they are known, whereas any deviation from isotopic equilibrium is unknown.

An estimation of the maximum ¹³C enrichment in the HCO₃⁻ reservoir owing to CO₂ degassing and CaCO₃ precipitation was made, using an open system Rayleigh distillation model, and published isotope fractionation factors. The effects of Rayleigh distillation on the δ¹³C value of the DIC reservoir can be modelled by:

$$(\delta + 1000)/(\delta_o + 1000) = f^{(\alpha_{p-r} - 1)} \quad (4.37)$$

where δ is the C isotope composition of HCO₃⁻, δ_o is the initial C isotope composition of HCO₃⁻, f is the fraction of HCO₃⁻ remaining at a given point in the fluids evolution, and α_{p-r} is the equilibrium carbon isotope fractionation factor between a bulk product and the HCO₃⁻ reactant. Because the C in HCO₃⁻ is evenly partitioned between CaCO₃ and CO₂ (g) during CaCO₃ precipitation, a fractionation factor between a bulk product and HCO₃⁻ can be defined such that

$$\alpha_{(bulk_product-HCO_3^-)} = 1/2(\alpha_{CO_2-HCO_3^-}) + 1/2(\alpha_{calcite-HCO_3^-}) \quad (4.38)$$

Using fractionation factors for α_{CO₂-HCO₃} and α_{calcite-HCO₃} of 0.9922 and 1.0010, respectively (Romanek *et al.*, 1992; Zhang *et al.*, 1995), the α_(bulk product-HCO₃) is 0.9966 at 15 °C. The oxygen isotope effects of CO₂ degassing, CaCO₃ precipitation, and H₂O formation, can be modelled using an analogous Rayleigh distillation approach with the following assumptions: There is no oxygen isotope exchange between DIC and water, and the fractionation factor between the bulk product and HCO₃⁻ is

$$\alpha_{(bulk_product-HCO_3^-)} = 2/6(\alpha_{CO_2-HCO_3^-}) + 3/6(\alpha_{calcite-HCO_3^-}) + 1/6(\alpha_{H_2O-HCO_3^-}) \quad (4.39)$$

or in proportion to the oxygen in each of the three products. Using fractionation factors for α_{CO₂-HCO₃}, α_{calcite-HCO₃} and α_{H₂O-HCO₃} of 1.0062, 0.9939, and 0.9667, respectively, α_(bulk product-HCO₃) is 0.9935 at 15 °C (Brenninkmeijer *et al.*, 1983; Kim and O'Neil, 1997; Usdowski and Hoefs, 1993).

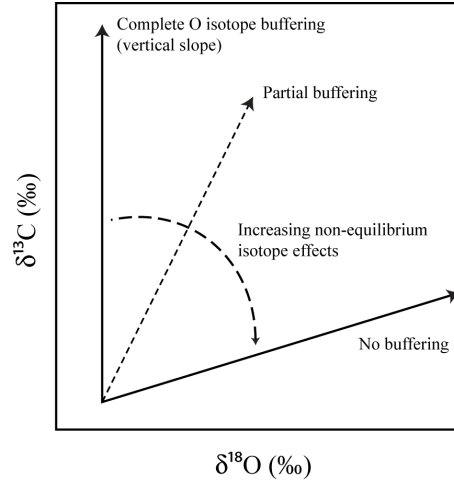


Figure 4.4-39 Changes in the $\delta^{18}\text{O}$ and $\delta^{13}\text{C}$ of HCO_3^- as a result of progressive loss of HCO_3^- during CO_2 degassing and CaCO_3 precipitation with different isotope effects. The $\delta^{18}\text{O}$ of HCO_3^- can either be maintained at a constant value by equilibration between DIC and H_2O through equations (4.41) and (4.42). In the absence of any oxygen exchange $\delta^{18}\text{O}_{\text{HCO}_3^-}$ will evolve, as HCO_3^- is removed from solution, according to the equilibrium fractionation between dissolved species, out gassing CO_2 and precipitating CaCO_3 . An intermediate situation is also possible. (Redrawn after Mickler *et al.*, 2006).

Similarly, the effects of batch degassing on the isotopic composition of the fluid can be expressed as (after Valley, 1986):

$$\delta = \delta_o - (1 - f) \cdot 1000 \cdot \ln \alpha_{p-r} \quad (4.40)$$

where the notations are as previously described. If crystallization of CaCO_3 is sufficiently rapid, HCO_3^- enriched in ^{18}O will be incorporated into CaCO_3 before ^{18}O re-equilibration occurs between HCO_3^- and the bulk water. This approach is an end-member calculation because it neglects CO_2 hydration and hydroxylation reactions (equations 4.41 and 4.42), which will buffer the oxygen isotopic composition of the HCO_3^- reservoir and reduce the magnitude of the oxygen isotope effects of CO_2 degassing. The relatively slow forward and backward reactions outlined in equations (4.41) and (4.42) will result in the HCO_3^- acquiring a $\delta^{18}\text{O}$ value closer to equilibrium with the large reservoir of oxygen in H_2O (Hendy, 1971). Note that in the pH range of interest, reaction (4.41) is dominant.

CO_2 hydration-dehydration



and

CO_2 hydroxylation



This model of progressive loss of HCO₃⁻ during calcium carbonate precipitation, while excluding oxygen isotope exchange between DIC and H₂O, will cause progressive ¹⁸O and ¹³C enrichment in the HCO₃⁻ reservoir, as shown in figures (4.4-37) to (4.4-39). Kinetic fractionation of HCO₃⁻ (aq) implies rapid rates of CO₂ degassing and carbonate precipitation, faster than the HCO₃⁻-H₂O equilibration reaction which operates on the 1000's to 10000's sec time-scale (Hendy, 1971).

4.4.7. Ancient Travertine Deposits

δ¹³C_{CaCO₃} of ancient travertine deposits (Dockrill, 2005) range from 2.5 to 6.5 ‰, the variation being attributed to fractionation during CO₂ degassing. Minimum δ¹³C_{CaCO₃} values 1‰ lower than modern travertine deposits suggest deposition from an isotopically lighter, less degassed reservoir of carbon. This suggests the δ¹³C of the DIC reservoir has evolved through time and was lighter during earlier periods of CO₂ leakage. Ancient travertines from Little Grand Fault (Dockrill, 2005) exhibit trends consistent with kinetic fractionation of the HCO₃⁻ reservoir. The lack of a positive correlation in δ¹³C and δ¹⁸O in Salt Wash Graben samples (Dockrill, 2005) may reflect under representation of the sample population or that these fluids were sufficiently degassed at the time of travertine deposition to suppress kinetic effects. The wide variation in δ¹⁸O_{CaCO₃} (Fig. 4.4-40) (δ¹⁸O SWG: 18.6 to 25.1 ‰; δ¹⁸O LGWF: 17.3 to 21.7 ‰) and values that range to compositions significantly heavier than the modern travertine deposits is attributed to larger concentrations of Paradox Formation brine in the groundwaters during past periods of leakage. Differences in the range of δ¹⁸O observed between each fault system reflect differences in the maximum flux of brine in each fault system.

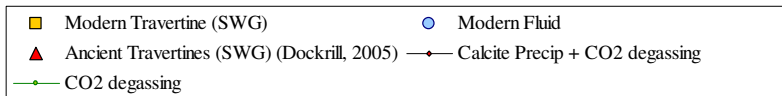
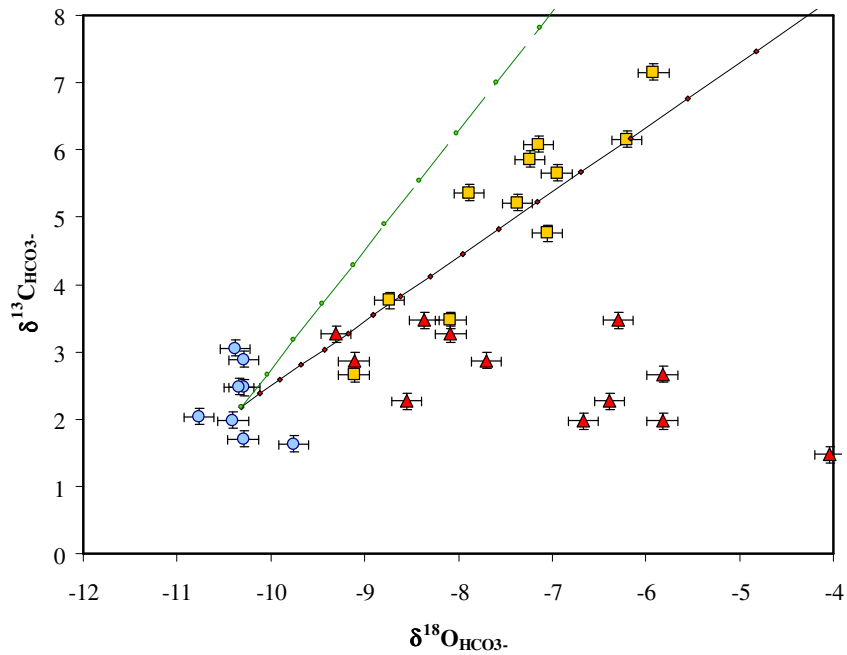
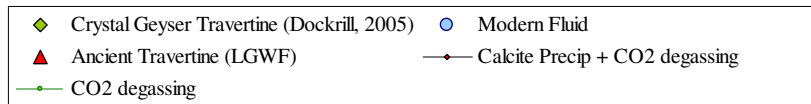
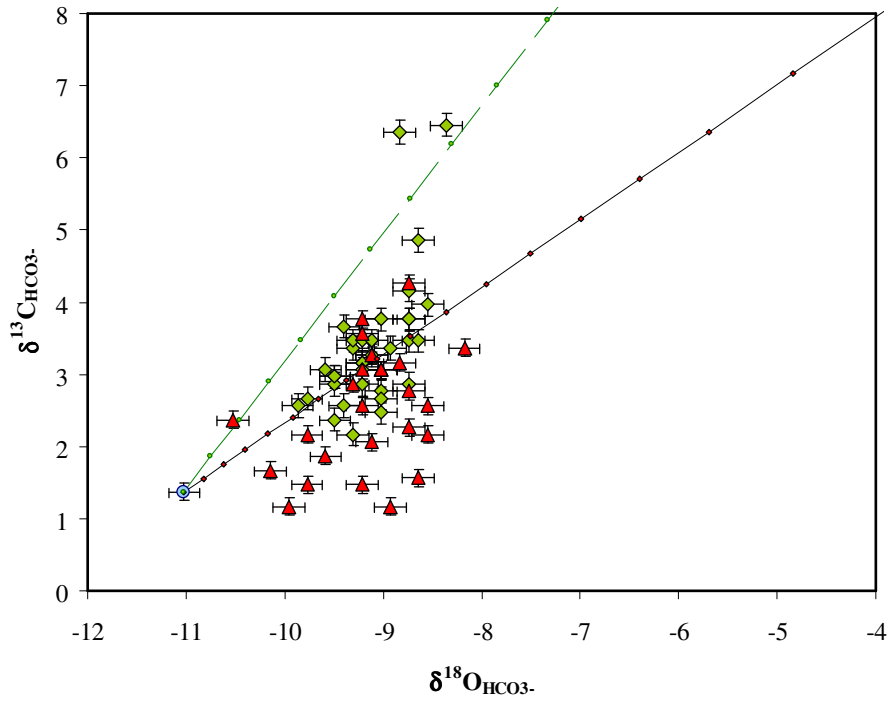


Figure 4.4-40 The $\delta^{18}\text{O}$ and $\delta^{13}\text{C}$ of HCO_3^- calculated from the isotopic composition of modern travertine samples and from ancient travertine samples from Little Grand Fault (a) and Salt Wash Graben (b). The composition of Crystal Geyser fluid and springs from SWG are shown. Lines are Rayleigh distillation models as in Fig. 4.4-36. The fraction models suggest that the modern fluid undergoes ~20% degassing before the initiation of calcite precipitation. Only the ancient travertines from LGF exhibit a correlation consistent with kinetic fractionation of the HCO_3^- reservoir. The wide range in $\delta^{18}\text{O}$ of the SWG samples is interpreted to reflect a wide variation in the range of brine fractions in the source fluid. In both instances the lowest $\delta^{13}\text{C}$ of HCO_3^- in the ancient travertine samples is between 1 to 1.5 ‰ lower than the modern samples which is interpreted to reflect progressive fraction of the initial $\delta^{13}\text{C}$ of the subsurface CO₂ reservoir through the life of the leaking site. This is most likely due to fraction of the $\delta^{13}\text{C}_{\text{CO}_2}$ due to in-situ degassing.

4.4.8. Aragonite Veins

The wide range of $\delta^{18}\text{O}$ observed in aragonite veins and modern travertine samples is indicative of variation in the $\delta^{18}\text{O}$ composition of the parent fluid as a result of both mixing of meteoric and brine fluid sources and modification by kinetic fraction of the solution HCO_3^- pool during CO₂ degassing and CaCO₃ deposition. Positive correlated $\delta^{18}\text{O}_{\text{CaCO}_3}$ and $\delta^{13}\text{C}_{\text{CaCO}_3}$ is a general indication that kinetic effects may be influencing isotopic fractionation during the precipitation of calcium carbonate, although other physical variables may also result in this correlation (e.g. fluid temperature, surface evaporation-condensation processes or progressive dissolution of a precursor carbonate phase and subsequent enrichment in ¹³C and ¹⁸O).

The range of $\delta^{18}\text{O}$ observed in aragonite and modern travertine samples exceeds that expected for likely temperature variations in shallow subsurface and surface environments. The 4 to 5 ‰ variation in $\delta^{18}\text{O}$ observed in aragonite veins would be equivalent to an ~20 to 25 °C variation in precipitation temperature. The slope of the trend in $\delta^{18}\text{O}$ versus $\delta^{13}\text{C}$ resulting from variation in precipitation temperature is significantly lower than the observed correlations. Aragonite deposition occurs at shallow subsurface to near surface depths and so evaporation-condensation processes are unlikely. Given that the stabilization of aragonite at low temperatures requires high [CO₃²⁻] and high levels of supersaturation, non-equilibrium fractionation is to be expected during its deposition.

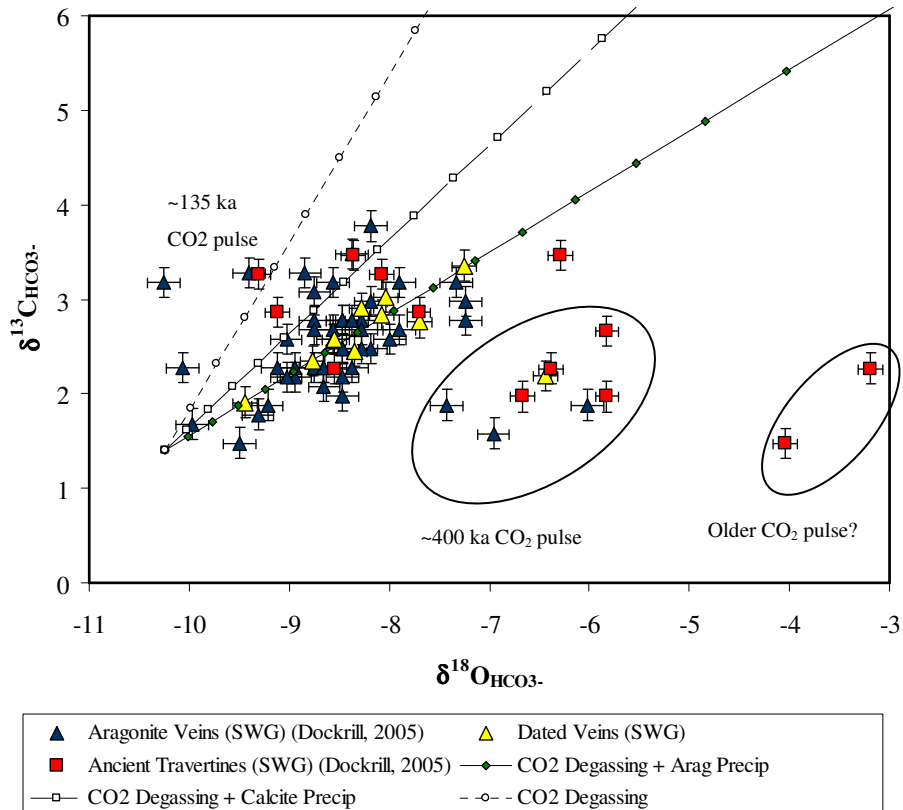
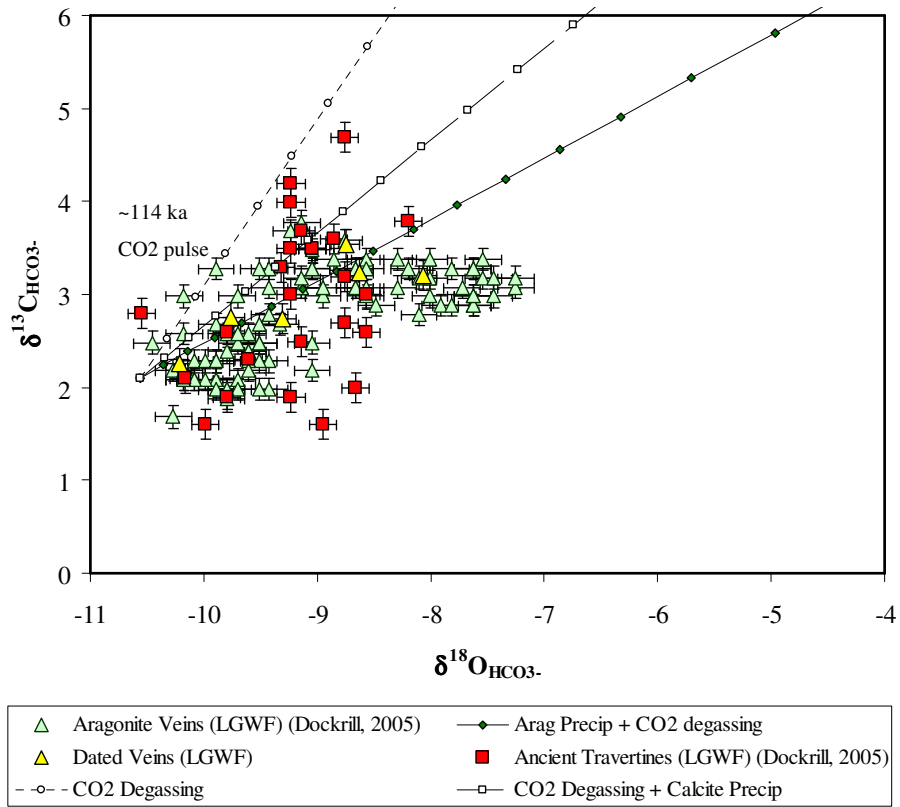


Figure 4.4-41 The $\delta^{18}\text{O}$ and $\delta^{13}\text{C}$ of HCO_3^- calculated from the isotopic composition of aragonite veins and ancient travertines from (a) LGF and (b) SWG (Dockrill, 2005). Dated aragonite samples (this study) are also shown and encompass the general trend of all samples in both fault systems. Both data sets do not fit a kinetic degassing model from an initial fluid of the same composition as the modern CO₂-charged waters (compare to Fig 4.4-40) suggesting derivation from a fluid with lower initial $\delta^{13}\text{C}_{\text{HCO}_3^-}$ and heavier $\delta^{18}\text{O}_{\text{H}_2\text{O}}$. Both fault systems exhibit variation in $\delta^{18}\text{O}$ attributed to variation in the brine additions. This is especially noticeable in SWG where clusters of compositions reflect distinct leakage events with progressively younger events having lighter $\delta^{18}\text{O}$ as the brine additions decline (see section 4.5-7). A corresponding decline in the average $\delta^{13}\text{C}$ of each cluster is attributed to the $\delta^{13}\text{C}_{\text{CO}_2(\text{g})}$ becoming increasingly heavy due to fractionation of the in-situ composition by exsolution of CO₂ in the subsurface. Within individual populations linear correlations in $\delta^{18}\text{O}$ and $\delta^{13}\text{C}$ are attributed to kinetic fractionation of the HCO_3^- pool. Travertines from LGF have compositions close to or lighter than their corresponding aragonite veins which is attributed to rapid ascent of the fluid with limited CO₂ degassing in the subsurface. Travertines from SWG are always lighter than their corresponding aragonite veins, attributed to extensive CO₂ degassing in the subsurface prior to effusion of fluid at the surface.

4.4.9. Altered Host Rock

Variation in the $\delta^{13}\text{C}$ of altered and calcite cemented Entrada Sandstone samples in travertine feeder systems is interpreted as reflecting degassing driven ¹²C depletion from an initial HCO_3^- reservoir of $\sim -0.7\text{‰}$. The variation in $\delta^{18}\text{O}$ of all samples is attributed to both differences in the proportions of fluid end-members and kinetic fractionation. The trends suggest that the initial $\delta^{13}\text{C}_{\text{HCO}_3^-}$ of the CO₂-charged fluids may have been $\sim 2\text{‰}$ lower than that observed in the modern system.

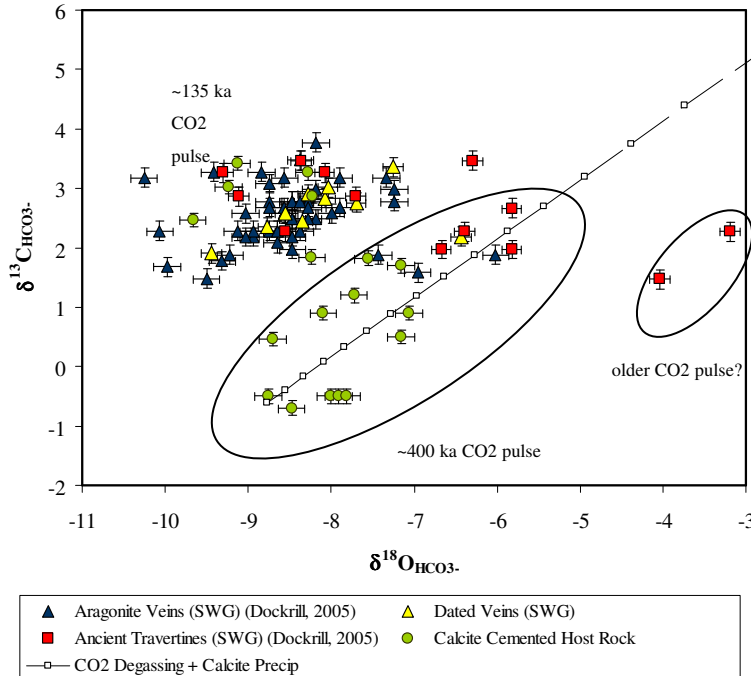


Figure 4.4-42 The $\delta^{18}\text{O}$ and $\delta^{13}\text{C}$ of HCO_3^- as above but including the values for altered Entrada Sandstone from SWG.

4.4.10. Implications for modern and ancient travertine formation

The presence of large kinetic isotope effects during precipitation of aragonite veins in travertine feeder systems suggests substantial CO₂ degassing from the ascending fluid, in the shallow subsurface, increasing Ω_{cc} , enforcing very rapid rates of CaCO₃ precipitation, sufficient to suppress equilibration of HCO₃⁻ and H₂O in solution.

The absence of a positive correlation in ¹⁸O versus ¹³C in ancient travertine samples from Salt Wash Graben is interpreted to reflect the slow equilibrium degassing of CO₂-charged fluids as they escape from the fault zone, having undergone extensive CO₂ degassing in the shallow subsurface.

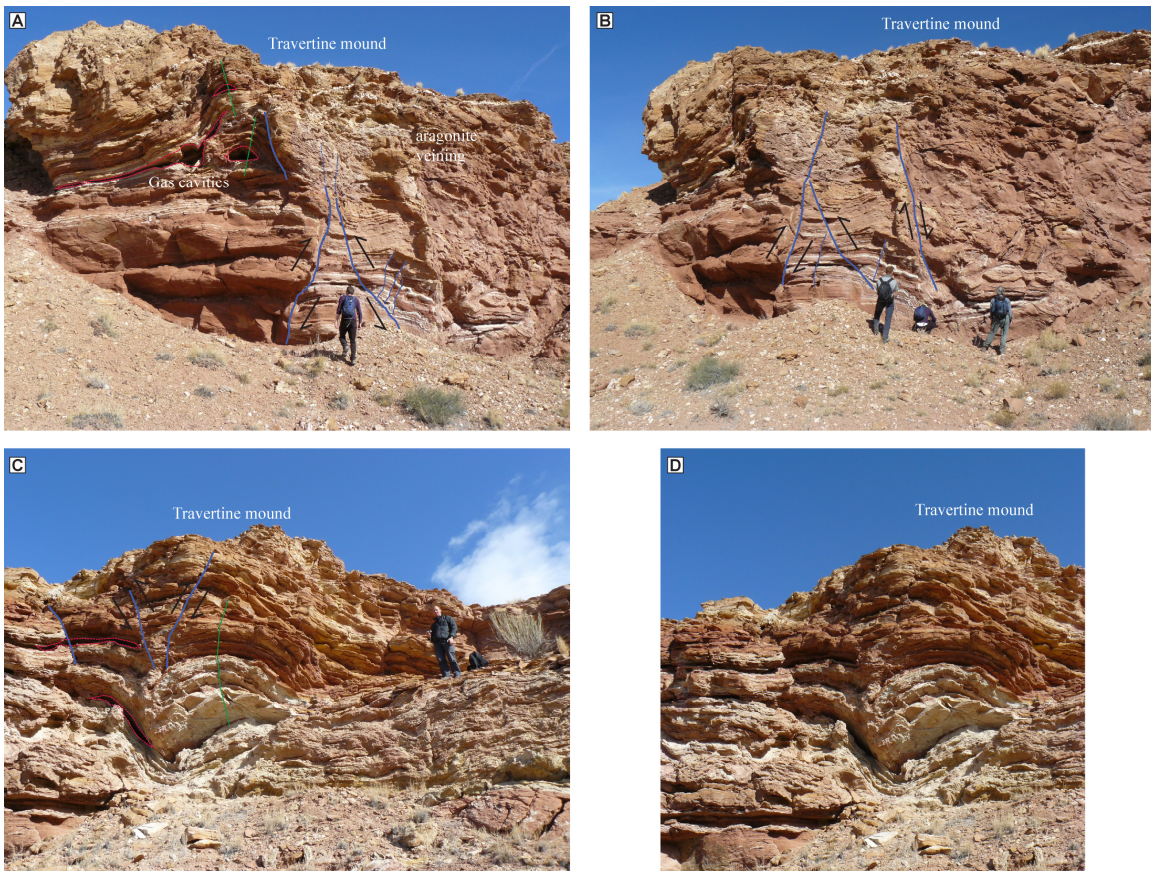


Figure 4.4-43 (a-d): Deformation and alteration beneath travertine mounds from Salt Wash Graben. The degassing of CO₂ in the shallow subsurface results in free gas accumulation and cavity formation inducing buoyant uplift of the surrounding rock volume and associated deformation. Cavity formation induces folding of the Entrada Sandstone which is in part accommodated by the formation of conjugate reverse fault sets. This active deformation will be important for the formation and maintenance of leakage pathways at shallow depth.

Conversely, positively correlated $\delta^{13}\text{C}$ and $\delta^{18}\text{O}$ of modern travertines, and ancient travertines from Little Grand Fault, are interpreted to reflect rapid CO₂ degassing and calcite precipitation as the effused fluid flows over the land surface. It is inferred that some largely undegassed fluid was able to escape to the surface at LGF imply rapid fluid velocities and leakage rates.

This is consistent with the observed morphologies of travertine deposits in each fault setting: individual travertines of LGF are up to 10 m thick, drape over fault scarps and local topographic features and are of relatively narrow lateral extent having degassed rapidly at the surface, depositing carbonate rapidly; travertines from SWG are much thinner (up to 4m), but of larger lateral extent having degassed slowly at the surface. Additionally, altered Entrada Sandstone beneath travertine mounds in SWG shows extensive deformation, faulting and folding attributed to accumulation of pockets of CO₂(g) in the subsurface and buoyant uplift of the surrounding rock volume (Fig. 4.4-43), a feature largely absent in LGF. Differences in the styles of leakage are interpreted to be a result of a) differences in the fault architecture; b) differences in the depth of the leaking reservoir; c) differences in the local hydrology d) differences in the hydraulic conductivities of the shallow lithologies. This is discussed further in section 4.5.8.

4.4.11. Reconstructing the CO₂ Leakage History

Variation in the $\delta^{18}\text{O}$, $\delta^{13}\text{C}$ and $^{87}\text{Sr}/^{86}\text{Sr}$ of U-series dated aragonite veins (Burnside, 2009) from Salt Wash Graben and Little Grand Fault record a history of CO₂ injection, migration, degassing and CO₂ promoted fluid-mineral reactions within the Navajo Aquifer. Both fault systems exhibit the same style of covariance in isotopic systems, although the timing and magnitude of events differ between the two.

4.4.11.1. Salt Wash Graben

The Navajo Aquifer was charged with CO₂ at some point prior to 413 ka and was later recharged with a second major pulse of CO₂ at ca. 135 ka. Enrichment in the $\delta^{13}\text{C}$ of aragonite of 1.13 ‰ between 413 ka and 219 ka, and 1.23 ‰ between 135 ka and 60 ka is interpreted to reflect CO₂ leakage and kinetic fraction of the fluid HCO₃⁻ reservoir via coupled CaCO₃ precipitation-CO₂ degassing.

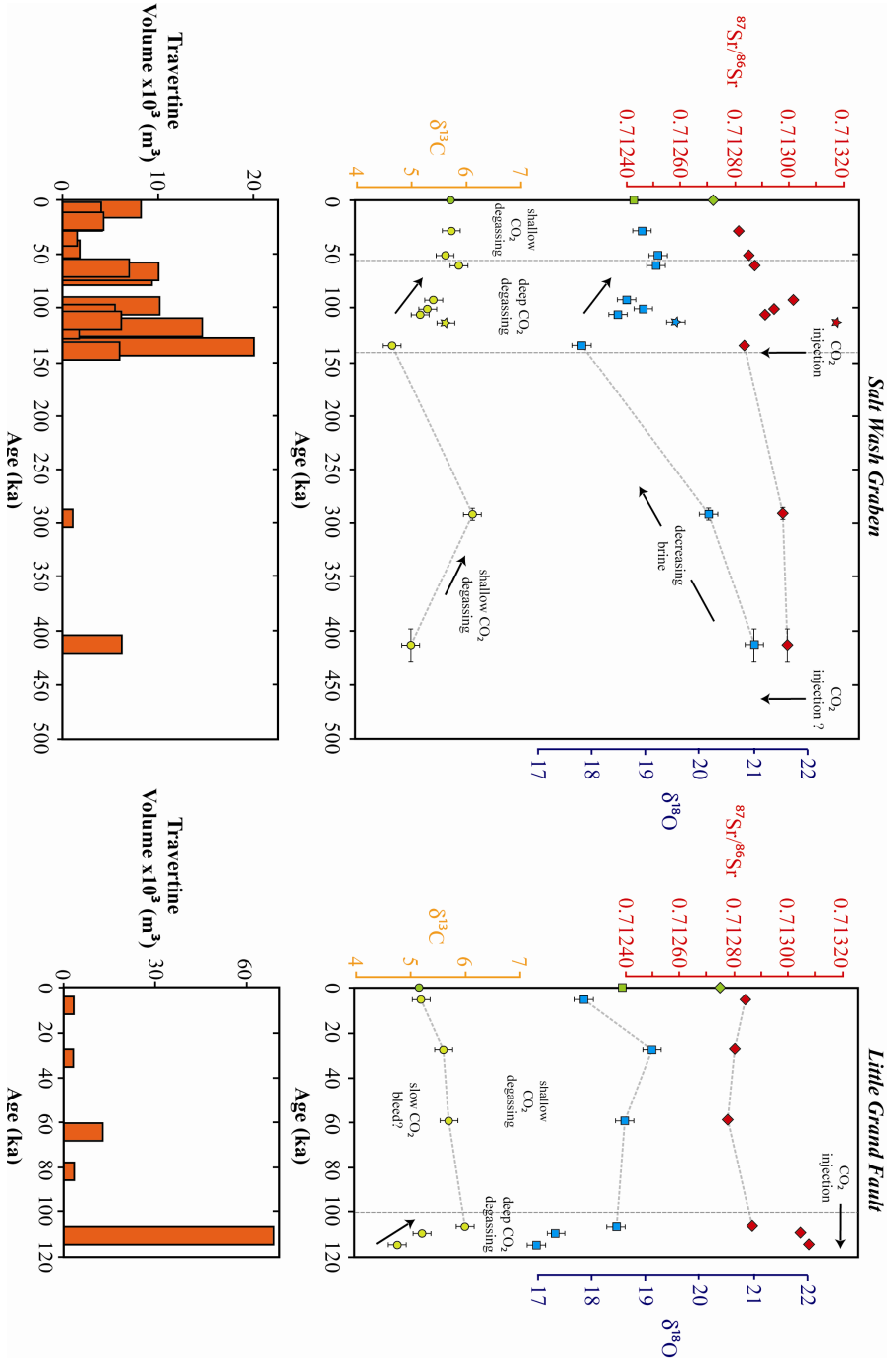


Figure 4.4-44 $\delta^{18}\text{O}$, $\delta^{13}\text{C}$ and $^{87}\text{Sr}/^{86}\text{Sr}$ of aragonite veins from Salt Wash Graben and Little Grand Fault plotted against their U-Th ages (Burnside, 2009). Travertine volumes are calculated from the maps of Dockrill, (2005). For SWG all samples are close to the intersection of the apex of the Green River and the northern fault of SWG, with the exception of the star symbol which lies 3.4 km further along the fault trace, in the direction of groundwater flow. Uncertainties are the 2σ of analytical uncertainties. Uncertainties for $^{87}\text{Sr}/^{86}\text{Sr}$ and most ages are smaller than the symbols used. Green symbols are the modern values for: SWG) for the lowest measured $\delta^{13}\text{C}$ and $\delta^{18}\text{O}$ travertine from SWG and its equivalent spring $^{87}\text{Sr}/^{86}\text{Sr}$ (Big Bubbling Spring); and LGF) The lowest measured values of ^{13}C and $\delta^{18}\text{O}$ travertine samples from Crystal Geyser of Dockrill (2005) and the Crystal Geyser fluid $^{87}\text{Sr}/^{86}\text{Sr}$. Travertine volumes are estimated from the maps of Burnside, (2007).

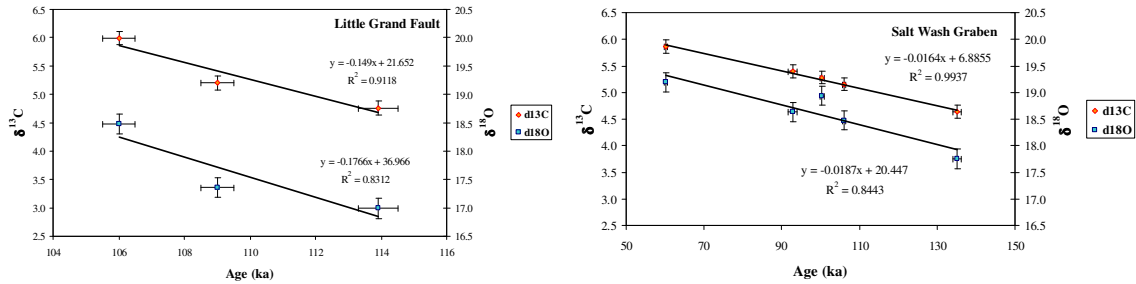


Figure 4.4-45 The change in $\delta^{13}\text{C}$ and $\delta^{18}\text{O}$ of aragonite with time, during periods of kinetic fractionation, for both LGF and SWG. The near identical slopes of $d\delta^{13}\text{C}/dt$ and $d\delta^{18}\text{O}/dt$ highlights that the same mechanism is modifying both isotopic systems.

Suppression of the $\delta^{13}\text{C}$ and $\delta^{18}\text{O}$ of aragonite between these two periods of degassing reflects introduction of a fresh unfractionated CO₂ charge at ca. 135ka, sufficient to suppress the $\delta^{18}\text{O}$ composition of the HCO₃⁻. The enrichment in both $\delta^{13}\text{C}$ and $\delta^{18}\text{O}$ from 135 ka to 60 ka reflects rapid leakage and kinetic fractionation of HCO₃⁻(aq), which implies rapid rates of CO₂ degassing and carbonate precipitation, faster than the HCO₃⁻-H₂O equilibration reaction which operates on the 1000's to 10000's sec time-scale (Hendy, 1971). Travertine mounds show a maximum volume at 135ka and the volume of travertine mounds decreases exponentially from 135ka to 60ka. The covariation of travertine volume and linearly increasing $\delta^{13}\text{C}$ and $\delta^{18}\text{O}$, and the initiation of an increase in ⁸⁷Sr/⁸⁶Sr are interpreted to reflect introduction of a new CO₂ charge at 135ka which saturated the reservoir fluid and produced a free gas phase. This CO₂-charge then degassed rapidly from 135ka to a state of under-saturation at 65ka. The linear covariation in $\delta^{13}\text{C}$ and $\delta^{18}\text{O}$ over these periods, and the similarity of $d\delta^{13}\text{C}/dt$ and $d\delta^{18}\text{O}/dt$ in each fault system reflects kinetic fraction of the HCO₃⁻ reservoir due to rapid rates of CaCO₃ precipitation as a result of a large degree of CaCO₃ oversaturation in the fluid caused by rapid rates of CO₂-degassing. This state of oversaturation is due to: a) rapid CO₂ degassing in the subsurface and; b) higher concentrations of Ca²⁺ and HCO₃⁻ in the ascending fluid following a CO₂-charge as the fluid moves towards equilibrium with respect to carbonate by dissolving dolomite in the reservoir under conditions of elevated *p*CO₂. High *p*CO₂, and consequently elevated Ca²⁺ and HCO₃⁻, will lower the depth at which over-saturation with respect to CaCO₃ is reached in the ascending fluid, promoting rapid rates of CaCO₃ deposition. As *p*CO₂ in the reservoir falls the point at which CaCO₃ super-saturation in the ascending fluid is reached will move closer to the surface and subsurface CaCO₃ deposition rates will decline, inhibiting kinetic fractionation of the HCO₃⁻ pool. A cessation in covarying $d\delta^{13}\text{C}/dt$ and $d\delta^{18}\text{O}/dt$ following these periods reflects a decline in the rate of CaCO₃ deposition due to a reduction in the CO₂ degassing rate and in-situ *p*CO₂, and consequently a lowering of fluid Ca²⁺ and HCO₃⁻ and Ω_{cc} at shallow depths. This reflects the depletion of the free gas phase and a return to CO₂ under saturated conditions.

$\delta^{18}\text{O}$ of aragonite progressively decreases from ca. 413 ka to ca. 135ka by 3.25 ‰ (Fig. 4.4-41 & 4.4-45). Initially high $\delta^{18}\text{O}$ of aragonite is interpreted to reflect heavy $\delta^{18}\text{O}_{\text{H}_2\text{O}}$ resulting from an increased proportion of Paradox formation brine in the early fluids, with progressively decreasing contributions to ca. 135ka, and constant contributions there after. Following the CO₂ charge at ca. 135ka $\delta^{18}\text{O}$ of aragonite progressively increases at the same rate as $\delta^{13}\text{C}$. Differences in the range of $\delta^{18}\text{O}$ between LGF and SWG reflect consistent differences in the volume of brine influx between each fault system, in both modern and ancient settings. This probably reflects intrinsic differences in the fault architecture and hydrological systems between each fault. The northern fault of Salt Wash Graben penetrates to greater depth than Little Grand Wash Fault (Dockrill, 2005). And as such the fault may also act as a more significant conduit to upward fluid movement.

4.4.11.2. $^{87}\text{Sr}/^{86}\text{Sr}$

Depression of the fluid $\delta^{13}\text{C}$ is accompanied by the initiation of exponentially increasing $^{87}\text{Sr}/^{86}\text{Sr}$. Increase in the $^{87}\text{Sr}/^{86}\text{Sr}$ of aragonite reflects an increased contribution of ^{87}Sr from silicate mineral dissolution following injection of CO₂ into the reservoir. Covariation of $\delta^{13}\text{C}$ and $^{87}\text{Sr}/^{86}\text{Sr}$ reflects a coupling between the CO₂-charge and mineral dissolution. Influxing CO₂ will suppress fluid pH and mineral saturation, elevate $[\text{H}^+]$ and enhance mineral dissolution rates. Sr incorporated into aragonite will be derived from three primary sources: 1) dissolved Sr carried in groundwater advected into the fault system; 2) high $^{87}\text{Sr}/^{86}\text{Sr}$ derived from silicate mineral hydrolysis and; 3) low $^{87}\text{Sr}/^{86}\text{Sr}$ derived from dolomite dissolution, within the zone of high CO₂-charge. Additionally, low $^{87}\text{Sr}/^{86}\text{Sr}$ may be added at the site of CO₂ injection derived from brine entrained in the CO₂ stream. The rate of change $d^{87}\text{Sr}/^{86}\text{Sr}/dt$ of aragonite will largely reflect the ratio of the rate of Sr liberation from silicate and dolomite dissolution assuming 1) the initial dissolved Sr flux and $^{87}\text{Sr}/^{86}\text{Sr}$ is constant; 2) the flux of Sr in groundwater is exceeded by the flux in Sr derived from mineral dissolution. The exponential increase in $^{87}\text{Sr}/^{86}\text{Sr}$ following introduction of the 135 ka CO₂ charge can reflect either; 1) initial dissolution of both silicate and dolomite, but at different rates, or; 2) that the rate of silicate mineral dissolution increased with time. The former explanation is the most likely and the form of $d^{87}\text{Sr}/^{86}\text{Sr}/dt$ suggests a decline in the rate of dolomite dissolution to ca 95ka. Inversion of the exponentially increasing trend in $^{87}\text{Sr}/^{86}\text{Sr}$ to an exponentially decreasing trend at ca 93 ka reflects groundwater Sr flux exceeding Sr-flux from mineral dissolution. This reflects slowing of the dissolution rate of silicate minerals over ca. 42 ka as the fluid loses CO₂ through degassing, pH is neutralized by reaction and pore-fluid chemistry moves towards equilibrium with the silicate mineral surface.

4.4.11.3. Little Grand Wash Fault

⁸⁷Sr/⁸⁶Sr declines exponentially from 114 ka to 106 ka and δ¹³C and δ¹⁸O increase (Fig. 4.4-45) concomitantly due to rapid CO₂-leakage and degassing. ⁸⁷Sr/⁸⁶Sr decline from an initially high value suggests injection of CO₂ prior to 114ka and that silicate dissolution rates declined as CO₂ saturation decreased. Between ca. 59ka and 5ka a gradual decline in δ¹³C coupled with increasing ⁸⁷Sr/⁸⁶Sr and δ¹⁸O is interpreted to reflect slow bleeding of a CO₂-brine mixture into the reservoir (Figs. 4.4-45 & 4.4-46).

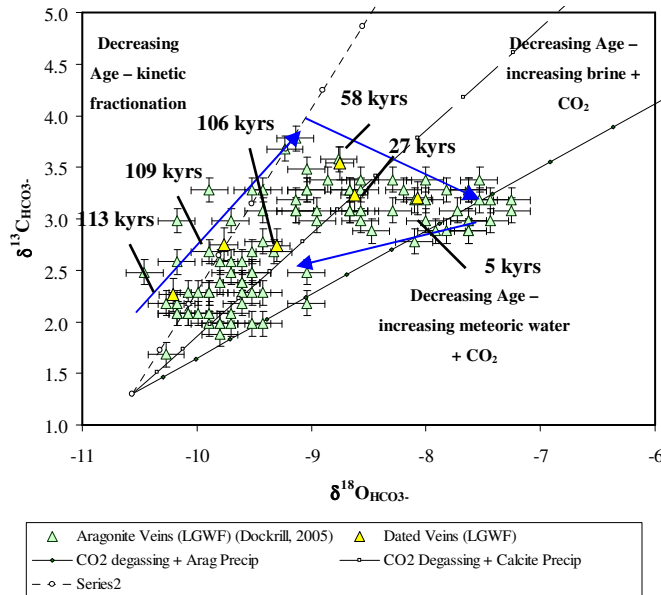


Figure 4.4-46 The δ¹³C and δ¹⁸O of HCO₃⁻ in equilibrium with aragonite veins from LGF. Fitting of kinetic fraction models implies degassing from a fluid reservoir with initial δ¹³C_{HCO₃⁻} lower than that observed in modern fluids. Dated veins constrain the trajectory of the evolution in isotopic composition of HCO₃⁻ through time.

4.4.12. Controls on Leakage

Differences between the slope of dδ¹³C/dt and dδ¹⁸O/dt, the time taken for the δ¹³C/δ¹⁸O trend to plateau, and the rate of travertine deposition (Fig. 4.4-45) reflect intrinsic differences in the CO₂-leakage rate of each fault. The trends record far more rapid CO₂ loss from Little Grand Fault. The volume of dated travertine records the mass of CO₂ leaked from each fault and the variation in the CO₂ leakage rate through time (Fig. 4.4-47). The mass of leaked CO₂ can be estimated by assuming that every litre of effused fluid deposited ~10 mmoles of CaCO₃ (Ca²⁺ loss is estimated from differences in Ca²⁺ concentration in spring waters and Ca²⁺ concentration after prolonged runoff) and that each litre of fluid was initially saturated with CO₂ at reservoir conditions. This calculation implies a similar cumulative loss of CO₂ from each fault: LGF; 1.2x10⁷ tonnes (CO₂) and SWG; 1.3x10⁷ tonnes (CO₂). Initial leakage rates are up to ~633 t/a and ~927 t/a for SWG

and LGF, respectively. However, average leakage rates of 50-100 t/a are more common. These leakage rates during periods of quiescence are comparable to modern CO₂ effusion rates of ~55 t/a measured at SWG by Allis *et al.*, (2005). Variation in the leakage rate is presented in figure (4.4-47). The ‘average’ large (600 Mw) coal burning power station in the USA produces 4-5x10⁶ t/a (CO₂) (IPCC, 2007). Many of these have been in existence since the 1950’s, giving a cumulative CO₂ production of ~2.3x10⁸ tonnes (CO₂). Whilst the magnitude of leaked CO₂ obviously depends on the volume of the initial CO₂-charge a fault leaking CO₂-saturated reservoir will therefore still leak at rates significantly lower than ‘leaking’ power stations.

The spatial-temporal pattern of travertine formation (Fig. 4.4-48), for both LGF and SWG, suggests that: a) a new CO₂-charge always initial exploits leakage pathways at the crest of the anticline (or zones of high structural complexity such as the easterly breached relay ramp); b) for SWG this central leakage site moves by small distances (10’s to 100’s meters) eastward with younger charges, in the direction of groundwater flow, suggesting the continued formation of new leakage pathways rather than the re-exploitation of older leakage pathways, at the anticline crest; c) with time from the initial introduction of a new CO₂-charge, leakage pathways spread from the anticline crest laterally along the fault trace. This spatial-temporal relationship is interpreted as reflecting: a) the establishment of new leakage pathways with the introduction of a new CO₂-charge due to mineral-fluid reactions at the cap-rock reservoir interface, and within fracture zones and the fault damage zone. These pathways are localized at the apex of the anticline initially, due to the buoyant accumulation of free-phase CO₂; b) these initial leakage pathways then become blocked by the deposition of carbonate within fractures; c) the lateral migration of leakage points as initial pathways become blocked and CO₂-charged fluids exploit, and initiate, more complex and ss hydraulically conductive leakage pathways along the length of the fault trace.

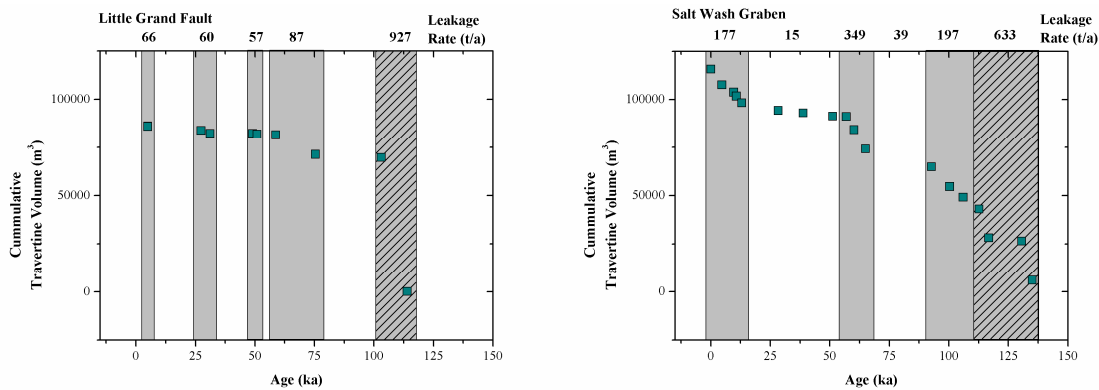


Figure 4.4-47 Variation in the cumulative travertine volume with time for LGF and SWG. Estimated leakage rates (tonnes (CO₂)/year) during periods of rapid CO₂ loss and quiescence are detailed at the top of each figure. Temporal data and surface travertine volumes are estimated from the maps of Burnside, (2007).

The spatial-temporal trend of travertine deposition (Fig. 4.4-48) implies an increase in the blocking rate of leakage pathways with time. This is interpreted to reflect progressive CO₂ loss from the reservoir and a decrease in in-situ $p\text{CO}_2$, which elevates Ω_{cc} in the upwelling fluid increasing the rate of carbonate deposition. Differences between the slope of this trend in each fault system record more rapid blocking rates in SWG than in LGF. This may be due to differences in reservoir depth (the Navajo Aquifer is located at ~500m depth at LGF and at ~250m depth at SWG) and thus differences in the in-situ $p\text{CO}_2$ at each fault, which imposes differences in the Ω_{cc} of the upwelling fluid.

Differences in the rate of CO₂-leakage at each fault may reflect differences in the volume of the initial CO₂-charge, depth to the host reservoir, the fracture blocking rate, local hydraulic head, pore over-pressure and intrinsic differences in the permeability structure of the fault damage zone, the stratigraphic architecture and reservoir-seal juxtaposition between each fault. Slow leakage rates at SWG, as compared to LGF, are largely due to the high throw, lower degree of reservoir-reservoir juxtaposition and higher shale gouge ratio (Dockrill, 2005) of this fault system. However, the hydraulic properties of the near surface lithologies may also impact on the leakage rate. Shallow lithologies at LGF comprise low permeability formations of the Curtis Formation and Mancos Shale, and at SWG the more permeable Entrada Sandstone. The observation of aragonite veining extending laterally some distance from individual travertine mounds and the extensive deformation associated with free gas accumulation in the subsurface, together with isotopic evidence discussed, suggests substantial degassing of CO₂ in the shallow subsurface at SWG. These features are largely absent from LGF suggesting fluids rapidly ascended leakage pathways without significant interaction with shallow formations. It is inferred that surface leakage at LGF has historically taken the form of active cold water geysering, which has actively stimulated leakage and has had a significant impact on the time taken for an individual CO₂ charge to dissipate. Additionally, higher levels of local hydraulic head at LGW will have helped sustain high rates of fluid discharge.

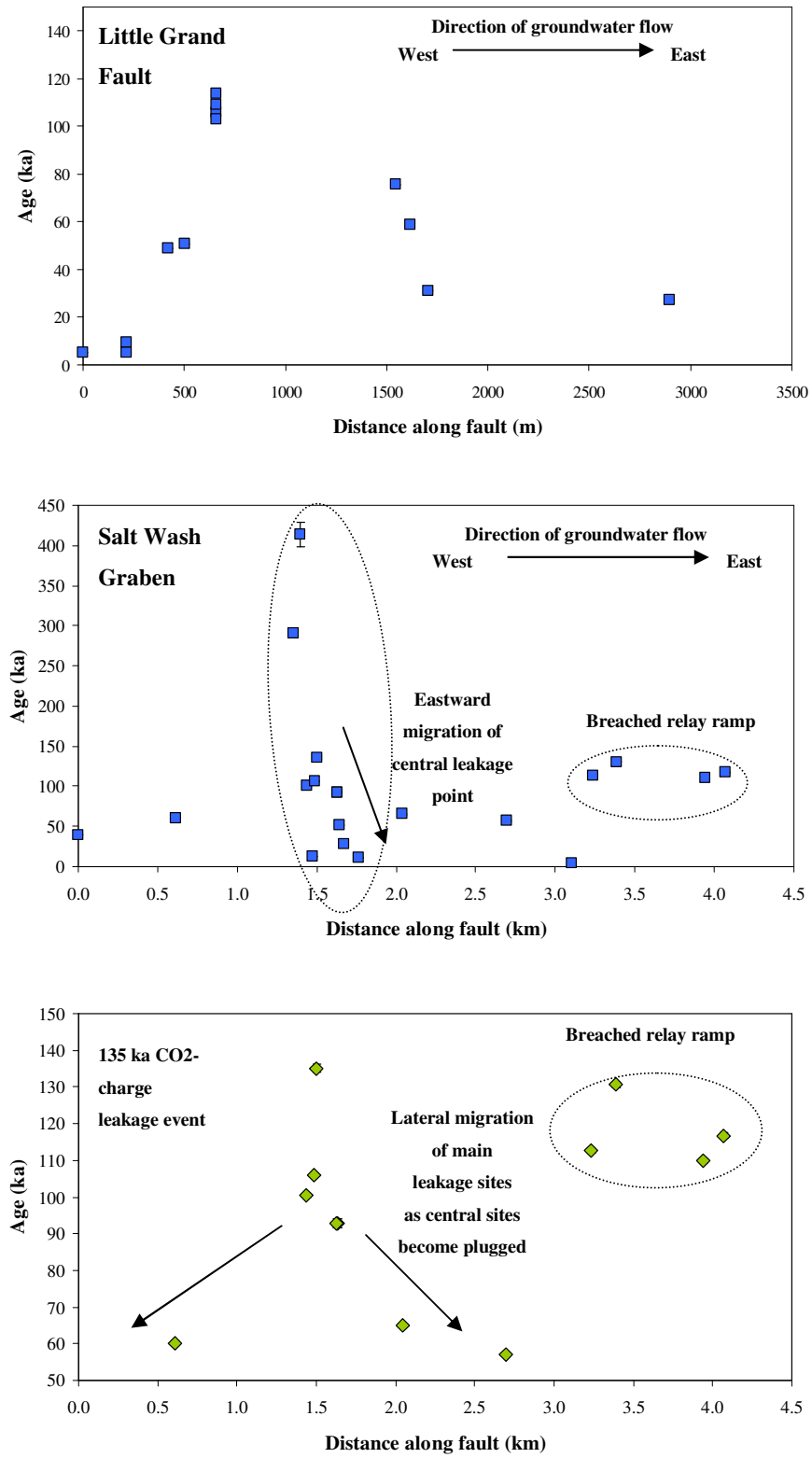


Figure 4.4-48 The spatial distribution of individual travertine mounds versus their age for LGF, SWG and for travertines associated with the 135ka leakage event at SWG. Spatial and temporal data from Burnside, (2007).

4.5. Conclusions

Extensive alteration and cementation in the Entrada Sandstone beneath surface travertine deposits preserves the geochemical and mineralogical impacts of interaction with CO₂-charged fluids. Feldspar grains show evidence of extensive corrosion and reprecipitation of silica, smectite and kaolinite on grain surfaces and within the local pore volume. Feldspar grains continue to dissolve even when coated with up to 10µm surface coatings of inter-grown clay minerals, suggesting the maintenance of porosity within the surface coating. This adds to the evidence that the presence of such a coating does not inhibit dissolution at the mineral surface.

High Mn and Fe concentrations in fracture and host rock calcite cements record elevated Mn²⁺ and Fe²⁺ concentrations in the parent fluid. Fe and Mn concentrations imply reducing Eh conditions (30 to -50 mV) in the parent fluid and a pH in the range 5.5 to 6.5, comparable to the Eh-pH conditions of the modern CO₂-charged groundwaters. This finding, together with hematite solubility modelling and field and petrographic observations of extensive dissolution of hematite grain coatings and Fe-oxide reprecipitation, suggests that CO₂-charged fluids alone are capable of dissolving and mobilizing Fe in these sediments. However, the precise control on Eh is uncertain. Equilibrium redox potentials for the SO₄²⁻-H₂S and CO₂-CH₄ redox couples are in the region of 0 to -200 mV and -200 to -500mV, respectively (Drever, 1997). The calculated Eh values are generally higher those expected for redox potentials controlled by either SO₄²⁻-H₂S or CO₂-CH₄ equilibrium. The range of values obtained is more comparable to redox potentials observed in groundwaters with low O-fugacity (e.g. White *et al.*, 1990).

Sr concentrations in these cements record mean calcite precipitation rates of 1.3x10⁻⁶ to 2.1x10⁻⁶ mol/m²/s, comparable to laboratory derived calcite precipitation rates, in fluids with moderate Mn/Ca and Fe/Ca, at Ω_{cc} of ~1 to 3. The overall variation in rate is large, from ~1x10⁻⁹ to ~1x10⁻⁵ mol/m²/s, probably reflecting both variation in the intrinsic rate and variation in the Sr/Ca of the parent fluid.

Mg and Sr concentrations in calcite cements away from fracture conduits record closed system fractionation of the fluid Sr/Ca and Mg/Ca by calcite precipitation, which elevated the Mg/Ca ratio sufficiently to allow kinetic stabilization of aragonite and the precipitation of poikilitic aragonite cements. However, other kinetic factors such as the Ω_{cc} of the fluid and [CO₃²⁻] most likely also contributed to this stabilization.

Ancient travertine deposits and aragonite veining record leakage of CO₂ from the Navajo Aquifer that initiated at ca 413 ka at Salt Wash Graben and at ca 114 ka at Little Grand Fault. At Salt Wash Graben a second injection of CO₂ at ca 135 ka initiated simultaneous variation in δ¹⁸O_{CaCO₃} and δ¹³C_{CaCO₃}, and a spike in ⁸⁷Sr/⁸⁶Sr which is interpreted to reflect near coeval injection of CO₂ into the aquifer and the initiation of surface leakage as a result of this injection.

Temporal trends in ⁸⁷Sr/⁸⁶Sr record enhanced silicate mineral dissolution rates following injection of this CO₂ charge, but dissolution rates decreased as CO₂ was lost from the reservoir, pH increased and saturation with respect to the dissolving mineral was approached (Chapter 3). Correlations in δ¹⁸O_{CaCO₃} and δ¹³C_{CaCO₃}, kinetic fractionation of the HCO₃⁻(aq) reservoir, the volume and rate of surface travertine formation and its spatial and temporal distribution suggest that initially leakage: a) occurred rapidly and at a constant rate, b) was localised at the anticline crest and c) occurred from a reservoir fluid saturated in CO₂, coexisting with a free-gas phase. Additionally, kinetic fractionation of HCO₃⁻(aq) during these periods implies rapid rates of CO₂ degassing and carbonate precipitation, faster than the HCO₃⁻-H₂O equilibration reaction which operates on the 1000's to 10000's sec time-scale (Hendy, 1971). A sharp inflection in leakage rate and an approximately concurrent cessation in kinetic fraction of the HCO₃⁻(aq) reservoir are interpreted to reflect depletion of the saturated CO₂ and a return to undersaturated conditions, after ~75ka of leakage. During this time leakage sites propagated laterally along the length of the fault trace as fracture conduits were blocked by carbonate deposition and new leakage pathways were exploited and opened by mineral-fluid reactions. Fracture blocking rates increased as the CO₂ charge dissipated, *p*CO₂ in the aquifer fell and the fluids became increasingly oversaturated in carbonate.

Whilst the cumulative CO₂ loss from both Little Grand Fault and Salt Wash Graben are of the same order of magnitude (~1x10⁷ tonnes CO₂), the time required to deplete the initial CO₂-charge to a state of CO₂-undersaturation (~8 ka versus ~75 ka), and leakage rates during this period (~927 t/a versus ~164 t/a), vary by an order of magnitude between the two fault systems. This is attributed primarily to intrinsic difference in the fault architecture and properties of the fault damage zone, including the shale gouge ratio and degree of reservoir-reservoir juxtaposition. However, the depth of the host reservoir, and thus maximum in-situ *p*CO₂, imposes difference in the fracture blocking rate in each fault which may impact the overall leakage rates. In addition the hydraulic properties of shallow lithologies appear to be important in controlling leakage rates where permeable formations allow migration of CO₂-charged fluids away from the fault damage zone, prolonging the fluid ascent time, enhancing CO₂ degassing in the shallow subsurface and promoting carbonate deposition and fracture blocking. This highlights the importance of accurately modelling the fault surface, damaged zone, shallow lithological properties and regional hydraulic gradients when modelling leakage from CO₂ storage sites. The findings suggest that in geological storage sites fault controlled CO₂ leakage rates from shallow CO₂ saturated fluids will be slow (relative to CO₂ emission rates from anthropogenic sources) and fracture conduits will seal through carbonate precipitation impeding leakage, but that this process is likely to take place on 100's to 1000's year time-scales.

Chapter 5

Fluid Inclusion Petrography of Diagenetic Bleaching in the Entrada Sandstone, Green River, Utah

5.1. Introduction

Across the Paradox Basin, adjacent to faults and preferentially in coarser grained sandstone units, originally red Jurassic sandstones are frequently bleached pale-yellow or white where hematite grain coatings have been dissolved by the passage of diagenetic fluids (Foxford *et al.*, 1996; Garden *et al.*, 2001). This bleaching has been attributed by various authors to a variety of different extra-formational fluids including hydrocarbon liquids, organic acids and methane (Beitler *et al.*, 2005; Bowen, 2005; Chan *et al.*, 2000, 2001; Eichhubl *et al.*, 2009; Garden *et al.*, 2001; Parry *et al.*, 2004), and carbon dioxide and hydrogen sulphide (Haszeldine *et al.*, 2005).

Regionally bleached sandstones record the passage of migrating diagenetic fluids over a variety of physical and temporal scales (e.g. Bowen *et al.*, 2007). Understanding their geochemical origin facilitates their use as a reservoir analogue, from which the petrophysical and geochemical controls on fluid flow can be made by direct observation. Additionally, exhumed reservoirs such as these provide the opportunity to examine the coupling of fluid transport and mineral-fluid interactions, directly (e.g. Bickle, 1992). Constraining the large-scale migration of fluids in the subsurface has traditionally only been possible via numerical simulation or by direct geochemical observations in well studied groundwater systems (e.g. O'Nions *et al.*, 1993) or hydrocarbon fields (e.g. Bradley *et al.*, 1986).

In this chapter the petrology and isotope geochemistry of large-scale diagenetic bleaching of the Entrada Sandstone at Salt Wash Graben is discussed. Fluid inclusions trapped in secondary minerals associated with this bleaching, and with bleaching in travertine feeder zones (discussed in Chapter 4) were examined using laser Raman microspectroscopic and microthermometric techniques, and the results are presented and discussed. Mineral hosted fluid inclusions may preserve fluid and vapour compositions at the time of trapping yielding information on the thermal, pressure and chemical regimes under which that mineral developed. The objectives of this chapter are to a) establish the composition of the volatile phase(s) (i.e. CH₄, CO₂, N₂, O₂, H₂,

H₂S, SO₂) associated with large-scale diagenetic bleaching of the Entrada Sandstone at Salt Wash Graben. b) To assess whether volatile phase(s) in addition to CO₂, were present in the ancient CO₂-system c) to derive thermal and pressure data which will inform on the relative timing of the large-scale diagenetic bleaching.

5.2. Methodology

5.1.1. Fluid Inclusions

When crystals grow or recrystallize in a fluid medium, growth irregularities result in the trapping of small portions of the fluid in the solid crystal, yielding primary fluid inclusions. Healing of fractures developed in existing crystal can also lead to the entrapment of secondary fluid inclusions.

5.1.1.1. Microthermometry

Microthermometry techniques provide information on the melting point of included aqueous fluids and the homogenisation temperature of two phase vapour-liquid mixtures. Measurement of the homogenization temperature (T_h) and temperature of last ice melting (T_m) in fluid inclusions provides information on the minimum temperature of the fluid inclusions formation and the salinity of fluids from which the cement(s) precipitated (Roedder, 1984).

5.1.1.2. T_m

Aqueous fluids in geological environments typically contain varying amounts of salt, dominantly NaCl, KCl or CaCl₂ (Bodnar, 2003). Salts and other solutes depress the melting point of ice, thus the temperature at which the last remaining ice in an inclusion melts will reflect the salinity of the fluid. The relationship between freezing point depression and salinity varies only slightly for the various species dominant in the fluid (Bodnar, 2003). Most researchers report their interpretations of freezing point depression in weight % NaCl equivalent, simply stating the salinity of fluid inclusions assuming all dissolved species to be NaCl. This yields a salinity that is fairly close to reality for many diagenetic systems (Roedder, 1984).

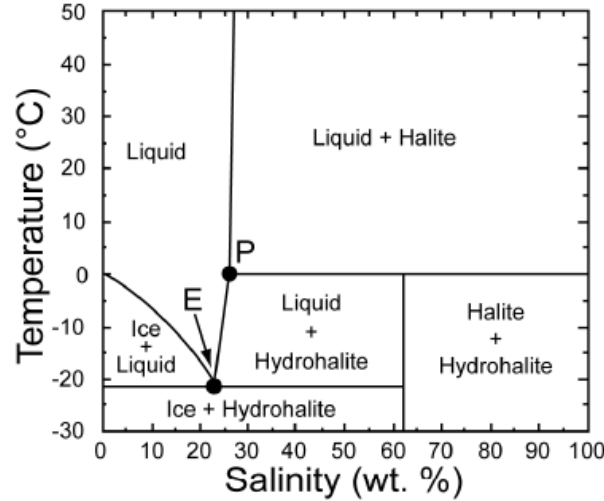


Figure 5.2-1 NaCl-H₂O phase diagram, after Bodnar, (2003). I = ice; L = liquid; HH = hydrohalite; H = halite; P = peritectic (0.1°C, 26.3 wt% NaCl); E = eutectic (-21.2°C, 23.2 wt% NaCl).

Figure (5.2.1) shows the H₂O-NaCl phase relations in the low temperature region, including the relationship between salinity and the ice melting temperature. Hall *et al.*, (1988) determined the freezing-point depression of H₂O-NaCl solutions ranging from pure water to the eutectic composition (23.2 wt% NaCl), and Bodnar (1993) presented a simple equation according to:

$$Salinity(wt\%) = 1.78\alpha - 0.0442\alpha^2 + 0.000557\alpha^3 \quad (5.1)$$

where α is the freezing point depression (FPD) in degrees Celsius (FPD is simply the negative of the freezing temperature). Equation (5.1) reproduces the original experimental data of Hall *et al.*, (1988) to better than ± 0.05 wt% NaCl at all temperatures from 0.0°C to -21.2°C, the eutectic temperature for H₂O-NaCl.

The presence of CO₂ in a fluid inclusion may affect the melting temperature obtained from phase relations determined in CO₂-free systems. However, in fluid inclusions which have both liquid and vapour phases, most CO₂ is contained in the vapour phase at the temperature of final ice melting (Roedder, 1984). Therefore, only very small CO₂ concentrations exist in the liquid phase, and thus the affect of CO₂ on the temperature of ice melting is considered insignificant (Frantz *et al.*, 1992). Frantz *et al.*, (1992) observed that the presence of up to 43.2 mol% CO₂ in individual inclusions had a negligible effect on final ice melting temperature.

5.1.1.3. T_h

A conspicuous feature of many aqueous fluid inclusions is a vapour or gas bubble. Phase separation (liquid and vapour) is a result of differential shrinkage of the host mineral and the inclusion fluid on cooling from the temperature of trapping to that of observation. Upon cooling

to room temperature, the fluid shrinks far more than the host, thus, the pressure in the inclusions drops below the saturation vapour pressure of the contained fluid and the fluid splits into two phases: liquid and vapour. Artificially heating a two-phase inclusion observed at ambient temperatures and observing the point of homogenisation provides information on the temperature of entrapment.

If a fluid inclusion is trapped from a homogeneous fluid below or on a boiling curve (i.e. under P-T conditions such that it was in equilibrium with either a vapour or gas phase) the temperature of homogenisation represents the actual trapping temperature of the inclusion. However, some inclusions have trapped fluids at a P-T combination above the liquid/vapour curve. In these, a bubble disappears on heating up from room temperature when the pressure and temperature have increased to the liquid/vapour curve, below the actual temperature at which the fluid was included. There can be a large difference between the measured T_h and the true trapping temperature (T_i). In order to obtain the true trapping temperatures of an inclusion trapped at high P-T conditions, a pressure correlation needs to be applied. However given that fluids within the studied system were included at temperatures significantly below the boiling curve for H₂O-NaCl-CO₂ systems this consideration is unnecessary.

5.1.2. Raman Microspectroscopy

The laser Raman microprobe (LRM) permits the spectroscopic analysis of solid, liquid and gas phases as small as a few micrometers. In this technique of molecular spectroscopy the sample is imaged through the high power objective of an optical microscope. The Raman effect is the shift in frequency that monochromatic light (e.g., laser light) undergoes during inelastic scattering (Burke, 2001). Only the spectral distribution of the inelastically scattered light emitted by the sample (Raman scattering) is of analytical interest, since it is caused by component-specific molecular vibrational and rotational phenomena in the sample. The scattered light is transmitted through the microscope into a double monochromator, step scanned, and detected with a monochannel photon-counting system (Seitz *et al.*, 1987). The spectra are recorded in terms of the amount of displacement from the frequency of the exciting (laser) radiation.

The accompanying spectra are plots of total counts vs. wave numbers (cm⁻¹). The photon count rate of the inelastically scattered radiation is a function of both the sample and the instrumental conditions (Burke, 2001). In regard to the former the Raman band intensities are largely proportional to the number of molecules in the scattering volume or the density (Long, 1977). Among the latter are the exciting laser power, the alignment of the laser in the optical system, the optical properties of the objectives, the chosen slit width, and the electronic parameters of the detection system (Burke, 2001). The total number of recorded counts depends upon the count rate, the counting time (signal integration time per step of the monochromator

during a scan), and the spacing of the steps (number of wave numbers between each step) (Seitz *et al.*, 1987). Analysing the spectra collected enables identification of the species that are contained within a fluid inclusion by identifying the unique band assemblage of individual species.

Multiple species in both the vapour and liquid phase of a fluid inclusion can be identified by laser Raman microprobe spectroscopy (Wopenka and Pasteris, 1987). Raman quantitative analysis based on Placzek's polarizability theory (Placzek, 1934) can be applied to derive a compositional analysis for Raman active species (e.g. H₂O, CO₂, CO, N₂, H₂S, SO₂, CH₄, O₂, H₂) in a fluid inclusions liquid and vapour phases. This allows estimates of the relative gas composition and the contribution of CO₂ in individual inclusions and distinct diagenetic events.

Theoretical estimates of the detection limits of Raman microprobes in general are in the pictogram (10⁻¹² g) range (Etz, 1979). As pointed out by Rosasco *et al.*, (1979), the detection limit for a species in a fluid inclusion depends upon the scattering efficiency of the species itself, the counting time and stepping interval, the Raman and optical properties of the host, the geometry of the inclusion, spectral interference (e.g., overlapping Raman peaks, fluorescence) from other components, and the stability of the species under the impinging laser beam. Using Raman spectroscopy, CO₂ can be detected to about 1 bar at ambient temperature (Rosso and Bodnar, 1995). A lack of appropriate standards prevents the quantification of instrumental detection limits in this study.

In this study Raman spectroscopy was used to identify CO₂ and other volatile bearing inclusions in distinct diagenetic assemblages and to provide a quantitative estimation of the gas composition of vapour bearing fluid inclusions. The pressure dependent bond configurations of some Raman active species (e.g. CO₂, CH₄ and N₂) allows features of the Raman spectra to be used to calculate vapour phase gas densities, dissolved gas concentrations in the liquid phase, entrapment pressures and thus entrapment depths.

5.1.2.1. The Spectrum of CO₂

The CO₂ molecule is linear and thus has four modes of vibration (Fig. 5.2-2); a symmetric stretching mode (ν_1), an antisymmetric stretching mode (ν_3), and two bending modes (ν_2a and ν_2b)

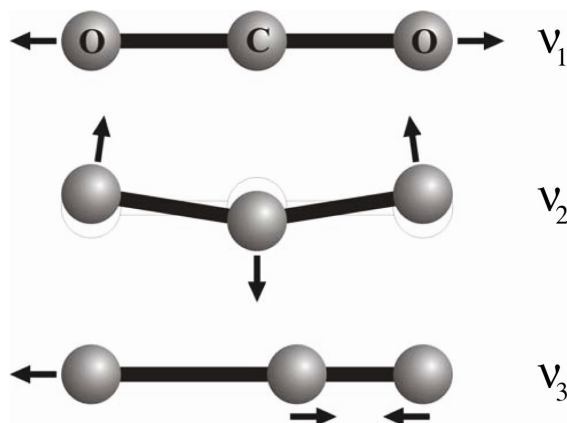


Figure 5.2-2 Schematic representation of the three fundamental vibrations of CO₂ (after Rosso and Bodnar, 1995)

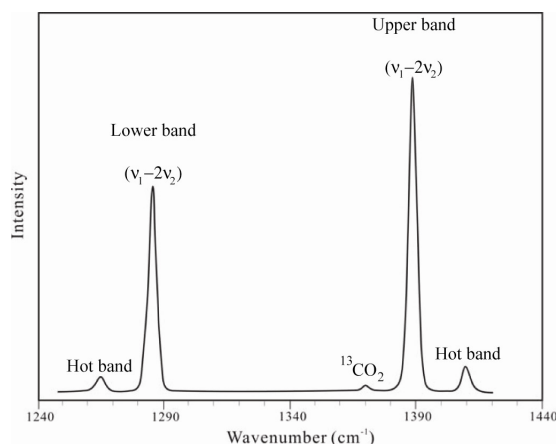


Figure 5.2-3 Typical Raman spectrum of CO₂ with background subtracted. Peaks marked $(\nu_1-2\nu_2)$ comprise the $\nu_1-2\nu_2$ Fermi diad. The hot bands are also coupled through Fermi resonance (modified after Rosso and Bodnar, 1995).

which have the same frequency of vibration and form a degenerate pair (Gordon and McCubbin, 1966) (Fig. 5.2-3). The symmetric stretching mode is the only predicted Raman-active vibration because the derivative of the change in total molecular polarizability during this motion is nonzero (Rosso and Bodnar, 1995).

Due to Fermi resonance, the admixed excited ν_1 and $2\nu_2$ states are split apart and two strong CO₂ bands are present in the Raman spectrum. These two bands are referred to as the $\nu_1-2\nu_2$ Fermi diad and have the approximate frequencies 1388 cm⁻¹ (upper band) and 1285 cm⁻¹ (lower band) (Gordon and McCubbin, 1966; Rosso and Bodnar, 1995) (Fig. 5.2-3). Another band type is represented by low intensity peaks flanking the Fermi diad, which are referred to as hot bands. Their resultant frequencies are approximately 1264 cm⁻¹ and 1409 cm⁻¹ (Fig. 5.2-3). They arise from transitions that originate in excited vibrational states higher in energy than the ground

vibrational state due to the thermal energy of the molecules (Rosso and Bodnar, 1995). The hot bands are also perturbed by Fermi resonance (Rosso and Bodnar, 1995). The intensity of the hot bands of the Raman spectra of CO₂ increases concomitantly with increased temperature of CO₂; at ambient temperatures they are typically not observable (Brown and Steeper, 1991).

5.1.2.2. Relative Gas Compositions

According to Placzek's (1934) polarizability theory, the area of a Raman peak (over a finite range of wave numbers) is a function of (1) the number of molecules of a certain species in the scattering volume (absolute concentration of the species), (2) the Raman scattering cross section of the species, (3) the irradiance of the specimen, and (4) the solid angle of light collection. If two or more Raman-active species in the same phase of a fluid inclusion are analyzed either at the same time or one immediately after the other, the irradiance, the scattering volume, and the angle of collection of light are assumed to be the same for all the species. Thus instrumental effects on peak height and area are negated and the ratio of two or more species can be estimated. In practice, for a two-component system, the experimental result in units of mole percentages (C_a , C_b) is the function of three ratios: one for the determined Raman peak area (A_a , A_b), one for the relative scattering cross sections (σ_a , σ_b) of the two species, and one for the instrumental efficiencies (η_a , η_b) for Raman scattered light at specific wavelengths and polarization orientation. The σ 's and η 's can be combined into "Raman quantification factors" (F_a , F_b) (Wopenka and Pasteris, 1987). The quantitative relationship between the relative concentration of two components, a and b , and their Raman peak areas reduce to a simple formula:

$$A_a/A_b = (C_a/C_b) \cdot (\sigma_a/\sigma_b) \cdot (\eta_a/\eta_b) = (C_a/C_b) \cdot (F_a/F_b) \quad (5.2)$$

This equation requires knowledge of the Raman scattering efficiencies (σ 's) for the different components and the instrumental efficiencies (η 's) for Raman scattering radiation arising from those components.

In calculating the mol% of CO₂ and CH₄ in gas mixtures the 1388 cm⁻¹ and 2917 cm⁻¹ peak are used as comparative bands. It has long been realized that the cross-section of a volatile changes with the total pressure in a given fluid inclusion (Rosso and Bodnar, 1995). For CH₄ and CO₂ in calibration gas mixtures up to 15 bars total pressure, Wopenka and Pasteris (1987) determined F-factors (relative to N₂) of 6.7 and 1.5, respectively, for their laser Raman microprobe. The ratio of these F-factors is 4.4. Such ratios for low density gas mixtures are the ones most appropriate for the species in gas bubbles in this study and are therefore adopted to quantify the contents of the vapour phase. For a CH₄-CO₂ supercritical fluid with a density of about 80 cm³/mole (about 80 bars at room temperature), the empirically determined F-factor ratio

is 2.9, a relative decrease of about 34% compared to the ratio obtained at low pressure (Seitz *et al.*, 1987).

However, the fact that there are several instrument-specific parameters makes it problematic to apply the above empirical F-factors to different instruments. Among the most important instrumental factors are the different sensitivities of the gratings and the detector system for Raman scattered light of different polarization orientations and/or wavelengths. The use of the microscope of a laser Raman spectrometer will cause additional optical effects due to different components (e.g., objective, beam splitter, lenses) (Wopenka and Pasteris, 1987). Since each optical component has its own spectral characteristics that are a function of both wavelength and polarization orientation of the interacting light, the published F-factors are only approximate solutions for the Raman instruments used in this study.

In fluid inclusions from high temperature geological systems, ductile strain (e.g. Hollister, 1989) or diffusion along dislocation edges (e.g. Cordier *et al.*, 1994) can lead to because enrichment of components such as CO₂ and NaCl as H₂O is soluble and can diffuse through the silicate lattice. In such a low temperature system as that examined these processes are not thought to significantly contribute to alteration of the fluid composition.

5.1.2.3. Gas Density

The sensitivity of bond configuration to the pressure on or density of a phase has been documented in the Raman spectra of gaseous CO₂ (Bertran, 1983), CH₄ (May *et al.*, 1959), and N₂. This effect has been previously noted in the spectra of natural fluid inclusions (e.g. Burke, 2001; Rosasco *et al.*, 1975; Dubessy *et al.*, 2001).

Many previous studies have documented the density-dependent band shift in Raman peaks of pure CO₂ (e.g., Wang & Wright, 1973; Bertrán, 1983; Garrabos *et al.*, 1989a,b; Rosso & Bodnar, 1995; Yamamoto & Kagi, 2006). In the spectrum of CO₂, the bands of the Fermi diad shift to lower wave numbers with increasing density. The frequency shift of the lower band has a higher density dependence than does the upper band. At the same time, the intensity ratio of the upper band to the lower band increases with increasing density (Garrabos *et al.*, 1980) The split (Δ) between the Fermi diad peaks increases with increasing density of CO₂ (e.g., Bertrán, 1983; Kawakami *et al.*, 2003). Rosso and Bodnar (1995) have calibrated the dependence of the Fermi diad separation on CO₂ density from a compilation of experimental results ranging from analyses of low density gaseous CO₂ to liquid CO₂ in the density range of 0.01– 1.20 g/cm³. Within this density range the relationship between Δ and density is assumed to be linear (Hacura *et al.*, 1997). This resulted in the following empirical fit suitable for estimating CO₂ densities (g/cm³):

$$\rho_{CO_2} = \frac{(\Delta - 102.68)}{2.49} \quad (5.3)$$

The overall precision of the determination of Δ is approximately 0.05 cm^{-1} which equates to $\pm 0.02 \text{ g/cm}^3$.

The total pressure (P_T) of a mixture of ideal gases is equal to the sum of the partial pressures of the individual gases in the mixture as stated by Dalton's law. For the vapour phase of a fluid inclusion containing CO_2 , CH_4 and H_2O vapour, P_T is defined as

$$P_T = P_{\text{CH}_4} + P_{\text{CO}_2} + P_{\text{H}_2\text{O}} \quad (5.4)$$

where P_{CH_4} , P_{CO_2} and $P_{\text{H}_2\text{O}}$ are the gas partial pressures of CH_4 , CO_2 and H_2O in the vapour phase. For fluid inclusions at room temperature the total pressure is essentially $P_{\text{CO}_2} + P_{\text{CH}_4}$ since the vapour pressure of water at ambient temperatures is negligible (Hedenquist and Henley, 1985).

The mole fraction of a gas component in a gas mixture is equal to the volumetric fraction of that component in a gas mixture. The mole fraction (x_i) of an individual gas component (i) in an ideal gas mixture can be expressed in terms of the component's partial pressure (P_i) or the moles of the component (n_i) as

$$x_i = \frac{P_i}{P_T} = \frac{n_i}{n} \quad (5.5)$$

and the partial pressure of an individual gas component in an ideal gas can be obtained using this expression:

$$P_i = x_i \cdot P_T \quad (5.6)$$

From the calculated CO_2 gas density the inclusion CO_2 partial pressure can be estimated from the combined ideal gas law expressed as a function of density and temperature as

$$P_{\text{CO}_2} = \rho_{\text{CO}_2} \cdot (R \cdot T) \quad (5.7)$$

where ρ_{CO_2} is the CO_2 gas density, P_{CO_2} is CO_2 partial pressure, R is the specific gas constant for CO_2 ($188.9 \text{ J/kg}\cdot\text{K}$) and T is absolute temperature at the time of the spectra acquisition. In inclusions containing only CO_2 in the vapour phase $P_{\text{CO}_2} = P_T$. The uncertainty associated with measurement of ρ_{CO_2} results in an uncertainty in P_{CO_2} of $\pm 1.03 \text{ MPa}$.

From the total inclusion pressure (P_T) the depth (m) of inclusion formation can be estimated, assuming a hydrostatic pressure gradient, according to

$$\text{Depth} = (P_T - P_{\text{atm}}) / (\rho_{\text{fluid}} \cdot g) \quad (5.8)$$

Where P_T is the inclusion pressure, P_{atm} is atmospheric pressure, ρ_{fluid} is the average density of the pore fluid (1.01 g/cm^3) and g is the acceleration due to gravity. Propagating the uncertainty in ρ_{CO_2} results in an uncertainty in the depth estimate of $\pm 96 \text{ m}$.

As shown by May *et al.*, (1959), the Raman spectrum of CH_4 in the fluid state depends on pressure. The wave number of the Raman peak for the symmetric C-H stretching mode (ν_1) decreases as pressure increases. Lu *et al.*, (2007) have quantified the dependency of the measured Raman shifts of C–H symmetric stretching band (ν_1) in the vapour phase with methane vapour pressures in inclusions from a compilation of experimental and natural fluid datasets. They derive a unified equation for the relationship between pressure and Raman peak position at isothermal conditions by using all available data, such that it can be applied reliably in any laboratory. The shift, D (in cm^{-1}) of ν_1 from ν_0 (2917.30 cm^{-1}), the CH_4 ν_1 peak position at near zero pressure (or density), with total inclusion pressure, P_T (in MPa) can be represented by

$$P_T = -0.0148 \cdot D^5 - 0.1791 \cdot D^4 - 0.8479 \cdot D^3 - 1.765 \cdot D^2 - 5.876 \cdot D \quad (5.9)$$

$$\text{where } D = \nu_{sample} - \nu_0 \quad (5.10)$$

Methane density, ρ_{CH_4} (g/cm^3), can be represented as a function of D as follows:

$$\rho_{CH_4} = -5.17331 \times 10^{-5} \cdot D^3 + 5.53081 \times 10^{-4} \cdot D^2 - 3.51387 \times 10^{-2} \cdot D \quad (5.11)$$

The uncertainty of D is estimated to be about 0.3 cm^{-1} , and therefore, the uncertainty of the calculated density of methane in vapour is about 0.012 g/cm^3 and the uncertainty of the calculated inclusion pressure is $\pm 1.34 \text{ MPa}$.

From an estimate of vapour phase gas partial pressure the concentration of a dissolved gas in equilibrium with the inclusion fluid can be calculated. For a dilute solution in equilibrium with $CO_2(g)$ the ideal gas vapour pressure of CO_2 is proportional to its mole fraction in the solution. The calculations utilise Henry's Law constant K_H , which relates the partial pressure of a gas P_i to its mole fraction in aqueous solution X_i according to:

$$P_i \alpha = K_H X_i \quad (5.12)$$

where α is the fugacity coefficient. For any non-electrolyte solution, the fugacity of the dissolved component, i , becomes closer to being directly proportional to the mole fraction x_i as x_i approaches zero. Such that in solutions with low gas concentrations, the fugacity coefficient will be close to unity so that it can safely be ignored. This study uses the expression for K_H (CO_2) generated by Wilkinson (2001) over the temperature range $0\text{-}350^\circ\text{C}$ and the salinity range $0.0\text{-}2.0 \text{ M NaCl}$ by regression of data from the studies of Ellis and Golding (1963) and references therein.

5.1.3. Sample Material

65 μ m thick doubly polished wafers for fluid inclusion analyses were made from ten samples of Entrada Sandstone host rock and vein material collected from exposures at Tenmile Butte, outcropping in the footwall of the northern fault of Salt Wash Graben. Sections were prepared from: i) two samples of gypsum veins petrographically associated with large-scale diagenetic bleaching of the Entrada Sandstone; ii) two samples of bleached sandstone; iii) one sample of unbleached sandstone, and; iv) five samples of aragonite veins, including samples of thick veins (>40cm thickness) and thin veins (<3mm) in bleached and unbleached host rock. Individual wafers were broken into fragments in order to enable multiple microthermometry runs from each sample.

5.1.4. Analytical Methods

Six representative samples were investigated using Raman microspectroscopy. Dispersive laser-Raman spectra were obtained at the University of Cambridge by means of a LabRam 300 spectrometer equipped with a 632.81 nm diode laser, a 1200 lines/mm diffraction grating and a CCD detector. The spectrometer is attached to an Olympus microscope, with 5 \times , 20 \times , 50 \times and 100 \times objective lenses, giving a lateral resolution down to \sim 1 μ m.

Raman spectra were collected at room temperature in the spectral window of 100-4000 cm^{-1} which covers the ν_1 - $2\nu_2$ bands of CO_2 at 1285 cm^{-1} and 1388 cm^{-1} and its two hot bands at 1264 cm^{-1} and 1409 cm^{-1} ; the N_2 band at 2328 cm^{-1} ; the SO_2 band at 1151 cm^{-1} ; the large stretching band of H_2O (2900 – 3700 cm^{-1}) and the ν_1 band of CH_4 at 2917 cm^{-1} (Pasteris *et al.*, 1988). Overlap of Raman bands from volatiles in inclusions with bands from the mineral hosts (typically 400 – 1000 cm^{-1}) does not usually occur.

Microthermometric measurements on fluid inclusions from two representative vein samples (one aragonite, one gypsum) were conducted at the University of Leeds using a Linkam heating-freezing stage. It was calibrated using the temperature of the CO_2 triple point (56.6 $^\circ\text{C}$) and H_2O triple point (0 $^\circ\text{C}$) and the critical homogenization of an H_2O fluid inclusion (374.1 $^\circ\text{C}$). The accuracy of measurement is \pm 0.1 $^\circ\text{C}$ in the range of -100 $^\circ\text{C}$ to +25 $^\circ\text{C}$, \pm 0.5 $^\circ\text{C}$ between 25 $^\circ\text{C}$ and 250 $^\circ\text{C}$ and increases linearly to \pm 1 $^\circ\text{C}$ at 374.1 $^\circ\text{C}$. During heating, the temperature was increased at a rate of 1 to 2 $^\circ\text{C}/\text{min}$ to minimize thermal-gradient effects. Homogenization temperatures were not corrected for pressure.

5.3. Results

5.1.5. Field Observations

At Green River bleaching of aeolian Lower to Middle Jurassic sandstones occurs to varying degrees in the footwalls of both Little Grand Fault and Salt Wash Graben (see Chapter 4, Fig. 4.4-1 for maps detailing the distribution of bleaching and sample localities). The distribution of bleaching in the footwalls of both faults is focused in the faulted fold axis of the Green River anticline (Fig. 5.3-1), though its spatial extent varies depending on the footwall lithologies. Along the more shale-rich Little Grand Wash fault footwall, bleaching is mainly confined to the lower, sand-rich sections of the Curtis Formation, with the bottom 2 m of the outcropping sandstone partially to completely bleached, while the next 4m contains sporadic, thin bleached horizons (1 to 10 cm thick) subparallel to bedding and thin bleached haloes (1 to 5cm thick) surrounding steeply-dipping fractures that are sporadically infilled with calcite or rare gypsum veins.

Along the more sand-rich rocks exposed in the footwall of the northern fault of Salt Wash Graben, the red Entrada Sandstone is extensively bleached to pale yellow-white and is especially well exposed at Tenmile Butte. The zone of bleaching, up to 8m thick, is localized to the stratigraphic base of the formation and extends up to 300m into the footwall. Above this contact, bleaching is mainly located around clusters of steeply-dipping fractures with bleached haloes up to 5 m wide, which are sporadically infilled with calcite or gypsum veins. The bleached zone is domal in structure and is coincident with the structural high formed by the anticlinal crest. The zone thins both down-dip, away from the fault trace and laterally E-W along the fault outcrop, eventually forming elongate stringers. The basal contact of the bleached zone with underlying unbleached rock is not exposed. The upper contact of the bleached zone with overlying unbleached rock is sharp, dips at a low angle over its length and terminates in bulbous fronts towards the north, east and west. It cross cuts stratigraphic boundaries and its macroscopic form is more influenced by the distance from faults and fracture conduits, than by permeability heterogeneity. Small-scale permeability heterogeneity, such as the presence of granulation seems or facies heterogeneity exerts controls on the geometry of the bleached front at the outcrop scale (Fig. 5.3-2).

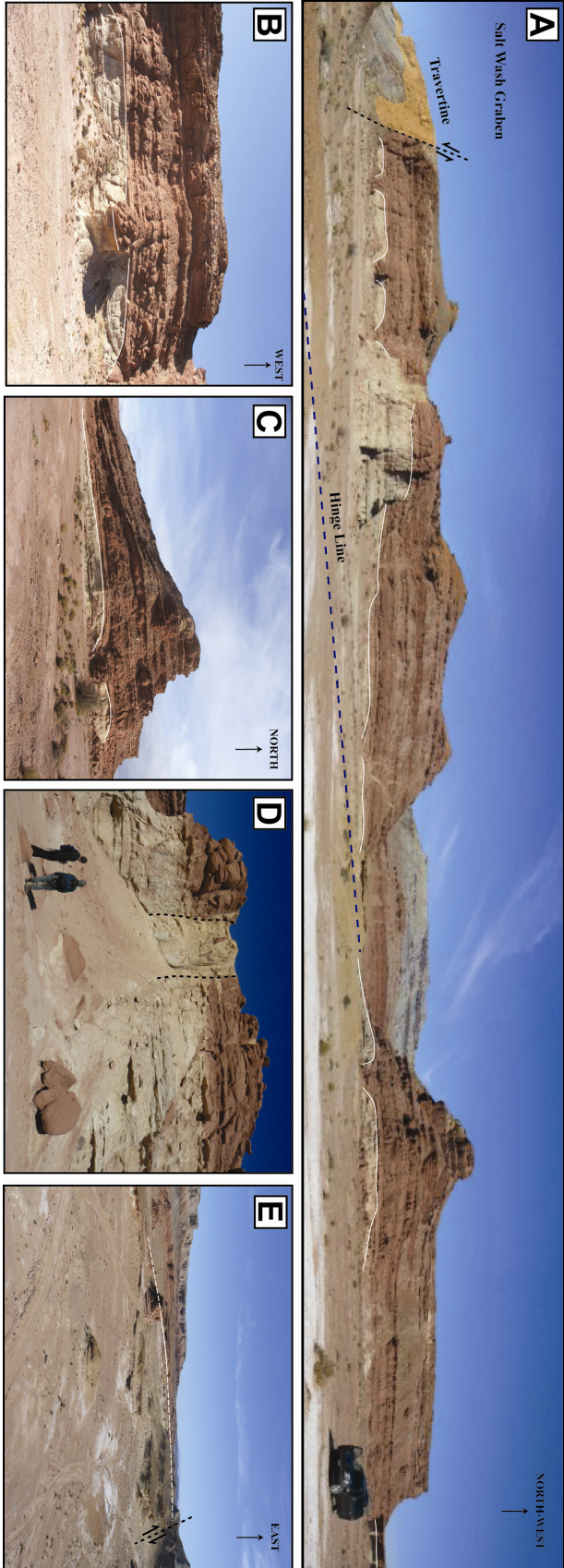


Figure 5.3-1 Tennile Butte, intersection of the Green River anticline and the northern fault of Salt Wash Graben. Field photographs showing the spectacular bleaching of the Entrada Sandstone (a-e). Bleaching is localised to a horizontally continuous 4-8m thick layer at the base of the Entrada Sandstone. d) The chimney structure, formed as an array of closely spaced subvertical fractures, through which the extra-formational bleaching fluid was introduced into the Entrada Sandstone, from deeper formations.

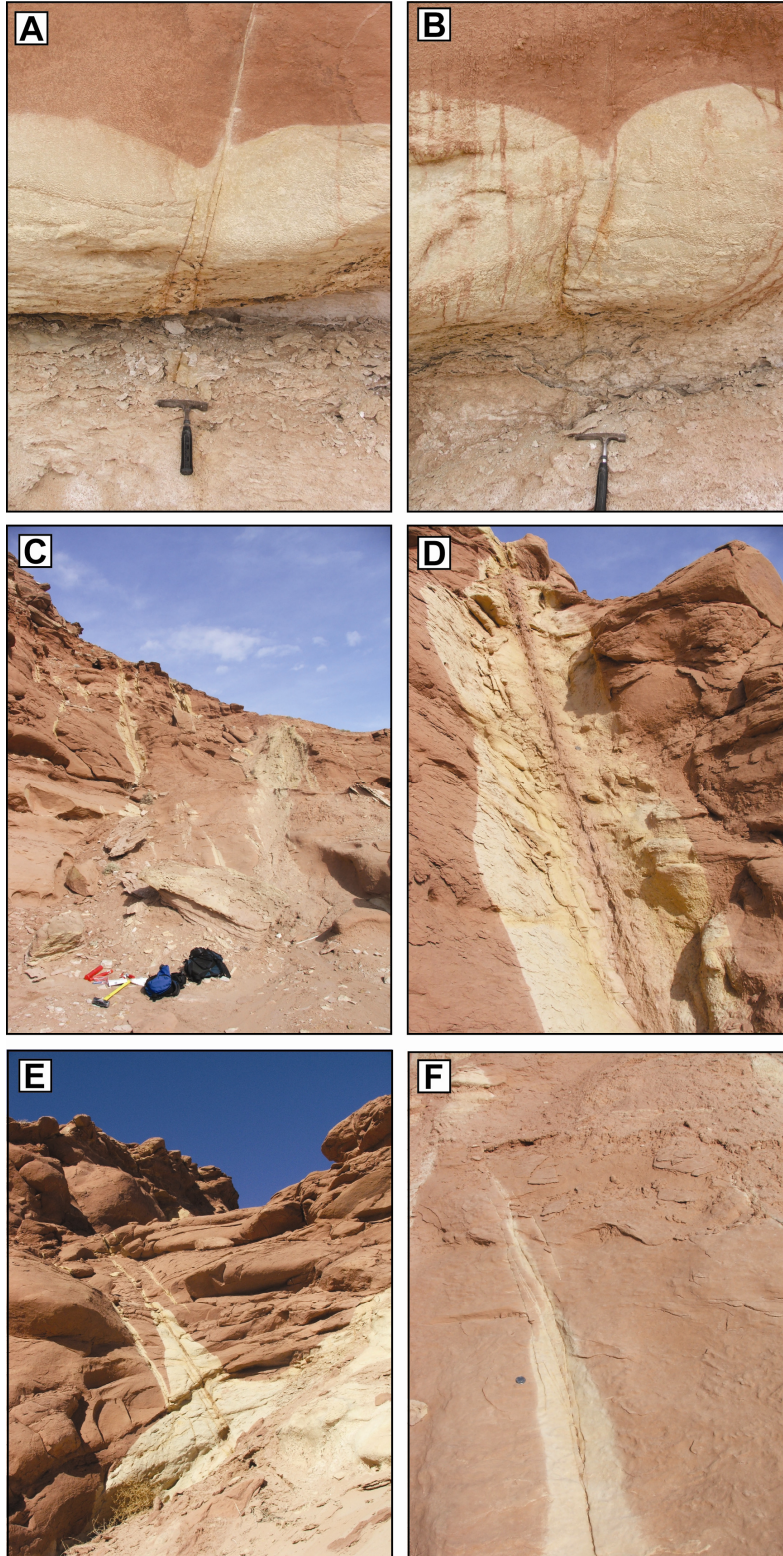


Figure 5.3-2 Field photographs showing granulation seams both enhancing (a) and impeding (b) propagation of the bleaching front. Steeply dipping fractures (c-d) extend from the larger bleached zone and commonly have bleached halos that thin and terminate m's to 10m's along the fracture length. Fracture cores occasionally contain reprecipitated Fe-oxides, indicating transport of Fe in solution and multiple generations of fluid flow. Scales: Hammer: 35cm, Coin: 2.5 cm.

5.1.6. Petrology and Cathodoluminescence

Bleached Entrada Sandstone samples average 6.2 vol.% feldspars and 70.8 vol.% detrital quartz grains, which are occasionally overgrown by euhedral and irregular quartz overgrowths (2.0 vol.%). Overgrowths surround both hematite and illite grain coatings and grains from which the haematitic coatings have been dissolved. Bleached sandstones samples average 2.9 vol.% illite and 1.1 vol.% kaolinite. Bleached samples average 3.3 vol.% corroded dolomite and abundant pore filling calcite (8.2 vol.%). Cryptocrystalline hematite and coarse crystalline Fe-oxides average 0.2 vol.% and 1.2 vol.% respectively. Scatter plots (Fig. 5.3-3) indicate potential paragenetic relationships between phases.

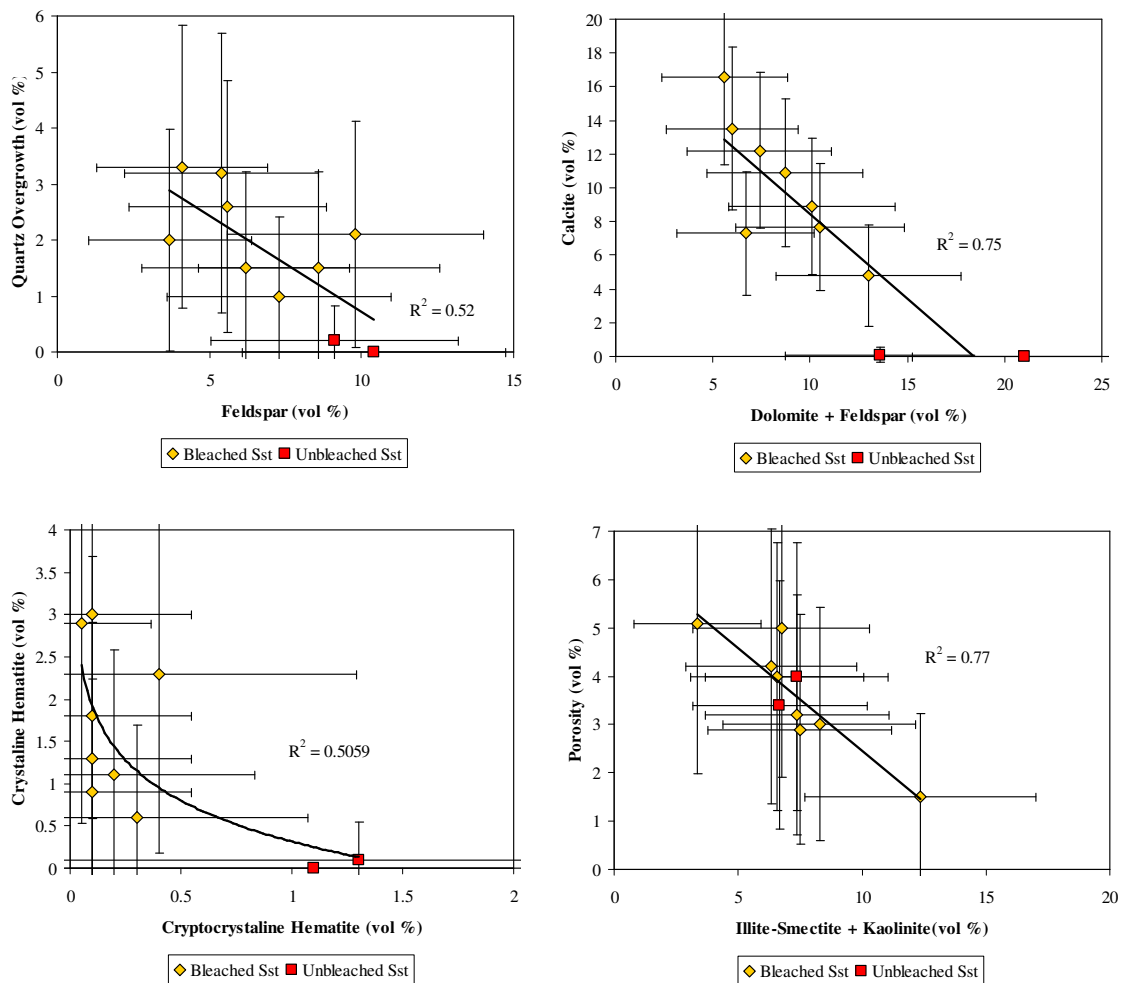


Figure 5.3-3 Scatter plots of the point counted mineralogies for samples of bleached and unbleached Entrada Sandstone. Negatively correlated volumes of quartz overgrowths and feldspar suggests derivation of silica from the dissolution of feldspar. Negative correlated volumes of dolomite+feldspar versus calcite suggest, at least in part, derivation of some Ca^{2+} for calcite precipitation from the dissolution of these phases. Negative correlated cryptocrystalline hematite and coarse Fe-oxide volumes suggest a non-detrital origin for coarse oxides and their formation from the dissolution and reprecipitation of cryptocrystalline hematite to coarse crystalline hematite. Porosity is occluded by calcite and clay precipitation.

Dolomite is present as an early cement and is often corroded and shows evidence of patchy recrystallization. Calcite rims sand grains and overgrows dolomite cement partially filling and completely occluding pore space. Calcite has a tabular, blocky habit and individual grains range in size from (5-45 μ m). Two distinct calcite phases can be identified based on cathodoluminescence properties (Fig. 5.3-4): 1) an early, pigmented, bright yellow-orange luminescent calcite that rims grains and overgrows dolomite and 2) a second later calcite phase that infills remaining pore space, overgrows earlier calcite cement, and is weakly orange-red or nonluminescent. The luminosity in calcite is relatively homogeneous with no evidence of zonation. The blocky texture of the calcite and homogenous CL pattern suggests partial recrystallization.

Minor amounts of pore-filling poikilotopic barite and sylvite were observed in samples from the base of the bleached zone. Intergrowths of calcite and sylvite towards the edges of these poikiloblasts suggest contemporaneous precipitation. Extensive occurrence of barite was described by Morrison and Parry (1986) and Breit *et al.*, (1990) from areas associated with collapsed salt cored anticlines to the south east of Green River, in the vicinity of the Moab fault. Based on the sulfur isotopic composition of barite found in the Upper Jurassic Morrison Formation, Breit *et al.*, (1990) attributed barite formation to fluids originating in the underlying Pennsylvanian evaporites.

Proximal to faults, and within fractures, gypsum veins (Fig. 5.3-5) (0.5-2mm thick) grew contemporaneously with calcite. Individual gypsum veins contain inclusions of pyrite and are paralleled by occasional hematite and magnetite liesegang bands (Fig. 5.3-6). Occasional calcite veins (0.25-1mm) cross cut and are cut by gypsum veins and contain inclusions of Fe-oxides.

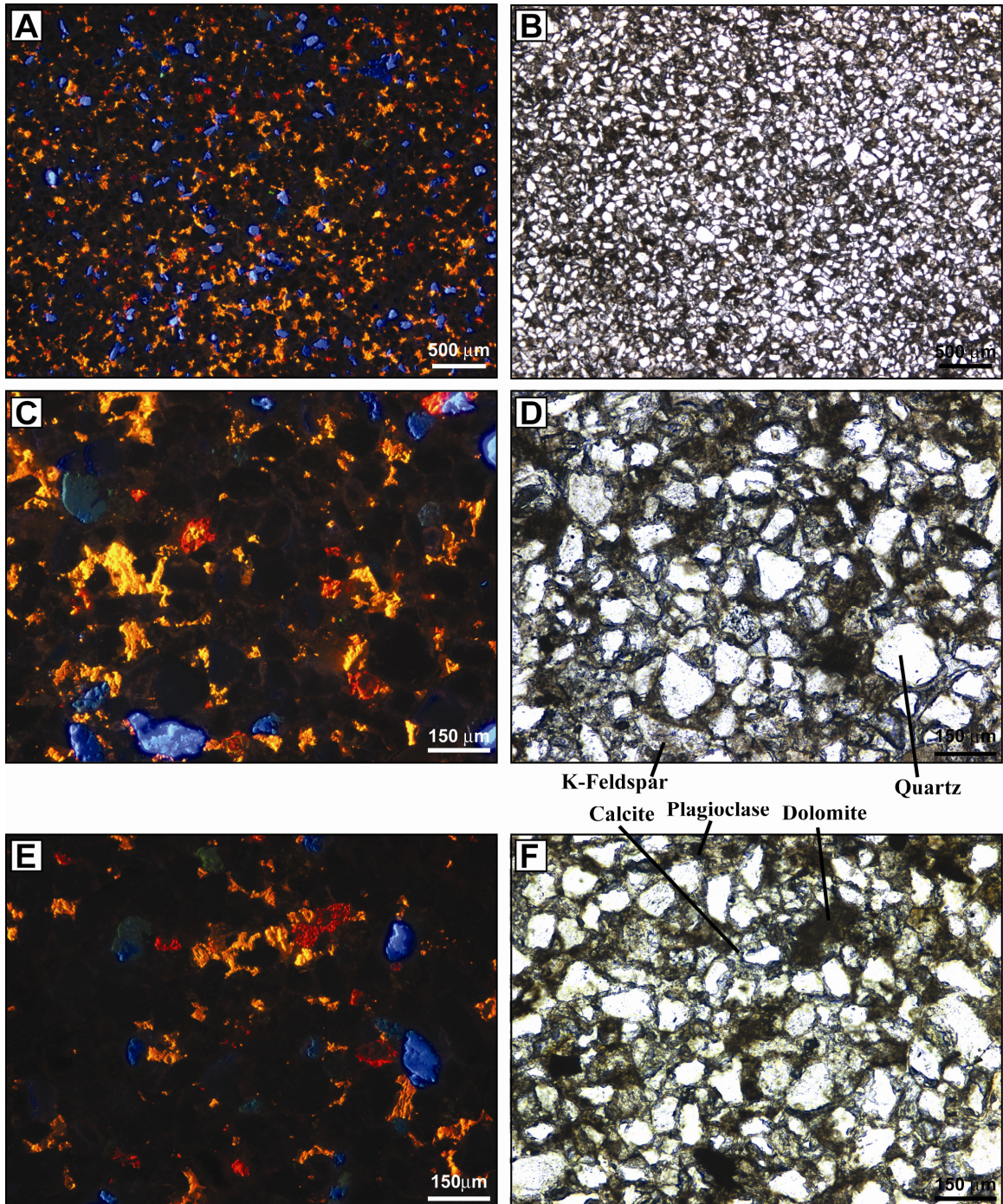


Figure 5.3-4 Typical cold CL and plane polarized light photomicrographs from bleached Entrada Sandstone from the fracture conduit (Fig. 5.3-1D) feeding the bleached zone. Ubiquitous calcite cements (yellow-orange CL) are pigmented and overgrow corroded dolomite rhombs (red CL).

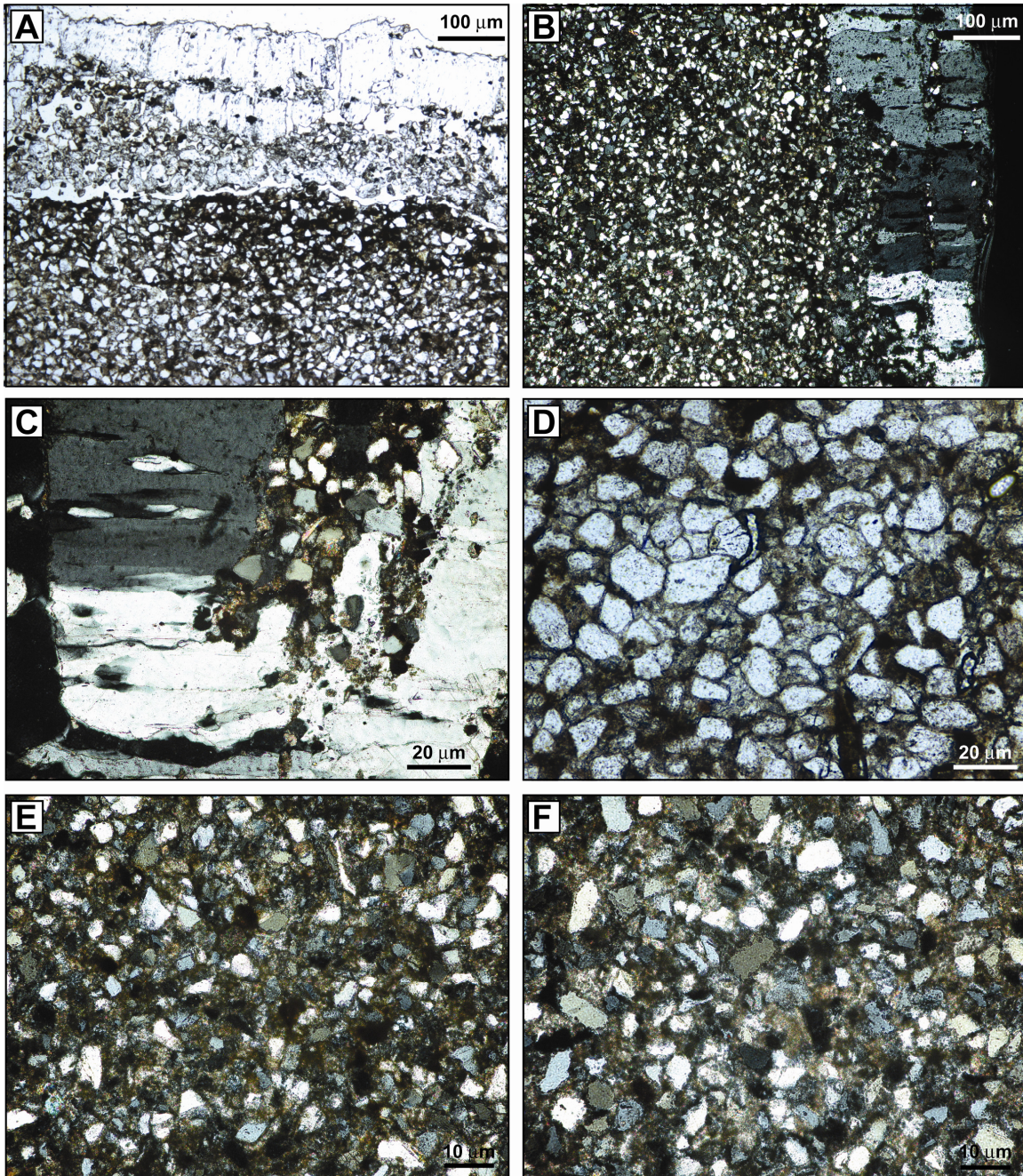


Figure 5.3-5 Typical plane and crossed polarized light photomicrographs from bleached Entrada Sandstone, in Fig. 5.3-4, adjacent to a fracture filling gypsum vein. Gypsum contains inclusions of calcite and pyrite. Secondary crystalline Fe-oxides (a-b) parallel the veinlet.

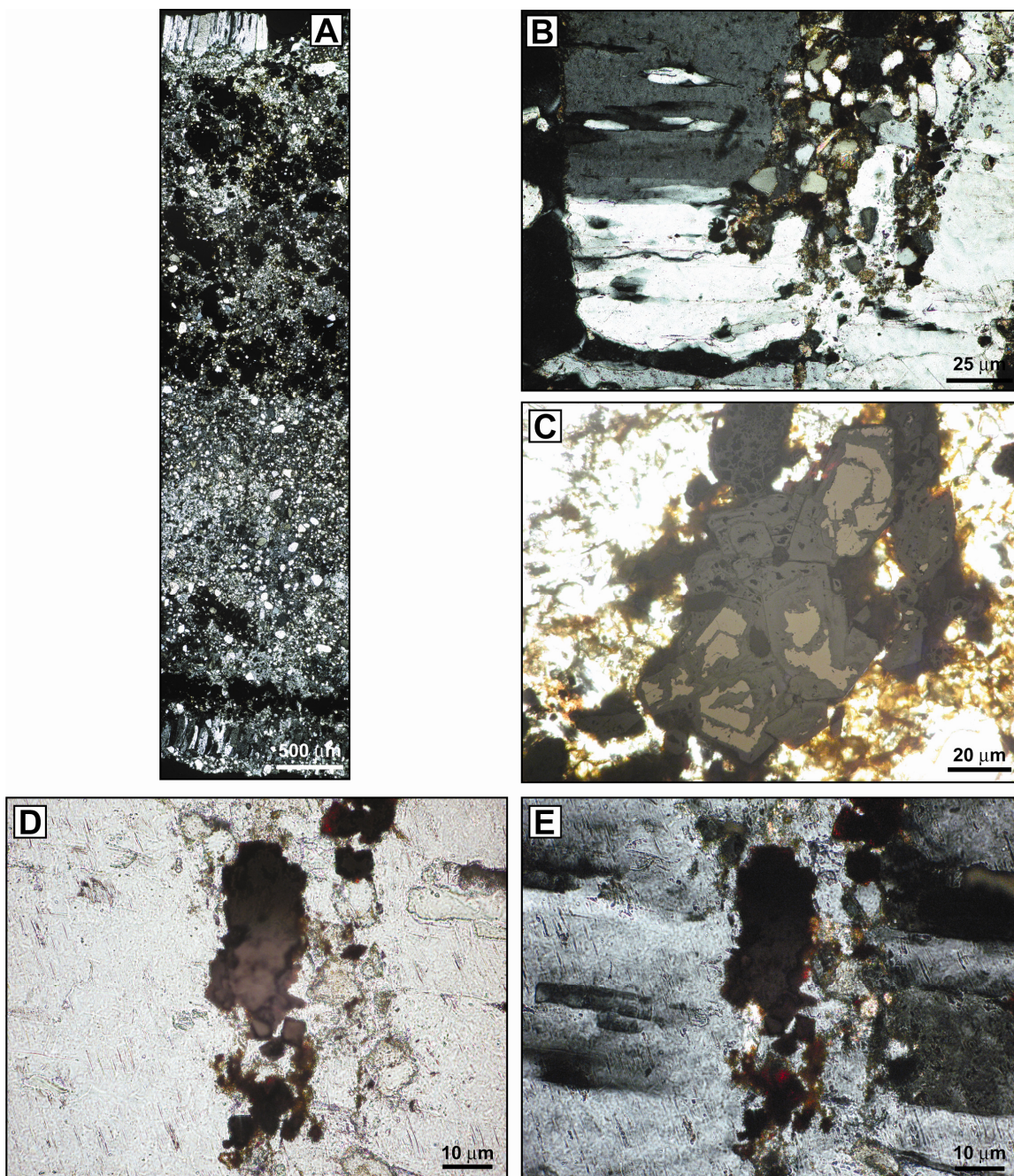


Figure 5.3-6 Typical plane and crossed polarized light photomicrographs from bleached Entrada Sandstone adjacent to a fracture filling gypsum vein showing: a) coarse hematite liesegang bands; c-e) coarse secondary hematite.

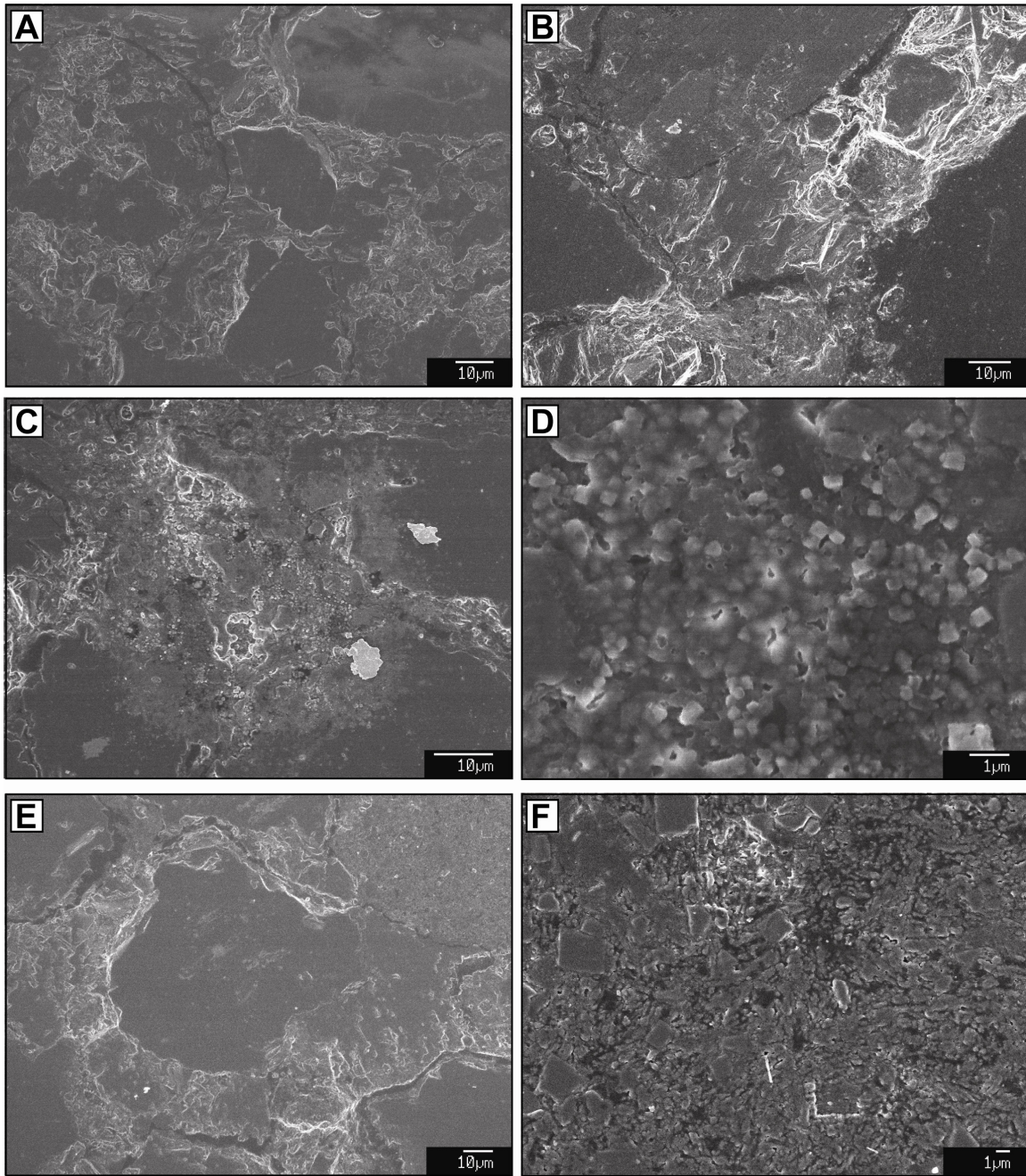


Figure 5.3-7 SEM images from bleached Entrada Sandstone showing: a-c) corroded feldspar grains and pore filling and grain rimming illite/smectite and kaolinite; d) amalgams of kaolinite and calcite; e) extensively corroded feldspar rimmed by calcite and kaolinite and; f) coarse amalgams of kaolinite and calcite.

5.1.7. Scanning Electron Microscopy

Samples contain corroded K-feldspar and plagioclase overgrown by patchy coatings of illite, illite-smectite and kaolinite (Fig. 5.3-7). Corroded feldspars contain abundant clay precipitates in adjoining pore space. Occasional remnant feldspar grains have been completely replaced by

coarse pore filling illite/smectite or kaolinite. Equant and irregular quartz overgrowths are visible occasionally. Pore filling kaolinite often inter-grows with small <0.5µm euhedral calcite.

5.1.8. XRD and XRF

X-ray diffraction patterns (Fig. 5.3-8) from bleached Entrada Sandstone include typical detrital minerals; quartz and K-feldspar and secondary minerals calcite, dolomite, kaolinite and mixed layer illite-smectite. Modal mineralogy (Table 5.3-1) was calculated from least squares mixing of mineral proportions to match whole rock compositions using the program MINSQ (Hermann & Berry, 2002). Recalculated modal mineral proportions are similar to those determined from point counting and exhibit similar patterns in the genetic relationships of detrital and secondary minerals. Whilst bleached sandstone is depleted in Fe ~25% of the initial Fe content remains.

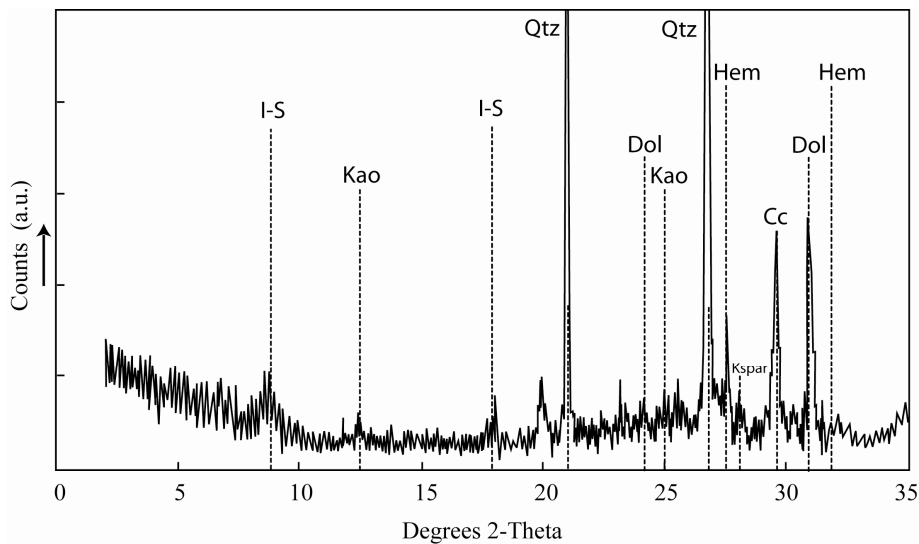


Figure 5.3-8 XRD pattern from bleached Entrada Sandstone.

Sample	Type	Qtz	Kspar	Plag	Dol	Kao	Hem	Cc	MnOx	Apt	Il	TOT	SSQ
RS060	B	65.4	10.7	5.7	6.4	0.3	0.4	3.5	0.00	0.0	7.5	100.0	0.8
RS029	R	64.4	13.2	5.9	10.3	0.0	2.0	0.0	0.04	0.1	3.9	100.0	1.5

Table 5.3-1 Modal Mineralogy of bleached (RS060) and unbleached (RS029) Entrada Sandstone recalculated from XRF analyses. Abbreviations: Qtz = Quartz, Kspar = K-feldspar, plag = plagioclase, Dol = dolomite, Cc = calcite, Kao = kaolinite, Hem = Fe₂O₃, MnOx = Mn-oxide, Apt = apatite, Il = illite/smectite

5.1.9. Discussion: Petrology of Diagenetic Bleaching in the Entrada Sandstone

Hematite grain coatings are the earliest determinable diagenetic event and reddening is considered to have occurred during earliest burial. (Walker *et al.*, 1979). Petrographic

observations and XRF analyses suggest that during bleaching cryptocrystalline hematite was dissolved and reprecipitated locally as coarse hematite grains and some Fe was transported, in solution. The red colour of the Entrada Sandstone is caused by the reflectance in the red part of the visible spectrum by cryptocrystalline hematite. However, reflectance in the red part of the spectrum decreases as hematite particle size increases. With increasing size from 0.1 to 0.8 μm , the colour progressively changes from orange to red to purple (Kerker *et al.*, 1979; Morris *et al.*, 1996). The colour of hematite changes to gray in the 5-10 μm -size range (Lane *et al.*, 1999) so that coarse-grained hematite is black or steel gray. The colour change in bleached sandstone is a result of changes in the grain size of hematite in addition to removal of Fe from the sandstone. Cryptocrystalline hematite grain coatings are largely absent in thin sections of bleached sandstones and modal (Fig. 5.3-3) and compositional measurements (Table 5.3-1) confirm the removal of hematite and Fe in bleached samples.

In unbleached Entrada Sandstone (Chapter 4, section 4.4.2.1) illite/smectite occurs as 1-5 μm thick pore-lining cements which generally dust entire detrital grains. Illite-smectite coating is absent or very thin at grain contacts. No detrital clay is observed in the Entrada Sandstone. Kaolinite occurs as authigenic pore filling cement which post dates dolomite cementation and is intimately associated with feldspar grains. Both these clay products are thought to represent alteration of silicate grains during burial. Volumetrically minor quartz overgrowths (<1%) were also precipitated during this episode. In bleached Entrada Sandstone reaction between volatile components in the extra-formational fluid and the host formation resulted in moderate dissolution of detrital feldspar grains and precipitation of additional grain rimming and pore-filling kaolinite and illite/smectite. This implies elevated $[\text{H}^+]$ in the bleaching fluid. Feldspar dissolution was accompanied by reprecipitation of silica as euhedral and irregular quartz overgrowths which crystallize on grains from which the hematite grain coatings have been removed. Feldspar and hematite dissolution was accompanied by calcite veining and cements which follow regional bleaching.

Calcite cement contents decreasing from ~17 vol. % close to the main feeder conduit (Fig.5.3-1D) to ~6 vol. % towards the northerly and easterly extremes of the bleached zone. Regionally the Entrada Sandstone is loosely cemented relative to the sandstones which are stratigraphically below and above it (Ohran, 1992). Dolomite occurs as pore filling rhombs in unbleached interdunal and dune facies sandstone. Regionally, dolomite was precipitated from an isotopically heavy fluid which may have originated as evaporated playa water on the Entrada dune field (Desborough and Poole, 1992). Regionally, calcite occurs mostly as a poikilotopic cement, well developed in the extreme upper and lower parts (30-50cm) of the Entrada Sandstone but is absent elsewhere (Ohran, 1992). This calcite cement is thought to be sourced from infiltration of CaCO_3 bearing solutions from formations above and below the Entrada during

early compaction (Ohran, 1992). Extensive calcite cementation in bleached sandstones is directly related to the bleaching event, which implies that the bleaching fluid was enriched in C and had elevated $[\text{HCO}_3^-]$.

Localization of bleaching to the base of the formation suggests derivation from a fluid denser than the original pore fluid. The presence of gypsum veining and pore-filling poikilotopic barite and sylvite cements suggest the involvement of a saline fluid enriched in SO_4^{2-} , Cl^- , Ba^{2+} and K^+ .

5.1.10. Isotope Geochemistry

5.1.10.1. Carbon and Oxygen Stable Isotopes

Tables B-VI and B-VII (Appendix B) displays the $\delta^{13}\text{C}$ and $\delta^{18}\text{O}$ of samples of the bulk Entrada Sandstone (both bleached and unbleached) and calcite veins associated with bleaching. Twenty three of the samples were collected from Tenmile Butte, Salt Wash Graben, from calcite veins, bleached and unbleached Entrada Sandstone. In addition twenty samples of the Navajo Sandstone were collected from core chips from petroleum exploration wells Salt Valley 22-34 and Salt Wash #1 (well details can be found in Appendix B, Table VII) which penetrate the Navajo Sandstone on the eastern limb of the Green River anticline. In both the sampled wells the Navajo Sandstone shows a progressive colour change from very pale-white to pale yellow over the entirety of the sampled interval and only the upper 5 to 10m were unbleached and retained the original red colouration. This data is projected in Figure 5.3-9, together with published data sets from carbonate cements, veins and concretions from bleached Jurassic Sandstones in the Moab and Courthouse syncline regions of the northern Paradox Basin (Beitler *et al.*, 2005, Chan *et al.*, 2000, Eichhubl *et al.*, 2009, Garden *et al.*, 2001).

5.1.10.2. $^{87}\text{Sr}/^{86}\text{Sr}$

$^{87}\text{Sr}/^{86}\text{Sr}$ of calcite veins in bleached Entrada Sandstone range from 0.712115 to 0.712645, $n=2$, and gypsum veins in bleached Entrada Sandstone range from 0.711837 to 0.711919, $n=3$. Analyses are presented in figure 5.3-10 against values for aragonite veins from the Green River anticline, the silicate fraction of the Entrada and Navajo Sandstone (Truini and Longworth, 2003), early diagenetic cements in these formations elsewhere in the Northern Paradox Basin (Goldstein *et al.*, 2008), secondary hematite concretions associated with bleaching of the Entrada Sandstone along the Moab Fault (Chan *et al.*, 2000), analyses of barite cements in the Morrison Formation from the Slickrock Mining District (Breit *et al.*, 1990) part of a large salt collapse structure and zone of upward brine movement from the Paradox formation, and values for the Paradox formation brine from the Greater Aneth Oil Field (Spangler *et al.*, 1996).

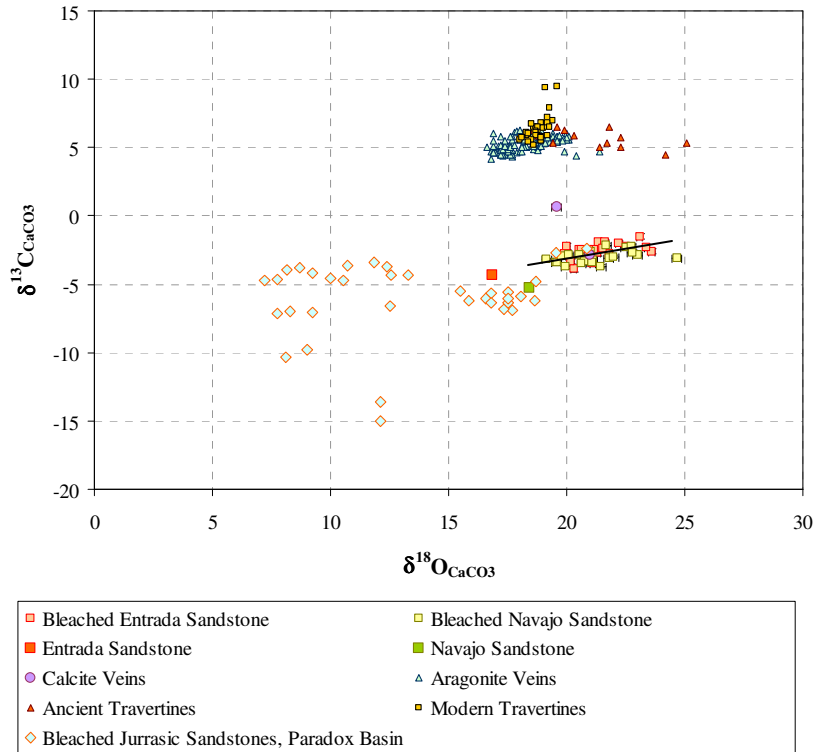


Figure 5.3-9 Stable isotope analyses for calcite cements and veins associated with bleached portions of the Entrada and Navajo Sandstones from this study. Included are a compilation of stable isotope analyses of calcite cements and veins associated with bleached Jurassic sandstones from the northern Paradox Basin (see text for references) and the isotopic composition of aragonite veins and modern and ancient travertine deposits associated with the leaking CO₂ system.

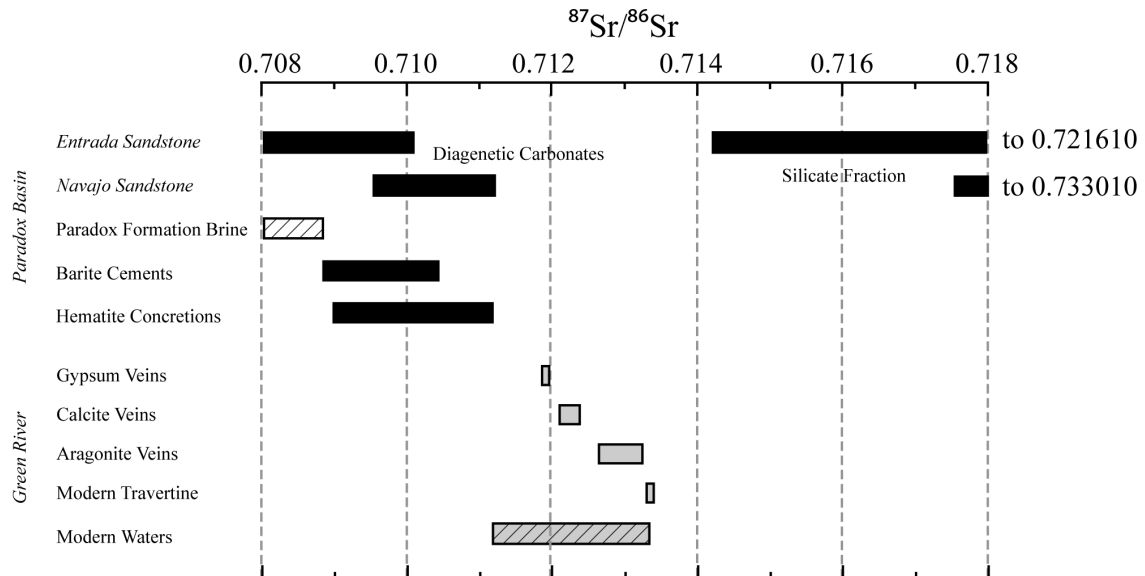


Figure 5.3-10 ⁸⁷Sr/⁸⁶Sr of aragonite, calcite and gypsum veins, modern travertine and modern CO₂-charged waters. Additionally the ⁸⁷Sr/⁸⁶Sr of diagenetic carbonate cements and the silicate fraction in the Navajo and Entrada Sandstones, Paradox Formation Brine, hematite concretions from bleached Jurassic Sandstones near Moab fault and salt collapse related barite cements are shown for reference. See text for references.

5.1.10.3. Discussion: Isotope Geochemistry

$\delta^{18}\text{O}_{\text{CaCO}_3}$ of bleached Entrada Sandstone samples range from 19.9 to 23.6 ‰ (V-SMOW) and $\delta^{13}\text{C}_{\text{CaCO}_3}$ values range from -1.5 to -3.9 ‰ (V-PDB) (Fig. 5.3-9). $\delta^{18}\text{O}_{\text{CaCO}_3}$ of bleached Navajo Sandstone range from 19.2 to 22.7 ‰ (V-SMOW) and $\delta^{13}\text{C}_{\text{CaCO}_3}$ values range from -2.2 to -3.7 ‰ (V-PDB) (Fig. 5.3-9). Calcite cements from both bleached Entrada and Navajo Sandstones exhibit a similar range and trends in $\delta^{13}\text{C}_{\text{CaCO}_3}$ and $\delta^{18}\text{O}_{\text{CaCO}_3}$ (Fig. 5.3-11). This suggests formation of calcite from a fluid of comparable isotopic composition at similar temperatures and implies that carbonate deposition occurred from a fluid migrating vertically through the stratigraphy.

$\delta^{18}\text{O}_{\text{H}_2\text{O}}$ calculated from $\delta^{18}\text{O}_{\text{CaCO}_3}$ (Fig. 5.3-11) (using the crystallization temperatures determined in section 5.1.13) of bleaching related cements in both Entrada and Navajo Sandstone is isotopically similar to that of carbonate associated with the modern CO_2 -system, but is heavier than calcite cements associated with bleaching in the wider Paradox Basin area (determined from various crystallizations temperatures reported in Beitler *et al.*, (2005), Chan *et al.*, (2000) and Garden *et al.*, (2001), ranging from ~30-80°C) (Fig. 5.3-11). Bleaching related waters elsewhere in the Paradox basin have been variably attributed to fluids of a largely meteoric origin (Beitler *et al.*, 2005, Eichhubl *et al.*, 2009, Garden *et al.*, 2001) or to mixtures of meteoric water and saline fluids derived from the Pennsylvanian evaporite formations (Chan *et al.*, 2000). The 3.7 to 3.8 ‰ variation in $\delta^{18}\text{O}$ observed here would imply an ~20°C variation in temperature over the course of precipitation if carbonate formed from an invariant, unfractionated fluid source. This range of temperature during deposition of calcite is unlikely. Additionally, the correlated trends in $\delta^{13}\text{C}$ and $\delta^{18}\text{O}$ does not follow that predicted for isotopic variation due to varying precipitation temperatures. The heavy $\delta^{18}\text{O}$ implies precipitation from a fluid enriched in ^{18}O . This is interpreted as reflecting precipitation from a fluid composed of a mixture of meteoric water and saline fluid derived from Pennsylvanian evaporite formations, but containing higher contributions of brine than observed elsewhere in the Paradox Basin.

$^{87}\text{Sr}/^{86}\text{Sr}$ of calcite and gypsum veins is radiogenic, and significantly more so than bleaching related hematite concretions from the Moab fault region (Chan *et al.*, 2000), Paradox Formation brines (Spangler *et al.*, 1996) or diagenetic cements origination from extremely brine enriched fluids (Breit *et al.*, 1990) (Fig. 5.3-10). $^{87}\text{Sr}/^{86}\text{Sr}$ is close to, but marginally less radiogenic than, carbonate cements associated with the ancient CO_2 system but overlaps with the range in $^{87}\text{Sr}/^{86}\text{Sr}$ observed in modern CO_2 -charged waters. The radiogenic $^{87}\text{Sr}/^{86}\text{Sr}$ suggests significant contributions of ^{87}Sr suggesting the role of a reactive fluid, enriched in H^+ , capable of dissolving significant quantities of silicate minerals in the host aquifer.

$\delta^{13}\text{C}$ of bulk rock bleached samples is on average ~5‰ lighter than the average $\delta^{13}\text{C}$ of carbonate cements associated with ancient travertines (Fig. 5.3-9). The analysed $\delta^{13}\text{C}$ and $\delta^{18}\text{O}$ will be a mechanical mixture of all carbonate phases present in the sample during powdering.

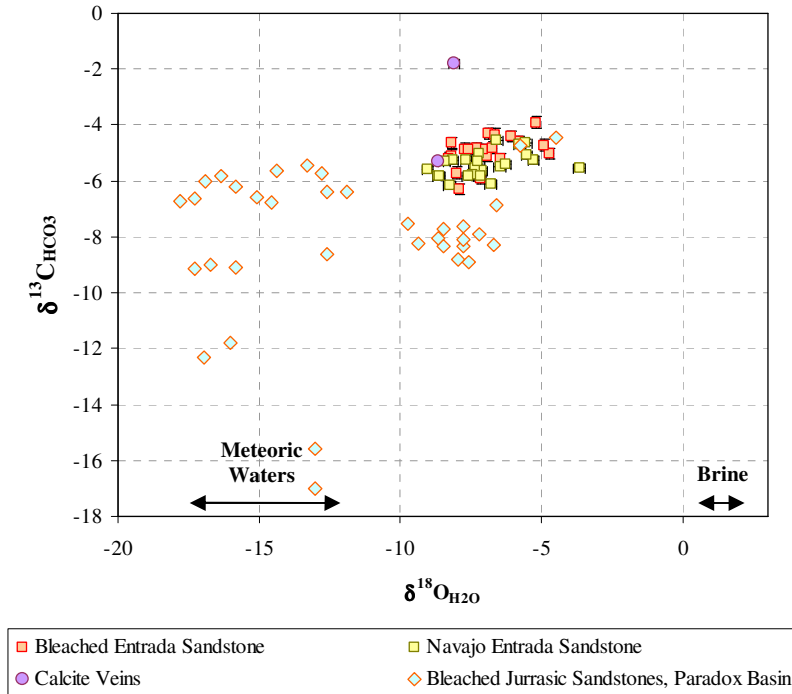


Figure 5.3-11 $\delta^{18}\text{O}_{\text{H}_2\text{O}}$ and $\delta^{13}\text{C}_{\text{HCO}_3}$ calculated from the isotopic composition of bleached Entrada and Navajo Sandstone samples using crystallization temperatures determined in section 5.1.13, uncorrected for dolomite.

The linear correlation in $\delta^{13}\text{C}$ and $\delta^{18}\text{O}$ passes through the composition of samples that contain only sabkha dolomite cements suggesting that the array in $\delta^{13}\text{C}$ and $\delta^{18}\text{O}$ represents a mixing line between this and an isotopically heavy carbon/oxygen source (Fig. 5.3-9). Dolomite formed at low temperatures (e.g. 25°C) typically should be enriched in ^{18}O by 5-7‰ compared to coexisting calcite (Clark and Fritz, 1997). Therefore the observed isotopic difference between early dolomite and later bleaching related calcite indicates that they were precipitated from different fluids. Due to the mixing of cements during sample preparation, the actual value of $\delta^{13}\text{C}$ and $\delta^{18}\text{O}$ of the calcite cements will be heavier than the bulk values measured. Recalculation of the precise $\delta^{13}\text{C}$ and $\delta^{18}\text{O}$ of individual samples is difficult without having bulk rock chemical analyses for each sample. However, point counted estimates suggest that between 30 to 70% of the C in individual bleached samples is derived from early dolomite cements. This implies that the average $\delta^{13}\text{C}$ of measured calcite is between -1.7‰ and +1.8‰ as apposed to the average measured bulk rock value of -2.5‰.

Secondary carbonate minerals forming in the presence of a precursor carbonate phase will derive ^{13}C and ^{12}C from the partial recrystallization of the precursor and from the addition of C from the pore fluid HCO_3^- reservoir. Carbonate volumes (up to ~ 20 vol. %) significantly in excess of those observed in samples containing only early diagenetic

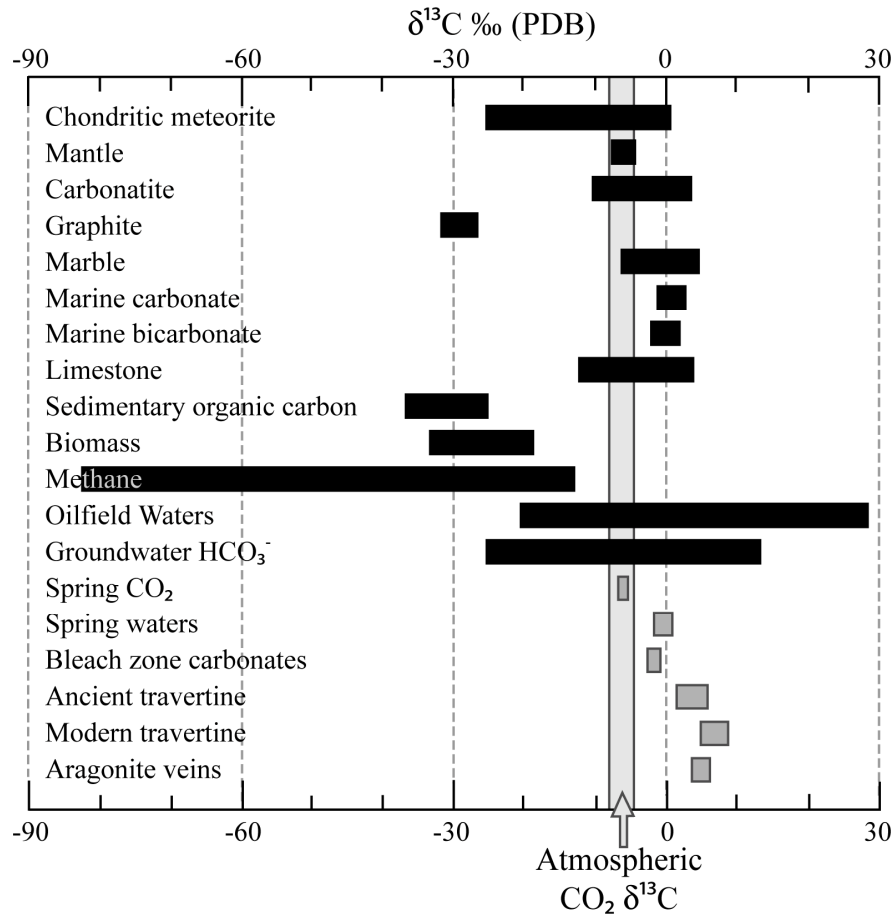


Figure 5.3-12 $\delta^{13}\text{C}$ of $\text{CO}_2(\text{g})$ and fluid from the modern CO_2 charged waters, carbonate cements in large-scale bleached zones, ancient and modern travertine and aragonite veins compare to the range of $\delta^{13}\text{C}$ in various geological environments and substances.

cements (up to ~10 vol. %) suggests significant addition of HCO_3^- from an external C reservoir. These distinct C sources are interpreted as being dolomite cement, observed in unaltered samples of both sandstones, related to early diagenetic sabkha deposits and an isotopically heavy source of C and O related to the bleaching fluid.

In this instance likely extra-formational carbon sources, for carbonate cementation during sediment exhumation, include bicarbonate produced from the transformation of organic matter during hydrocarbon generation (Battani *et al.*, 2000; Butala *et al.*, 2000), or geogenic CO_2 sourced from decarbonation reactions involving clay-carbonate mineral diagenetic reactions in deeper formations (Chapter 2, section 2.4.3). Calcite precipitated from the breakdown of hydrocarbon has $\delta^{13}\text{C}_{\text{CaCO}_3}$ values as low as -20‰ (Tucker and Wright, 1996; Wood and Boles, 1991) and are typically in the range -20 to -10‰. Diagenetic and metamorphic CO_2 would have about the same $\delta^{13}\text{C}_{\text{CO}_2(\text{g})}$ as the carbonate mineral source because fractionation is only about ~1‰ at 150°C (Friedman and O’Neil, 1977). It is therefore unlikely, but not impossible, that this ^{13}C enriched HCO_3^- arose from hydrocarbon breakdown. Early $\delta^{13}\text{C}_{\text{HCO}_3^-}$ in the ancient CO_2 system

was certainly as light as 1‰ (Chapter 4, section 4.4.8), may have had values as low as -0.7‰ (Chapter 4, section 4.4.9) and has certainly evolved from lighter to heavier $\delta^{13}\text{C}_{\text{HCO}_3}$ through time. $\delta^{13}\text{C}_{\text{HCO}_3}$ calculated from the $\delta^{13}\text{C}_{\text{CaCO}_3}$, corrected for C derived from dolomite, for samples from which point count estimates of dolomite/calcite is available, have values between ~ -3.52 to -0.56 ‰. Which is lighter than the $\delta^{13}\text{C}_{\text{HCO}_3}$ in modern and ancient CO_2 systems, but not only moderately so. The heavy $\delta^{13}\text{C}$ may therefore have arisen from crustally sourced, unfractionated CO_2 and/or from a mixture of CO_2 and a lighter, hydrocarbon C source, although this cannot be conclusively confirmed from C-isotopes alone.

5.1.11. Fluid Inclusion Petrography

Fluid inclusions examined in this study occur in aragonite, calcite, gypsum, and in quartz overgrowths surrounding detrital quartz grains. Most of the fluid inclusions examined in this study are found in aragonite (Fig. 5.3-13) and gypsum (Fig. 5.3-14) crystals and in healed microfractures within, and quartz overgrowths surrounding, detrital quartz grains (Fig. 5.3-15). Only quartz overgrowths possessing a clear petrographic link to, and contemporaneous timing with, the overall diagenetic assemblage and event of interest were analysed. Petrographic criteria for the acceptance of a genetic link between quartz overgrowth and other diagenetic phases include i) the observation of intergrowths or solid inclusions of the other diagenetic phases of interest within quartz ii) a consistent vapour/liquid ratio between inclusions in overgrowths and other cements. Necking-down or stretching textures were observed and avoided. Primary and secondary inclusions were distinguished by their relationships to crystallographic surfaces and microfractures, respectively.

Primary inclusions within aragonite crystals (Fig. 5.3-13) are typically small (1-5 μm), single or two phase (aqueous liquid \pm vapour), ovoid and occur in dense clusters along growth and cleavage planes (A1 type) (e.g. Fig. 5.3-13A-F). Larger type A1 inclusions (10-20 μm) typically have a subhedral to euhedral negative crystal shape (e.g. Fig. 5.3-13F). Primary fluid inclusions in aragonite also occur at impinging crystal boundaries (type A2), where they typically trap both aqueous and hydrocarbon liquids (e.g. Fig. 5.3-13B,E,F) and occur as single (aqueous or hydrocarbon), two (aqueous and/or hydrocarbon and/or vapour) or three phase inclusions (aqueous, liquid hydrocarbon and vapour). Curvilinear arrays of secondary fluid inclusions also occur along healed microfractures (A3 type) (e.g. Fig. 5.3-13B,C).

Gypsum crystals (Fig. 5.3-14) contain a variety of primary inclusion types, ranging from clusters of small equant inclusions (1-5 μm) along growth and cleavage planes (type G1), to larger irregular inclusions (8-20 μm) along growth planes and between impinging crystal boundaries (type G2).

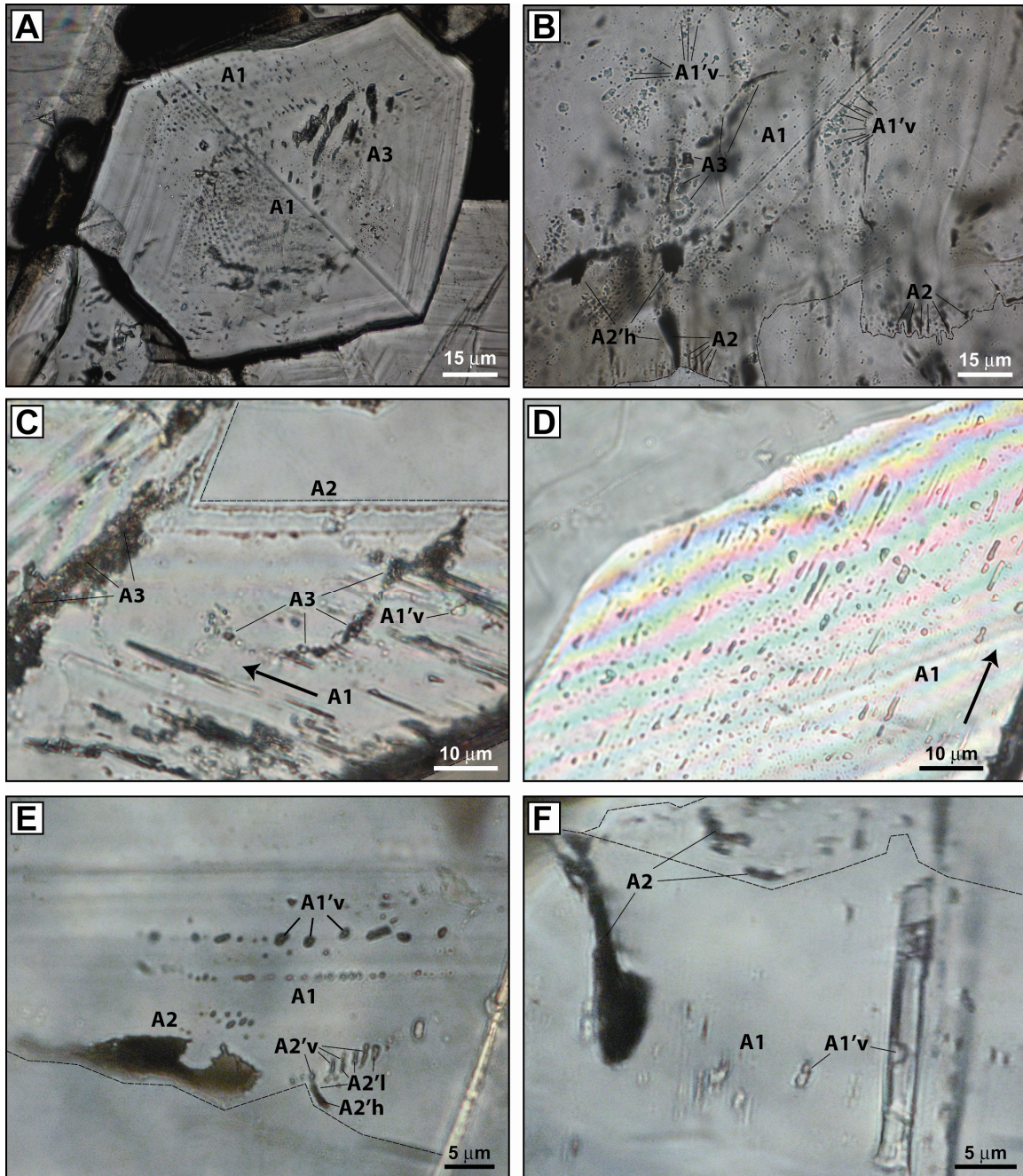


Figure 5.3-13 Photomicrographs illustrating the various primary and secondary fluid inclusions types observed in aragonite crystals from vein and matrix samples of the Entrada Sandstone, Salt Wash graben, Green River.

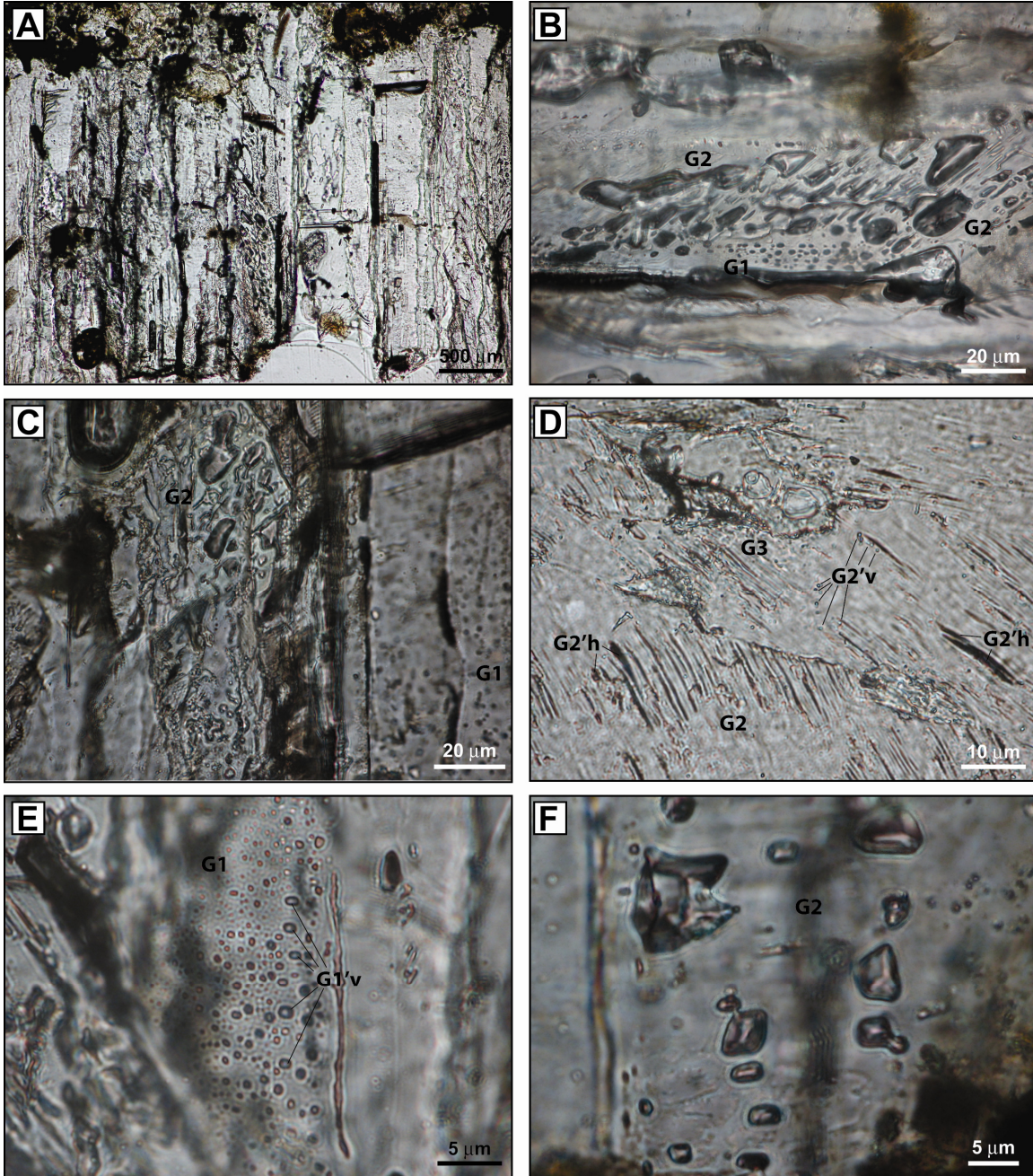


Figure 5.3-14. Photomicrographs illustrating the various primary and secondary fluid inclusions types observed in gypsum crystals from vein samples of the Entrada Sandstone, Salt Wash graben, Green River.

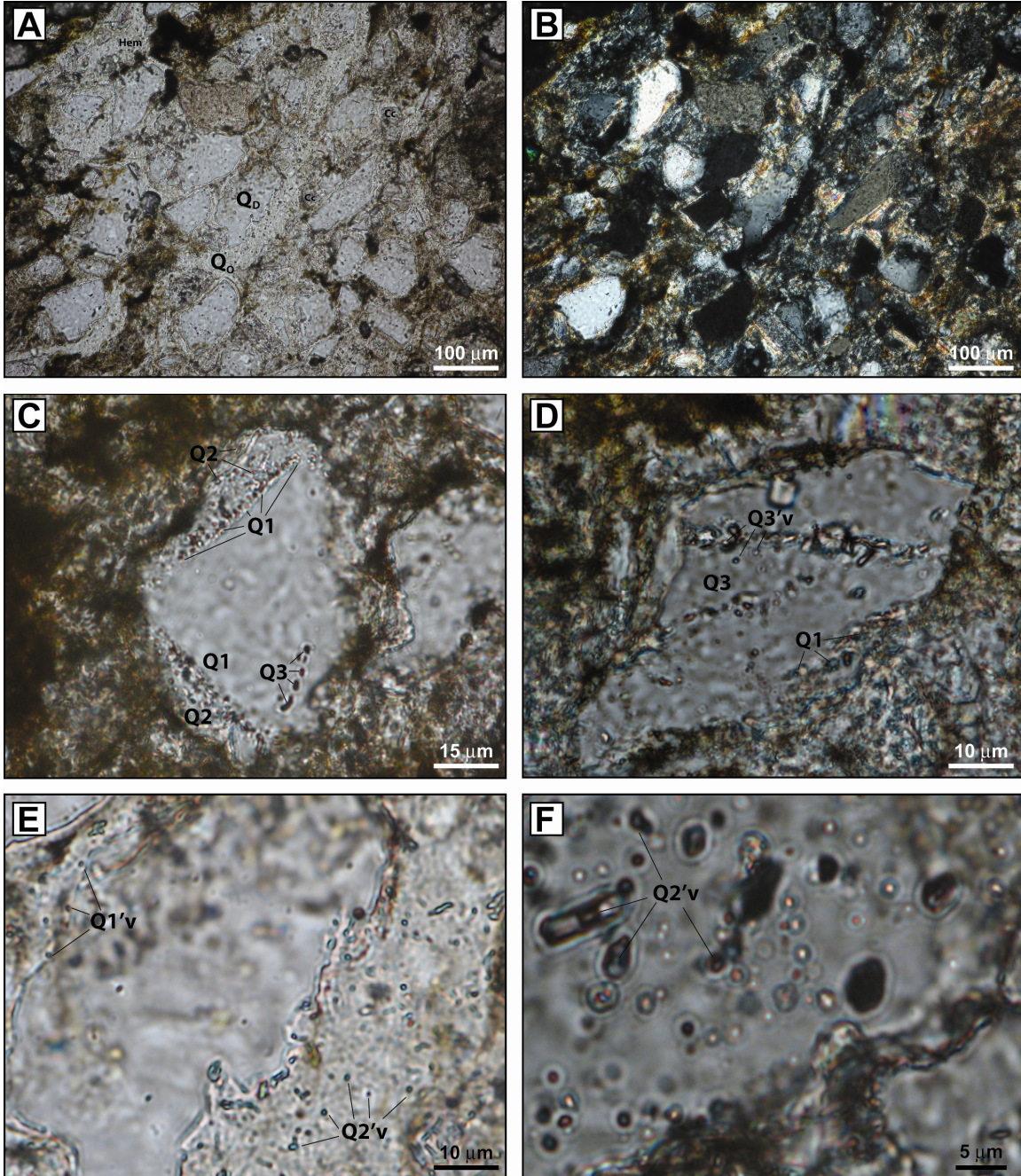


Figure 5.3-15. Photomicrographs illustrating the various primary and secondary fluid inclusions types observed in quartz crystals from vein and matrix samples of the Entrada Sandstone, Salt Wash graben, Green River.

Small (2-8 μ m), primary fluid inclusions within quartz overgrowths (Fig. 5.3-15) are found on the boundary between detrital grains and overgrowths (type Q1) and, less commonly, within the overgrowths themselves (type Q2). Most primary fluid inclusions show a subhedral to euhedral negative crystal shape. Curvilinear arrays of small (2-6 μ m), secondary fluid inclusions also occur along healed microfractures (Q3 type).

5.1.12. Raman Spectroscopy

The optical properties of fluid inclusions that are ‘ideal’ for Raman analysis are the same as those that are desirable for microthermometric analysis, i.e., high optical clarity, sufficient size ($> 5 \mu\text{m}$ desirable), and shallow depth below the sample surface. The chosen inclusions are generally between 2 to 15 μm in size. They occur in clusters or have an isolated occurrence. All the fluid inclusions which were examined by LRM spectroscopy contain two phases, liquid and vapour at room temperature. The vapour phase volume ranges from ~ 2 to $\sim 15\%$. Inclusions sufficiently large to allow reliable LRM analysis on their vapour bubbles proved difficult to find. Due to the small size of inclusions in carbonate minerals and the turbidity of the host, targeting these inclusions for LRM is highly problematic. Due to the close proximity to the homogenization temperature, vibration and Brownian motion of vapour bubbles makes them difficult to target with the laser: movement of vapour bubbles would lead to distorted spectra, with enhanced bands of the volatiles when the bubbles are on target and subdued bands when the bubbles moved off the laser beam.

Over 120 fluid inclusions were examined by LRM in this study. CO_2 and CH_4 were detected as volatiles. It was found that the volatile content varies strongly in these inclusions: some show moderate intensities for the H_2O , CO_2 or CH_4 bands, while others show only weak or no signal. The vast majority of the fluid inclusions analysed contained only H_2O and no other volatile components were detected. This is either because the vapour bubble was not accurately targeted; the volatile content was below the detection limit of the apparatus or the inclusion was devoid of volatile material.

CO_2 was identified in eight fluid inclusions. CO_2 and CH_4 were found to coexist in three. The compositions of volatile species of these fluid inclusions are displayed in Table 5.2. As Fig. 5.3-16 shows, the CO_2 bands can be easily resolved against the bands of the host mineral. Superposition of the two $\nu_1-2\nu_2$ bands of CO_2 on the broad but low quartz bands can be clearly resolved. No other volatiles were found in this fluid inclusion, indicating that the inclusion primarily contains water vapour and CO_2 .

Three inclusions were found to contain CH_4 as a coexisting species. In the vapour phase spectrum (Fig. 5.3-18), for example, the CH_4 band at 2916.5 cm^{-1} is present together with the two $\nu_1-2\nu_2$ bands of CO_2 , highlighting the presence of both CO_2 and CH_4 . The results of the calculations of gas composition, CO_2 and CH_4 gas density, inclusion pressure and formation depth and the dissolved content of CO_2 and CH_4 in the inclusion fluid are presented in Table 5.2. Peak areas used to calculate gas composition were determined from Raman spectra, after baseline correction, using a Gaussian curve fitting algorithm in Origin Pro (version 7.0, OriginLab Corporation, Northampton, MA).

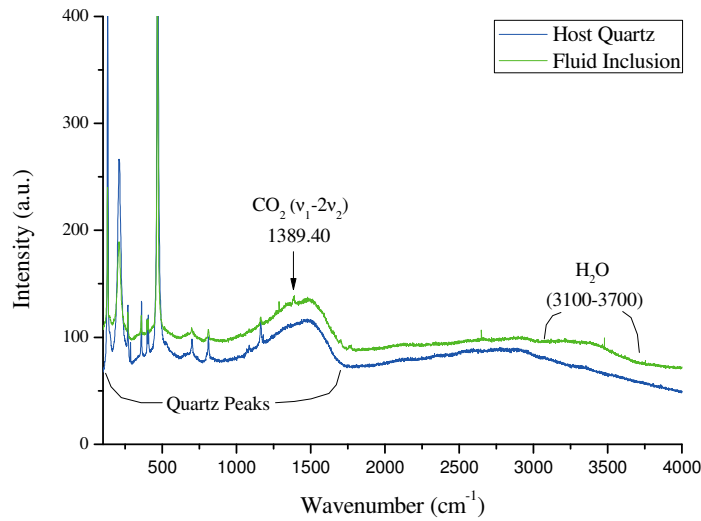


Figure 5.3-16. Raman spectra of the host and the vapour phase of a fluid inclusion in a quartz overgrowth associated with an aragonite bearing sample from the feeder zone of an ancient travertine deposit in the Entrada sandstone, Salt Wash Graben, Green River. The main $\nu_1-2\nu_2$ peak of CO₂ is visible at 1389.40 cm⁻¹. The broad peak 3100-3700 cm⁻¹ corresponds to a weak ν_1 vibration of H₂O vapour.

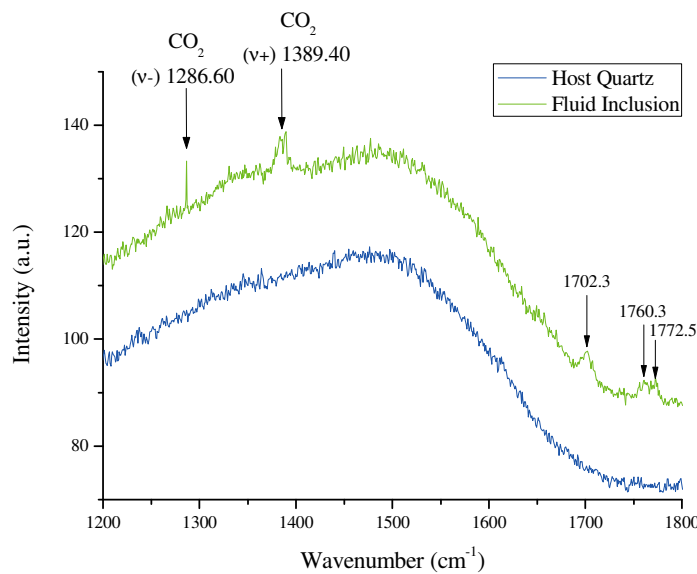


Figure 5.3-17. Close up of the region 1200-1800 cm⁻¹ for the Raman spectra of the host and the vapour phase of a fluid inclusion in a quartz overgrowth associated with an aragonite bearing sample from the feeder zone of an ancient travertine deposit, Salt Wash Graben, Green River. The upper and lower $\nu_1-2\nu_2$ peaks of CO₂ are visible at 1389.40 and 1286.60 cm⁻¹ respectively.

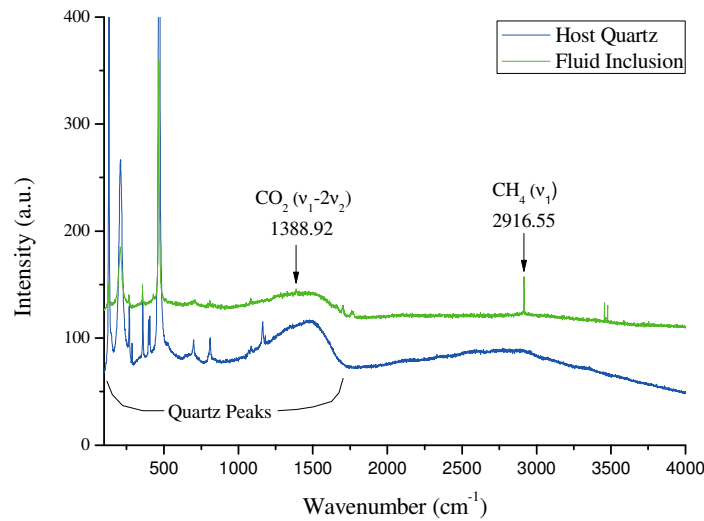


Figure 5.3-18. Raman spectra of the host and the vapour phase of a fluid inclusion in a quartz overgrowth associated with gypsum in a sample from a bleached zone in the Entrada Sandstone, Salt Wash Graben, Green River. The main ν_1 - $2\nu_2$ peak of CO₂ is visible at 1388.92 cm⁻¹. The ν_1 peak of CH₄ is visible at 2916.5 cm⁻¹.

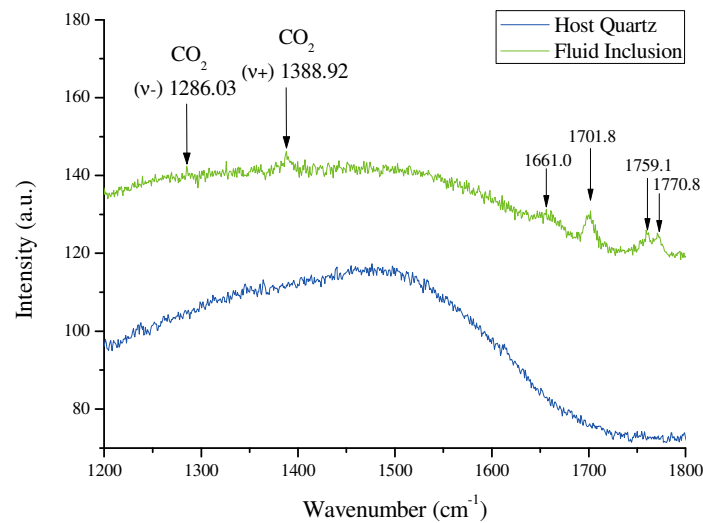


Figure 5.3-19. Close up of the region 1200-1800 cm⁻¹ for the Raman spectra of the host and the vapour phase of a fluid inclusion in a quartz overgrowth associated with gypsum in a sample from a bleached zone in the Entrada Sandstone, Salt Wash Graben, Green River. The upper and lower ν_1 - $2\nu_2$ peaks of CO₂ are visible at 1388.92 and 1286.03 cm⁻¹ respectively.

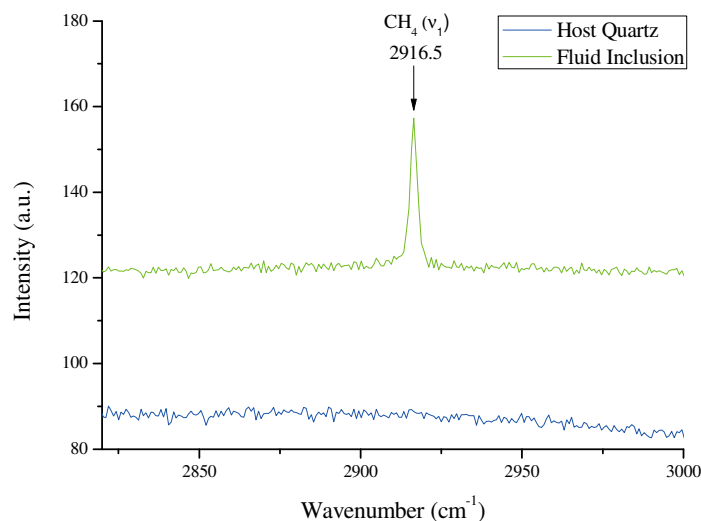


Figure 5.3-20. Close up of the region 2825-3000 cm^{-1} for the Raman spectra of the host and the vapour phase of a fluid inclusion in a quartz overgrowth associated with gypsum in a sample from a bleached zone in the Entrada Sandstone, Salt Wash Graben, Green River. The ν_1 peak of CH_4 is visible at 2916.5 cm^{-1} .

5.1.13. Microthermometry

T_m and T_h of analysed fluid inclusions are displayed in Figs. 5.3-21 and 5.3-22. Fig. 5.3-23 shows T_h and T_m for those fluid inclusions from which both quantities could be analysed. The salinity (in terms of total weight % Na, K, Ca, Mg, Cl, SO_4 and HCO_3) and the emanation temperature of modern CO_2 -spring fluids are included in these figures for comparison. Due to the turbidity of both minerals visual determination of melting point temperature was problematic and T_m could only be determined for $\sim 1/3$ of inclusions examined. The majority of inclusions examined possessed or nucleated a gas bubble upon cooling. Homogenization temperatures were measured on inclusions upon heating, following melting point determination.

Homogenization temperatures and salinity estimates for the two specimens examined fall into distinct clusters (Fig. 5.3-23). Fluid salinities (1.31-2.82 wt% salt) and homogenisation temperatures (16.1-17.5 $^{\circ}\text{C}$) for inclusions in aragonite ($n = 12$) lie within the range of salinity (0.38-1.90 wt% salt) and temperatures (14.7-27.0 $^{\circ}\text{C}$) of modern CO_2 -charged fluids at Green River ($n = 10$). Fluid salinities (2.49-6.95 wt% salt) and homogenisation temperatures (22.1-27.1 $^{\circ}\text{C}$) for inclusions in gypsum ($n = 25$) formed from more saline fluid, at moderately higher formation temperatures.

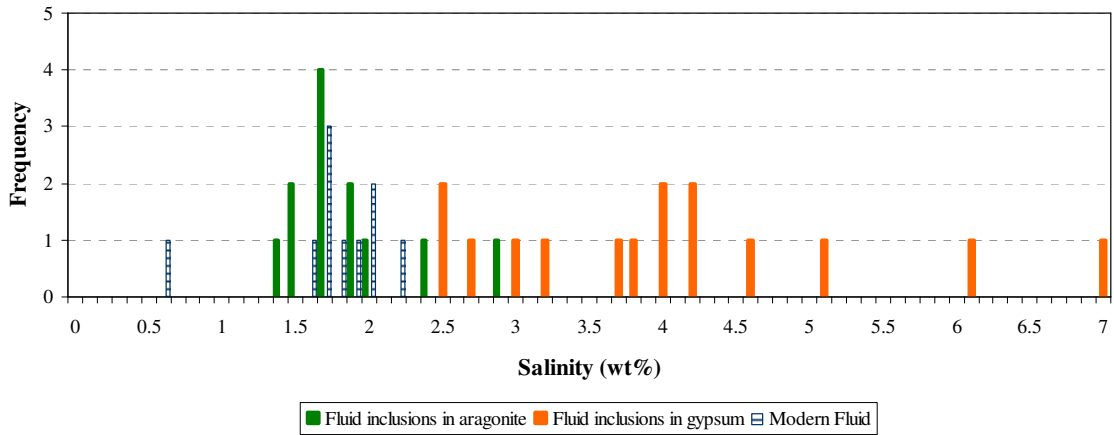


Figure 5.3-21. Fluid salinities, estimated from last ice melting temperatures (T_m), for primary aqueous inclusions in aragonite and gypsum veins from the Entrada Sandstone, Salt Wash Graben, Green River. The salinities of modern CO₂-charged fluids are included for comparison.

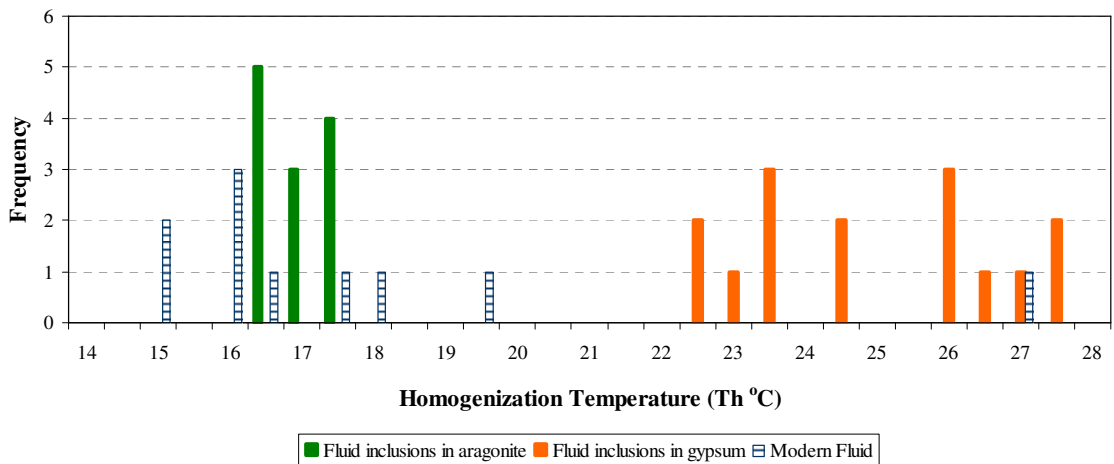


Figure 5.3-22. Homogenization temperatures (T_h) of primary aqueous inclusion in aragonite and gypsum veins from the Entrada Sandstone, Salt Wash Graben, Green River. The emanation temperatures of modern CO₂-charged fluids are included for comparison.

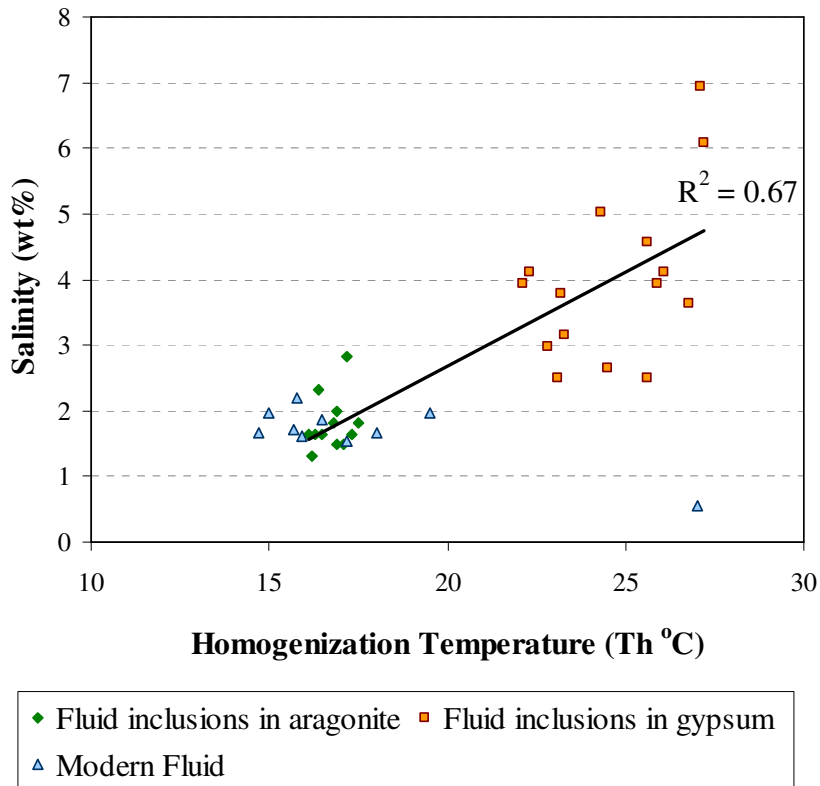


Figure 5.3-23. Fluid salinities versus homogenization temperatures of primary aqueous inclusion in aragonite and gypsum veins from the Entrada Sandstone, Salt Wash Graben, Green River.

5.4. Discussion: Fluid Inclusion Petrology

Aragonite crystals and associated quartz overgrowths contain: i) primary single phase aqueous inclusion of moderate salinity (1.31-2.82 wt% salt); ii) primary two phase inclusions of saline fluid and both pure CO₂ (100 mol% CO₂) and a single inclusion with mixed CO₂ and CH₄ vapour (92 mol% CO₂, 8 mol% CH₄) and; iii) primary inclusions of liquid hydrocarbon, aqueous fluid and vapour (vapour composition could not be determined with LRM due to the fluorescence of the hydrocarbon phase). Homogenisation temperatures (16.1-17.5 °C) and vapour phase densities (0.01-0.05 ±0.02 g/cm³) attest to inclusion at low pressures (0.41-2.49 ±1.03 MPa) at shallow burial depths (29-221 ±97 m) during the most recent periods of basin exhumation. Fluid salinities, entrapment temperatures and dissolved CO₂ concentrations (0.06-0.88 ±0.33 mol/l) for these fluid inclusions fall with the ranges of those quantities observed in the modern CO₂-charged fluids at Green River. This suggests that aragonite and its associated alteration textures formed from a fluid of composition similar to that of the modern CO₂-charged fluids. The brine content of this fluid, based on the measured salinities of the inclusions, would have been within the range of those observed in the modern CO₂-charged fluids or ~1 wt% more saline.

CO₂ was only observed in the vapour phase of a small number of the actual inclusions examined in aragonite bearing samples (4 out of 52 examined). This is thought to be due to difficulties in accurately targeting the vapour phase, the small size of the vapour bubble (typically <1.5 µm) and the very close proximity of the CO₂ concentrations to the theoretical detection limit of LRM.

Gypsum crystals and associated quartz overgrowths examined in this fluid inclusion study are petrologically associated with large-scale diagenetic bleaching of the Entrada Sandstone at the crest of the Green River anticline. Gypsum crystals and associated quartz overgrowths contain: i) primary single phase aqueous inclusion of high salinity (2.49-6.95 wt% salt); ii) primary two phase inclusions of saline fluid and both pure CO₂ (100 mol% CO₂) and mixed CO₂ and CH₄ vapour (88-73 mol% CO₂, 11-27 mol% CH₄) and; iii) primary inclusions of liquid hydrocarbon, aqueous fluid and vapour (vapour composition could not be determined with LRM due to the fluorescence of the hydrocarbon phase). Homogenisation temperatures (22.1-27.1 °C) and vapour phase densities (0.04-0.09 ±0.02 g/cm³) attest to inclusion at higher pressures (2.28-4.56 ±1.03 MPa) and burial depths (202-413 ±97m) than inclusions formed in aragonite associated samples. Based on burial curves for the Entrada Sandstone in the area surrounding Green River (Nuccio and Condon, 1996), modified for local variations in burial depth due to the structural high formed by the Green River anticline, the interval from which these samples were taken passed through the burial depth range 200-400 ±97 m between 2.1-5.5 ±1.5 Ma (Fig 5.4-1).

Fluid salinities, entrapment temperatures and formation pressures suggest that gypsum and the large-scale diagenetic bleaching formed during the latest stages of basin exhumation from a saline fluid enriched in brines derived from the Pennsylvanian evaporite formations. In a plot of homogenization temperature versus fluid salinity (Fig. 5.3-23) values for the two sets of examined fluid inclusions fall along an approximately linear array of increasing fluid salinity with increasing entrapment temperature. Possible explanations for this apparent correlation included i) the transport of 'hot' brine into the Entrada Sandstone ii) a correlation between pore fluid salinity and temperature where increasing temperatures reflect higher burial depths and fluid inclusions of greater age. Given that fluids passively migrating along faults are likely to lose heat through thermal conduction it seems unlikely that basinal brines would carry significant heat into shallower formations. Thus, increasing salinity with increasing entrapment temperature most likely records a decrease in the proportion of Paradox formation brine entering the Entrada sandstone with time.

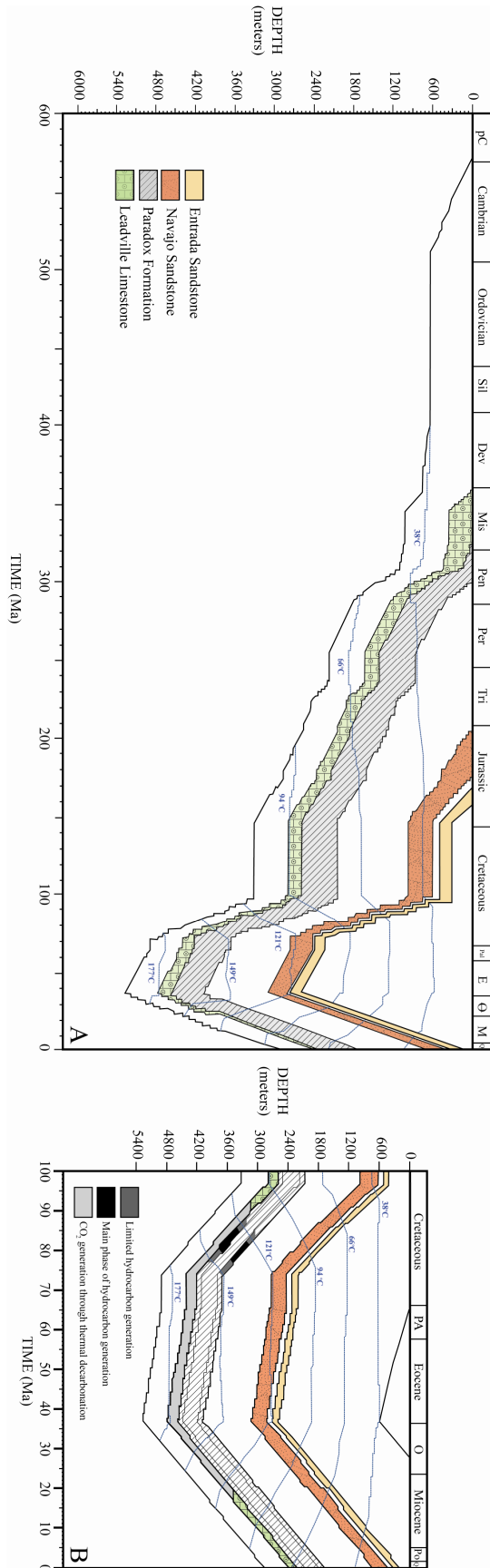


Figure 5-4-1 Burial and thermal model for the Paradox Basin in the vicinity of Green River (after Nuccio and Condon, 1996). A) Cambrian through present. B) Expanded time scale illustrating 100Ma to present.

A number of single, two and three phase hydrocarbon bearing primary fluid inclusions were observed in all the sample types analyzed. CH₄ is present in the vapour phase of three of the primary fluid inclusions; two in gypsum (17-21 mol% CH₄), and one in aragonite (8 mol% CH₄). CH₄ may have been derived from: i) dissolved or free phase gas migrating with the CO₂/brine mixture entering the Entrada Sandstone; ii) exsolved from a liquid hydrocarbon phase that entered the Entrada Sandstone during deep burial; iii) exsolved from a liquid hydrocarbon phase that migrated along with the CO₂/brine mixture; iv) the reduction of CO₂ to form CH₄ via the reaction:



However, this reaction requires elevated temperatures and redox conditions improbable in shallow diagenetic systems (Berndt *et al.*, 1996; Horita and Berndt 1999; McCollom and Seewald 2001). Migration of both liquid hydrocarbons and CH₄, along with a CO₂ bearing free gas phase or CO₂-saturated brine, would be aided by the high solubility of CO₂ in hydrocarbon liquids (e.g. Dehima *et al.*, 1999) and the resulting reduction in oil viscosity: a process akin to natural enhanced oil recovery. Gypsum bearing samples contain a higher proportion of CH₄ bearing inclusions, and the vapour phase of these inclusions contains a higher proportion of CH₄ relative to CO₂ than does the aragonite bearing samples (only a single CH₄ bearing inclusion was observed in aragonite, with low mol% CH₄ relative to CO₂). This general trend of apparently decreasing CH₄ content with time may reflect a flushing of the hydrological system, with hydrocarbon liquids and CH₄ being stripped from the system by CO₂ rich fluids and gases.

CH₄ would be a suitable redox agent for the reduction of Fe³⁺ and dissolution of hematite. However, CH₄ was not observed in all the volatile bearing inclusions, the rest contained only CO₂ and CO₂ is the dominant volatile phase in all volatile bearing inclusions. Reductive dissolution of hematite would be enhanced by pH suppression at high *p*CO₂ and by the overall availability of H⁺ (e.g. Cornell and Giovanoli, 1993). Kinetically rapid dissolution of hematite may explain the sharp nature of the contact between bleached and unbleached sandstone (e.g. Fig. 5.3-2). Additionally, isotopically light HCO₃⁻ derived from the break down of CH₄, mixed with isotopically heavy HCO₃⁻ derived from crustally sourced CO₂ may explain measured values of δ¹³C_{CaCO₃} lighter than those observed in the young leaking CO₂ system (section 5.1.10.3).

The paragenesis of the Entrada Sandstone is presented in figure 5.4-2, which shows the relative timing and duration of diagenesis observed in this study to regional diagenetic episodes and to local and regional geological events. Detrital fragments of locally derived pisolites and travertine have recently been discovered in the fluvial Lower Cretaceous Yellow Cat Member of the Cedar Mountain Formation, at Crystal Geysers Dinosaur Quarry, near Crystal Geysers (Suarez *et al.*, 2007a, 2007b). The similar morphology and mineralogy of these fragments to actively forming travertine at Crystal Geysers led those authors to attributed their formation to CO₂-

charged springs. Additionally, extensive carbonate, Fe-oxide, and silicate alteration, including chemical bleaching of the sediment, at the Temple Mountain uranium district, on the edge of the San Rafael Swell have been attributed to CO₂-charged fluids and dated at ~13Ma (Morrison and Parry, 1988). These finding suggests that CO₂-charged fluids have been leaking from local Green River area for considerably longer periods than is evident from persevered surface travertine deposits and that CO₂-hosting paleo-reservoirs could be expected in now exhumed sandstone formations.

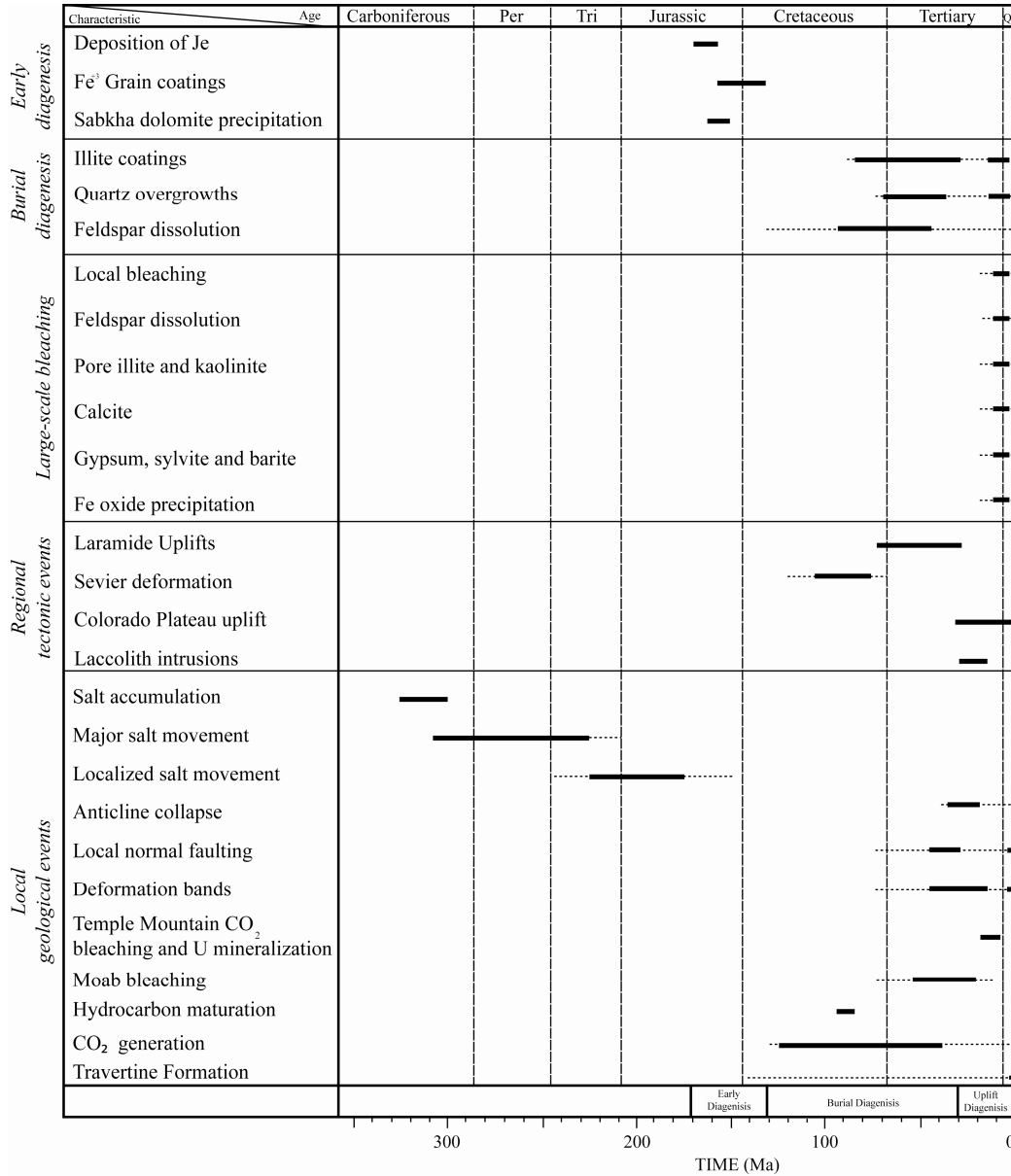


Figure 5.4-2 Paragenesis of the Entrada Sandstone in the vicinity of Green River Interpreted paragenetic relationships of diagenetic alteration and associated geological events constructed from age data of Beitler *et al.*, 2005; Condon, 1997; Dockrill, 2005; Doelling *et al.*, 1988; Morrison and Parry, 1988; McKnight, 1940; Nuccio and Condon, 1996; Suarez *et al.*, 2007a.

5.5. Conclusions

Mineral assemblages in samples from travertine feeder systems contain low salinity aqueous single and two phase primary fluid inclusions and single, two and three phase hydrocarbon bearing primary fluid inclusions. The aqueous fluid contained in these inclusions was trapped at a comparable temperature to, and is of salinity similar to that of modern CO₂ charged fluids escaping along normal faults of the Salt Wash Graben and Little Grand Fault systems. Vapour densities, inclusion pressures and homogenisation temperatures suggest these inclusions formed within the most recent periods of basin exhumation at very shallow burial depths (<200 m). The CO₂ content of these fluid inclusions is similar to that of the modern fluid but ranges to higher concentrations. This may represent the trapping of less CO₂-degassed fluid than that which is seen escaping to the surface today. A single inclusion was observed to contain a low concentration of CH₄ suggesting the intermittent presence of CH₄ in the CO₂-rich gas phase associated with travertine formation.

Mineral assemblages in samples from zones of extensive Fe³⁺ bleaching in the Entrada Sandstone contain primary fluid inclusions of moderately saline aqueous fluid, CO₂ and CH₄ vapour and occasional liquid hydrocarbon bearing two and three phase primary inclusions. Vapour densities, inclusion pressures and homogenisation temperatures attest to the formation of these inclusions at shallow burial depth, during basin exhumation, in the last 2.1-5.5 ±1.5 Ma. Fluid salinities are higher than those observed in modern fluid at Green River which suggests an increased component of Paradox formation brine in these older entrapped fluids in agreement with petrological observations and isotopic evidence presented in section 5.1.10.3. The presence of a CO₂ rich vapour phase with moderate quantities of CH₄ is attributed to mobilization of hydrocarbons and CH₄ by migrating CO₂ bearing fluids and gases. The CH₄ dissolved in this fluid would be a suitable redox agent for the reduction of Fe³⁺ to Fe²⁺, and the high concentrations of CO₂ would significantly enhance the solubility and dissolution rate of hematite by lowering pH and increasing the availability of H⁺.

Sample	Type	Host Mineral	Gas Composition					v_1	ρ_{CH_4}	P_T	Depth	Dissolved CO ₂	Dissolved CH ₄
				$\Delta v_1 - 2v_2$	ρ_{CO_2}	P_{CO_2}	Depth						
					(g/cm ³)	(MPa)	(m)		(g/cm ³)	(MPa)	(m)	(mol/l)	(mol/l)
RS073	B	Quartz	CO ₂ (73%), CH ₄ (27%)	102.89	0.04	2.28	202	2916.50	0.028	3.94	356	1.05	0.36
RS061	B	Gypsum	CO ₂ (89%), CH ₄ (11%)	102.90	0.09	4.56	413	2916.49	0.029	3.98	360	1.30	0.15
RS066	B	Gypsum	CO ₂ (100%)	102.84	0.06	3.32	298					1.18	
RS061	B	Quartz	CO ₂ (100%)	102.81	0.05	2.74	244					0.97	
RS069	Y-B	Quartz	CO ₂ (100%)	102.75	0.03	1.45	125					0.14	
RS069	Y-B	Quartz	CO ₂ (100%)	102.72	0.02	0.83	67					0.29	
RS069	Y-B	Aragonite	CO ₂ (100%)	102.80	0.05	2.49	221					0.88	
RS069	Y-B	Quartz	CO ₂ (92%), CH ₄ (8%)	102.70	0.01	0.41	29	2917.27	0.001	0.17	7	0.06	0.005

Table 5.5-1 Details of the gas composition, gas densities, inclusions pressures, formation depths for the vapour phase of primary fluid inclusions in vein and matrix samples associated with large-scale diagenetic bleaching (B) and bleaching in ancient travertine feeder systems (Y-B) in the Entrada Sandstone, Salt Wash Graben, Green River.

Chapter 6

Discussion and Conclusions

Understanding the geochemical behaviour of anthropogenic carbon dioxide stored in geological reservoirs, over a range of time-scales, is crucial for quantifying the risk of leakage and the evolution of the sequestered form of that CO₂ through the life of an individual storage site. Prediction of the long-term fate of this carbon dioxide requires determination of the relevant gas-fluid-mineral reactions and their chemical kinetics (e.g. Xu *et al.*, 2004). These gas-fluid-mineral reactions may act either to increase the stability of stored CO₂ by precipitating carbonate minerals or enhance leakage by corroding well cements, existing boreholes, cap rocks and fault seals. Modelling the progress of such reactions is frustrated by uncertainties in the absolute mineral surface reaction rates and the significance of other rate-limiting steps in natural systems (see White and Brantley, 2003 for a complete review). It is well established that silicate dissolution rates in the natural environment are typically 2 to 5 orders of magnitude slower than, far-from-equilibrium, laboratory-derived rates at similar pH and temperature conditions (White and Brantley, 2003), and the laboratory rates are typically the only rates available for simulations (e.g. Knauss *et al.*, 2005; White *et al.*, 2005; Xu *et al.*, 2004). Quantification of the kinetics of fluid-mineral reactions in natural systems, rich in CO₂, is thus required for the accurate prediction of the long-term performance of geological storage sites.

This thesis uses the chemical evolution of groundwater from the Jurassic Navajo Sandstone, part of a leaking natural accumulation of CO₂ at Green River, Utah, in the Colorado Plateau, USA, to place constraints on the rates and potential controlling mechanisms of the mineral-fluid reactions, under elevated CO₂ pressures, in a natural system. Surface carbonate deposits and cementation within the footwall of the local fault systems record multiple injections of CO₂ into the Navajo Aquifer and leakage of CO₂ from the site over ca. 400,000 years. Geochemical and petrological methods are employed to examine the mineralogical consequences of this fluid-mineral interaction. The stable and radiogenic isotopic composition of these deposits are examined and used to interpret the physical and chemical processes controlling the long-term leakage of CO₂ from the underlying Navajo Aquifer. Additionally, large scale zones of mineralization and mineralogical alteration in the overlying Entrada Sandstone are examined; the role of CO₂ and other volatile phases (e.g. CH₄, H₂S, organic acids) in the production of this alteration is investigated using petrographic techniques and the analysis of volatile bearing, mineral hosted fluid inclusions. The key findings of this thesis are summarized below.

6.1. Carbon Storage Site Analogue, Green River, Utah

6.1.1. Summary of the CO₂-charged Groundwater Hydrogeochemistry

Crustally sourced CO₂, produced from diagenetic reactions in the Leadville Limestone, at depth within the Paradox Basin, migrates vertically through the stratigraphy mixing with and dissolving into basinal brines of the Paradox Formation. These CO₂-charged brines migrate along the Little Grand and Salt Wash fault systems into the shallow White Rim and Navajo Aquifers where they mix with meteorically derived groundwaters, flowing along hydraulic gradients from zones of recharge in the San Rafael Swell to zones of discharge near the confluence of the Green and Colorado Rivers. This passive migration of CO₂ is analogous to leakage of a deep geological CO₂ reservoir into shallower aquifer systems. CO₂ leaks to the surface through the fault damage zone of the Little Grand and Salt Wash fault systems and through a number of abandoned petroleum exploration wells.

Time-series analysis of the fluid isogeochemistry from the largest of these leakage sites, Crystal Geyser, has provided important insights into the plumbing of fault leakage and the role of CO₂-driven cold water geysering in stimulating and enhancing CO₂ leakage rates. Cold water geysering of Crystal Geyser, driven by CO₂-degassing, causes pressure depletion in the Navajo Aquifer. This stimulates influx of CO₂-charged brines from deeper formations, most likely from the White Rim Sandstone, on the time-scale of the geysering events, which mix with chemically distinct fluids in the host aquifer. The physical process of CO₂ gas-driven geysering is therefore an important mechanism for the stimulation of vertical fluid and gas migration in the subsurface and will be important for prolonging effusion from leaking wells in CO₂ storage sites. Estimates of the average annual CO₂ emissions from Crystal Geyser range from 5694 ± 1708 t/a to 12702 ± 3810 t/a. Combining these with estimates of the annual fluid flux results in average CO₂ concentrations of ~ 4 to 10 mol L⁻¹, greatly exceeding the maximum solubility of CO₂ in the Navajo Aquifer. This strongly implies that CO₂, in addition to brine, is imbibed through the Little Grand fault as a consequence of the geysering process and is added to the Navajo Aquifer close to the site of Crystal Geyser.

CO₂ entering the Navajo Sandstone groundwater system dissolves into the formation water, suppressing pH and mineral saturation in the fluid promoting dissolution of silicate and carbonate minerals in the host aquifer. The introduction of this CO₂ increases the fluids capacity to accept dissolved solids by lowering the pH and the saturation state of the groundwater, enhancing mineral dissolution. As a result, the CO₂-rich groundwaters evolve towards very high solute concentrations after prolonged water-rock interaction. In geological CO₂ storage sites this

processes will ultimately enhance the fluids capacity to accept dissolved CO₂, through ionic complexation, thereby enhancing solubility trapping.

The groundwater chemistry is controlled by a mix of kinetically rapid, equilibrated mineral-fluid reactions and disequilibrated reactions where the mineral surface dissolution kinetics are slow or the saturation state of the reacting phase is controlled by an additional rate limiting step. The dominant controlling reactions are the dissolution of plagioclase (An₃₈) and K-feldspar which result in increasing concentrations of Na⁺, K⁺ and Al³⁺ as the groundwaters evolve. These phases, in addition to quartz, dominate the mineralogy of the Navajo Sandstone. With progressive flow through the aquifer, feldspar hydrolysis reactions consume H⁺ and liberate solutes to solution which increase mineral saturation in the fluid. The concentration of dissolved silica, derived from the dissolution of silicate minerals, is controlled by equilibrium with an amorphous silica phase. Kaolinite and smectite are the dominant stable clay minerals and reaction products of feldspar dissolution. Equilibrium with silica maintains most groundwater samples within the kaolinite stability field. Because *a*SiO₂(aq) is fixed by the precipitation of an amorphous silica phase, kaolinite will not regulate the dissolved Al³⁺ concentration (Deutsch, 1997) and its concentration will be regulated by the dissolution of silicate minerals.

The fault damage zones of the Little Grand fault and Salt Wash Graben are altered and cemented by the passage of CO₂-charged fluids. Feldspar grains show evidence of extensive corrosion and reprecipitation of silica, smectite and kaolinite on grain surfaces and within the local pore volume. Feldspar grains continue to dissolve even when coated with up to 10µm surface coatings of inter-grown clay minerals, suggesting the maintenance of porosity within the surface coating. This adds to the evidence that the presence of such a coating does not inhibit dissolution at the mineral surface.

6.1.2. Fluid-Mineral Reaction Kinetics

Silicate Mineral Dissolution

Using the evolution of the CO₂-charged groundwater chemistry along defined flow paths the kinetics of the dissolution reactions controlling groundwater chemistry was investigated. The progress of individual reactions, inferred from changes in groundwater chemistry was modelled using mass balance techniques. The mineral reactions are close to stoichiometric with plagioclase and K-feldspar dissolution largely balanced by precipitation of clay minerals and carbonate. Mineral modes, in conjunction with published surface area measurements and flow rates estimated from hydraulic head measurements, are then used to quantify the kinetics of feldspar dissolution. The close to equilibrium plagioclase dissolution rates derived from mass balance and hydrological modelling range from $10^{-13.74 \pm 0.11/0.15} \text{ mol}\cdot\text{m}^{-2}\cdot\text{s}^{-1}$ to $10^{-18.63 \pm 0.6/1.5} \text{ mol}\cdot\text{m}^{-2}\cdot\text{s}^{-1}$. K-feldspar dissolution rates range from $10^{-15.45 \pm 0.08/0.09} \text{ mol}\cdot\text{m}^{-2}\cdot\text{s}^{-1}$ to $10^{-17.42 - 0.27/0.81} \text{ mol}\cdot\text{m}^{-2}\cdot\text{s}^{-1}$. These

rates are 1 to 3 orders of magnitude slower than rates determined by laboratory experiments at similar temperatures and pH, and 1 to 3 orders of magnitude faster than rates determined in the same aquifer under alkaline groundwater conditions. The enhancement of feldspar dissolution rates in this study area, relative to those determined by Zhu (2005) for alkaline groundwater, is attributed to the introduction of CO₂ which depresses silicate mineral saturation in the fluids. The finding that the Green River system is close to thermodynamic saturation adds to the evidence that the 2–5 orders of magnitude discrepancy between laboratory and field rates may, in part, be explained by differences in the thermodynamic state of experimental and natural fluids (c.f. Burch *et al.*, 1993; White and Brantley, 2003).

The range of rates and the rate:Δ*G_r* dependence observed at Green River suggest that feldspar dissolution rate laws should include exponentially declining rates close to equilibrium (Δ*G_r* < -10kJ/mol), over a wider range (and slower absolute values) of dissolution rate than previously suggested by experimental studies. These findings suggest that mineral-fluid reactions in CO₂ hosting reservoirs will be promoted by the state of disequilibrium induced by the introduction of CO₂ and highlight the importance of including a rate:Δ*G_r* dependence in the geochemical modelling of the long term interactions of CO₂-fluid-rock in geological storage reservoirs. This suggests that in the earliest stages of CO₂ injection in storage sites systems can be expected to be highly undersaturated with respect to minerals comprising the host reservoir and reaction rates will be fast, occurring at low Δ*G_r*.

Carbonate Precipitation Kinetics in CO₂-leaking Faults

The fault damage zones of Little Grand fault and Salt Wash Graben are heavily veined and cemented with carbonate where CO₂-charged fluids ascend to the surface, degassing CO₂ which drives carbonate supersaturation in the fluid. The precipitation of carbonate in CO₂ leaking faults has important implications for the long term performance of these leakage conduits as carbonate precipitation may eventual block leakage pathways. The kinetics of calcite precipitation were quantified by measuring the concentrations of trace elements known to exhibit a kinetically dependent liquid-solid partitioning. Sr concentrations in calcite cements within the fault damage zone record mean calcite precipitation rates of 1.3x10⁻⁶ to 2.1x10⁻⁶ mol/m²/s, comparable to laboratory derived calcite precipitation rates, in fluids with moderate Mn/Ca and Fe/Ca, at Ω_{cc} of ~1 to 3. The overall variation in rate is large, from ~1x10⁻⁹ to ~1x10⁻⁵ mol/m²/s, probably reflecting both variation in the intrinsic rate and variation in the Sr/Ca of the parent fluid. This suggests that far-from-equilibrium carbonate precipitation, which blocks fracture conduits and causes the leaking system to self-seal, driven by CO₂ degassing in the shallow subsurface, can be accurately modeled with laboratory derived rates.

The continued study of fluid-rock interactions in natural settings may help further elucidate the relationship between rate and ΔG_r for a range of mineral phases, in the close-to-equilibrium region which is so difficult to assess experimentally. These results must be tempered with the understanding that large uncertainties exist in the quantification of modelling parameters in natural settings, especially reactive mineral surface area, indirect sampling of reservoir fluids and the hydro-geological setting. The long duration of reaction accessible in natural studies, whilst allowing access to controlling factors of real mineral weathering such as near equilibrium rate dependence, also introduces uncertainty as many model parameters may change through the duration of the 'experiment'. The change in porosity and reacting mineral surface through the duration of the natural experiment cannot easily be factored into the calculation of the controlling rates. Heterogeneity in reservoir hydraulic properties, mineralogy and fluid chemistry also lead to uncertainty in the calculation of rates.

Heavy Metal Mobilization in CO₂-rich Fluids

The modern CO₂-charged groundwaters contain high quantities of dissolved Fe²⁺ and Mn²⁺. Superposition of Eh, pH and $a_{\text{Fe}^{2+}}$ suggests that the redox state of the fluid is controlled by low oxygen fugacity and fixed by the Fe³⁺/Fe²⁺ redox couple through equilibration with hematite. This has important implications for the mobilization and transport of metals in CO₂ storage sites and is analogous to iron mobilization processes recently observed at the Frio test CO₂-injection site (Hovorka *et al.*, 2006; Karaka *et al.*, 2006; Smyth *et al.*, 2009). This suggests that, even in the absence of an additional reductant, deep O₂-depleted groundwaters in CO₂ storage sites will derive high metal concentrations from the pH suppression induced by large quantities of dissolved CO₂.

The fault damage zones of the Little Grand fault and Salt Wash Graben are altered and cemented by the passage of CO₂-charged fluids. This alteration includes dissolution and remobilization of pre-existing Fe-oxide grain coatings, which bleaches the sediment from a distinctive ochre red to pale yellows and white at scales of mm's to cm's. High Mn and Fe concentrations are observed in fracture and host rock calcite cements within the mineralized portions of the damage zone. These cements record elevated Mn²⁺ and Fe²⁺ concentrations in the ancient CO₂-charged groundwaters. The measured Fe and Mn concentrations were combined with equilibrium modelling techniques to derive groundwater Eh (30 to -50 mV) and pH (5.5 to 6.5) conditions. These ancient groundwater compositions are comparable to the Eh-pH conditions of the modern CO₂-charged groundwaters. This finding, together with hematite solubility modelling and field and petrographic observations of extensive dissolution of hematite grain coatings and Fe-oxide reprecipitation, suggests that CO₂-charged fluids alone are capable of dissolving and mobilizing Fe in these sediments. However, the precise control on Eh is uncertain.

Equilibrium redox potentials for the SO_4^{2-} - H_2S and CO_2 - CH_4 redox couples are in the region of 0 to -200 mV and -200 to -500mV, respectively (Drever, 1997). The calculated Eh values are generally higher than those expected for redox potentials controlled by either SO_4^{2-} - H_2S or CO_2 - CH_4 equilibrium. The range of values obtained is more comparable to redox potentials observed in groundwaters with low O-fugacity (e.g. White *et al.*, 1990).

Analogous km-scale sandstone bleaching of the Entrada Sandstone is observed at the apex of the Green River anticline. Mineral assemblages in samples from zones of extensive Fe^{3+} bleaching in the Entrada Sandstone contain primary fluid inclusions of moderately saline aqueous fluid, CO_2 and CH_4 vapour and occasional liquid hydrocarbon bearing two and three phase primary inclusions. Vapour densities, inclusion pressures and homogenisation temperatures attest to the formation of these inclusions at shallow burial depth, during basin exhumation, in the last 2.1-5.5 \pm 1.5 Ma. The presence of a CO_2 -rich vapour phase with moderate quantities of CH_4 is attributed to mobilization of hydrocarbons and CH_4 by migrating CO_2 bearing fluids and gases. The CH_4 dissolved in this fluid would be a suitable redox agent for the reduction of Fe^{3+} to Fe^{2+} , and the high concentrations of CO_2 would significantly enhance the solubility and dissolution rate of hematite by lowering pH and increasing the availability of H^+ .

CO_2 has played an important role in the dissolution and mobilization of metal oxides in all of these sandstone aquifer systems. This has important implications for trace and heavy metal mobilization in CO_2 storage sites as solubilisation of heavy metal bearing minerals in shallow groundwater systems is of concern for the contamination of potable water sources (e.g. Wang and Jaffe, 2004). Further work on understanding the kinetics of these reactions, and their coupling to advective and diffusive fluid transport process, is of critical importance to the accurate prediction of the performance of CO_2 storage sites.

6.1.3. CO_2 Leakage from Fault Systems

Ancient surface travertine deposits along the trace of the Little Grand fault and Salt Wash Graben and carbonate veining within the fault damage zones record leakage of CO_2 from the Navajo Sandstone over a ca 400,000 year period (Burnside, 2009). CO_2 leakage initiated at ca 413 ka from Salt Wash Graben and at ca 114 ka from Little Grand Fault (Burnside, 2009). Temporal variation in the $\delta^{18}\text{O}_{\text{CaCO}_3}$ and $\delta^{13}\text{C}_{\text{CaCO}_3}$ of these deposits reflects multiple injections of CO_2 into the underlying Navajo Sandstone from deeper formations, at 10,000's year intervals. These new pulses of CO_2 are enriched in ^{12}C and ^{16}O , dissolving to form $\text{HCO}_3^-(\text{aq})$ with a light stable isotopic composition, which is inherited by the daughter carbonate precipitates. Following the injection of individual CO_2 pulses, leakage and CO_2 degassing drives a progressive Rayleigh distillation of the $\text{HCO}_3^-(\text{aq})$ reservoir and the precipitating carbonate becomes increasingly enriched in ^{13}C and ^{18}O as a consequence. Kinetic fractionation of $\text{HCO}_3^-(\text{aq})$ during these periods

implies rapid rates of CO₂ degassing and carbonate precipitation, faster than the HCO₃⁻-H₂O equilibration reaction which operates on the 1000's to 10000's sec time-scale (Hendy, 1971). Periods of progressive isotopic fractionation correlate with periods of rapid surface travertine accumulation. The linear variation in δ¹⁸O_{CaCO₃} and δ¹³C_{CaCO₃} with time reflects constant rates of CO₂ degassing over 10's kyrs. Correlations in δ¹⁸O_{CaCO₃} and δ¹³C_{CaCO₃}, kinetic fractionation of the HCO₃⁻(aq) reservoir, the volume and rate of surface travertine formation and its spatial and temporal distribution suggest that initially leakage: a) occurred rapidly and at a constant rate, b) was localised at the anticline crest and c) occurred from a reservoir fluid saturated in CO₂, coexisting with a free-gas phase. A sharp inflection in leakage rate and an approximately concurrent cessation in kinetic fraction of the HCO₃⁻(aq) reservoir are interpreted to reflect depletion of the saturated CO₂ and a return to undersaturated conditions, after ~75ka of leakage. During this time leakage sites propagated laterally along the length of the fault trace as fracture conduits were blocked by carbonate deposition and new leakage pathways were exploited and opened by mineral-fluid reactions. Fracture blocking rates increased as the CO₂ charge dissipated, *p*CO₂ in the aquifer fell and the fluids became increasingly oversaturated in carbonate.

Whilst the cumulative CO₂ loss from both Little Grand Fault and Salt Wash Graben are of the same order of magnitude (~1x10⁷ tonnes CO₂), the time required to deplete the initial CO₂-charge to a state of CO₂-undersaturation (~8 ka versus ~75 ka), and leakage rates during this period (~927 t/a versus ~164 t/a), vary by an order of magnitude between the two fault systems. These leakage rates are also an order of magnitude slower than rates calculated for Crystal Geysers which range between 5694 ± 1708 t/a to 12702 ± 3810 t/a, depending upon assumptions about eruption frequency. Differences in leakage rates between the two fault systems is attributed primarily to intrinsic difference in the fault architecture and properties of the fault damage zone, including the shale gouge ratio and degree of reservoir-reservoir juxtaposition. However, the depth of the host reservoir, and thus maximum in-situ *p*CO₂, imposes difference in the fracture blocking rate in each fault which may impact the overall leakage rates. In addition the hydraulic properties of shallow lithologies appear to be important in controlling leakage rates where permeable formations allow migration of CO₂-charged fluids away from the fault damage zone, prolonging the fluid ascent time, enhancing CO₂ degassing in the shallow subsurface and promoting carbonate deposition and fracture blocking. This highlights the importance of accurately modelling the fault surface, damaged zone, shallow lithological properties and regional hydraulic gradients when modelling leakage from CO₂ storage sites. The findings suggest that in geological storage sites fault controlled CO₂ leakage rates from shallow CO₂ saturated fluids will be slow (relative to CO₂ emission rates from anthropogenic sources) and fracture conduits will seal through carbonate precipitation impeding leakage, but that this process is likely to take place on 100's to 1000's year time-scales.

6.1.4. Future Work

The interaction of fluid-mineral systems is of great importance in a range of Earth System processes including surface weathering, continental scale alteration of the crust, the behaviour and evolution of hydrothermal systems and a range of industrial processes including the long-term containment of nuclear waste and the sequestration of CO₂. Establishing reliable rates for silicate mineral dissolution and its controls also has important implications for many fundamental aspects of the long term relationship between silicate weathering, global climate (Berner and Berner, 1997) and global elemental cycling (Lasaga et al., 1994).

Further work on groundwater systems over a range of pH conditions, bulk rock mineralogies and fluid residence times is crucial for understanding in-situ dissolution kinetics for the wide variety of mineral structures, and over a range of mineral saturations. Further work on the evolution of mineral surface areas over the long durations of surface mineral weather is vitally important to understand the role of the truly reactive mineral surface, as apposed to the bulk mineral surface, and how the evolution of this surface is coupled to properties of the contacting fluid and the duration of reaction. Ultimately it is likely that a range of transport phenomena are important in controlling fluid-mineral interactions at various scales. Further investigation of mineral reaction kinetics in a range of weathering environments under different conditions of water saturation and fluid velocities is crucial to understanding this coupling.

The role of microbial activity in mediating and catalysing a range of in-situ fluid-mineral reactions is beginning to be appreciated (e.g. Edwards et al., 2005, Fein, 2000). Continued work on understanding the ecology of subsurface microbial systems and the role of microbes in modifying the mineral surface, the production of metabolic by-products that enhance mineral solubilities and mediation of groundwater solute chemistry is crucial for the accurate modelling of large-scale mineral weathering in both surface and subsurface systems.

The further understanding of the long-term containment of CO₂ will be greatly aided by continued work on natural analogue sites. Investigation of the geochemical evolution of a range of CO₂-accumulations, in a variety of host lithologies, is vital to understanding the underlying fluid-mineral interactions, and their coupling to physical processes, that influence the long term mineralization of CO₂. The study of a number of 'failed' natural CO₂ accumulations, many of which exhibit evidence of leakage in the geological past but which are now secure, well help understand the coupling between geochemical and physical processes, that both enhance leakage and ultimately lead to its containment.

References

- AAGAARD P. & HELGESON H. (1977) Thermodynamic and kinetic constraints on the dissolution of feldspars. *Geol. Soc. Am., Abstr. Programs*.
- AAGAARD P. & HELGESON H. (1983) Activity/composition relations among silicates and aqueous solutions: II. Chemical and thermodynamic consequences of ideal mixing of atoms on homological sites in montmorillonites, illites, and mixed-layer clays. *Clays Clay Miner*, **31**, 207-217.
- ALLIS R., BERGFELD D., MOORE J., MCCLURE K., MORGAN C., CHIDSEY T., HEATH J. & MCPHERSON B. (2005) Implications of results from CO₂ flux surveys over known CO₂ systems for long-term monitoring. United States Geological Survey.
- ALLIS R., CHIDSEY T., GWYNN W., MORGAN C., WHITE S., ADAMS M. & MOORE J. (2001) Natural CO₂ reservoirs on the Colorado Plateau and southern Rocky Mountains: Candidates for CO₂ sequestration. 14–17 United States Geological Survey.
- AMRHEIN C. & SUAREZ D. (1992) Some factors affecting the dissolution kinetics of anorthite at 25 C. *Geochimica et Cosmochimica Acta*, **56**, 1815-1826.
- ANDERSON G.M. (1976) Error propagation by the Monte Carlo method in geochemical calculations. *Geochim. Cosmochim. Acta*, **40**, 1533–1538.
- ANDREWS J. & WILSON G. (1987) The composition of dissolved gases in deep groundwaters and groundwater degassing. *Saline Water and Gases in Crystalline Rocks*, 245–252.
- APPELO C. & POSTMA D. (2005) *Geochemistry, groundwater and pollution*. Taylor & Francis, London.
- ARNÓRSSON S. & STEFÁNSSON A. (1999) Assessment of feldspar solubility constants in water in the range 0 to 350 C at vapor saturation pressures. *Am. J. Sci*, **299**, 173-209.
- ARVIDSON R., ERTAN I., AMONETTE J. & LUTTGE A. (2003) Variation in calcite dissolution rates: A fundamental problem? *Geochimica et Cosmochimica Acta*, **67**, 1623-1634.
- ARVIDSON R. & MACKENZIE F. (2000) Temperature Dependence of Mineral Precipitation Rates Along the CaCO₃–MgCO₃ Join. *Aquatic Geochemistry*, **6**, 249-256.
- ASSAYAG N., BICKLE M., KAMPMAN N. & BECKER J. (2009) Carbon isotopic constraints on CO₂ degassing in cold-water Geysers, Green River, Utah. *Energy Procedia*, **1**, 2361-2366.
- ASSAYAG N., MATTER J., ADER M., GOLDBERG D. & AGRINIER P. (2009) Water–rock interactions during a CO₂ injection field-test: Implications on host rock dissolution and alteration effects. *Chemical Geology*, **262**, 406-414.
- BAARS D. (1962) Permian System of Colorado Plateau. *Assoc. Petroleum Geologists Bull*, **46**, 149-218.
- BAARS D. & SEAGER W. (1970) Stratigraphic control of petroleum in White Rim sandstone Permian in and near Canyonlands National Park, Utah. *AAPG bulletin*, **54**, 709-718.
- BAARS D. & STEVENSON G. (1981) *Tectonic evolution of the Paradox basin, Utah and Colorado*.
- BACHU S. (2008) CO₂ storage in geological media: Role, means, status and barriers to deployment. *Progress in Energy and Combustion Science*, **34**, 254-273.
- BACHU S., BONIJOLY D., BRADSHAW J., BURRUSS R., HOLLOWAY S., CHRISTENSEN N. & MATHIASSEN O. (2007) CO₂ storage capacity estimation: Methodology and gaps. *International Journal of Greenhouse Gas Control*, **1**, 430-443.
- BAER J. & RIGBY J. (1978) Geology of the Crystal Geyser and the environmental implications of its effluent, Grand County, Utah. *Utah Geology*, **5**.
- BALLENTINE C. (1997) Resolving the mantle He/Ne and crustal ²¹Ne/²²Ne in well gases. *Earth and Planetary Science Letters*, **152**, 233-249.
- BALLENTINE C., VAN KEKEN P., PORCELLI D. & HAURI E. (2002) Numerical models, geochemistry and the zero-paradox noble-gas mantle. *Philosophical Transactions: Mathematical, Physical and Engineering Sciences*, 2611-2631.
- BARNABY R. & RSIMSTIDT J. (1989) Redox conditions of calcite cementation interpreted from Mn and Fe contents of authigenic calcites. *Bulletin of the Geological Society of America*, **101**, 795.
- BARNES I. & HEM J. (1973) Chemistry of subsurface waters. *Annual review of earth and planetary sciences*, **1**, 157-181.
- BARNES I., IRWIN W. & WHITE D. (1978) Global distribution of carbon-dioxide discharges and major zones of seismicity. *Global distribution of carbon-dioxide discharges and major zones of seismicity*, **12**.
- BARRANTE J.R. (1974) *Applied Mathematics for Physical Chemistry*. Prentice-Hall, Englewood Cliffs, New Jersey.

- BASOLO F. & PEARSON R. (1967) *Mechanism of Inorganic Reactions*. John Wiley, London.
- BATTANI A., SARDA P. & PRINZHOFER A. (2000) Basin scale natural gas source, migration and trapping traced by noble gases and major elements: the Pakistan Indus basin. *Earth and Planetary Science Letters*, **181**, 229-249.
- BEAUBIEN S., LOMBARDI S., CIOTOLI G., ANNUNZIATELLIS A., HATZIYANNIS G., METAXAS A. & PEARCE J. (2004) Potential Hazards of CO₂ leakage in storage systems—learning from natural systems. *GHGT7, Vancouver*, 5–8.
- BECK J., BERNDT M. & SEYFRIED JR W. (1992) Application of isotopic doping techniques to evaluation of reaction kinetics and fluid/mineral distribution coefficients: An experimental study of calcite at elevated temperatures and pressures. *Chemical Geology*, **97**, 125-144.
- BECKER J. (2005) Quantification of Himalayan Metamorphic CO₂ Fluxes: Impact on Global Carbon Budgets. Ph.D. Thesis, University of Cambridge, UK.
- BEIG M. & LÜTTGE A. (2006) Albite dissolution kinetics as a function of distance from equilibrium: Implications for natural feldspar weathering. *Geochimica et Cosmochimica Acta*, **70**, 1402-1420.
- BEITLER B., PARRY W. & CHAN M. (2005) Fingerprints of fluid flow: chemical diagenetic history of the Jurassic Navajo Sandstone, southern Utah, USA. *Journal of Sedimentary Research*, **75**, 547.
- BERG A. & BANWART S. (2000) Carbon dioxide mediated dissolution of Ca-feldspar: implications for silicate weathering. *Chemical Geology*, **163**, 25-42.
- BERNDT M., ALLEN D. & SEYFRIED JR W. (1996) Reduction of CO₂ during serpentinization of olivine at 300 C and 500 bar. *Geology*, **24**, 351.
- BERNER R. (1975) The role of magnesium in the crystal growth of calcite and aragonite from sea water. *Geochimica et Cosmochimica Acta*, **39**, 489-494.
- BERNER R. & HOLDREN JR G. (1977) Mechanism of feldspar weathering: some observational evidence. *Geology*, **5**, 369.
- BERNER R. & MORSE J. (1974) Dissolution kinetics of calcium carbonate in sea water; IV, Theory of calcite dissolution. *American Journal of Science*, **274**, 108.
- BERTRÁN J. (1983) Study of the Fermi doublet $n_{01} \rightarrow 2n_{02}$ in the Raman spectra of CO₂ in different phases. *Spectrochimica Acta Part A: Molecular Spectroscopy*, **39**, 119-121.
- BETHKE C. (1989) Modeling subsurface flow in sedimentary basins. *International Journal of Earth Sciences*, **78**, 129-154.
- BICKLE M. (1992) Transport mechanisms by fluid-flow in metamorphic rocks: oxygen and strontium decoupling in the Trois Seigneurs Massif - a consequence of kinetic dispersion? . *American Journal of Science*, **292**, 289-316.
- BICKLE M. (2009) Geological carbon storage. *Nature Geoscience*, **2**, 815-818.
- BICKLE M., BUNBURY J., CHAPMAN H., HARRIS N., FAIRCHILD I. & AHMAD T. (2003) Fluxes of Sr into the headwaters of the Ganges. *Geochimica et Cosmochimica Acta*, **67**, 2567-2584.
- BISCHOFF J. & FYFE W. (1968) Catalysis, inhibition, and the calcite-aragonite problem;[Part] 1, The aragonite-calcite transformation. *American Journal of Science*, **266**, 65.
- BLAKE R. & WALTER L. (1999) Kinetics of feldspar and quartz dissolution at 70–80 C and near-neutral pH: Effects of organic acids and NaCl. *Geochimica et Cosmochimica Acta*, **63**, 2043-2059.
- BLAKEY R. (2008) Pennsylvanian-Jurassic Sedimentary Basins of the Colorado Plateau and Sothern Rocky Mountains. *The Sedimentary Basins of the United States and Canada*, 245.
- BLUM A. & LASAGA A. (1991) The role of surface speciation in the dissolution of albite. *Geochimica et Cosmochimica Acta*, **55**, 2193-2201.
- BLUM A. & STILLINGS L. (1995) Feldspar dissolution kinetics. *Reviews in Mineralogy and Geochemistry*, **31**, 291.
- BLUM J., EREL Y. & BROWN K. (1993) ⁸⁷Sr/⁸⁶Sr ratios of Sierra Nevada stream waters: Implications for relative mineral weathering rates. *Geochimica et Cosmochimica Acta*, **57**, 5019-5025.
- BODELL J. & CHAPMAN D. (1982) Heat flow in the north-central Colorado Plateau. *J. geophys. Res.*, **87**, 2869-2884.
- BODINE M., HOLLAND H. & BORCSIK M. (1965) Coprecipitation of manganese and strontium with calcite. In: *Postmagmatic Ore Deposition*, 401-406. Prauge.
- BODNAR R. (2003) Introduction to fluid inclusions. *Fluid Inclusions: Analysis and Interpretation. Mineral. Assoc. Can., Short Course Ser.*, **32**, 1-8.
- BÖTTCHER M. (1998) Manganese (II) partitioning during experimental precipitation of rhodochrosite–calcite solid solutions from aqueous solutions. *Marine Chemistry*, **62**, 287-297.
- BOTTOMLEY D. & VEIZER J. (1992) The nature of groundwater flow in fractured rock: Evidence from the isotopic and chemical evolution of recrystallized fracture calcites from the Canadian Precambrian Shield. *Name: Geochimica et Cosmochimica Acta*.

- BOWEN B. (2005) Sandstone Bleaching and Iron Concretions: An index to fluid pathways and diagenetic history of the Jurassic Navajo Sandstone, Southern Utah. Ph.D. Thesis, University of Utah, USA.
- BOWEN B., MARTINI B., CHAN M. & PARRY W. (2007) Reflectance spectroscopic mapping of diagenetic heterogeneities and fluid-flow pathways in the Jurassic Navajo Sandstone. *AAPG bulletin*, **91**, 173.
- BRADLEY M., MAYSON H. & WILKINS K. (1986) An Integrated Approach to Refining Reservoir Description Through Monitoring Fluid Movements in the Prudhoe Bay Reservoir. In: *SPE Annual Technical Conference and Exhibition*, New Orleans, Louisiana.
- BRAND U. & VEIZER J. (1980) Chemical diagenesis of a multicomponent carbonate system: 1. Trace elements. *Journal of Sedimentary Petrology*, **50**, 1219-1236.
- BRANTLEY S., BLAI A., CREMEENS D., MACINNIS I. & DARMODY R. (1993) Natural etching rates of feldspar and hornblende. *Aquatic Sciences-Research Across Boundaries*, **55**, 262-272.
- BRANTLEY S., KUBICKI J. & WHITE A. (2007) *Kinetics of water-rock interaction*. Springer Verlag, New York.
- BREIT G., GOLDBERGER M., SHAW D. & SIMMONS E. (1990) Authigenic barite as an indicator of fluid movement through sandstones within the Colorado Plateau. *Journal of Sedimentary Petrology*, **60**, 884-896.
- BREIT G.N. (2002) USGS Water Database. United States Geological Survey.
- BRENNINKMEIJER C.A.M., KRAFT P. & MOOK W.G. (1983) Oxygen isotope fractionation between CO₂ and H₂O. *Chemical Geology*, **41**, 181-190.
- BRICKER O. (1965) Some stability relations in the system Mn-O₂-H₂O at 25 and one atmosphere total pressure. *American Mineralogist*, **50**, 1296-1354.
- BROWN M. & STEEPER R. (1991) CO₂-based thermometry of supercritical water oxidation. *Applied Spectroscopy*, **45**, 1733-1738.
- BUDD D., HAMMES U. & VACHER H. (1993) Calcite cementation in the upper Floridan aquifer: A modern example for confined-aquifer cementation models? *Geology*, **21**, 33.
- BUHMANN D. & DREYBRODT W. (1985) The kinetics of calcite dissolution and precipitation in geologically relevant situations of karst areas: 2. Closed system. *Chemical Geology*, **53**, 109-124.
- BULLEN T., WHITE A., BLUM A., HARDEN J. & SCHULZ M. (1997) Chemical weathering of a soil chronosequence on granitoid alluvium: II. Mineralogical and isotopic constraints on the behavior of strontium. *Geochimica et Cosmochimica Acta*, **61**, 291-306.
- BURCH T., NAGY K. & LASAGA A. (1993) Free energy dependence of albite dissolution kinetics at 80 °C and pH 8. *Chemical Geology*, **105**, 137-162.
- BURKE E. (2001) Raman microspectrometry of fluid inclusions. *Lithos*, **55**, 139-158.
- BURKE W., DENISON R., HETHERINGTON E., KOEPNICK R., NELSON H. & OTTO J. (1982) Variation of seawater ⁸⁷Sr/⁸⁶Sr throughout Phanerozoic time. *Geology*, **10**, 516.
- BURKHARD M. & KERRICH R. (1988) Fluid regimes in the deformation of the Helvetic nappes, Switzerland, as inferred from stable isotope data. *Contributions to Mineralogy and Petrology*, **99**, 416-429.
- BURKHARD M., KERRICH R., MAAS R. & FYFE W. (1992) Stable and Sr-isotope evidence for fluid advection during thrusting of the Glarus nappe (Swiss Alps). *Contributions to Mineralogy and Petrology*, **112**, 293-311.
- BURNS S., BAKER P. & SHOWERS W. (1988) The factors controlling the formation and chemistry of dolomite in organic-rich sediments: Miocene Drakes Bay Formation, California. In: *SEPM Society for Sedimentary Research*, 41.
- BURNSIDE N. (2007) Using Spring Deposits to Track the Evolution of Fluid Pathways Through Faults: Little Grand Wash Fault and Salt Wash Graben, Utah, USA. In: *GSA Annual Meeting*, Denver, Colorado, USA.
- BURNSIDE N., DOCKRILL B., SHIPTON Z.K. & ELLAM R.M. (2009) Dating and constraining leakage rates from a natural analogue for CO₂ storage: the Little Grand Wash and Salt Wash faults, Utah, USA. In: *Faults and Top seals: From Pore to Basin Scale*, EAGE, 21-24 Montpellier, France.
- BUSENBERG E. & PLUMMER L. (1986) A comparative study of the dissolution and crystal growth kinetics of calcite and aragonite. *Studies in Diagenesis*, **105**, 139-168.
- BUSENBERG E., PLUMMER L. & PARKER V. (1984) The solubility of strontianite (SrCO₃) in CO₂-H₂O solutions between 2 and 91 °C, the association constants of SrHCO₃⁺(aq) and SrCO₃(aq) between 5 and 80 °C, and an evaluation of the thermodynamic properties of Sr²⁺(aq) and SrCO₃ (cr) at 25 °C and 1 atm total pressure. *Geochim. Cosmochim. Acta*, **48**, 2021-2035.
- BUTALA S., MEDINA J., TAYLOR T., BARTHOLOMEW C. & LEE M. (2000) Mechanisms and kinetics of reactions leading to natural gas formation during coal maturation. *Energy and Fuels*, **14**, 235-259.
- CAINE J., EVANS J. & FORSTER C. (1996) Fault zone architecture and permeability structure. *Geology*, **24**, 1025.

- CAMPBELL J. & DENVER C. (1980) Lower Permian depositional systems and Wolfcampian paleogeography, Uncomphagre Basin, eastern Utah and southwestern Colorado. 327-340 Soc. Econ. Paleontol. Miner.
- CAPPA J. & RICE D. (1995) *Carbon dioxide in Mississippian rocks of the Paradox Basin and adjacent areas, Colorado, Utah, New Mexico, and Arizona*. United States Geological Survey.
- CARPENTER A. & OGLESBY T. (1976) A model for the formation of luminescently zoned calcite cements and its implications. In: *Geological Society of America, Abstracts with Programs*, 469-470.
- CARTWRIGHT I., WEAVER T., TWEED S., AHEARNE D., COOPER M., CZAPNIK K. & TRANTER J. (2002) Stable isotope geochemistry of cold CO₂-bearing mineral spring waters, Daylesford, Victoria, Australia: sources of gas and water and links with waning volcanism. *Chemical Geology*, **185**, 71-91.
- CASEY W. & BUNKER B. (1990) Leaching of mineral and glass surfaces during dissolution. *Reviews in Mineralogy and Geochemistry*, **23**, 397.
- CASEY W., WESTRICH H. & HOLDREN G. (1991) Dissolution rates of plagioclase at pH= 2 and 3. *American Mineralogist*, **76**, 211.
- CHAN M., PARRY W. & BOWMAN J. (2000) Diagenetic hematite and manganese oxides and fault-related fluid flow in Jurassic sandstones, southeastern Utah. *AAPG bulletin*, **84**, 1281.
- CHAN M., PARRY W., PETERSEN E. & HALL C. (2001) ⁴⁰Ar/³⁹Ar age and chemistry of manganese mineralization in the Moab and Lisbon fault systems, southeastern Utah. *Geology*, **29**, 331.
- CHEN T., NEVILLE A. & YUAN M. (2006) Influence of Mg²⁺ on CaCO₃ formation—bulk precipitation and surface deposition. *Chemical Engineering Science*, **61**, 5318-5327.
- CHESTER F. (1994) Effects of temperature on friction: Constitutive equations and experiments with quartz gouge. *J. geophys. Res.*, **99**, 7247-7261.
- CHESTER F., EVANS J. & BIEGEL R. (1993) Internal structure and weakening mechanisms of the San Andreas fault. *J. geophys. Res.*, **98**, 771-786.
- CHESTER F. & LOGAN J. (1986) Implications for mechanical properties of brittle faults from observations of the Punchbowl fault zone, California. *Pure and Applied Geophysics*, **124**, 79-106.
- CHIDSEY JR T. (2005) Dolomitization of the Mississippian Leadville Limestone, Paradox Basin, SE Utah. United States Geological Survey.
- CHOI H., KOH Y., BAE D., PARK S., HUTCHEON I. & YUN S. (2005) Estimation of deep-reservoir temperature of CO₂-rich springs in Kangwon district, South Korea. *Journal of Volcanology and Geothermal Research*, **141**, 77-89.
- CHOU L. & WOLLAST R. (1985) Steady-state kinetics and dissolution mechanisms of albite. *Am. J. Sci.*, **285**, 963-993.
- CLARK I. & FRITZ P. (1997) *Environmental isotopes in hydrogeology*. CRC Press.
- CLOW D., MAST M., BULLEN T. & TURK J. (1997) Strontium 87/strontium 86 as a tracer of mineral weathering reactions and calcium sources in an alpine/subalpine watershed, Loch Vale, Colorado. *Water Resources Research*, **33**, 1335-1351.
- CONDON S. (1997) *Geology of the Pennsylvanian and Permian cutler group and Permian Kaibab limestone in the Paradox Basin, southeastern Utah and southwestern Colorado*. United States Geological Survey.
- COOK P. (2006) Carbon dioxide capture and geological storage: research, development and application in Australia. *International Journal of Environmental Studies*, **63**, 731-749.
- COOLEY M., HARSHBARGER J., AKERS J. & HARDT W. (1969) Regional hydrogeology of the Navajo and Hopi Indian reservations. *Arizona, New Mexico, and Utah: US Geological Survey Professional Paper*, **521**.
- CORNELL R. & GIOVANOLI R. (1993) Acid dissolution of hematites of different morphologies. *Clay Minerals*, **28**, 223-223.
- COUDRAIN-RIBSTEIN A., GOUZE P. & DE MARSILY G. (1998) Temperature-carbon dioxide partial pressure trends in confined aquifers. *Chemical Geology*, **145**, 73-89.
- COX S. (1995) Faulting processes at high fluid pressures: An example of fault valve behavior from the Wattle Gully fault. *Victoria, Australia: Journal of Geophysical Research*, **100**, 12841-12859.
- COYLE M. (2009) Likely Outcomes in the National Debate over Greenhouse Gas Emissions—a public policy analysis. *Senior Honors Projects*, 136.
- CULLERS R. (1995) The controls on the major-and trace-element evolution of shales, siltstones and sandstones of Ordovician to Tertiary age in the Wet Mountains region, Colorado, USA. *Chemical Geology*, **123**, 107-131.
- CURTI E. (1999) Coprecipitation of radionuclides with calcite: estimation of partition coefficients based on a review of laboratory investigations and geochemical data. *Applied Geochemistry*, **14**, 433-445.
- CZERNICHOWSKI-LAURIOL I., ROCHELLE C., SPRINGER N., BROSSE E., SANJUAN B., LANINI S. &

- THIÉRY D. (1999) «SACS»-Saline aquifer CO₂-storage. *Final Report of Work Area*, **3**.
- DAMEN K., FAAIJ A., VAN BERGEN F., GALE J. & LYSÉN E. (2005) Identification of early opportunities for CO₂ sequestration—worldwide screening for CO₂-EOR and CO₂-ECBM projects. *Energy*, **30**, 1931-1952.
- DEFREYTES K. (1965) Carbonate equilibria: a graphic and algebraic approach. *Limnology and Oceanography*, **10**, 412-426.
- DEINES P., HARMON R. & LANGMUIR D. (1974) Stable carbon isotope ratios and the existence of a gas phase in the evolution of carbonate ground waters. *Geochimica et Cosmochimica Acta*, **38**, 1147-1164.
- DESBOROUGH G. & POOLE F. (1992) Interdune carbonate evaporites on primary bounding surfaces in the eolian Jurassic Navajo Sandstone of southeastern Utah. In: *SEPM*, 7. Utah, USA.
- DEUTSCH W. (1997) *Groundwater geochemistry: fundamentals and applications to contamination*. CRC Press.
- DHIMA A., DE HEMPTINNE J.-C. & JOSE J. (1999) Solubility of Hydrocarbons and CO₂ Mixtures in Water under High Pressure. *Industrial & Engineering Chemistry Research*, **38**, 3144-3161.
- DICK J. (2008) Calculation of the relative metastabilities of proteins using the CHNOSZ software package. *Geochemical Transactions*, **9**, 10.
- DICKINSON W. & SNYDER W. (1978) Plate tectonics of the Laramide orogeny. *Laramide Folding Associated With Basement Block Faulting in the Western United States*, 355-366.
- DOCKRILL B. (2005) Understanding Leakage from a Fault Sealed CO₂ Reservoir in East Central Utah: A Natural Analogue Applicable to CO₂ Storage. Ph.D. Thesis, University of Dublin, Trinity College, Ireland.
- DOCKRILL B. & SHIPTON Z. (2010) Structural controls on leakage from a natural CO₂ geologic storage site: central Utah, U.S.A. *Journal of Structural Geology*. *in press*.
- DOELLING H. (1988) Geology of Salt Valley Anticline and Arches National Park, Grand County, Utah. *Salt deformation in the Paradox region, Utah: Utah Geological and Mineral Survey Bulletin*, **122**, 1-60.
- DOELLING H., ROSS M. & MULVEY W. (2002) Geologic Map of the Moab 7.5' Quadrangle, Grand County, Utah. *Utah Geological Survey Map*, **181**, 34.
- DREVER J. (1994) The effect of land plants on weathering rates of silicate minerals. *Geochimica et Cosmochimica Acta*, **58**, 2325-2332.
- DREVER J. (1997) *The Geochemistry of Natural Waters*. Prentice Hall, Upper Saddle River, NJ.
- DREVER J. & CLOW D. (1995) Weathering rates in catchments. *Reviews in Mineralogy and Geochemistry*, **31**, 463.
- DREYBRODT W. (1988) *Processes in Karst Systems: Physics, Chemistry, and Geology*. Springer-Verlag New York.
- DREYBRODT W., BUHMANN D., MICHAELIS J. & USDOSWSKI E. (1992) Geochemically controlled calcite precipitation by CO₂ outgassing: Field measurements of precipitation rates to theoretical predictions. *Chem. Geol.*, **97**, 287-296.
- DREYBRODT W., LAUCKNER J., ZAIHUA L., SVENSSON U. & BUHMANN D. (1996) The kinetics of the reaction CO₂ + H₂O → H⁺ + HCO₃⁻ as one of the rate limiting steps for the dissolution of calcite in the system H₂O-CO₂-CaCO₃. *Geochimica et Cosmochimica Acta*, **60**, 3375-3381.
- DROMGOOLE E. & WALTER L. (1990) Inhibition of calcite growth rates by Mn²⁺ in CaCl₂ solutions at 10, 25, and 50 °C. *Geochimica et Cosmochimica Acta*, **54**, 2991-3000.
- DROMGOOLE E. & WALTER L. (1990) Iron and manganese incorporation into calcite: Effects of growth kinetics, temperature and solution chemistry. *Chemical Geology*, **81**, 311-336.
- DUAN Z. & SUN R. (2003) An improved model calculating CO₂ solubility in pure water and aqueous NaCl solutions from 273 to 533 K and from 0 to 2000 bar. *Chemical Geology*, **193**, 257-271.
- DUAN Z., SUN R., ZHU C. & CHOU I. (2006) An improved model for the calculation of CO₂ solubility in aqueous solutions containing Na⁺, K⁺, Ca²⁺, Mg²⁺, Cl⁻, and SO₄²⁻. *Marine Chemistry*, **98**, 131-139.
- DUBESSY J., BUSCHAERT S., LAMB W., PIRONON J. & THIÉRY R. (2001) Methane-bearing aqueous fluid inclusions: Raman analysis, thermodynamic modelling and application to petroleum basins. *Chemical Geology*, **173**, 193-205.
- DULINSKI M. & ROZANSKI K. (1990) Formation of ¹³C/¹²C isotope ratios in speleothems: a semi-dynamic model. *Radiocarbon*, **32**, 7-16.
- EDMUNDS W., MILES D. & COOK J. (1984) A comparative study of sequential redox processes in three British aquifers. *Hydrochemical balances of freshwater systems*, 55-70.
- EDWARDS, K., BACH, W., McCOLLOM, T., (2005) Geomicrobiology in oceanography: microbe-mineral interactions at and below the seafloor. *Trends in Microbiology*, **13**, 449-456.

- EICHHUBL P., DAVATZ N. & BECKER S. (2009) Structural and diagenetic control of fluid migration and cementation along the Moab fault, Utah. *AAPG bulletin*, **93**, 653.
- ELLIS A. & GOLDING R. (1963) The solubility of carbon dioxide above 100 degrees C in water and in sodium chloride solutions. *American Journal of Science*, **261**, 47.
- EMBERLEY S., HUTCHEON I., SHEVALIER M., DUROCHER K., GUNTER W. & PERKINS E. (2004) Geochemical monitoring of fluid-rock interaction and CO₂ storage at the Weyburn CO₂-injection enhanced oil recovery site, Saskatchewan, Canada. *Energy*, **29**, 1393-1401.
- EMBERLEY S., HUTCHEON I., SHEVALIER M., DUROCHER K., MAYER B., GUNTER W. & PERKINS E. (2005) Monitoring of fluid-rock interaction and CO₂ storage through produced fluid sampling at the Weyburn CO₂-injection enhanced oil recovery site, Saskatchewan, Canada. *Applied Geochemistry*, **20**, 1131-1157.
- ETZ E. (1979) Raman microprobe analysis: principles and applications. *Scanning Electron Microscopy*, **1**, 67-82.
- EVANS J., HEATH J., SHIPTON Z., KOLESAR P., DOCKRILL B., WILLIAMS A., KIRCHNER D., LACHMAR T. & NELSON S. (2004) Natural Leaking CO₂-charged Systems as Analogs for Geologic Sequestration Sites. Utah State University.
- FAIMAN D., RAVIV D. & ROSENSTREICH R. (2007) Using solar energy to arrest the increasing rate of fossil-fuel consumption: The southwestern states of the USA as case studies. *Energy Policy*, **35**, 567-576.
- FAIRCHILD I. (1983) Chemical controls of cathodoluminescence of natural dolomites and calcites: new data and review. *Sedimentology*, **30**, 579-583.
- FAIRCHILD I., BORSATO A., TOOTH A., FRISIA S., HAWKESWORTH C., HUANG Y., MCDERMOTT F. & SPIRO B. (2000) Controls on trace element (Sr-Mg) compositions of carbonate cave waters: implications for speleothem climatic records. *Chemical Geology*, **166**, 255-269.
- FANTIDIS J. & EHHALT D. (1970) Variations of the carbon and oxygen isotopic composition in stalagmites and stalactites: evidence of non-equilibrium isotopic fractionation. *Earth and Planetary Science Letters*, **10**, 136-144.
- FEIN, J. (2000) Quantifying the effects of bacteria on adsorption reactions in water-rock systems. *Chemical Geology*, **169**, 265-280.
- FERNANDEZ-DIAZ L., PUTNIS A., PRIETO M. & PUTNIS C. (1996) The role of magnesium in the crystallization of calcite and aragonite in a porous medium. *Journal of Sedimentary Research-Section A-Sedimentary Petrology and Processes*, **66**, 482-491.
- FLEURY M., BERNE P. & BACHAUD P. (2009) Diffusion of dissolved CO₂ in caprock. *Energy Procedia*, **1**, 3461-3468.
- FLOWERS R., WERNICKE B. & FARLEY K. (2008) Unroofing, incision, and uplift history of the southwestern Colorado Plateau from apatite (U-Th)/He thermochronometry. *Geological Society of America Bulletin*, **120**, 571.
- FOXFORD K.A., GARDEN I.R., GUSCOTT S.C., BURLEY S.D., LEWIS J.M., WALSH J.J. & WATTERSON J. (1996) The field geology of the Moab Fault. In: *Geology and resources of the Paradox Basin: Utah Geological Association Guidebook* (Ed. A.C. Huffman), Vol. **25**.
- FRANK J., CARPENTER A. & OGLESBY T. (1982) Cathodoluminescence and composition of calcite cement in the Taum Sauk Limestone (Upper Cambrian), southeast Missouri. *Journal of Sedimentary Petrology*, **52**, 631-638.
- FRANTZ J., POPP R. & HOERING T. (1992) The compositional limits of fluid immiscibility in the system H₂O-NaCl-CO₂ as determined with the use of synthetic fluid inclusions in conjunction with mass spectrometry. *Chemical Geology*, **98**, 237-255.
- FREETHEY G. & CORDY G. (1991) Geohydrology of Mesozoic Rocks in the Upper Colorado River Basin in Arizona, Colorado, New Mexico, Utah, and Wyoming, Excluding the San Juan Basin. USGS Professional Paper 1411-C.
- FRIEDMAN I. & O'NEIL J. (1977) *Compilation of stable isotope fractionation factors of geochemical interest*. USGPO.
- FRIEDMANN S. (2007) Geological carbon dioxide sequestration. *Elements*, **3**, 179.
- GABITOV R., GAETANI G., WATSON E., COHEN A. & EHRlich H. (2008) Experimental determination of growth rate effect on U⁶⁺ and Mg²⁺ partitioning between aragonite and fluid at elevated U⁶⁺ concentration. *Geochimica et Cosmochimica Acta*, **72**, 4058-4068.
- GAETANI G. & COHEN A. (2006) Element partitioning during precipitation of aragonite from seawater: A framework for understanding paleoproxies. *Geochimica et Cosmochimica Acta*, **70**, 4617-4634.
- GALE J. (2004) Geological storage of CO₂: What do we know, where are the gaps and what more needs to be done? *Energy*, **29**, 1329-1338.
- GARDEN I., GUSCOTT S., BURLEY S., FOXFORD K., WALSH J. & MARSHALL J. (2001) An exhumed palaeo-hydrocarbon migration fairway in a faulted carrier system, Entrada Sandstone of SE Utah, USA. *Geofluids*, **1**, 195-213.

- GARRABOS Y., CHANDRASEKHARAN V., ECHARGUI M. & MARSAULT-HERAIL F. (1989) Density effect on the raman fermi resonance in the fluid phases of CO₂. *Chemical Physics Letters*, **160**, 250-256.
- GARRABOS Y., ECHARGUI M. & MARSAULT-HERAIL F. (1989) Comparison between the density effects on the levels of the Raman spectra of the Fermi resonance doublet of the ¹²C ¹⁶CO₂ and ¹³C ¹⁶O₂ molecules. *The Journal of Chemical Physics*, **91**, 5869-5881.
- GARRABOS Y., TUFEU R., LE NEINDRE B., ZALCZER G. & BEYSENS D. (1980) Rayleigh and Raman scattering near the critical point of carbon dioxide. *The Journal of Chemical Physics*, **72**, 4637.
- GARRELS R. & CHRIST C. (1965) Minerals, solutions, and equilibria. *Harper and Row, New York*.
- GASCOYNE M. (1983) Trace-element partition coefficients in the calcite-water system and their paleoclimatic significance in cave studies. *Journal of Hydrology*, **61**, 213-222.
- GAUCHER E., TOURNASSAT C., JACQUOT E., ALTMANN S. & VINSOT A. (2007) Improvements in the modelling of the porewater chemistry of the Callovian-Oxfordian formation. In: *Clays in Natural and Engineered Barriers*, Lille, France.
- GAUS I. (2009) Role and impact of CO₂-rock interactions during CO₂ storage in sedimentary rocks. *International Journal of Greenhouse Gas Control*.
- GAUS I., AZAROUAL M. & CZERNICHOWSKI-LAURIOL I. (2005) Reactive transport modelling of the impact of CO₂ injection on the clayey cap rock at Sleipner (North Sea). *Chemical Geology*, **217**, 319-337.
- GAUTIER J., OELKERS E. & SCHOTT J. (1994) Experimental study of K-feldspar dissolution rates as a function of chemical affinity at 150 C and pH 9. *Geochimica et Cosmochimica Acta*, **58**, 4549-4560.
- GHERARDI F., XU T. & PRUESS K. (2007) Numerical modeling of self-limiting and self-enhancing caprock alteration induced by CO₂ storage in a depleted gas reservoir. *Chemical Geology*, **244**, 103-129.
- GIAMMAR D., BRUANT R. & PETERS C. (2005) Forsterite dissolution and magnesite precipitation at conditions relevant for deep saline aquifer storage and sequestration of carbon dioxide. *Chemical Geology*, **217**, 257-276.
- GILFILLAN S. (2006) Deep magmatic degassing and the Colorado Plateau uplift. Ph.D. Thesis, University of Manchester, UK.
- GILFILLAN S., BALLENTINE C., HOLLAND G., BLAGBURN D., LOLLAR B., STEVENS S., SCHOELL M. & CASSIDY M. (2008) The noble gas geochemistry of natural CO₂ gas reservoirs from the Colorado Plateau and Rocky Mountain provinces, USA. *Geochimica et Cosmochimica Acta*, **72**, 1174-1198.
- GILFILLAN S., LOLLAR B., HOLLAND G., BLAGBURN D., STEVENS S., SCHOELL M., CASSIDY M., DING Z., ZHOU Z. & LACRAMPE-COULOUME G. (2009) Solubility trapping in formation water as dominant CO₂ sink in natural gas fields. *Nature*, **458**, 614-618.
- GIVEN R. & WILKINSON B. (1985) Kinetic control of morphology, composition, and mineralogy of abiogenic sedimentary carbonates. *Journal of Sedimentary Petrology*, **55**, 109-119.
- GLEDHILL D. & MORSE J. (2006) Calcite dissolution kinetics in Na-Ca-Mg-Cl brines. *Geochimica et Cosmochimica Acta*, **70**, 5802-5813.
- GLENNON J. & PFAFF R. (2005) The operation and geography of carbon dioxide-driven, cold-water geysers. *GOSA Transactions*, **9**, 184-192.
- GODDARD J. & EVANS J. (1995) Chemical changes and fluid-rock interaction in faults of crystalline thrust sheets, northwestern Wyoming, USA. *Journal of Structural Geology*, **17**, 533-547.
- GOLDSTEIN H., REYNOLDS R., REHEIS M., YOUNT J. & NEFF J. (2008) Compositional trends in aeolian dust along a transect across the southwestern United States. *J. geophys. Res.*, **113**.
- GONZALEZ L. & LOHMANN K. (1988) Controls on mineralogy and composition of speleothem carbonates: Carlsbad Caverns, New Mexico. *Paleokarst: New York, Springer-Verlag*, 81-101.
- GORDON H. & MCCUBBIN T. (1966) The 2.8-micron bands of CO₂. *Journal of Molecular Spectroscopy*, **19**, 137-154.
- GOUGH C., SHACKLEY S., HOLLOWAY S., BENTHAM M., BULATOV I. & MCLACHLAN C. (2005) An integrated assessment of Carbon dioxide capture and storage in the UK. British Geological Survey.
- GOUVEIA F. & FRIEDMANN S. (2006) Timing and prediction of CO₂ eruptions from Crystal Geyser, UT, United States. Dept. of Energy.
- GOUVEIA F., JOHNSON M., LEIF R. & FRIEDMANN S. (2005) Aerometric measurement and modeling of the mass of CO₂ emissions from Crystal Geyser, Utah. UCRL-TR-211870, Lawrence Livermore National Lab., Livermore, CA (USA).
- GROVER JR G. & READ J. (1983) Paleoquifer and deep burial related cements defined by regional cathodoluminescent patterns, Middle Ordovician carbonates, Virginia. *Bulletin*, **67**, 1275-1303.
- GUNTER W., WIWEHAR B. & PERKINS E. (1997) Aquifer disposal of CO₂-rich greenhouse gases: extension of the time scale of experiment for CO₂-sequestering reactions by

- geochemical modelling. *Mineralogy and Petrology*, **59**, 121-140.
- GUTJAHR A., DABRINGHAUS H. & LACMANN R. (1996) Studies of the growth and dissolution kinetics of the CaCO₃ polymorphs calcite and aragonite. 2. The influence of divalent cation additives on the growth and dissolution rates. *J. Cryst. Growth*, **158**, 310–315.
- HACURA A. (1997) High pressure Raman study of Fermi resonance in CO₂ in gaseous CO₂-N₂ mixtures. *Physics Letters A*, **227**, 237-240.
- HADIZADEH J. (1994) Interaction of cataclasis and pressure solution in a low-temperature carbonate shear zone. *Pure and Applied Geophysics*, **143**, 255-280.
- HALL D., STERNER S. & BODNAR R. (1988) Freezing point depression of NaCl-KCl-H₂O solutions. *Economic Geology*, **83**, 197.
- HAMILTON J., BRANTLEY S., PANTANO C., CRISCENTI L. & KUBICKI J. (2001) Dissolution of nepheline, jadeite and albite glasses: toward better models for aluminosilicate dissolution. *Geochimica et Cosmochimica Acta*, **65**, 3683-3702.
- HANSHAW B. & HILL G. (1969) Geochemistry and hydrodynamics of the Paradox basin region, Utah, Colorado, and New Mexico: Chem. *Geology*, **4**, 263-294.
- HASZELDINE R., QUINN O., ENGLAND G., WILKINSON M., SHIPTON Z., EVANS J., HEATH J., CROSSEY L., BALLENTINE C. & GRAHAM C. (2005) Natural geochemical analogues for carbon dioxide storage in deep geological porous reservoirs, a United Kingdom perspective. *Oil & Gas Science and Technology*, **60**, 33-49.
- HAVET T. & HEIJNEN W. (1965) Cathodoluminescence activation and zonation in carbonate rocks: an experimental approach. *Interpretation*, **1972**.
- HEATH J. (2004) Hydrogeochemical Characterization of Leaking Carbon Dioxide-Charged Fault Zones in East-Central Utah. Masters Thesis, Utah State University, USA.
- HEDENQUIST J. & HENLEY R. (1985) The importance of CO₂ on freezing point measurements of fluid inclusions; evidence from active geothermal systems and implications for epithermal ore deposition. *Economic Geology*, **80**, 1379.
- HELGESON H. (1969) Thermodynamics of hydrothermal systems at elevated temperatures and pressures. *American Journal of Science*, **267**, 729.
- HELGESON H., BROWN T., NIGRINI A. & JONES T. (1970) Calculation of mass transfer in geochemical processes involving aqueous solutions. *Geochimica et Cosmochimica Acta*, **34**, 569-592.
- HELGESON H., GARRELS R. & MACKENZIE F. (1969) Evaluation of irreversible reactions in geochemical processes involving minerals and aqueous solutions--II. Applications. *Geochimica et Cosmochimica Acta*, **33**, 455-481.
- HELLMANN R. (1994) The albite-water system: Part I. The kinetics of dissolution as a function of pH at 100, 200, and 300 C. *Geochimica et Cosmochimica Acta*, **58**, 595-595.
- HELLMANN R. (1999) The dissolution behavior of albite feldspar at elevated temperatures and pressures: the role of surface charge and speciation. *Mitteilungen der Osterreichischen Mineralogischen Gesellschaft*, **144**, 69–100.
- HELLMANN R., PENISSON J., HERVIG R., THOMASSIN J. & ABRIOUX M. (2003) An EFTEM/HRTEM high-resolution study of the near surface of labradorite feldspar altered at acid pH: evidence for interfacial dissolution-reprecipitation. *Physics and Chemistry of Minerals*, **30**, 192-197.
- HELLMANN R. & TISSERAND D. (2006) Dissolution kinetics as a function of the Gibbs free energy of reaction: An experimental study based on albite feldspar. *Geochimica et Cosmochimica Acta*, **70**, 364-383.
- HENDY C. (1971) The isotopic geochemistry of speleothems-I. The calculation of the effects of different modes of formation on the isotopic composition of speleothems and their applicability as palaeoclimatic indicators. *Geochimica et Cosmochimica Acta*, **35**, 801-824.
- HEREFORD A., KEATING E., GUTHRIE G. & ZHU C. (2007) Reactions and reaction rates in the regional aquifer beneath the Pajarito Plateau, north-central New Mexico, USA. *Environmental Geology*, **52**, 965-977.
- HERMAN J. & LORAH M. (1987) CO₂ outgassing and calcite precipitation in Falling Spring Creek, Virginia, U. S. A. *Chemical Geology*, **62**, 251-262.
- HERMAN J. & LORAH M. (1988) Calcite precipitation rates in the field: measurement and prediction for a travertine-depositing stream. *Geochimica et Cosmochimica Acta*, **52**, 2347-2355.
- HERRMANN W. & BERRY R. (2002) MINSQ-a least squares spreadsheet method for calculating mineral proportions from whole rock major element analyses. *Geochemistry: Exploration, Environment, Analysis*, **2**, 361.
- HITE R. & BUCKNER D. (1981) Stratigraphic correlations, facies concepts, and cyclicity in Pennsylvanian rocks of the Paradox basin. 147–160 United States Geological Survey.
- HODSON M. (2003) The influence of Fe-rich coatings on the dissolution of anorthite at pH 2.6. *Geochimica et Cosmochimica Acta*, **67**, 3355-3363.
- HOLDREN JR G. & SPEYER P. (1987) Reaction rate-surface area relationships during the early stages of weathering. II. Data on eight additional feldspars. *Geochimica et Cosmochimica Acta*, **51**, 2311-2318.

- HOLLOWAY S., PEARCE J., HARDS V., OHSUMI T. & GALE J. (2007) Natural emissions of CO₂ from the geosphere and their bearing on the geological storage of carbon dioxide. *Energy*, **32**, 1194-1201.
- HOOD J. & PATTERSON D. (1984) Bedrock aquifers in the northern San Rafael Swell area. *Utah, with special emphasis on the Navajo Sandstone: State of Utah Department of Natural Resources Technical Publication*, **78**, 128.
- HORITA J. (2002) Profilometer-based study of nanometer-to millimeter-scale growth kinetics of calcite from CO₂-rich fluids. In: *GSA Annual Meeting*, Denver, Colorado, USA.
- HORITA J. & BERNDT M. (1999) Abiogenic methane formation and isotopic fractionation under hydrothermal conditions. *Science*, **285**, 1055.
- HOUSE W. (1981) Kinetics of crystallisation of calcite from calcium bicarbonate solutions. *Journal of the Chemical Society, Faraday Transactions 1*, **77**, 341-359.
- HOVORKA S., BENSON S., DOUGHTY C., FREIFELD B., SAKURAI S., DALEY T., KHARAKA Y., HOLTZ M., TRAUTZ R. & NANCE H. (2006) Measuring permanence of CO₂ storage in saline formations: the Frio experiment. *Environmental Geosciences*, **13**, 105.
- HUANG Y. & FAIRCHILD I. (2001) Partitioning of Sr²⁺ and Mg²⁺ into calcite under karst-analogue experimental conditions. *Geochimica et Cosmochimica Acta*, **65**, 47-62.
- HUBBERT M. & RUBEY W. (1959) Mechanics of fluid-filled porous solids and its application to overthrust faulting. *Geological Society of America Bulletin*, **70**, 115-166.
- HUNTOON J., DUBIEL R., STANESCO J., MICKELSON D. & CONDON S. (2002) Permian-Triassic depositional systems, paleogeography, paleoclimate, and hydrocarbon resources in Canyonlands and Monument Valley, Utah. *GSA Field Guides*, **3**, 33.
- HUTCHEON I. & ABERCROMBIE H. (1990) Fluid-rock interactions in thermal recovery of bitumen, Tucker Lake pilot, Cold Lake, Alberta. *Prediction of reservoir quality through chemical modeling: AAPG Memoir*, **49**, 161-169.
- HUTCHEON I. & ABERCROMBIE H. (1990) Carbon dioxide in clastic rocks and silicate hydrolysis. *Geology*, **18**, 541-544.
- HUTCHEON I., ABERCROMBIE H. & KROUSE H. (1990) Inorganic origin of carbon dioxide during low temperature thermal recovery of bitumen: Chemical and isotopic evidence. *Geochimica et Cosmochimica Acta*, **54**, 165-171.
- HUTCHEON I., ABERCROMBIE H. & KROUSE H. (1990) Carbon dioxide production in thermal recovery: Chemical and isotopic evidence and applications. *Geochimica et Cosmochimica Acta*, **59**, 165-171.
- ICHIKUNI M. (1973) Partition of strontium between calcite and solution: effect of substitution by manganese. *Chemical Geology*, **11**, 315-319.
- INDERMÜHLE A., STOCKER T., JOOS F., FISCHER H., SMITH H., WAHLEN M., DECK B., MASTROIANNI D., TSCHUMI J. & BLUNIER T. (1999) Holocene carbon-cycle dynamics based on CO₂ trapped in ice at Taylor Dome, Antarctica. *Nature*, **398**, 121-126.
- INGRI N. (1978) Aqueous silicic acid, silicates and silicate complexes. *Biochemistry of silicon and related problems. Plenum Press, New York*, 3-51.
- INSKEEP W. & BLOOM P. (1985) An evaluation of rate equations for calcite precipitation kinetics at pCO₂ less than 0.01 atm and pH greater than 8. *Geochimica et Cosmochimica Acta*, **49**, 2165-2180.
- INSKEEP W., NATER E., BLOOM P., VANDERVOORT D. & ERICH M. (1991) Characterization of laboratory weathered labradorite surfaces using X-ray photoelectron spectroscopy and transmission electron microscopy. *Geochim. Cosmochim. Acta*, **55**, 787-800.
- IPCC W. (2007) Climate change 2007: the physical science basis. *Summary for Policy Makers, Contribution of Working Group I to the Fourth Assessment Report of the Intergovernmental Panel on Climate Change*.
- IRWIN W. & BARNES I. (1975) Effect of geologic structure and metamorphic fluids on seismic behavior of the San Andreas fault system in central and northern California. *Geology*, **3**, 713.
- JACOBSON R. & USDOWSKI H. (1976) Partitioning of strontium between calcite, dolomite and liquids: An experimental study under higher temperature diagenetic conditions, and a model for the prediction of mineral pairs for geothermometry. *Contributions to Mineralogy and Petrology*, **59**, 171-185.
- JAMES B. & BARTLETT R. (2000) Redox phenomena. *Handbook of Soil Science*.
- JANSSEN C., LAUBE N., BAU M. & GRAY D. (1998) Fluid regime in faulting deformation of the Waratah Fault Zone, Australia, as inferred from major and minor element analyses and stable isotopic signatures. *Tectonophysics*, **294**, 109-130.
- JANSSEN C., MICHEL G., BAU M., LÜDERS V. & MÜHLE K. (1997) The North Anatolian Fault Zone and the role of fluids in seismogenic deformation. *The Journal of Geology*, **105**, 387-404.
- JOHNSON J. & NITAO J. (2003) Reactive transport modeling of geologic CO₂ sequestration at Sleipner. *Greenhouse Gas Control Technologies*, **1**, 327-332.

- JOHNSON J., NITAO J., STEEFEL C. & KNAUSS K. (2001) Reactive transport modeling of geologic CO₂ sequestration in saline aquifers: the influence of intra-aquifer shales and the relative effectiveness of structural, solubility, and mineral trapping during prograde and retrograde sequestration. In: *NETL Conference on Carbon Sequestration.*, 14-17.
- JOHNSON T. & DEPAOLO D. (1994) Interpretation of isotopic data in groundwater-rock systems: Model development and application to Sr isotope data from Yucca Mountain. *Water Resources Research*, **30**.
- JOYCE D. & HOLLOWAY J. (1993) An experimental determination of the thermodynamic properties of H₂O-CO₂-NaCl fluids at high pressures and temperatures. *Geochimica et Cosmochimica Acta*, **57**, 733-733.
- KAMPMAN N., BICKLE M., BECKER J., ASSAYAG N. & CHAPMAN H. (2009) Feldspar dissolution kinetics and Gibbs free energy dependence in a CO₂-enriched groundwater system, Green River, Utah. *Earth and Planetary Science Letters*, **284**, 473-488.
- KASZUBA J., JANECKY D. & SNOW M. (2003) Carbon dioxide reaction processes in a model brine aquifer at 200 C and 200 bars: implications for geologic sequestration of carbon. *Applied Geochemistry*, **18**, 1065-1080.
- KASZUBA J., JANECKY D. & SNOW M. (2005) Experimental evaluation of mixed fluid reactions between supercritical carbon dioxide and NaCl brine: Relevance to the integrity of a geologic carbon repository. *Chemical Geology*, **217**, 277-293.
- KATZ B. & BULLEN T. (1996) The combined use of ⁸⁷Sr/⁸⁶Sr and carbon and water isotopes to study the hydrochemical interaction between groundwater and lakewater in mantled karst. *Geochimica et Cosmochimica Acta*, **60**, 5075-5087.
- KAWAKAMI Y., YAMAMOTO J. & KAGI H. (2003) Micro-Raman densimeter for CO₂ inclusions in mantle-derived minerals. *Applied Spectroscopy*, **57**, 1333-1339.
- KEATING E. & BAHR J. (1998) Reactive transport modeling of redox geochemistry: Approaches to chemical disequilibrium and reaction rate estimation at a site in northern Wisconsin. *Water Resources Research*, **34**.
- KEELING C. & WHORF T. (2005) Atmospheric CO₂ records from sites in the SIO air sampling network. *Trends: A compendium of data on global change*, 16-26.
- KELLEY V. (1958) Tectonics of the region of the Paradox Basin. 31 Utah Geological and Mineralogical Survey.
- KENNEDY B., KHARAKA Y., EVANS W., ELLWOOD A., DEPAOLO D., THORSEN J., AMBATS G. & MARINER R. (1997) Mantle fluids in the San Andreas fault system, California. *Science*, **278**, 1278.
- KENOYER G. & BOWSER C. (1992) Groundwater chemical evolution in a sandy silicate aquifer in northern Wisconsin 1. Patterns and rates of change. *Water Resources Research*, **28**.
- KENOYER G. & BOWSER C. (1992) Groundwater chemical evolution in a sandy silicate aquifer in Northern Wisconsin 2. Reaction modeling. *Water Resources Research*, **28**.
- KERKER M., SCHEINER P., COOKE D. & KRATOHVIL J. (1979) Absorption index and color of colloidal hematite. *J. Colloid Interface Sci*, **71**, 176-187.
- KHARAKA Y., COLE D., HOVORKA S., GUNTER W., KNAUSS K. & FREIFELD B. (2006) Gas-water-rock interactions in Frio Formation following CO₂ injection: Implications for the storage of greenhouse gases in sedimentary basins. *Geology*, **34**, 577.
- KHARAKA Y., COLE D., THORSEN J., KAKOUREOS E. & NANCE H. (2006) Gas-water-rock interactions in sedimentary basins: CO₂ sequestration in the Frio Formation, Texas, USA. *Journal of Geochemical Exploration*, **89**, 183-186.
- KIKUTA K., HONGO S., TANASE D. & OHSUMI T. (2005) Field test of CO₂ injection in Nagaoka, Japan. In: *Proceedings of the 7th International Conference on Green House Gas Control Technology*, 1367-1372.
- KIM K. (2002) Plagioclase weathering in the groundwater system of a sandy, silicate aquifer. *Hydrological Processes*, **16**, 1793-1806.
- KIM S., O'NEIL J., HILLAIRES-MARCEL C. & MUCCI A. (2007) Oxygen isotope fractionation between synthetic aragonite and water: influence of temperature and Mg²⁺ concentration. *Geochimica et Cosmochimica Acta*, **71**, 4704-4715.
- KIM S. & O'NEIL J. (1997) Equilibrium and nonequilibrium oxygen isotope effects in synthetic carbonates. *Geochimica et Cosmochimica Acta*, **61**, 3461-3475.
- KINSMAN D. & HOLLAND H. (1969) The co-precipitation of cations with CaCO₃-IV. The co-precipitation of Sr²⁺ with aragonite between 16° and 96° C. *Geochimica et Cosmochimica Acta*, **33**, 1-17.
- KITANO Y. & HOOD D. (1965) The influence of organic material on the polymorphic crystallization of calcium carbonate. *Geochimica et Cosmochimica Acta*, **29**, 29-41.
- KNAUSS K., JOHNSON J. & STEEFEL C. (2005) Evaluation of the impact of CO₂, co-contaminant gas, aqueous fluid and reservoir rock interactions on the geologic sequestration of CO₂. *Chemical Geology*, **217**, 339-350.
- KNAUSS K. & WOLERY T. (1986) Dependence of albite dissolution kinetics on pH and time at 25 C and 70 C. *Geochimica et Cosmochimica Acta*, **50**, 2481-2497.

- KORBØL R. & KADDOUR A. (1995) Sleipner vest CO₂ disposal-injection of removed CO₂ into the Utsira formation. *Energy Conversion and Management*, **36**, 509-512.
- LACHENBRUCH A. & SASS J. (1980) Heat flow and energetics of the San Andreas fault zone. *J. geophys. Res.*, **85**, 6185-6222.
- LANE M., MORRIS R. & CHRISTENSEN P. (1999) An extensive deposit of crystalline hematite in Terra Meridiani, Mars. In: *Lunar and Planetary Sciences*, 1469.
- LASAGA A. (1981) Rate laws of chemical reactions. *Reviews in Mineralogy and Geochemistry*, **8**, 1.
- LASAGA A. (1982) Toward a master equation in crystal growth. *American Journal of Science*, **282**, 1264.
- LASAGA A. (1995) Fundamental approaches in describing mineral dissolution and precipitation rates. *Reviews in Mineralogy*, **31**, 23-86.
- LASAGA A. (1998) *Kinetic theory in the earth sciences*. Princeton University Press, Princeton
- LASAGA A. & LUTTGE A. (2004) Mineralogical approaches to fundamental crystal dissolution kinetics. *American Mineralogist*, **89**, 527.
- LEE E. & KROTHER N. (2001) A four-component mixing model for water in a karst terrain in south-central Indiana, USA. Using solute concentration and stable isotopes as tracers. *Chemical Geology*, **179**, 129-143.
- LEE Y. & MORSE J. (1999) Calcite precipitation in synthetic veins: implications for the time and fluid volume necessary for vein filling. *Chemical Geology*, **156**, 151-170.
- LEE Y., MORSE J. & WILTSCHKO D. (1996) An experimentally verified model for calcite precipitation in veins. *Chemical Geology*, **130**, 203-215.
- LEITNER W. (2003) A greener solution. *Nature*, **423**, 930-931.
- LEWICKI J., BIRKHOLZER J. & TSANG C. (2007) Natural and industrial analogues for leakage of CO₂ from storage reservoirs: identification of features, events, and processes and lessons learned. *Environmental Geology*, **52**, 457-467.
- LI S., DONG M., LI Z., HUANG S., QING H. & NICKEL E. (2005) Gas breakthrough pressure for hydrocarbon reservoir seal rocks: implications for the security of long-term CO₂ storage in the Weyburn field. *GEOFLUIDS-OXFORD*, **5**, 326.
- LICHTNER P. (1988) The quasi-stationary state approximation to coupled mass transport and fluid-rock interaction in a porous medium. *Geochimica et Cosmochimica Acta*, **52**, 143-165.
- LINDBERG R. & RUNNELLS D. (1984) Ground water redox reactions: An analysis of equilibrium state applied to Eh measurements and geochemical modeling. *Science*, **225**, 925.
- LIN-HUA S. & ATKINSON T. (1985) Dissolved iron in chalk groundwaters from Norfolk, England. *Quarterly Journal of Engineering Geology & Hydrogeology*, **18**, 261.
- LIPPMANN F. (1973) *Sedimentary carbonate minerals*. Springer Verlag.
- LOGAN J. & DECKER C. (1994) Cyclic fluid flow along faults. *Hickman, Stephen, Sibson, Richard, and Bruhn, Ronald eds*, 6-10.
- LONG D. (1977) *Raman spectroscopy*. McGraw-Hill New York.
- LORAH M. & HERMAN J. (1988) The chemical evolution of a travertine-depositing stream: geochemical processes and mass transfer reactions. *Water Resources Research*, **24**.
- LORENS R. (1978) A study of biological and physical controls on the trace metal content of calcite and aragonite. Ph.D. Thesis, University of Rhode Island, USA.
- LORENS R. (1981) Sr, Cd, Mn and Co distribution coefficients in calcite as a function of calcite precipitation rate. *Geochimica et Cosmochimica Acta*, **45**, 553-561.
- LORENS R. & BENDER M. (1980) The impact of solution chemistry on *Mytilus edulis* calcite and aragonite. *Geochimica et Cosmochimica Acta*, **44**, 1265-1278.
- LOVELY D.R. & GOODWIN S. (1988) Hydrogen concentrations as an indicator of the predominant terminal electron accepting process in aquatic sediments. *Geochim. Cosmochim. Acta* **52**, 11-18.
- LU X., WATSON A., GORIN A. & DEANS J. (2005) Measurements in a low temperature CO₂-driven geysiring well, viewed in relation to natural geysers. *Geothermics*, **34**, 389-410.
- MACHEL H. (1985) Cathodoluminescence in calcite and dolomite and its chemical interpretation. *Geoscience Canada*, **12**.
- MAHER K., STEEFEL C., DEPAOLO D. & VIANI B. (2006) The mineral dissolution rate conundrum: Insights from reactive transport modeling of U isotopes and pore fluid chemistry in marine sediments. *Geochimica et Cosmochimica Acta*, **70**, 337-363.
- MALDAL T. & TAPPEL I. (2004) CO₂ underground storage for Snøhvit gas field development. *Energy*, **29**, 1403-1411.
- MANN M., AMMANN C., BRADLEY R., BRIFFA K., CROWLEY T., HUGHES M., JONES P., OPPENHEIMER M., OSBORN T. & OVERPECK J. (2003) On past

- temperatures and anomalous late-20th century warmth. *Eos*, **84**, 256–258.
- MARINI L. (2007) *Geological sequestration of carbon dioxide: thermodynamics, kinetics, and reaction path modeling*. Elsevier Science.
- MARSHALL B. & MAHAN S. (1994) Strontium Isotope Geochemistry of Soil and Playa Deposits Near Yucca Mountain, Nevada. *High Level Radioactive Waste Management* 2685-2691.
- MASON R. (1987) Ion microprobe analysis of trace elements in calcite with an application to the cathodoluminescence zonation of limestone cements from the Lower Carboniferous of South Wales, U. K. *Chemical Geology*, **64**, 209-224.
- MATTER J., TAKAHASHI T. & GOLDBERG D. (2007) Experimental evaluation of in situ CO₂-water-rock reactions during CO₂ injection in basaltic rocks: Implications for geological CO₂ sequestration. *Geochemistry Geophysics Geosystems*, **8**, Q02001.
- MAY A., HENESIAN M. & BYER R. (1978) The CW coherent anti-Stokes Raman spectrum of the nu₁ band of CH₄ and its pressure dependence. *Canadian Journal of Physics*, **56**, 248.
- MAY F. (2005) Alteration of Wall Rocks by CO₂-Rich Water Ascending in Fault Zones: Natural Analogues for Reactions Induced by CO₂ Migrating Along Faults in Siliciclastic Reservoir and Cap Rocks. *Oil & Gas Science and Technology*, **60**, 19-32.
- MCCOLLOM T. & SEEWALD J. (2001) A reassessment of the potential for reduction of dissolved CO₂ to hydrocarbons during serpentinization of olivine. *Geochimica et Cosmochimica Acta*, **65**, 3769-3778.
- MCINTIRE W. (1963) Trace element partition coefficients--a review of theory and applications to geology. *Geochimica et Cosmochimica Acta*, **27**, 1209-1264.
- MCPHERSON B. & LICHTNER P. (2001) CO₂ sequestration in deep aquifers. In: *NETL Conference on Carbon Sequestration*, 1-8.
- MELBOURNE P., VICTORIA A. & ARGONNE I. (1991) Redox Reactions on Colloidal Metals and Metal Oxides. *Kinetics and catalysis in microheterogeneous systems*, 303.
- MEYER H. (1984) The influence of impurities on the growth rate of calcite. *Journal of crystal growth*, **66**, 639-646.
- MILLER S., NUR A. & OLGAARD D. (1996) Earthquakes as a coupled shear stress-high pore pressure dynamical system. *Geophysical Research Letters*, **23**, 197-200.
- MIRSKY A. & TREVES S. (1962) Heavy Minerals of Pre-Morrison Jurassic Rocks, Lucero Uplift, Northwestern New Mexico: ABSTRACT.
- MOLENAAR C. (1981) Mesozoic stratigraphy of the Paradox basin: An overview. 119–127 United States Geological Survey.
- MOOK W., BOMMERSON J. & STAVERMAN W. (1974) Carbon isotope fractionation between dissolved bicarbonate and gaseous carbon dioxide. *Earth and Planetary Science Letters*, **22**, 169.
- MOORE J., ADAMS M., ALLIS R., LUTZ S. & RAUZI S. (2003) CO₂ mobility in natural reservoirs beneath the Colorado Plateau and southern Rocky Mountains: An example from the Springerville-St. Johns field, Arizona and New Mexico. In: *Proc. 2nd. Nat. Conf. Carb. Seq.*, 5-8.
- MOORE J., ADAMS M., ALLIS R., LUTZ S. & RAUZI S. (2005) Mineralogical and geochemical consequences of the long-term presence of CO₂ in natural reservoirs: An example from the Springerville–St. Johns Field, Arizona, and New Mexico, USA. *Chemical Geology*, **217**, 365-385.
- MORRIS J., DETWILER R., FRIEDMANN S., VOROBIEV O. & HAO Y. (2009) The large-scale effects of multiple CO₂ injection sites on formation stability. *Energy Procedia*, **1**, 1831-1837.
- MORRIS R., GOLDEN D. & BELL III J. (1996) Low-temperature reflectivity spectra of red hematite and the color of Mars. *Journal of Geophysical Research-Planets*, **102**.
- MORRISON S. & PARRY W. (1988) Age and formation conditions of alteration associated with a collapse structure, Temple Mountain uranium district, Utah. *Bulletin of the Geological Society of America*, **100**, 1069.
- MORSE J. (1986) The surface chemistry of calcium carbonate minerals in natural waters: an overview. *Marine Chemistry*, **20**, 91-112.
- MORSE J. & ARVIDSON R. (2002) The dissolution kinetics of major sedimentary carbonate minerals. *Earth Science Reviews*, **58**, 51-84.
- MORSE J. & BENDER M. (1990) Partition coefficients in calcite: Examination of factors influencing the validity of experimental results and their application to natural systems. *Chemical Geology*, **82**, 265-277.
- MORSE J., WANG Q. & TSIO M. (1997) Influences of temperature and Mg:Ca ratio on CaCO₃ precipitates from seawater. *Geology*, **25**, 85.
- MUCCI A. & MORSE J. (1983) The incorporation of Mg²⁺ and Sr²⁺ into calcite overgrowths: influences of growth rate and solution composition. *Geochimica et Cosmochimica Acta*, **47**, 217-233.
- MUCCI A. & MORSE J. (1984) The solubility of calcite in seawater solutions of various magnesium concentration, It=

- 0.697 m at 25 C and one atmosphere total pressure. *Geochimica et Cosmochimica Acta*, **48**, 815-822.
- MUIR I., BANCROFT G., SHOTYK W. & NESBITT H. (1990) A SIMS and XPS study of dissolving plagioclase. *Geochimica et Cosmochimica Acta*, **54**, 2247-2256.
- MUIR I. & NESBITT H. (1991) Effects of aqueous cations on the dissolution of labradorite feldspar. *Name: Geochimica et Cosmochimica Acta*.
- MURAKAMI T., KOGURE T., KADOHARA H. & OHNUKI T. (1998) Formation of secondary minerals and its effect on anorthite dissolution. *American Mineralogist*, **83**, 1209-1219.
- MUSGROVE M. & BANNER J. (1993) Regional ground-water mixing and the origin of saline fluids: Midcontinent, United States. *Science*, **259**, 1877.
- NAGY K. & LASAGA A. (1990) The effect of deviation from equilibrium on the kinetics of dissolution and precipitation of kaolinite and gibbsite. *Chemical Geology*, **84**, 283-285.
- NAGY K. & LASAGA A. (1992) Dissolution and precipitation kinetics of gibbsite at 80C and pH 3: the dependence on solution saturation state. *Geochim. Cosmochim. Acta*, **56**, 3093-3111.
- NANCOLLAS G. & REDDY M. (1971) The crystallization of calcium carbonate. II. Calcite growth mechanism *Journal of Colloid and Interface Science*, **37**, 824-830.
- NESBITT H. & MUIR I. (1988) SIMS depth profiles of weathered plagioclase and processes affecting dissolved Al and Si in some acidic soil solutions. *Nature*, **334**, 336-338.
- NICOT J. (2008) Evaluation of large-scale CO₂ storage on fresh-water sections of aquifers: An example from the Texas Gulf Coast Basin. *International Journal of Greenhouse Gas Control*, **2**, 582-593.
- NIEL PLUMMER L., PARKHURST D. & THORSTENSON D. (1983) Development of reaction models for ground-water systems. *Geochimica et Cosmochimica Acta*, **47**, 665-685.
- NIEMANN J. & READ J. (1988) Regional cementation from unconformity-recharged aquifer and burial fluids, Mississippian Newman Limestone, Kentucky. *Journal of Sedimentary Research*, **58**, 688.
- NORDBOTTEN J., CELIA M., BACHU S. & DAHLE H. (2005) Semianalytical solution for CO₂ leakage through an abandoned well. *Environ. Sci. Technol*, **39**, 602-611.
- NORTON D. (1974) Chemical mass transfer in the Rio Tanama system, west-central Puerto Rico. *Geochimica et Cosmochimica Acta*, **38**, 267-277.
- NUCCIO V. & CONDON S. (1996) *Burial and thermal history of the Paradox Basin, Utah and Colorado, and petroleum potential of the Middle Pennsylvanian Paradox Formation*. United States Geological Survey.
- OELKERS E., GISLASON S. & MATTER J. (2008) Mineral carbonation of CO₂. *Elements*, **4**, 333.
- OELKERS E. & SCHOTT J. (2005) Geochemical aspects of CO₂ sequestration. *Chemical Geology*, **217**, 183-186.
- OELKERS E., SCHOTT J. & DEVIDAL J. (1994) The effect of aluminum, pH, and chemical affinity on the rates of aluminosilicate dissolution reactions. *Geochimica et Cosmochimica Acta*, **58**, 2011-2024.
- OGLESBY T. (1976) A model for the distribution of manganese, iron and magnesium in authigenic calcite and dolomite cements in the Upper Smackover Formation in eastern Mississippi. *Missouri, Columbia*, **122**.
- OLDENBURG C. (2007) Migration mechanisms and potential impacts of CO₂ leakage and seepage. *Carbon Capture and Sequestration: Integrating Technology, Monitoring and Regulation*.
- OLDENBURG C. & UNGER A. (2003) On leakage and seepage from geologic carbon sequestration sites: unsaturated zone attenuation. *Vadose Zone Journal*, **2**, 287.
- O'NIONS R., BALLENTINE C., HALLIDAY A., MCKENZIE D. & COLEMAN M. (1993) Rare Gas Studies of Basin Scale Fluid Movement [and Discussion]. *Philosophical Transactions: Physical Sciences and Engineering*, **344**, 141-156.
- OOMORI T., KANESHIMA H., MAEZATO Y. & KITANO Y. (1987) Distribution coefficient of Mg²⁺ ions between calcite and solution at 10-50 C. *Marine Chemistry*, **20**, 327-336.
- ORHAN H. (1992) Importance of dust storms in the diagenesis of sandstones: a case study, Entrada sandstone in the Ghost Ranch area, New Mexico, USA. *Sedimentary geology*, **77**, 111-122.
- OXBURGH E., O'NIONS R. & HILL R. (1986) Helium isotopes in sedimentary basins. *Nature(London)*, **324**, 632-635.
- OXBURGH R., DREVER J. & SUN Y. (1994) Mechanism of plagioclase dissolution in acid solution at 25 C. *Geochimica et Cosmochimica Acta*, **58**, 661-669.
- PACES T. (1972) Chemical characteristics and equilibration in natural water-felsic rock-CO₂ system. *Geochimica et Cosmochimica Acta*, **36**, 217-240.
- PACES T. (1978) Reversible control of aqueous aluminum and silica during the irreversible evolution of natural waters. *Geochimica et Cosmochimica Acta*, **42**, 1487-1493.
- PALANDRI J. & KHARAKA Y. (2002) Ferric Iron-Bearing Sediments as a Mineral Trap for Geologic CO₂

- Sequestration: Iron Reduction Using SO₂ or H₂S Waste Gas. In: *AGU Fall Meeting Abstracts*, 5.
- PALANDRI J., ROSENBAUER R. & KHARAKA Y. (2005) Ferric iron in sediments as a novel CO₂ mineral trap: CO₂-SO₂ reaction with hematite. *Applied Geochemistry*, **20**, 2038-2048.
- PAQUETTE J., VALI H. & MUCCI A. (1996) TEM study of Pt-C replicas of calcite overgrowths precipitated from electrolyte solutions. *Geochimica et Cosmochimica Acta*, **60**, 4689-4699.
- PARKHURST D. & APPELO C. (1999) User's guide to PHREEQC (version 2)—a computer program for speciation, batch-reaction, one-dimensional transport, and inverse geochemical calculations. *US Geological Survey Water-Resources Investigations Report*, **99**, 310.
- PARRY M., CANZIANI O. & PALUTIKOF J. (2007) *Climate Change 2007: impacts, adaptation and vulnerability: contribution of Working Group II to the fourth assessment report of the Intergovernmental Panel on Climate Change*. Cambridge University Press.
- PARRY W., CHAN M. & BEITLER B. (2004) Chemical bleaching indicates episodes of fluid flow in deformation bands in sandstone. *AAPG bulletin*, **88**, 175.
- PAUWELS H., FOUILLAC C., GOFF F. & VUATAZ F. (1997) The isotopic and chemical composition of CO₂-rich thermal waters in the Mont-Dore region (Massif-Central, France). *Applied Geochemistry*, **12**, 411-427.
- PEARCE J. (2004) Natural analogues for the geological storage of CO₂. Final report of the Nascent project. *British Geological Survey Technical Report 122*.
- PEARCE J., CHADWICK A., KIRBY G. & HOLLOWAY S. (2006) The objectives and design of generic monitoring protocols for CO₂ storage. 19-22 British Geological Survey.
- PEARCE J., CZERNICHOWSKI-LAURIOL I., LOMBARDI S., BRUNE S., NADOR A., BAKER J., PAUWELS H., HATZIYANNIS G., BEAUBIEN S. & FABER E. (2004) A review of natural CO₂ accumulations in Europe as analogues for geological sequestration. *Geological Society London Special Publications*, **233**, 29.
- PEARCE J., HOLLOWAY S., WACKER H., NELIS M., ROCHELLE C. & BATEMAN K. (1996) Natural occurrences as analogues for the geological disposal of carbon dioxide. *Energy Conversion and Management*, **37**, 1123-1128.
- PETERSON F. & TURNER-PETERSON C. (1987) The Morrison Formation of the Colorado Plateau: recent advances in sedimentology, stratigraphy, and paleotectonics. *Hunteria*, **2**, 1-18.
- PETIT J., JOUZEL J., RAYNAUD D., BARKOV N., BARNOLA J., BASILE I., BENDER M., CHAPPELLAZ J., DAVIS M. & DELAYGUE G. (1999) Climate and atmospheric history of the past 420,000 years from the Vostok ice core, Antarctica. *Nature*, **399**, 429-436.
- PHILIBERT C. & PODKANSKI J. (2005) International Energy Technology Collaboration and Climate Change Mitigation. Case Study 4: Clean Coal Technologies. *International Energy Agency, Paris*.
- PINGITORE JR N. & EASTMAN M. (1986) The coprecipitation of Sr²⁺ with calcite at 25 C and 1 atm. *Geochimica et Cosmochimica Acta*, **50**, 2195-2203.
- PINGITORE N. (1988) The coprecipitation of manganese (II) with calcite: an experimental study. *Marine Chemistry*, **25**, 107-120.
- PLACZEK G. (1934) *Handbook of Radiology VI*.
- PLUMMER L., PARKHURST D. & WIGLEY T. (1979) Critical review of the kinetics of calcite dissolution and precipitation. In: *Chemical Modeling in Earth Sciences*, 537-573.
- PONNAMPERUMA F., LOY T. & TIANCO E. (1969) Redox equilibria in flooded soils: II. The manganese oxide systems. *Soil Science*, **108**, 48.
- POTTER R. & ROSSMAN G. (1979) The manganese-and iron-oxide mineralogy of desert varnish. *Chemical Geology*, **25**, 79-94.
- POTTS P., WEBB P. & WATSON J. (1984) Energy-dispersive X-ray fluorescence analysis of silicate rocks for major and trace elements. *X-ray Spectrometry*, **13**, 2-15.
- PRUESS K. (2004) Numerical simulation of CO₂ leakage from a geologic disposal reservoir, including transitions from super- to subcritical conditions, and boiling of liquid CO₂. *SPE Journal*, **9**, 237-248.
- PRUESS K. (2005) Numerical studies of fluid leakage from a geologic disposal reservoir for CO₂ show self-limiting feedback between fluid flow and heat transfer. *Lawrence Berkeley National Laboratory*.
- PRUESS K. (2006) On leakage from geologic storage reservoirs of CO₂. *Lawrence Berkeley National Laboratory*.
- PRUESS K. (2008) On CO₂ fluid flow and heat transfer behavior in the subsurface, following leakage from a geologic storage reservoir. *Environmental Geology*, **54**, 1677-1686.
- PRUESS K., XU T., APPS J. & GARCIA J. (2003) Numerical modeling of aquifer disposal of CO₂. *SPE Journal*, **8**, 49-60.
- PYTKOWICZ R. (1965) Calcium carbonate saturation in the ocean. *Limnology and Oceanography*, **10**, 220-225.

- RAHMSTORF S. (2003) Timing of abrupt climate change: A precise clock. *Geophys. Res. Lett.*, **30**, 1510.
- RAISWELL R. & FISHER Q. (2004) Rates of carbonate cementation associated with sulphate reduction in DSDP/ODP sediments: implications for the formation of concretions. *Chemical Geology*, **211**, 71-85.
- RAKOVAN J. & REEDER R. (1996) Intracrystalline rare earth element distributions in apatite: Surface structural influences on incorporation during growth. *Geochimica et Cosmochimica Acta*, **60**, 4435-4445.
- REDDY M. (1977) Crystallization of calcium carbonate in the presence of trace concentrations of phosphorus-containing anions: I. Inhibition by phosphate and glycerophosphate ions at pH 8.8 and 25. *Journal of crystal growth*, **41**, 287-295.
- REDDY M., PLUMMER L. & BUSENBERG E. (1981) Crystal growth of calcite from calcium bicarbonate solutions at constant PCO_2 and 25° C: a test of a calcite dissolution model. *Geochimica et Cosmochimica Acta*, **45**, 1281-1289.
- REDDY M. & WANG K. (1980) Crystallization of Calcium Carbonate in the Presence of Metal Ions I. Inhibition by Magnesium Ion at pH 8. 8 and 25 degree C. *Journal of crystal growth*, **50**, 470-480.
- REED S. (2005) *Electron microprobe analysis and scanning electron microscopy in geology*. Cambridge University Press, Cambridge.
- RIGBY J. (1987) Stratigraphy and structure of the San Rafael Reef Utah; A major monocline of the Colorado Plateau. *Rocky Mountain Section of the Geological Society of America*, 269.
- RIMSTIDT J., BALOG A. & WEBB J. (1998) Distribution of trace elements between carbonate minerals and aqueous solutions. *Geochimica et Cosmochimica Acta*, **62**, 1851-1863.
- RINEHART J. (1980) *Geysers and geothermal energy*. Springer Verlag.
- ROCHELLE C., PEARCE J. & HOLLOWAY S. (1999) The underground sequestration of carbon dioxide: containment by chemical reactions in the deep geosphere. *Chemical Containment of Waste in the Geosphere*, 117.
- ROEDDER E. (1984) Fluid inclusions: Review. *Mineral. Mineral. Soc. Am.*, **12**, 644.
- ROMANEK C., GROSSMAN E. & MORSE J. (1992) Carbon isotopic fractionation in synthetic aragonite and calcite: effects of temperature and precipitation rate. *Geochimica et Cosmochimica Acta*, **56**, 419-430.
- ROSASCO G. & ROEDDER E. (1979) Application of a new Raman microprobe spectrometer to nondestructive analysis of sulfate and other ions in individual phases in fluid inclusions in minerals. *Geochimica et Cosmochimica Acta*, **43**, 1907-1915.
- ROSENBAUER R., KOKSALAN T. & PALANDRI J. (2005) Experimental investigation of CO₂-brine-rock interactions at elevated temperature and pressure: Implications for CO₂ sequestration in deep-saline aquifers. *Fuel processing technology*, **86**, 1581-1597.
- ROSSO K. & BODNAR R. (1995) Microthermometric and Raman spectroscopic detection limits of CO₂ in fluid inclusions and the Raman spectroscopic characterization of CO₂. *Geochimica et Cosmochimica Acta*, **59**, 3961-3975.
- ROWE G. & BRANTLEY S. (1993) Estimation of the dissolution rates of andesitic glass, plagioclase and pyroxene in a flank aquifer of Poás Volcano, Costa Rica. *Chemical Geology*, **105**, 71-87.
- RUDNICKI J. & WAWERSIK W. (1999) Report looks at sequestering CO₂ beneath Earth's surface. *Eos Trans. AGU*, **80**, 607.
- RUTQVIST J., VASCO D. & MYER L. (2009) Coupled reservoir-geomechanical analysis of CO₂ injection at In Salah, Algeria. *Energy Procedia*, **1**, 1847-1854.
- SAYLOR B. & ZERAI B. (2004) Injection and trapping of carbon dioxide in deep saline aquifers. *Energy, Waste and the Environment: A Geochemical Perspective*, 285.
- SCHILLING F., BORM G., WÜRDEMANN H., MÖLLER F. & KÜHN M. (2009) Status Report on the First European on-shore CO₂ Storage Site at Ketzin (Germany). *Energy Procedia*, **1**, 2029-2035.
- SCHNEIDER S. (2004) Abrupt non-linear climate change, irreversibility and surprise. *Global Environmental Change*, **14**, 245-258.
- SCHOFIELD S. & JANKOWSKI J. (2004) Hydrochemistry and isotopic composition of Na-HCO₃-rich groundwaters from the Ballimore region, central New South Wales, Australia. *Chemical Geology*, **211**, 111-134.
- SCHWERTMANN U. (1991) Solubility and dissolution of iron oxides. *Plant and Soil*, **130**, 1-25.
- SEITZ J., PASTERIS J. & WOPENKA B. (1987) Characterization of CO₂-CH₄-H₂O fluid inclusions by microthermometry and laser Raman microprobe spectroscopy- Inferences for clathrate and fluid equilibria. *Geochimica et Cosmochimica Acta*, **51**, 1651-1664.
- SHAFIEE S. & TOPAL E. (2008) An econometrics view of worldwide fossil fuel consumption and the role of US. *Energy Policy*, **36**, 775-786.
- SHERWOOD LOLLAR B., BALLENTINE C. & ONIONS R. (1997) The fate of mantle-derived carbon in a continental sedimentary basin: Integration of C He relationships and

- stable isotope signatures. *Geochimica et Cosmochimica Acta*, **61**, 2295-2307.
- SHIPTON Z., EVANS J., DOCKRILL B., HEATH J., WILLIAMS A., KIRSCHNER D. & KOLESAR P. (2005) Natural leaking CO₂-charged systems as analogs for failed geologic storage reservoirs. *The CO₂ Capture and Storage Project (CCP)*.
- SHIPTON Z., EVANS J., KIRSCHNER D., KOLESAR P., WILLIAMS A. & HEATH J. (2004) Analysis of CO₂ leakage through 'low-permeability' faults from natural reservoirs in the Colorado Plateau, east-central Utah. *Geological Society London Special Publications*, **233**, 43.
- SHIRAKI R. & BRANTLEY S. (1995) Kinetics of near-equilibrium calcite precipitation at 100 C: An evaluation of elementary reaction-based and affinity-based rate laws. *Geochimica et Cosmochimica Acta*, **59**, 1457-1471.
- SOMMER S. (1972) Cathodoluminescence of carbonates, 2. Geological applications. *Chemical Geology*, **9**, 275-284.
- SOONG Y., FAUTH D., HOWARD B., JONES J., HARRISON D., GOODMAN A., GRAY M. & FROMMELL E. (2006) CO₂ sequestration with brine solution and fly ashes. *Energy Conversion and Management*, **47**, 1676-1685.
- SOONG Y., GOODMAN A., MCCARTHY-JONES J. & BALTRUS J. (2004) Experimental and simulation studies on mineral trapping of CO₂ with brine. *Energy Conversion and Management*, **45**, 1845-1859.
- SORAI M., OHSUMI T. & ISHIKAWA M. (2005) Nanoscale surface observation of feldspar dissolved under supercritical CO₂-water-mineral system. *Energy*, **30**, 2334-2343.
- SPANGLER L., NAFTZ D. & PETERMAN Z. (1996) Hydrology, chemical quality, and characterization of salinity in the Navajo aquifer in and near the Greater Aneth oil field. *San Juan County, Utah: US Geological Survey Water-Resources Investigations Report*, 96-4155.
- STEVENS S., PEARCE J., RIGG A. & SYDNEY N. (2001) Natural analogs for geologic storage of CO₂: An integrated global research program. United States Geological Survey.
- STRAZISAR B., ZHU C. & HEDGES S. (2006) Preliminary modeling of the long-term fate of CO₂ following injection into deep geological formations. *Environmental Geosciences*, **13**, 1.
- STUMM W., MORGAN J. & DREVER J. (1996) *Aquatic chemistry*. Wiley New York.
- SUAREZ C., SUAREZ M., TERRY JR D. & GRANDSTAFF D. (2007) Rare earth element geochemistry and taphonomy of the Early Cretaceous Crystal Geyser Dinosaur Quarry, east-central Utah. *Palaaios*, **22**, 500.
- SUAREZ M., SUAREZ C., KIRKLAND J., GONZÁLEZ L., GRANDSTAFF D. & TERRY JR D. (2007) Sedimentology, stratigraphy, and depositional environment of the Crystal Geyser Dinosaur Quarry, east-central Utah. *Palaaios*, **22**, 513.
- SUEKANE T., NOBUSO T., HIRAI S. & KIYOTA M. (2008) Geological storage of carbon dioxide by residual gas and solubility trapping. *International Journal of Greenhouse Gas Control*, **2**, 58-64.
- SURANA V. & WARREN I. (1969) The leaching of goethite. *Trans. Inst. Min. Metall., Sect. C: Miner. Proc. Extr. Metall.*, **78**, 133.
- TAFT W. (1967) Physical chemistry of formation of carbonates. *Carbonate Rocks: Origin, Occurrence and Classification*, 151.
- TAGIROV B. & SCHOTT J. (2001) Aluminum speciation in crustal fluids revisited. *Geochimica et Cosmochimica Acta*, **65**, 3965-3992.
- TAKU IDE S., JESSEN K. & ORR F. (2007) Storage of CO₂ in saline aquifers: Effects of gravity, viscous, and capillary forces on amount and timing of trapping. *International Journal of Greenhouse Gas Control*, **1**, 481-491.
- TAYLOR A., BLUM J. & LASAGA A. (2000) The dependence of labradorite dissolution and Sr isotope release rates on solution saturation state. *Geochimica et Cosmochimica Acta*, **64**, 2389-2400.
- TAYLOR A., BLUM J., LASAGA A. & MACINNIS I. (2000) Kinetics of dissolution and Sr release during biotite and phlogopite weathering. *Geochimica et Cosmochimica Acta*, **64**, 1191-1208.
- TESORIERO A. & PANKOW J. (1996) Solid solution partitioning of Sr²⁺, Ba²⁺, and Cd²⁺ to calcite. *Geochimica et Cosmochimica Acta*, **60**, 1053-1063.
- TRIMBLE L. & DOELLING H. (1978) Geology and uranium-vanadium deposits of the San Rafael River mining area. *Emery County, Utah: Utah Geological and Mineral Survey Bulletin*, **113**, 122.
- TRIPATI A., ROBERTS C. & EAGLE R. (2009) Coupling of CO₂ and Ice Sheet Stability Over Major Climate Transitions of the Last 20 Million Years. *Science*, 1178296v1178291.
- TRUINI M. & LONGSWORTH S. (2003) Hydrogeology of the D aquifer and movement and ages of ground water determined from geochemical and isotopic analyses, Black Mesa area, northeastern Arizona. US Dept. of the Interior, US Geological Survey.
- TRUINI M. & LONGSWORTH S. (2003) *Hydrogeology of the D aquifer and movement and ages of ground water determined from geochemical and isotopic analyses, Black Mesa area, northeastern Arizona*. US Dept. of the Interior, US Geological Survey.

- TUCKER M. & WRIGHT V. (1996) *Carbonate sedimentology*. Blackwell Science.
- TUNUSOGLU O., SHAHWAN T. & EROGLU A. (2007) Retention of aqueous Ba²⁺ ions by calcite and aragonite over a wide range of concentrations: Characterization of the uptake capacity, and kinetics of sorption and precipitate formation. *GEOCHEMICAL JOURNAL-JAPAN*, **41**, 379.
- USDOWSKI E. & HOEFS J. (1993) Oxygen isotope exchange between carbonic acid, bicarbonate, carbonate, and water: A re-examination of the data of McCrea (1950) and an expression for the overall partitioning of oxygen isotopes between the carbonate species and water. *Geochimica et Cosmochimica Acta*, **57**, 3815-3818.
- VAHRENKAMP V. & SWART P. (1990) New distribution coefficient for the incorporation of strontium into dolomite and its implications for the formation of ancient dolomites. *Geology*, **18**, 387.
- VALLEY J. (1986) Stable isotope geochemistry of metamorphic rocks. *Reviews in Mineralogy and Geochemistry*, **16**, 445.
- VAN DER ZWAAN B. & GERLAGH R. (2009) Economics of geological CO₂ storage and leakage. *Climatic Change*, **93**, 285-309.
- VEIZER J. (1977) Diagenesis of pre-Quaternary carbonates as indicated by tracer studies. *Journal of Sedimentary Research*, **47**, 565.
- VEIZER J. (1983) Trace elements and isotopes in sedimentary carbonates. *Reviews in Mineralogy and Geochemistry*, **11**, 265.
- VEIZER J. (1983) Chemical diagenesis of carbonates: theory and application of trace element technique. *Stable Isotopes in Sedimentary Geology: Society of Economic Paleontologists and Mineralogists, Short Course*, **10**, 3.1-3.100.
- VELBEL M. (1989) Effect of chemical affinity on feldspar hydrolysis rates in two natural weathering systems. *Chemical Geology*, **78**, 245-253.
- VOGEL J., GROOTES P. & MOOK W. (1970) Isotopic fractionation between gaseous and dissolved carbon dioxide. *Zeitschrift für Physik A Hadrons and Nuclei*, **230**, 225-238.
- WALKER T.R. (1979) A study of global sand seas: Red color in dune sand. In: *A study of global sand seas: U.S. Geological Survey Professional Paper* (Ed. E.D. McKee), Vol. **105**.
- WALTHAM T. (2001) Crystal Geyser-Utah's cold one. *Geology Today*, **17**, 22-24.
- WANG C. & WRIGHT R. (1973) Effect of density on the Raman scattering of molecular fluids. I. A detailed study of the scattering polarization, intensity, frequency shift, and spectral shape in gaseous N. *The Journal of Chemical Physics*, **59**, 1706.
- WANG S. & JAFFE P. (2004) Dissolution of a mineral phase in potable aquifers due to CO₂ releases from deep formations; effect of dissolution kinetics. *Energy Conversion and Management*, **45**, 2833-2848.
- WANG Y. & XU H. (2001) Prediction of trace metal partitioning between minerals and aqueous solutions: a linear free energy correlation approach. *Geochimica et Cosmochimica Acta*, **65**, 1529-1543.
- WATSON E. & LIANG Y. (1995) A simple model for sector zoning in slowly grown crystals: Implications for growth rate and lattice diffusion, with emphasis on accessory minerals in crustal rocks. *American Mineralogist*, **80**, 1179-1187.
- WEIGEL J. (1986) Selected hydrologic and physical properties of Mesozoic formations in the upper Colorado River Basin in Arizona. *Colorado, Utah, and Wyoming excluding the San Juan Basin: US Geological Survey Water-Resources Investigations Report*, 86-4170.
- WELHAM N., MALATT K. & VUKCEVIC S. (2000) The stability of iron phases presently used for disposal from metallurgical systems—a review. *Minerals Engineering*, **13**, 911-931.
- WERNBERG T. (1998) Multicomponent groundwater transport with chemical equilibrium and kinetics: Model development and evaluation. *Hydrological Sciences Journal/Journal des Sciences Hydrologiques*, **43**, 299-317.
- WHELAN J. & STUCKLESS J. (1992) Paleohydrologic Implications of the Stable Isotopic Composition of Secondary Calcite Within the Tertiary Volcanic Rocks of Yucca Mountain, Nevada. *High Level Radioactive Waste Management 1572-1581*.
- WHITE A., BLUM A., SCHULZ M., BULLEN T., HARDEN J. & PETERSON M. (1996) Chemical weathering rates of a soil chronosequence on granitic alluvium: I. Quantification of mineralogical and surface area changes and calculation of primary silicate reaction rates. *Geochimica et Cosmochimica Acta*, **60**, 2533-2550.
- WHITE A. & BRANTLEY S. (1995) Chemical weathering rates of silicate minerals: an overview. *Chemical weathering rates of silicate minerals*, **31**, 1-22.
- WHITE A. & BRANTLEY S. (2003) The effect of time on the weathering of silicate minerals: why do weathering rates differ in the laboratory and field? *Chemical Geology*, **202**, 479-506.
- WHITE A., PETERSON M. & SOLBAU R. (1990) Measurement and interpretation of low levels of dissolved oxygen in ground water. *Ground Water*, **28**, 584-590.

- WHITE S., ALLIS R., MOORE J., CHIDSEY T., MORGAN C., GWYNN W. & ADAMS M. (2005) Simulation of reactive transport of injected CO₂ on the Colorado Plateau, Utah, USA. *Chemical Geology*, **217**, 387-405.
- WHITE W. (1997) Thermodynamic equilibrium, kinetics, activation barriers, and reaction mechanisms for chemical reactions in karst terrains. *Environmental Geology*, **30**, 46-58.
- WIELAND E., WEHRLI B. & STUMM W. (1988) The coordination chemistry of weathering: III. A generalization on the dissolution rates of minerals. Name: *Geochimica et Cosmochimica Acta*.
- WILKINSON J. (2001) Fluid inclusions in hydrothermal ore deposits. *Lithos*, **55**, 229-272.
- WILKINSON M. & DAMPIER M. (1990) The rate of growth of sandstone-hosted calcite concretions. *Geochimica et Cosmochimica Acta*, **54**, 3391-3399.
- WILKINSON M., GILFILLAN S., RS H. & BALLENTINE C. (2008) Plumbing the Depths: Testing Natural Tracers of Subsurface CO₂ Origin and Migration, Utah. *Carbon dioxide sequestration in geological media—State of the science: AAPG Studies*, **59**.
- WILLIAMS G. (1983) The rate of hydration of carbon dioxide in natural waters. *Ecological Bulletins*, 281-289.
- WILSON M. & MONEA M. (2004) IEA GHG Weyburn CO₂ Monitoring and Storage Project Summary Report 2000-2004. 3, 5-9.
- WOOD J. & BOLES J. (1991) Evidence for episodic cementation and diagenetic recording of seismic pumping events, North Coles Levee, California, U. S. A. *Applied Geochemistry*, **6**, 509-521.
- WOPENKA B. & PASTERIS J. (1987) Raman intensities and detection limits of geochemically relevant gas mixtures for a laser Raman microprobe. *Analytical Chemistry*, **59**, 2165-2170.
- WORDEN R. (2006) Dawsonite cement in the Triassic Lam Formation, Shabwa basin, Yemen: A natural analogue for a potential mineral product of subsurface CO₂ storage for greenhouse gas reduction. *Marine and Petroleum Geology*, **23**, 61-77.
- WYCHERLEY H., FLEET A. & SHAW H. (1999) Some observations on the origins of large volumes of carbon dioxide accumulations in sedimentary basins. *Marine and Petroleum Geology*, **16**, 489-494.
- XU T., APPS J. & PRUESS K. (2004) Numerical simulation of CO₂ disposal by mineral trapping in deep aquifers. *Applied Geochemistry*, **19**, 917-936.
- XU T., APPS J. & PRUESS K. (2005) Mineral sequestration of carbon dioxide in a sandstone-shale system. *Chemical Geology*, **217**, 295-318.
- XU T., APPS J., PRUESS K. & YAMAMOTO H. (2007) Numerical modeling of injection and mineral trapping of CO₂ with H₂S and SO₂ in a sandstone formation. *Chemical Geology*, **242**, 319-346.
- YAMAMOTO J. & KAGI H. (2006) Extended micro-Raman densimeter for CO₂ applicable to mantle-originated fluid inclusions. *Chemistry Letters*, **35**, 610-611.
- ZEEBE R. & WOLF-GLADROW D. (2001) *CO₂ in seawater: equilibrium, kinetics, isotopes*. Elsevier Science.
- ZHANG J., QUAY P. & WILBUR D. (1995) Carbon isotope fractionation during gas-water exchange and dissolution of CO₂. *Geochimica et Cosmochimica Acta*, **59**, 107-114.
- ZHONG S. & MUCCI A. (1989) Calcite and aragonite precipitation from seawater solutions of various salinities: Precipitation rates and overgrowth compositions. *Chemical Geology*, **78**, 283-299.
- ZHONG S. & MUCCI A. (1993) Calcite precipitation in seawater using a constant addition technique: A new overall reaction kinetic expression. *Geochimica et Cosmochimica Acta*, **57**, 1409-1417.
- ZHONG S. & MUCCI A. (1995) Partitioning of rare earth elements (REEs) between calcite and seawater solutions at 25 C and 1 atm, and high dissolved REE concentrations. *Geochimica et Cosmochimica Acta*, **59**, 443-453.
- ZHOU G. & ZHENG Y. (2003) An experimental study of oxygen isotope fractionation between inorganically precipitated aragonite and water at low temperatures. *Geochimica et Cosmochimica Acta*, **67**, 387-399.
- ZHU C. (2000) Estimate of recharge from radiocarbon dating of groundwater and numerical flow and transport modeling. *Water Resources Research*, **36**, 2607-2620.
- ZHU C. (2005) In situ feldspar dissolution rates in an aquifer. *Geochimica et Cosmochimica Acta*, **69**, 1435-1453.
- ZHU C., VEBLEN D., BLUM A. & CHIPERA S. (2006) Naturally weathered feldspar surfaces in the Navajo Sandstone aquifer, Black Mesa, Arizona: Electron microscopic characterization. *Geochimica et Cosmochimica Acta*, **70**, 4600-4616.
- ZUDDAS P. & MUCCI A. (1994) Kinetics of calcite precipitation from seawater: I. A classical chemical kinetics description for strong electrolyte solutions. *Geochimica et Cosmochimica Acta*, **58**, 4353-4362.
- ZUDDAS P. & MUCCI A. (1998) Kinetics of calcite precipitation from seawater: II. The influence of the ionic strength. *Geochimica et Cosmochimica Acta*, **62**, 757-766.

Appendix A

Spring Geochemistry Data Tables

A.1. Gas Isotope Geochemistry

Table A.1-I $\delta^{13}\text{C}$ of $\text{CO}_2(\text{g})$ collected from CO_2 -charged springs during the 2006 and 2007 field seasons.

<i>2006 Data</i>			
Sample	Spring/Geyser	$\delta^{13}\text{C}_{\text{CO}_2(\text{g})}$ (VPDB)	Notes
UT0601	Crystal Geyser	-7.31	
UT0602	Torrey's Spring	-6.79	
UT0603	Tenmile Geyser	-7.55	Slow Freeze
UT0605	Pseudo Tenmile Geyser	-7.28	
UT0605A	Pseudo Tenmile Geyser	-7.32	
UT0606	Chaffin Ranch	-7.25	
UT0608	Airport Well	-6.61	
UT0609	Big Bubbling Spring	-6.97	Excess Water
UT0610	Small Bubbling Spring	-7.02	
UT0611	Seep, Big Bubbling Spring	-7.18	
UT0615	Tumble Weed Geyser	-6.72	
UT0617	Side Seep, Crystal Geyser	-7.30	
<i>2007 Data</i>			
Sample	Spring/Geyser	$\delta^{13}\text{C}_{\text{CO}_2(\text{g})}$ (VPDB)	Notes
GR07g001	Pseudo-Tenmile Geyser	-7.54	
GR07g006	Big Bubbling	-7.21	
GR07g003	Torreys Spring	-7.39	
GR07g004	Airport Well	-6.29	Excess Water
GR07g005	Small Bubbling Spring	-6.98	
GR07g002	Tenmile Geyser	-7.34	
GR07g012	Crystal Geyser	-7.33	
GR07g009	Chaffin Ranch	-6.88	Eruption
GR07g008	Chaffin Ranch	-6.20	Pre-eruption

A.2. CO₂-spring Fluid Chemistry & Isotope Data

Table A.2-I Major and minor element and isotope data from the CO₂-charged springs, 2006 and 2007 field seasons. Alkalinity [Alk] was titrated in the field. 2007 data includes field determined redox potentials (mV).

<i>2006 Data</i>																	
Spring/Sample Name	Temp	pH	Al³⁺	Ba²⁺	Ca²⁺	Fe	K⁺	Mg²⁺	Mn	Na⁺	Si	Sr²⁺	Cl⁻	SO₄²⁻	[Alk]	DIC	⁸⁷Sr/⁸⁶Sr
	°C		μmol/l	μmol/l	mmol/l	μmol/l	mmol/l	mmol/l	μmol/l	mmol/l	mmol/l	μmol/l	mmol/l	mmol/l	meq/l	mmol/l	
Green River Airport Well	27.0	6.18	3.6	0.14	19.7	4.6	2.15	7.95	22.7	18.11	922.8	112.7	2.59	19.06	37.08	75.59	0.712660
Crystal Geyser	18.0	6.46	4.9	0.10	21.8	44.4	7.98	9.02	25.1	159.02	186.7	142.9	137.94	26.46	68.86	107.37	0.712588
Small Bubbling Spring	17.2	6.17	3.2	0.12	18.2	2.3	7.35	8.88	19.0	160.27	139.7	138.0	128.63	26.65	56.54	118.89	0.711755
Big Bubbling Spring	17.5	6.30	5.1	0.10	21.6	2.7	9.36	8.55	7.2	212.87	135.7	157.4	178.29	32.17	66.04	116.33	0.712798
Side Seep, Big Bubbling	16.5	6.21	5.0	0.11	19.1	4.0	9.23	8.65	7.5	211.26	131.0	131.0	170.47	30.12	59.69	118.75	0.713053
Pseudo-Tenmile Geyser	15.0	6.52	4.3	0.08	19.3	19.2	9.55	8.09	2.2	228.04	136.7	164.2	177.98	31.20	62.06	93.33	0.713327
Torrey's Spring	15.8	6.59	4.8	0.13	23.5	48.0	11.02	7.93	19.1	251.29	152.3	145.0	193.14	30.16	78.72	111.63	0.712720
Tenmile Geyser	15.7	6.58	5.0	0.14	22.2	83.1	6.79	9.44	18.5	219.01	159.5	236.3	165.19	14.30	58.21	83.19	0.712554
Tumble Weed Geyser	15.9	6.46	5.0	0.12	18.8	5.2	8.11	8.90	12.1	189.25	144.3	153.5	132.88	19.74	62.12	97.94	0.712663
Chaffin Ranch Geyser	14.7	6.73	5.0	0.08	26.0	67.6	7.58	9.78	17.4	193.54	134.0	165.5	128.39	14.54	76.12	100.15	0.712581

<i>2007 Data</i>																				
Spring/Sample Name	Eh	Temp	pH	Al³⁺	Ba²⁺	Ca²⁺	Fe	K⁺	Mg²⁺	Mn	Na⁺	Si	Sr²⁺	Cl⁻	SO₄²⁻	DIC	⁸⁷Sr/⁸⁶Sr	δ¹³C_{DIC}	δ¹⁸O	³H
	mV	°C		μmol/l	μmol/l	mmol/l	μmol/l	mmol/l	mmol/l	μmol/l	mmol/l	μmol/l	μmol/l	mmol/l	mmol/l	mmol/l		(VPDB)	(SMOW)	TU
Green River Airport Well	-42	26.8	6.18	4.6	0.09	22.18	106.0	2.19	8.82	24.0	20.55	993.0	104.2	2.59	20.93	66.73	N/A	-1.83	-14.48	0.50
Crystal Geyser	-5	16.9	6.37	5.8	0.08	26.13	230.6	9.35	9.63	28.4	163.56	199.8	147.1	121.77	25.58	120.96	0.712719	-0.85	-14.52	0.30
Small Bubbling Spring	-7	19.2	6.14	4.3	0.07	19.81	61.1	8.82	9.54	19.2	164.80	143.4	128.5	131.07	25.44	90.83	0.712530	-1.17	-14.25	N/A
Big Bubbling Spring	-32	17.7	6.26	5.0	0.05	23.20	123.3	11.42	9.35	6.8	218.28	138.2	148.6	183.64	30.12	85.79	0.712721	-0.48	-13.88	0.30
Side Seep, Big Bubbling	-32	17.9	6.25	4.3	0.10	20.79	118.0	11.03	9.28	9.7	213.47	148.9	127.5	161.41	30.33	94.80	N/A	-0.39	-13.77	N/A
Pseudo-Tenmile Geyser	6	15.8	6.42	4.7	0.04	20.72	107.9	11.38	8.53	1.9	223.76	126.9	150.7	153.07	31.61	95.81	N/A	-0.59	-13.76	0.70
Torreys Spring	-40	16.4	6.51	5.8	0.04	25.41	144.2	13.40	8.41	19.8	247.39	123.8	132.6	229.42	31.41	118.75	0.712617	0.74	-13.86	0.70
Tenmile Geyser	-23	18.5	6.55	5.0	0.06	24.08	55.9	7.81	10.13	19.0	220.07	131.6	221.3	197.61	19.71	110.01	0.711788	-1.67	-13.21	0.30
Tumble Weed Geyser	-32	17.9	6.42	6.0	0.03	28.26	263.7	8.62	10.34	17.9	192.66	115.7	154.4	179.45	25.91	84.53	0.713056	-0.19	-13.82	0.40
Chaffin Ranch Geyser	-35	16.0	6.75	5.8	0.02	27.58	267.2	8.62	10.33	17.4	194.19	112.4	147.1	145.74	26.22	118.59	N/A	-0.63	-13.76	0.50

A.3. Crystal Geyser Fluid Chemistry & Isotope Data

Table A.3-I Major and minor element and isotope data from temporal samples through the build up to, and course of, a large-scale eruption of Crystal Geyser.

Sample	Time	pH	Temp °C	Al ³⁺	Ba ²⁺	Ca ²⁺	Fe	K ⁺	Mg ²⁺	Mn	Na ⁺	Si	Sr ²⁺	Cl	SO ₄ ²⁻	DIC	δ ¹⁸ O	δ ¹³ C _{DIC}	⁸⁷ Sr/ ⁸⁶ Sr
				μmol/l	μmol/l	mmol/l	μmol/l	mmol/l	mmol/l	μmol/l	mmol/l	μmol/l	mmol/l	μmol/l	μmol/l	mmol/l	mmol/l	mmol/l	(VSMOW)
CG1	12:00:00	6.52	17.0	5.8	0.08	26.1	231	9.3	9.6	28	164	200	147	123	24.7	109	-14.36	-0.69	0.712712
CG2	12:30:00	6.38	18.1	5.4	0.08	26.3	236	9.4	9.6	28	164	203	149	124	24.9	111	-14.32	-0.92	0.712704
CG3	13:00:00	6.48	18.3	5.8	0.07	26.1	246	9.5	9.6	28	166	203	149	126	24.9	101	-14.35	-0.52	0.712707
CG4	13:30:00	6.38	18.1	6.1	0.09	26.3	250	9.6	9.7	28	169	204	149	129	25.0	103	-14.32	-0.61	0.712723
CG5	14:00:00	6.38	18.2	5.4	0.07	25.8	246	9.7	9.7	27	170	205	148	128	25.2	119	-14.51	-0.81	0.712726
CG6	14:30:00	6.47	18.2	6.2	0.07	26.0	239	9.6	9.5	27	168	199	148	122	24.2	93	-14.48	-0.51	0.712723
CG7	15:00:00	6.51	18.8	5.3	0.08	25.9	229	9.5	9.5	27	169	200	148	123	24.2	90	-14.54	-0.63	0.712723
CG8	15:30:00	6.38	18.7	6.0	0.08	25.7	241	9.7	9.6	27	171	204	147	130	25.5	109	-14.44	-0.94	0.712726
CG9	15:47:00	6.57	18.1	6.0	0.07	26.3	251	9.6	9.6	27	171	201	150	129	25.2	95	-14.43	-0.22	0.712729
CG10	15:55:10	6.57	17.7	6.1	0.08	26.5	252	9.4	9.7	30	163	202	148	123	25.0	98	-14.46	-0.73	0.712698
CG11	16:02:00	6.55	17.3	5.7	0.08	26.3	248	9.2	9.6	30	160	199	148	121	24.6	88	-14.49	-0.19	0.712696
CG12	16:06:00	6.57	17.7	5.8	0.08	26.2	257	9.1	9.6	29	158	202	149	122	24.9	96	-14.50	-0.29	0.712685
CG13	16:10:00	6.55	17.8	5.9	0.07	26.5	258	9.1	9.7	30	158	206	150	119	24.1	102	-14.51	-0.47	0.712669
CG14	16:16:30	6.55	17.8	6.0	0.08	26.5	264	9.1	9.8	30	157	207	151	117	24.2	82	-14.52	-0.35	0.712674
CG15	16:33:00	6.55	18.7	5.7	0.08	26.7	280	8.6	10.0	31	149	203	154	112	23.9	93	-14.55	-0.42	0.712613
CG16	17:00:00	6.53	18.2	5.4	0.08	26.8	281	8.1	10.2	32	133	205	158	97	22.4	93	-14.61	-0.23	0.712551
CG17	17:30:00	6.56	16.6	5.5	0.08	26.7	276	7.8	10.2	32	128	202	159	98	22.7	86	-14.64	-0.42	0.712524

A.4. Paradox Formation Brine Analyses

Table A.4-I Major solute chemistry of brine analyses from the Paradox Formation, Paradox Basin, compiled from the USGS produced water database Breit, (2002).

Lat	Long	API	Interval	pH	<i>mmol/l</i>						
					Ca	K	Mg	Na	HCO3	Cl	SO4
37.32	-109.25	4303706099	DESERT CREEK	7.6	113		38	550	3	846	1
38.14	-109.81	4303706346	PARADOX	8.3	52		46	572	0	719	26
37.09	-109.5	4303705082	PARADOX	8	16		66	578	19	623	50
38.15	-109.8	4303706350	PARADOX	8.2	135		47	596	3	931	14
37.08	-109.5		PARADOX	8	32		31	638	16	649	50
37.08	-109.49	4303705074	PARADOX	7.1	51		19	663	19	700	42
38.15	-109.8	4303706350	PARADOX	6.8	187		40	674	3	1100	14
37.05	-109.49	4303705047	PARADOX	7.18	66		62	703	20	869	36
37.07	-109.6	43037005068	PARADOX	8.3	57	12	50	739	15	880	35
37.3	-109.18	4303706002	PARADOX HERMOSA	6.8	177		77	793	2	1298	1
37.07	-109.6	4303705068	PARADOX LOWER	7.4	62	13	53	797	14	959	34
37.07	-109.6	4303705068	PARADOX	7.6	60	13	53	811	16	965	35
37.07	-109.6	43037005068	PARADOX	7.8	60	13	51	811	17	959	35
37.39	-109.46		ISMAY	6.6	100	10	39	870	5	1111	21
37.09	-109.61	4303705077	PARADOX	7.1	135		75	892	19	1241	26
37.09	-109.61	4303705077	PARADOX	7.1	105		53	943	19	1185	28
37.66	-109.59	43037006292	ISMAY UPPER	7.4	174		53	944	2	1326	35
37.05	-109.59	4303705057	PARADOX	6	195		117	973	9	1551	19
37.07	-109.31	4303705067	PARADOX	7.9	162		113	996	8	1467	36
38.59	-109.96	4301905035	PARADOX	5.4	182		97	1044	1	1574	16
37.04	-109.22	4303705041	ISMAY LOWER	8	73	8	53	1059	6	1308	7
			DESERT CREEK	7.2	187	7	70	1171	2	1664	13
37.42	-109.42	4303706216	PARADOX	7.4	105		70	1179	2	1805	21
37.3	-109.25		PARADOX	7.2	267		97	1249	2	1946	14
37.09	-109.08	4303705080	ISMAY LOWER	7.3	133	8	91	1393	4	1828	10
37.03	-109.53	4303720291	ISMAY LOWER	7.3	82		56	1415	23	1612	28
37.32	-109.32		PARADOX	8.3	236		64	1428	4	1974	24
			DESERT CREEK	7.2	223	17	90	1544	2	2172	7
37.09	-109.08	4303705080	ISMAY LOWER	7.1	147	8	112	1554	5	2059	8
37.26	-109.1	4303706545	ISMAY UPPER LOWER	7.2	170	11	79	1611	3	2087	15
37.26	-109.1	4303706545	ISMAY UPPER LOWER	7.4	182	10	60	1652	2	2115	15
38.34	-109.59	4303706415	PARADOX	6.7	49		22	1670	8	1721	42
37.08	-109.14	4303705075	PARADOX	7.5	94		44	1687	3	1907	27
37.3	-109.14	4303705990	PARADOX	7	210		216	1689	2	2510	14
37.26	-109.1	4303706545	ISMAY UPPER LOWER	7.4	188	11	73	1693	3	2200	11
37.26	-109.1	4303706545	ISMAY UPPER LOWER	7	188	10	79	1701	2	2228	15
37.68	-109.5	43037006294	PARADOX	7.4	281		112	1706	3	2460	15
37.08	-109.14	4303705075	PARADOX	7.5	115		50	1739	7	2032	15
37.26	-109.1	4303706545	ISMAY UPPER LOWER	5.5	188	11	79	1762	1	2285	10
37.26	-109.1	4303706545	ISMAY UPPER LOWER	7.3	194	13	73	1763	3	2285	11
37.26	-109.1	4303706545	ISMAY UPPER LOWER	5	206	11	79	1781	1	2341	10

Table A.4-I continued

Lat	Long	API	Interval	pH	<i>mmol/l</i>						
					Ca	K	Mg	Na	HCO3	Cl	SO4
37.29	-109.5	43037005903	PARADOX ISMAY	6.2	556		226	1806		3357	6
37.24	-109.11	4303705658	ISMAY	8.1	213		80	1826	3	2370	18
37.22	-109.11	4303705483	ISMAY LOWER	7.1	195		80	1827	3	2341	17
37.26	-109.1	4303706545	ISMAY UPPER LOWER	5.7	206	11	97	1830	1	2426	10
37.29	-109.14	4303705902	ISMAY LOWER	8.7	201	7	104	1831	1	2426	9
37.26	-109.1	4303706545	ISMAY UPPER LOWER	7	206	13	79	1838	2	2398	10
37.3	-109.14	4303705990	PARADOX	6.9	196		115	1892	2	2482	15
37.3	-109.18	4303706002	PARADOX HERMOSA	7.7	241		177	1988	5	2528	8
			PARADOX ISMAY	7.2	421		203	2012	1	3244	7
37.62	-109.48		PARADOX ISMAY	7.8	413		151	2021	3	3131	7
37.29	-109.44		PARADOX ISMAY	6.2	360		241	2028		3216	8
37.72	-109.15	4303706303	PARADOX		302		201	2030	1	3013	10
37.3	-109.31	4303705976	DESERT CREEK	6.6	451		158	2041	1	3244	7
37.22	-109.11	4303705483	ISMAY	6.7	216		83	2054	1	2629	11
37.68	-109.5	43037006294	PARADOX	6.8	358		179	2072	2	3120	13
37.22	-109.11	4303705483	ISMAY	6.6	223		87	2088	2	2686	11
37.25	-109.07	4303705704	ISMAY LOWER	5.7	221		99	2100	1	2713	13
37.31	-109.56	4303706071	ISMAY LOWER	8.2	187		100	2182	2	2708	24
37.68	-109.5	43037006294	PARADOX	6.7	377		230	2264	2	3456	10
37.24	-109.29	4303705649	DESERT CREEK	6.9	376		166	2316	2	3385	6
37.25	-109.34		DESERT CREEK	6.8	398		294	2349	1	3723	4
37.27	-109.25	4303705805	PARADOX	6.7	447		185	2388	2	3639	6
37.16	-109.57		PARADOX	5.3	357		190	2392	1	3469	9
37.22	-109.26	4303705485	DESERT CREEK	6.8	360		181	2574	2	3639	8
37.31	-109.54	4303706094	PARADOX	7.2	320		142	2596	4	3498	10
37.29	-109.25	4303705918	DESERT CREEK	6.7	518		233	2600	2	4090	6
37.29	-109.35		DESERT CREEK	7	548		196	2753	2	4231	5
37.33	-109.19	4303706157	PARADOX	6.9	629		140	2807	5	4316	12
37.24	-109.34	4303705648	PARADOX	6.6	455		270	2868	2	4299	9
37.3	-109.29	4303706000	DESERT CREEK	6.5	488		188	2887	1	4231	4
37.29	-109.52		PARADOX	6.5	548		218	2989		4513	5
37.33	-109.26		PARADOX UPPER	6.2	568		227	3068	8	4639	6
37.31	-109.32	4303706111	PARADOX P 3		517		156	3103	1	4441	4
37.3	-109.05	4303705993	PARADOX	5.2	262		80	3140	1	3808	8
37.19	-109.07	4303705304	PARADOX	6.7	771		220	3220	3	5190	5
37.28	-109.29	4303705868	PARADOX C D	7	540		194	3302	3	4752	8
37.54	-109.34	4303706269	PARADOX	5	465		188	3385		4682	4
37.54	-109.33		PARADOX	6.2	464		115	3415	1	4569	4
37.3	-109.05	4303705993	PARADOX ISMAY	6.5	308		143	3426	2	4316	6
37.28	-109.27	4303705835	PARADOX C D	7.2	417		129	3431	6	4500	9
37.3	-109.18	4303706002	PARADOX	5.8	824		281	3565	8	5745	12
38.59	-109.96	4301905035	PARADOX	6.4	192		60	3754	2	4231	14

A.5. Uncertainty Analysis

Fully propagated errors in the calculated reaction rates were derived, using the Gaussian error propagation method (Barrante, 1974), from the elemental uncertainties of analytically determined parameters and the parametric uncertainties of all modelled components. Given that all the variables in the calculation of mineral reaction rates are uncorrelated, and therefore statistically independent, the linear error propagation method of Anderson (1976) can be used to calculate the uncertainty in reaction rates arising from uncertainty in the individual parameters used.

Uncertainty in the brine corrected fluid composition was determined using a linear error propagation method, taking into account an assumed 3% analytical uncertainty in the measured CO₂-spring fluid composition and the standard deviation in the concentration of each solute in the brine, determined from a compilation of brine compositions for fluids in Pennsylvanian strata in the northern Paradox Basin (Breit, 2002; Spangler *et al.*, 1996).

$$\begin{aligned} \sigma_{k_c}^2 = & \left(\left[\left(\frac{\sigma_{k_s}}{k_s} \right)^2 + \left(\frac{\sigma_{Cl_s}}{Cl_s} \right)^2 + \left(\frac{\sigma_{Cl_B}}{Cl_B} \right)^2 \right]^{0.5} \cdot \frac{k_s}{(1 - Cl_s / Cl_B)} \right)^2 \\ & + \left(\left[\left(\frac{\sigma_{k_B}}{k_B} \right)^2 + \left(\frac{\sigma_{Cl_s}}{Cl_s} \right)^2 + \left(\frac{\sigma_{Cl_B}}{Cl_B} \right)^2 + \left(\frac{\sigma_{Cl_s}}{Cl_s} \right)^2 + \left(\frac{\sigma_{Cl_B}}{Cl_B} \right)^2 \right]^{0.5} \cdot \frac{(Cl_s / Cl_B) \cdot k_B}{(1 - Cl_s / Cl_B)} \right)^2 \end{aligned} \quad (A1)$$

Uncertainties in the modelled mass transfer coefficients were determined by treating the mass balance equations as a set of dependent linear equations and propagating the error on the corrected element concentrations.

$$\begin{aligned} \sigma_{M_{Kspar}}^2 = & \left\{ \frac{\sigma_{K_f}}{b_{K,Kspar}} \right\}^2 + \left\{ \frac{\sigma_{K_i}}{b_{K,Kspar}} \right\}^2 + \left\{ \left(b_{K,Smct} \cdot \sigma_{Mg_f} \right) \cdot \left(\frac{\sigma_{Mg_f}}{b_{Mg,Smct}} \right) \cdot \left(\frac{\sigma_{Mg_f}}{b_{K,Kspar}} \right) \right\}^2 \\ & + \left\{ \left(b_{K,Smct} \cdot \sigma_{Mg_i} \right) \cdot \left(\frac{\sigma_{Mg_i}}{b_{Mg,Smct}} \right) \cdot \left(\frac{\sigma_{Mg_i}}{b_{K,Kspar}} \right) \right\}^2 \end{aligned} \quad (A2)$$

$$\text{where} \quad \sigma_{m_{r,k}}^2 = \sigma_{k_{final}}^2 + \sigma_{k_{initial}}^2 \quad (A3)$$

Uncertainty in $\partial M_j / \partial z$ resulting from the fit of $M_j - dz$ was computed as

$$\left(\frac{\partial M_j / \partial z}{\partial M_j / \partial z}\right)^2 = \left(\frac{\sigma A}{A}\right)^2 + \left(\frac{\sigma B}{B}\right)^2 + \left(\frac{\sigma B}{z}\right)^2 + 2 \frac{\sigma A}{A} \frac{\sigma B}{B} \rho_{AB} \quad (\text{A4})$$

$$\text{where } \rho_{ab} = \frac{COV_{AB}}{\sqrt{COV_{AA}} \cdot \sqrt{COV_{BB}}} \quad (\text{A5})$$

and A and B are the fitting terms in equation (A4).

The uncertainty in calculated reaction rates, resulting from uncertainty in individual parameters used in the calculation can be computed as follows, assuming all parameters are statistically independent:

$$\sigma R_j^2 = \left\{ \left(\frac{M_j \omega_o}{S_j} \right) \sigma \phi \right\}^2 + \left\{ \left(-\frac{M_j \omega_o \phi}{S_j^2} \right) \sigma S_j \right\}^2 + \left\{ \left(\frac{\omega_o \phi}{S_j} \right) \sigma M_j \right\}^2 + \left\{ \left(\frac{M_j \phi}{S_j} \right) \sigma \omega_o \right\}^2 \quad (\text{A6})$$

Model parameters that are derived from compilations of published data have values of the mean of these compilations and uncertainties of one standard error. An average of laboratory determined hydraulic conductivities of the Navajo Sandstone (Hood and Patterson, 1984) was used, giving a mean conductivity value ($n = 91$) of 0.47m/day with ± 0.06 m/day variation. Effective porosity values for the Navajo Sandstone vary from 10% to 35% ($n = 129$) (Cooley *et al.*, 1969; Hood and Patterson, 1984; Weigel, 1986; Freethy 1988), with a volume-weighted average of 20.03% with $\pm 4.4\%$ variation. Individual mineral abundances used in these calculations were determined as the mean of the normative mineral abundances calculated from the whole rock data of this study and Bowen (2004) and the mineral compositional analyses of this study. Variation in individual mineral abundances was taken as one standard error of the mean of these analyses. The error associated with bulk surface area measurements ($n = 7$) was taken to be ± 0.06 m/g, one standard error of the BET measurements of Zhu (2005). From these the uncertainty in mineral surface area was calculated as

$$\sigma S_j^2 = (\sigma s_j \cdot v_j \cdot (1 - \phi) \cdot \rho)^2 + (\sigma \phi \cdot s_j \cdot v_j \cdot \rho)^2 + (\sigma v_j \cdot s_j \cdot (1 - \phi) \cdot \rho)^2 \quad (\text{A7})$$

Uncertainties in the free energies of the reactions are determined as a square root of the sum of the products of activity uncertainties ($\pm 5\%$ of the calculated activities) and derivatives of ΔG_r , taken with respect to activities and equilibrium constants of equation

(20) and (23), all raised to the square. For the dissolution of K-feldspar this expression has the form

$$\sigma_{\Delta G}^2 = RT \left[\left(\frac{0.95\sigma_{a_{K^+}}}{a_{K^+}} \right)^2 + \left(\frac{0.05\sigma_{a_{Na^+}}}{a_{Na^+}} \right)^2 + \left(\frac{\sigma_{a_{Al(OH)_2^+}}}{a_{Al(OH)_2^+}} \right)^2 + \left(\frac{3\sigma_{a_{H_4SiO_4}}}{a_{H_4SiO_4}} \right)^2 + \left(\frac{2\sigma_{a_{H^+}}}{a_{H^+}} \right)^2 + \left(\frac{\sigma_{a_{K_{eq}}}}{K_{eq}} \right)^2 \right] \quad (A8)$$

The standard deviations of ΔG_r are on average 0.5–1 kJ/mol.

Appendix B

Petrographic, XRF and Petrophysical Data: Navajo Sandstone

B.1. XRF Analyses

Table B.B-I Major element XRF analyses for Entrada and Navajo Sandstone samples.

sample	RS026	RS044	RS045a	RS046	RS056	RS060b	SV001	SV002	SV008	SV009
wt. %	Navajo	Navajo	Navajo	Navajo	Entrada	Entrada	Navajo	Navajo	Navajo	Navajo
SiO₂	94.05	90.25	72.51	92.57	75.06	77.15	81.05	80.92	77.56	74.71
TiO₂	0.083	0.169	0.243	0.091	0.288	0.262	0.292	0.294	0.287	0.301
Al₂O₃	2.77	4.08	4.43	2.87	6.76	5.88	5.80	5.53	5.95	6.04
Fe₂O₃	0.26	0.46	1.11	0.21	1.39	0.92	1.54	1.47	1.74	1.56
MnO	0.004	0.003	0.072	0.004	0.037	0.031	0.050	0.059	0.099	0.098
MgO	0.02	0.12	3.82	0.11	1.76	1.53	0.97	1.01	1.81	1.89
CaO	0.05	0.65	5.95	0.14	4.73	4.57	3.22	3.36	4.84	5.51
Na₂O	0.06	0.07	0.09	0.15	0.45	0.40	0.18	0.26	0.31	0.33
K₂O	1.52	2.05	2.16	1.83	2.36	2.09	2.30	2.14	2.20	2.18
P₂O₅	0.033	0.046	0.053	0.015	0.080	0.072	0.076	0.077	0.101	0.107
LOI	0.49	1.34	9.50	1.03	6.69	6.66	4.48	4.62	6.26	7.40
Total	99.35	99.24	99.93	99.02	99.60	99.57	99.96	99.73	101.14	100.12
ppm										
Ba	285	387	358	297	352	308	313	381	389	663
Cr	8	15	16	12	20	16	18	26	23	20
Ni	8	7	11	8	11	7	12	6	9	13
S%	0.01	0.11	0.01	0.11	0.01	0.12	0.02	0.03	0.02	0.03

Please Note: Ba, Cr, Ni and S values presented here are only approximate and are for information purposes only.

B.2. Electron Probe Data: Navajo Sandstone

Table B.B-II Recalculated probe data for Navajo Sandstone samples. Abbreviations: K-spar = K-feldspar, plag = plagioclase, Smct = smectite, Dolo = dolomite, Cc = calcite

wt% oxides		Sample												
Slide No.	RS026													
Phase	K-spar													
Na ₂ O	0.63	0.32	0.36	0.24	0.62	0.68	0.55	1.13	0.40	0.59	0.41	0.88	0.34	
MgO	0.004	0.000	0.007	0.000	0.002	0.001	0.002	0.003	0.004	0.004	0.003	0.002	-0.001	
FeO	-0.003	0.083	0.212	0.107	0.015	-0.002	0.074	0.033	0.063	0.041	0.030	0.059	0.127	
CaO	0.042	0.060	0.043	0.024	0.027	0.030	0.017	0.049	0.007	0.000	0.090	0.056	0.039	
BaO	0.25	0.77	0.71	0.53	0.43	0.28	0.36	0.10	0.39	0.05	0.38	0.03	0.19	
K ₂ O	15.98	16.14	16.16	16.56	16.24	16.18	16.07	15.67	16.64	16.51	16.59	16.05	16.54	
SrO	0.13	0.08	0.09	0.02	0.04	0.05	0.02	-0.01	0.00	0.03	0.03	-0.01	0.01	
SiO ₂	63.99	63.34	63.04	63.41	63.64	63.78	64.38	65.24	65.29	65.55	63.51	64.23	63.81	
Al ₂ O ₃	17.97	18.22	18.43	18.27	18.25	18.26	18.19	18.09	17.85	18.09	18.66	18.34	18.16	
TiO ₂	-0.02	-0.07	-0.07	-0.05	-0.05	-0.03	-0.05	0.00	-0.05	0.00	-0.03	0.02	-0.01	
Total	99.00	99.04	99.06	99.16	99.27	99.27	99.68	100.31	100.64	100.87	99.71	99.68	99.22	
Na	0.057	0.029	0.033	0.022	0.056	0.062	0.050	0.101	0.036	0.052	0.037	0.079	0.031	
Mg	0.000	0.000	0.000	0.000	0.000	0.000	0.000	0.000	0.000	0.000	0.000	0.000	0.000	
Ca	0.002	0.003	0.002	0.001	0.001	0.002	0.001	0.002	0.000	0.000	0.005	0.003	0.002	
Ba	0.005	0.014	0.013	0.010	0.008	0.005	0.006	0.002	0.007	0.001	0.007	0.001	0.003	
K	0.955	0.969	0.971	0.993	0.971	0.966	0.954	0.921	0.980	0.967	0.989	0.951	0.988	
Sr	0.003	0.002	0.003	0.001	0.001	0.001	0.001	0.000	0.000	0.001	0.001	0.000	0.000	
Si	2.998	2.981	2.969	2.980	2.982	2.984	2.995	3.005	3.013	3.009	2.966	2.985	2.988	
Al	0.992	1.011	1.023	1.012	1.008	1.007	0.998	0.982	0.971	0.979	1.027	1.005	1.002	
Sum	5.01	5.01	5.02	5.02	5.03	5.03	5.01	5.01	5.01	5.01	5.03	5.03	5.02	
Slide No.	RS026													
Phase	K-spar													
Na ₂ O	0.40	0.25	0.23	0.51	0.31	0.79	1.10	0.16	0.61	0.55	0.43	0.57	0.74	
MgO	-0.003	0.006	0.009	0.002	0.005	0.005	0.005	-0.002	0.003	0.000	0.002	0.004	0.003	
FeO	0.060	0.039	0.031	0.035	0.057	0.024	0.008	0.028	0.023	0.121	0.064	0.023	0.031	
CaO	0.068	0.037	0.023	0.060	0.016	0.063	0.058	0.020	0.036	0.089	0.011	0.053	0.054	
BaO	0.04	1.18	0.87	0.10	0.03	0.05	0.04	0.10	0.28	0.05	0.16	0.74	0.16	
K ₂ O	16.38	16.68	16.15	16.43	16.48	16.13	15.67	17.10	16.50	16.47	16.54	16.21	16.27	
SrO	-0.04	0.00	0.00	0.03	0.03	0.02	0.01	-0.01	0.01	0.01	0.00	0.00	0.02	
SiO ₂	63.25	63.81	62.96	63.21	64.54	64.66	63.59	64.70	65.17	65.37	65.78	64.62	64.56	
Al ₂ O ₃	18.03	18.57	18.26	18.28	17.56	18.57	18.27	18.16	18.31	18.33	18.37	18.09	18.65	
TiO ₂	-0.01	-0.16	-0.12	-0.01	0.00	-0.01	-0.01	0.00	-0.03	-0.01	-0.02	-0.08	-0.02	
Total	98.22	100.57	98.55	98.66	99.02	100.31	98.74	100.28	100.95	101.00	101.38	100.32	100.48	
Na	0.036	0.023	0.021	0.046	0.028	0.070	0.100	0.015	0.054	0.049	0.038	0.051	0.066	
Mg	0.000	0.000	0.001	0.000	0.000	0.000	0.000	0.000	0.000	0.000	0.000	0.000	0.000	
Ca	0.003	0.002	0.001	0.003	0.001	0.003	0.003	0.001	0.002	0.004	0.001	0.003	0.003	
Ba	0.001	0.022	0.016	0.002	0.000	0.001	0.001	0.002	0.005	0.001	0.003	0.013	0.003	
K	0.987	0.990	0.975	0.987	0.984	0.950	0.937	1.011	0.968	0.964	0.964	0.959	0.958	
Sr	0.000	0.000	0.000	0.001	0.001	0.001	0.000	0.000	0.000	0.000	0.000	0.000	0.000	
Si	2.988	2.970	2.978	2.977	3.019	2.985	2.982	2.998	2.996	2.998	3.004	2.997	2.979	
Al	1.004	1.019	1.018	1.014	0.968	1.010	1.009	0.992	0.992	0.991	0.989	0.989	1.015	
Sum	5.02	5.03	5.01	5.03	5.00	5.02	5.03	5.02	5.02	5.01	5.00	5.01	5.03	

Table B.II. continued

wt% oxides		Sample											
Slide No.	RS026	RS044	RS044	RS044									
Phase	K-spar												
Na₂O	0.76	0.40	0.25	0.26	0.58	0.74	0.24	0.28	0.63	1.22	0.66	1.08	0.73
MgO	0.001	0.002	0.008	0.002	0.003	0.000	0.004	0.000	0.001	0.001	0.004	0.002	0.003
FeO	0.062	0.043	0.039	0.040	0.133	0.036	0.036	0.040	0.015	0.136	0.016	0.008	0.012
CaO	0.050	0.003	0.030	0.054	0.028	0.014	0.023	0.054	0.014	0.066	0.027	0.053	0.028
MnO	0.000	0.000	0.017	0.016	0.021	0.006	-0.001	0.004	0.000	0.000	0.000	0.000	0.005
BaO	0.48	1.42	0.15	0.20	1.11	0.36	0.59	0.38	0.28	0.36	0.78	0.28	0.25
K₂O	16.04	16.23	16.88	16.84	15.77	16.07	16.04	16.32	16.37	15.51	15.99	15.70	15.97
SrO	0.09	0.07	0.00	0.02	0.10	0.00	0.00	0.01	0.00	0.03	0.08	0.01	0.05
SiO₂	64.79	64.06	64.72	64.90	64.25	65.76	64.76	64.71	65.00	65.24	64.28	65.30	65.18
Al₂O₃	18.38	18.71	18.10	18.62	18.76	18.71	18.31	18.15	18.32	18.54	17.57	18.12	18.47
TiO₂	0.000	0.000	0.000	0.000	0.000	0.000	0.000	0.000	0.000	0.000	0.000	0.000	0.000
Total	100.66	100.94	100.19	100.96	100.76	101.71	100.00	99.94	100.63	101.11	99.40	100.54	100.70
Na	0.068	0.036	0.022	0.023	0.052	0.066	0.021	0.025	0.056	0.108	0.060	0.096	0.065
Mg	0.000	0.000	0.001	0.000	0.000	0.000	0.000	0.000	0.000	0.000	0.000	0.000	0.000
Ca	0.002	0.000	0.001	0.003	0.001	0.001	0.001	0.003	0.001	0.003	0.001	0.003	0.001
Ba	0.009	0.026	0.003	0.004	0.020	0.007	0.011	0.007	0.005	0.007	0.014	0.005	0.004
K	0.944	0.959	0.998	0.988	0.931	0.933	0.948	0.966	0.963	0.906	0.955	0.922	0.936
Sr	0.002	0.002	0.000	0.001	0.003	0.000	0.000	0.000	0.000	0.001	0.002	0.000	0.001
Si	2.989	2.970	3.000	2.985	2.972	2.993	3.001	3.002	2.996	2.988	3.010	3.005	2.995
Al	1.000	1.022	0.989	1.010	1.023	1.004	1.000	0.992	0.995	1.001	0.970	0.982	1.001
Sum	5.02	5.02	5.02	5.02	5.01	5.00	4.98	5.00	5.02	5.02	5.01	5.01	5.01

Slide No.	RS045	RS045	RS045b										
Phase	K-spar												
Na₂O	0.57	0.51	0.71	0.49	0.74	0.65	0.59	0.38	0.33	0.34	0.39	0.65	0.29
MgO	0.004	0.004	0.004	0.000	0.004	0.003	0.002	0.004	0.003	0.002	0.000	0.006	0.007
FeO	0.057	0.004	0.073	0.000	0.062	0.057	0.016	0.018	0.003	0.017	0.029	0.041	0.018
CaO	0.075	0.028	0.043	0.018	0.051	0.061	0.028	0.006	0.072	0.084	0.029	0.089	0.092
MnO	0.002	0.000	0.010	0.000	0.011	0.00	0.008	0.000	0.000	0.00	0.000	0.000	0.007
BaO	0.32	0.16	0.04	0.08	0.10	0.05	0.47	0.01	0.05	0.04	0.01	0.04	0.05
K₂O	15.99	16.34	16.25	16.25	15.98	16.08	15.99	16.65	16.04	16.29	16.68	15.97	16.74
SrO	0.03	0.000	0.000	0.000	0.000	0.000	0.01	0.000	0.05	0.04	0.00	0.05	0.02
SiO₂	64.30	64.59	64.46	64.39	64.64	64.71	64.58	64.65	64.23	64.58	64.90	64.45	63.81
Al₂O₃	18.05	17.39	17.48	17.90	17.64	17.62	17.57	17.65	18.61	18.30	17.68	18.45	18.83
TiO₂	0.000	0.000	0.01	0.00	0.000	0.01	0.000	0.01	-0.01	0.00	0.00	0.01	0.000
Total	99.41	99.02	99.10	99.14	99.23	99.24	99.27	99.37	99.40	99.69	99.72	99.75	99.88
Na	0.052	0.046	0.064	0.044	0.067	0.058	0.053	0.034	0.030	0.030	0.035	0.059	0.026
Mg	0.000	0.000	0.000	0.000	0.000	0.000	0.000	0.000	0.000	0.000	0.000	0.000	0.000
Ca	0.004	0.001	0.002	0.001	0.003	0.003	0.001	0.000	0.004	0.004	0.001	0.004	0.005
Ba	0.006	0.003	0.001	0.002	0.002	0.001	0.009	0.000	0.001	0.001	0.000	0.001	0.001
K	0.951	0.976	0.970	0.968	0.951	0.956	0.953	0.991	0.951	0.965	0.989	0.945	0.993
Sr	0.001	0.000	0.000	0.000	0.000	0.000	0.000	0.000	0.001	0.001	0.000	0.001	0.001
Si	2.999	3.023	3.015	3.007	3.015	3.017	3.017	3.015	2.987	2.997	3.016	2.988	2.967
Al	0.992	0.959	0.964	0.985	0.970	0.968	0.967	0.970	1.020	1.001	0.968	1.008	1.032
Sum	5.01	5.01	5.02	5.01	5.01	5.01	5.00	5.01	4.99	5.00	5.01	5.01	5.03

Table B.II. continued

wt% oxides		Sample											
Slide No.	RS045b	RS045b	RS045b	RS046	SV009	SV009	SV009	SV009	SV009	SV009	SV009	SV009	SV009
Phase	K-spar	K-spar	K-spar	K-spar	plag	plag	plag	plag	plag	plag	plag	plag	plag
Na₂O	0.69	0.55	0.73	0.50	7.95	6.99	6.11	7.35	6.69	7.78	6.43	7.13	6.82
MgO	0.002	0.003	0.002	0.002	0.00	0.00	0.02	0.00	0.00	0.00	0.00	0.00	0.00
FeO	0.025	0.017	0.004	0.027	0.05	0.05	0.10	0.03	0.03	0.03	0.03	0.06	0.07
CaO	0.058	0.023	0.050	0.023	6.78	7.74	8.71	7.33	7.98	6.88	8.31	7.63	7.47
MnO	0.003	0.021	0.009	0.00	0.00	0.00	0.00	0.00	0.00	0.01	0.01	-0.02	0.01
BaO	0.28	0.17	0.27	0.55	0.02	0.02	0.00	0.00	0.00	0.04	0.05	0.02	0.03
K₂O	16.26	16.60	16.19	16.37	0.37	0.57	0.39	0.25	0.47	0.15	0.64	0.51	0.39
SrO	0.06	0.00	0.06	0.07	0.06	0.06	0.03	0.06	0.06	0.02	0.00	0.01	0.03
SiO₂	64.91	65.34	65.06	64.57	58.87	58.87	58.93	58.88	58.73	57.94	58.29	58.50	59.10
Al₂O₃	18.27	17.87	18.31	17.56	26.84	26.84	26.45	26.60	26.70	26.54	26.79	26.34	26.50
TiO₂	0.00	0.00	0.00	0.00	0.00	0.00	0.00	0.00	0.01	0.00	0.00	0.00	0.01
Total	100.56	100.59	100.69	99.67	100.94	101.14	100.68	100.44	100.63	99.38	100.53	100.18	100.42
Na	0.062	0.049	0.065	0.045	0.683	0.600	0.525	0.633	0.576	0.679	0.555	0.618	0.587
Mg	0.000	0.000	0.000	0.000	0.000	0.000	0.001	0.000	0.000	0.000	0.000	0.000	0.000
Ca	0.003	0.001	0.002	0.001	0.322	0.367	0.414	0.349	0.380	0.332	0.397	0.365	0.356
Ba	0.005	0.003	0.005	0.010	0.000	0.000	0.000	0.000	0.000	0.001	0.001	0.000	0.000
K	0.957	0.976	0.951	0.975	0.021	0.032	0.022	0.014	0.026	0.008	0.036	0.029	0.022
Sr	0.002	0.000	0.002	0.002	0.001	0.001	0.001	0.001	0.001	0.001	0.000	0.000	0.001
Si	2.995	3.012	2.996	3.013	2.609	2.606	2.615	2.617	2.609	2.606	2.597	2.614	2.626
Al	0.994	0.971	0.994	0.966	1.402	1.400	1.383	1.394	1.398	1.407	1.407	1.387	1.388
Sum	5.02	5.01	5.02	5.01	5.04	5.01	4.97	5.01	4.99	5.03	4.99	5.02	4.98

Slide No.	GS006												
Phase	Illite												
Na₂O	0.11	0.10	0.09	0.12	0.08	0.09	0.09	0.11	0.09	0.09	0.11	0.10	0.09
MgO	0.66	0.67	0.68	0.65	0.66	0.66	0.66	0.67	0.67	0.66	0.66	0.66	0.67
FeO	1.08	1.10	1.08	1.11	1.09	1.11	1.12	1.14	1.12	1.11	1.09	1.12	1.13
CaO	0.14	0.14	0.14	0.14	0.14	0.14	0.15	0.15	0.15	0.15	0.15	0.15	0.15
MnO	0.000	0.03	0.000	0.00	0.000	0.000	0.000	0.01	0.02	0.01	0.02	0.000	0.00
BaO	0.000	0.000	0.00	0.02	0.000	0.04	0.00	0.00	0.00	0.04	0.03	0.01	-0.04
K₂O	8.67	8.85	8.66	9.03	8.68	8.85	8.83	8.71	8.93	8.89	8.90	9.01	8.77
SrO	0.000	0.02	0.03	0.02	0.000	0.01	0.000	0.000	0.000	0.000	0.000	0.000	0.000
SiO₂	47.62	47.46	47.72	47.49	47.70	47.19	47.23	47.97	47.56	47.37	47.80	47.51	47.63
Al₂O₃	19.83	20.01	20.04	20.13	20.00	19.96	20.07	20.04	20.22	20.00	19.99	20.09	20.07
TiO₂	0.02	0.03	0.03	0.03	0.02	0.03	0.02	0.03	0.02	0.02	0.03	0.02	0.02
Total	78.13	78.42	78.47	78.74	78.38	78.09	78.17	78.81	78.78	78.34	78.76	78.67	78.54
Na	0.034	0.032	0.027	0.038	0.026	0.029	0.028	0.032	0.027	0.028	0.035	0.031	0.029
Mg	0.157	0.160	0.161	0.154	0.156	0.158	0.158	0.158	0.159	0.158	0.155	0.156	0.158
Fe	0.143	0.147	0.144	0.147	0.145	0.149	0.150	0.150	0.149	0.148	0.144	0.149	0.150
Ca	0.023	0.024	0.024	0.024	0.024	0.024	0.025	0.025	0.025	0.025	0.026	0.026	0.026
K	1.763	1.798	1.755	1.829	1.761	1.807	1.799	1.756	1.806	1.809	1.799	1.826	1.778
Sr	0.000	0.002	0.003	0.002	0.000	0.001	0.000	0.000	0.000	0.000	0.000	0.000	0.000
Si	7.593	7.557	7.576	7.543	7.581	7.551	7.543	7.585	7.540	7.554	7.577	7.549	7.564
Al	3.727	3.756	3.750	3.768	3.746	3.764	3.778	3.735	3.779	3.759	3.734	3.762	3.757
Sum	13.4	13.5	13.4	13.5	13.4	13.5	13.5	13.4	13.5	13.5	13.5	13.5	13.5

Table B.II. continued

wt% oxides		Sample											
Slide No.	SV009												
Phase	Smct												
Na₂O	0.181	0.226	0.199	0.186	0.214	0.168	0.194	0.182	0.163	0.183	0.178	0.171	0.184
MgO	3.727	3.685	3.701	3.743	3.714	3.734	3.819	3.739	3.635	3.717	3.632	3.667	3.678
FeO	1.692	1.667	1.715	1.729	1.712	1.684	1.777	1.645	1.726	1.686	1.705	1.723	1.738
CaO	0.148	0.151	0.152	0.153	0.154	0.155	0.155	0.156	0.156	0.157	0.158	0.158	0.158
MnO	0.013	0.016	0.000	0.000	0.002	0.000	0.004	-0.026	0.004	0.000	0.009	0.000	0.000
BaO	0.041	0.025	0.006	0.000	0.000	0.014	0.013	-0.006	0.008	0.021	0.002	0.000	0.049
K₂O	3.185	3.205	3.197	3.199	3.195	3.197	3.173	3.210	3.189	3.207	3.153	3.193	3.180
SrO	0.000	0.000	0.000	0.000	0.000	0.010	0.000	0.000	0.015	0.016	0.003	0.000	0.000
SiO₂	55.730	56.601	56.018	56.264	56.184	56.349	55.377	56.336	55.804	56.540	54.425	56.032	55.467
Al₂O₃	28.002	27.986	28.088	28.073	28.060	27.975	27.875	28.274	28.056	28.083	27.979	28.123	28.017
TiO₂	0.022	0.029	0.024	0.018	0.021	0.021	0.024	0.020	0.021	0.024	0.022	0.026	0.022
Total	94.710	95.574	95.065	95.308	95.236	95.300	94.387	95.527	94.777	95.630	93.266	95.025	94.443
Na	0.02	0.03	0.02	0.02	0.03	0.02	0.02	0.02	0.02	0.02	0.02	0.02	0.02
Mg	0.36	0.35	0.35	0.36	0.36	0.36	0.37	0.36	0.35	0.35	0.36	0.35	0.36
Fe	0.091	0.089	0.092	0.093	0.092	0.090	0.096	0.088	0.093	0.090	0.094	0.093	0.094
Ca	0.010	0.010	0.010	0.010	0.011	0.011	0.011	0.011	0.011	0.011	0.011	0.011	0.011
Mn	0.001	0.001	0.000	0.000	0.000	0.000	0.000	0.000	0.000	0.000	0.001	0.000	0.000
Ba	0.001	0.001	0.000	0.000	0.000	0.000	0.000	0.000	0.000	0.001	0.000	0.000	0.001
K	0.26	0.26	0.26	0.26	0.26	0.26	0.26	0.26	0.26	0.26	0.26	0.26	0.26
Si	3.60	3.62	3.60	3.61	3.61	3.61	3.59	3.60	3.60	3.61	3.57	3.60	3.59
Al	2.13	2.11	2.13	2.12	2.12	2.11	2.13	2.13	2.13	2.12	2.17	2.13	2.14
Sum	6.48	6.47	6.48	6.47	6.48	6.47	6.49	6.47	6.47	6.47	6.49	6.47	6.48
Slide No.	SV002	SV002	SV002	SV002	SV002	SV002	GR007						
Phase	Dolo	Dolo	Dolo	Dolo	Dolo	Dolo	Cc						
Na₂O	0.000	0.013	0.003	0.022	0.025	0.039	0.004	0.000	0.008	0.002	0.002	0.000	0.000
MgO	20.68	20.05	20.34	20.95	22.30	21.34	0.24	0.25	0.09	0.41	0.10	0.36	0.12
FeO	0.05	0.22	0.12	0.18	0.26	0.31	0.02	0.01	0.02	0.18	0.10	0.46	0.01
CaO	32.02	30.78	31.92	30.33	30.65	30.13	55.14	56.51	56.08	57.44	56.14	52.37	54.60
MnO	0.032	0.166	0.002	0.000	0.025	0.013	0.178	0.068	0.268	0.133	0.168	0.738	0.000
K₂O	0.031	0.123	0.057	0.003	0.018	0.023	0.045	0.031	0.046	0.127	0.057	0.077	0.041
SrO	0.033	0.000	0.016	0.005	0.000	0.012	0.025	0.008	0.034	0.074	0.005	0.025	0.020
BaO	0.000	0.000	0.042	0.000	0.021	0.000	0.000	0.016	-0.045	0.019	0.054	0.000	0.000
CO₂	47.14	48.64	47.50	48.51	46.71	48.14	44.17	43.05	43.34	41.40	43.27	45.38	45.04
Total	52.86	51.36	52.50	51.49	53.29	51.86	55.84	56.95	56.66	58.60	56.73	54.62	54.96
Na	0.000	0.001	0.000	0.001	0.002	0.002	0.000	0.000	0.000	0.000	0.000	0.000	0.000
Mg	0.954	0.915	0.936	0.954	1.029	0.975	0.006	0.006	0.002	0.010	0.003	0.009	0.003
Fe	0.001	0.006	0.003	0.004	0.007	0.008	0.000	0.000	0.000	0.003	0.001	0.006	0.000
Ca	1.061	1.009	1.056	0.993	1.016	0.989	0.983	1.017	1.008	1.051	1.010	0.927	0.966
Mn	0.001	0.004	0.000	0.000	0.001	0.000	0.003	0.001	0.004	0.002	0.002	0.010	0.000
K	0.001	0.005	0.002	0.000	0.001	0.001	0.001	0.001	0.001	0.003	0.001	0.002	0.001
Sr	0.001	0.000	0.000	0.000	0.000	0.000	0.000	0.000	0.000	0.001	0.000	0.000	0.000
Ba	0.000	0.000	0.001	0.000	0.000	0.000	0.000	0.000	0.000	0.000	0.000	0.000	0.000
CO₃	1.991	2.032	2.002	2.024	1.973	2.013	1.004	0.987	0.992	0.966	0.991	1.023	1.015
Sum	4.010	3.971	4.000	3.977	4.028	3.988	1.997	2.013	2.008	2.036	2.009	1.977	1.985

B.3. Petrophysical Data: Navajo Sandstone

Table B.B-III Porosity, permeability and hydraulic conductivity of the Navajo Sandstone, compiled from Weigel, (1986)¹ and Hood and Patterson, (1984)². Abbreviations: perm = permeability, Hydr Cond = hydraulic conductivity, Poro = effective porosity, Hor = horizontal, Ver = vertical, Ref = reference.

(ft/day)				%		Ref	(ft/day)				%		Ref
perm		Hydr Cond		Poro	Ref		perm		Hydr Cond		Poro	Ref	
Hor	Ver	Hor	Ver				Hor	Ver					
1.8	7.9	11	9.9	30.8	1			0.58	0.055	20.9	1		
			1.2	0.18	12.8	1			1.6	26.8	1		
1.6	1.1	0.72	0.46	23.2	1			0.7	0.089		1		
				13.7	1				1.5	25.2	1		
				15.5	1			0.34	0.27	21.3	1		
				13.3	1	0.64	0.54			24.3	1		
			0.011	13	1					13.4	1		
			1.3	15.1	1			0.017		14.3	1		
				12.5	1			1.2		0.75	21.3		
0.063	0.039	0.038	0.024	11.6	1					23	1		
	2.7		0.93	18	1	1.3	1.2	0.52		21.4	1		
				28.6	1	1.2				18	1		
3.5	4.7	2.8		20.7	1			2.2			1		
4.7	2.4			18.5	1			0.64			1		
3.8				20	1			0.89		22.8	1		
8.7				20.7	1			0.56		21.9	1		
9.6	8.4	5.8		20	1			0.78	0.52	20.5	1		
1.2		0.19		20.6	1			0.41	0.52	20.7	1		
	0.83		0.22	19.2	1			2.5		25.9	1		
				21	1			0.33	0.17	20.4	1		
3.1	0.79	0.55		22.1	1			0.47	0.12	20.4	1		
				15.6	1			1		24.3	1		
	3.1		1.3	19.1	1			1.4		25	1		
0.034	0.032	0.013	0.0041	14.1	1			1.4		25.9	1		
				10.5	1			0.17	0.067	22.3	1		
				19.8	1			0.45	0.43	22.3	1		
				21.2	1			0.78		22	1		
		0.91		20.7	1			0.66		23.1	1		
				27.4	1			0.4		24.1	1		
2.8	2.1	1.8	1.2	26.8	1			0.015	0.035	22.5	1		
	2.6		42	15.8	1			0.38	0.25	22.5	1		
				17.6	1			0.55		24.7	1		
0.43	0.29			17.5	1			0.43		25.2	1		
				22	1				0.24	13.8	1		
				21.2	1				1.1	26.1	1		
				19.9	1			0.0079	0.021		1		
0.76				16.5	1				1.7	13.9	1		
2.4				16.4	1				1.5	20.9	1		
1.7				15.9	1			2.7	0.91	17.4	1		
2.4				12.7	1				0.91	14	1		
2.3				14.1	1			0.0022	0.0011	16.1	1		

perm		(ft/day) Hydr Cond		% Poro		Ref
Hor	Ver	Hor	Ver			
		0.88	0.46	14.2		1
		0.43	0.25	25.6		1
		5.2		26.5		1
		1.4				1
5.5	6.5	2.4	2.4	28.3		1
		1.1				1
		0.93				1
		0.49				1
		1				1
				25		1
		0.0022		22.1		1
		0.64	0.41	23		1
		0.38	0.22	26		1
		2	0.24			1
		7.5	0.53	22		1
		0.78	0.27			1
		7.6	0.5	22		1
				22		1
		3.4	2	25		1
		3.2	0.7	15		1
		1.9	5	24		1
		3	0.8	17		1
		1.6	3	15		1
		2.4				1
		0.33				1
		1.7				1
		0.006				1
		0.055				1
		0.21				1
		4.2	2.2	28		1
				30		1
		5	2.3	19		1
		4.5	4.6	27		1
		0.002	0.005	15		1
		0.12	0.099	11		1
			0.17	14		1
		6.1	4.5	30		1
		0.3	0.11	11		1
		0.034		11.5		2
		0.029		11.4		2
		2.5		19.4		2
		1.6				2
				18.5		2
		5.1		19.6		2
		0.17		20.6		2
		0.49		22.1		2

Table B.III continued

perm		(ft/day) Hydr Cond		% Poro		Ref
Hor	Ver	Hor	Ver			
				0.011	14.1	2
				0.0089	13.8	2
				<0.00002	6.7	2
				<0.00002	6.7	2
				0.8	20.7	2
				1.6	26.3	2
				1.5		2
					17.5	2
				1.4	21.2	2
					24.3	2
					24.1	2
					23.1	2
					22.8	2
				0.46	21.4	2

B.4. Sample Details

Table B.B-IV Sample localities, rock types and analyses. Abbreviations: Lat = latitude, Long = longitude, Alt = altitude, PWD = powder, TS = thin section, MW = micro-wafer, XRF = x-ray florescence. ‘Lithology’ describes the unit/formation type and whether the samples are of the bulk host rock (Rock), a vein (vein) or a travertine (trav). ‘Type’ describes whether the sample is bleached (B), unbleached/red (R) or obviously bleached and carbonate cemented Y-B.

Code	Lat.	Long.	Alt (m)	Location	PWD	TS	MW	XRF	Lithology	Type
RS001	38.96618	-110.22624	*	Green River Airport Well	x				Travertine	Trav N/A
RS004	38.96618	-110.22624	*	Green River Airport Well	x				Travertine	Trav N/A
RS005	38.76350	-110.12744	*	Chaffin Ranch	x				Travertine	Trav N/A
RS006	38.86272	-110.10125	*	Tenmile Geyser	x				Travertine	Trav N/A
RS007	38.85873	-110.07277	*	Torreys Spring	x				Travertine	Trav N/A
RS020	38.98344	-110.53357	1680	San Rafael River	x	x			White Rim	Rock B
RS021	38.98347	-110.53360	1657	San Rafael Swell	x	x			White Rim	Rock B
RS024	38.93354	-110.45022	1454	San Rafael Swell	x	x			White Rim	Rock R-B
RS026	38.93353	-110.41688	1409	Black Dragon Canyon	x	x		x	Navajo Sst	Rock R
RS027	38.92959	-110.41925	1314	Black Dragon Canyon	x	x			Entrada Sst	Rock Y-B
RS029	38.92959	-110.41925	1318	Black Dragon Canyon	x				Entrada Sst	Rock R
RS041	38.94825	-110.44040	*	Black Dragon Canyon	x				Wingate Sst.	Rock B
RS044	38.94586	-110.43100	1345	Black Dragon Canyon		x		x	Navajo Sst	Rock B
RS045a	38.94544	-110.42973	1341	Black Dragon Canyon		x		x	Navajo Sst	Rock R
RS045b	38.94544	-110.42973	1341	Black Dragon Canyon		x			Navajo Sst	Rock R
RS046	38.94548	-110.42975	*	Black Dragon Canyon		x		x	Navajo Sst	Rock R
RS048	38.87023	-110.11190	1248	Near Big Bubbling Spring		x			Entrada Sst	Rock Y-B
RS052a	38.86842	-110.10816	1286	Near Big Bubbling Spring	x	x			Entrada Sst	Rock Y-B
RS052b	38.86842	-110.10816	1286	Near Big Bubbling Spring	x	x			Entrada Sst	Rock Y-B
RS053	38.86622	-110.10348	1263	Tenmile Butte	x	x			Entrada Sst	Rock B
RS054a	38.86824	-110.10208	1269	Tenmile Butte	x				Entrada Sst	Vein B
RS055	38.86717	-110.09952	1261	Tenmile Butte	x	x			Entrada Sst	Rock B
RS056a	38.86696	-110.09933	1268	Tenmile Butte	x	x		x	Entrada Sst	Vein B
RS056b	38.86696	-110.09933	1268	Tenmile Butte	x	x			Entrada Sst	Rock B
RS057	38.86756	-110.10040	1278	Tenmile Butte	x	x			Entrada Sst	Rock B
RS058	38.86770	-110.10076	1268	Tenmile Butte	x	x			Entrada Sst	Rock B

Table B.IV *continued*

Code	Lat.	Long.	Alt (m)	Location	PWD	TS	MW	XRF	Lithology	Type	
RS059	38.86770	-110.10076	1268	Tenmile Butte					Entrada Sst	Rock	R
RS060	38.86731	-110.10248	1257	Tenmile Butte	x	x		x	Entrada Sst	Rock	R-B
RS061	38.86731	-110.10248	1257	Tenmile Butte	x	x			Entrada Sst	Rock	B
RS062	38.86780	-110.10178	*	Tenmile Butte	x	x			Entrada Sst	Rock	B
RS063	38.86643	-110.10234	*	Tenmile Butte	x	x			Entrada Sst	Rock	B
RS065	38.86493	-110.09981	1277	Tenmile Butte					Entrada Sst	Rock	B
RS066	38.86488	-110.09982	1267	Tenmile Butte	x	x	x		Entrada Sst	Vein	B
RS067	38.86487	-110.09982	1266	Tenmile Butte	x				Entrada Sst	Vein	B
RS068	38.86550	-110.10105	1262	Tenmile Butte	x				Entrada Sst	Rock	B
RS069a	38.86532	-110.10098	1277	Tenmile Butte	x	x	x		Entrada Sst	Vein	B
RS069b	38.86532	-110.10098	*	Tenmile Butte		x			Entrada Sst	Vein	B
RS070	38.86514	-110.10070	1277	Tenmile Butte	x	x			Entrada Sst	Vein	B
RS071a	38.86543	-110.10160	1274	Tenmile Butte	x	x	x		Entrada Sst	Vein	B
RS071b	38.86563	-110.10152	1274	Tenmile Butte	x	x	x		Entrada Sst	Vein	B
RS071c	38.86563	-110.10139	1274	Tenmile Butte	x		x		Entrada Sst	Vein	B
RS072	38.86563	-110.10139	1274	Tenmile Butte	x				Entrada Sst	Vein	B
RS073	38.86655	-110.10241	1281	Tenmile Butte	x	x	x		Entrada Sst	Rock	B
RS090a	38.87023	-110.11190	*	Big Bubbling Spring	x	x	x		Entrada Sst	Vein	R-B
RS090b	38.87023	-110.11190	*	Big Bubbling Spring	x				Entrada Sst	Vein	R-B
RS090c	38.87023	-110.11190	*	Big Bubbling Spring	x				Entrada Sst	Vein	R-B
RS090d	38.87023	-110.11190	*	Big Bubbling Spring	x				Entrada Sst	Vein	R-B
RS091a	38.87265	-110.11662	*	Small Bubbling Spring	x				Travertine	Trav	N/A
RS091b	38.87265	-110.11662	*	Small Bubbling Spring	x				Travertine	Trav	N/A
RS092a	38.87023	-110.11190	*	Big Bubbling Spring	x				Entrada Sst	Vein	B
RS092b	38.87023	-110.11190	*	Big Bubbling Spring	x				Entrada Sst	Vein	B
RS093a	38.86717	-110.09952	*	Tenmile Butte	x				Entrada Sst	Vein	B
RS093b	38.86717	-110.09952	*	Tenmile Butte	x				Entrada Sst	Vein	B
RS093c	38.86717	-110.09952	*	Tenmile Butte	x				Entrada Sst	Vein	B
RS094	38.86272	-110.10125	*	Tenmile Geysers	x				Travertine	Trav	N/A

Table B.B-V Details for petroleum exploration wells sampled in this study, including; well details, API No., localities, rock types and the intervals from which samples were collected. The 'code' at the bottom of each table is the generic sample code for that well.

	Green River					
Well Name	Unit 1. (Amerada Hess)	Mt Fuel Supply Geyser	Grand Fault 14-24	Government Smoot #2	Salt Valley 22-34	Sharp State #1
API	4301910030	4301930124	4301511182	4301916048	4301911188	4301910817
Latitude	38.9331	38.8749	38.9661	38.8086	38.8563	38.8599
Longitude	-110.1307	-110.1128	-110.2262	-110.0668	-110.0341	-110.0621
Elevation (m)	1244	1259	1284	1311	1319	1372
Sample Form.	Navajo Sst.	Navajo Sst.	Navajo Sst.	Navajo Sst.	Navajo Sst.	Navajo Sst.
Start Depth (m)	445	381	640	195	137	149
End Depth (m)	539	430	765	274	293	216
Thickness (m)	94	49	125	79	155	67
Smpl Spcing (m)	3	3	3	3	3	6
Samples	7	6	9	6	12	5
Code	GR00X	MF00X	GF00X	GS00X	SV00X	SS00X

Well Name	Salt Wash #1	Silliman #1	Culburtson #1	Forest Governmnt #1	North Salt Wash #1
API	4301910831	4301910406	4301911521	4301510373	4301930282
Latitude	38.8087	38.9331	38.9409	38.8837	38.8232
Longitude	-110.0390	-110.1410	-110.1221	-110.1334	-110.0526
Elevation (m)	1310	1259	1349	1329	1352
Sample Form.	Navajo Sst.	White Rim	White Rim	Leadville	Leadville
Start Depth (m)	143	756	938	1685	2700
End Depth (m)	271	799	1026	1713	2705
Thickness (m)	128	43	88	28	5
Smpl Spcing (m)	6	3	2	2	1
Samples	9	6	6	4	4
Code	SW00X	SI00X	CU00X	FG00X	NSW00X

B.5. Rock Isotope Data

Table B.B-VI $\delta^{18}\text{O}$, $\delta^{13}\text{C}$ and $^{87}\text{Sr}/^{86}\text{Sr}$ for rock samples

Code	Location	VSMOW $\delta^{18}\text{O}$	PDB $\delta^{13}\text{C}$	% Carbonate	$^{87}\text{Sr}/^{86}\text{Sr}$	% error	Lithology	Type
RS001	Airport Well, east side of geyser	17.8	7.8		0.713342	7	Travertine	Trav N/A
RS004	Airport Well, north side of geyser	16.7	6.6	97%			Travertine	Trav N/A
RS005	Chaffin Ranch	20.9	9.1	98%			Travertine	Trav N/A
RS006	Tenmile Geyser, west of vent	20.2	3.4				Travertine	Trav N/A
RS007	Torreys Spring	20.7	8.3	76%			Travertine	Trav N/A
RS020	San Rafael River		3.5	0%			White Rim	Rock B
RS021	San Rafael Swell		0.1	0%			White Rim	Rock B
RS024	San Rafael Swell		-1.0	5%			White Rim	Rock R-B
RS026	Black Dragon Canyon		4.3	8%			Navajo Sst	Rock R
RS027	Black Dragon Canyon		-3.1	6%			Entrada Sst	Rock Y-B
RS029	Black Dragon Canyon		-2.9	5%			Entrada Sst	Rock R
RS041	Black Dragon Canyon		-6.0	11%			Wingate Sst.	Rock B
RS044	Black Dragon Canyon						Navajo Sst	Rock R
RS045a	Black Dragon Canyon		-2.4	4%			Navajo Sst	Rock R
RS045b	Black Dragon Canyon		-4.2	0%			Navajo Sst	Rock R
RS046	Black Dragon Canyon						Navajo Sst	Rock R
RS048	Near Big Bubbling Spring		3.3				Entrada Sst	Rock Y-B
RS052a	Near Big Bubbling Spring	19.8	4.6	44%			Entrada Sst	Rock Y-B
RS052b	Near Big Bubbling Spring	19.8	5.7	63%			Entrada Sst	Rock Y-B
RS053	Tenmile Butte	21.2	-2.5	2%			Entrada Sst	Rock B
RS054a	Tenmile Butte	18.7	6.1	89%			Entrada Sst	Vein B
RS055	Tenmile Butte	18.8	6.2	65%			Entrada Sst	Rock B
RS056a	Tenmile Butte	19.2	5.8				Entrada Sst	Vein B
RS056b	Tenmile Butte	20.9	-2.4	7%			Entrada Sst	Rock B
RS057	Tenmile Butte	20.0	-2.7	5%			Entrada Sst	Rock B
RS058	Tenmile Butte	21.4	-1.9	5%			Entrada Sst	Rock B

Table B.IV *continued*

Code	Location	VSMOW $\delta^{18}\text{O}$	PDB $\delta^{13}\text{C}$	% Carbonate	$^{87}\text{Sr}/^{86}\text{Sr}$	% error	Lithology	Type
RS059	Tenmile Butte	16.8	-4.4				Entrada Sst	Rock R
RS060	Tenmile Butte		2.9	1%			Entrada Sst	Rock R-B
RS061	Tenmile Butte	20.0	-2.2	4%			Entrada Sst	Rock B
RS062	Tenmile Butte	21.6	-1.9	2%			Entrada Sst	Rock B
RS063	Tenmile Butte	21.5	-2.4	6%			Entrada Sst	Rock B
RS065	Tenmile Butte, southern cliff	19.9	-2.8				Entrada Sst	Rock B
RS066	Tenmile Butte, southern cliff		-2.9	0%			Entrada Sst	Vein B
RS067	Tenmile Butte, southern cliff	19.6	0.6	2%	0.712645	8	Entrada Sst	Vein B
RS068	Tenmile Butte, southern cliff	20.5	-2.4	8%			Entrada Sst	Rock B
RS069a	Tenmile Butte, southern cliff	18.7	5.8	91%			Entrada Sst	Vein B
RS069b	Tenmile Butte, southern cliff						Entrada Sst	Vein B
RS070	Tenmile Butte	20.5	4.6	43%			Entrada Sst	Vein B
RS071a	Tenmile Butte	18.6	5.8	100%	0.713035	10	Entrada Sst	Vein B
RS071b	Tenmile Butte	18.8	5.9	87%			Entrada Sst	Vein B
RS071c	Tenmile Butte	18.5	5.7	96%			Entrada Sst	Vein B
RS072	Tenmile Butte	18.7	5.9	61%			Entrada Sst	Vein B
RS073	Tenmile Butte	20.7	-2.5	16%	0.711829	7	Entrada Sst	Rock B
RS090a	Near Big Bubbling Spring	19.5	6.4	54%			Entrada Sst	Vein R-B
RS090b	Near Big Bubbling Spring		6.6	49%			Entrada Sst	Vein R-B
RS090c	Near Big Bubbling Spring		6.7	87%			Entrada Sst	Vein R-B
RS090d	Near Big Bubbling Spring		6.6	111%			Entrada Sst	Vein R-B
RS091a	Small Bubbling Spring	18.7	4.2	34%	0.712115	7	Travertine	Trav N/A
RS091b	Small Bubbling Spring		5.0	44%			Travertine	Trav N/A
RS092a	Near Big Bubbling Spring	19.7	6.1	62%			Entrada Sst	Vein B
RS092b	Near Big Bubbling Spring		6.3	85%			Entrada Sst	Vein B
RS093a	Tenmile Butte	18.2	5.3	52%			Entrada Sst	Vein B
RS093b	Tenmile Butte		4.8	100%			Entrada Sst	Vein B
RS093c	Tenmile Butte		4.9	103%			Entrada Sst	Vein B
RS094	Tenmile Geyser	19.6	6.0	59%			Travertine	Trav N/A

Table B.B-VII

Code	Powder	Thin Section	Location	Sample Description	Lithology	(m) Depth	VSMOW $\delta^{18}\text{O}$	PDB $\delta^{13}\text{C}$	% Carb
SV001	x	x	Green River Anticline	Salt Valley 22-34	Navajo Sst	137	20.0	-3.7	5.4%
SV002	x	x	Green River Anticline	Salt Valley 22-35	Navajo Sst	149	19.6	-3.4	7.1%
SV003	x		Green River Anticline	Salt Valley 22-36	Navajo Sst	168	20.9	-3.1	5.9%
SV004	x		Green River Anticline	Salt Valley 22-37	Navajo Sst	183	20.1	-2.9	9.6%
SV005	x		Green River Anticline	Salt Valley 22-38	Navajo Sst	201	19.2	-3.2	12.1%
SV006	x		Green River Anticline	Salt Valley 22-39	Navajo Sst	213	20.6	-2.8	17.4%
SV007	x		Green River Anticline	Salt Valley 22-40	Navajo Sst	229	19.6	-3.4	10.2%
SV008	x		Green River Anticline	Salt Valley 22-41	Navajo Sst	241	19.8	-2.9	8.4%
SV009	x	x	Green River Anticline	Salt Valley 22-42	Navajo Sst	259	22.5	-2.3	10.4%
SV010	x		Green River Anticline	Salt Valley 22-43	Navajo Sst	274	22.7	-2.2	12.0%
SV011	x	x	Green River Anticline	Salt Valley 22-44	Navajo Sst	290	21.0	-2.6	16.0%
SV012			Green River Anticline	Salt Valley 22-45	Navajo Sst	305			
SW001	x		Green River Anticline	Salt Wash #1	Navajo Sst	143	23.0	-2.8	
SW002	x		Green River Anticline	Salt Wash #1	Navajo Sst	158	20.8	-3.3	
SW003	x		Green River Anticline	Salt Wash #1	Navajo Sst	174	21.8	-3.1	
SW004	x		Green River Anticline	Salt Wash #1	Navajo Sst	189	21.0	-2.9	
SW005	x		Green River Anticline	Salt Wash #1	Navajo Sst	204	21.7	-2.1	
SW006	x		Green River Anticline	Salt Wash #1	Navajo Sst	219	20.6	-3.4	
SW007	x		Green River Anticline	Salt Wash #1	Navajo Sst	235	22.8	-2.7	
SW008	x		Green River Anticline	Salt Wash #1	Navajo Sst	250	22.0	-3.0	
SW009	x		Green River Anticline	Salt Wash #1	Navajo Sst	265	21.1	-3.4	

B.6. Point Counting Data: Entrada Sandstone

Table B.B-VIII Point count estimates (expressed as vol% of thin section) for major mineral phases in Entrada Sandstone Samples averaged over 200 counts per slide. Abbreviations: Qtz = Quartz, Qtz Ovrgrth = Quartz Overgrowth, Feld = feldspar, Dol = dolomite, Cc = calcite, Hem = hematite cryptocrystalline, Crys Oxides = coarse Fe-oxides, Illite Coat = illite grain coating, Illite Pore = pore filling illite, Kaol = kaolinite, Poro = porosity

Sample	Type	<i>vol% of slide</i>										
		Qtz	Qtz Ovrgrth	Feld	Dol	Cc	Hem	Crys Oxide	Illite Coat	Illite Pore	Kaol	Poro
RS057	B	71.9	3.3	4.1	2.6	7.3	0.1	0.9	1.4	2.1	0.3	5.9
RS073	B	73.9	2	3.7	3.7	12.2	0.2	1.1	1.8	0.8	0.6	0.8
RS062	B	67.7	1.5	6.2	4.3	7.7	0.3	0.6	1.1	1.4	1.1	8.1
RS061	B	70.9	2.1	9.8	3.2	4.8	0.4	2.3	0.3	0.7	0.4	5.1
RS058	B	69.5	1	7.3	2.8	8.9	0.1	1.3	3.2	1.6	3.3	1.5
RS027	R	73.9	0.2	9.1	4.5	0.1	1.3	0.1	1.7	1.7	0.3	7.9
RS029	R	70.4	0	10.4	10.6	0	1.1	0	1.8	1.3	0.1	3.4
RS069	Y-B	66.2	3.2	5.4	0.2	16.6	0.1	1.8	1.8	1.3	0.8	3.2
RS052	Y-B	67.3	2.6	5.6	0.4	13.5	0.6	3	1.9	0.9	0.5	4
RS090	Y-B	62.9	1.5	8.6	0.1	10.9	0.5	2.9	1.6	2.5	0.2	10

B.7. Aragonite Vein Isotope Data

Table B-IX Aragonite vein isotope data, travertine volumes and distance along fault trace from most westerly (up groundwater flow direction) travertine, for Salt Wash Graben and Little Grand Fault.

Sample/Travertine	Age (ka)	σ (ka)	Distance		$^{87}\text{Sr}/^{86}\text{Sr}$	σ	$\delta^{13}\text{C}$ (PDB)	$\delta^{18}\text{O}$ (VSMOW)
			Along Fault (km)	Travertine Volume (m^3)				
<i>Salt Wash Graben</i>								
SW1	0.11	0.63	3.94	8162				
SW2	4.79	0.03	3.10	3741				
SW3	9.75	0.05	5.88	2041				
SW4	10.79	0.04	1.76	3401				
SW5	13.07	0.06	1.48	4081				
SW.03.52K	28.38	0.24	1.67	1275	0.712812	1.4E-05	5.74	18.92
SW6	38.91	0.16	0.00	1700				
SW.06.27A	51.29	0.25	1.64	170	0.712851	1.4E-05	5.61	19.22
SW7	57.01	0.41	2.70	6802				
SW03.65N	60.19	0.44	0.61	10101	0.712872	1.6E-05	5.87	19.19
SW8	65.09	0.33	2.04	9353				
SW.03.56H	92.79	1.12	1.63	10203	0.713019	1.6E-05	5.40	18.64
SW06.17D	100.38	0.56	1.44	5510	0.712947	1.6E-05	5.28	18.94
SW.06.18C	106.09	0.42	1.49	6122	0.712915	1.4E-05	5.16	18.47
SW02.36J	112.80	0.63	3.23	14879	0.713173	1.6E-05	5.63	19.54
SW9	116.79	0.69	4.07	1700				
SW10	130.67	0.83	3.39	20406				
SW.06.19C	135.14	1.14	1.50	5986	0.712834	1.4E-05	4.64	17.76
SW.06.22A	291.31	5.59	1.36	816	0.712979	1.4E-05	6.13	20.16
SW.06.16B	413.47	15.13	1.40	6122	0.712998	1.4E-05	5.00	21.01
<i>Little Grand Fault</i>								
LG1	5.03	0.04	0.00	240				
LG.03.50A	5.06	0.04	0.22	2047	0.712731	1.4E-05	5.19	17.87
LG.03.51Q	27.41	0.08	0.66	1588	0.712703	1.6E-05	5.61	19.13
LG2	31.22	0.08	0.66	36				
LG3	49.09	0.30	0.66	335				
LG4	50.89	0.32	1.62	388				
LG.03.48F	58.80	0.40	2.89	10213	0.712680	1.4E-05	5.71	18.63
LG5	75.50	0.46	0.42	1621				
LG.03.42AX	106.00	0.50	0.50	69660	0.712750	1.4E-05	5.99	18.48
LG.03.42AF	109.00	0.50	1.55		0.712883	1.8E-05	5.20	17.36
LG.03.42AD	113.91	0.60	1.70		0.712907	1.4E-05	4.76	16.99
LG6	9.48	0.04	0.22					
LG7	103.17	0.50	0.66					

Appendix C

Eh-pH Diagrams

C.1. Calculation of Mn-oxyhydroxide solubility

Fluid-mineral equilibrium with ‘typical’ well crystalline Mn-oxyhydroxide suggests that Mn^{2+} concentrations in groundwater at any given Eh and pH should be much higher than Fe^{2+} , but this is rarely observed. It has commonly been noted that when Mn^{2+} and Fe^{2+} solution concentrations for typical clastic and carbonate groundwater systems are superimposed on their respective activity contours the redox conditions defined from the Mn content (assuming equilibrium with a ‘typical’ Mn-oxyhydroxide) do not coincide with those defined on the basis of Fe (e.g. Barnaby and Rsimstidt, 1989; Edmunds *et al.*, 1986). A similar phenomenon is observed in CO_2 -charged fluids suggesting that groundwaters are not in equilibrium with any of the Mn-oxyhydroxide phases considered in construction of typical Eh-pH stability diagrams. This could reflect a) the absence of a true Mn-oxyhydroxide phase 2) disequilibrium between porewater Mn^{2+} and Mn-oxyhydroxides 3) pore waters are in equilibrium with Mn-oxyhydroxides of different thermodynamic stability than those used to construct stability diagrams. Given the ubiquitous presence of Mn-oxyhydroxide minerals in sedimentary environments (1) is unlikely (e.g. Bricker, 1965; Potter and Rossman 1979). The compatibility with measured aFe^{2+} , pH and Eh with known Fe-oxyhydroxides suggests equilibrium is maintained. Thus (3) seems the most likely explanation given the variable composition, crystallinity and thermodynamic stability of naturally occurring Mn-oxyhydroxide minerals.

Manganese chemistry in natural systems is complex and not well understood. Mn exists in several possible oxidation states and commonly forms complex nonstoichiometric oxyhydroxides, with highly variable crystallinity (Ponnamperuma *et al.*, 1969). Detailed studies of Mn oxide mineralogy from various sedimentary environments indicate that Mn oxides other than pyrolusite (MnO_2) are dominant (see

Taylor *et al.*, 1964). Consequently it is valid to assume that Mn^{2+} concentrations are controlled by equilibrium with a relatively insoluble ‘complex’ MnO_2 phase.

The thermodynamic stability of the Mn-oxyhydroxides governing Mn^{2+} solubility in the CO_2 charged fluids can be evaluated by estimating the *apparent* standard free energy of formation of a *hypothetical* Mn-oxide phase in equilibrium with the CO_2 charged fluids using the Nernst equation, measured fluid $a_{Mn^{2+}}$, pH and assuming Pt-electrode-measured Eh potentials approximate the actual Eh. Assuming the controlling redox reaction;



For which the equilibrium constant (K_{MnO_2}) can be written as;

$$K_{MnO_2} = \frac{a_{Mn^{2+}} \cdot a_{H_2O}^2}{a_{H^+}^4 \cdot a_{e^-}^2} \quad (C.2)$$

Where $Eh = 10^{-a_{e^-}}$ (C.3)

And using the Nernst equation

$$\Delta E^\circ = \frac{RT}{nF} \ln[K] \quad (C.4)$$

The apparent standard state free energy of formation can be defined as

$$\Delta G_f^\circ = -nF\Delta E^\circ \quad (C.5)$$

Where ΔE° is the standard state cell potential, n is the number of electrons involved in the reaction, F is the Farady constant, R is the gas constant and T is temperature ($^\circ K$). This yields an average estimated $\Delta G_f MnO_2 = -144640 \text{ kJ mol}^{-1}$. Stability diagrams constructed using this estimated ΔG_f (Fig. C.1-1) demonstrate that the Mn^{2+} activity contours are depressed towards more reducing conditions and define Eh conditions consistent with those predicted from the iron equilibria discussed in Chapter 2 section 2.4.7.

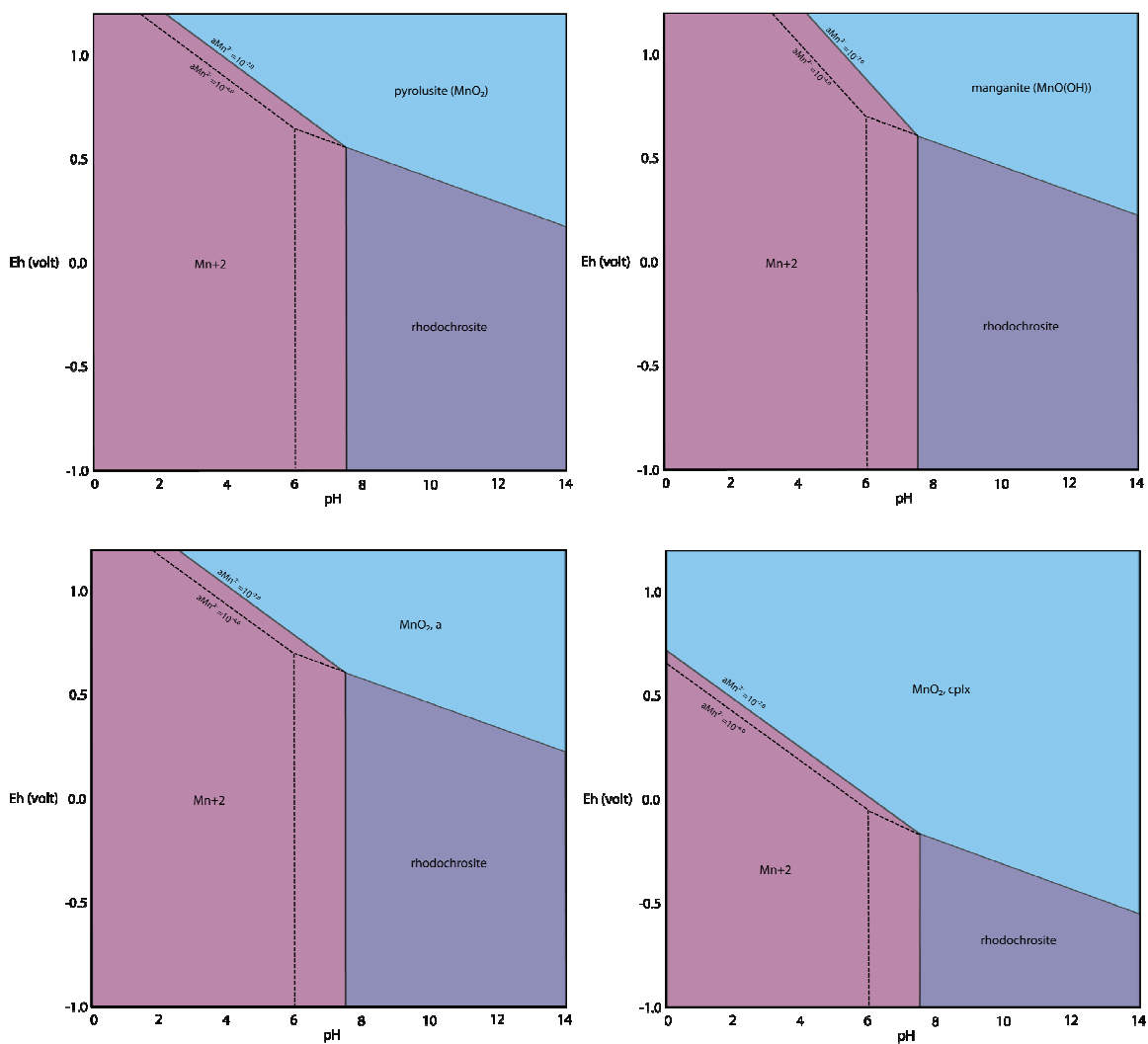


Figure C.1-1 Eh-pH stability fields for the important Mn-oxyhydroxides in typical clastic aquifers, at 25°C, $\log(\text{Mn}_{\text{TOT}}) = -3$ and -4 . Calculated using CHNOSZ (Dick, 2008). $\text{MnO}_2, \text{cplx}$ is the *hypothetical* Mn-oxide phase whose solubility has been calculated from measured spring pH, Eh and Mn concentrations.